Heterometallic Complexes as Models of Enzymatic Active Sites

Thesis by
Davide Lionetti

In Partial Fulfillment of the Requirements
for the Degree of Doctor of Philosophy

CALIFORNIA INSTITUTE OF TECHNOLOGY
Division of Chemistry and Chemical Engineering
Pasadena, California
2016
(Defended on September 3rd, 2015)

To Mom, Dad, Sarah, and Stephanie.

"And we shouldn't be here at all, if we'd known more about it before we started. But I suppose it's often that way. […] But that's not the way of it with the tales that really mattered, or the ones that stay in the mind. Folk seem to have been just landed in them, usually their paths were laid that way, as you put it. But I expect they had lots of chances, like us, of turning back, only they didn't. And if they had, we shouldn't know, because they'd have been forgotten."

– Samwise Gamgee (J.R.R. Tolkien, *The Lord of the Rings*)

"I'm the Doctor, and you're in the biggest library in the Universe. Look me up."

– The Tenth Doctor

ACKNOWLEDGMENTS

As I try to wrap my head around the six years I have spent at Caltech I find myself battling with the sense that I will never really be happy with what is written in this paragraph (surprising, I know). I had wanted to take a moment to summarize what the graduate school experience has meant to me, to distill these years to their essence so that, together with the science described in the rest of this dissertation, it could stand as a record of my time here. The truth, however, is that it is impossible to adequately boil down my experience to a few sentences, or even a few paragraphs, or pages. My years at Caltech have been the most complex and intricate experience of my life – its myriad facets are reflected in the numerous people I am about to thank.

There are a handful of things I can state with some certainty. I have not had the easiest time through the last six years. I have learned much (although never enough) about chemistry and science in general, but also about life. I have had the privilege to work with and learn from some of the smartest and most hard-working people I will ever meet. My time here has been challenging, edifying, rewarding (sometimes), and frustrating (often). I do not know if a year (or ten) will be enough for me to look back and come up with a good way to describe this time in fewer than way too many words. I do know, however, that I would have never gotten the chance to even be in this position had it not been for the help, support, and guidance of a large number of people who got me to where I stand today. Although surely doomed to be laughably inadequate, these are my thanks to them.

The first person I would like to thank is my advisor, Theodor Agapie. With his enthusiasm for science (and his predilection for crazy ligands) Theo was the person who really sold me on Caltech when I first visited, back in March 2009. When I joined his group later that fall, Theo was actually the one who first trained me in the laboratory and got me started on my first project. I owe Theo a significant debt of gratitude for his help in those early days in the lab, the innumerable discussions about all sorts of chemistry, and his excitement about new ideas (however crazy), but also for helping me learn how to teach chemistry in the classroom and to write about science. Outside the lab, Theo was to me also a kindred hiking spirit; it was great to get the chance to spend time hiking on our group camping trips, and chats with Theo taught me a lot about hiking at higher altitudes than I was used to (who knew the Alps I grew up in could

suddenly feel so small) and about the various trails in the wonderful Sierras. Theo, I hope I have repaid the trust you put in me when you took me into your group, and I look forward to hearing about the future endeavors of the Agapie group.

The CCE division at Caltech is an incredible gathering of great minds, and I want to thank the members of my thesis committee, in particular, Profs. John Bercaw, Dennis Dougherty, and Harry Gray, for the lessons they taught me about how to think about and design my research projects and for their insightful assessment of my research proposals. It is great to have had such great people in my corner. The collegial mindset of the Chemistry division as a whole was an extremely important factor in my decision to come to Caltech and one that I hope will always be preserved.

As a member of the Agapie group, it has been a privilege to work with so many people who coupled amazing intellectual abilities with an indefatigable work ethic, and at the same time made it possible to survive Caltech without going (completely) crazy. Emily Tsui always asked the challenging questions and held me to the highest standards of work, and taught me a lot about…well, really about everything chemistry. She was my partner in crime both for hiking (Langley! Whitney!) and forgetting about work for a while over a drink or two at the Athenaeum (#Excellence). Madalyn Radlauer was one of the most positive people I have ever met, and her support was incredibly helpful when I was having a rough time (so, often). She was dedicated and unrelenting in her work as well as in her striving to always be a force for confidence and optimism. I owe my thanks to Maddy also for forcing me to get out and unplug every now and then and find time to play some board games and eventually to get me to start my first D&D campaign in ages, which was awesome. Sibo Lin and Paul Kelley were also incredibly hard-working, contributing to setting the example for the younger students, and they were key co-conspirators in many of our gaming escapades. Sandy Suseno and Jacob Kanady were the two other students in my class, and I am glad I was able to rely on two such smart people for support during my time here. Sandy, you are indomitable. Sandy's ability to always push through everything and get the job done was admirable and a source of inspiration when I felt stuck. Sandy could also always be counted on to find the best places to grab a bite whether in Los Angeles or anywhere we were traveling to, and our road trips to the Bay Area were fantastic. Jacob and I worked in the same glovebox for several years and built (most of) our high-vacuum line together, managing

to never kill each other even when we were not seeing eye to eye. Kyle Horak has been a trustworthy friend for the last three years – thanks for letting me run my crazy chemistry theories and my many questions by you, thanks for always being a sounding board for me, and for always letting me tag along with you and Sandy without ever making me feel like a third wheel, you guys are awesome. I hope Kyle keeps never backing down, always holding other researchers to his high standards. Josh Buss was a more recent addition to the group but he was quick to show his talents – his meticulousness and work ethic in the lab were commendable, and his tenaciousness on the trails and his wilderness expertise got us safely through many a hike (many thanks for not just leaving Emily, Sibo, and me up at the Whitney windows that one time, I am sure you were tempted). Guy Edouard, thanks for always being yourself and somehow always having kind words for me (and go Pats!), and thanks to Dave Herbert for letting me join him on his project when I came back from leave. Thanks to all the other members of the Agapie group for all their continued support. Good luck to the current members of the group, make sure you keep upholding our group's standards even in the face of the difficult projects you are working on – I am expecting great things.

I want to thank the people in other research groups and among the staff who helped me in my work – thanks to Jon Rittle and Niklas Thompson for their help with Mössbauer and to our collaborators at LBNL (Junko Yano, Rosalie Tran) and UC Davis (R. David Britt, Luo Lu) for XAS and EPR studies, respectively. Thanks to Larry Henling for teaching me so much about X-ray diffraction and for being entertaining even when I kept you at work late at night to mount terrible crystal after terrible crystal. Thanks to Mike Takase and the late Mike Day for their work in the crystallography facility, which played such a hugely important role in many of our projects. Thanks to Rick Gerhart for being willing week after week to try and fix more and more broken parts of our high-vacuum line, and for keeping me company every time I walked into his shop asking for more help. Thanks to the people at Resnick (Stewart and Lynda Resnick for their support, Neil Fromer, Heidi Rusina) for building a great group of smart people to promote thinking about multidisciplinary approaches to sustainability.

Thanks to my undergraduate advisor at the University of Notre Dame, Seth Brown, for first getting me excited about inorganic chemistry and setting me on the way that

led me here to Caltech. Thanks also for talking me through my troubles while I returned from leave and for showing me that you always supported me and believed in me.

Thanks to the people who let my unathletic self play sports with them – the Cp All-Stars softball teams were always awesome and it was a tremendous amount of fun to play with them for six seasons. Thanks also to our soccer group, going very strong in my last year here, it was great to get to kick a ball around again after such a long time.

Thanks to Jan Aura for keeping me sane and never letting me fall away, even from across the ocean. Thanks to Toby and Perplexed (and Super) and everyone else for everything from day one (for some of them a long time ago) to now.

Okay, now, I hope that everyone got though all that because this is the "last-but-not-least" part which, cliché notwithstanding, is extremely important to me. I want to thank my Mom and Dad and my sister Sarah for their unwavering support over the past six years as well as through everything that came before. I first moved away to the U.S. at sixteen, and yet Mom and Dad have always made sure I felt as if they were just around the corner. They made a point of visiting me in California every year so that I would never forget that they were there for me (which, I mean, I am sure it was extra-hard giving how little there is to do and see in California – just kidding, of course I know they would have visited me anyway). When I took my medical leave of absence they let me move back into their home and got me back on my feet, and without that opportunity I would not be writing this dissertation today. This work is their crowning achievement, not mine. My sister Sarah is awesome, and I am so very proud of her – she does not know, but I brag about her a lot. Thanks for being great and for having me over in Cardiff a few times over these past five years – oh and thanks again for getting us tickets to the Olympics, that was amazing.

Finally – I want to thank you, Stephanie, for being wonderful and for still being here, five years later. We used to be upset at the universe that we would not get our chance, and yet here we are – I know it has not always been easy, but it has meant the world to have you with me. Thank you for your unending support, for always believing in me, for indulging (and enabling) my craziness, and for always being in my head (and letting me be in yours). I love you, and I cannot wait for what is next.

With that, thanks for indulging me in these overlong but long overdue acknowledgments, we will get to Science now. Allons-y!

PREFACE

Parts of this thesis have been adapted from published articles co-written by the author and articles that are currently in preparation

The following article was reproduced in part with permission from the Royal Society of Chemistry:

"Metal-Templated Ligand Architectures for Trinuclear Chemistry: Tricopper Complexes and Their O_2 Reactivity" D. Lionetti, M. W. Day, T. Agapie, *Chem. Sci.*, **2013**, *4*, 785-790.

The following article was reproduced in part with permission from the American Chemical Society:

"Heterometallic Triiron-Oxo/Hydroxo Clusters: Effect of Redox-Inactive Metals" Herbert, D. E.; Lionetti, D.; Rittle, J.; Agapie, T.; *J. Am. Chem. Soc.*, **2013**, *135*, 19075.

RESPECTIVE CONTRIBUTIONS

Parts of the work described in this thesis are the result of collaborative efforts, without which these studies would not have been possible. Specific notes are included for compounds synthesized by other researchers and spectroscopic characterization carried out by our collaborators.

In Chapter 2, the late Dr. Michael W. Day was responsible for refining the solid-state structure of complex **4-Y**.

In Chapter 4, several **32-M** and **33-M** were first synthesized and characterized by Dr. David E. Herbert, who laid the foundations of this project. Complex **31-Fe** was first synthesized by Dr. Emily Y. Tsui. Mössbauer studies were carried out by Jonathan Rittle and Niklas Thompson in the group of Prof. Jonas Peters. The analysis of structural and spectroscopic data leading to the reassignment of the structure of clusters **27-M**/**28-M** was carried out in close collaboration with Dr. Sandy Suseno. EPR experiments on **27-M** and **28-M** clusters (M = Ca, Sr) were performed by Luo Lu and Prof. R. David Britt at the University of California – Davis. Kurtis M. Carsch carried out the computational work related to these structural reassignments. Studies of the OAT reactivity of Mn_3 oxo-hydroxo and cubane clusters were performed by Dr. Sandy Suseno, Dr. Emily Y. Tsui, and Dr. Jacob S. Kanady. Larry Henling and Dr. Michael Takase aided in X-ray diffraction studies.

In Appendix A, Zn complexes **A.1** and **A.2** were first synthesized by Dr. David E. Herbert. Yuji Niishi first synthesized and characterized Zn_3 complexes **A.24** and **A.25**.

ABSTRACT

This dissertation describes studies on two multinucleating ligand architectures: the first scaffold was designed to support tricopper complexes, while the second platform was developed to support tri- and tetrametallic clusters.

In Chapter 2, the synthesis of yttrium (and lanthanide) complexes supported by a tripodal ligand framework designed to bind three copper centers in close proximity is described. Tricopper complexes were shown to react with dioxygen in a 1:1 $[Cu_3]/O_2$ stoichiometry to form intermediates in which the O–O bond was fully cleaved, as characterized via UV-Vis spectroscopy and determination of the reaction stoichiometry. Pre-arrangement of the three Cu centers was pivotal to cooperative O_2 activation, as mono-copper complexes reacted differently with dioxgyen. The reactivity of the observed intermediates was studied with various substrates (reductants, O-atom acceptors, H-atom donors, Brønsted acids) to determine their properties. In Chapter 3, the reactivity of the same yttrium-tricopper complex with nitric oxide was explored. Reductive coupling to form a *trans*-hyponitrite complex (characterized by X-ray crystallography) was observed via cooperative reactivity by an yttrium and a copper center on two distinct tetrametallic units. The hyponitrite complex was observed to release nitrous oxide upon treatment with a Brønsted acid, supporting its viability as an intermediate in nitric oxide reduction to nitrous oxide.

In Chapter 4, a different multinucleating ligand scaffold was employed to synthesize heterometallic triiron clusters containing one oxide and one hydroxide bridges. The effects of the redox-inactive, Lewis acidic heterometals on redox potential was studied by cyclic voltammetry, unveiling a linear correlation between redox potential and heterometal Lewis acidity. Further studies on these complexes showed that the Lewis

acidity of the redox-inactive metals also affected the oxygen-atom transfer reactivity of these clusters. Comparisons of this reactivity with manganese systems, collaborative efforts to reassign the structures of related manganese oxo-hydroxo clusters, and synthetic attempts to access related dioxo clusters are also described.

In Appendix A, ongoing efforts to synthesize new clusters supported by the same multinucleating ligand platform are described. Studies of novel approaches towards ligand exchange in tetrametallic clusters and incorporation of new supporting and bridging ligand motifs in trinuclear complexes are presented.

TABLE OF CONTENTS

CHAPTER 1

HETEROMETALLIC EFFECTS ON ELECTRON TRANSFER AND REACTIVITY OF SYNTHETIC MULTINUCLEAR COMPLEXES

–

EFFECTS OF REDOX-INACTIVE METALS ON REDOX PROCESSES

The text for this chapter was reproduced in part from:

D. Lionetti, S. Suseno, T. Agapie, *Review Manuscript in Preparation.*

Abstract

Discrete synthetic models of the many heterometallic systems that are involved in intriguing chemical transformations in biological enzymes as well as heterogeneous catalysts have received considerable attention for the insight they offer into the various interactions between different metal centers and their effects on reactivity. In particular, systems that display effects of redox-inactive metals on processes involving electron transfer have attracted significant interest due to their relevance to biological water oxidation, which is performed by a heterometallic cluster containing both redox-active (Mn) and redox-inactive (Ca) metals. Systematic studies of the effects of redox-inactive metals on the redox processes carried out by heterometallic complexes have demonstrated the influence of these Lewis acidic metals on electron transfer as well as group transfer reactions such as oxygen- and hydrogen-atom transfers. The many elegant reports of this type of heterometallic effect have contributed to the identification of general trends of effects of redox-inactive metals on redox reactivity of metal complexes.

1. INTRODUCTION

"The whole is other than the sum of its parts"

Though hardly developed with chemistry in mind,[1,2] the often-cited main tenet of Gestalt psychology is nonetheless surprisingly applicable to the fields of bioinorganic chemistry and catalysis. Multiple different metal centers placed in close proximity (the 'whole') can exhibit cooperative and synergistic effects that give rise to chemical properties and reactivity pathways that are often quite different from those that each constituent metal (the 'part') possess individually. In Nature, enzymes whose active sites contain multiple metal centers are often responsible for transformations requiring the transfer of multiple electrons and are involved in processes as diverse as oxidative (water oxidation by Photosystem II), reductive (O_2 reduction by cytochrome *c* oxidase and N_2 fixation by nitrogenase), and hydrolytic (phosphate esters hydrolysis by purple acid phosphatases) reactivity. Similarly to biological active sites, heterogeneous materials used for analogous transformations (e.g. water oxidation and O_2 reduction) also display heterometallic effects on reactivity as shown for many mixed-metal oxide materials.

Interest in many of the transformations effected by heterometallic enzymes for a variety of applications, from fuel cell catalysis to solar energy capture and storage, has driven numerous efforts to mimic both the structure and function of these multimetallic assemblies with synthetic models.[3-16] In particular, much attention has been devoted to studying the interactions between different metals in synthetic heterometallic complexes, and to how these interactions affect electron transfer and chemical reactivity.[6,17,18] Research in discrete heterometallic complexes is hindered by synthetic challenges and difficult characterization of reactive species. Nonetheless,

many elegant examples have been presented in the literature that display intriguing properties and reactivity. This Review aims to provide a detailed overview of the literature concerning discrete mixed-metal complexes of first-row transition metals for which heterometallic effects on electron transfer and reactivity have been systematically studied, with a particular focus on those systems that are mimics, structural or conceptual, of heterometallic enzymatic active sites. Many heterometallic clusters have been reported, for example in the context of single molecule magnetism; such molecules will not be covered in this Review, unless these complexes have also provided insight into heterometallic effects related to electron transfer and chemical reactivity. Although all heterometallic enzymes will be highlighted herein to provide a lens through which to interpret the observations of heterometallic effects, certain active sites have been more thoroughly studied, and more model systems have thus been constructed as mimics of these multimetallic assemblies. Therefore, their respective discussion in the present Review is weighted accordingly.

Biological enzymes that have been structurally characterized to contain heterometallic active sites are shown in Figure 1, along with the chemical reaction(s) they catalyze. Strikingly, many of these small-molecule transformations are among the most sought-after targets in fields such as energy science – e. g. oxygen reduction and hydrogen oxidation for fuel cell development, water oxidation and proton reduction for water splitting using solar energy, CO_2 fixation for greenhouse gas capture, nitrogen fixation to supplement the energy-intensive Haber-Bosch process.[12,19-27] The metals included in these active sites are also extremely varied: first-row transition metals from manganese to zinc are represented, together with calcium (an alkaline earth metal) and molybdenum (a second row transition metal). This diversity is a result of the different

environmental constraints experienced by different organisms, and it showcases the potential for inexpensive, abundant first-row transition metals for use in catalysis relevant to energy conversion.[23] In the present Review, a brief overview of the features of each of these heterometallic active sites will be provided to place the discussion of structural and functional models of each enzyme in its proper context. Nonetheless, since comprehensive reviews have been published on several of these heterometallic enzymes, detailed discussion of the biological, structural, and chemical features of each enzyme will be excluded.

The research highlighted in the present Review is organized into two main sections. In the first section, reports studying the effects of redox-*inactive* metals on redox processes will be described. The oxidative chemistry involving these systems will be discussed in the context of the role of the redox-inactive calcium center in the oxygen evolving complex (OEC, a Mn_4CaO_n cluster) of Photosystem II (PSII),[28] and a second part will focus on reductive chemistry. The second main section will be devoted to synthetic multimetallic complexes displaying two different first-row transition metals, and these systems will be discussed in the context of the respective enzyme they aim to model [not included in the present chapter]. As mentioned previously, heterometallic enzymes have received varying levels of attention, some resulting in fewer synthetic models being characterized and their properties studied. The relative abundance of model systems for different active sites will be reflected in this Review, leading to more detailed discussion of certain enzymes and transformations.

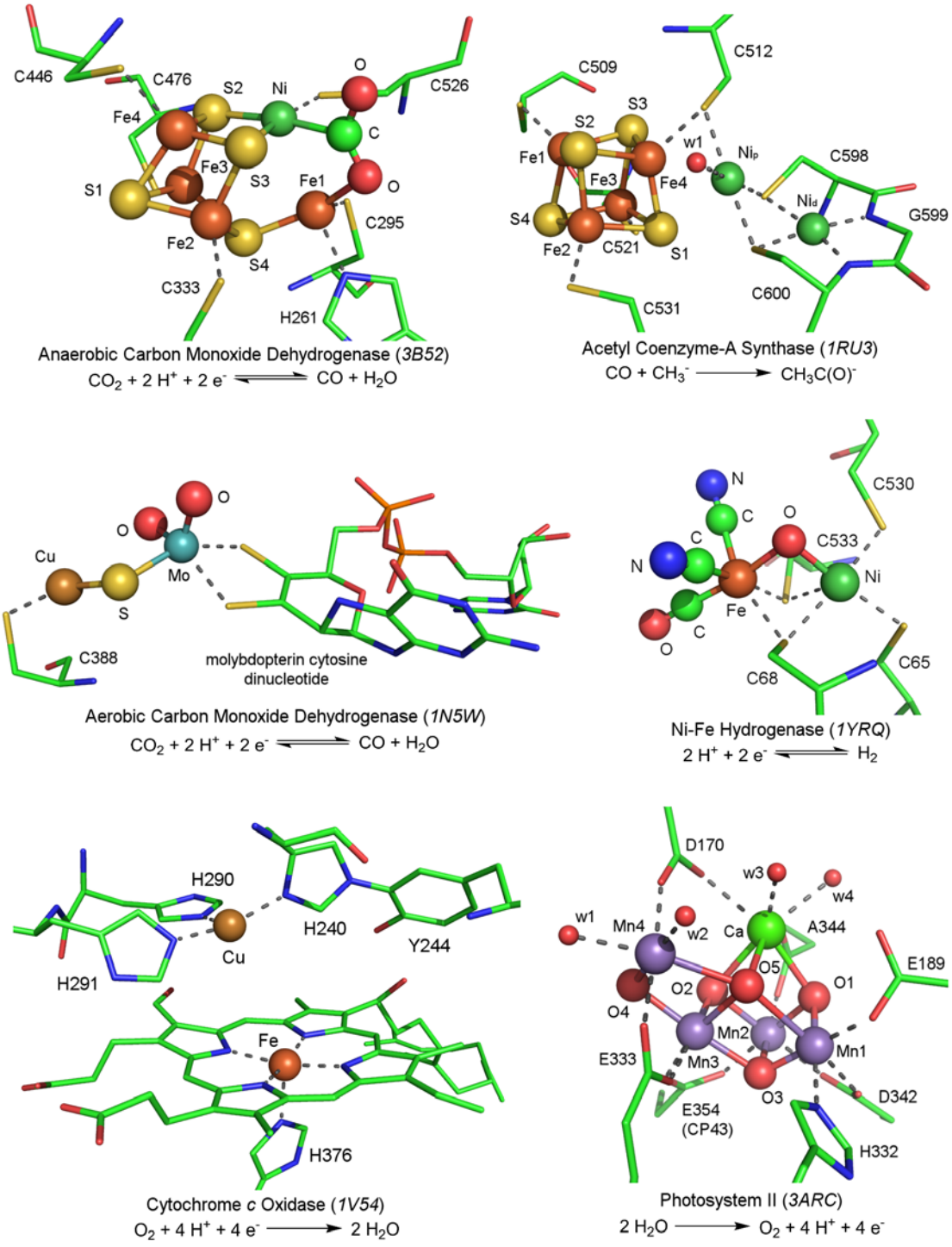

Figure 1. Structural representations of heterometallic active sites in biological enzymes and reaction(s) catalyzed. Protein Data Bank codes in parentheses. Structures rendered with PyMol.[29]

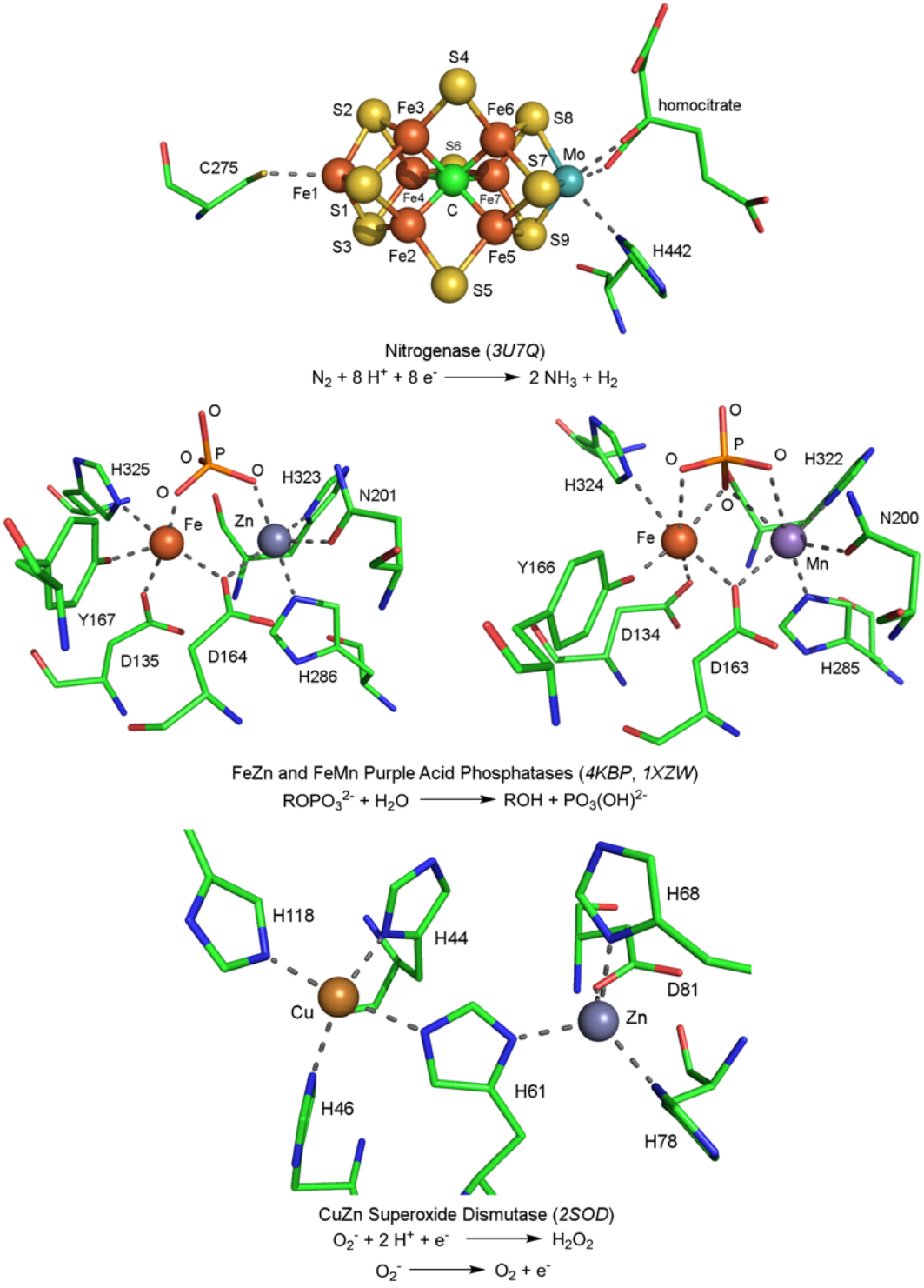

Figure 1 (cont'd). Structural representations of heterometallic active sites in biological enzymes and reaction(s) catalyzed. Protein Data Bank codes in parentheses. Structures rendered with PyMol.[29]

Table 1. Abbreviations, PDB codes, and metal composition of heterometallic enzymatic active sites.

Enzyme	Abbreviation	Structure PDB code	Metal Centers	Ref.
Anaerobic Carbon Monoxide Dehydrogenase	CODH	*3B52*	Fe_4Ni	[30]
Aerobic Carbon Monoxide Dehydrogenase	aeroCODH	*1N5W*	CuMo	[31]
Acetyl Coenzyme-A Synthase	ACS	*1RU3*	Fe_4Ni_2	[32]
Cytochrome *c* Oxidase	C*c*O	*1V54*	CuFe	[33]
Nitrogenase	-	*3U7Q*	Fe_7Mo	[34]
Photosystem II	PSII	*3ARC*	Mn_4Ca	[35]
NiFe Hydrogenase	-	*1YRQ*	NiFe	[36]
CuZn Superoxide Dismutase	SOD	*2SOD*	CuZn	[37]
Purple Acid Phosphatases	PAP	*4KBP, 1XZW*	FeZn, FeMn	[38,39]

2. EFFECTS OF REDOX-INACTIVE METALS ON REDOX PROCESSES

2.1 Redox-Inactive Metals in Redox-Active Biological Systems: the Oxygen Evolving Complex

The presence of a calcium center in the oxygen evolving complex (OEC) of Photosystem II (PSII) is one of the great puzzles involving heterometallic enzymes. The OEC is a multimetallic assembly composed of four manganese centers and a single Ca^{2+} center bridged by oxido ligands, and is the sole means of biological production of dioxygen in organisms ranging from cyanobacteria, to algae, to higher plants.[28] Nearly all of the O_2 in the Earth's atmosphere, necessary to sustain life as we know it, has been photosynthetically generated over billions of years by enzymes containing this type of heteromultimetallic active site.[40-42] In order to oxidize water to dioxygen, the OEC must

accumulate four oxidizing equivalents – four consecutive photons absorbed by the PSII Reaction Center result in the transfer of four electrons (and, concomitantly, four protons) from the OEC to yield the reactive species responsible for water oxidation and O_2 release, which return the site to its reduced state. While the identities of some of the redox states (S-states) in the catalytic cycle (known as the Kok cycle) have been elucidated via various spectroscopic methods, the full mechanism of O_2 evolution remains elusive.[28,43-48] Amongst the many mechanistic questions that remain open to date is the role of the calcium center housed in the "cubane" ($[Mn_3O_4Ca]$) subsite of the OEC, which is required for enzymatic activity and cannot be substituted for any other metal to give a functional enzyme – with one exception: substitution with strontium recovers ~40% of activity.[49-51] The surprising aspect of calcium's involvement resides in the fact that although the OEC needs to access high oxidation states to oxidize water, it requires Ca^{2+} – which is redox-inactive at biological potentials – to function.

Studies of biological water oxidation driven by a desire to exploit this reaction in photodriven water splitting for artificial energy conversion have generated numerous mechanistic proposals for O_2 evolution by the OEC.[12,17,28,48,51] In particular, the formation of the O–O bond has been the focus of much interest as the key step preceding O_2 release. Mechanisms involving nucleophilic attack by a water or hydroxide ligand on the electrophilic oxygen of a high-valent Mn–oxo species or radical coupling of bridging or terminal oxide or hydroxide ligands have been proposed on the basis of various spectroscopic studies involving X-ray absorption spectroscopy (XAS), electron paramagnetic resonance (EPR), and mass spectrometry techniques, as well as by computation. Elucidation of the role of calcium in this transformation has also attracted

interest given its unique ability to engender enzymatic activity. Substitution studies with a variety of other redox-active and redox-inactive metals revealed that Sr^{2+} is the only other metal to yield a functional enzyme (albeit with reduced reaction rates),[49-51] and one that largely maintains an analogous structure to the biological OEC.[28] The inability of other metals of similar size (e.g. cadmium) to promote catalysis has been taken as an indication that the role of calcium is not merely structural.[51,52] Calcium's importance in substrate binding and/or activation has been suggested on the basis of the similar Lewis acidities of Ca^{2+} and Sr^{2+}.[17,52-55] Effects of calcium on proton-coupled electron transfer (PCET) have been proposed, as well as the possibility of calcium's involvement in tuning of the redox potential of the OEC.[56-58] Notably, in another enzyme known to incorporate a redox-inactive metal in an active site responsible for a redox process, the Zn^{2+} center in CuZn superoxide dismutase has been proposed to affect the redox potential of the nearby Cu^{2+} center (facilitating superoxide oxidation to dioxygen), as well as protonation and H-bonding within the active site in the second half of the catalytic cycle (superoxide reduction).[37]

In the last decade, interest in the effects of redox-inactive metals on redox processes has been further piqued by discoveries in the field of heterogeneous catalysis. Mixed-metal oxides, including materials incorporating both redox-active and redox-inactive components, have gained significant attention as electrocatalysts in energy conversion processes such as the oxygen evolution reaction (OER)[59-67] and the oxygen reduction reaction (ORR),[62,67-69] which are central to the development of solar electrolytic water-splitting devices[19,70,71] and fuel cells.[72] In fact, intriguing parallels have been discovered between certain heterogoenous water oxidation catalysts and their biological counterpart, the OEC. Examples of heterometallic manganese birnessites exhibiting

electrocatalytic OER activity have been reported that display a striking structural resemblance to the OEC, with heterometallic cubane subsites bridged to additional manganese centers (Figure 2).[63]

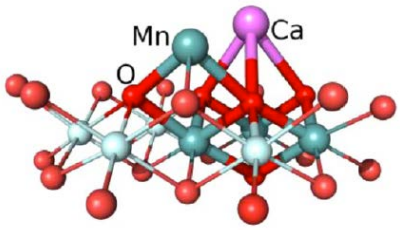

Figure 2. Schematic drawing of one proposed structure of calcium-doped manganese oxide (birnessite) material.[63]

Similar to the case of the OEC, the role of the redox-inactive metals in these heterogeneous catalysts has not yet been elucidated. However, the study of the effects of redox-inactive metals on redox processes has blossomed during the past two decades, and such effects have now been reported in a number of discrete molecular systems. The variety and flexibility of the platforms that have been investigated have engendered many elegant systematic studies of the effects of metal centers that are redox-inactive at relevant potentials on chemical transformations involving the transfer of electrons. In many cases, such studies were undertaken expressly to model the role of Ca^{2+} in the OEC, although the structural motifs involved have often differed from the biological assembly.

The ever-increasing variety of discrete molecular model systems for which effects of redox-inactive metals on electron transfer processes have been observed speaks to the generality of this type of heterometallic influence. The present section of this Review highlights the literature reports in which this type of heterometallic effect has been systematically studied. Systems that display oxidative behavior, including electron

transfer, H- and O-atom transfer, and O_2 release, will be discussed first, as the more direct models of the activity of the biological OEC, oxidation of water. A second unit will focus on heterometallic effects in systems involved in reductive reactivity, including O_2 and N_2 activation and O–O bond cleavage in metal-bound peroxide and superoxide species.

2.2 Redox-Inactive Metal Effects on Oxidative Reactivity

2.2.1. Heterometallic Effects in 'Classical' Inorganic Oxidants.

The first reports on the effects of redox-inactive alkali and alkaline earth metal additives on the redox properties of discrete molecular systems were published in the early 1990s, and focused on several high-valent transition metal-oxo species used as oxidizing agents in organic chemistry. Ruthenate ($[RuO_2(OH)_3]^{2-}$),[73] chromate ($[Cr_2O_7]^{2-}$),[74] permanganate ($[MnO_4]^-$),[74-77] ferrate ($[FeO_4]^{2-}$),[78] and nitridoosmate ($[OsO_3(N)]^-$)[79,80] were shown to be more effective oxidants in the presence of a variety of Lewis acidic species, including several Group 1 and 2 metals. In the seminal work on these systems, Lau and coworkers reported enhancement of oxidation of the unactivated C–H bonds in cyclohexane under mild conditions by ruthenate, chromate, permanganate, and ferrate in the presence of excess Lewis acidic additives. Formation of cyclohexanone was accelerated by addition of Zn^{2+}, Al^{3+}, Fe^{3+}, Cu^{2+}, Mg^{2+}, and Li^+ salts (usually in ~5-fold excess), and this effect was observed to be mildly anion-dependent: chloride salts were more effective than trifluoromethanesulfonate ($^-$OTf) variants, which in turn led to faster rates than acetate ($^-$OAc) salts. In these studies, rate acceleration was proposed to be the result of a positive shift in the oxidation potential of the high-valent species due to binding of a Lewis acidic metal center to the M–O moieties of the oxidant. Mere electrostatic effects were ruled out as a chief contributor

to this effect in the case of ruthenate based on the observation that trifluoroborate (BF_3) – a coordinating but *neutral* Lewis acid – led to rate acceleration, while the positively charged but non-coordinating tetraphenylphosphonium cation (PPh_4^+) did not affect reaction rates.

Scheme 1. Proposed Catalytic Cycle for Lewis-Acid Assisted Hydroxylation of Cyclohexane by Osmium Nitride Complexes

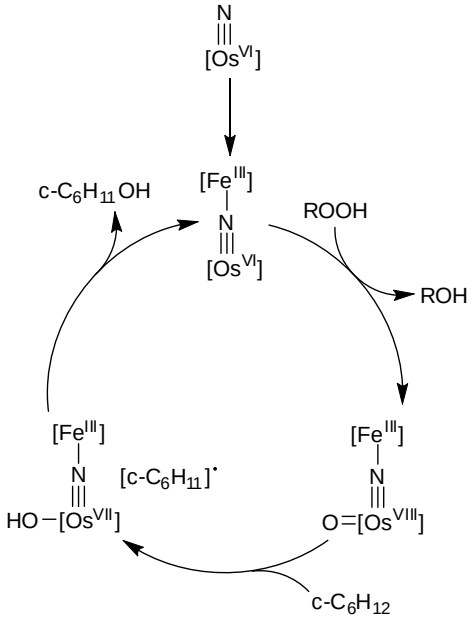

These early mechanistic postulations led the way for more thorough investigations in later studies, in which both Lau and Lee undertook more rigorous analysis of specific oxidant-Lewis acid formulations to determine the mechanism of rate acceleration. Lau and coworkers studied the stoichiometric oxidation of alkanes by $[OsO_3(N)]^-$ in the presence of $FeCl_3$.[79,80] On the basis of kinetic and spectroscopic studies, the proposed active oxidant species was one in which Fe^{3+} was bound to the nitride ligand of the nitridoosmate complex. When the $[OsO_3(N)]^-/FeCl_3$ formulation was used in a catalytic study, the metal species involved in catalysis were determined to be $[Cl_4Os^{VI–VIII}(N)]$ species, which also bind Fe^{3+} via the N^{3-} ligand (Scheme 1). The more reduced

of these complexes could undergo O-atom transfer from a sacrificial oxidant (H_2O_2) to form a Fe-bound [$Cl_4(O)Os^{VIII}(N)$] complex, a species assumed to be active towards C–H bond activation. In accordance with this interpretation, [$Cl_4Os^{VI}(N)$] was found to be a competent precatalyst for alkane oxidation in the presence of $FeCl_3$ and inorganic or organic peroxides.

When simple hydrocarbons are used as substrates for C–H bond activation, as described thus far, the lack of suitable donor motifs makes binding of substrate by Lewis acidic metal species *before* oxidation impossible. However, when the substrate contains heteroatoms, an alternate mechanism can be outlined in which coordination of the Lewis acid to the substrate activates the latter towards oxygen atom transfer from the oxidant.[76] Lee and coworkers examined this possibility in the oxidation of thioanisoles by permanganate in the presence of Lewis acids.[75] Kinetic data revealed that the reaction proceeded via association of the Lewis acid salt with permanganate, followed by binding of the sulfide at the Mn^{VII} center. Two subsequent O-atom transfer steps then yielded the observed sulfone product. Possible mechanisms involving formation of a Lewis acid–substrate intermediate, or a sulfide–permanganate intermediate, or an initial single electron-transfer step were discarded on the basis of kinetic data, isotopic labelling of the substrate, and substrate substituent effects.

Lewis acid-induced enhancement of C–H bond oxidation by permanganate has been shown by Lau and coworkers to allow for rapid oxidation of aliphatic alcohols under mild conditions.[77] Reaction of $KMnO_4$ with methanol was greatly accelerated (up to 10^7-fold) by the presence of Lewis acids (Ba^{2+}, Ca^{2+}, Zn^{2+}, and Sc^{3+} salts, and BF_3). Unlike earlier studies, in which both Lewis acidic metals and counteranions were varied concurrently, this approached focused on a single class of metal salts ($^-$OTf),

simplifying comparisons between the effects of the different metal species. Using the pK_a's of metal aquo complexes as a measure of Lewis acidity,[81,82] a linear correlation between reaction rate and Lewis acidity of the redox-inactive metal can be observed (Figure 3).

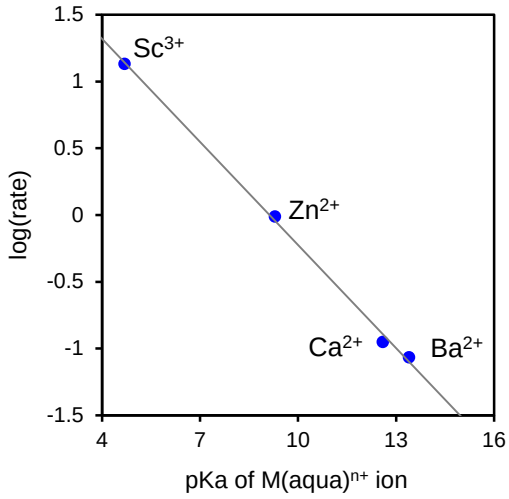

Figure 3. Plot of log(rate) vs. pKa of $M(aqua)^{n+}$ ion for MeOH oxidation by permanganate in the presence of Lewis acid additives. Derived from data from ref. 75.

It is important to note at this point that in these studies, as will be the case for many of the systems described in this section, structural characterization is rarely available for the heterometallic species responsible for the reactivity of interest (in this case, oxygen atom transfer). While spectroscopic data has often provided information on the interactions between high-valent metal-oxo species and redox-inactive metal centers (as with the binding of Fe^{3+} to the nitride ligand of nitridoosmate species outlined above), large excesses of Lewis acidic additives were usually required to ensure complete formation of the target heterometallic species. The dynamic nature of these binding processes makes conclusive identification of reactive species difficult, which in turn complicates interpretation of reactivity data as any mechanistic proposals must account

for the possible existence of pre-equilibria and other such dynamic processes that may be responsible for the observed effects on reactivity.

2.2.2 Binding of Redox-Inactive Metal Ions to Redox-Active Metal Species Via Ligand Backbone

Some of the earliest attempts to facilitate interactions between redox-inactive metal centers and high-valent metal-oxo species have included efforts to append additional donor moieties to ligand scaffolds known to support metal-oxo motifs. Concurrently with the aforementioned studies on inorganic oxidants, investigations on multidentate ligand frameworks that support discrete high-valent Mn–oxo species led to the development of scaffolds with multiple, differentiated binding sites that facilitated systematic studies of binding of redox-inactive metals in proximity to a high-valent Mn center. Horwitz and coworkers devised the incorporation of a crown ether moiety into salen/salophen ligand scaffolds.[83-86] Reaction of Mn^{II} complexes of these ligands with O_2 yielded bimetallic species in which the Mn centers were bridged by one or two oxide ligands depending on the flexibility of the multidentate ligand framework. In the case of a more rigid phenylene in the salen backbone, the Mn_2 species displayed a single oxido bridge between two Mn^{III} centers (**1**).[83] Incorporation of two Lewis acidic ions per dimer, one per crown ether moiety as determined by spectrometric titrations, was accomplished without the need for excess cations in solution due to the strong binding affinities of the crown motifs. Binding of cations led to shifts in the electrochemical reduction potential of the Mn–O–Mn species to more positive values, more so with increasing Lewis acidity of the ions. The 2-e^- Mn^{III}–O–Mn^{III}/Mn^{II}–O–Mn^{II} couple ($E°$ = -0.47 V vs. Fc^+/Fc in **1**) was observed to shift from -0.36 (K^+) to -0.14 vs. Fc^+/Fc (Ca^{2+}) as shown in Table 1. Unfortunately, due to the limited number of redox-inactive

metals screened and to their narrow range of Lewis acidities (all relevant metal aquo complexes fall within a window of only 2-2.5 pK_a units), extrapolative analysis of the correlation between Lewis acidity and reduction potentials would be misleading.

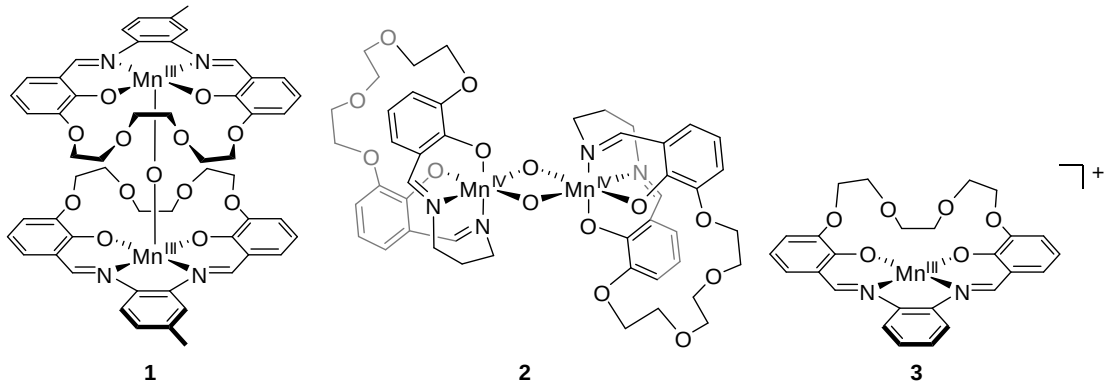

Figure 4. [Mn_2] complexes of ligands bearing crown ether moieties for binding of redox-inactive metal ions.

A similar effect on redox potential was observed in a related system in which the less rigid propanediamine backbone allows for rearrangement of the salophen ligand around each Mn center, yielding dioxo complex **2**.[85] Incorporation of redox-inactive metal ions in this Mn^{IV}–$(O)_2$–Mn^{IV} species led to shifts in the potential of both redox events observable by cyclic voltammetry – the $[Mn^{IV}_2]/[Mn^{III}Mn^{IV}]$ and $[Mn^{III}Mn^{IV}]/[Mn^{III}_2]$ couples, respectively. As expected, binding of a more Lewis acidic ion resulted in a greater positive shift in potential, from -0.535 and -1.15 V vs. Fc^+/Fc for K^+, to -0.135 and -0.49 V for Ca^{2+} (Table 1). As in the case of the singly bridged dimer, however, the Lewis acids utilized in this study (K^+, Na^+, Ba^{2+}, and Ca^{2+}) display Lewis acidities too similar to quantitatively extrapolate a reliable trend for the effect of Lewis acidity on redox potential. EPR studies were conducted on the mixed-valent Mn^{III}–$(O)_2$–Mn^{IV} analog of **2** (obtained via chemical reduction), although only subtle effects of cation binding were observed on the antiferromagnetically coupled Mn

centers. Monomeric Mn complex **3** was also studied, and displayed similar effects of binding of redox-inactive metals of comparable Lewis acidity on its redox potential.

Table 2. Electrochemical data for complexes **1**-**3** in the presence of various cationic additives. Potentials given in V vs. Fc^+/Fc.

Redox-Inactive Metal	pK_a[a]	E^o(1)[b, 83]	E^o(2)[c, 85]	E^o(3)[d, 86]
-	-	-0.47	-0.97, -1.55	-
K^+	15-15.5[e]	-0.355	-0.535, -1.15	-0.380
Na^+	14.8	-	-0.64, -0.99	-0.355
Li^+	13.8	-0.325	-	-
Ba^{2+}	13.4	-0.18	-0.24, -0.53	-0.180
Ca^{2+}	12.6	-0.135	-0.135, -0.49	-0.120

[a] pK_a of metal aquo ions.[81] [b] $[Mn^{III}Mn^{III}]/[Mn^{II}Mn^{II}]$ couple. [c] $[Mn^{IV}Mn^{IV}]$ /$[Mn^{III}Mn^{IV}]$ and $[Mn^{III}Mn^{IV}]/[Mn^{III}Mn^{III}]$ couples, respectively. [d] $[Mn^{III}]/[Mn^{II}]$ couple. [e] An exact pK_a value for K^+ comparable with the scale used herein for other metal ions is not available.

In these crown ether-based systems, OAT reactivity was studied only for heterometallic complexes derived from **1**, but the propensity of the cation-bound species to undergo single-electron transfer with potential O-atom acceptors precluded systematic OAT studies. Using a Mn–oxo complex supported by a macrocyclic ligand with additional backbone donor moieties for interaction with a second metal center, Collins and coworkers reported the effects of redox-inactive metal additives on the oxygenation of a phosphine substrate.[87] Mn^V–oxo species of tetraanionic ligands such as the tetraamidomacrocyclic ligand (TAML) in complex **4** often display diminished ET and OAT reactivity due to the stabilization of the high-valent Mn center by the electron-rich ligand set. However, introduction of a nitrogen donor in the backbone arene of this ligand provided a suitable site for binding of a second metal center, resulting in an enhancement of the reactivity of **4**.

Scheme 2. Reactivity of Complex **4** with PPh_3 in the Presence of Lewis Acids.

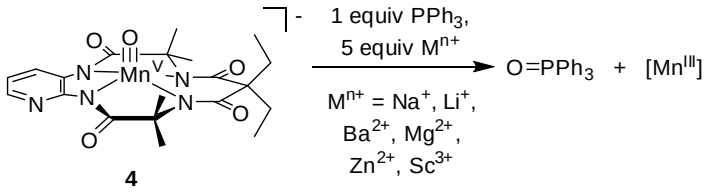

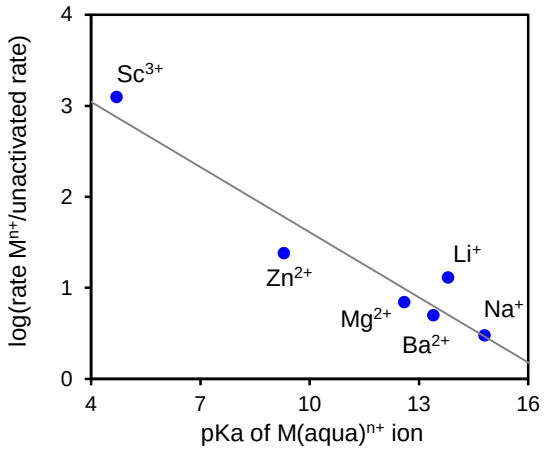

Figure 5. Plot of log(rate M^{n+}/unactivated rate) vs. pKa of the metal aquo complex for oxygen atom transfer to PPh_3 by **4** in the presence of redox inactive metal ions. Derived from data from ref. 85.

Complex **4** was found to bind a variety of redox-inactive ions (Na^+, Li^+, Ba^{2+}, Zn^{2+}, Mg^{2+}, and Sc^{3+}, though not K^+), and this interaction was thought to involve both the backbone pyridine N donor and the closest carbonyl O moiety, which provided a bidentate binding site. The absence of direct binding to the manganyl moiety was inferred from the blueshift of the ν(Mn–O) IR band, indicative of increased donation from the oxo ligand. A stronger Mn–O interaction was considered consistent with reduced donation of electron density from the macrocyclic ligand upon binding of a second metal center to its backbone. Direct binding of a Lewis acidic ion to the Mn–O moiety, on the other hand, would result in a redshift of said manganyl vibration. Binding of Lewis acids led to acceleration of the rate of PPh_3 oxygenation by **4**, and the extent

of this effect grew with increasing Lewis acidity. Upon further analysis, it can be shown that the logarithms of the relative rates of PPh_3 oxygenation (reaction rates were reported by the authors as relative rates with respect to the rate of oxygenation in the absence of Lewis acidic additives) correlate linearly with the Lewis acidity of the respective ions (Figure 5). The lack of binding in the case of K^+ can also be explained in terms of Lewis acidity, as K^+ is amongst the least Lewis acidic of the alkali/alkaline earth metals.

Redox-inactive metal additives were also observed to affect the ability of **4** to perform catalytic oxygenation of C–H bonds. In the absence of metal additives, **4** did not react with 2,3-dimethyl-2-butene (Scheme 3). However, in the presence of redox-inactive metals (Zn^{2+}, Mg^{2+}, or Sc^{3+}) **4** catalyzed the oxygenation of this substrate to yield 2,3-dimethylbut-3-en-2-ol as the major product. 2-methyl-1-butene-3-one (resulting from oxidation of the alcohol) and 2,2,3,3-tetramethyloxirane (resulting from olefin epoxidation) were observed as side products to varying extents with different Lewis acids (the cleanest reactivity was observed with Zn^{2+}, which yielded a 95:5:0 alcohol/ketone/epoxide product mixture).

Scheme 3. Lewis Acid-Induced Catalytic Oxygenation Reactivity of Complex **4**.

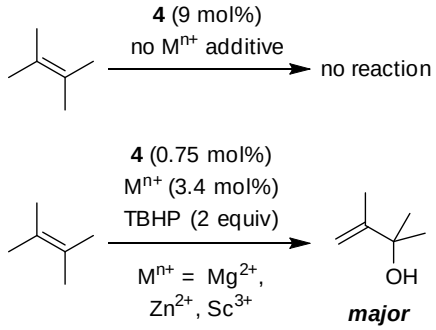

In the absence of the more extensive crown ether binding motif used by Horwitz and coworkers, the addition of an excess of redox-inactive metal salt to TAML complex

4 was necessary to engender the enhanced oxygenation reactivity. The effects of redox-inactive metal ion concentration on the rate of phosphine oxygenation were explicitly studied, but the results do not appear to fit any trends – increase in the Lewis acid/[Mn] ratio from 5:1 to 60:1 affected the reaction rate of various Lewis acids differently (1.2- to 2-fold rate increases were observed). The case of Na^+ was however a clear outlier, as the use of 60:1 Na^+/[Mn] ratio resulted in a 169-fold increase in rate. This observation was explained on the basis of the possible binding of a second Na^+ to **4**. Furthermore, the possibility of binding of multiple Mn complexes to the same cation (in the case of the larger Ca^{2+} for example) was inferred from nonisosbestic behaviour in spectrometric titration experiments. The dynamic processes involved in cation binding and the consequent lack of structural characterization for the reactive species in substrate oxygenation complicates the assignment of the observed rate effects.

2.2.3 Binding of Redox-Inactive Metals to Metal-Oxo Motifs: Effects on Single Electron Transfer

The majority of the reports that have described the redox-inactive metal effects on redox processes have focused on systems in which Lewis acidic metal centers interact with high-valent metal-oxo motifs by direct coordination to the oxo ligand, rather than via binding to the supporting ligand scaffold. This type of interaction has been shown to strongly influence the ET, OAT, and HAT reactivity of high-valent metal-oxo complexes. The reports of these effects represent some of the broadest systematic studies of the effects of Lewis acidic metals on redox processes.

Amongst the most substantial contributions to this field, the groups of Fukuzumi and Nam have provided extensive and often quantitative analyses of the effects of redox-inactive metals on reactions involving electron transfer. These studies have

focused on three multidentate ligand platforms that are capable of supporting high-valent metal-oxo species (Figure 6), and have involved Fe and Mn complexes containing M–O (oxo) or M–(O_2^{2-}) (peroxo) motifs.

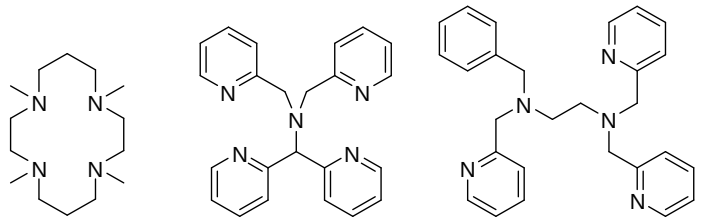

5 **6** **7**

Figure 6. Tetra- and pentadentate neutral ligands used to support high-valent metal-oxo species.

The first such report described the effects of binding of redox-inactive metal ions to the Fe^{IV}–O complex supported by macrocyclic ligand **5**. Fukuzumi and coworkers found that the presence of Sc^{3+} induced a change in the reactivity of complex **8** (Scheme 4),[88] previously reported as the first crystallographically characterized non-heme Fe^{IV}–O species.[89] While complex **8** could only be reduced once by ferrocene, it was able to undergo a second reduction by the same reagent following addition of Sc^{3+} (1-8 equiv.). When $Sc^{3+}$was introduced before the addition of reductant, a single 2-e^- event was observed spectrometrically. Kinetic studies carried out via UV-Vis spectroscopy confirmed that the reaction proceeded via a rate-determining 1-e^- reduction, followed by a fast second electron transfer step. The weaker Lewis acid Ca^{2+} also induced a similar shift in the reactivity of **8**, albeit only when present in large excess (40 equivalents, vs. 1-8 for Sc^{3+}). These observations were consistent with the increased oxidizing power (i.e. a positive shift in reduction potential) of the Fe^{IV}–O motif upon

binding of Lewis acids, and supported the possible redox-tuning role of redox-inactive metals in biological systems and heterogeneous catalysts.

Scheme 4. Reactivity of Complex **8** with Reductants and Redox-Inactive Metal Salts.

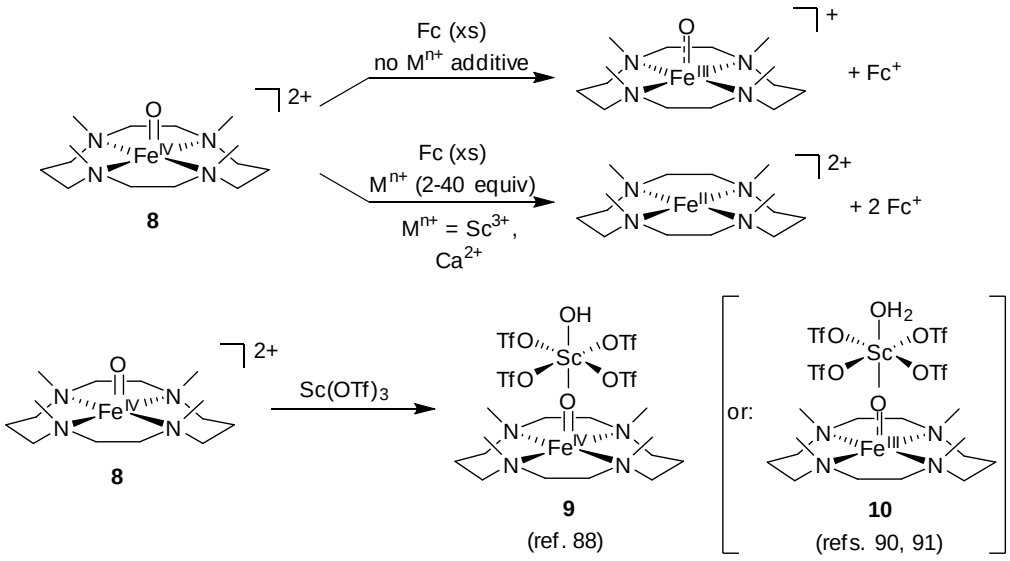

Direct evidence for binding of Sc^{3+} to the Fe^{IV}–O moiety was provided by X-ray crystallography (Scheme 4). The crystal structure of the product of reaction of **8** with $Sc(OTf)_3$ was assigned by the authors as $[Fe^{IV}]$–(O)–$Sc(OTf)_4(OH)]$ complex **9**. To date, this is the only structurally characterized high-valent metal-oxo species with an oxo-bound metal ion, highlighting the difficulties in accurately characterizing reactive species involving weak (and therefore often dynamic) binding of Lewis acids to redox-active metal complexes. Even in this unique case for which crystallographic characterization of the heterometallic species of interest is available, the assignment of the structure obtained from XRD analysis has been disputed. A report by Stewart argued that comparison of bond metrics as well as density functional theory (DFT) calculations suggest formulation of the species as the more reduced $[Fe^{III}]$–(O)–$Sc(OTf)_4(H_2O)$ complex **10**.[90] This new assignment was corroborated by a later report

by Que, Jr. and coworkers, who provided Mössbauer, XANES, and EPR data and described chemical reactivity indicating that **10** contained a Fe^{III}, not Fe^{IV}, center.[91]

Analysis of the effects of a broader series of redox-inactive metal additives was reported for Fe-peroxide complex **11** supported by the same macrocyclic ligand. Binding of redox-inactive metals (Sr^{2+}, Ca^{2+}, Zn^{2+}, Lu^{3+}, Y^{3+}, and Sc^{3+}) to the peroxide moiety in **11** was shown to lead to formation of heterobimetallic species **12-M**, which were characterized by UV-Vis, EPR, and EXAFS spectroscopies and mass spectrometry (Scheme 5).[92,93] The redox-inactive metals were found to markedly affect the electrochemical behavior of the bimetallic complexes. As the Lewis acidity of the bound ion increased, the potentials for both redox events observed for **12-M** by cyclic voltammetry (one oxidation and one reduction event, both 1-e^- irreversible processes) were shifted to more positive values (Table 3). Complexes of more Lewis acidic metals (M = Zn^{2+}, Y^{3+}, Lu^{3+}, Sc^{3+}) did not display an oxidation wave (see Sections 2.2.5 and 2.3.3 for details on reactivity).

Scheme 5. Formation of Heterobimetallic Peroxo-Bridged Complexes **12-M**.

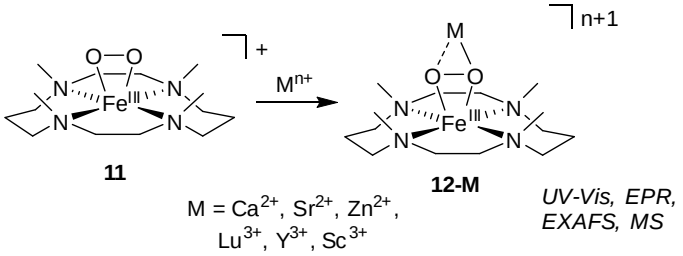

Table 3. Electrochemical data for complexes **11** and **12-M** in the presence of various cationic additives.[93] Potentials given in V vs. Fc^+/Fc.

Complex	pK_a(M)[a]	E_{ox}	E_{red}
11	-	0.54	-0.81
12-Sr	13.2	0.56	-0.77
12-Ca	12.6	0.58	-0.75
12-Zn	9.3	-[b]	-0.54
12-Y	8.04	-[b]	-0.22
12-Lu	7.90	-[b]	-0.24
12-Sc	4.7	-[b]	+0.00

[a] pK_a of metal aquo ions. [b] No oxidation wave observed.

Tetrapyridine ligand **6** (Figure 6) has also been studied for its ability to support a Fe^{IV}–oxo complex (**13**), which was crystallographically characterized (Scheme 6).[94] The extensive studies on the effects of Lewis acid additives on the reactivity of **13** have made this one of the most thoroughly analyzed systems for heterometallic effects. The 1-e^- reduction potential (E_{red}) of **13** was determined to be 0.13 V (vs. Fc^+/Fc), making reduction of **13** by $[Fe^{II}(bpy)_3]^{2+}$ (E_{ox} = 0.68 vs. Fc^+/Fc) inaccessible.[95] Addition of Sc^{3+} was however observed to allow this ET process, indicating a substantial potential shift. The reduction potential of **13** in the presence of Sc^{3+} was sufficiently positive that an ET equilibrium was observed with the weaker reductant $[Ru^{II}(bpy)_3]^{2+}$ (E_{ox} = 0.86). The calculated range of E_{red} for **13** was 0.88-0.97 V, indicative of a ~0.8 V increase in reduction potential upon Sc^{3+} binding.

Investigation of the effects of Sc^{3+} concentration on E_{red}, as well as studies of the kinetics of ET, revealed that binding of two Sc^{3+} ions occurred at high [Sc^{3+}] concentrations (30 equiv.). Rate acceleration (up to 10^8-fold at high [Sc^{3+}]) for ET from

13 to Fc was also observed in the presence of Sc^{3+} as well as other redox-inactive metal ions (Y^{3+}, Lu^{3+}, Zn^{2+}, Mg^{2+}, and Ca^{2+}). Using a Lewis acidity scale based on the interaction of redox-inactive metals with the superoxide anion as measured via EPR spectroscopy,[96] the authors showed that $\log(k_n)$ values (k_n = first and second order rate of ET) were linearly correlated with Lewis acidity. The presence of Brønsted acids was also found to affect the reduction potential of complex **13**. Addition of triflic acid (HOTf) to **13** resulted in a shift in reduction potential to 1.17 V (vs. Fc^+/Fc) – an even greater effect than in the case of Sc^{3+} (~ 1 V).[97] Analysis of the correlation between the concentration of HOTf and the observed reduction potential revealed that two equivalents of HOTf could bind to **13,** akin to what had been observed for Sc^{3+}.

Scheme 6. ET Reactivity of Fe^{IV}–O Complex **13** in the Presence of Cations

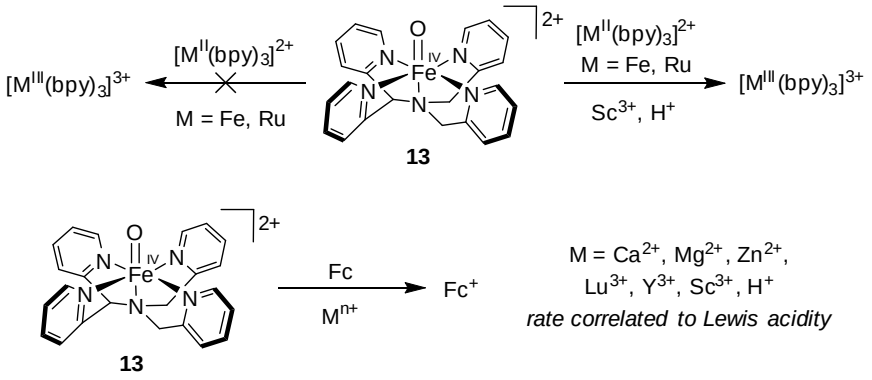

The ET behavior of systems supported by ligands **5** and **6** in the presence of metal salts has been described by the authors as *metal-coupled electron transfer* (MCET), a process analogous to proton-coupled electron transfer (PCET) but involving metal cations.[98,99] The effects of both H^+ and metal salts on complexes such as **13** can be ascribed to the stronger interaction of these redox-inactive cations with the more reduced Fe complexes. The greater thermodynamic stabilization of the reduced complex vs. its oxidized analog due to the increase in binding affinity upon reduction facilitates the

transfer of electrons to the complex, effectively shifting its reduction potential to more positive values according to the Nerst equation as shown by (1):

$$\Delta E_{\text{red}} = \frac{RT}{F} ln \left[\frac{K_{red}[M^{n+}]}{K_{ox}[M^{n+}] + 1} \right], \qquad (1)$$

where ΔE_{red} is the shift in one-electron reduction potential of a given species, K_{red} and K_{ox} are the binding constants for complexes of cations with the reduced and oxidized species, respectively, and $K_{\text{red}}[M^{n+}] >> 1$. [98]

Scheme 7. Reactivity of Mn^{IV}–O Complexes with Redox-Inactive Metal Ions and Effects on Redox Potential

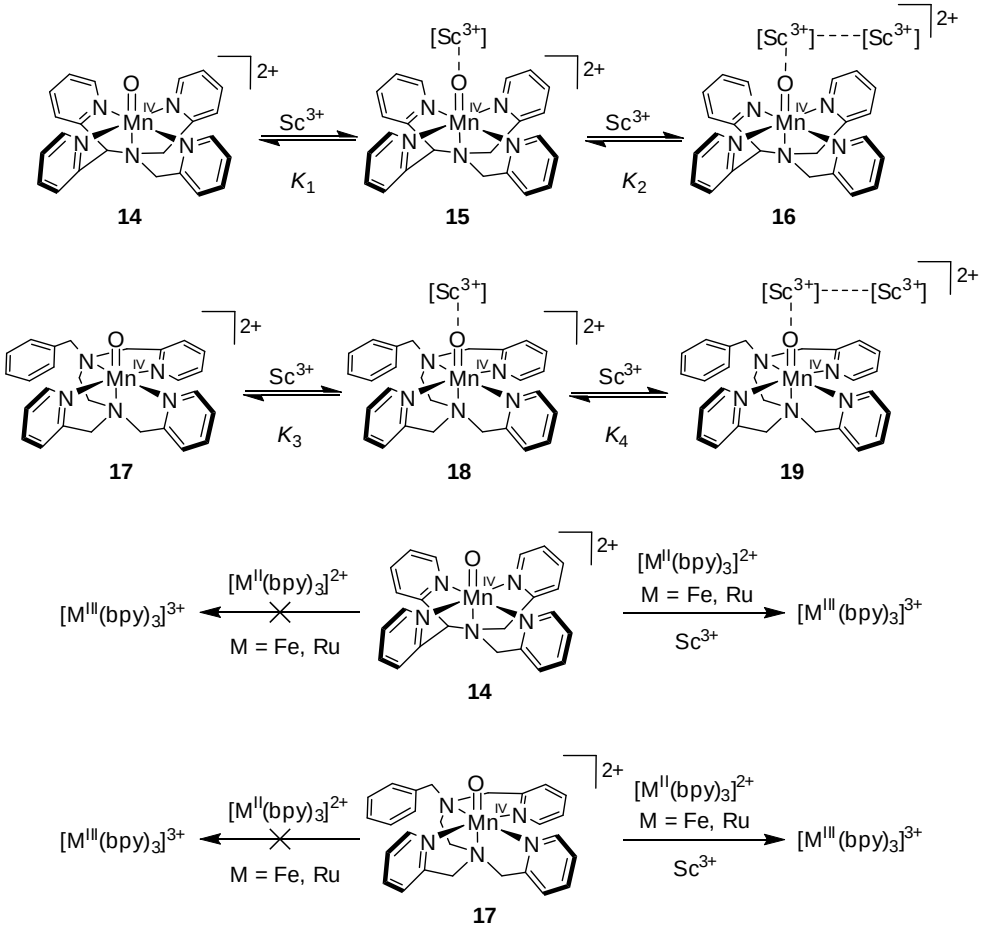

Studies on ligands **6** and **7** have been extended to Mn complexes, as it was found that these frameworks could also support Mn^{IV}–O species (**14** and **17**, Scheme 7).[100] Complex **14** was shown to be a metastable species ($t_{1/2}$ = 2 h at 25 °C) and was prepared

from a Mn^{II} precursor by reaction with iodosobenzene (PhIO). Its assignment as a Mn^{IV}–O complex was confirmed via EPR, ESI-MS, and XANES/EXAFS spectroscopies. Similarly to its Fe analog, **14** was found to bind up to two Sc^{3+} ions. 1:1 and 1:2 [Mn]-Sc^{3+} adducts **15** and **16** were observed to be more stable than **14** ($t_{1/2}$ at 25 °C = 12 h and 1 d, respectively), and the equilibrium binding constants for the two processes were analysed spectrometrically.[101] Addition of 1 equiv. Sc^{3+} was sufficient to fully convert **14** to **15** ($K_1 >> 10^4$ M^{-1}), whereas full formation of **16** required excess Sc^{3+} (5 equiv.; $K_2 = 6.1 \times 10^3$ M^{-1}). Analogous studies were carried out with Mn^{IV} species **17**, which displayed a similar, albeit slightly lesser, ability to bind Sc^{3+} ions ($K_3 = 4.0 \times 10^3$ M^{-1}, $K_4 = 1.2 \times 10^3$ M^{-1}). Cation-bound species **15-16** and **18-19** were characterized via EPR, EXAFS, and ESI-MS spectroscopic techniques. Structural data obtained via EXAFS was consistent with elongation of Mn–O distances by ~0.05 Å, indicating binding of cations at the Mn-oxo motif.

Binding of redox-inactive ions to **14** and **17** resulted in shifts in their reduction potential consistent with the authors' observations on the related Fe system. In the presence of Sc^{3+}, these species could oxidize poor reductants such as dibromoferrocene and $[Ru^{II}(bpy)_3]^{2+}$ (E_{ox} = 0.33 and 0.86 V vs. Fc^+/Fc), which were unreactive with **14** and **17** in the absence of additive.[101] The reduction potentials for species **14**-**19**, calculated from redox titration experiments, are listed in Table 4.

Table 4. Reduction potentials of complexes **14-21** determined via spectrometric redox titrations. Potentials given in V vs. Fc^+/Fc.

Complex	Additive (# bound)	E_{red}	Ref.
14	-	0.42	[100]
15	$Sc(OTf)_3$ (1)	0.93	[101]
16	$Sc(OTf)_3$ (2)	1.04	[101]
20	HOTf (2)	1.27	[102]
17	-	0.4	[103]
18	$Sc(OTf)_3$ (1)	0.9	[101]
19	$Sc(OTf)_3$ (2)	0.98	[101]
21	HOTf (2)	1.12	[102]

Scheme 8. Reactivity of Mn^{IV}–O Complexes with Redox-Inactive Metal Ions and Effects on Redox Potential

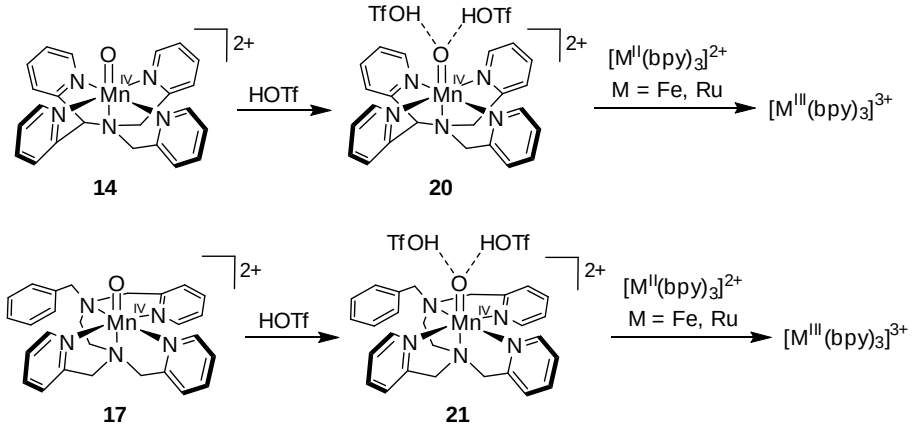

Studies of the effects of HOTf on **14** and **17** were also reported. Spectrometric titrations and kinetic data supported the formation of 1:2 $[Mn^{IV}]/[HOTf]$ adducts **20** and **21** upon addition of HOTf.[102] On the basis of EXAFS data and DFT calculations, however, the structures of HOTf adducts **20** and **21** were assigned differently from those of Sc^{3+}-bound **16** and **19**. In the case of Sc^{3+}, the authors invoked binding of a

single cation directly to the Mn^{IV}–O motif, with the second metal center located in the second coordination sphere, possibly interacting with the Mn complex via triflate anions. On the other hand, binding of two HOTf directly to the Mn^{IV}–O via H-bonding interactions was proposed in **20** and **21**. The reduction potentials of the HOTf adducts were determined via redox titration, and **20** and **21** were found to be slightly stronger oxidants than the respective $(Sc^{3+})_2$ adducts **16** and **19** (Table 4).

Although the reduction potentials observed in Mn species interacting with Lewis or Brønsted acids are more positive than in the analogous Fe species, the shifts in reduction potential of Mn^{IV} species engendered by cation binding were lower than those for Fe^{IV} complexes. The larger changes in potentials are consistent with the stronger binding of cations to the Fe^{IV}–O motif evident from the binding constants determined spectrometrically. Further studies of the OAT and HAT reactivity of these systems are highlighted in Section 2.2.4.

Scheme 9. Tautomerization Reactivity of **23** with Zn^{2+}.

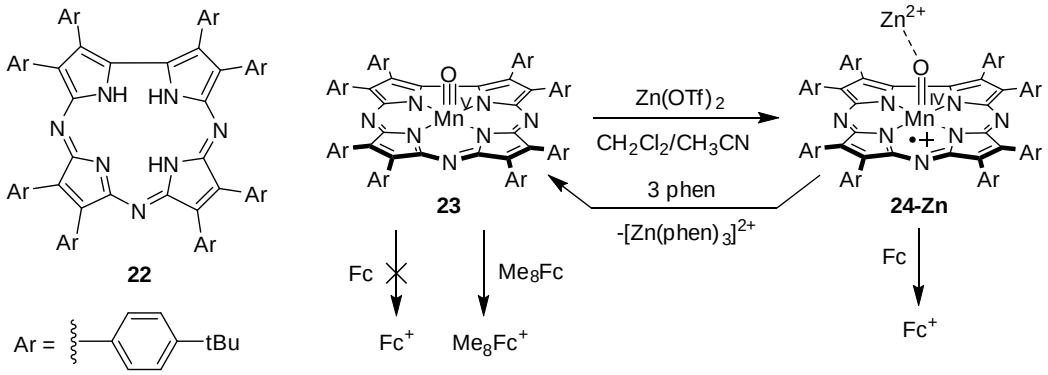

Binding of Lewis acids was found to have a remarkable effect on a corrolazine-supported Mn–oxo species studied by Goldberg and coworkers.[104] Porphyrine-like ligands such as corrolazines are more electron-rich than the neutral ligands described above, and therefore allow access to higher-valent manganese-oxo complexes. Using

an octakis(*p-tert*-butylphenyl)corrolazine ligand (**22**, Scheme 9), a Mn^{V}–oxo complex (**23**) was isolated. This diamagnetic species was unreactive towards ferrocene due to its low reduction potential, although it could oxidize the stronger reductant octamethylferrocene (Me_8Fc, E_{ox} = -0.80 V vs. Fc^{+}/Fc), generating a two-electron reduced Mn^{III} species. Addition of one equivalent of $Zn(OTf)_2$ to **23** resulted in clean conversion to a paramagnetic species whose spectroscopic features were consistent with formation of a corrole cation radical. Since Zn^{2+} is redox-inactive at these potentials, oxidation of the corrolazine ring indicated reduction of the Mn center to Mn^{IV}. The product species was therefore assigned as the valence tautomer complex **24-Zn**. Treatment of **24-Zn** with 1,10-phenanthroline (phen) resulted in sequestration of the Zn^{2+} cation and consequent regeneration of the starting Mn^{V} complex, confirming Zn^{2+} binding. Unlike in the case of Fe^{IV}–O and Mn^{IV}–O moieties supported by neutral ligands as described above, only a 1:1 adduct is formed by addition of Zn^{2+} to **23** even in the presence of excess Zn^{2+}. Complex **24-Zn** was found to be reduced by ferrocene, yielding a one-electron reduced Mn^{IV} complex with a closed-shell corrolazine ring. Analogous conversions to Mn^{IV}/corrolazine radical cation species were observed upon addition of $B(C_6F_5)_3$ and HBF_4. Group transfer reactivity of these species will be described in the next section.

2.2.4 Binding of Redox-Inactive Metals to Metal-Oxo Motifs: Effects on OAT and HAT

Together with single ET studies, the reactivity pathways most commonly investigated for heterometallic effects are oxgyen- and hydrogen-atom transfers. Many of the systems described in the last section that display effects of redox-inactive metal cations on their redox potential and on rates of ET are also active for OAT and/or

HAT. A handful of additional systems have also been reported to exhibit effects on OAT/HAT, although studies of their ET behavior have not been described in detail, and are included in the present section.

Scheme 10. OAT Reactivity of Complex **13** with Thioanisoles and Reactivity Modulation by Lewis Acidic Additives

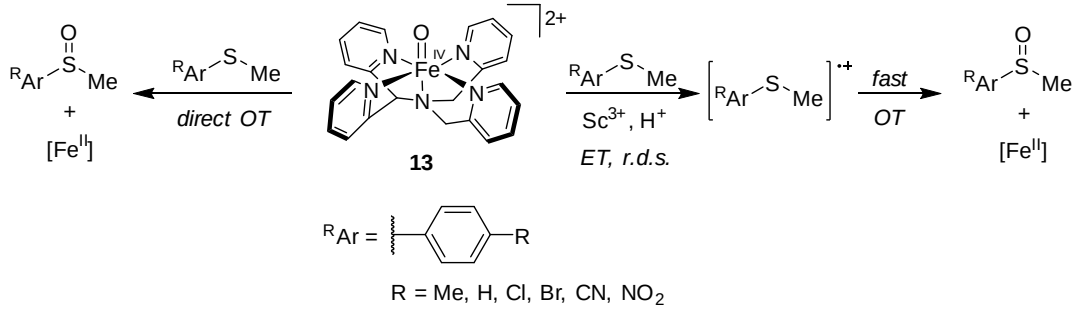

The groups of Nam and Fukuzumi have extended many of their analyses of the interactions of redox-inactive metal ions and Fe^{IV}– and Mn^{IV}–oxo complexes supported by neutral N-donor ligands to investigation of OAT and HAT reactivity. The presence of Lewis acids was found to affect OAT from complex **13** to sulfides. The rate of oxidation of thioanisoles by **13** was greatly accelerated (up to 10^2-fold) by addition of Sc^{3+}.[99] In fact, the mechanism of thioanisole oxidation was found to shift from direct O-atom transfer in the absence of Sc^{3+} (a 2-e^- step) to metal-coupled electron transfer followed by fast O-atom transfer (two 1-e^- processes) when Sc^{3+} was present (Scheme 10). This effect was ascribed to the large driving force for electron transfer that resulted from binding of Sc^{3+} to the iron-oxo complex as described in Section 2.2.3. When this driving force was lowered – e.g. in reactions with more electron-poor thioanisoles (R = CN, NO_2) – rate acceleration by Sc^{3+} was also lower. Analysis of the kinetic data for OAT to a series of substituted thioanisoles in the presence of Sc^{3+} (20 equiv.) revealed a dependence of the observed OAT rate on the calculated driving force for ET from

thioanisoles to **13**. This relationship was determined to fit the parameters of the Marcus theory of adiabatic outer-sphere electron transfer,[105] indicating a rate-determining ET step. Treatment of **13** with electron-rich *p*-methoxythioanisole in the presence of Sc^{3+} resulted in formation of *p*-methoxythioanisole radical cation as observed by UV-Vis spectroscopy, further supporting the proposal of a shift in mechanism and an initial ET step.

Though not involving a second metal center, reactivity of **13** with olefins was found to be strongly affected by triflic acid. HOTf was found to promote OAT from complex **13** to olefins to yield epoxides (Scheme 11). Similar to the reactivity with thioanisoles, HOTf accelerated the reaction of **13** with styrene derivatives, which are unreactive with **13** in the absence of additives.[106] Reaction between olefins and **13** was determined to occur via an initial PCET step as implicated by the dependence of the observed reaction rate on the ET driving force for various substituted styrenes. Transfer of the O atom (possibly via $O^{\bullet-}$ transfer) could then take place. The metal-containing product isolated following reactivity is Fe^{III} complex **25**, likely from comproportionation between Fe^{II} and Fe^{IV} species. As a result of the balance of electrons involved in reactivity, therefore, the maximum theoretical yield of epoxide was 50% (observed yields were 42-45%).

Scheme 11. Epoxidation Reactivity of Complex **13** in the Presence of HOTf

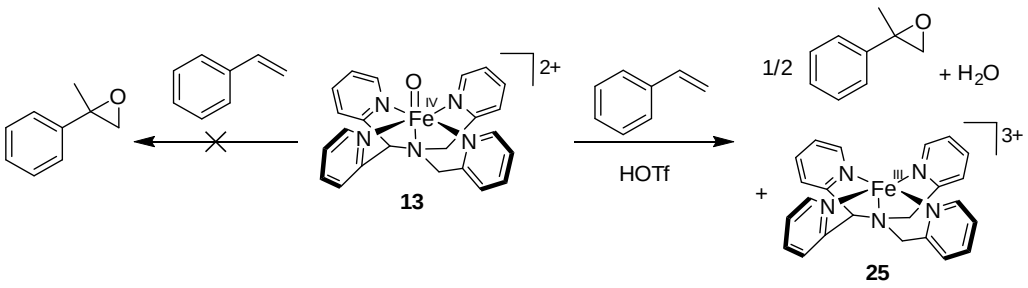

Modulation of the reactivity of complex **13** by Sc^{3+} was also studied for the reaction with *N*,*N*-dimethylanilines.[107] Sc^{3+} addition engendered a shift in the product

distribution as well as an acceleration of the overall reaction rate. In the absence of Sc^{3+}, reaction of **13** with *N,N*-dimethylaniline (DMA) proceeded via an electron-transfer/proton-transfer pathway leading to demethylation of the aniline (Scheme 12a). Addition of Sc^{3+} accelerated the initial electron transfer step, but also hindered proton

Scheme 12. Reactivity of **13** with N,N-dimethylaniline(a) in the Presence and (b) Absence of $Sc(OTf)_3$.

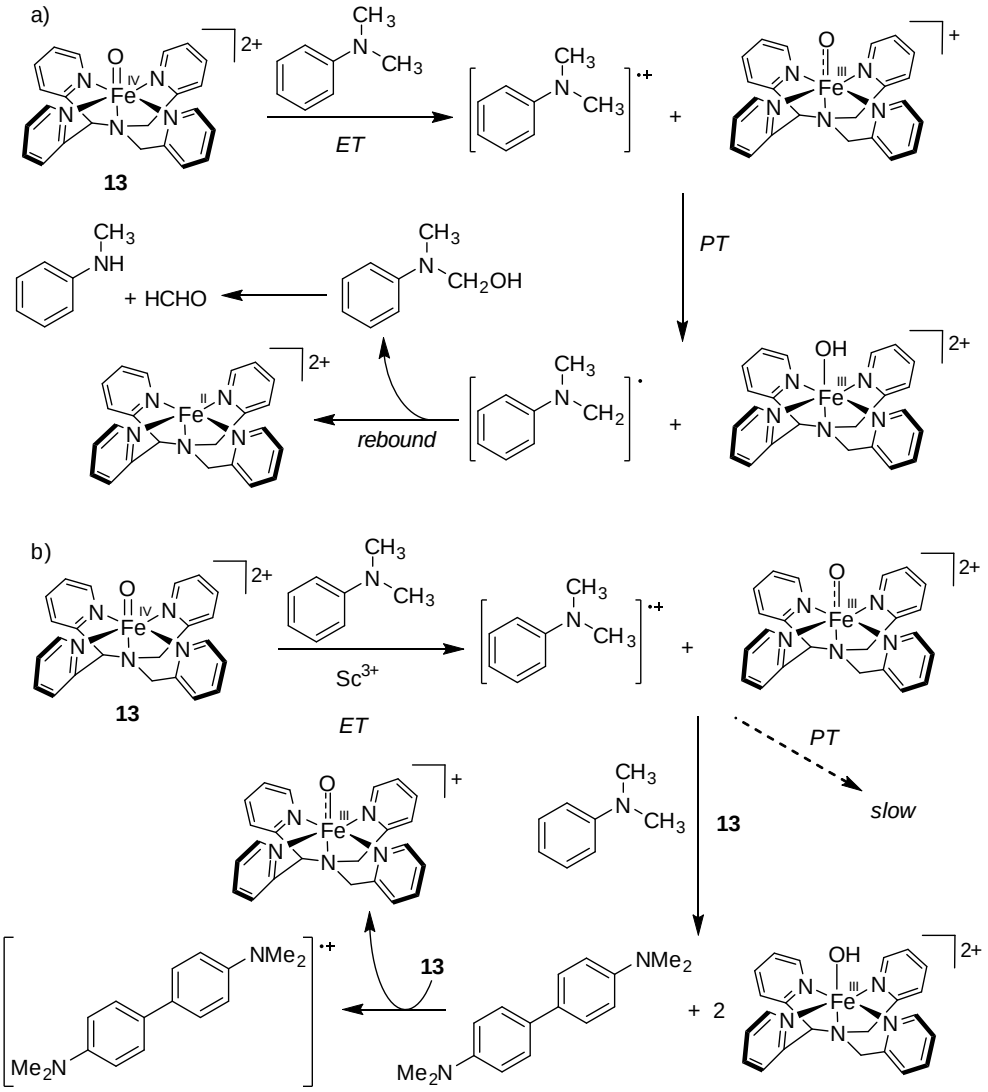

transfer to the Fe^{IV}–O moiety due to binding of Sc^{3+} at the same site. The slower rate of proton transfer favored nucleophilic attack by free DMA and subsequent oxidation by additional **13** to yield the dimerized tetramethylbenzidine radical cation ($TMB^{\bullet+}$) as

the final product (Scheme 12b). When a pathway to dimerization was not available – i.e. when *para*-substitution was introduced in the substrate aniline – proton transfer to the Sc^{3+}-bound Fe^{IV}–O species was observed to eventually occur, leading to demethylation.

Studies of HAT reactivity with complex **13** have focused on toluene derivatives as substrates. Complex **13** itself only displayed slow reactivity with toluene analogs, and the large kinetic isotope effect (KIE = 31) suggested a classical H-atom transfer mechanism followed by oxygen rebound to yield benzylic alcohols (Scheme 13).[97] Addition of $Sc(OTf)_3$ and HOTf resulted in ~2-100- and ~100-1000-fold increase in observed reaction rates, respectively. The small kinetic isotope effect observed at high concentrations of HOTf (KIE = 1 in the presence of 200 equiv. HOTf) indicated a shift in mechanism. As in the thioanisole and olefin cases, the first, rate-determining step in this reaction was assigned as a metal- or proton-coupled ET from substrate to **13**. Since the metal-containing product was identified as Fe^{III} species **25** (see Scheme 11) the second reaction step (transfer of O to the radical formed via ET) may involve comproportionation of Fe^{II} and Fe^{IV} species.

Scheme 13. Reactivity of Complex **13** with Toluene Derivatives.

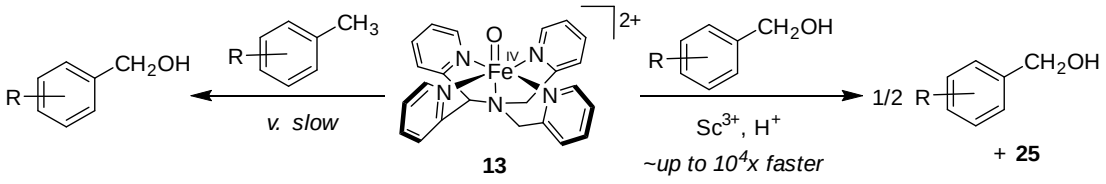

Mn complex **14**, supported by the same ligand scaffold as Fe species **13**, has been reported to display analogous OAT and HAT reactivity. The effects of Sc^{3+} binding on the group transfer reactivity of **14** were initially studied in the reaction of complexes **14** (no additives), **15** (one bound Sc^{3+}), and **16** (two bound Sc^{3+}) with thioanisoles. While

all three species underwent overall two-electron reduction processes consistent with O–atom transfer to substrate, the adducted species displayed faster (up to 22,000-fold) reaction rates.[100] Rate acceleration effects were ascribed to a similar shift in OAT mechanism from direct OAT to rate-determining MCET/PCET followed by oxygen transfer (Scheme 14), again based on rate dependence on ET driving force. Similar enhancements of reaction rates were observed when HOTf was used as the additive instead of $Sc(OTf)_3$.[102]

Scheme 14. Effects of $Sc(OTf)_3$ on OAT and HAT Reactivity of Mn Complex **14**-**16**.

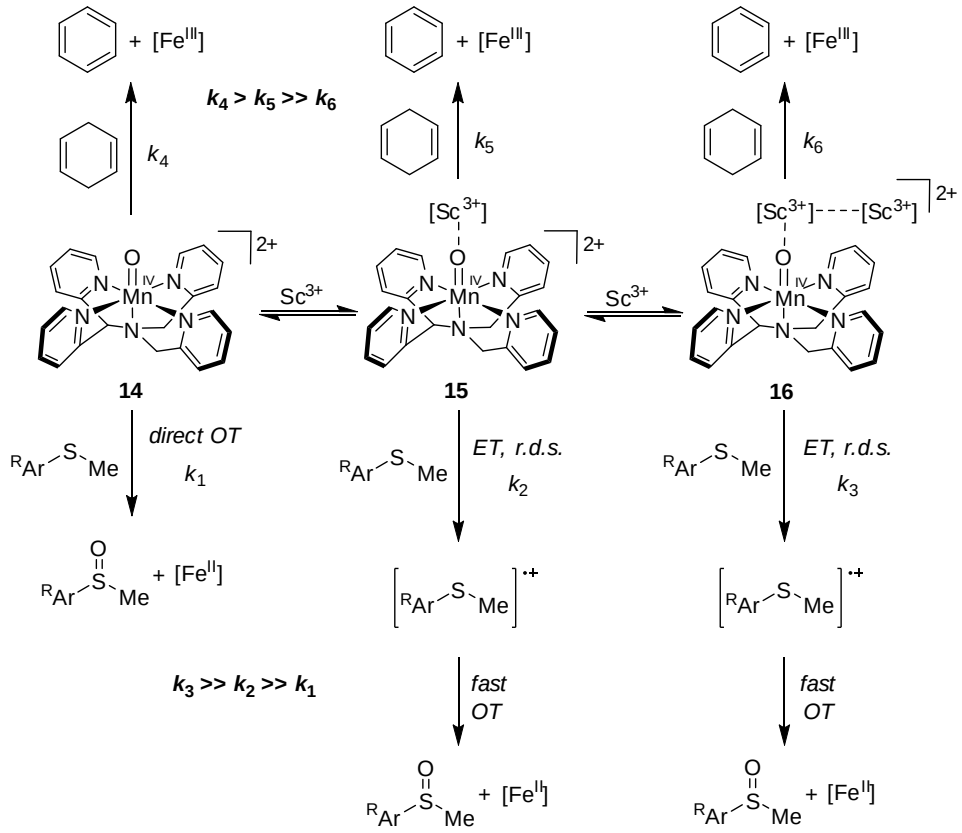

In studies that have not been reported for the related Fe system, effects of addition of $Sc(OTf)_3$ and HOTf on the rate of HAT to **14** were found to track inversely to those observed for OAT. Reaction of complex **14** with 1,4-cyclohexadiene (CHD) was 5 and 180 times faster than the 1:1 and 1:2 $[Mn]/Sc^{3+}$ adducts **15** and **16**, respectively.[100] This

change in relative reactivity was ascribed to the different steric requirements for the two reactions. While the rate-determining ET step in oxidation of thioanisoles is largely uninfluenced by the steric constraints due to Sc^{3+} binding, significant interaction between substrate and the Mn–O moiety is likely necessary in H-atom transfer. Sc^{3+} binding in **15** and **16** sterically hinders this interaction, resulting in slower reaction rates. Consistent with this steric argument, HOTf adduct **20** displayed HAT rates intermediate between those of **14** and **16** (~4-fold slower than **14**).[102] The smaller steric profile of the HOTf moieties (vs. the larger $Sc(OTf)_3$) resulted in a lesser extent of rate decrease in the case of HOTf than in that of $Sc(OTf)_3$. Parallel studies involving complexes **17-19** and **21** were reported, and yielded analogous results for both OAT and HAT reactivity.

Scheme 15. Effects of Binding of Lewis Acids on OAT and HAT Reactivity of Corrolazine-Supported Mn Complex **23**.

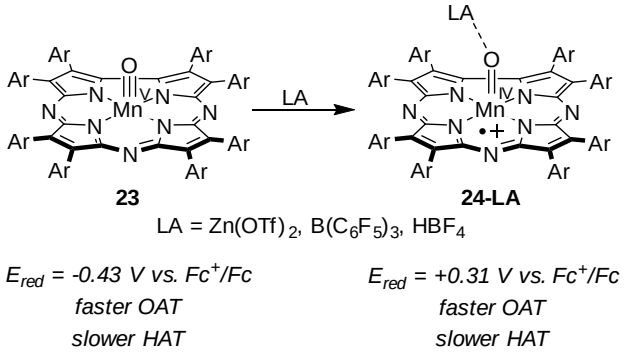

Studies by Goldberg and coworkers have shown that the effects of redox-inactive metal binding at a Mn^{V}–O supported by a corrolazine ligand extended to the OAT and HAT reactivity of this complex. Binding of Zn^{2+} to **23** to give valence tautomer complex **24-Zn** also resulted in slower rates (up to 10^4-fold) of OAT to phosphine substrates with respect to **23**.[108] Similar results were obtained when the Lewis acid $B(C_6F_5)_3$ or the Brønsted acid HBF_4 were used to generate the respective valence

tautomers **24-B(C_6F_5)$_3$** and **24-H** (Scheme 15) Analysis of various substituted triarylphosphines revealed that complexes **24-LA** were differently affected by the electronics of the substrate. While OAT reactivity was hindered by valence tautomerization, HAT processes were mildly enhanced, with **24-Zn** displaying rates ~3-fold faster than those for **23**. The observation of a faster HAT (a 1-e^- process) for valence tautomer **24-Zn** was rationalized on the basis of its reduction potential being ~0.7 V more positive than that of **23**. On the other hand, since OAT reactivity was assumed to occur via a concerted 2-e^- step (due to the high oxidation potential of triarylphosphines), the authors surmised that reactivity would be more closely influenced by the electrophilicity of the oxo ligand (higher in Mn^V complex **23** than in Mn^{IV} species **24-Zn**).

Scheme 16. Sc^{3+}-Induced Formation of a Co^{IV} Complex.

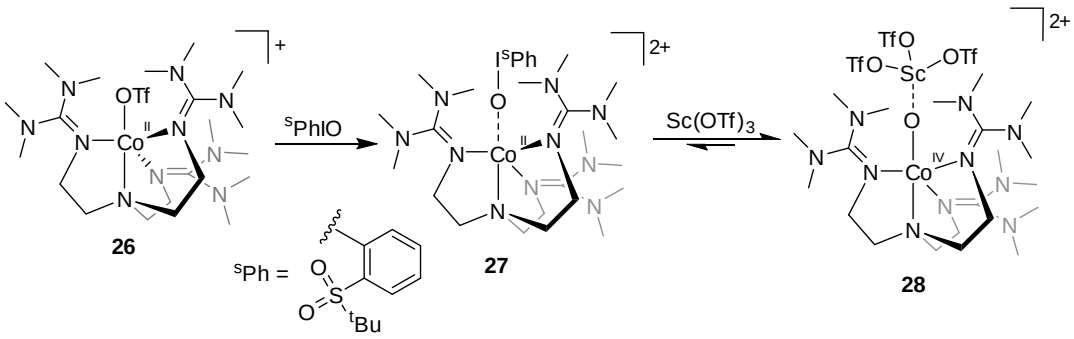

A single system involving a high-valent Co–oxo species binding redox-inactive metal ions has been described to date.[109] Co^{II} complex **26**, supported by the tripodal, neutral TMG_3tren ligand (TMG_3tren = tris[2-*N*-tetramethylguanidyl)ethyl]amine, Scheme 16), was shown to react with 2-(*tert*-butylsulfonyl) iodosobenzene (^{s}PhIO, an analog of PhIO soluble in organic solvents; 3 equiv.) to generate a new species in which a ^{s}PhIO molecule was bound to the Co^{II} center, with no electron transfer having occurred (**27**, Scheme 16).[109] The assignment of this product was made by the authors

on the basis of the similarity of EPR and XAS data to that of **26**, indicating that the Co had remained in the +2 oxidation state. The observation of mere coordination of ^{s}PhIO to the Co complex was ascribed to the inaccessibility of the Co^{II}/Co^{IV} couple in the given neutral ligand set. However, reaction between **26** and ^{s}PhIO in the presence of $Sc(OTf)_3$ resulted in generation of a species with different spectroscopic features. EPR, XAS, and EXAFS analyses indicated the presence of a more highly oxidized Co center than in **26** or **27**. A fifth O/N donor (together with the four ligand-based ones) located closer to Co than the ligand N donors was also observed. These observations led to the formulation of this product as $[Co^{IV}]$–O–$[Sc^{3+}]$ complex **28**. Sc^{3+}-bound complex **28** was found to be a more competent one-electron oxidant than **27**, reacting with both ferrocene and 1,1'-dibromoferrocene (E_{ox} = 0.31 V vs. Fc^{+}/Fc), while **27** was not reduced by the latter. Despite their differences in oxidation state and oxidizing power, complexes **27** and **28** displayed similar rates of OAT to triphenylphosphine (PPh_3), both of which were much lower than an analogous Fe^{IV}–O complex previously reported in the literature. Complex **27** exhibited a faster rate of HAT from 9,10-dihydroanthracene than the Sc-bound complex **28**. The differences between these Co complexes and their literature Fe precedent may be explained in terms of the higher oxyl radical character found in the Co–O motif than in the analogous Fe–O one.

The assignment of complex **28** as a $[Co^{IV}]$–O–$[Sc^{3+}]$ species, made by the authors in the original report on this chemistry, has since been challenged by other researchers. Borovik and coworkers have disagreed with the authors' assignment on the basis of their comparison of the above system with Co complexes supported by a different tripodal scaffold for which structural characterization by XRD methods was available.[110] In the single-crystal X-ray diffraction structure of a heterobimetallic Co^{III}

complex supported by a trianionic tris(sulfonamido) framework (**29**, Figure 7), a Co–O(H) bond distance of 1.85 Å was observed. This measure was identical to the Co–O distance in **28** as determined via EXAFS. Furthermore, Ray and coworkers had relied on the assignment of the observed 1.24 eV shift in edge energy in the XANES spectrum of **28** as evidence for the 2-e$^-$oxidation of a Co^{II} species to Co^{IV}. However, in the report by Borovik and coworkers the edge energy for Co^{III} complex **30** differed by 1.42 eV from its Co^{II} analog, even though these complexes were separated by a single oxidation state. Borovik and coworkers therefore proposed that a more accurate assignment of **28** would be as a Co^{III} complex bridged to Sc^{3+} by an $^-$OH ligand (**30**).

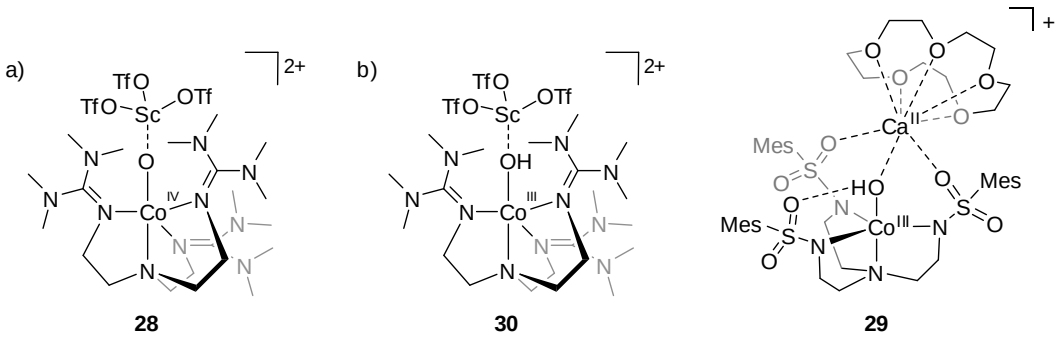

Figure 7. Structural assignments of complex **28** proposed by (a) Ray et al.[109] and (b) Borovik et al.,[110] and (c) the heterometallic Co^{III} complex **29** reported by Borovik et al.[110]

Cross-bridged cyclam-supported Mn^{II} and Mn^{IV} complexes **31** and **32** (Scheme 17) represent another example of reactivity modulation by Lewis acidic ions, and are involved in one of the rare examples of this type of heterometallic effects on a catalytic process. Complex **31** was found to be a competent, though sluggish, catalyst for oxygen atom transfer to thioanisole.[111] Addition of redox-inactive metal salts (Na^+, Mg^{2+}, Ca^{2+}, Al^{3+}, Sc^{3+}, Y^{3+}, and Yb^{3+}) to **31** led to a more efficient catalytic system, with accelerated oxygenation rates and increased conversion and yield. In stoichiometric studies with

Al^{3+} as an additive, Mn^{IV} species **32** also showed a moderate increase in sulfoxidation activity. In both the catalytic and stoichiometric systems, use of benzyl phenyl sulfide as substrate resulted in low sulfoxide yields, with C–S bond cleavage products representing a large fraction of the organic material produced. This observation was consistent with a mechanism similar to that for Fe- and Mn–oxo species reported by Nam and Fukuzumi[97,101] as described above – the initial step in the reaction was postulated to be MCET from thioanisole to the Mn complex. Formation of the S-centered radical in benzyl phenyl sulfide via oxidation by a Mn^{IV} species resulted in radical rearrangement, which accounted for the observed distribution of organic products. Yin and coworkers' investigation of stoichiometric oxygenation of triphenylphosphine by **32** is of particular note because it included direct rate comparison for a broad series of redox-inactive, Lewis acidic metals. Further analysis of the data from this report shows that log(reaction rate) and cation Lewis acidity are linearly correlated (Figure 8).

Scheme 17. Reactivity of Mn^{II} and Mn^{IV} Complexes Supported by Macrocyclic Ligand Scaffold.

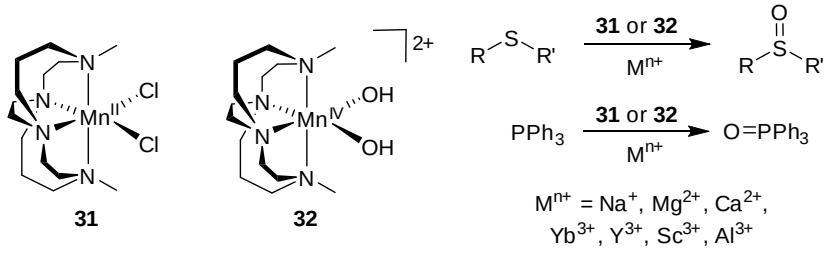

Cation binding to complex **31** and **32** also accelerated their rate of HAT from ethylbenzene, but these improvements were observed to be modest and the yields low. It must be noted that no structural characterization of the redox-inactive metal-bound species is available for either stoichiometric or catalytic systems. The oxidatively

competent species has been putatively assigned as a [Mn]–O–M^{n+} species by analogy with other published systems, but the cation binding processes in these complexes have not been elucidated further.

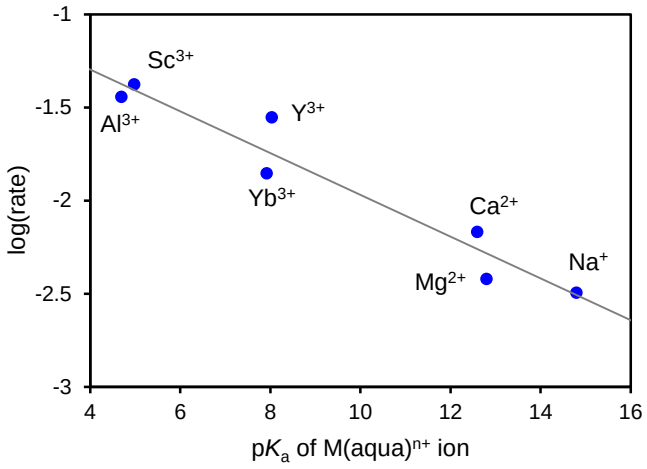

Figure 8. Plot of log(rate) vs. pKa of the metal aquo complex for oxidation of PPh_3 to $O{=}PPh_3$ by **32**. Derived from data from ref. 109.

As indicated by the many reports highlighted in this section, it is clear that the reactivity of redox-active complexes in the presence of Lewis acidic additives has been studied extensively. Binding of cations to the Fe–O, Mn–O, and Co–O motifs resulted in marked effects on reduction potential, which in turn engendered shifts in the mechanism of group transfer reactions including OAT and HAT. The substantial tuning of the redox potential of these redox-active complexes by Lewis acids resulted in many different transformations sharing a similar rate-determining step, an MCET or PCET process, including thioanisole and phosphine oxygenation, olefin epoxidation, and benzylic C–H bond oxidation. These results highlight the ability of redox-inactive moieties to profoundly affect redox processes without direct participation in the transfer of electrons.

2.2.5 Redox-Inactive Metal Effects on O_2 Release from Metal Peroxides.

Despite the elegance of the many examples of redox-inactive metal effects on oxidative behavior of redox-active complexes, none of these systems are involved in the specific reactivity that is displayed by the biological system that has inspired much of this work – water oxidation and O_2 evolution by the OEC. Although no report of the redox-inactive metal effects on water oxidation by homogeneous metal complexes has appeared in the literature, a recent publication by the groups of Nam and Fukuzumi has described effects of redox-inactive cations on the release of O_2 from Fe-peroxide species.[93,112] The modulation of the redox potential of complex **11** by bound Lewis acids was previously described in Section 2.2.3. An oxidation wave was observed electrochemically for complex **11** as well as cation-bound complexes **12-Ca** and **12-Sr**, though this redox event was absent from the CV of the adducts of other Lewis acids. The irreversible nature of this cathodic wave was shown to be due to the release of O_2 upon 1-e^- oxidation. Chemical oxidation of **11**, **12-Ca**, and **12-Sr** with ceric ammonium nitrate ($(NH_4)_2Ce(NO_3)_6$, CAN) also resulted in the release of O_2, which was detected by GC/MS methods (Scheme 18). Complexes **12-M** (M = Zn^{2+}, Lu^{3+}, Y^{3+}, Sc^{3+}), for which an oxidation wave was not observed by cyclic voltammetry, did not react with CAN, and no release of O_2 was detected (*vide infra* for reductive reactivity observed with more Lewis acidic ions).

It is notable that Ca^{2+} and Sr^{2+} are the only redox-inactive metals for which O_2 release from the Fe-peroxide complex is observed, because of their biological relevance – Ca^{2+} contained in the native OEC, and Sr^{2+} is the only metal that can recover any activity when substituting Ca^{2+}.[28,49,50] However, the observation that Lewis acid-free complex **11** is also capable of releasing O_2 upon oxidation implies that the role of Ca^{2+}

in the OEC cannot solely be to *promote* O_2 release. It is possible however, that Ca^{2+} (and Sr^{2+}) aids OEC function by *not hindering* release of O_2 (while also playing other roles), whereas a more Lewis acidic ion may prevent this step in water oxidation. Since the peroxide motif in **11** is not derived from H_2O, these findings shed little light on the mechanism of O–O bond formation. Nonetheless, they provide useful information on the subsequent reaction step – peroxide oxidation and O_2 release – and on the influence of redox-inactive metals on these processes.

Scheme 18. Lewis Acid-Induced O_2 Release from Fe-Peroxide Complexes.

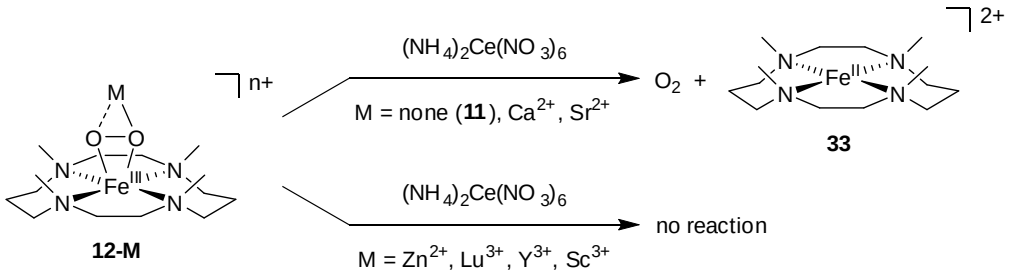

2.2.6 Redox-Inactive Metal Effects on ET and OAT in Cluster Complexes.

As described earlier, a key shortcoming of many of the systems studied for redox-inactive metal effects on redox processes is the lack of structural characterization of the reactive species that are directly responsible for ET, OAT, or HAT. The paucity of conclusive information on the structure of these species – which are often accessed by addition of excess amounts of Lewis acid additives – can complicate the interpretation of reactivity data. One of the means of avoiding this downside is to construct heterometallic complexes in which both redox-active and redox-inactive metal centers are bound to ligand scaffolds that preserve the structure of the cluster. Such constructs preclude the need for the use of excess amounts of redox-inactive metals, thereby simplifying structural characterization by XRD analysis and other spectroscopic techniques.

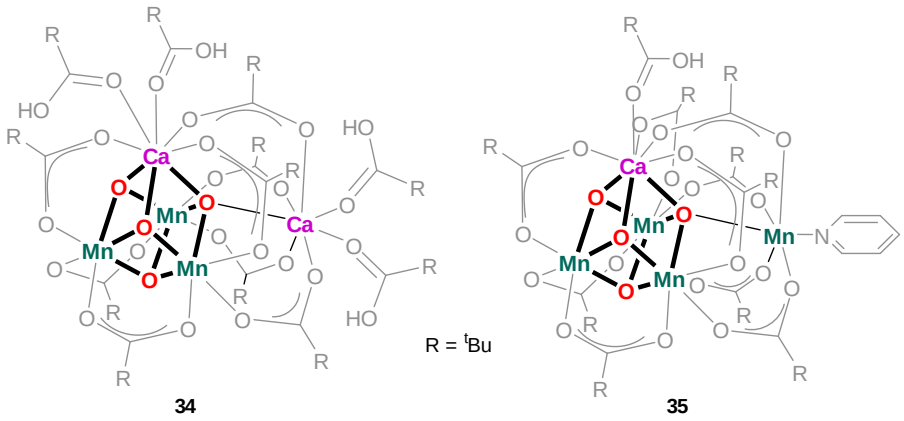

Figure 9. Models of the OEC synthesized via self-assembly.

The design of model complexes of polynuclear heterometallic clusters (such as the oxygen evolving complex itself) presents synthetic inorganic chemists with many challenges. The difficulty of precisely constructing such intricate complexes has forced researchers to rely heavily on self-assembly techniques. This synthetic approach offers very limited control on the stoichiometry and structure of the complexes that are isolated. Nonetheless, this strategy has been employed with occasional success in the modelling of the structure of the OEC. In 2011, Christou and coworkers were able to isolate a carboxylate-supported $Mn_3Ca_2O_4$ complex (**34**, Figure 9) containing a Mn_3CaO_4 cubane-like moiety analogous to that observed in the OEC.[113] The fourth, 'dangler' Mn center in the OEC was absent in **34** – its position was occupied by a second Ca atom. Spectroscopic studies corroborated that **34** was a reasonable structural model of the cubane subsite of the OEC. More recently, in 2015, Zhang, Dau, Dong, and coworkers reported the synthesis of an oxide-bridged cluster with the same metal composition as the OEC, displaying a cubane motif with a dangling Mn center (**35**).[114] This complex, supported by pivalate, pivalic acid, and pyridine ligands, was accessed via a one-pot procedure involving Mn and Ca acetate salts, pivalic acid, and permanganate (as O-atom transfer agent) followed by recrystallization in the presence

of pyridine. Electrochemical studies on **35** revealed multiple accessible redox states, which were interpreted by the authors in light of the S-state cycle of the biological OEC (**35** was isolated in the $[Mn^{III}_2Mn^{IV}_2]$ oxidation state, corresponding to the S_1 state). EPR studies further related complex **35** to the OEC, highlighting the usefulness of this model.

Despite reports of successful attempts in targeting specific clusters of this complexity via self-assembly, rational design of ligand scaffolds capable of supporting clusters would allow for higher control over the synthetic protocol. This approach would furthermore provide a strategy to systematically effect changes to various cluster features (e.g. structure, metal stoichiometry, supporting ligand sets, etc.) to allow structure-function relationship studies. In targeting synthetic models of biological iron-sulfur clusters, Holm and coworkers have relied on a site-differentiation approach in which a homometallic cluster fragment was supported by a multinucleating ligand scaffold. The resulting desymmetrized complex allowed incorporation of a heterometal in a facile and predictable manner to obtain series of heterometallic clusters. By adapting this approach designed for iron-sulfur clusters, our group has been able to isolate oxide-bridged clusters with specific metal compositions. Implementation of a strategy involving a multinucleating ligand provided a $[Mn_3CaO_4]$ model of the cubane subsite of the OEC, as well as allowing substitution of the Ca center for a variety of redox-active and redox-inactive metals. The same ligand scaffold has been used to study related Mn_3 and Fe_3 heterometallic complexes displaying a lower extent of oxide incorporation. The three resulting series represent one of the first systematic studies of the effects of Lewis acidity on the ET and OAT properties of fully structurally characterized clusters.

A triarylbenzene framework bearing three alkoxide and six pyridine donors (**36**) was shown to support homotrimetallic complexes of first-row transition metals[115,116] These complexes were used as precursors for preparation of tetrametallic metal-oxido clusters. Synthesis of higher-nuclearity species was achieved via treatment with an oxidant/O-atom source in the presence of a salt of the desired redox-inactive metal or, alternatively, via transmetallation from pre-formed heterometallic clusters bearing less Lewis acidic heterometals. Modification of reaction conditions allowed isolation of clusters displaying differences in ligand coordination mode and displaying varying oxygen-atom incorporation and, consequently, metal oxidation states. Treatment of the Mn^{II}_3 complex **37-Mn** with PhIO in the presence of $Ca(OTf)_2$, $Sr(OTf)_2$, $Na(OTf)$, or $Y(OTf)_3$ led to isolation of oxo/hydroxo complexes (**38-M**, Scheme 19). An analogous Zn complex was obtained via transmetallation from **38-M**.[82] In these complexes, the binding mode of the multidentate ligand observed in the trimetallic precursor was maintained: each alkoxide bridged two Mn centers and the two pyridine donors on each arm were bound to adjacent Mn centers. All four metal centers were observed to be bridged by an oxide ligand, while the apical, redox-inactive metal and one basal Mn center were bridged by a hydroxide ligand. The apical metal coordination sphere was completed by two acetate ligands (bridging to the two remaining Mn centers) and anions or solvent molecules, depending on metal identity. In two cases (Sr^{2+}, Na^+), the clusters were isolated as dimers. Assigment of the Mn oxidation states revealed a $[Mn^{III}_3]$ core. Notably, these clusters were originally characterized as containing two oxide ligands, implying different oxidation states (one electron more oxidized). The adjusted structural assignment was made on the basis of structural comparisons with the analogous Fe_3 complexes (*vide infra*), as well as EPR data and DFT calculations.[117]

Scheme 19. Synthesis of Heterometallic Mn_3 and Fe_3 Clusters

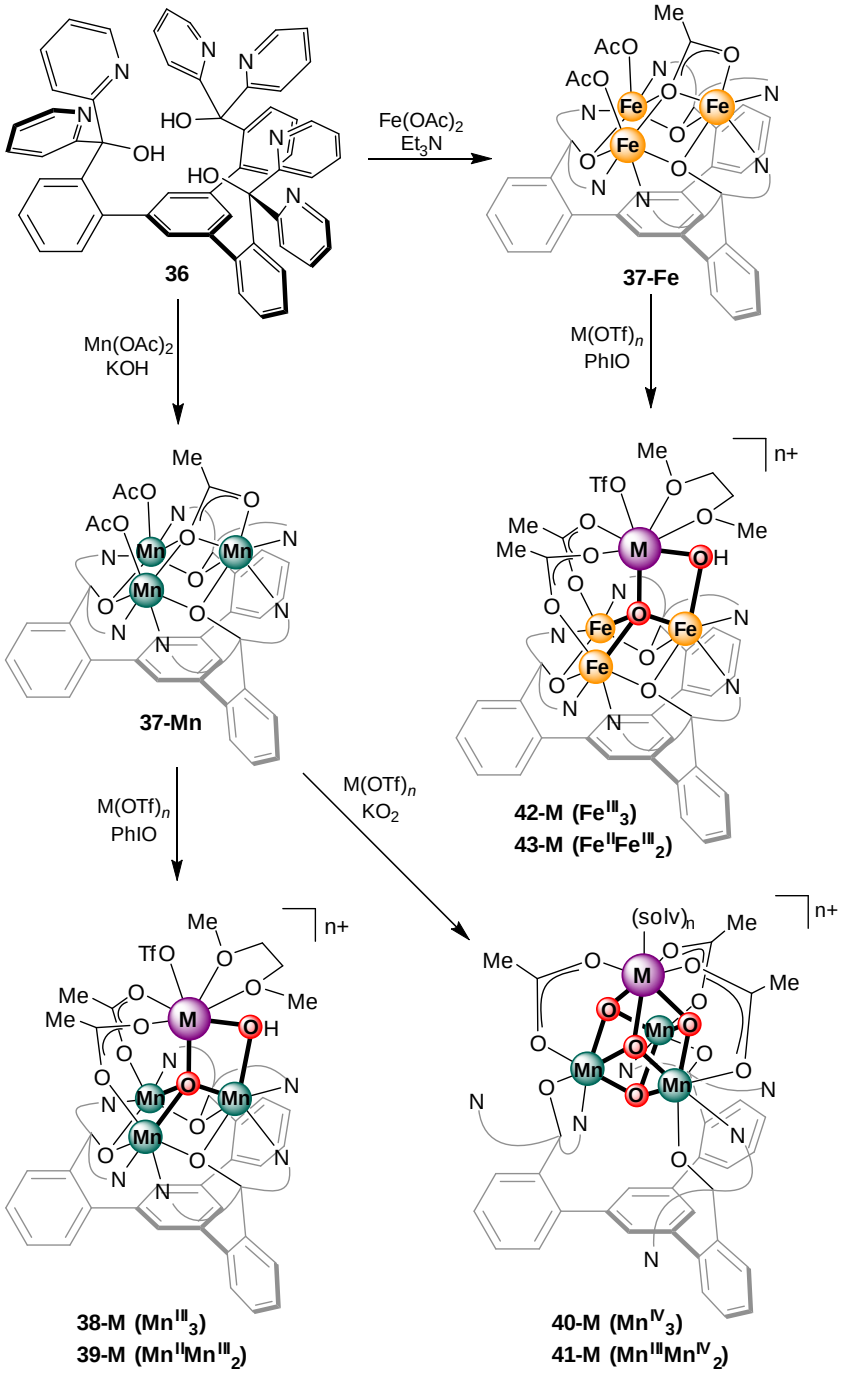

The Lewis acidity of the redox-inactive metal incorporated in the clusters directly influenced the electronics of the cluster as displayed in the shift in redox potential across the series of compounds. Electrochemical data indicated that $E_{1/2}$ values for the

$[Mn^{III}_3]/[Mn^{III}_2Mn^{II}]$ couple ranged from -0.30 V vs. Fc^+/Fc for **38-Na** to +0.42 V for **38-Y**. The $E_{1/2}$ values correlated linearly with Lewis acidity as measured by the pK_a value of the metal aquo ions of these redox-inactive metals (Figure 10).[81] Furthermore, the broad range of Lewis acidities investigated allowed for a more accurate quantitative interpretation of the trend than literature reports focusing on narrow Lewis acidity windows. For complexes **38-M**, a change of one pK_a unit corresponded to a potential shift of ~0.1 V. These results confirmed that redox-tuning of clusters by Lewis acids is a possible role of redox-inactive metals in both biological systems (e.g. PSII) and heterogeneous materials (e.g. birnessites).

A separate series of complexes was obtained via a slight modification of the conditions used to isolate complexes **38-M**. Treatment of the same Mn^{II}_3 precursor **37-Mn** in the presence of Ca^{2+} or Sr^{2+} with potassium superoxide (in place of PhIO) led to formation of tetraoxide clusters displaying a Mn_3MO_4 'cubane' structural motif, with the redox-inactive metal again situated at the site-differentiated apical position.[118,119] As observed in the XRD-derived structures for these complexes, a shift in the binding mode of the multidentate ligand was engendered by incorporation of the four oxide ligands, resulting in terminal alkoxide donors and one unbound pyridine on each ligand arm. Acetate ligands bridged each face of the *pseudo*-C_{3v}-symmetric cubane core (the overall complexes have *pseudo*-C_3 symmetry). The Mn centers in complexes **40-Ca** and **40-Sr** were in the Mn^{IV} oxidation state. Related clusters with different metal compositions were accessible via transmetallation from **40-Ca** with a variety of alkali, alkaline earth, rare earth, and transition metal salts.[120-122] Furthermore, the analogous all-Mn cubane complex was isolated by treatment of **37-Mn** with permanganate, which could supply all the required oxidizing, O-atom, and Mn equivalents.[118] In this case, the

cluster was isolated in the $Mn^{III}_2Mn^{IV}_2$ oxidation state (**41-Mn**). Similar to what was observed for the clusters **38-M**, the electronics of the cubane complexes were markedly affected by the Lewis acidity of the apical metal. The redox potentials for the $[Mn^{III}Mn^{IV}_2]/[Mn^{IV}_3]$ couple in these complexes, ranging from -0.944 V vs. Fc^+/Fc for **40-Sr** to 0.29 V for **41-Mn**, are listed in Table 5. These values also correlated linearly with Lewis acidity (Figure 10). Despite the differences in structure and overall oxidation state between the two series of clusters, a similar linear fit slope was observed for complexes **38-M** and **40-M** (~ 0.10 V/pK_a unit).

It is notable that the cubane clusters **40-Ca** and **40-Sr** displayed nearly-identical redox potentials, as they contain the only two metals that can be incorporated in the biological OEC to obtain a functional enzyme (the native enzyme in the case of Ca^{2+}, a less efficient analog in the case of Sr^{2+}). Furthermore, the large difference in potential between **40-Ca** and **41-Mn** (>1.2 V) may suggest a possible role of Ca^{2+} in H_2O oxidation in PSII.[118] To oxidize water, storage of four oxidizing equivalents within the OEC cluster is required. The presence of the redox-inactive Ca^{2+} dication may enable buildup of localized charge at the Mn centers, facilitating oxidation. While the overall charge of the tetrametallic cores in **40-Ca** and **41-Mn** is the same ($[M_3M'O_4]^{6+}$), their redox potential is vastly different. As a consequence, in **41-Mn**, a $[Mn^{III}_2Mn^{IV}_2]$ core is observed, whereas three Mn^{IV} centers are accessed in **40-Ca**.

Table 5. Electrochemical redox potentials of Mn oxo-hydroxo, Mn tetraoxo, and Fe oxo-hydroxo complexes. Potentials given in V vs. Fc^+/Fc.

M	pK_a[a]	38-M[a]	40-M[a]	42-M[a]
Na^+	14.8	-0.305	-	-
Sr^{2+}	13.2	-0.072	-0.944	-0.49
Ca^{2+}	12.6	-0.071	-0.94	-0.48
Ni^{2+}	9.4	-	-0.599	-
Zn^{2+}	9.3	0.163	-0.628	-0.20
La^{3+}	9.06	-	-0.487	-0.08
Cu^{2+}	9.02	-	-0.589	-
Nd^{3+}	8.43	-	-0.435	-
Gd^{3+}	8.35	-	-0.432	-
Eu^{3+}	8.31	-	-0.429	-
Tb^{3+}	8.16	-	-0.408	-
Dy^{3+}	8.1	-	-0.413	-
Y^{3+}	8.04	0.419	-0.428	-
Yb^{3+}	7.92	-	-0.381	-
Sc^{3+}	4.79	-	-0.246	0.07
Fe^{3+}	2.81	-	0.291	-
Co^{3+}	0.66	-	0.258	-
Mn^{3+}	0.1	-	0.29	-

[b] pK_a of $M(aqua)^{n+}$ complex.[81] [b] $[Mn^{III}_3]/[Mn^{III}_2Mn^{II}]$ couple. [c] $[Mn^{III}Mn^{IV}_3]/[Mn^{III}_2Mn^{IV}_2]$ couple. [d] $[Fe^{III}_3]/[Fe^{III}_2Fe^{II}]$ couple.

Complexes containing a fourth redox-active metal are a peculiar subset of cubane clusters **41-M**. In these species (M = Fe, Co, Ni, Cu) the apical metal could affect the oxidation state of the isolated complexes.[121] Transmetallation from **40-Ca** with Fe^{2+} led to isolation of a cluster in the $[Fe^{III}Mn^{III}Mn^{IV}_2]$ oxidation state (**41-Fe**), as assigned by Mössbauer spectroscopy. Under similar conditions with Co^{2+}, **40-Co** was accessed in

an intermediate oxidation state between [$Co^{III}Mn^{III}Mn^{IV}_2$] and [$Co^{II}Mn^{IV}_3$]. A key difference between the cyclic voltammograms of the four clusters discussed was that two redox events were observed for **41-Fe** and **40-Co**, while **40-Ni** and **40-Cu** displayed only one redox event within the *ca.* 3 V range of solvent window (dimethylacetamide, DMA). The redox potentials observed from cyclic voltammetry studies of these clusters may give insight into the differences in performance of mixed-metal oxides used for ORR and/or OER catalysts and Li-ion batteries. In the latter case, where the presence of other transition metals (Fe, Co, Ni and Cu) strongly influences the response of $LiMn_2O_4$ spinel as cathodes in lithium cells, [123-125] the possibility of two redox processes being accessible in the case of **41-Fe** and **40-Co** vs. only one event in **40-Ni** and **40-Cu** suggested that the presence of a more electronegative metal center shifted the reduction of Mn towards more positive potentials. This difference could be attributed to the more covalent Fe^{3+}–oxo or Co^{3+}–oxo interaction based on these apical metals being more electronegative than Ni^{2+} or Cu^{2+}, thus allowing more facile electron transfer to the basal Mn centers.

Recently, desymmetrization of a C_3-symmetryic cubane complex and binding of a fifth metal center to the tetranuclear cluster was reported. Binding of a single additional metal center was attempted with **40-Ca** to target a full model of the OEC cluster ([Mn_4CaO_n]). Substitution of two of the $^-$OAc ligands in **40-Ca** with a multidentate bis(oximate) ligand yielded complex **44** (Scheme 20), though its insolubility in organic solvents prevented its structural characterization.[126] While substitution of the Ca^{2+} center in tris(acetate) complex **40-Ca** with more Lewis acidic metals was observed to be facile, the bis(oximate) ligand in **44** was observed to prevent this undesired process. Treatment of **44** with excess AgOTf led to binding of Ag^+ to the cluster as determined

by XRD (**45-Ag**) – though the poor quality of the crystal samples only provided connectivity information.

Scheme 20. Incorporation of a Fifth Metal Center in Cubane Cluster **40-Ca**.

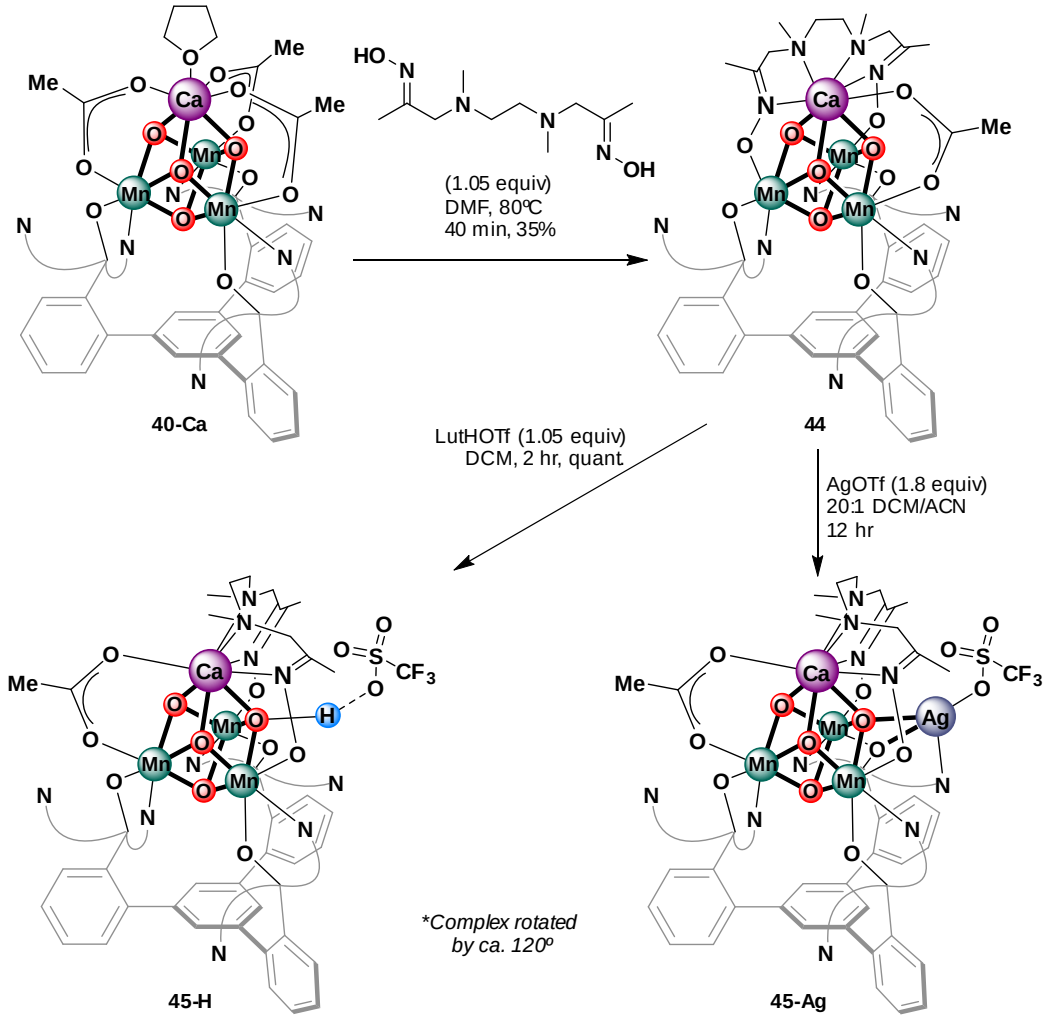

Binding of Ag^+ to the cluster occurred via one of the μ_3-O ligands from the cubane motif, and one of the unbound pyridines and one Mn-bound alkoxide from the multinucleating ligand framework. The coordination sphere of Ag^+ was completed by $^-$OTf. Treatment of **44** with HOTf (in the form of protonated 2,6-lutidine) resulted in protonation at the same μ_3-O ligand (**45-H**), indicating that the desymmetrization of **40-Ca** resulted in accumulation of electron density at a specific oxide ligand.

A third series of heterometallic clusters supported by this same multidentate ligand was built on Fe_3 complex **37-Fe**, analogous to the Mn_3 species **37-Mn**. Under similar conditions to those used to isolate clusters **38-M**, structurally analogous oxo/hydroxo clusters **42-M** (M = Ca^{2+}, Sr^{2+}) were obtained.[127] Observation of hydroxo-bridged clusters has been assumed to be a result of the instability of the [M^{IV}–O] species (M = Mn, Fe) that would result from four-electron oxidation of precursors **37-M** by PhIO. Any [M^{IV}–O] species generated during the reaction may be sufficiently oxidizing to abstract an H-atom (likely from solvent), yielding the hydroxide-bridged clusters. The assignment of the μ_2-bridge in clusters **42-M** as a hydroxo moiety was indicated by charge balance in the solid state structure, bond metrics of the Fe–O(H) bond (too long for a Fe^{III}–O bond based on literature examples), and the confirmation of Fe oxidation states via Mössbauer spectroscopy. Under analogous reaction conditions, addition of $Sc(OTf)_3$ in place of $Ca(OTf)_2$ led to isolation of the 1-e^- reduced Sc^{3+} cluster **43-Sc**. Sc^{3+} complex **42-Sc** may be a sufficiently strong oxidant to be reduced *in situ* by any [Fe^{II}] species in solution. Transmetallation from the Ca complex yielded clusters **42-Zn** and **42-La** to provide a five-complex series with redox-inactive metals spanning nine pK_a units. Three of the clusters were characterized in the $Fe^{III}Fe^{II}_2$ oxidation state (**43-M**) (M = Sc^{3+}, Ca^{2+}, and La^{3+}), the latter two via chemical reduction with cobaltocene ($E_{1/2}$ = -1.34 V vs. Fc^+/Fc). Oxidation states were again confirmed by Mössbauer spectroscopy. Crystallographic characterization revealed that the one-electron reduction event occurred at one of the two Fe centers that are *not* bound to the hydroxide bridge. This observation is intriguing as it implied that H-atom abstraction from one of these reduced complexes would proceed via transfer of the hydroxide proton concurrent with the electron transfer from a Fe center not directly bound to the

source of the proton, and only few reports have described this type of H-atom transfer reactivity. As with the other two cluster series, complexes **42-M** displayed a shift in redox potential upon changes in the Lewis acidity of the apical metal, with the $[Fe^{III}_3]/[Fe^{III}_2Fe^{II}]$ couple ranging from -0.49 V vs. Fc^+/Fc for Ca^{2+}/Sr^{2+} to +0.70 for Sc^{3+}.

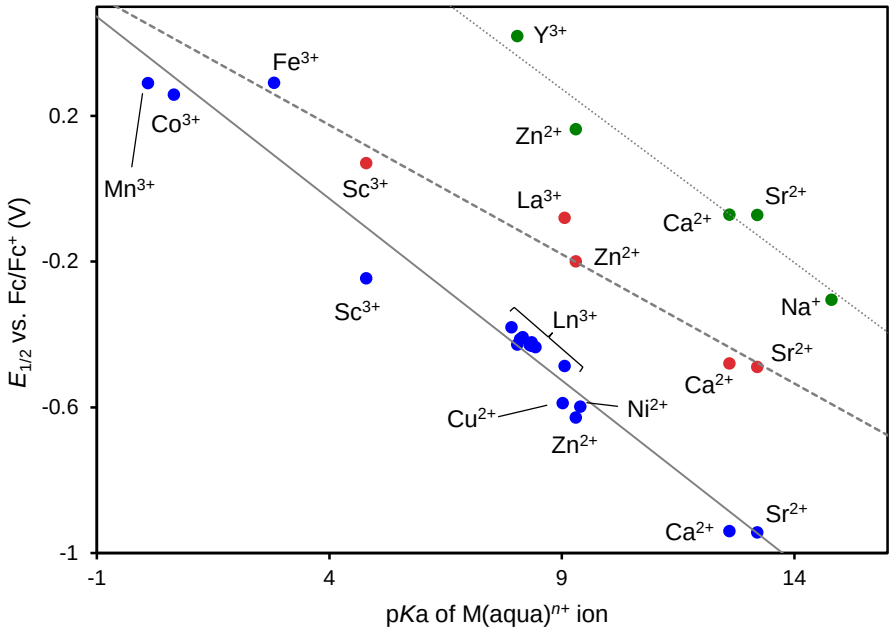

Figure 10. Plots of redox potential vs. Lewis acidity for **40-M** (blue),[118-121] **42-M** (green),[127] and **38-M** clusters (red).[82] Ln^{3+} = La^{3+}, Nd^{3+}, Eu^{3+}. Gd^{3+}, Tb^{3+}, Dy^{3+}, Yb^{3+}, Y^{3+}.

All potentials for **42-M** complexes are listed in Table 5. As before, $E_{1/2}$ values correlated linearly with the pK_a of the metal aquo complexes. However, the slope of the linear fit for the Fe_3 complexes was different, ~0.07 V/pK_a unit, from those of either Mn_3 series (Figure 10). One possible explanation for this observation is based on a similar analysis to that described by Nam and Fukuzumi for metal-coupled electron transfer.[18,98] The shift in redox potential of a redox-active species upon binding of a cation is due to the stronger interaction of this Lewis acid with the reduced complex

than with the oxidized species. Quantitatively, this shift is described by equation (1), which cannot be applied to the case of clusters **38**-**43** because the redox-inactive metals are always bound in these systems. Nonetheless, qualitatively, the potential shift in complexes **38-M** and **42-M** can be interpreted as the result of stronger interactions between a Lewis acid and the trimetallic core in the reduced state vs. the oxidized state. Since the Mn and Fe centers in complexes **38-M** and **42-M** are in identical coordination environments, their respective Lewis acidities can be used as reporters of their abilities to interact with bridging ligands. The drop in Lewis acidity upon reduction from M^{3+} to M^{2+} is larger for Mn (~11 pK_a units) than for Fe (~7 pK_a units).[128] Therefore, the interaction between the Mn center and its ligands will be more weakened by reduction than that of a corresponding Fe center, resulting in larger accumulation of electron density on the brdiging ligands in the case of Mn than for Fe. As a consequence, a larger gain in interaction between the redox-inactive metal ion and these ligands is expected in Mn complexes than in their Fe counterparts, resulting in larger relative stabilization of reduced Mn centers vs. Fe ones. The stronger interaction between redox-inactive metal and bridging ligands in Mn complexes **38-M** results in a larger shift in redox potential as a function of Lewis acidity than for Fe complexes **42-M**, giving rise to the different linear correlations between Lewis acidity and redox potential. Unfortunately, the differences in structure and overall oxidation state between clusters **38-M** and **40-M** make an analogous analysis to explain their similar redox potential trend impossible. The observation of a similar trend in the presence of said large structural and electronic differences, however, may hint at a pure coincidental reason for the observation of the similar slope in Figure 10 for clusters **38-M** and **40-M**.

Together with redox potential, the Lewis acidity of the redox-inactive metals incorporated into complexes **38-M**, **40-M** and **42-M** was also found to influence the rate of OAT from the clusters to phosphine substrates. Complexes from each series were reacted with various phosphines (trimethyl-, triethyl-, or triphenylphosphine), and the relative OAT rates displayed by these systems followed the same trends as their redox potentials.[117] Reaction conditions and the rates observed in these studies are listed in Table 6. Complexes **40/41-M**, from the least oxidizing cubane series, displayed the slowest rates of OAT as monitored via ^{1}H nuclear magnetic resonance (^{1}H NMR). Mn_3 oxo/hydroxo complexes **38/39-M** exhibited the fastest rates of OAT, in accordance with their more positive redox potentials. Fe_3 complexes **42/43-M** displayed intermediate reactivity, akin to their intermediate redox potentials. In the case of **40/41-M**, the metal-containing products were identified as trioxo complexes **46-M** (Scheme 21), in which the site of the bottom oxide ligand was vacant. Structural identification of metal-containing products was unsuccessful for either set of oxo/hydroxo complexes, though NMR data for the products of reactions involving complexes **38/39-M** showed broad paramagnetic signals consistent with $[Mn^{II}_3]$ complexes similar to **37-Mn**.

Table 6. OAT Reactivity of Complexes **38-M**-**43-M**.[117]

Complex	M_3 Ox. State	pK_a[a]	Substrate (equiv.)	Time	T(°C)
40-Sc	Mn^{IV}_3	4.8	PMe_3 (2)	N.R.[b]	r.t.
40-Ca	Mn^{IV}_3	12.9	PMe_3 (2)	N.R.	r.t.
41-Mn	$Mn^{IV}_2Mn^{III}$	0.1	PMe_3 (2)	15 min	r.t.
41-Co	$Mn^{IV}_2Mn^{III}$	0.66	PMe_3 (2)	2 h	r.t.
41-Sc	$Mn^{IV}_2Mn^{III}$	4.8	PMe_3 (10)	1.5 weeks	r.t.
41-Sc	$Mn^{IV}_2Mn^{III}$	4.8	PMe_3 (10)	35 h	50 °C
41-Gd	$Mn^{IV}_2Mn^{III}$	8.4	PMe_3 (10)	>2 weeks	r.t.
41-Gd	$Mn^{IV}_2Mn^{III}$	8.4	PMe_3 (10)	50 h	50 °C
(38-Y)$_2$[c]	Mn^{III}_3	8.6	PEt_3 (10)	15 min	r.t.
(38-Y)$_2$[c]	Mn^{III}_3	8.6	PPh_3 (10)	30 min	r.t.
38-Ca	Mn^{III}_3	12.9	PEt_3 (10)	3 h	r.t.
38-Ca	Mn^{III}_3	12.9	PPh_3 (10)	20 h	r.t.
39-Y	$Mn^{III}_2Mn^{II}$	8.6	PEt_3 (10)	30 min	r.t.
39-Y	$Mn^{III}_2Mn^{II}$	8.6	PPh_3 (10)	1 h	r.t.
39-Ca	$Mn^{III}_2Mn^{II}$	12.9	PEt_3 (10)	36 h	r.t.
42-La	Fe^{III}_3	9.06	PPh_3 (10)	24 h	r.t.
42-Ca	Fe^{III}_3	12.9	PPh_3 (10)	N.R.	r.t.
43-Sc	$Fe^{III}_2Fe^{II}$	4.8	PMe_3 (10)	14 h	r.t.
43-La	$Fe^{III}_2Fe^{II}$	9.06	PMe_3 (10)	130 h	r.t.
43-Ca	$Fe^{III}_2Fe^{II}$	12.9	PMe_3 (10)	270 h	r.t.

[a] pK_a of $M(aqua)^{n+}$ complex.[81] [b] N.R. = no reaction. [c] complex **38-Y** was isolated as a dimer

Scheme 21. OAT Reactivity of Clusters **38-M**-**43-M**.

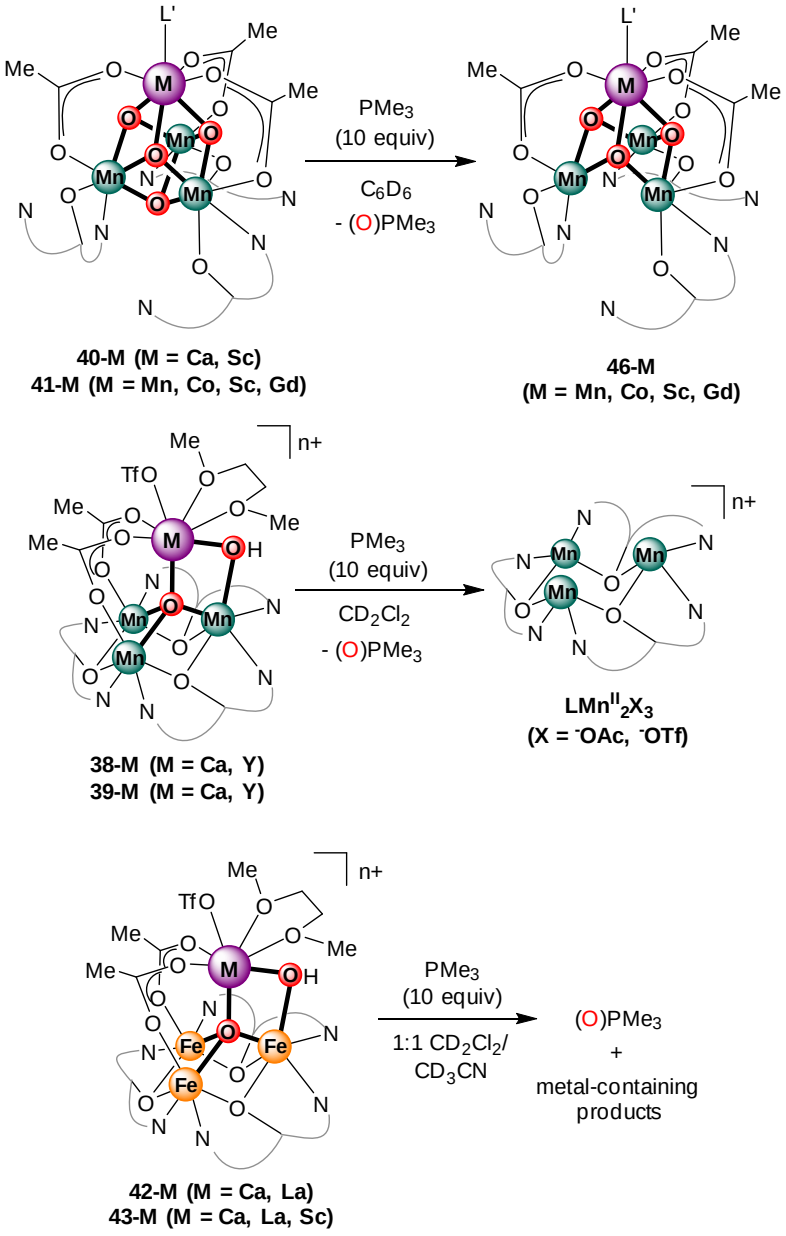

2.3 Effects of Redox-Inactive Metals on Reductive Reactivity

Although most of the reports of redox-inactive metal effects on redox processes have focused on oxidative chemistry, several instances of effects on substrate reduction have also been described. These systems have been involved in O_2 reduciton, O–O bond cleavage in peroxides, and N_2 reduction, among others.

2.3.1 Electron Transfer

The modulation of the ET behaviour of a Ce^{III} complex by redox-inactive metals whose binding was shown to affect ligand reorganization was reported by the groups of Walsh and Schelter. Binding of alkali metal centers (Li^+, Na^+, K^+, Cs^+) to a homoleptic (S)-binolate Ce^{III} complex occurred with coordination of three ions to the O moieties of adjacent binolate ligands to give heterotetrametallic complexes **47-M** (Scheme 22).[129,130] The identity of the redox-inactive metal displayed a marked effect on the redox behavior of complexes **47-M**, as shown in Table 7. The irreversible redox events observed via cyclic voltammetry were observed to shift by 0.6 and 0.3 V for the anodic and cathodic peak currents, respectively. The large peak-peak separations observed in the cyclic voltammograms of these complexes were rationalized by the authors in terms of the slow kinetics of heterogeneous ET. Surprisingly, although the ET rates from cyclic voltammetry were observed to be faster for the less Lewis acidic ions ($k_{Li} < k_{Na} < k_K < k_{Cs}$), the rates of chemical oxidation of **47-M** followed the inverse trend. This result was taken to indicate a shift in ET mechanism from outer-sphere to inner-sphere ET. The steric accessibility of the Ce center, higher for the smaller Li^+ ion than the larger K^+, strongly affected the latter process, leading to faster (up to 120-fold) chemical oxidation of **47-Li** than **47-Na** and **47-K**.

Scheme 22. Modulation of Reactivity of Ce Complexes by Alkali Metals.

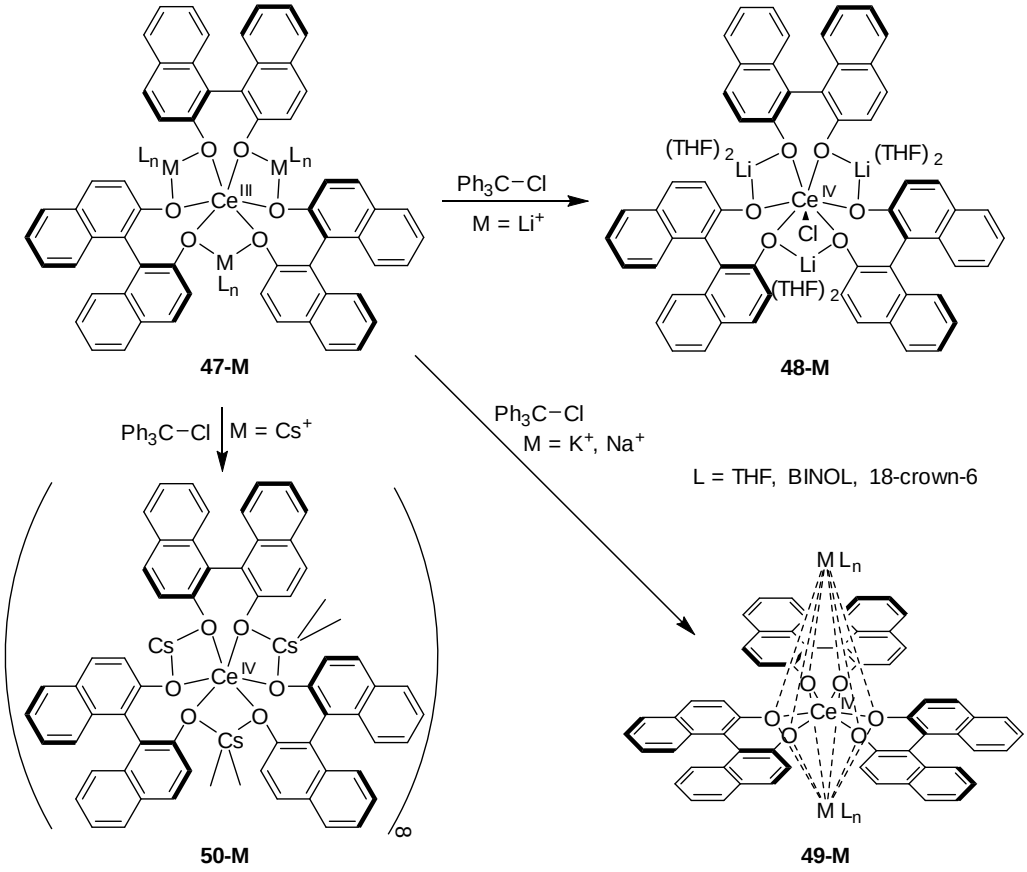

Chemical oxidation also resulted in the isolation of different products depending on the identity of the alkali metal. Oxidation of **47-Li** resulted in halide incorporation into the Ce^{IV} product (**48-Li**) and retention of the three Li^+ centers. However, upon oxidation, complexes of Na^+ and K^+ underwent loss of M–X (M = alkali metal, X = halide) and displayed a shift in binding mode of the two remaining redox-inactive ions to the axial faces of the tris(binolate) Ce^{IV} complex (**49-M**). This result was consistent with the large differences observed electrochemically between **47-Li** and the other alkali metal complexes. Oxidation of complex **47-Cs**, finally, led to isolation of a coordination polymer in which adjacent Ce complexes were linked via Cs–O and Cs–π interactions (**50-Cs**). Effects of the Lewis acidity of the alkali metals on the redox potential and

ligand-to-metal charge transfer (LMCT) band in the UV-Vis spectra of complexes **48**-**50** were also observed, although the structural differences in these complexes complicate direct comparison of these values (Table 7).

Table 7. Electrochemical and UV-Vis data for complexes **47**-**50**.[129,130] Potentials given in V vs. Fc^+/Fc.

Complex	pK_a[a] of Alkali Ions	E_{pa}	E_{pc}	$E_{1/2}$	LMCT[b]
47-Li	13.8	-0.475	-1.065	-	-
47-Na	14.8	-0.905	-1.245	-	-
47-K	15-15.5[c]	-1.065	-1.365	-	-
47-Cs	~15.5[c]	-1.100	-1.290	-	-
48-Li	13.8	-	-	-0.885	2.05
49-Na	14.8	-	-	-1.163	2.20
49-K	15-15.5[c]	-	-	-1.245	2.25
50-Cs	~15.5[c]	-	-	-1.275	2.30

[a] pK_a of metal aquo ions. [b] $1/\lambda_{max}$($\times 10^{-4}$ cm^{-1}). [c] An exact pK_a value for K^+ and Cs^+ comparable with the scale used herein for other metal ions is not available.

2.3.2 O_2 Reduction.

The most extensive screening of the effects of Lewis acidic metal salts on the same system is the study of O_2 activation by a Co porphyrin species by Fukuzumi, Otera, and coworkers.[131,132] Tetraphenylporphyrin-Co complex **51** displayed no reactivity with O_2, in agreement with its high oxidation potential (E_{ox}(**51**) = -0.03 V, $E_{red}(O_2)$ = -1.24 V vs. Fc^+/Fc). Addition of redox inactive metal salts resulted in one-electron reduction of O_2 as monitored by UV-Vis and EPR spectroscopies (Scheme 22). The rate of electron transfer increased dramatically as Lewis acidity increased. A plot of log(k) vs. Lewis

acidity (measured via Fukuzumi's EPR method)[96] revealed a striking linear correlation highlighting the rate-accelerating effects of binding of M^{n+} ions to superoxide.

Scheme 22. Modulation of O_2 Reduction with Complex **51** by Lewis Acids.

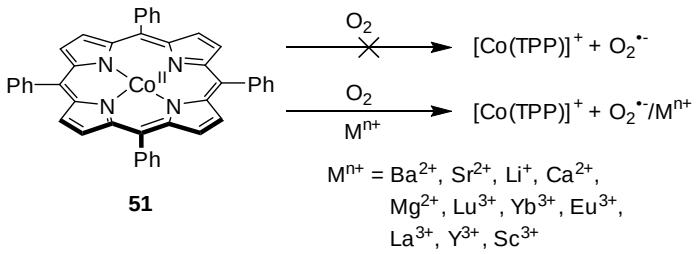

51

Scheme 23. Reactivity of Complexes **52-M** in the Presence of Redox-Inactive Metals.

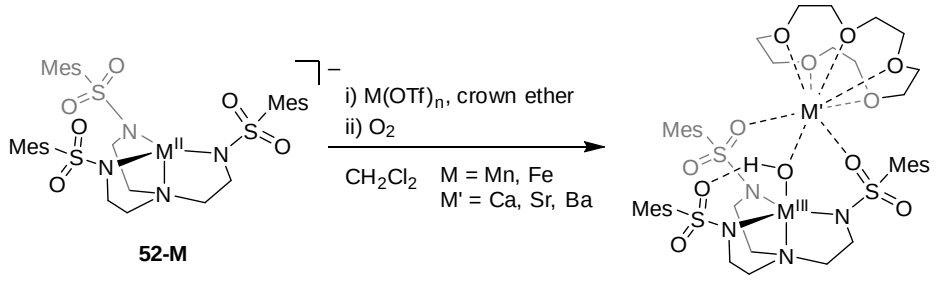

52-M

53-M-M'

Redox-inactive metal effects on O_2 reduction were also observed by Borovik and coworkers in their studies on a tripodal tris(sulfonamido) ligand scaffold (Scheme 23).[133,134] Monometallic species **52-M** (M = Mn, Fe) displayed only slow reactivity towards O_2. Rate of O_2 reduction was however accelerated by the presence of Lewis acidic metal salts (Ca^{2+}, Sr^{2+}, Ba^{2+}). Crystallographic characterization of the products of these reactions revealed heterobimetallic complexes **53-M-M'** in which the redox-active metal center (now in the M^{III} oxidation state) was bridged to the redox-inactive metal center by a hydroxide ligand. The sulfonamido S–O groups were key to stabilization of these complexes, as they served as additional donors for the redox-inactive metals, and these moieties also provided a H-bonding network to support the OH bridge (Scheme 23).

Table 8. Kinetic data for reaction of complex **52-Fe** with O_2 in the presence of Lewis acids.[133]

Lewis Acid	pK_a[a]	Initial Rate (s^{-1})	Rate Relative to 52-Fe
-	-	$2.2 \pm 0.1 \times 10^{-4}$	1
Ba^{2+}	13.4	$2.3 \pm 0.6 \times 10^{-3}$	10
Sr^{2+}	13.2	$7.4 \pm 1.6 \times 10^{-3}$	34
Ca^{2+}	12.6	$7.9 \pm 0.4 \times 10^{-3}$	36

[a] pK_a of metal aquo ions.[81]

Table 9. Electrochemical data for complexes **53-M-M**.[133,134]

Complex	pK_a[a]	$E_{1/2}$
53-Fe-Ca	12.6	-1.13
53-Fe-Sr	13.2	-1.12
53-Fe-Ba	13.4	-1.22
53-Mn-Ca	12.6	-0.72
53-Mn-Sr	13.2	-0.70
53-Mn-Ba	13.4	-0.76

[a] pK_a of metal aquo ions.[81]

Isotopic labelling confirmed that the oxygen atom in the OH bridge was derived from molecular O_2. However, the stoichiometry of the reaction and the source of the hydroxide proton were not discussed by the authors. Analysis of the rate acceleration by the redox-inactive ions showed that Ca^{2+} and Sr^{2+} displayed similar effects, while rate enhancement by Ba^{2+} was lower (Table 8). The similar electrochemical behavior of the Ca^{2+} and Sr^{2+} complexes led the authors to assert that Lewis acidity was not sufficient to explain the observed trends (Table 9). At the same time, the differences in size between the two ions notwithstanding, Ca^{2+} and Sr^{2+} do display similar Lewis acidities, whether measured by the pK_a of the metal aquo complex or by the method of Fukuzumi.[96,131] Similarity of the effects of these two ions on the same system may

therefore be expected. A possible mechanism for the O_2 activation reaction was also proposed by the authors, involving initial formation of a Mn- or Fe-bound superoxide species that is stabilized by interaction with the redox-inactive metal, akin to the reactivity observed by Fukuzumi and coworkers with complex **51**.

Scheme 24. Reactivity of **52-Fe** with NMO in the Absence of Redox-Inactive Metals

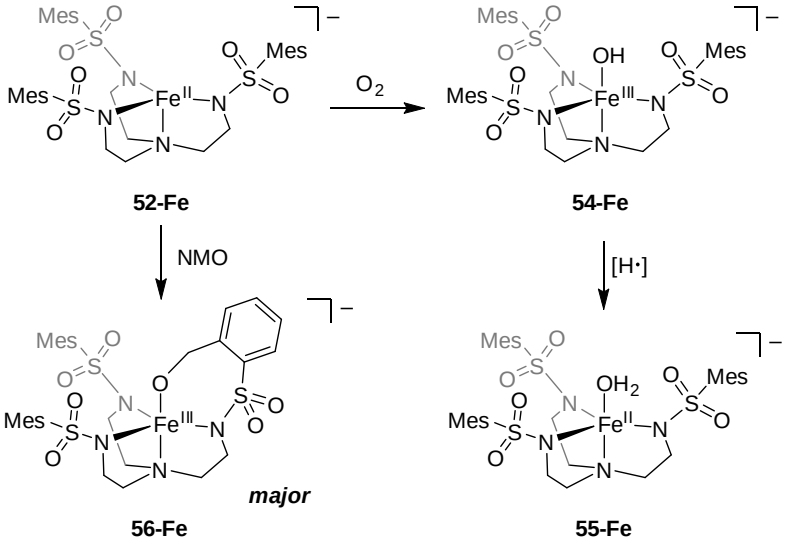

Another effect of redox-inactive metals on the reactivity complex **52-Fe** besides the modulation of the O_2 activation rate was reported by the same group. Complexes **53-Fe-M** could be accessed via use of O_2 or 4-methylmorpholine-*N*-oxide (NMO) as oxidant. Reaction of **52-Fe** with O_2 was sluggish, and generation of the monometallic hydroxide **54-Fe** was followed by decomposition to water-adduct **55-Fe** via putative H-atom abstraction from solvent (Scheme 24).[135] NMO gave rise to faster reactivity, and although similar yields of heterometallic complexes could be obtained in the presence of redox-inactive metals as for the reaction with O_2, in the absence of Lewis acidic additives ligand oxidation product **56-Fe** was isolated instead. This result indicated that the presence of redox-inactive metals can prevent ligand decomposition, though further elaboration on the mechanism of this effect was not provided.

Studies on complexes of two redox-active metals have also been performed on the same ligand framework, and bear mention here. A heterobimetallic Fe^{III}–(OH)–Mn^{II} complex (**57-Fe-Mn**) was prepared in which Fe was bound to the tripodal ligand scaffold and a Mn center supported by a trimethyltriazacyclononane ligand was coordinated to the complex via two of the sulfonamido groups (Scheme 25).[136] While in the case of redox-inactive metals the redox potential of the complex was sensitive to the identity of the second metal, [FeMn] species **57-Fe-Mn** displayed reduced electronic communication via the hydroxo bridge. In fact, the two redox processes observed in electrochemical studies of **57-Fe-Mn** (the $[Fe^{III}Mn^{II}]/[Fe^{II}Mn^{II}]$ and $[Fe^{III}Mn^{II}]/[Fe^{III}Mn^{III}]$ couples) occurred at the same potentials as in the respective homometallic Fe^{III}–(OH)–Fe^{II} (**57-Fe-Fe**) and Mn^{III}–(OH)–Mn^{II} (**57-Mn-Mn**) complexes, even though the Lewis acidities of the ions involved are different (Table 10). This difference in metal effects is likely to be due to the increased covalent character of the bonding in Fe–(OH)–Mn species with respect to the much more ionic bonds in complexes of redox-inactive metals, which result in lower electronic communication.

Table 10. Electrochemical data for complexes **57-M-M**.[136]

Complex	$E_{1/2}^{a,c}$	$E_{1/2}^{b,c}$
57-Fe-Mn	-0.88 (10.6)	0.71 (2.2)
57-Fe-Fe	-0.87 (9.4)	0.36 (2.2)
57-Mn-Mn	-0.47 (10.6)	0.71 (-0.6)

[a] $[M^{II}M^{III}]/[M^{II}M^{II}]$ couple. [b] $[M^{III}M^{III}]/[M^{III}M^{II}]$ couple. [c] Value in parenthesis corresponds to pK_a of metal aquo ion of metal center not involved in ET for the redox couple of interest.[128]

Scheme 25. Synthesis of Heterometallic Complex **57-Fe-Mn** and structures of homometallic complexes **57-Fe-Fe** and **57-Mn-Mn**

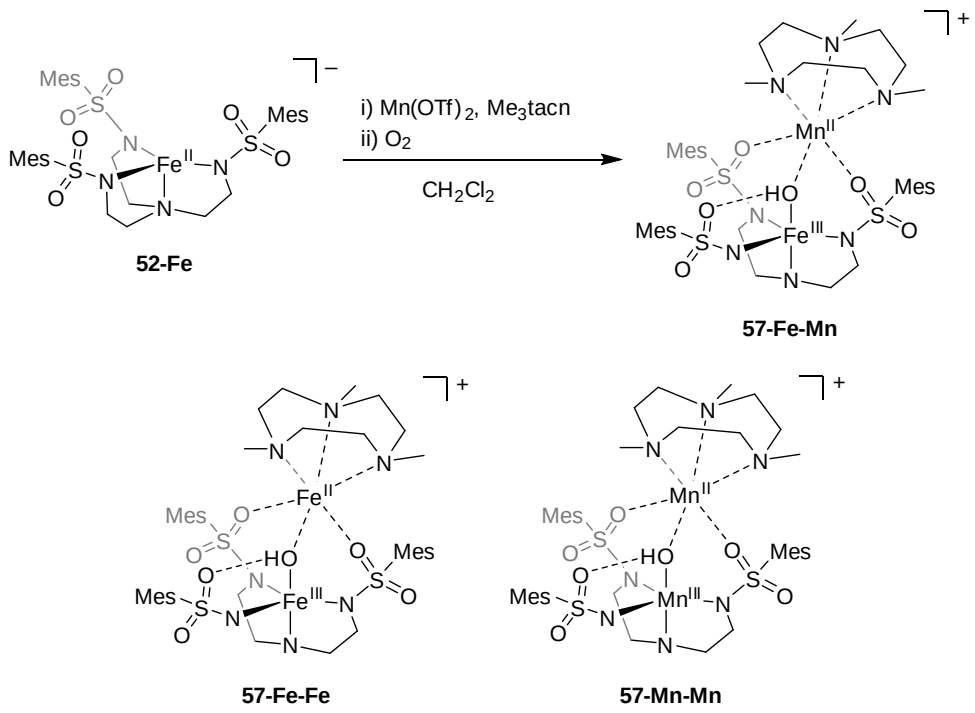

Effects of a strong Lewis acid (Sc^{3+}) on the product of O_2 reduction by a Cu catalyst have been reported by Karlin, Fukuzumi, and coworkers.[137] Cu complex **58** had been previously reported to catalyse the 4-e^- reduction of O_2 to H_2O by decamethylferrocene (Fc*) in the presence of strong Brønsted acids.[138] When H^+ sources were replaced by Sc^{3+}, peroxide (O_2^{2-}) was instead the product of O_2 reduction (Scheme 26). Use of other tricationic metal additives of lower Lewis acidity lowered the catalytic reactivity but still led to production of peroxide. Kinetic data indicated that ET from Fc* to **58** was the rate-determining step of the catalytic reaction. The observed shift in reaction product is notable, as formation of peroxide during O_2 reduction is a common undesired reaction pathway observed in catalytic processes relevant to fuel cell design. This study has provided new information on the factors that may contribute to this type of shift in reactivity by O_2 reduction catalysts.

Scheme 26. Modulation of O_2 Reduction Catalysis with Cu Complex **58** by Lewis Acidic Additives.

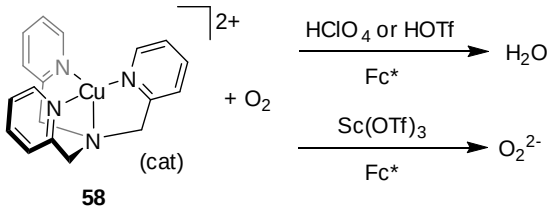

2.3.3 O–O Bond Cleavage in Metal-Peroxide Complexes.

Several reports of the effects of redox-inactive metals on the reductive cleavage of the O–O bond in metal-bound peroxide moieties have been reported. Fukuzumi, Nam, and coworkers[92,93] as well as Que, Jr.[139] and coworkers simultaneously reported that complexes **12-M** underwent reactivity with chemical reductants to generate Fe^{IV}–O complex **8**, the product of the 2-e^- cleavage of the peroxide moiety (Scheme 27). The two groups described the use of reductants such as tetraphenylborate (Ph_4B^-), ferrocene, and 1-benzyl-1,4-dihydronicotinamide dimer ($(BNA)_2$) to carry out this reduction. Notably, cleavage of the O–O bond did not occur when reductants were added to the monometallic precursor **11** (though formation of Fe^{IV}–O is observed in the presence of Ph_4B^- *and* H^+). Since the rate of reduction correlated with Lewis acidity ($k_{Zn} < k_{Lu} < k_Y < k_{Sc}$), and screening of a series of reductants showed that the ET reorganization energy is identical for both complexes, effects on rate were solely derived from the shifts in reduction potential of **12-M**.[92]

Scheme 27. Reactivity of Peroxo-Bridged Complexes **12-M** with Reductants.

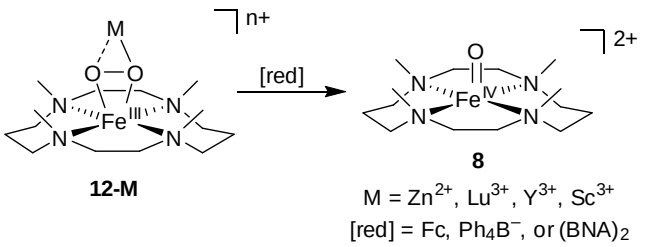

In their studies on bimetallic activation of O_2, Ray, Driess, and coworkers discovered that nickel-superoxo complex **59**, supported by the bidentate, monoanionic nacnac$^-$ ligand, was reduced by K metal by one electron to give the heterobimetallic $\mu,\eta^2{:}\eta^2$-peroxide complex **60**.[140] While this species was stable towards further reactivity, transmetallation with a Zn^{2+} source resulted in isolation of a [NiZn] complex with two bridging hydroxides (**62**). This observation was consistent with the increased electrophilicity of the bridging peroxide unit upon binding of the stronger Lewis acid Zn^{2+}, which favored abstraction of two H-atoms (presumably from solvent) to yield the product of O–O bond cleavage. DFT calculations supported a possible reaction intermediate in which the O–O has already been cleaved, carrying one unpaired electron on each O atom. This species (**61**) was postulated to be responsible for the observed H–atom abstraction events that led to product formation.

Scheme 28. Reactivity of Ni-Superoxo Complex **59** with K and Zn^{2+}.

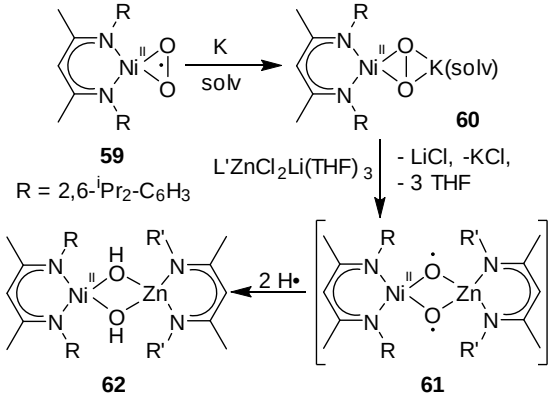

Reduction of the superoxo moiety in **59** was also observed in the reaction with a Cu^I species. Binding of Cu^I complex **63**, supported by *N*,*N*,*N'*,*N'*,*N''*-pentamethyl-dipropylenetriamine, prompted cleavage of the O–O bond via a three-electron reduction of the superoxo moiety and concurrent oxidation of the bimetallic [NiCu] unit to yield [Ni^{III}–(μ-O)$_2$–Cu^{III}] complex **64** (Scheme 29).[141] This bis(μ-O) species

exhibited different reactivity to its homometallic analogues. The oxide ligands in **64** were found to be nucleophilic and readily reacted with exogenous electrophiles such as aldehydes and benzoyl chlorides. No reaction was observed with nucleophilic substrates such as triphenylphosphine, which were however reactive towards homometallic analogs of **64** ([Ni_2] and [Cu_2] complexes). **64** also underwent HAT from weak X–H bonds (1,3-cyclohexadiene, 9,10-dihydroanthracene, 2,4-di-*tert*-butylphenol).

Scheme 29. Reactivity of **59** with Cu^I Complex **63**.

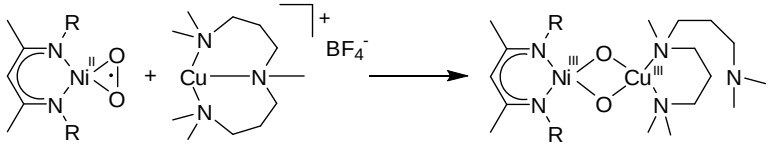

Finally, O–O bond cleavage was also observed in the reaction of **59** with Fe^I complex **65** (Scheme 30).[142] However, the high reactivity of the putative [Ni^{III}–$(O)_2$–Fe^{III}] species **66** thus obtained (supported by DFT calculations) resulted in C–H bond activation of the ligand framework, yielding a heterobimetallic [NiFe] complex bridged by one hydroxide and one alkoxide ligand (**67**)

Scheme 30. Cleavage of the O–O Bond in **59** by Fe Complex **65** and Subsequent reactivity.

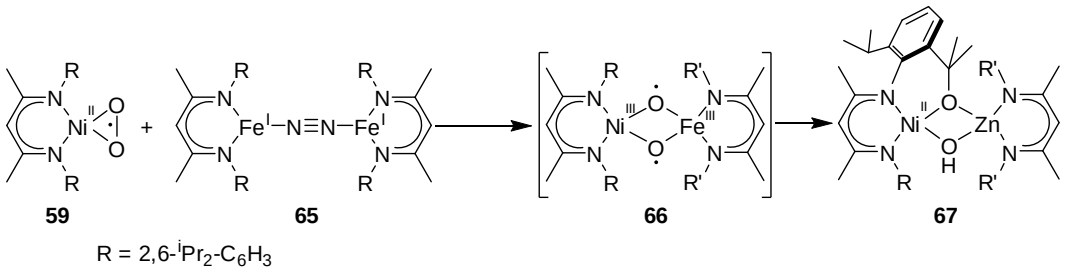

2.3.4 N_2 Reduction

Recent reports by the group of Holland have demonstrated N–N bond cleavage by iron complexes favoured by cooperation with alkali metal ions. Using a β-diketiminate Fe^{II} complex (**68**), dinitrogen activation resulting in complete N–N bond cleavage was achieved in the presence of potassium graphite as reductant (Scheme 31).[143] The isolated product was crystallographically characterized as a Fe_4 complex incorporating two nitride ligands derived from N_2, one of which is bridging between two iron and two potassium centers (**69-K**). Complex **69-K** generated ammonia in 82±4% yield when treated with ethereal HCl. Likewise, ammonia can be generated from **69-K** by addition of dihydrogen, albeit the NH_3 yield from hydrogenation is lower (42±2%).

Scheme 31. Dinitrogen Activation by Complex **68** in the Presence of Alkali Metals.

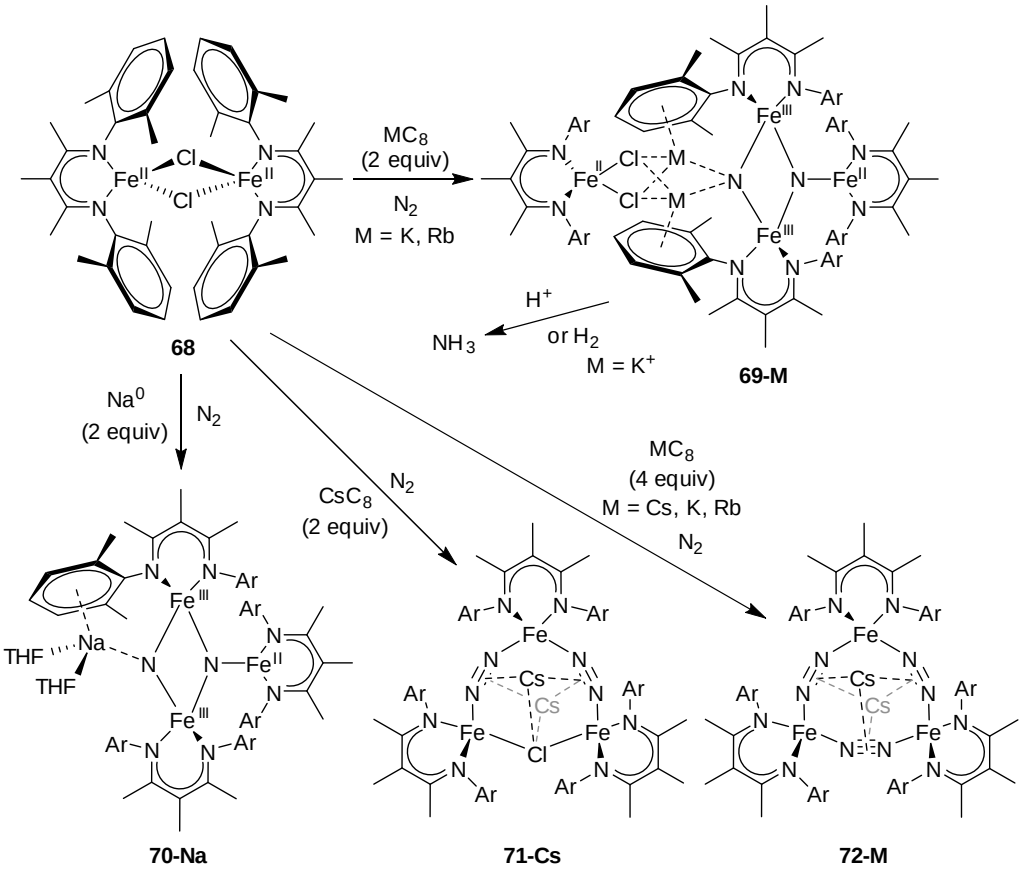

The role of potassium in the dinitrogen activation reaction was studied by density functional theory methods, and while gas-phase calculations supported a considerable stabilizing role by K^+, introduction of solvent effects limited this interaction.[144] To gain further insight into the role of K/K^+ in the observed reactivity, analogous studies with other alkali metals were performed.[145] Under the same reaction conditions, use of reductant RbC_8 (2 equiv.) yielded the corresponding Rb-containing Fe_4 complex **69-Rb**, isostructural to but more thermally stable than **69-K**. Treatment of **68** with Na^0 under an N_2 atmosphere yielded a novel product of N–N bond cleavage, **70-Na**, containing three Fe centers and a single Na^+, possibly due to the smaller size of the cation. Surprisingly, reaction of CsC_8 (2 equiv.) with **58** did not result in N_2 cleavage, but rather yielded complex **71-Cs**, which contained two intact N_2 units. Increase of the amount of CsC_8 added (4 equiv.) did not engender cleavage of N_2; a Fe_3 complex containing *three* intact N_2 molecules (**72-Cs**) was instead observed. Analogous complexes with K^+ and Rb^+ (**72-K** and **72-Rb**) were obtained by increasing the stoichiometry of the respective reductants (1:4 **68**/MC_8, M = K^+, Rb^+). Since the extent of N_2 cleavage was not regulated by the number of reducing equivalents provided, and since the reducing power of the various reductants was assumed to be similar (given their analogous $M^+C_8^-$ nature), the reactivity of this system was rationalized on the basis of the geometry of the species formed in the presence of different amounts of reductant. Given the structures of **69-K**, **69-Rb**, and **70-Na**, the authors postulated that attack of three [Fe^I] units on a single N_2 moiety was required for N–N bond cleavage, which was prevented by the presence of extra alkali ions via the formation of species such as **71-Cs** and **72-M**. This study represents an interesting example of modulation

of reactivity by metal cations not based on Lewis acidity or electronic effects, but rather on the cation size and its effect on complex geometry.

Scheme 32. N_2 Activation by Al–M Complexes.

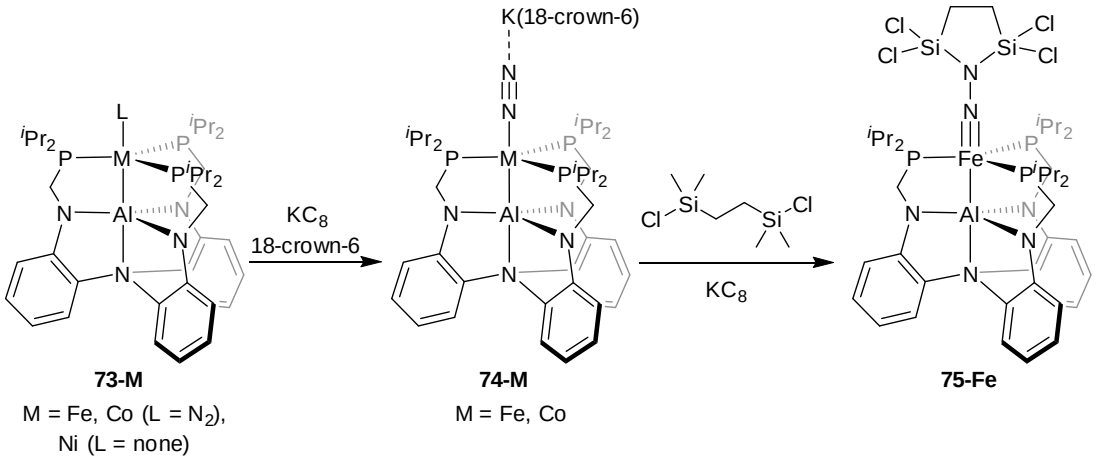

N_2 activation by heterometallic complexes was studied by Lu and coworkers using a tripodal ligand scaffold decorated with both hard (anionic N) and soft (neutral P) donors to support [Al-M] complexes **73-M** (M = Fe^0, Co^0, Ni^0).[146] **73-Fe** and **73-Co** were observed to bind a N_2 ligand, whose IR stretching frequency indicated only minor activation. For complexes **73-Ni** and **73-Co**, the M–Al distances were close to the sum of the covalent radii for Al and Ni and Al and Co respectively, while the observed Al–Fe distance in **73-Fe** was longer. These observations were mirrored in the redox behavior of the three species, with the reduction potential for **73-Fe** being less influenced by Al and displaying a much more negative redox potential for the [M^0/M^{I}] couple than **73-Co**. Chemical one-electron reduction of **73-Fe** and **73-Co** yielded complexes **74-Fe** and **74-Co**, respectively (Scheme 32). These reduced complexes displayed lower N–N vibrational frequencies as well as shorter of M–Al distances, consistent with generation of a M→Al dative interaction for both Co and Fe.[147] The solid-state structure of **74-Fe** also showed an interaction between the bound N_2 moiety

and the crown ether-complexed K^+ countercation. Further chemical reduction of **74-Fe** with KC_8 in the presence of bis(chlorodimethylsilyl)ethane yielded iron disilylhydrazido complex **75-Fe**, in which the distal nitrogen of the N_2 moiety was functionalized.

2.3.5 Formate Reduction

Lewis acidic cocatalysts were shown to greatly enhance turnover number (TON) and turnover frequency (TOF) in the dehydrogenation of formate by a momonuclear Fe catalyst. Via study of an analogous stoichiometric reaction, Schneider, Hazari, and coworkers determined that binding of Lewis acids facilitated release of CO_2 from complex **76**.[148] This effect was hypothesized to arise from stabilization of intermediate H-bound formate complex **77** by Lewis acidic additives (Na^+, Li, K^+, Cs, Ca^{2+}, Mg^{2+}, $B(C_6F_5)_3$) leading to CO_2 extrusion and formation of dihydride **78**, which could then react further with formic acid, releasing H_2 and closing the catalytic cycle.

Scheme 33. Lewis Acid-Assisted Dehydrogenation of Formate.

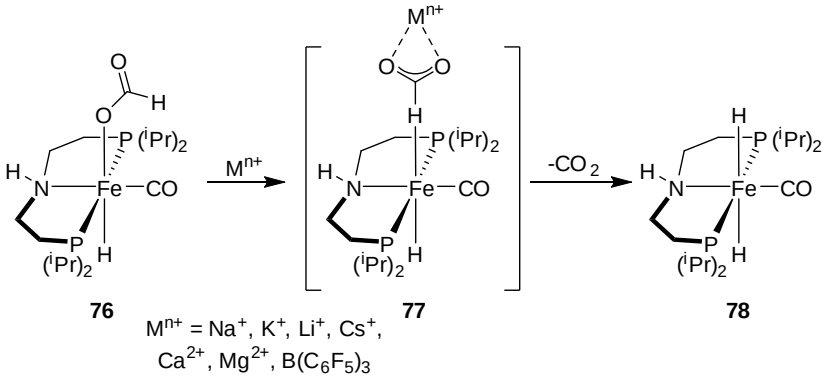

3. CONCLUSIONS

Lewis acidic metal centers can profoundly affect redox processes even when unable to directly participate in electron transfer. The ability of redox-inactive metals to

modulate the redox potential of redox-active complexes engenders effects on the activity of these species towards electron and group transfer reactions as well as on the kinetics of ET, OAT, and HAT. These effects contribute to the enhancement of activity of otherwise unreactive species, prompt shifts in the mechanism of certain transformations, and can affect product selectivity in various chemical reactions. The ever-growing number of examples of this type of heterometallic effects speaks to the ubiquity of these influences, which represent a useful potential tool for modulation of reactivity of redox-active complexes. Furthermore, the many reports of these effects provide useful perspective on the roles that redox-inactive, Lewis acidic species may play in systems relevant to biology and heterogeneous catalysis, such as the oxygen evolving complex in Photosystem II and the many mixed-metal heterogeneous catalysts reported for water oxidation and O_2 reduction. While questions about the role played by redox-inactive metal centers in the actual mechanisms of these challenging transformations remain open, the outstanding work in this field continues to provide us with the tools to attempt to answer them.

4. REFERENCES

(1) Wong, B. *Nat. Methods* **2010**, *7*, 863.

(2) Wong, B. *Nat. Methods* **2010**, *7*, 941.

(3) Adams, R. D.; Cotton, F. A. *Catalysis by Di- and Polynuclear Metal Cluster Complexes*; Wiley-VCH, 1998.

(4) Appel, A. M.; Bercaw, J. E.; Bocarsly, A. B.; Dobbek, H.; DuBois, D. L.; Dupuis, M.; Ferry, J. G.; Fujita, E.; Hille, R.; Kenis, P. J. A.; Kerfeld, C. A.; Morris, R. H.; Peden, C. H. F.; Portis, A. R.; Ragsdale, S. W.; Rauchfuss, T. B.; Reek, J. N. H.; Seefeldt, L. C.; Thauer, R. K.; Waldrop, G. L. *Chem. Rev.* **2013**, *113*, 6621.

(5) Braunstein, P.; Rosé, J. *Heterometallic Clusters in Catalysis*; Wiley-VCH, 1999.

(6) Buchwalter, P.; Rose, J.; Braunstein, P. *Chem. Rev.* **2015**, *115*, 28.

(7) Collman, J. P.; Boulatov, R.; Sunderland, C. J.; Fu, L. *Chem. Rev.* **2004**, *104*, 561.

(8) Cooper, B. G.; Napoline, J. W.; Thomas, C. M. *Catal. Rev. - Sci. Eng.* **2012**, *54*, 1.

(9) Gavrilova, A. L.; Bosnich, B. *Chem. Rev.* **2004**, *104*, 349.

(10) Guczi, L. *Supported Bimetallic Catalysts Derived from Molecular Metal Complexes*; Elsevier Science Publishers B. V., 1986; Vol. 29.

(11) Harrop, T. C.; Mascharak, P. K. *Coord. Chem. Rev.* **2005**, *249*, 3007.

(12) Karkas, M. D.; Verho, O.; Johnston, E. V.; Akermark, B. *Chem. Rev.* **2014**, *114*, 11863.

(13) Kim, E.; Chufan, E. E.; Kamaraj, K.; Karlin, K. D. *Chem. Rev.* **2004**, *104*, 1077.

(14) Lee, S. C.; Holm, R. H. *Chem. Rev.* **2004**, *104*, 1135.

(15) Lee, S. C.; Lo, W.; Holm, R. H. *Chem. Rev.* **2014**, *114*, 3579.

(16) Tard, C.; Pickett, C. J. *Chem. Rev.* **2009**, *109*, 2245.

(17) Tsui, E. Y.; Kanady, J. S.; Agapie, T. *Inorg. Chem.* **2013**, *52*, 13833.

(18) Nam, W.; Lee, Y. M.; Fukuzumi, S. *Acc. Chem. Res.* **2014**, *47*, 1146.

(19) Lewis, N. S.; Nocera, D. G. *Proc. Natl. Acad. Sci. USA* **2006**, *103*, 15729.

(20) Faunce, T. A.; Lubitz, W.; Rutherford, A. W.; MacFarlane, D. R.; Moore, G. F.; Yang, P. D.; Nocera, D. G.; Moore, T. A.; Gregory, D. H.; Fukuzumi, S.; Yoon, K. B.; Armstrong, F. A.; Wasielewski, M. R.; Styring, S. *Energy Environ. Sci.* **2013**, *6*, 695.

(21) Pagliaro, M.; Konstandopoulos, A. G.; Ciriminna, R.; Palmisano, G. *Energy Environ. Sci.* **2010**, *3*, 279.

(22) Suntivich, J.; May, K. J.; Gasteiger, H. A.; Goodenough, J. B.; Shao-Horn, Y. *Science* **2011**, *334*, 1383.

(23) Du, P. W.; Eisenberg, R. *Energy Environ. Sci.* **2012**, *5*, 6012.

(24) Kondratenko, E. V.; Mul, G.; Baltrusaitis, J.; Larrazabal, G. O.; Perez-Ramirez, J. *Energy Environ. Sci.* **2013**, *6*, 3112.

(25) Kucharski, T. J.; Tian, Y. C.; Akbulatov, S.; Boulatov, R. *Energy Environ. Sci.* **2011**, *4*, 4449.

(26) Poizot, P.; Dolhem, F. *Energy Environ. Sci.* **2011**, *4*, 2003.

(27) Fukuzumi, S.; Hong, D. C. *Eur. J. Inorg. Chem.* **2014**, 645.

(28) Yano, J.; Yachandra, V. *Chem. Rev.* **2014**, *114*, 4175.

(29) The PyMOL Molecular Graphics System, Version 1.3r1, Schrodinger, LLC

(30) Jeoung, J. H.; Dobbek, H. *Science* **2007**, *318*, 1461.

(31) Dobbek, H.; Gremer, L.; Kiefersauer, R.; Huber, R.; Meyer, O. *Proc. Natl. Acad. Sci. USA* **2002**, *99*, 15971.

(32) Svetlitchnyi, V.; Dobbek, H.; Meyer-Klaucke, W.; Meins, T.; Thiele, B.; Romer, P.; Huber, R.; Meyer, O. *Proc. Natl. Acad. Sci. USA* **2004**, *101*, 446.

(33) Tsukihara, T.; Shimokata, K.; Katayama, Y.; Shimada, H.; Muramoto, K.; Aoyoma, H.; Mochizuki, M.; Shinzawa-Itoh, K.; Yamashita, E.; Yao, M.; Ishimura, Y.; Yoshikawa, S. *Proc. Natl. Acad. Sci. USA* **2003**, *100*, 15304.

(34) Spatzal, T.; Aksoyoglu, M.; Zhang, L. M.; Andrade, S. L. A.; Schleicher, E.; Weber, S.; Rees, D. C.; Einsle, O. *Science* **2011**, *334*, 940.

(35) Umena, Y.; Kawakami, K.; Shen, J. R.; Kamiya, N. *Nature* **2011**, *473*, 55.

(36) Volbeda, A.; Martin, L.; Cavazza, C.; Matho, M.; Faber, B. W.; Roseboom, W.; Albracht, S. P. J.; Garcin, E.; Rousset, M.; Fontecilla-Camps, J. C. *J. Biol. Inorg. Chem.* **2005**, *10*, 239.

(37) Tainer, J. A.; Getzoff, E. D.; Beem, K. M.; Richardson, J. S.; Richardson, D. C. *J. Mol. Biol.* **1982**, *160*, 181.

(38) Klabunde, T.; Strater, N.; Frohlich, R.; Witzel, H.; Krebs, B. *J. Mol. Biol.* **1996**, *259*, 737.

(39) Schenk, G.; Gahan, L. R.; Carrington, L. E.; Mitic, N.; Valizadeh, M.; Hamilton, S. E.; de Jersey, J.; Guddat, L. W. *Proc. Natl. Acad. Sci. USA* **2005**, *102*, 273.

(40) Allen, J. F.; Martin, W. *Nature* **2007**, *445*, 610.

(41) Bekker, A.; Holland, H. D.; Wang, P. L.; Rumble, D.; Stein, H. J.; Hannah, J. L.; Coetzee, L. L.; Beukes, N. J. *Nature* **2004**, *427*, 117.

(42) Des Marais, D. J. *Science* **2000**, *289*, 1703.

(43) Joliot, P.; Barbieri, G.; Chabaud, R. *Photochem. Photobiol.* **1969**, *10*, 309.

(44) Kok, B.; Forbush, B.; Mcgloin, M. *Photochem. Photobiol.* **1970**, *11*, 457.

(45) McEvoy, J. P.; Brudvig, G. W. *Chem. Rev.* **2006**, *106*, 4455.

(46) Siegbahn, P. E. M. *Acc. Chem. Res.* **2009**, *42*, 1871.

(47) Vinyard, D. J.; Ananyev, G. M.; Dismukes, G. C. *Annu. Rev. Biochem.* **2013**, *82*, 577.

(48) Blomberg, M. R. A.; Borowski, T.; Himo, F.; Liao, R. Z.; Siegbahn, P. E. M. *Chem. Rev.* **2014**, *114*, 3601.

(49) Ghanotakis, D. F.; Babcock, G. T.; Yocum, C. F. *FEBS Lett.* **1984**, *167*, 127.

(50) Boussac, A.; Rutherford, A. W. *Biochemistry* **1988**, *27*, 3476.

(51) Brudvig, G. W. *Phil. Trans. R. Soc. B* **2008**, *363*, 1211.

(52) Lee, C. I.; Lakshmi, K. V.; Brudvig, G. W. *Biochemistry* **2007**, *46*, 3211.

(53) Pecoraro, V. L.; Baldwin, M. J.; Caudle, M. T.; Hsieh, W. Y.; Law, N. A. *Pure Appl. Chem.* **1998**, *70*, 925.

(54) Vrettos, J. S.; Stone, D. A.; Brudvig, G. W. *Biochemistry* **2001**, *40*, 7937.

(55) Yachandra, V. K.; Yano, J. *J. Photochem. Photobiol. B* **2011**, *104*, 51.

(56) Yachandra, V. K.; Sauer, K.; Klein, M. P. *Chem. Rev.* **1996**, *96*, 2927.

(57) Lohmiller, T.; Cox, N.; Su, J. H.; Messinger, J.; Lubitz, W. *J. Biol. Chem.* **2012**, *287*, 24721.

(58) RiggsGelasco, P. J.; Mei, R.; Ghanotakis, D. F.; Yocum, C. F.; PennerHahn, J. E. *J. Am. Chem. Soc.* **1996**, *118*, 2400.

(59) Smith, R. D. L.; Prevot, M. S.; Fagan, R. D.; Trudel, S.; Berlinguette, C. P. *J. Am. Chem. Soc.* **2013**, *135*, 11580.

(60) Smith, R. D. L.; Prevot, M. S.; Fagan, R. D.; Zhang, Z. P.; Sedach, P. A.; Siu, M. K. J.; Trudel, S.; Berlinguette, C. P. *Science* **2013**, *340*, 60.

(61) Trotochaud, L.; Ranney, J. K.; Williams, K. N.; Boettcher, S. W. *J. Am. Chem. Soc.* **2012**, *134*, 17253.

(62) Yuan, C.; Wu, H. B.; Xie, Y.; Lou, X. W. D. *Angew. Chem. Int. Ed.* **2014**, *53*, 1488.

(63) Zaharieva, I.; Najafpour, M. M.; Wiechen, M.; Haumann, M.; Kurz, P.; Dau, H. *Energy Environ. Sci.* **2011**, *4*, 2400.

(64) Wiechen, M.; Zaharieva, I.; Dau, H.; Kurz, P. *Chem. Sci.* **2012**, *3*, 2330.

(65) Merrill, M. D.; Dougherty, R. C. *J. Phys. Chem. C.* **2008**, *112*, 3655.

(66) McCrory, C. C. L.; Jung, S. H.; Peters, J. C.; Jaramillo, T. F. *J. Am. Chem. Soc.* **2013**, *135*, 16977.

(67) Liang, Y. Y.; Wang, H. L.; Zhou, J. G.; Li, Y. G.; Wang, J.; Regier, T.; Dai, H. J. *J. Am. Chem. Soc.* **2012**, *134*, 3517.

(68) Ding, K. Q. *Int. J. Electrochem. Sci.* **2010**, *5*, 72.

(69) Suntivich, J.; Gasteiger, H. A.; Yabuuchi, N.; Nakanishi, H.; Goodenough, J. B.; Shao-Horn, Y. *Nat. Chem.* **2011**, *3*, 546.

(70) Gray, H. B. *Nat. Chem.* **2009**, *1*, 112.

(71) Kanan, M. W.; Nocera, D. G. *Science* **2008**, *321*, 1072.

(72) Suntivich, J.; Gasteiger, H. A.; Yabuuchi, N.; Nakanishi, H.; Goodenough, J. B.; Shao-Horn, Y. *Nat. Chem.* **2011**, *3*, 647.

(73) Lau, T. C.; Mak, C. K. *J. Chem. Soc. Chem. Comm.* **1993**, 766.

(74) Lau, T. C.; Wu, Z. B.; Bai, Z. L.; Mak, C. K. *J. Chem. Soc. Dalton Trans.* **1995**, 695.

(75) Xie, N.; Binstead, R. A.; Block, E.; Chandler, W. D.; Lee, D. G.; Meyer, T. J.; Thiruvazhi, M. *J. Org. Chem.* **2000**, *65*, 1008.

(76) Lai, S.; Lee, D. G. *Tetrahedron* **2002**, *58*, 9879.

(77) Zhang, D. Q.; Duan, A. J.; Zhao, Z.; Wang, X. Q.; Jiang, G. Y.; Liu, J.; Wang, C. Y.; Jin, M. C. *Catal. Today* **2011**, *175*, 477.

(78) Ho, C. M.; Lau, T. C. *New J. Chem.* **2000**, *24*, 587.

(79) Yiu, S. M.; Wu, Z. B.; Mak, C. K.; Lau, T. C. *J. Am. Chem. Soc.* **2004**, *126*, 14921.

(80) Yiu, S. M.; Man, W. L.; Lau, T. C. *J. Am. Chem. Soc.* **2008**, *130*, 10821.

(81) Perrin, D. D.; International Union of Pure and Applied Chemistry. Commission on Equilibrium Data. *Ionisation constants of inorganic acids and bases in aqueous solution*; 2nd ed.; Pergamon Press: Oxford Oxfordshire ; New York, 1982.

(82) Tsui, E. Y.; Tran, R.; Yano, J.; Agapie, T. *Nat. Chem.* **2013**, *5*, 293.

(83) Horwitz, C. P.; Ciringh, Y. *Inorg. Chim. Acta* **1994**, *225*, 191.

(84) Horwitz, C. P.; Warden, J. T.; Weintraub, S. T. *Inorg. Chim. Acta* **1996**, *246*, 311.

(85) Horwitz, C. P.; Ciringh, Y.; Weintraub, S. T. *Inorg. Chim. Acta* **1999**, *294*, 133.

(86) Ciringh, Y.; GordonWylie, S. W.; Norman, R. E.; Clark, G. R.; Weintraub, S. T.; Horwitz, C. P. *Inorg. Chem.* **1997**, *36*, 4968.

(87) Miller, C. G.; Gordon-Wylie, S. W.; Horwitz, C. P.; Strazisar, S. A.; Peraino, D. K.; Clark, G. R.; Weintraub, S. T.; Collins, T. J. *J. Am. Chem. Soc.* **1998**, *120*, 11540.

(88) Fukuzumi, S.; Morimoto, Y.; Kotani, H.; Naumov, P.; Lee, Y. M.; Nam, W. *Nat. Chem.* **2010**, *2*, 756.

(89) Rohde, J. U.; In, J. H.; Lim, M. H.; Brennessel, W. W.; Bukowski, M. R.; Stubna, A.; Munck, E.; Nam, W.; Que, L. *Science* **2003**, *299*, 1037.

(90) Swart, M. *Chem. Commun.* **2013**, *49*, 6650.

(91) Prakash, J.; Rohde, G. T.; Meier, K. K.; Jasniewski, A. J.; Van Heuvelen, K. M.; Munck, E.; Que, L. *J. Am. Chem. Soc.* **2015**, *137*, 3478.

(92) Lee, Y. M.; Bang, S.; Kim, Y. M.; Cho, J.; Hong, S.; Nomura, T.; Ogura, T.; Troeppner, O.; Ivanovic-Burmazovic, I.; Sarangi, R.; Fukuzumi, S.; Nam, W. *Chem. Sci.* **2013**, *4*, 3917.

(93) Bang, S.; Lee, Y. M.; Hong, S.; Cho, K. B.; Nishida, Y.; Seo, M. S.; Sarangi, R.; Fukuzumi, S.; Nam, W. *Nat. Chem.* **2014**, *6*, 934.

(94) Kaizer, J.; Klinker, E. J.; Oh, N. Y.; Rohde, J. U.; Song, W. J.; Stubna, A.; Kim, J.; Munck, E.; Nam, W.; Que, L. *J. Am. Chem. Soc.* **2004**, *126*, 472.

(95) Morimoto, Y.; Kotani, H.; Park, J.; Lee, Y. M.; Nam, W.; Fukuzumri, S. *J. Am. Chem. Soc.* **2011**, *133*, 403.

(96) Fukuzumi, S.; Ohkubo, K. *Chem. Eur. J.* **2000**, *6*, 4532.

(97) Park, J.; Morimoto, Y.; Lee, Y. M.; Nam, W.; Fukuzumi, S. *Inorg. Chem.* **2014**, *53*, 3618.

(98) Fukuzumi, S.; Ohkubo, K. *Coord. Chem. Rev.* **2010**, *254*, 372.

(99) Park, J.; Morimoto, Y.; Lee, Y. M.; Nam, W.; Fukuzumi, S. *J. Am. Chem. Soc.* **2011**, *133*, 5236.

(100) Chen, J.; Lee, Y. M.; Davis, K. M.; Wu, X.; Seo, M. S.; Cho, K. B.; Yoon, H.; Park, Y. J.; Fukuzumi, S.; Pushkar, Y. N.; Nam, W. *J. Am. Chem. Soc.* **2013**, *135*, 6388.

(101) Yoon, H.; Lee, Y. M.; Wu, X.; Cho, K. B.; Sarangi, R.; Nam, W.; Fukuzumi, S. *J. Am. Chem. Soc.* **2013**, *135*, 9186.

(102) Chen, J.; Yoon, H.; Lee, Y. M.; Seo, M. S.; Sarangi, R.; Fukuzumi, S.; Nam, W. *Chem. Sci.* **2015**, *6*, 3624.

(103) Yoon, H.; Morimoto, Y.; Lee, Y. M.; Nam, W.; Fukuzumi, S. *Chem. Commun.* **2012**, *48*, 11187.

(104) Leeladee, P.; Baglia, R. A.; Prokop, K. A.; Latifi, R.; de Visser, S. P.; Goldberg, D. P. *J. Am. Chem. Soc.* **2012**, *134*, 10397.

(105) Marcus, R. A. *Annu. Rev. Phys. Chem.* **1964**, *15*, 155.

(106) Park, J.; Lee, Y. M.; Ohkubo, K.; Nam, W.; Fukuzumi, S. *Inorg. Chem.* **2015**, *54*, 5806.

(107) Park, J.; Morimoto, Y.; Lee, Y. M.; You, Y.; Nam, W.; Fukuzumi, S. *Inorg. Chem.* **2011**, *50*, 11612.

(108) Zaragoza, J. P. T.; Baglia, R. A.; Siegler, M. A.; Goldberg, D. P. *J. Am. Chem. Soc.* **2015**, *137*, 6531.

(109) Pfaff, F. F.; Kundu, S.; Risch, M.; Pandian, S.; Heims, F.; Pryjomska-Ray, I.; Haack, P.; Metzinger, R.; Bill, E.; Dau, H.; Comba, P.; Ray, K. *Angew. Chem. Int. Ed.* **2011**, *50*, 1711.

(110) Lacy, D. C.; Park, Y. J.; Ziller, J. W.; Yano, J.; Borovik, A. S. *J. Am. Chem. Soc.* **2012**, *134*, 17526.

(111) Dong, L.; Wang, Y. J.; Lv, Y. Z.; Chen, Z. Q.; Mei, F. M.; Xiong, H.; Yin, G. C. *Inorg. Chem.* **2013**, *52*, 5418.

(112) Lionetti, D.; Agapie, T. *Nature* **2014**, *513*, 495.

(113) Mukherjee, S.; Stull, J. A.; Yano, J.; Stamatatos, T. C.; Pringouri, K.; Stich, T. A.; Abboud, K. A.; Britt, R. D.; Yachandra, V. K.; Christou, G. *Proc. Natl. Acad. Sci. USA* **2012**, *109*, 2257.

(114) Zhang, C. X.; Chen, C. H.; Dong, H. X.; Shen, J. R.; Dau, H.; Zhao, J. Q. *Science* **2015**, *348*, 690.

(115) Tsui, E. Y.; Kanady, J. S.; Day, M. W.; Agapie, T. *Chem. Commun.* **2011**, *47*, 4189.

(116) Tsui, E. Y.; Day, M. W.; Agapie, T. *Angew. Chem. Int. Ed.* **2011**, *50*, 1668.

(117) Lionetti, D.; Suseno, S.; Tsui, E. Y.; Lu, L.; Britt, R. D.; Carsch, K. M.; Agapie, T., *Manuscript in preparation*.

(118) Kanady, J. S.; Tsui, E. Y.; Day, M. W.; Agapie, T. *Science* **2011**, *333*, 733.

(119) Tsui, E. Y.; Agapie, T. *Proc. Natl. Acad. Sci. USA* **2013**, *110*, 10084.

(120) Lin, P. H.; Takase, M. K.; Agapie, T. *Inorg. Chem.* **2015**, *54*, 59.

(121) Suseno, S.; Agapie, T., *Manuscript in preparation.*

(122) Kanady, J. S.; Mendoza-Cortes, J. L.; Tsui, E. Y.; Nielsen, R. J.; Goddard, W. A.; Agapie, T. *J. Am. Chem. Soc.* **2013**, *135*, 1073.

(123) Caballero, A.; Cruz, M.; Hernan, L.; Melero, M.; Morales, J.; Castellon, E. R. *J. Electrochem. Soc.* **2005**, *152*, A552.

(124) Arora, P.; Popov, B. N.; White, R. E. *J. Electrochem. Soc.* **1998**, *145*, 807.

(125) Malyovanyi, S. M.; Andriiko, A. A.; Monko, A. P. *J. Solid State Electrochem.* **2003**, *8*, 7.

(126) Kanady, J. S.; Lin, P. H.; Carsch, K. M.; Nielsen, R. J.; Takase, M. K.; Goddard, W. A.; Agapie, T. *J. Am. Chem. Soc.* **2014**, *136*, 14373.

(127) Herbert, D. E.; Lionetti, D.; Rittle, J.; Agapie, T. *J. Am. Chem. Soc.* **2013**, *135*, 19075.

(128) Hawkes, S. J. *J. Chem. Educ.* **1996**, *73*, 516.

(129) Robinson, J. R.; Carroll, P. J.; Walsh, P. J.; Schelter, E. J. *Angew. Chem. Int. Ed.* **2012**, *51*, 10159.

(130) Robinson, J. R.; Gordon, Z.; Booth, C. H.; Carroll, P. J.; Walsh, P. J.; Schelter, E. J. *J. Am. Chem. Soc.* **2013**, *135*, 19016.

(131) Ohkubo, K.; Menon, S. C.; Orita, A.; Otera, J.; Fukuzumi, S. *J. Org. Chem.* **2003**, *68*, 4720.

(132) Fukuzumi, S. *Chem. Lett.* **2008**, *37*, 808.

(133) Park, Y. J.; Cook, S. A.; Sickerman, N. S.; Sano, Y.; Ziller, J. W.; Borovik, A. S. *Chem. Sci.* **2013**, *4*, 717.

(134) Park, Y. J.; Ziller, J. W.; Borovik, A. S. *J. Am. Chem. Soc.* **2011**, *133*, 9258.

(135) Cook, S. A.; Ziller, J. W.; Borovik, A. S. *Inorg. Chem.* **2014**, *53*, 11029.

(136) Sano, Y.; Weitz, A. C.; Ziller, J. W.; Hendrich, M. P.; Borovik, A. S. *Inorg. Chem.* **2013**, *52*, 10229.

(137) Kakuda, S.; Rolle, C. J.; Ohkubo, K.; Siegler, M. A.; Karlin, K. D.; Fukuzumi, S. *J. Am. Chem. Soc.* **2015**, *137*, 3330.

(138) Fukuzumi, S.; Kotani, H.; Lucas, H. R.; Doi, K.; Suenobu, T.; Peterson, R. L.; Karlin, K. D. *J. Am. Chem. Soc.* **2010**, *132*, 6874.

(139) Li, F. F.; Van Heuvelen, K. M.; Meier, K. K.; Munck, E.; Que, L. *J. Am. Chem. Soc.* **2013**, *135*, 10198.

(140) Yao, S. L.; Xiong, Y.; Vogt, M.; Grutzmacher, H.; Herwig, C.; Limberg, C.; Driess, M. *Angew. Chem. Int. Ed.* **2009**, *48*, 8107.

(141) Kundu, S.; Pfaff, F. F.; Miceli, E.; Zaharieva, I.; Herwig, C.; Yao, S. L.; Farquhar, E. R.; Kuhlmann, U.; Bill, E.; Hildebrandt, P.; Dau, H.; Driess, M.; Limberg, C.; Ray, K. *Angew. Chem. Int. Ed.* **2013**, *52*, 5622.

(142) Yao, S. L.; Herwig, C.; Xiong, Y.; Company, A.; Bill, E.; Limberg, C.; Driess, M. *Angew. Chem. Int. Ed.* **2010**, *49*, 7054.

(143) Rodriguez, M. M.; Bill, E.; Brennessel, W. W.; Holland, P. L. *Science* **2011**, *334*, 780.

(144) Figg, T. M.; Holland, P. L.; Cundari, T. R. *Inorg. Chem.* **2012**, *51*, 7546.

(145) Grubel, K.; Brennessel, W. W.; Mercado, B. Q.; Holland, P. L. *J. Am. Chem. Soc.* **2014**, *136*, 16807.

(146) Rudd, P. A.; Liu, S. S.; Gagliardi, L.; Young, V. G.; Lu, C. C. *J. Am. Chem. Soc.* **2011**, *133*, 20724.

(147) Rudd, P. A.; Planas, N.; Bill, E.; Gagliardi, L.; Lu, C. C. *Eur. J. Inorg. Chem.* **2013**, *2013*, 3898.

(148) Bielinski, E. A.; Lagaditis, P. O.; Zhang, Y. Y.; Mercado, B. Q.; Wurtele, C.; Bernskoetter, W. H.; Hazari, N.; Schneider, S. *J. Am. Chem. Soc.* **2014**, *136*, 10234.

CHAPTER 2

SYNTHETIC MODELS OF THE MULTICOPPER OXIDASES: TRICOPPER COMPLEXES AND THEIR O_2 REACTIVITY

The text for this chapter was reproduced in part from:

D. Lionetti, M. W. Day, T. Agapie, *Chem. Sci.*, **2013**, *4*, 785-790

Abstract

A trinucleating framework was assembled by templation of a heptadentate ligand around yttrium and lanthanides. The generated complexes orient three sets of two or three N-donors each for binding additional metal centers. Addition of three equivalents of copper(I) leads to the formation of tricopper(I) species. Reactions with dioxygen at low temperatures generate species whose spectroscopic features are consistent with a μ_3,μ_3-dioxo-tricopper complex. Reactivity studies were performed with a variety of substrates. The dioxo-tricopper species deprotonates weak acids, undergoes oxygen atom transfer with one equivalent of triphenylphosphine to yield triphenylphosphine oxide, and abstracts two hydrogen atom equivalents from tetramethylpiperidine-N-hydroxide (TEMPO-H). Thiophenols reduce the oxygenated species to a Cu^{I}_3 complex and liberate two equivalents of disulfide, consistent with a four-electron, four-proton process.

INTRODUCTION

Many biological enzymes responsible for transformations involving the transfer of multiple electrons rely on active sites containing multiple metal centers to carry out their function.[1-3] The reduction of dioxgyen to water, a reaction requiring the transfer of four electrons and four protons, has garnered considerable attention because of its relevance to the development of fuel cell technology for environmentally benign production of energy.[4-6] The multicopper oxidases (MCOs) are a family of enzymes that couple the reduction of O_2 to H_2O to one-electron oxidations of organic or metal substrates.[2,7] The ability of these enzymes to fully reduce O_2, coupled with their involvement in biological processes as diverse as lignin formation and degradation, wound healing, and iron metabolism has generated substantial interest in elucidating their properties and the mechanism of their enzymatic activity.[7-10]

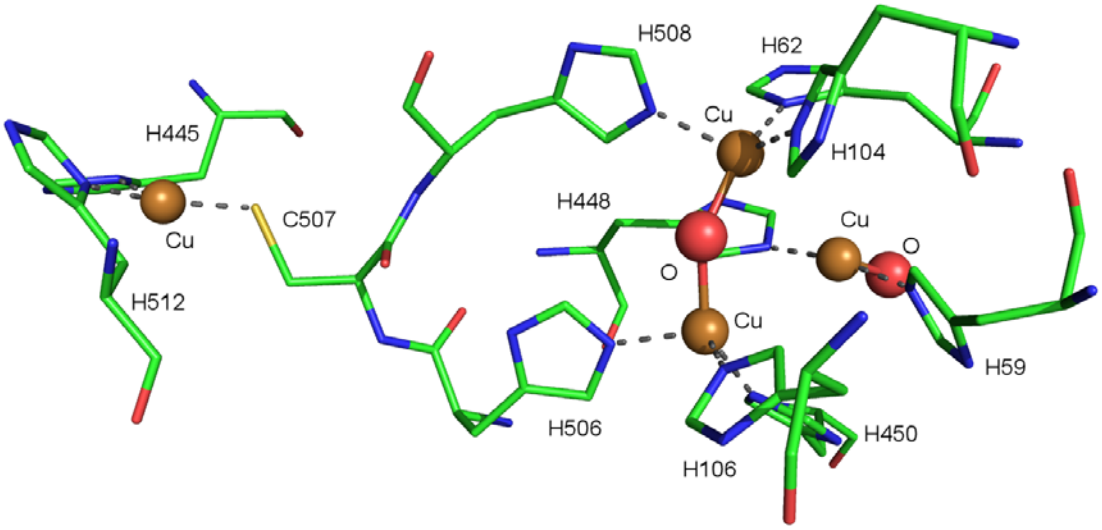

Figure 1. Active site of ascorbate oxidase in the oxidized state (PDB: *1AOZ*).[11]

The active site of MCOs (Figure 1) is composed of three copper centers located in close proximity (~3.5-4.0 Å).[11] This Cu_3 assembly is the site of O_2 binding and reduction to water, a process which has been extensively studied with spectroscopic and

computational methods.[8,9] A fourth Cu center is located ~13 Å from the trinuclear site, and serves as an electron shuttle from substrate (which binds in its vicinity) to the Cu_3 site. O_2 reduction has been determined to occur at this active site in two sequential 2-e^- steps. Binding of O_2 to the fully reduced form of the enzyme and reduction by two electron results in formation of a μ_3-1,1,2-peroxide intermediate (**PI**, Scheme 1). The first reduction event is the rate-determining step, and is followed by a second, fast 2-e^- reduction to fully cleave the O–O bond. Transfer of four electrons via the fourth Cu center, and protonation of the O_2-derived moieties liberates two molecules of water and regenerates the reduced enzyme, concurrent with oxidation of four equivalents of substrate.

Scheme 1. Mechanism of O_2 Reduction to H_2O by MCO Enzymes.[9]

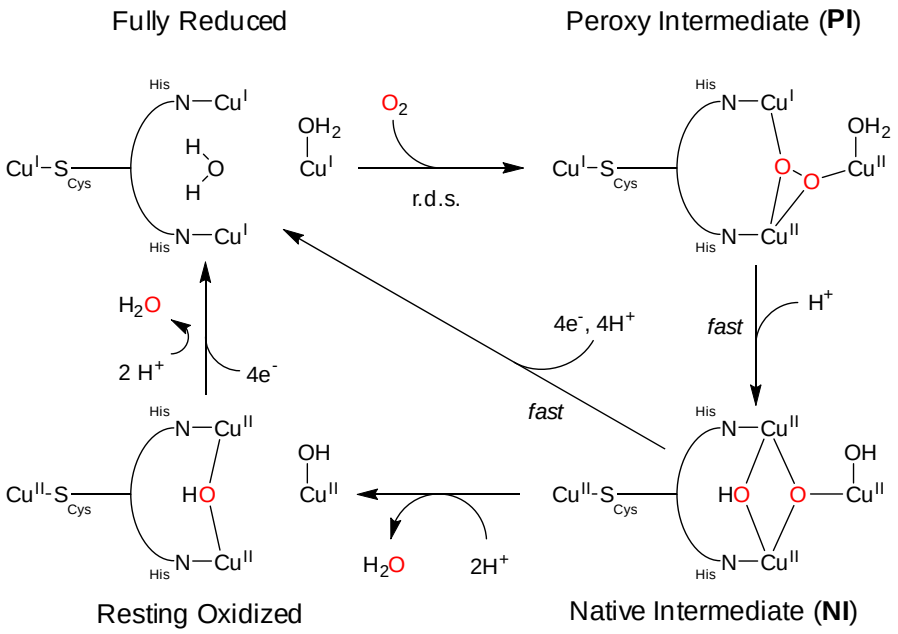

Synthetic efforts to model the structural and functional features of MCOs have focused on the tricopper site where O_2 activation occurs. Mononuclear Cu^I complexes have been shown to self-assemble upon reaction with O_2 to form a $[Cu^{II}_2Cu^{III}(\mu_3\text{-}O)_2]$

species, though only at low O_2 concentrations (at higher O_2:Cu ratios, [Cu^{III}–$(O)_2$–Cu^{III}] species are usually formed).[12-15] An alternate strategy has been the employment of trinucleating frameworks that aimed at inducing cooperative reactivity by placing Cu centers in close proximity.[16-27] Most systems investigated are rather flexible and do not faciliate cooperative trinuclear reactivity. Macrocyclic ligands have been shown to bind three Cu^{II} centers, but O_2 reactivity has not been reported with these systems.[28] Beyond tricopper models, recent ligand-design synthetic efforts have been reported on trinuclear complexes of manganese, iron, cobalt, and zinc.[29-37]

In previous work in our group, 1,3,5-triarylbenzene frameworks have been investigated which are capable of supporting multimetallic systems.[31,38-40] The reaction of O_2 with a tricopper(I) complex based on this framework was complicated in part because of the presence of alcohol groups which lead to a bridged alkoxide species upon oxidation to Cu^{II}.[39] A novel multinucleating ligand framework was therefore designed that would bear Cu-binding motifs on each arm of a tripodal scaffold. Templating the ligand framework around a central metal center (yttrium or a lanthanide) would favor placing of the three arms in close proximity, facilitating cooperative reactivity of the three Cu centers. The present chapter describes the synthesis and O_2 reactivity of tetrametallic [MCu_3] complexes.

RESULTS AND DISCUSSION

Synthesis and Reactivity of Yttrium-Tricopper Complexes

Group 3 and lanthanide ions are known to bind heptadentate, tripodal [O_3N_4]-trisphenoxide-trisimine-amine ligands in a fashion that positions carbon substituents (*tert*-butyl groups) *ortho*- to the phenoxide oxygen about 3 to 4 Å apart from each other.[41-45] This separation is in the range observed for the copper centers in MCOs.[11]

Substitutions with multidentate moieties at these positions were therefore expected to allow for binding of three metal centers in close proximity. Additionally, the specific Cu-ligating moieties (dipicolylamine motifs) were selected to allow for orthogonal binding of different metals (e.g. first row transition metals vs. lanthanides or yttrium) at the desired sites.

Scheme 2. Synthesis of [YCu_3] Complex **4-Y**.

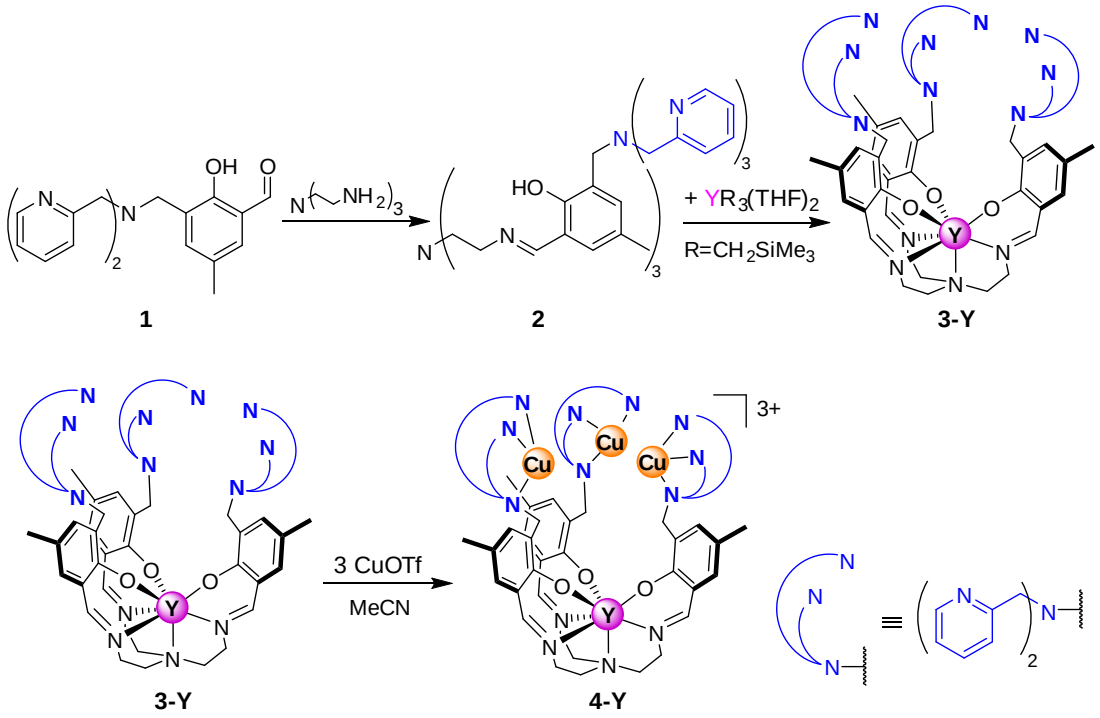

Toward assembling such multinucleating ligand architecture, a variant (**2**) of the [O_3N_4]-trisphenoxide-trisimine-amine framework with dipicolylamine substitutents was prepared via a condensation between tris(2-amino-ethyl)amine and three equivalents of previously reported aldehyde **1** (Scheme 2).[46] Metallation was performed via alkane elimination with an yttrium trialkyl precursor. NMR spectroscopic characterization showed a single phenoxide and pyridine environment, consistent with yttrium binding to the [O_3N_4]-trisphenoxide-trisimine-amine moiety to generate a high-symmetry species (**3-Y**). Addition of three equivalents of Cu^I precursor

($Cu(CH_3CN)_4OTf$) dissolved in acetonitrile (MeCN) to a suspension of **3-Y** in MeCN led to the generation of a homogeneous mixture and to a color change from light yellow to gold. In contrast to **3-Y**, the generated species was soluble in acetonitrile but insoluble in less polar solvents (e.g.: THF) suggesting the formation of an ionic complex.

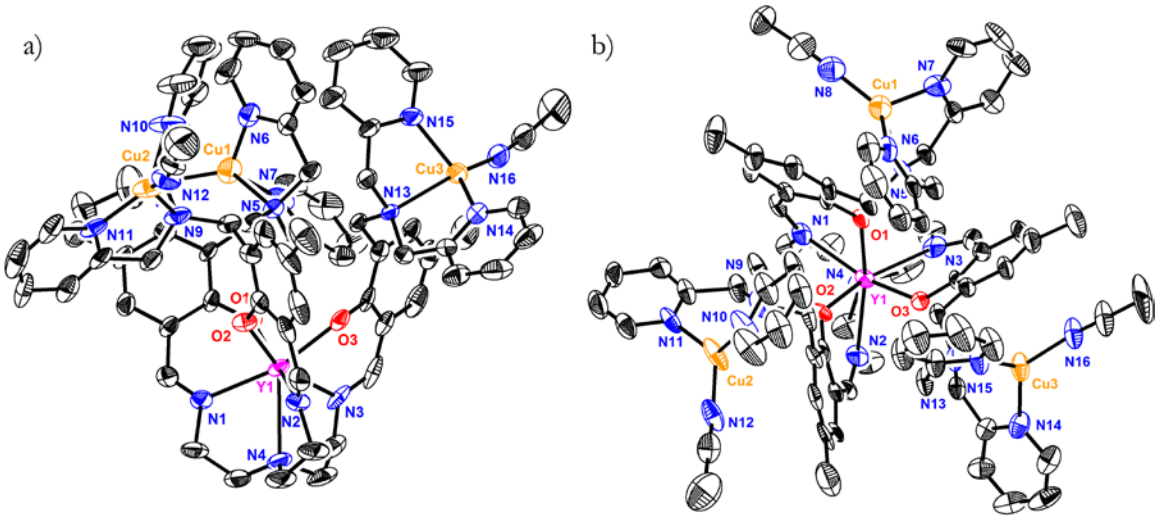

Figure 2. Solid-state structure of the tricationic portion of complex **4-Y** (a) side-on and (b) top-down, along the $Y–N_{axial}$ vector. Thermal ellipsoids shown at 50% probability. Hydrogen atoms omitted for clarity.

Single-crystal X-ray diffraction (XRD) studies showed the formation of a tricationic [YCu_3] species, **4-Y** (Figure 2), in which the seven-coordinate yttrium center was bound to the [O_3N_4]-trisphenoxide-trisimine-amine site and the three copper centers were coordinated to the dipycolylamine moieties. Acetonitrile molecules bound to the copper centers completed the distorted tetrahedral coordination environments. Substantial disorder was present in the obtained structure, which made location of the three triflate (^-OTf) ions impossible amid a large number of solvent molecules. Crystals of higher quality could not be obtained due to the extreme instability of species **4-Y** in air (even when in crystalline form), which put very short limits on the amount of time

available for manipulation and selection of crystals for XRD. Nonetheless, the data was of sufficient quality to unambiguously assign the metal-containing portion of the complex.

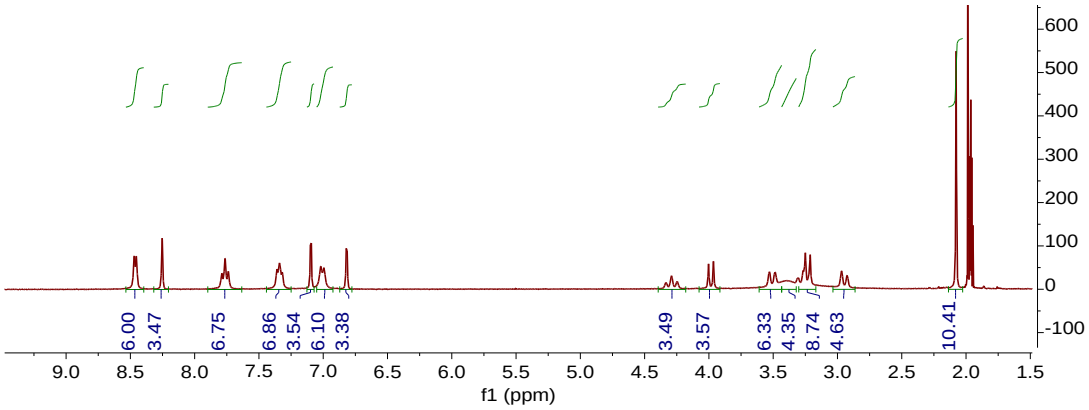

Figure 3. ^{1}H NMR spectrum of **4-Y** in CD_3CN. Note the presence of only seven signals in the aromatic region (6.5-8.5 ppm), consistent with fluxional behavior of **4-Y** to give a C_{3v}-symmetric species in solution at room temperature.

The selectivity for yttrium binding to the [O_3N_4] motif despite the presence of nine additional nitrogen donors was notable, and indicated that this strategy may be more general with respect to changes in the nature of chelating ligands and metals decorating the [YO_3N_4] unit. In the solid-state, the copper centers were twisted away from each other, leading to Cu-Cu separations of ~9 Å. Although the solid-state structure displayed a *pseudo*-C_3 environment, ^{1}H NMR studies showed only one environment for each pyridine proton (Figure 3). This indicated that in solution the conformation of the molecule is fluxional, and that therefore the copper centers could potentially approach closer orientations.

To explore the possible cooperativity between its three copper centers, reactivity of **4-Y** with O_2 was explored. The extensive literature on the reactivity of Cu complexes with O_2 has generated a wealth of spectroscopic information on the intermediates that

can be accessed by given Cu species.[47] UV-Vis spectroscopy has been especially useful in identifying Cu/O_2 complexes, as different [Cu_xO_y] give rise to unique features in the ultraviolet-visible range. The reaction of compound **4-Y** with O_2 was monitored by UV-Vis spectroscopy at low temperatures (Figure 4, blue). A new species was generated within a minute at -78 ºC and within seconds at -40 ºC. The UV-Vis features observed following O_2 addition agreed closely with those reported in the literature for the [$Cu^{II}_2Cu^{III}(\mu_3\text{-}O)_2$] core, in which the O–O bond has been fully cleaved to give two oxide ligands that bridge across all three Cu centers (Table 1). The low-temperature intermediate generated in the reaction of compound **4-Y** with O_2 was therefore assigned as bis(μ_3-O) complex **5-Y** (Scheme 3).

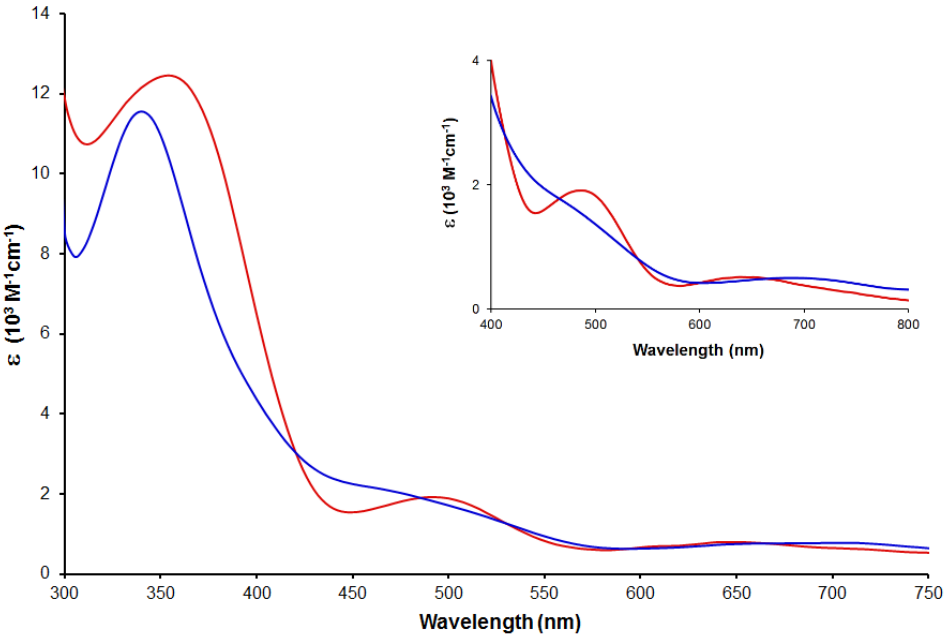

Figure 4. UV-Vis spectra of solutions of **5-Y** (red) and **12-Y** (blue) in 3:2 toluene/acetonitrile at -40 ºC. Inset: expanded view of the 400-800 nm region.

Scheme 3. Reaction of [Cu^{I}_3] Complex **4-Y** with O_2.

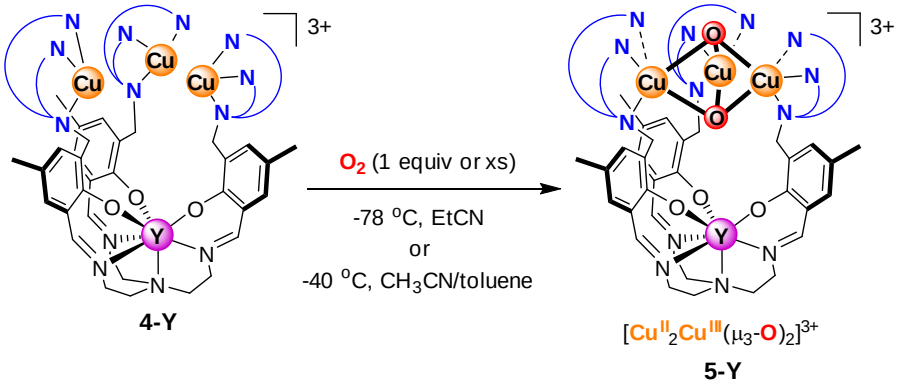

Table 1. Spectroscopic Features of [$Cu^{II}_2Cu^{III}(\mu_3\text{-}O)_2$] Complexes

6 λ_{max}, nm, (ε, $M^{-1}cm^{-1}$)[12]	**7** λ_{max}, nm, (ε, $M^{-1}cm^{-1}$)[14]	**8** λ_{max}, nm, (ε, $M^{-1}cm^{-1}$)[15]	**5-Y** λ_{max}, nm, (ε, $M^{-1}cm^{-1}$)	**13-Y** λ_{max}, nm, (ε, $M^{-1}cm^{-1}$)
290 (12,500)	-		-	-
355 (15,000)	343 (12,000)	328 (10,700)	355 (12,400)	340 (11,500)
480 (1,400)	515 (1,000)	420 (1,500)	480 (1,910)	455 (2,160)
620 (800)	685 (800)	590 (835)	640 (800)	690 (760)

Previously, the only Cu complexes shown to generate this type of 3:1 Cu/O_2 intermediate were mononuclear species supported by bidentate ligands: *N,N,N',N'*-tetraalkylcyclohexanediamines (**6**), reported by Stack *et al.*; *N,N*-dimethyl-2-picolylethanamine (**7**), reported by Itoh *el al.*; and, more recently, 4-(2,2-dimethylhydrazino)-dimethylhydrazone-3-penten-2-one (**8**), described by Tolman *et al.* (Figure 5).[12-15,48,49] For these mononuclear Cu complexes, formation of the [Cu_3] species is driven by low O_2 concentration ([Cu^{I}]/O_2 > 10:1). At lower [Cu]/O_2 ratios, formation of [Cu^{III}–$(O)_2$–Cu^{III}] complexes is usually observed for these complexes, and binding of an additional [Cu^{I}] complex (when present in excess) to this intermediate generates the bis(μ_3-O) species.[47]

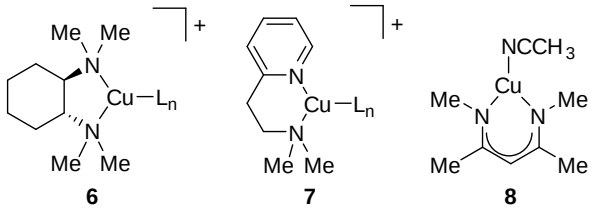

Figure 5. Mononuclear Cu^{I} complexes that can generate $[Cu_3(\mu_3\text{-}O)_2]$ complexes upon reaction with O_2.

Scheme 4. Synthesis of $[YCu_3]$ Complex **12-Y** and Its Reactivity with O_2.

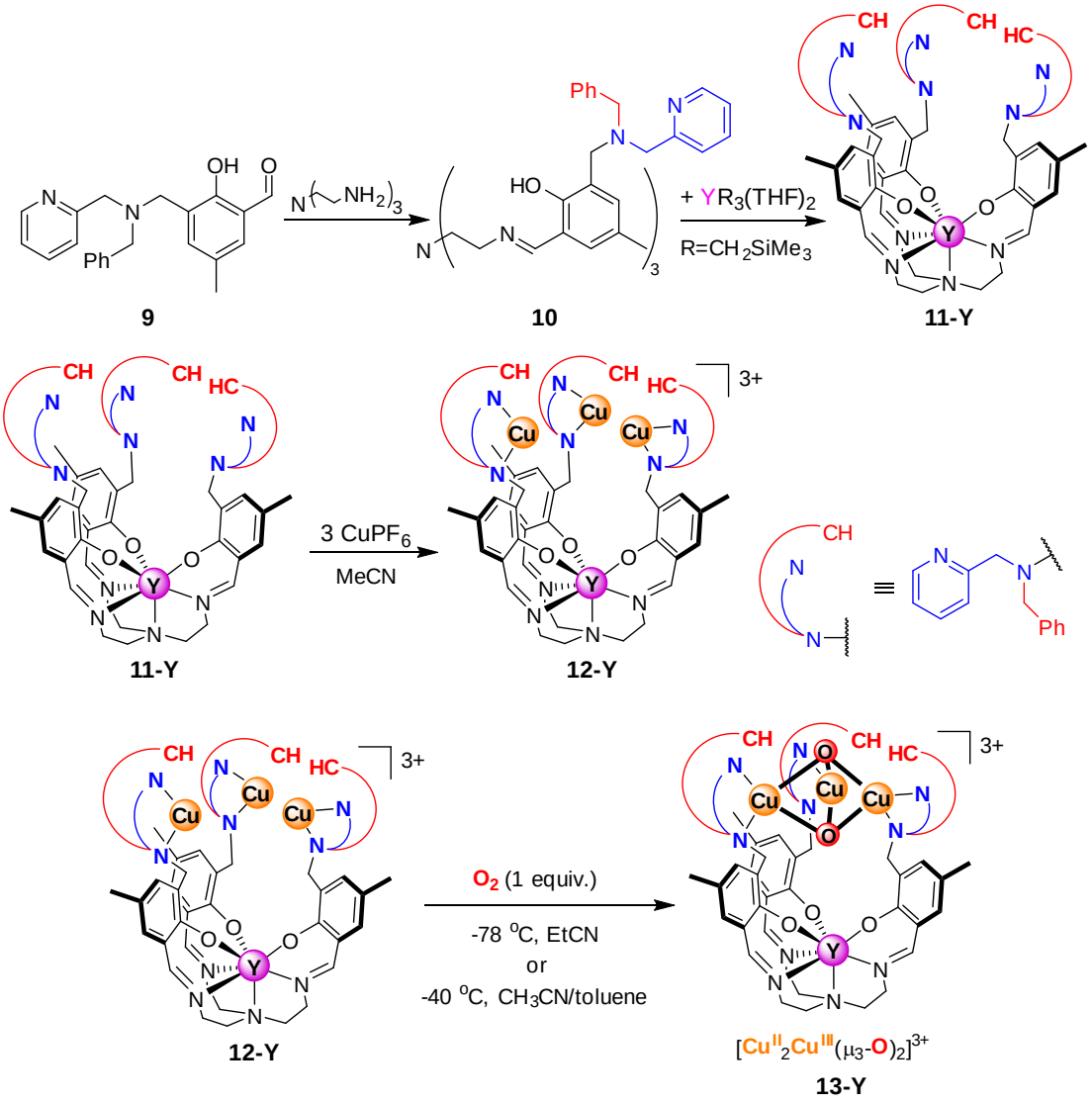

Intermediate **5-Y** was observed to be stable for at least 24 hours at -78 °C (<10% bleaching of UV-Vis signal); about 30% decay occurred over the same timeframe at -

40 °C. At 25 °C, complete decay was observed within minutes. Volumetric measurements carried out with a Toepler pump indicated that 0.97±0.01 equivalents of O_2 were consumed per equivalent of **4-Y**, supporting the formation of a complex with the $[Cu_3O_2]$ stoichiometry.

While literature examples of bis(μ_3-O) complexes were supported by bidentate ligands, three N donors were available to each Cu center in **5-Y** from the dipicolylamine motifs (all N donors are bound to Cu in **4-Y** as shown by the aforementioned XRD studies). To gain insight into whether all three available ligands are bound to Cu in **5-Y**, the behavior of the present architecture with other donor sets was tested. A ligand variant with only two N donors per Cu-binding moiety was synthesized for comparison – on each arm, one pyridyl ligand was replaced with a phenyl group (**10**, Scheme 4). $[YCu_3]$ complex **12-Y** was prepared, and its reaction with O_2 led to a new species with spectroscopic features similar to those of **5-Y** (Figure 4). Spectroscopic comparison with **6**, **7**, and **8** (Table 1), as well as the reaction stoichiometry, supported the assignment of species **5-Y** and **13-Y** as displaying the $[Cu^{II}_2Cu^{III}(\mu_3\text{-}O)_2]$ motif. No evidence of the presence of H_2O_2 was observed when a solution of **5** was treated with formic acid (5 equiv) and Ti(IV)oxysulfate solution.[15,50] EPR studies of **5-Y** were undertaken, and revealed a qualitatively similar spectrum to those reported in the literature for the $[Cu_3O_2]$ species obtained from **6** and **8** (Figure 6).[15,49] Resonance Raman experiments on **5-Y** were attempted, but due to the observation of fluorescence from the ligand phenoxides no useful data could be obtained. Finally, electrospray ionization mass spectroscopy (ESI-MS) analysis of a solution of **5-Y** displayed no molecular ion, but rather a number of smaller fragments, as is the case for all tricopper complexes studied herein (a molecular ion was observed for mono-Cu complexes **14**

and **15**). The synthesis of **5-Y** and **13-Y** was notable given the lack of precedent for preassembled trinuclear copper complexes that show similar reactivity with O_2. The generation of **5-Y** was particularly noteworthy given that previous studies of copper-dipicolylamine complexes do not report trinuclear reactivity.[51] This difference in behavior indicates that the formation of the $Cu^{II}_2Cu^{III}(\mu_3\text{-}O)_2$ unit in this case may be a consequence of preassembling the three copper centers in close proximity.

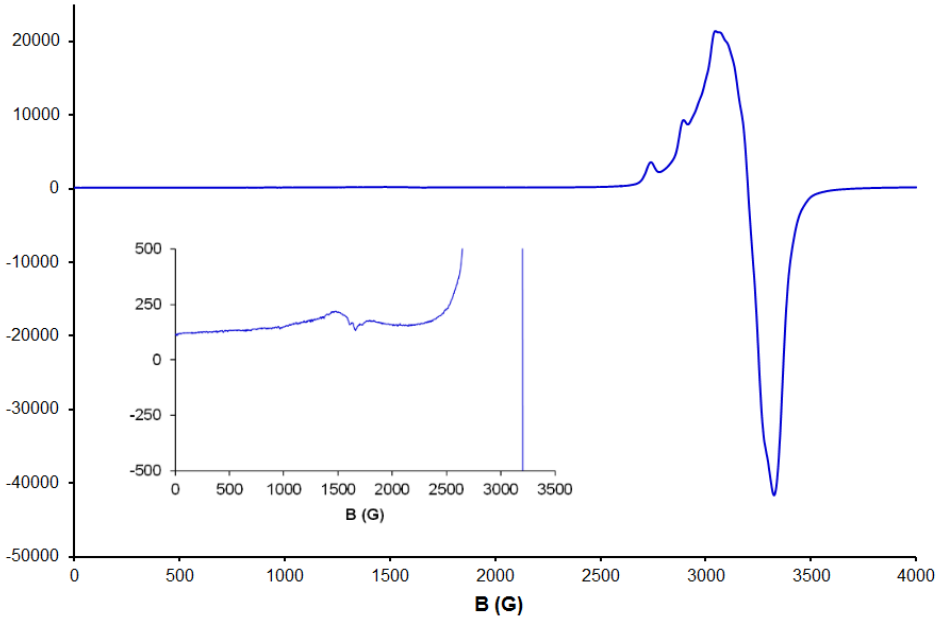

Figure 6. EPR spectrum of **5-Y** (20mM) in 1:1 propionitrile/toluene at 15 K. The inset displays an enlarged view of the g~4 region. Frequency: 9.374 GHz. Power: 0.644mW.

Synthesis and Reactivity of Mono-Copper Analogs

To further test this hypothesis, two related monocopper complexes were prepared, **14** and **15**, both displaying copper-dipicolylamine moieties (Scheme 5). In **14**, the yttrium binding site was removed and substituted with a methyl-aryl ether fragment. Complex **15**, on the other hand, was more closely related to **4-Y**, as it contained the Y-binding $[O_3N_4]$ motif, but only one of its arms was decorated with a dipicolylamine moiety, resulting in binding of a single Cu center. If intermolecular copper self-assembly

reactivity upon reaction with O_2 was responsible for the spectroscopic features of **5-Y** and **13-Y**, mononuclear Cu^I complexes **14** and/or **15** were expected to undergo reactivity similar to **4-Y** and **12-Y**, given the steric and electronic similarities of the Cu centers. Nonetheless, reaction of either of these mono-Cu complexes with O_2 was observed to result in species with spectroscopic features different from **5-Y** and **12-Y** (Figure 7). Even substantial increase in Cu concentration (0.2-10.0 mM) did not lead to observation of the spectroscopic signature of the $[Cu^{II}_2Cu^{III}(\mu_3\text{-}O)_2]$ core. In contrast, **5-Y** and **12-Y** were formed at concentrations as low as 0.05 mM. The literature intermolecular examples were generated at concentrations of 10 mM (complexes **6** and **7**) or 1.0 mM (complex **8**). These findings suggested that precursors **4-Y** and **12-Y** underwent intramolecular, cooperative reactivity and, therefore, that formation of the $[Cu^{II}_2Cu^{III}(\mu_3\text{-}O)_2]$ motif was facilitated by the presence of the three Cu centers prearranged in close proximity on the same ligand framework.

Scheme 5. Mononuclear Cu^I Complexes for Reactivity Comparison to Tricopper Cu_3Y Variants.

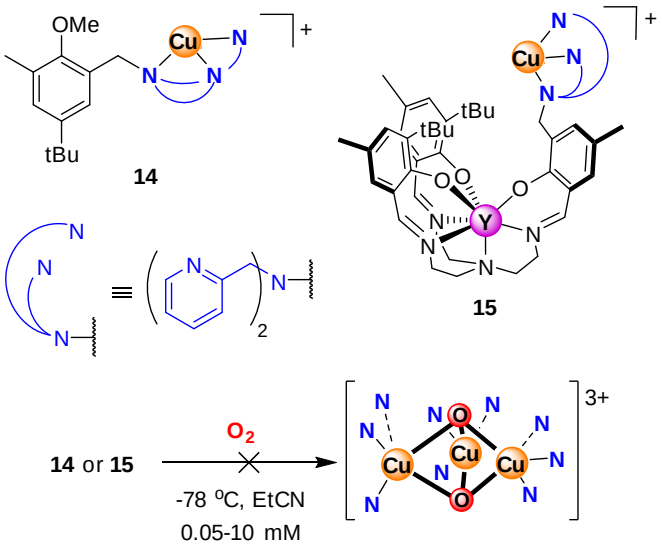

Facilitation of trinuclear cooperative reactivity by the tetrametallic, tricopper architecture in **4-Y** has implications to the reaction of O_2 in biological systems, in which the three Cu centers are kept in close proximity by the protein scaffold. Furthermore, MCOs bind the three copper centers using a total of eight histidines. Compound **5-Y** displays nine N-donors for three coppers, which represents a more accurate model of biological systems (eight total N donors for three Cu centers)[11] than previous model complexes that displayed a total of six nitrogen donors for the $[Cu_3O_2]$ moiety – though in the present case coordination of all nitrogens has not been confirmed structurally. Although studies of multicopper proteins have not shown evidence of a $[Cu^{II}_2Cu^{III}(\mu_3\text{-}O)_2]$ moiety,[9] bur rather for a bridging peroxide species, investigations of this moiety in a model system are expected to further our understanding of O_2 activation at tricopper sites.

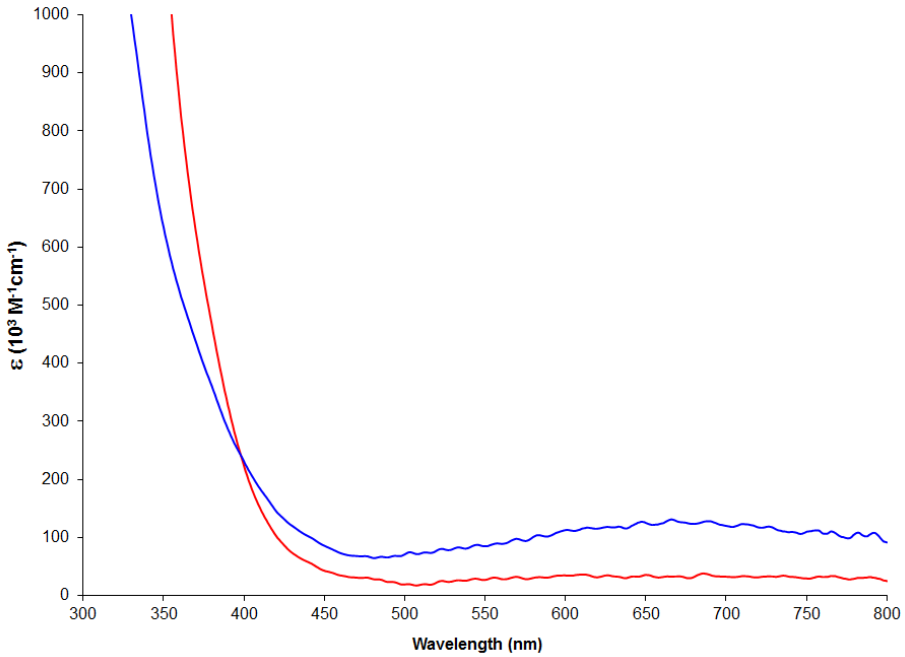

Figure 7. UV-Vis spectra of solutions of **14** (blue) and **15** (red) after addition of dioxygen in 1:1 propionitrile/tetrahydrofuran at -78 °C.

Synthesis and Reactivity of Other Lanthanide-Tricopper Complexes

In order to determine whether geometric changes in the ligand architecture would induce changes in reactivity, [$LnCu_3$] complexes analogous to **4-Y** (Ln=La, Ce, Nd, Eu, Lu) were investigated (Scheme 6). The size of the central Ln^{3+} ion was known to affect the relative orientation of the three phenoxide arms, with the propeller-like turn of the aromatic rings varying from 27.3º to 47.7º from the N_{axial}–Ln vector.[52] Complexes **4-Ln** were prepared by protonolysis with suitable $Ln(HMDS)_3$ reagents (HMDS=hexamethydisilazide) followed by metalation with $Cu(CH_3CN)_4OTf$. Full characterization of complexes **4-La** and **4-Lu** was obtained, including elemental analysis. **4-Ce**, **4-Nd**, **4-Eu**, on the other hand, could only be characterized by their (paramagnetic) ^1H NMR spectra.

Scheme 6. Synthesis of Lanthanide Complexes and Reactivity with O_2

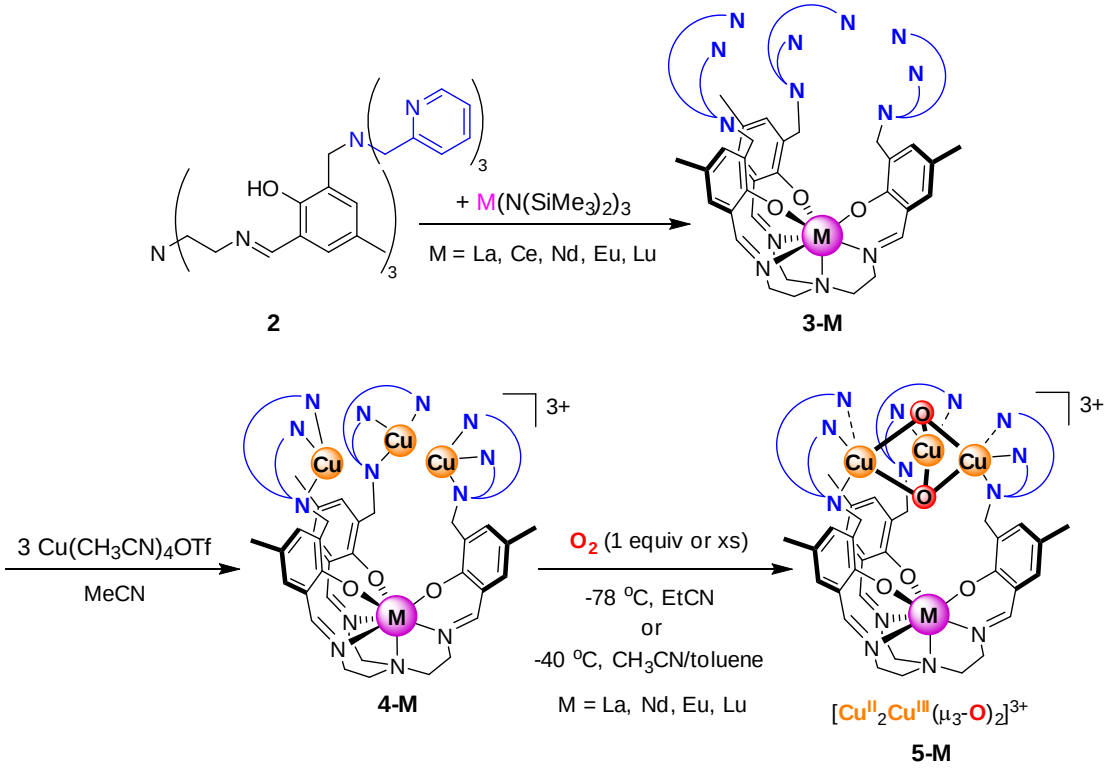

Monitoring of O_2 reactivity of **4-La**, **4-Nd**, **4-Eu**, and **4-Lu** via UV-Vis spectroscopy revealed reactivity analogous to [Cu_3Y] complexes **4-Y** and **12-Y** (Figures 8 and 9). The similar reactivity of complexes of lanthanides of different sizes (from largest, La, to smallest, Lu)[53] further highlighted the ability of the present architecture to engender cooperative reactivity among the three Cu centers regardless of the nature of the central templating metal.

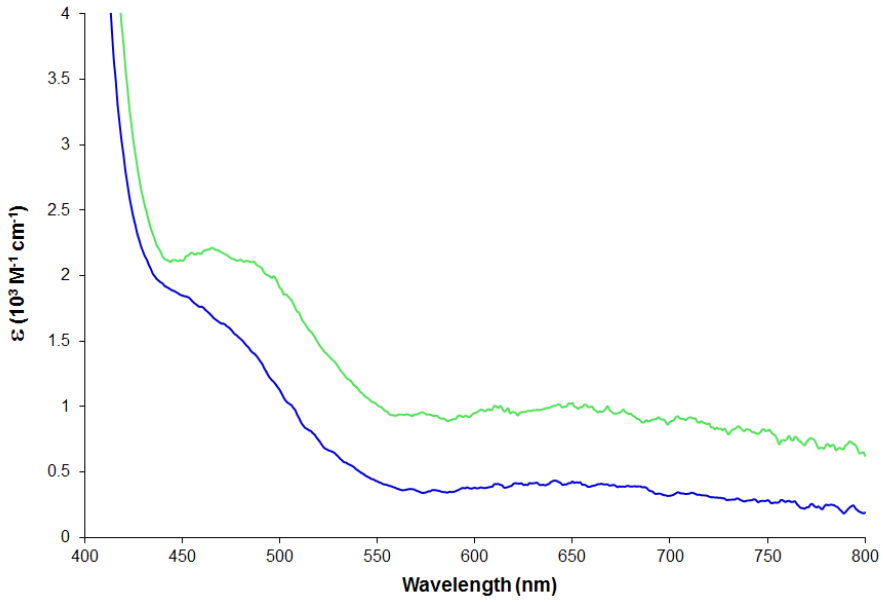

Figure 8. UV-vis spectra of reaction of **4-La** (blue) and **4-Lu** (green) in 1:1 toluene/EtCN at -78 °C.

Investigation of Ce^{III} complexes was undertaken to introduce an intriguing new element in the exploration of tetrametallic Cu_3 complexes. In the MCOs, the biological system our scaffold aimed to model, due to the presence of a fourth Cu center, all metal centers are in the Cu^{II} oxidation state following the 4-e^- reduction of O_2. In **5-M** and **12-M**, on the other hand, one of the Cu centers must access the Cu^{III} oxidation state, as only three metals are involved in O_2 reduction. Unlike the other rare earths

investigated in this study, Ce^{III} has an accessible redox couple (Ce^{IV}/Ce^{III}), and may therefore become involved in O_2 reduction via electron transfer.

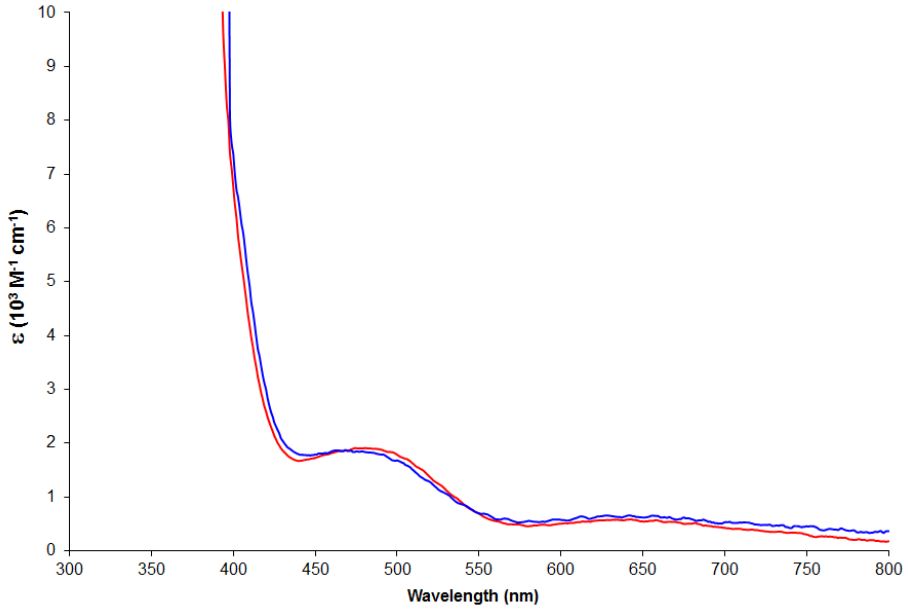

Figure 9. UV-Vis spectrum of reaction of **4-Nd** (red) and **4-Eu** (blue) with O_2 in 1:1 toluene/EtCN at -78 °C.

To gain insight into whether Ce^{III} participation in O_2 reduction was possible, we targeted complexes **3-Ce** and **4-Ce**. Unfortunately, both of these compounds were discovered to be extremely sensitive to even trace O_2 – under conditions for which no oxidation was observed with other **3-M** and **4-M** complexes – which greatly complicated identification of the compounds and exploration of their reactivity. The higher reactivity of **3-Ce** with O_2 than that found in most $[Cu^{I}_{3}]$ complexes was particularly surprising, with a change in color becoming evident in UV-Vis samples even faster than they could be connected to the inert gas feed at the spectrophotometer. As seen in Figure 10, evidence for oxidation of **3-Ce** (a shoulder at ~450 nm) was seen even in the first recorded UV-Vis, in agreement with an observed slight darkening in color. Upon further reaction with O_2, a clearer feature at 485 nm (ε = 3000 M^{-1} cm^{-1})

appeared. An independently synthesized Ce^{IV} species supported by the same multidentate ligand framework (**16**, Scheme 7) displayed a similar feature at 520 nm (ε = 4,400 M^{-1} cm^{-1}), together with a more intense transition at 345 nm (ε = 16,900 M^{-1} cm^{-1}), as shown in Figure 11.

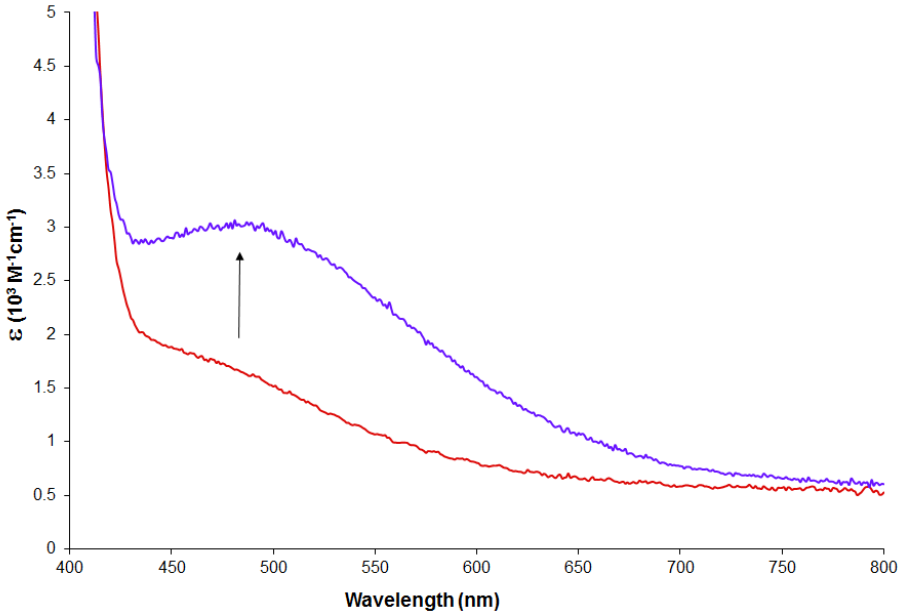

Figure 10. UV-Vis spectra of **3-Ce** before (red) and after (purple) reaction with O_2 in 1:1 toluene/EtCN at -78 °C.

Scheme 7. Synthesis of **16**.

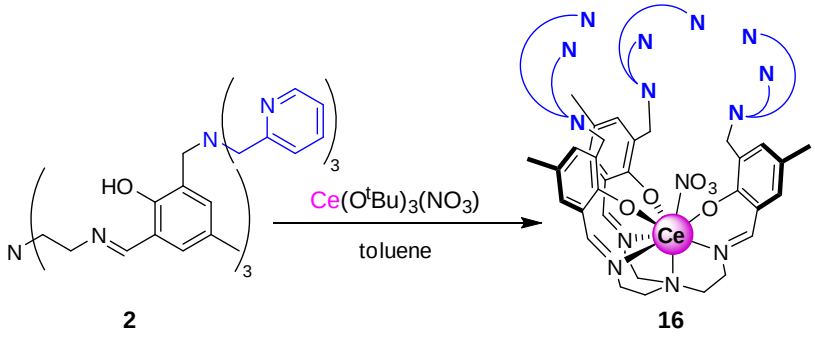

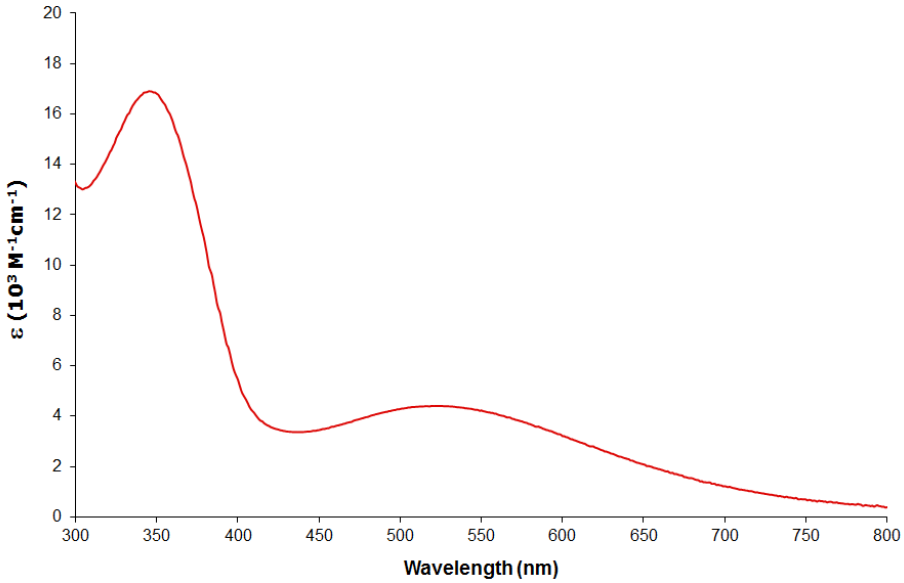

Figure 11. UV-vis spectrum of **16** in CH_3CN.

Metallation of **3-Ce** with $Cu(CH_3CN)_4OTf$ afforded **4-Ce** (neither **3-Ce** nor **4-Ce** could be obtained in analytically pure form). Reaction of **4-Ce** with O_2 gave rise to a different UV-Vis signature from both **4-M** complexes *and* **3-Ce** (Figure 12 and 13). This observation was promising, as it suggested the possibility that Ce^{III} may be involved in O_2 reduction by **4-Ce**. On the basis of reactivity of the **4-M** complexes, incorporation of Ce should not preclude formation of a $[Cu_3(\mu_3\text{-}O)_2]$ on the basis of its size. The absence of the spectral signature of the bis(μ_3-O) intermediate was therefore consistent with the formation of an intermediate with more reduced Cu centers – possibly a hitherto unreported $[Cu^{II}_3(\mu_3\text{-}O)_2]$ species. Unfortunately, no further characterization of the products of reaction of **3-Ce** and **4-Ce** with O_2 could be obtained – structural or spectroscopic.

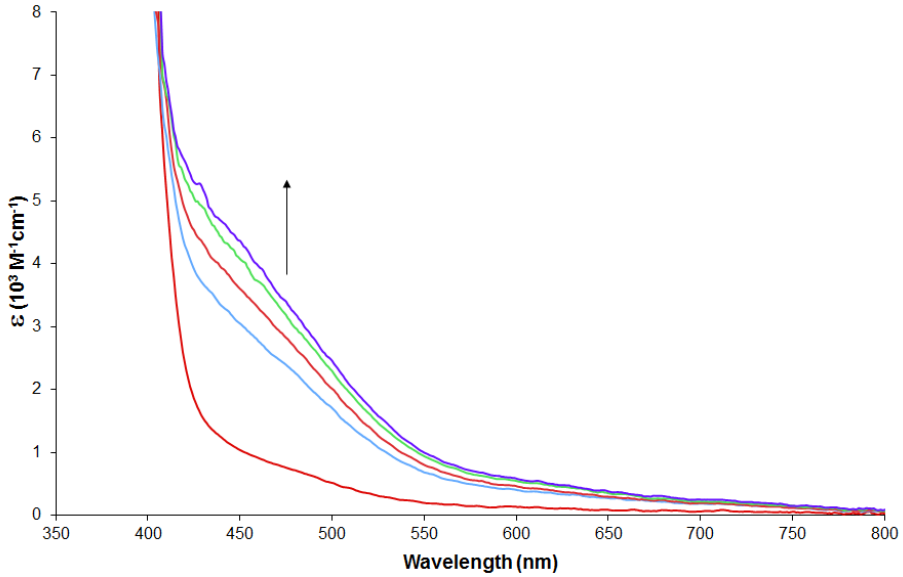

Figure 12. UV-Vis spectra of reaction of **4-Ce** with O_2 in 1:1 toluene/EtCN at -78 °C.

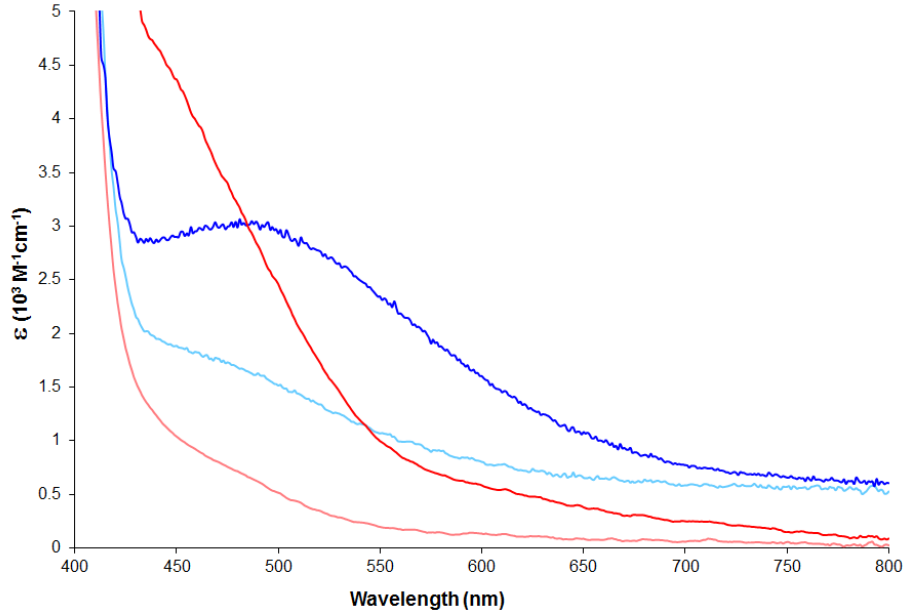

Figure 13. Comparison of UV-Vis spectra for reaction of **3-Ce** (blue traces) and **4-Ce** (red traces) with O_2 in 1:1 toluene/EtCN at -78 °C. Lighter and darker lines correspond to spectra before and after addition of O_2, respectively.

Reactivity of $[Cu_3O_2]^{3+}$ Intermediates

To gain insight into their properties and to further compare them to literature reports, the reactivities of intermediates **5-Y** and **13-Y** were explored. Reactions of **5-Y** and **13-Y** with substituted ferrocenes were performed to estimate their reduction potentials, similar to what had been reported in the literature for products of O_2 activation by copper complexes.[12,54,55] In each case, the 450-480 nm band decayed completely over 6 h upon treatment with decamethylferrocene (Fc*, $E_{1/2}$ = -0.59 vs. Fc^+/Fc, 4 equiv.)[56] at -40 °C (Figure 14 and 15). Treatment with 1,1'-dimethylferrocene (Me_2Fc, $E_{1/2}$ = -0.12 V vs. Fc^+/Fc)[56] over the same time period did not lead to decay of **5-Y** or **13-Y** beyond background decomposition.

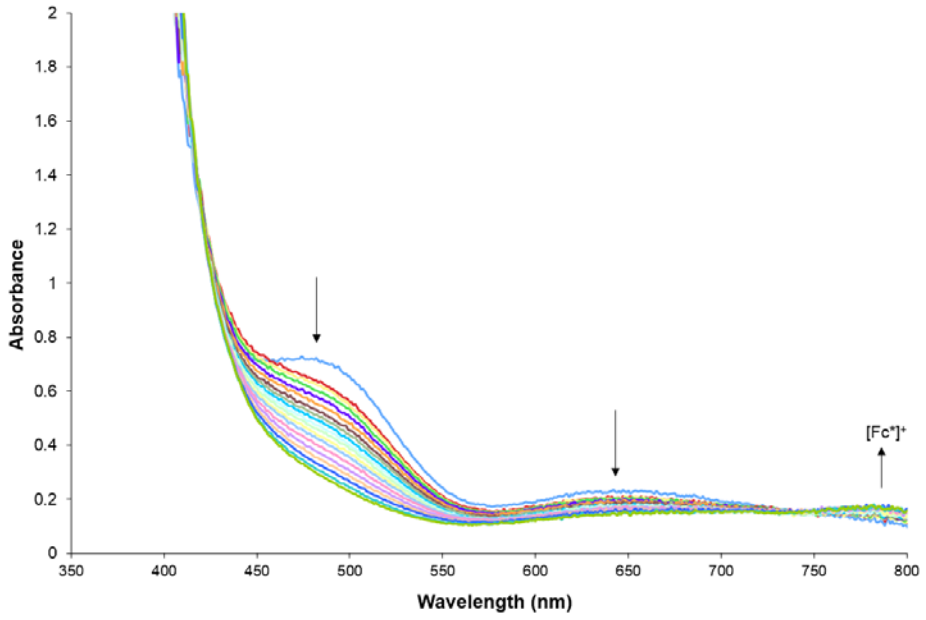

Figure 14. UV-Vis spectra of reaction of **5-Y** (0.30 mM) with decamethylferrocene (4 equiv.) in 1:1 toluene/CH_3CN at -40 °C. Scan interval: 20 min. Total reaction time: 6 hours.

These results indicated that the reduction potentials of both **5-Y** and **13-Y** are between -0.59 and -0.12 V vs. Fc^+/Fc. In contrast, the reduction potentials of the first two

reported $[Cu_3O_2]$ species generated from **6** and **7** were found to be between 0.21 and 0 V vs. Fc^+/Fc as determined by analogous reactivity with acetylferrocene and ferrocene, respectively.[12] Furthermore, several $Cu^{III}_2(\mu_2\text{-}O)_2$ species were reported to have a reduction potential near 0.1 V vs. Fc^+/Fc.[57] Hence, **5-Y** and **13-Y** are significantly weaker oxidants. This may be due to the presence of electron-rich phenoxide substituents on the nitrogen donors. Indeed, the $[Cu_3O_2]$ motif generated from **8** reported by Tolman and coworkers, supported by more electron rich, anionic ligands, were unreactive toward even the more reducing decamethylferrocene.[15]

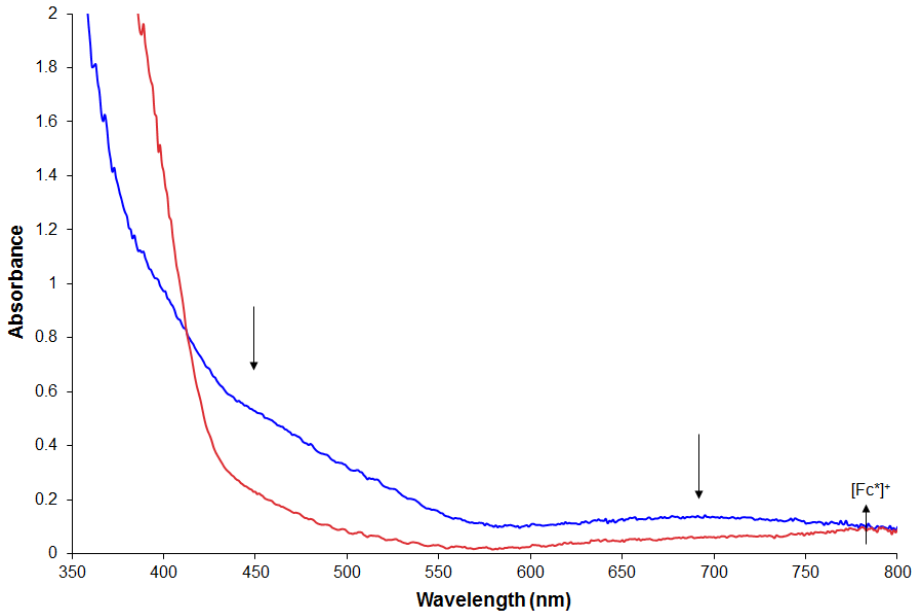

Figure 15. UV-Vis spectrum of **13-Y** (0.182 mM, blue) at -40 °C; and after reaction with decamethylferrocene (5 equiv.) at -40 °C (red) over 6 hours.

Compound **5-Y** reacted with 2,4-di-*tert*-butylphenol at -40 °C as observed via UV-Vis spectroscopy. According to GC-MS and ^{1}H NMR spectroscopy, the phenol starting material was quantitatively recovered upon work-up. This behavior is in contrast to that of other bis$(\mu_3\text{-}O)_2$ moieties supported by neutral ligands, which generated biphenol.[12,14] It has been previously proposed that the phenol coordination to copper precedes

dimerization.[14] The higher coordination number of **5-Y** may block phenol binding to the copper centers. However, the analogous reaction of **13-Y** – which has one less N-donor available per Cu center – with phenol also failed to yield dimerized product. This observation suggested that steric bulk, rather than coordination number, may be the reason for the differences in reactivity between **5-Y** and **13-Y** and other $[Cu_3O_2]$ moieties. Reaction of **5-Y** with a less bulky phenol (4-tertbutylphenol) also showed no evidence of oxygenation or C–C coupling. Furthermore, H-atom abstraction by the $[Cu_3O_2]$ moiety was ruled out when reaction with 2,4,6-tri-*tert*-butylphenol was observed to not give rise to the known 2,4,6-tri-*tert*-butylphenoxyl radical as monitored by UV-Vis spectroscopy. Hence the observed reactivity was proposed to involve only protonation, and not reduction, of the $[Cu_3O_2]$ moiety. The reactivity of **5-Y** with a variety of acids was therefore studied. Treatment of **5** at -40 °C with triethylammonium triflate (pK_a=18.5 in acetonitrile)[58] resulted in complete bleaching of the 485 and 645 nm bands over 4 hours. Treatment of **5** with weaker acids led to slightly slower reactions, as monitored by UV-Vis spectroscopy: 1,8-diazabicyclo[5.4.0]undec-7-enium triflate (pK_a=24.34)[58], and pyrrole (pK_a=34.6)[58], reacted with **5-Y** to 50-70% completion in 6 hours (Figures 16-18). Although a pK_a value could not conclusively be assigned to **5-Y**, reaction with acids as weak as pyrrole was consistent with reactivity with phenols (pK_a>25)[58] also involving protonation events.

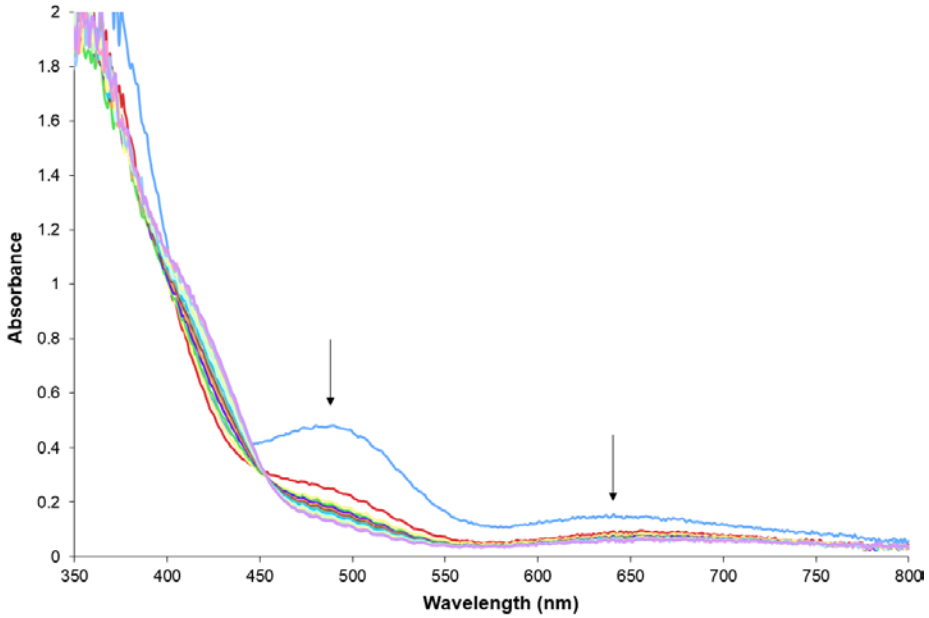

Figure 16. UV-Vis spectrum of reaction of **5-Y** (0.17 mM) with [Et_3NH][OTf] (10 eq) in 3:2 toluene/acetonitrile at -40 °C. Scan interval: 20 minutes. Total reaction time: 4 hours.

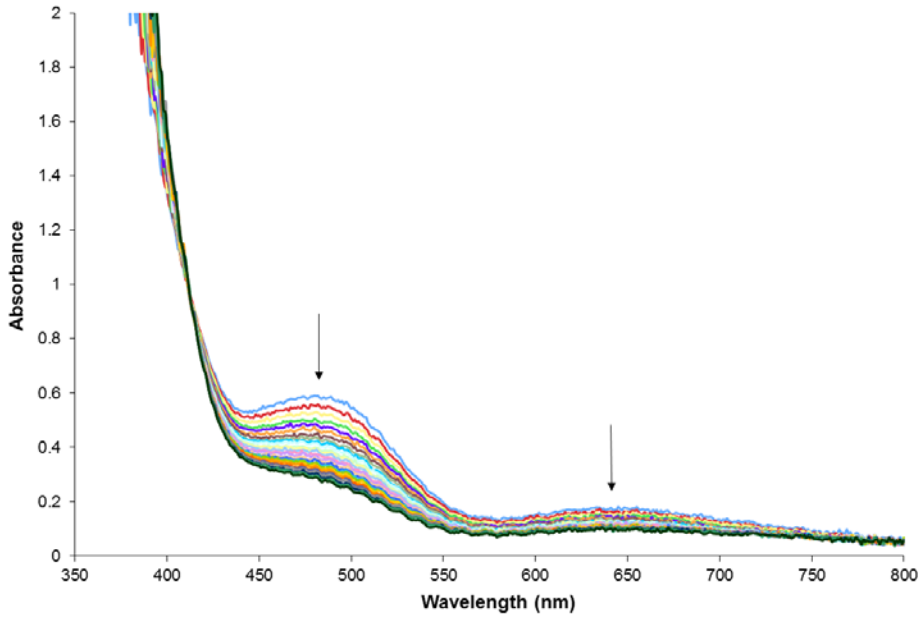

Figure 17. UV-Vis spectrum of reaction of **5-Y** (0.20 mM) with [DBU-H][OTf] (5 eq) in 3:2 toluene/acetonitrile at -40 °C. Scan interval: 20 minutes. Total reaction time: 6 hours.

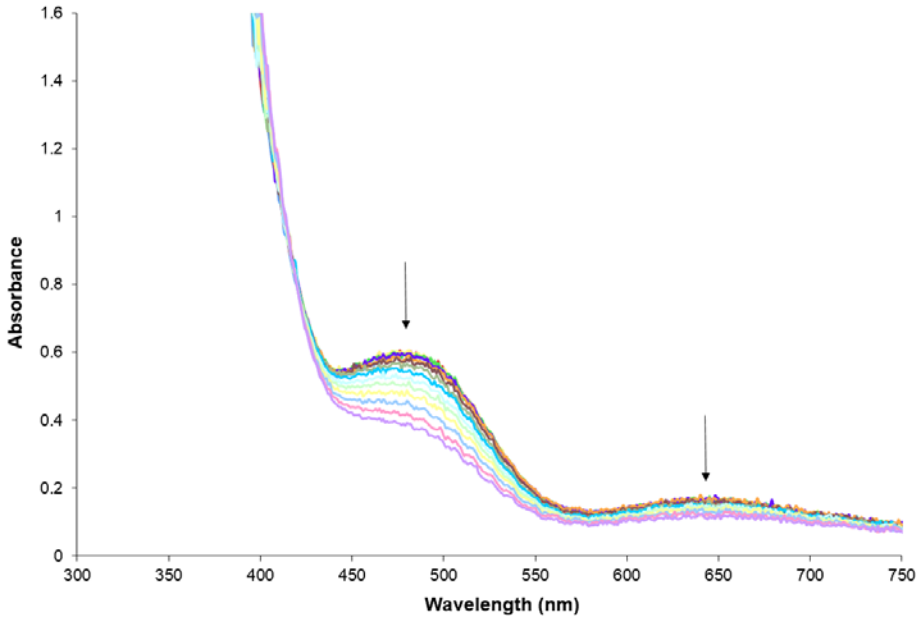

Figure 18. UV-Vis spectrum of reaction of **5-Y** (0.20 mM) with pyrrole (5 eq) at -40 °C, in 3:2 toluene/acetonitrile. Scan interval: 20 minutes. Total reaction time 6 h.

The reactions of **5-Y** with phosphine and H-atom transfer agents were investigated (Scheme 8). Intermediate **5-Y** was found to react to completion with triphenylphosphine (5 equiv.) in 3 hours to give triphenylphosphineoxide (0.84 ± 0.10 equiv., ^{31}P-NMR spectroscopy). In contrast, treatment of **13-Y** with PPh_3 yielded ~2 equivalents of (O)PPh_3, suggesting that the lower coordination number of the Cu centers in **7** and consequent steric bulk facilitated access to the second oxygen atom by phosphine. Decay of the spectroscopic signature of **5-Y** was also observed upon treatment with *N*-hydroxy-2,2,6,6-tetramethylpiperidine (TEMPO–H, pK_a>41 in acetonitrile[59]), and the reaction reached completion in 4 hours (Figure 19). The faster rate of reaction than expected, based on the pK_a of TEMPO–H, suggested that a different type of process was occurring. Integration of the electron paramagnetic resonance (EPR) signal of the TEMPO–H reaction solution and comparison to a standard solution of TEMPO radical[49] indicated that two equivalents of TEMPO

radical were generated per $[Cu_3O_2]$ moiety. Hence, compound **5-Y** was performing formal H-atom abstraction, rather than just deprotonation, in the reaction with TEMPO–H. No reaction was observed with 9,10-dihydroanthracene or toluene. The observed trend in reactivity therefore reflected the trend in X–H bond dissociation energies for these substrates (70 kcal/mol for TEMPO–H,[60] 74 kcal/mol for dihydroanthracene,[61] and 88 kcal/mol for toluene[62]).

Scheme 8. Reactivity of $[Cu_3O_2]$ Species with O- and H-Atom Acceptors.

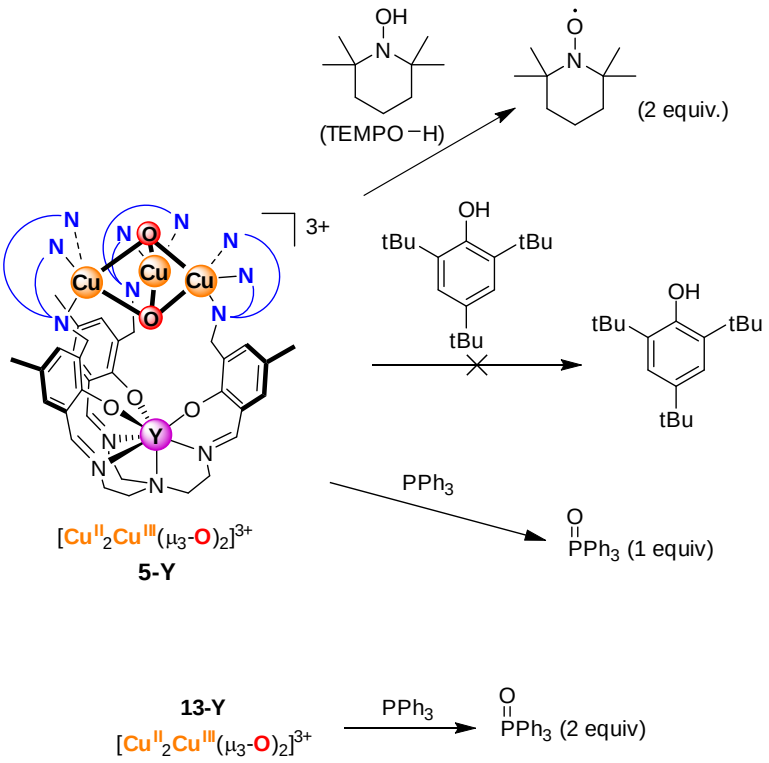

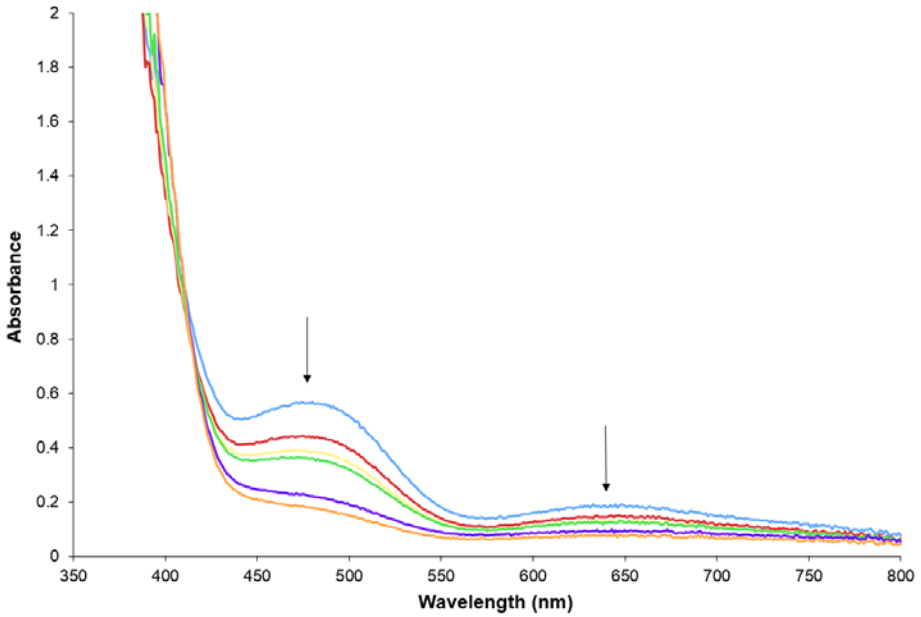

Figure 19. UV-Vis spectrum of reaction of **5-Y** (0.126 mM) with TEMPO–H in propionitrile at -78 °C. Scan interval: 30 minutes. Total reaction time: 4 hours.

The reactivity of complex **5-Y** with thiol reducing agents was also investigated. Upon treatment with 4-*tert*-butylthiophenol (Scheme 9) a solution of **5-Y** turned from orange-brown to yellow within seconds. After anaerobic workup at room temperature, the reaction mixture was observed to contain two equivalents of the diaryldisulfide product **17** by ^{1}H NMR, which corresponded to an overall transfer of four protons and four reducing equivalents to complex **5-Y**. A reduced, diamagnetic tricopper species was recovered in near-quantitative yield and was found to display *ca.* one bound thiophenol ligand by ^{1}H NMR. The identity of the recovered tricopper complex (**18**) was confirmed by independent synthesis via addition of 4-*tert*-butyl-thiophenol to **4-Y** (Scheme 9). Therefore, unlike TEMPO-H, thiophenol was found to be capable of delivering the four electrons and four protons necessary for full reduction of the $[Cu^{II}_2Cu^{III}O_2]$ core in **5-Y** to $[Cu^{I}_3]$. Reaction of **5-Y** with excess thiophenol in the presence of excess O_2 also yielded only two equivalents of disulfide **17**, indicating that

binding of thiophenol to the [Cu^{I}_3] species formed upon reduction of **5-Y** inhibits its reaction with dioxygen. This was confirmed by exposure of **18** to O_2 which led to no observed reactivity. A solution of **5-Y** that was allowed to warm to room temperature to yield the decomposition products of **5-Y** still displayed reactivity with 4-*tert*-butylthiophenol. However, this protocol gave a lower yield of **17** (50 %), and the reduced tricopper species **18** was observed (~50% yield, ^{1}H NMR) but could not be isolated cleanly.

Scheme 9. Reactivity of Complex **5-Y** with Thiophenols

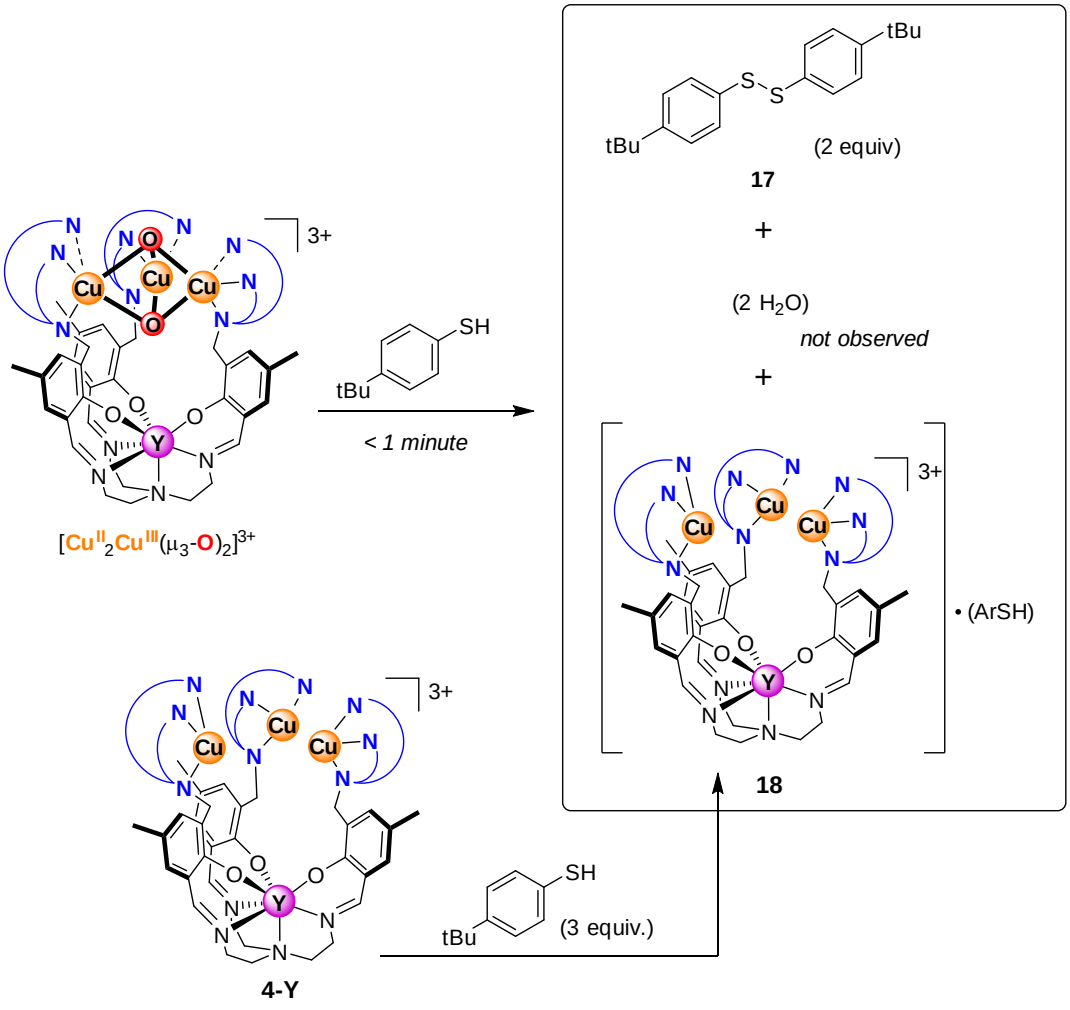

Table 2. Summary of Reactivity of Complexes **5-Y** and **13-Y**.

Complex	Substrate	Reaction Time	Completion (%)	Product[a]
		One-Electron Reductants		
5-Y	Fc*	6 h	100	$[Fc^*]^+$
5-Y	Me_2Fc	6 h	N.R.	-
13-Y	Fc*	6 h	100	$[Fc^*]^+$
13-Y	Me_2Fc	6 h	N.R.	-
		Brønsted Acids		
5-Y	$[Et_3NH][OTf]$	4 h	100	$(Et_3N)^a$
5-Y	[DBU–H][OTf]	6 h	~70	$(DBU)^a$
5-Y	2,4-di-*tert*-butylphenol	6 h	~70	(2,4-di-*tert*-butyl phenoxide)[a]
5-Y	pyrrole	6 h	~50	$(pyrrolide)^a$
		H-Atom Donors		
5-Y	TEMPO–H	4 h	100	TEMPO• (1 equiv)
5-Y	ArSH	1 minute	100	ArS–SAr (2 equiv)
		O-Atom Acceptors		
5-Y	PPh_3	4 h	100	$O{=}PPh_3$ (1 equiv)
13-Y	PPh_3	4 h	100	$O{=}PPh_3$ (2 equiv)

[a] Products not directly observed.

The reactivity of intemediates **5-Y** and **13-Y** is summarized in Table 2. The present $[Cu_3(\mu_3\text{-}O)_2]$ moiety was a weaker oxidant relative to other dicopper and tricopper oxo species with reported reduction potentials. This may explain its lack of oxidative C–C

coupling reactivity with alkylphenols.[63] X–H bond activation by **5-Y** was observed only with substrates that have weak X–H bonds. Since X–H bond activation is controlled by both the reduction potential and basicity of the metal-oxo species,[64-67] it was not surprising that, despite a qualitatively basic motif as shown by its reactivity with weak acids, reactivity with stronger X–H bonds was not observed, in view of the more negative reduction potential. This behavior is consistent with the function of tricopper sites in MCOs, which are oxidases and hence do not perform C–H oxygenations. Oxygenation reactivity would likely be detrimental to these proteins, as it would lead to the functionalization of amino-acid side chains near the tricopper site (inaccessible to the oxidation substrates).

CONCLUSIONS

In summary, ligand frameworks displaying a total of sixteen or thirteen oxygen and nitrogen donors were selectively templated by Y^{3+} and lanthanides (La^{3+}, Ce^{3+}, Eu^{3+}, Nd^{3+}, Lu^{3+}) binding to a tripodal $[O_3N_4]$-trisphenoxide-trisimine-amine moiety. The remaining three pycolylamine-based metal binding sites were used to bind Cu^{I} centers. Reactions of these $[Cu^{I}_3Y]$ complexes with O_2 generated $[Cu^{II}_2Cu^{III}(\mu_3\text{-}O)_2]$ motifs according to spectroscopic comparison to literature compounds and the measured reaction stoichiometry. Since two related mononuclear dipicolylamine-supported Cu complexes do not generate $[Cu^{II}_2Cu^{III}(\mu_3\text{-}O)_2]$ species, the preorganized tricopper core was determined to be necessary for this reactivity with O_2. Similarly to multicopper oxidases, the close arrangement of three metal centers led to cooperative activation of O_2. Compound **5-Y** was less oxidizing than previously reported $[Cu^{II}_2Cu^{III}(\mu_3\text{-}O)_2]$ complexes and did not perform phenol dimerization. This observation was possibly due to the availability of an additional nitrogen donor per arm in **5-Y** vs. the bidentate

ligands reported in the literature to support analogous intermediates. However, oxygenation of triphenylphosphine and activation of the weak O–H bond of TEMPO–H were observed. Oxidation of thiol to generate two equivalents of diaryldisulfide highlighted the ability of **5-Y** to be reduced back to a $[Cu^{I}_{3}]$ core using four electrons and four protons. Starting from **4-Y**, the overall process corresponded to the reduction of O_2 to H_2O. The structural features that led to the differences between the present system and previous reports of analogous intermediates were not fully elucidated, although both steric and electronic effects on reactivity were observed. The molecular architectures reported here are expected to be generally applicable to the assembly of multimetallic complexes for a variety of transformations including multielectron redox processes and acid-base chemistry.

EXPERIMENTAL SECTION

General considerations.

All procedures were carried out using standard Schlenk techniques or in an M. Braun glovebox filled with purified nitrogen unless stated otherwise. All reactions involving metal reagents were carried out in the glovebox. Anhydrous THF was purchased from Aldrich in 18 L Pure-Pac™ containers. Anhydrous dichloromethane, acetonitrile, diethyl ether, and THF were purified by sparging vigorously with nitrogen for 15 minutes and then passing under nitrogen pressure through a column of activated A2 alumina (Zapp's). Anhydrous DMF was purchased from Sigma-Aldrich and stored under nitrogen over 4 Å molecular sieves. Spectrophotometric-grade acetone was purchased from Sigma-Aldrich, dried over calcium sulfate, vacuum-transferred onto additional calcium sulfate, vacuum-transferred a second time, and stored in the glovebox. Propionitrile was purchased from Sigma-Aldrich and dried over CaH_2. All non-dried solvents used were reagent grade or better. All NMR solvents were purchased from Cambridge Isotope Laboratories, Inc. NMR solvents were dried as follows: CD_3CN and CD_2Cl_2 over calcium hydride, C_6D_6 over sodium benzophenone ketyl. All NMR solvents were degassed by three freeze-pump-thaw cycles and vacuum-transferred prior to use. ^1H NMR and ^{13}C NMR spectra were recorded on a Varian 300 MHz instrument or on a Varian 400 MHz instrument, with shifts reported relative to TMS as determined by observation of the residual solvent peak. Unless otherwise noted, all commercially available materials were used as received. $Y(CH_2SiMe_3)_3(THF)_2$ and all $Ln(NSiMe_3)_2)_3$ (Ln = La, Ce, Nd, Eu, Lu) salts were prepared according to published procedures.[68,69] UV-Vis spectra were collected on a Varian 50Bio spectrophotometer using a Schlenk-adapted 1 cm quartz cuvette. Low-temperature

UV-Vis spectra were obtained using a Varian dip-probe (661.202-UV, 10 mm) and a custom-made glass vessel.

Synthesis of 2.

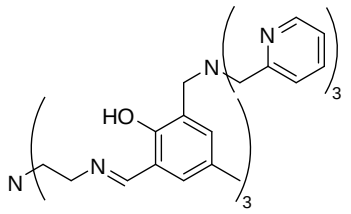

2

In a Schlenk tube, aldehyde **1** (0.617 g, 1.78 mmol)[70] and tris(2-aminoethyl)amine (0.088 mL, 0.592 mmol, 0.33 equiv) were added against positive nitrogen pressure. Dry methanol (15 mL) was added via cannula transfer and the reaction was stirred at room temperature for 16 hours. Volatile materials were removed under vacuum to yield the product as a yellow powder (91%). ^{1}H-NMR (300 MHz, C_6D_6): δ 14.08 (s, 3H, ArO*H*), 8.43 (s, 6H, Ar*H*), 7.69 (s, 3H, ArC*H*NCH$_2$), 7.62 (m, 6H, Ar*H*), 7.55 (br s, 6H, Ar*H*), 7.13 (m, 6H, Ar*H*), 6.58 (m, 6H, Ar*H*), 5.75 (s, 3H, Ar*H*), 4.12 (s, 6H, NC*H*$_2$Ar) 4.10 (s, 12H, NC*H*$_2$Ar), 3.02 (br s, 6H, NC*H*$_2$CH$_2$N), 2.19 (br s, 6H, NCH$_2$C*H*$_2$N), 2.09 (s, 9H, C*H*$_3$Ar) ppm. ^{13}C-NMR (101 MHz, CD_2Cl_2): δ 166.18 (Ar*C*HN), 160.21 (Ar), 157.63 (Ar), 148.96 (Ar), 135.43 (Ar), 133.90 (Ar), 130.62 (Ar), 126.52 (Ar), 126.04 (Ar), 122.23 (Ar), 121.28 (Ar), 118.33 (Ar), 60.06 (N*C*H$_2$Ar), 57.99 (N*C*H$_2$Ar), 55.79 (NCH$_2$*C*H$_2$N), 51.96 (N*C*H$_2$CH$_2$N), 20.22 (Ar*C*H$_3$) ppm. HRMS (FAB), $C_{69}H_{76}N_{13}O_3$: calculated m/z = 1134.619; observed m/z = 1134.6188 ($M+H^+$).

Synthesis of 3-Y.

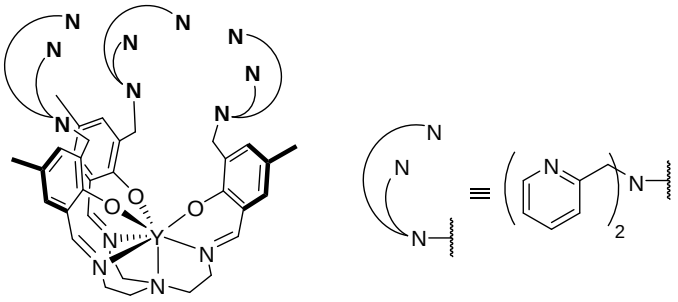

3-Y

In a 20 mL scintillation vial, **2** (0.0538 g, 0.047 mmol) was dissolved in THF (5 mL), and the solution was frozen in a cold well. A solution in THF (3 mL) of $Y(CH_2SiMe_3)_3(THF)_2$ (0.0235 g, 0.047 mmol, 1 equiv) was also frozen in the cold well. The thawing yttrium alkyl solution was added dropwise to the thawing ligand solution. The reaction mixture was stirred at room temperature for 4 h, during which time it turned from yellow to green to green-blue. The volatile materials were removed *in vacuo* to give a greenish solid. The solid was washed with hexane, diethyl ether, benzene, and THF. The THF filtrate was collected and evaporated to give 0.037 g of yttrium complex product as a yellow powder (64%). ^{1}H-NMR (300 MHz, CD_2Cl_2): δ 8.38 (s, 6H, *o*-Py*H*), 7.98 (s, 3H, ArC*H*NCH$_2$), 7.48 (m, 6H, Py*H*), 7.38 (m, 6H, Py*H*), 7.09 (d, 2.4 Hz, 3H, Ar*H*), 7.02 (m, 6H, Py*H*), 6.60 (d, 2.4 Hz, 3H, Ar*H*), 4.13 (m, 3H, ArC*H*H'N), 3.56 (m, 15H, NC*H*$_2$Ar+NC*H*$_2$C*H*$_2$N), 3.28 (m, 3H, NCH*H'*Ar), 3.17 (m, 3H, NC*H*H'Ar), 2.99 (m, 6H, NC*H*$_2$Ar), 2.14 (s, 9H, C*H*$_3$Ar) ppm. ^{13}C-NMR (101 MHz, CD_2Cl_2): δ 167.95 (Ar*C*HN), 164.33 (Ar), 161.06 (Ar), 148.43 (Ar), 136.47 (Ar), 135.62 (Ar), 132.77 (Ar), 128.15 (Ar), 122.76 (Ar), 121.37 (Ar), 121.09 (Ar), 120.81 (Ar), 59.86 (N*C*H$_2$Ar), 59.30 (N*C*H$_2$Ar), 57.96 (NCH$_2$*C*H$_2$N), 52.08 (N*C*H$_2$CH$_2$N), 20.11 (Ar*C*H$_3$) ppm. HRMS (FAB), $C_{69}H_{76}N_{13}O_3Y$: calculated m/z = 1220.502; observed m/z = 1220.505 ($M+H^+$).

Synthesis of 3-La.

In a glovebox, 0.1917 g **2** (169 μmol) was dissolved in THF and the solution frozen. Separately, La[N(SiMe$_3$)$_2$]$_3$ (0.1048 g, 169 μmol, 1 equiv) was dissolved in THF and this solution also frozen. Upon thawing, the La solution was added to the stirring ligand solution dropwise. The solution was allowed to warm to room temperature. After 2 hours, volatiles were removed *in vacuo*. The resulting solid was washed with hexanes, diethyl ether, toluene, and THF. The THF fraction was collected and volatiles removed *in vacuo* to give the desired product as a yellow powder (0.0978 g, 46%). ^{1}H-NMR (400 MHz, CD_2Cl_2): δ 8.41 (s, 6H, *o*-Py*H*), 8.02 (s, 3H, ArC*H*NCH$_2$), 7.48 (m, 6H, Py*H*), 7.36 (m, 6H, Py*H*), 7.10 (d, 2.4 Hz, 3H, Ar*H*), 7.02 (m, 6H, Py*H*), 6.70 (d, 2.4 Hz, 3H, Ar*H*), 3.67 (m, 6H, NC*H*$_2$C*H*$_2$N), 3.54 (s, 12H, NC*H*$_2$Ar), 3.43 (s, 6H, NCH$_2$Ar), 2.80 (m, 6H, NC*H*$_2$C*H*$_2$N), 2.36 (s, 3H, NC*H*H'Ar), 2.18 (s, 9H, C*H*$_3$Ar) 1.29 (m, 3H, NCH*H'*Ar). ^{13}C-NMR (101 MHz, CD_2Cl_2): δ 167.28 (Ar*C*HN), 163.88 (Ar), 160.75 (Ar), 148.49 (Ar), 135.79 (Ar), 135.67 (Ar), 133.02 (Ar), 128.01 (Ar), 122.77 (Ar), 121.51 (Ar), 121.27 (Ar), 121.17 (Ar), 61.30 (N*C*H$_2$), 59.63 (N*C*H$_2$), 59.17 (N*C*H$_2$), 52.70 (N*C*H$_2$), 20.03 (Ar*C*H$_3$) ppm. HRMS (FAB), $C_{69}H_{73}LaN_{13}O_3$: calculated m/z = 1270.502; observed m/z = 1270.500 ($M+H^+$).

Synthesis of 3-Ce.

Prepared according to analogous procedure to **3-La**. Isolated as an orange powder (45%). ^{1}H-NMR (300 MHz, CD_2Cl_2): δ 17.33 (3H), 10.67 (3H), 8.72 (3H), 7.38 (6H), 6.88 (6H), 6.65 (6H), 5.98 (6H), 3.67 (9H), 3.32 (12H), 1.78 (6H), 0.39 (6H), -8.68 (6H) ppm.

Synthesis of 3-Nd.

Prepared according to analogous procedure to **3-La**. Isolated as a green powder (44%). ^{1}H-NMR (300 MHz, CD_2Cl_2): δ 28.85, 12.00, 9.48, 7.97, 6.88, 5.32, 4.09, 2.50, 0.29, -1.08, -10.80 ppm.

Synthesis of 3-Eu.

Prepared according to analogous procedure to **3-La**. Isolated as a yellow powder (46%). ^{1}H-NMR (300 MHz, CD_2Cl_2): δ 24.26, 12.95, 9.65, 8.56, 8.05, 7.23, 4.21, 3.35, 1.27, -0.04, -0.58, -27.93 ppm.

Synthesis of 3-Lu.

Prepared according to analogous procedure to **3-La**. Isolated as a yellow powder (46%). ^{1}H-NMR (400 MHz, CD_2Cl_2): δ 8.37 (s, 6H, *o*-Py*H*), 8.01 (s, 3H, ArC*H*NCH$_2$), 7.49 (m, 6H, Py*H*), 7.33 (m, 6H, Py*H*), 7.14 (d, 2.4 Hz, 3H, Ar*H*), 7.02 (m, 6H, Py*H*), 6.64 (d, 2.4 Hz, 3H, Ar*H*), 4.19 (m, 3H, NC*H*$_2$), 3.39 (m, 18H, NC*H*$_2$), 3.05 (m, 9H, NC*H*$_2$), 2.18 (s, 9H, C*H*$_3$Ar). ^{13}C-NMR (101 MHz, CD_2Cl_2): δ 167.91 (Ar*C*HN), 164.94 (Ar), 161.15 (Ar), 148.45 (Ar), 136.32 (Ar), 135.59 (Ar), 132.40 (Ar), 128.78 (Ar), 122.65 (Ar), 121.33 (Ar), 121.04 (Ar), 59.41 (N*C*H$_2$), 57.65 (2 superimposed signals, N*C*H$_2$), 52.18 (N*C*H$_2$), 20.13 (Ar*C*H$_3$) ppm. HRMS (FAB), $C_{69}H_{73}LuN_{13}O_3$: calculated m/z = 1306.537; observed m/z = 1306.535 ($M+H^+$).

Synthesis of 4-Y.

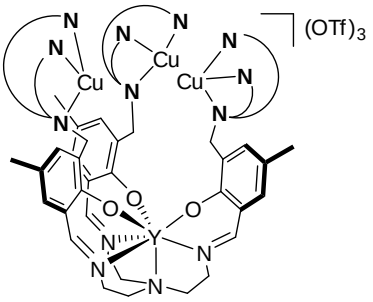

4-Y

Yttrium complex **3-Y** (0.2189 g, 0.179 mmol) was suspended in CH_3CN (4 mL). A solution of $Cu(CH_3CN)_4OTf$ (0.2028 g, 0.538 mmol, 3 equiv) in THF (3 mL) was added dropwise. The solution turned from cloudy and yellow to clear and golden. The solution was filtered through Celite and the solvent removed *in vacuo* to yield the yttrium-tricopper complex **4** in near-quantitative yield. ^{1}H-NMR (300 MHz, CD_3CN): δ 8.45 (s, 6H, *o*-Py*H*), 8.23 (s, 3H, ArC*H*NCH_2), 7.77 (m, 6H, Py*H*), 7.38 (m, 6H, Py*H*), 7.08 (d, 2.4 Hz, 3H, Ar*H*), 7.00 (m, 6H, Py*H*), 6.79 (d, 2.4 Hz, 3H, Ar*H*), 4.32 (m, 3H, ArC*H*H'N), 3.98 (m, 3H, NCH*H'*Ar), 3.51 (m, 18H, NCH_2Ar+NCH_2CH_2N), 2.94 (m, 6H, NCH_2Ar), 2.05 (s, 9H, CH_3Ar) ppm. ^{13}C-NMR (101 MHz, CD_3CN): δ 167.73 (ArCHN), 164.03 (Ar), 157.40 (Ar), 148.64 (Ar), 138.23 (Ar), 137.70 (Ar), 134.50 (Ar), 125.41 (Ar), 123.74 (Ar), 123.41 (Ar), 121.74 (Ar), 120.69 (Ar), 58.65 (NCH_2Ar), 57.59 (NCH_2CH_2N), 54.39 (NCH_2Ar), 19.34 (ArCH_3) ppm. Elemental analysis: Calculated for $C_{78}H_{81}Cu_3F_9N_{16}O_{12}S_3Y$: C 47.28, H 4.12, N 11.31. Found: C 46.93, H 4.00, N 11.02.

Synthesis of 4-La.

Prepared from **3-La** according to analogous procedure to **4-Y**. Isolated in quantitative yield as a golden yellow powder. ^{1}H-NMR (400 MHz, CD_3CN): δ 8.45 (s, 6H, *o*-Py*H*), 8.14 (s, 3H, ArC*H*NCH_2), 7.60 (m, 6H, Py*H*), 7.28 (m, 6H, Py*H*), 6.97 (d,

2.4 Hz, 3H, Ar*H*), 6.82 (d, 2.4 Hz, 3H, Ar*H*), 6.78 (m, 6H, Py*H*), 4.25-3.25 (m, 21H, NC*H*$_2$), 3.11 (m, 9H, NC*H*$_2$), 2.05 (s, 9H, C*H*$_3$Ar). ^{13}C-NMR (101 MHz, CD_3CN): δ 167.99 (Ar*C*HN), 164.06 (Ar), 157.54 (Ar), 148.48 (Ar), 138.25 (Ar), 137.50 (Ar), 135.40 (Ar), 125.03 (Ar), 123.55 (Ar), 123.32 (Ar), 122.01 (Ar), 121.01 (Ar), 60.69 (N*C*H$_2$), 60.18 (N*C*H$_2$), 59.45 (N*C*H$_2$), 55.25 (N*C*H$_2$), 19.14 (Ar*C*H$_3$) ppm. Elemental analysis: Calculated for $C_{78}H_{81}Cu_3F_9LaN_{16}O_{12}S_3$: C 46.12, H 4.02, N 11.03. Found: C 46.02, H 3.90, N 10.84.

Synthesis of 4-Ce.

Prepared from **3-Ce** according to analogous procedure to **4-Y**. Isolated as a golden yellow powder in quantitative yield. ^{1}H-NMR (300 MHz, CD_3CN): δ 15.15, 8.60, 8.37, 7.71, 7.59, 7.28, 6.56, 6.17, 3.69, 2.62, -1.08 ppm.

Synthesis of 4-Nd.

Prepared from **3-Nd** according to analogous procedure to **4-Y**. Isolated as a dark golden powder in quantitative yield. ^{1}H-NMR (300 MHz, CD_3CN): δ 25.99, 9.60, 8.68, 8.36, 7.79, 7.35, 7.16, 6.10, 3.08, 2.06, -0.90 ppm.

Synthesis of 4-Eu

Prepared from **3-Eu** according to analogous procedure to **4-Y**. Isolated as a golden yellow powder in quantitative yield. ^{1}H-NMR (300 MHz, CD_3CN): δ 10.24, 8.43, 7.60, 7.25, 4.73, 4.00, 3.89, 0.46, -0.07, -21.92 ppm.

Synthesis of 4-Lu.

Prepared from **3-Lu** according to analogous procedure to **4-Y**. Isolated as a golden yellow powder (quantitative). ^{1}H-NMR (300 MHz, CD_3CN): δ 8.47 (s, 6H, *o*-Py*H*), 8.25 (s, 3H, ArC*H*NCH$_2$), 7.77 (m, 6H, Py*H*), 7.34 (m, 6H, Py*H*), 7.16 (d, 2.4 Hz, 3H, Ar*H*), 7.03 (m, 6H, Py*H*), 6.85 (d, 2.4 Hz, 3H, Ar*H*), 4.30 (m, 3H, ArC*H*H'N), 3.86 (m, 3H, NCH*H'*Ar), 3.58-2.76 (m, 24H, NCH_2), 2.10 (s, 9H, CH_3Ar). ^{13}C-NMR (101 MHz, CD_3CN): δ 167.65 (Ar*C*HN), 164.67 (Ar), 157.46 (Ar), 148.64 (Ar), 138.28 (Ar), 137.61 (Ar), 134.31 (Ar), 125.79 (Ar), 123.75 (Ar), 123.35 (Ar), 122.03 (Ar), 121.59 (Ar), 58.64 (N*C*H$_2$), 57.48 (two superimposed peaks, N*C*H$_2$), 54.21 (N*C*H$_2$), 19.36 (Ar*C*H$_3$) ppm. Elemental analysis: Calculated for $C_{78}H_{81}Cu_3F_9LuN_{16}O_{12}S_3$: C 45.32, H 3.95, N 10.84. Found: C 45.22, H 3.77, N 10.76.

Synthesis of 5-M.

All intermediates **5-M** were prepared analogously. The protocol for preparation of **5-Y** is given here as example. Compound **5-Y** was prepared *in situ* in a UV-Vis vessel equipped with a fiber-optic dip probe for low temperature studies. A solution of complex 4 in propionitrile, 1:1 toluene/acetonitrile, or 3:2 toluene/acetonitrile (~0.2 mM) was prepared in a glovebox and 12 mL were added to the UV-Vis cell. The dip probe setup was sealed and taken out on the benchtop, where the cell was cooled to -78°C (propionitrile) or -40°C (toluene/acetonitrile). A small portion of the same solvent was saturated with dioxygen on a Schlenk line by vigorous bubbling for a few minutes, after which 2 mL of said solution were added to the UV-Vis cell via syringe. Formation of **-5-Y** was complete instantaneously (-40 °C) or in about 1 minute (-78°C).

Table 3. Spectroscopic Features of $[Cu^{II}_2Cu^{III}(\mu_3\text{-}O)_2]$ Complexes from the Present Study. All λ_{max} values in nm (ε values in M^{-1} cm^{-1}).

6 λ_{max}, nm, (ε, $M^{-1}cm^{-1}$)[12]	**7** λ_{max}, nm, (ε, $M^{-1}cm^{-1}$)[14]	**8** λ_{max}, nm, (ε, $M^{-1}cm^{-1}$)[15]	**5-Y** λ_{max}, nm, (ε, $M^{-1}cm^{-1}$)	**13-Y** λ_{max}, nm, (ε, $M^{-1}cm^{-1}$)
290 (12,500)	-		-	-
355 (15,000)	343 (12,000)	328 (10,700)	355 (12,400)	340 (11,500)
480 (1,400)	515 (1,000)	420 (1,500)	480 (1,910)	455 (2,160)
620 (800)	685 (800)	590 (835)	640 (800)	690 (760)

Volumetric measurement of O_2 consumption

To determine the stoichiometry of the reaction between **4-Y** and O_2, a solution of **4-Y** in acetonitrile was degassed via three freeze-pump-thaw cycles on a high-vacuum line. While the solution was still frozen, a known amount of O_2 (~10 equiv) was measured with a volumetric Schlenk bulb and added to the reaction vessel. The reaction solution was warmed to -40ºC and stirred for one hour, during which the solution changed in color from yellow to dark brown. The solution was again frozen using a dry-ice/acetone bath (-78ºC), and the gas present in the headspace was measured with a Toepler pump.[71] Three freeze-pump-thaw cycles were carried out on the final reaction solution to recover all unreacted gases. Table 4 summarizes the results of three separate runs of volumetric measurements. Per equivalent of 4, 0.97 $\pm$ 0.01 equivalents of O_2 were consumed.

Determination of H_2O_2 release by Ti(IV)oxysulfate titration

To determine whether species **5-Y** is a peroxide complex, a solution of **5-Y** prepared as described above was treated with formic acid (5 equiv), after which a solution of

Ti(IV)oxysulfate was added. The absence of increased absorbance at 408 nm indicated that no H_2O_2 was released within the limits of detection.[15,50]

Table 4. Results of volumetric O_2 measurements. Volumetric bulb volume = 33.0 mL, Toepler pump volume = 30.32 mL.

#	Amount of 4 (mmol)	T (K)	O_2 added (mmHg)	mol O_2 added	Final O_2 (mmHg)	Final O_2 (mmol)	mmol O_2 used	Equiv. used
1	0.0413	295	220.5	0.3955	216.0	0.3560	0.0395	0.97
2	0.0353	295	191.0	0.3426	187.5	0.3090	0.0336	0.95
3	0.0436	293	200.0	0.3612	192.0	0.3186	0.0426	0.98

Reactions of 5-Y with substrates

Reactivity of **5-Y** with substrates was first investigated under UV-Vis conditions to monitor the decay of **5-Y**. Species **5-Y** was formed as described above at -78 ºC; the desired reagent was solubilized in 1 mL of reaction solvent in the glovebox and added to the UV-Vis dip probe vessel via syringe. The reaction was monitored via UV-Vis spectroscopy; reaction was deemed to occur when bands corresponding to **5-Y** decreased by more than 15%.

For certain substrates (phenols, PPh_3, thiophenols, *p*-methylbenzylalcohol) reactivity with **5-Y** was also studied at larger scale to isolate and identify reaction products. In these cases, **5-Y** was prepared by exposure of a solution of **4-Y** in acetonitrile/toluene to excess O_2 on a Schlenk line at -40 ºC. Excess O_2 was removed by three freeze-pump-thaw cycles, and the desired substrate added as an acetonitrile/toluene solution under inert atmosphere. The solution was then stirred at -40 ºC until disappearance of the dark orange/brown color indicative of **5-Y**. The solution was then warmed to room temperature and the solvent removed *in vacuo*. The

reaction vessel was returned to a glovebox where the residue was studied under inert atmosphere with the appropriate spectroscopic techniques.

Reaction with triphenylphosphine was worked up by extraction of the dried reaction mixture with diethyl ether and the product was quantified by integration of its ^{31}P-NMR spectroscopy against excess triphenylphosphine starting material.

Reaction with TEMPO-H was monitored by UV-Vis spectroscopy and the product (TEMPO radical) was quantified by EPR spectroscopy via comparison to an authentic sample of TEMPO•.

Reaction with 4-*tert*-butylthiophenol was worked up by extraction of the dried reaction mixture with diethyl ether and the product was quantified by NMR spectroscopy. Thiophenol-bound complex **18** was synthesized by addition of thiophenol to **5-Y** and analysis by ^{1}H- and ^{13}C-NMR spectroscopy and ESI-MS.

Synthesis of 9.

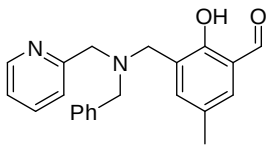

9

To a THF solution of 3-(chloromethyl)-2-hydroxy-5-methylbenzaldehyde (0.8969 g, 4.94 mmol) was added N-benzyl-N-(2-picolyl)amine (0.979 g, 4.94 mmol, 1 equiv). The solution turns from light brown to yellow. Triethylamine (2.4 mL, 17.28 mmol, 3.5 equiv) was added, and a yellow precipitate formed. The solution was allowed to stir at room temperature for 1 hour. The mixture was then filtered through Celite and the solvent removed *in vacuo* to obtain 1.465 g of crude product as a thick yellow oil (86%), which was carried on without further purification. ^{1}H-NMR (300 MHz, CD_2Cl_2): δ

10.33 (s, 1H, ArC*H*O), 8.59 (m, 1H, Ar*H*), 7.67 (m, 1H, Ar*H*), 7.41 (m, 9H, Ar*H*), 3.80 (s, 2H, NC*H*$_2$Ar), 3.76 (s, 2H, NC*H*$_2$Ar), 3.69 (s, 2H, NC*H*$_2$Ar), 3.48 (s, 1H, ArO*H*), 2.28 (s, 3H, C*H*$_3$Ar) ppm. ^{13}C-NMR (101 MHz, CD_2Cl_2): δ 191.90 (Ar*C*HO), 159.06 (Ar), 158.16 (Ar), 148.87 (Ar), 138.11 (Ar), 137.32 (Ar), 136.66 (Ar), 129.06 (Ar), 128.33 (Ar), 128.13 (Ar), 128.10 (Ar), 125.27 (Ar), 123.04 (Ar), 122.52 (Ar), 122.22 (Ar), 58.57 (N*C*H$_2$Ar), 57.84 (N*C*H$_2$Ar), 54.84 (N*C*H$_2$Ar), 55.45 (N*C*H$_2$Ar), 19.99 (Ar*C*H$_3$) ppm. HRMS (FAB), $C_{22}H_{23}N_2O_2$: calculated m/z = 3471760; observed m/z = 347.1775 ($M+H^+$).

Synthesis of 10.

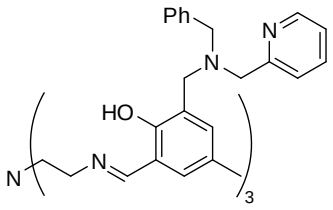

10

In a Schlenk tube, aldehyde **9** (1.465 g, 4.267 mmol, 3 equiv) was dried under vacuum for 1 hour. Tris(2-aminoethyl)amine (0.20 mL, 1.351 mmol, 1 equiv) was added via syringe under positive N_2 pressure. Dry methanol (15 mL) was transferred via cannula, and the mixture was stirred at room temperature for 12 hours. The solution was filtered through Celite and SiO_2, and the solvent removed *in vacuo* from the filtrate to obtain a yellow oil. The crude product was purified via SiO_2 column chromatography using 1% triethylamine in methanol as the eluent to obtain 0.640 g of product as a yellow solid (40%). ^{1}H-NMR (300 MHz, C_6D_6): δ 14.03 (s, 3H, ArO*H*), 8.38 (s, 6H, Ar*H*), 7.65 (s, 3H, NC*H*Ar), 7.51 (s, 3H, Ar*H*), 7.43 (m, 3H, Ar*H*), 7.13 (m, 12H, Ar*H*), 6.52 (m, 3H, Ar*H*), 5.72 (s, 3H, Ar*H*), 4.01 (s, 6H, NC*H*$_2$Ar), 4.00 (s, 6H, NC*H*$_2$Ar),

2.97 (br s, 6H, NC*H*$_2$CH$_2$N), 2.97 (br s, 6H, NCH$_2$C*H*$_2$N), 2.04 (s, 9H, C*H*$_3$Ar) ppm. ^{13}C-NMR (101 MHz, CD_2Cl_2): δ 166.19 (Ar*C*HN), 160.48 (Ar), 157.65 (Ar), 148.90 (Ar), 139.72 (Ar), 135.76 (Ar), 133.57 (Ar), 130.51 (Ar), 128.62 (2 superimposed peaks, Ar), 128.09 (2 superimposed peaks, Ar), 126.69 (Ar), 126.58 (Ar), 126.27 (Ar), 122.09 (Ar), 121.22 (Ar), 118.32 (Ar) 59.77 (N*C*H$_2$Ar), 58.45 (N*C*H$_2$Ar), 57.98 (NCH$_2$*C*H$_2$N), 55.45 (N*C*H$_2$CH$_2$N), 51.40 (N*C*H$_2$Ar), 20.24 (Ar*C*H$_3$) ppm. HRMS (FAB), $C_{72}H_{79}N_{10}O_3$: calculated m/z = 1131.634; observed m/z = 1131.6306 ($M+H^+$).

Synthesis of 11-Y.

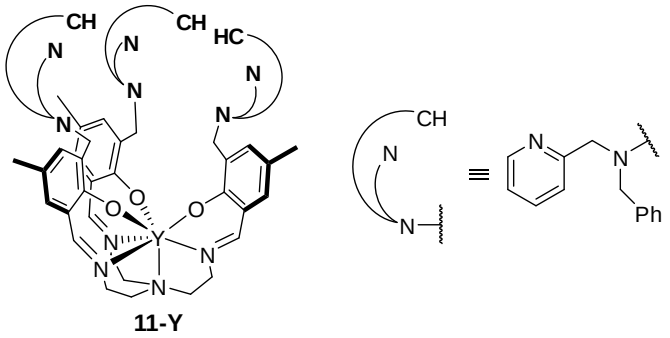

11-Y

Yttrium complex **11-Y** was prepared from **10** in a manner analogous to complex **3** (0.1505 g, 53%). %). ^{1}H-NMR (300 MHz, CD_2Cl_2): δ 8.40 (m, 3H, Ar*H*), 8.03 (s, 3H, NC*H*Ar), 7.50 (m, 3H, Ar*H*), 7.37 (m, 3H, Ar*H*), 7.28 (m, 15H, Ar*H*), 7.04 (m, 3H, Ar*H*), 6.71 (br s, 3H, Ar*H*), 4.12 (m, 3H, NC*H*H'), 3.48 (m, 21H, NC*H*$_2$), 2.95 (m, 3H, NCH*H'*), 2.79 (m, 3H, NC*H*$_2$), 2.22 (s, 9H, C*H*$_3$Ar) ppm. ^{13}C-NMR (101 MHz, CD_2Cl_2): δ 167.93 (Ar*C*HN), 164.35 (Ar), 161.36 (Ar), 148.41 (Ar), 140.77 (Ar), 136.16 (Ar), 135.64 (Ar), 132.61 (Ar), 128.92 (Ar), 128.77 (Ar), 128.67 (Ar), 127.73 (Ar), 126.13 (Ar), 122.57 (Ar), 121.45 (Ar), 121.06 (Ar), 120.76 (Ar), 59.57 (N*C*H$_2$), 59.16 (N*C*H$_2$), 57.87 (N*C*H$_2$), 57.73 (N*C*H$_2$), 51.71 (N*C*H$_2$), 20.18 (Ar*C*H$_3$) ppm. Elemental analysis: Calc for $C_{72}H_{75}N_{10}O_3Y$: C 71.04, H 6.21, N 11.51. Found: C 70.87, H 6.11, N 11.54.

Synthesis of 12-Y.

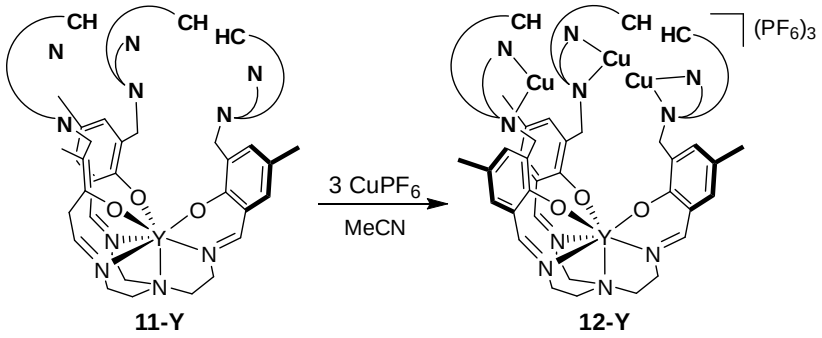

Yttrium-tricopper complex **12-Y** was prepared from **11-Y** in a manner analogous to complex **4** using $Cu(CH_3CN)_4PF_6$ as Cu^I source (0.164 g, 95%). ^{1}H-NMR (300 MHz, CD_3CN): δ 8.14 (m, 3H, Ar*H*), 8.04 (s, 3H, NC*H*Ar), 7.22 (m, 3H, Ar*H*), 7.20 (m, 21H, Ar*H*), 7.01 (m, 3H, Ar*H*), 6.56 (br s, 3H, Ar*H*), 4.15 (m, 3H, NC*H*H'), 3.62 (m, 3H, NCH_2), 3.48 (m, 18H, NCH_2), 3.15 (m, 3H, NCH*H*'), 2.96 (m, 3H, NCH_2), 2.10 (s, 9H, CH_3Ar) ppm. ^{13}C-NMR (101 MHz, CD_3CN): δ 168.06 (Ar*C*HN), 163.16 (Ar), 158.79 (Ar), 148.37 (Ar), 137.80 (Ar), 136.69 (Ar), 128.08 (Ar), 127.54 (Ar), 126.34 (Ar), 123.62 (Ar), 128.67 (Ar), 123.28 (Ar), 122.44 (Ar), 121.60 (Ar), 60.49 (N*C*H$_2$), 58.85 (N*C*H$_2$), 58.76 (N*C*H$_2$), 57.52 (N*C*H$_2$), 54.95 (N*C*H$_2$), 19.29 (Ar*C*H$_3$) ppm. Elemental analysis: Calculated for $C_{78}H_{84}Cu_3F_{18}N_{13}O_3P_3Y$: C 47.65, H 4.31, N 9.26. Found: C 47.78, H 4.38, N 9.19.

Synthesis of 13-Y.

Compound **13-Y** was prepared in a manner analogous to complexes **5-M**. Identification by means of mass spectroscopy (ESI) was unsuccessful.

Reactions of 13-Y with substrates.

Reactions of compound **13-Y** with substrates were carried out in a manner analogous to reactions of complex **5-Y**.

Reaction with triphenylphosphine was worked up by extraction of the dried reaction mixture with diethyl ether and the product was quantified by integration of its ^{31}P-NMR spectroscopy against excess triphenylphosphine starting material. The Cu-containing residue was dissolved in acetonitrile and was found to be a reduced tricopper(I) species.

Scheme 10. Synthetic Pathway for Monoucleating Ligand and Monocopper Complex

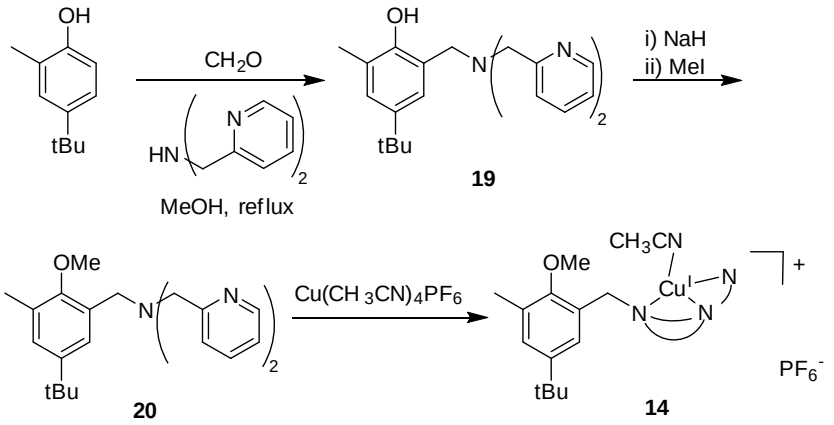

Synthesis of 19.

4-tert-butyl-2-methylphenol (4.136 g, 25.18 mmol), formaldehyde (37% in water, 8.249 g, 0.1 mol, 4 equiv), and dipicolylamine (5.017 g, 25.18 mmol, 1 equiv) were dissolved in methanol and the mixture was refluxed overnight. The mixture was then cooled and a white precipitate formed. The solution was filtered to obtain the clean product as a colorless solid (6.134 g, 65 %). ^{1}H-NMR (300 MHz, C_6D_6): δ 11.00 (s, 1H, ArO*H*), 8.41 (m, 2H, Ar*H*), 7.19 (d, 1H, Ar*H*), 7.05 (m, 2H, Ar*H*), 6.94 (m, 3H, Ar*H*), 6.50 (m, 2H, Ar*H*), 3.79 (s, 4H, NCH_2Py), 3.62 (s, 2H, NCH_2Ar), 2.54 (s, 3H, ArCH_3), 1.29 (s, 6H, C(CH_3)$_3$) ppm. ^{13}C-NMR (101 MHz, C_6D_6): δ 158.64 (Ar), 154.04 (Ar),

148.84 (Ar), 140.39 (Ar), 135.78 (Ar), 127.27 (Ar), 124.43 (Ar), 124.37 (Ar), 122.85 (Ar), 121.54 (Ar), 121.35 (Ar), 58.99 (N*C*H_2Py), 57.56 (N*C*H_2Ar), 33.58 (Ar*C*(CH_3)$_3$), 31.54 (ArC(*C*H_3)$_3$), 16.59 (Ar*C*H_3) ppm. HRMS (FAB), $C_{24}H_{30}N_3O$: calculated m/z = 376.2389; observed m/z = 372.2381.

Synthesis of 20.

Compound **19** (2.0671 g, 5.50 mmol) was dried on a Schlenk line overnight in a Schlenk tube. THF was transferred to the reaction flask via cannula. NaH (0.1651 g, 6.88 mmol, 1.25 equiv) was added against positive N_2 pressure. The solution turned cloudy, and gas evolution was observed. After 1 hour, MeI (0.52 mL, 8.26 mmol, 1.5 eq) was added via syringe. The solution was stirred at 70 °C for four hours, after which it was cooled and extracted with DCM/H_2O. The organic layer was dried over $MgSO_4$, filtered, and evaporated to give the product as a dark red oil (1.801 g, 84%). ^{1}H-NMR (300 MHz, C_6D_6): δ 8.18 (m, 2H, Ar*H*), 7.51 (s, 1H, Ar*H*), 7.28 (m, 2H, Ar*H*), 6.86 (m, 3H, Ar*H*), 6.35 (m, 2H, Ar*H*), 3.74 (s, 4H, NC*H*$_2$Py), 3.63 (s, 2H, NC*H*$_2$Ar), 3.05 (s, 3H, ArOC*H*$_3$), 1.93 (s, 3H, ArC*H*$_3$), 1.04 (s, 6H, C(C*H*$_3$)$_3$) ppm. ^{13}C-NMR (101 MHz, C_6D_6): δ 160.29 (Ar), 155.35 (Ar), 148.98 (Ar), 145.96 (Ar), 135.43 (Ar), 131.28 (Ar), 129.86 (Ar), 126.72 (Ar), 125.29 (Ar), 122.48 (Ar), 121.35 (Ar), 60.15 (N*C*H_2Py), 59.68 (N*C*H_2Ar), 52.81 (ArO*C*H_3), 34.03 (Ar*C*(CH_3)$_3$), 31.36 (ArC(*C*H_3)$_3$), 16.11 (Ar*C*H_3) ppm. HRMS (FAB), $C_{25}H_{32}N_3O$: calculated m/z = 390.2545; observed m/z = 390.2529 ($M+H^+$).

Synthesis of 14.

Compound **20** was dried under vacuum at 70 °C for four hours, after which it was brought into the glovebox. A MeCN solution of $Cu(CH_3CN)_4PF_6$ (0.1466 g, 0.393 mmol) was added dropwise to a stirring THF solution of **12** (0.1532 g, 0.393 mmol). The solution changed color from red to dark golden. The solvent was removed *in vacuo* to obtain the product in near-quantitative yield. ^{1}H-NMR (300 MHz, CD_6CN): δ 8.51 (m, 2H, Ar*H*), 7.76 (m, 2H, Ar*H*), 7.34 (m, 5H, Ar*H*), 7.11 (br s, 1H, Ar*H*), 3.99 (br s, 2H, NC*H*$_2$Ar), 3.84 (s, 2H, NC*H*$_2$Py), 3.06 (s, 3H, ArOC*H*$_3$), 2.23 (s, 3H, ArC*H*$_3$), 1.23 (s, 6H, C(C*H*$_3$)$_3$) ppm. ^{13}C-NMR (101 MHz, CD_3CN): δ 153.12 (Ar), 155.45 (Ar), 148.74 (Ar), 146.29 (Ar), 137.69 (Ar), 130.43 (Ar), 128.79 (Ar), 127.27 (Ar), 127.05 (Ar), 123.79 (two overlapping peaks, Ar), 60.12 (N*C*H$_2$Py), 58.88 (N*C*H$_2$Ar), 54.88 (ArO*C*H$_3$), 33.77 (Ar*C*(CH$_3$)$_3$), 30.63 (ArC(*C*H$_3$)$_3$), 15.60 (Ar*C*H$_3$) ppm. Elemental analysis: Calculated for $C_{27}H_{34}CuF_6N_4OP$: C 50.74, H 5.36, N 8.77. Found: C 51.02, H 5.29, N 8.62.

Reaction of 14 with O_2.

Compound **14** was reacted with O_2 in a manner analogous to complexes **4-M** and **12-Y**. λ_{max}, nm (ε, $M^{-1}cm^{-1}$): 675 (100).

Scheme 11. Synthethic pathway to **15**.

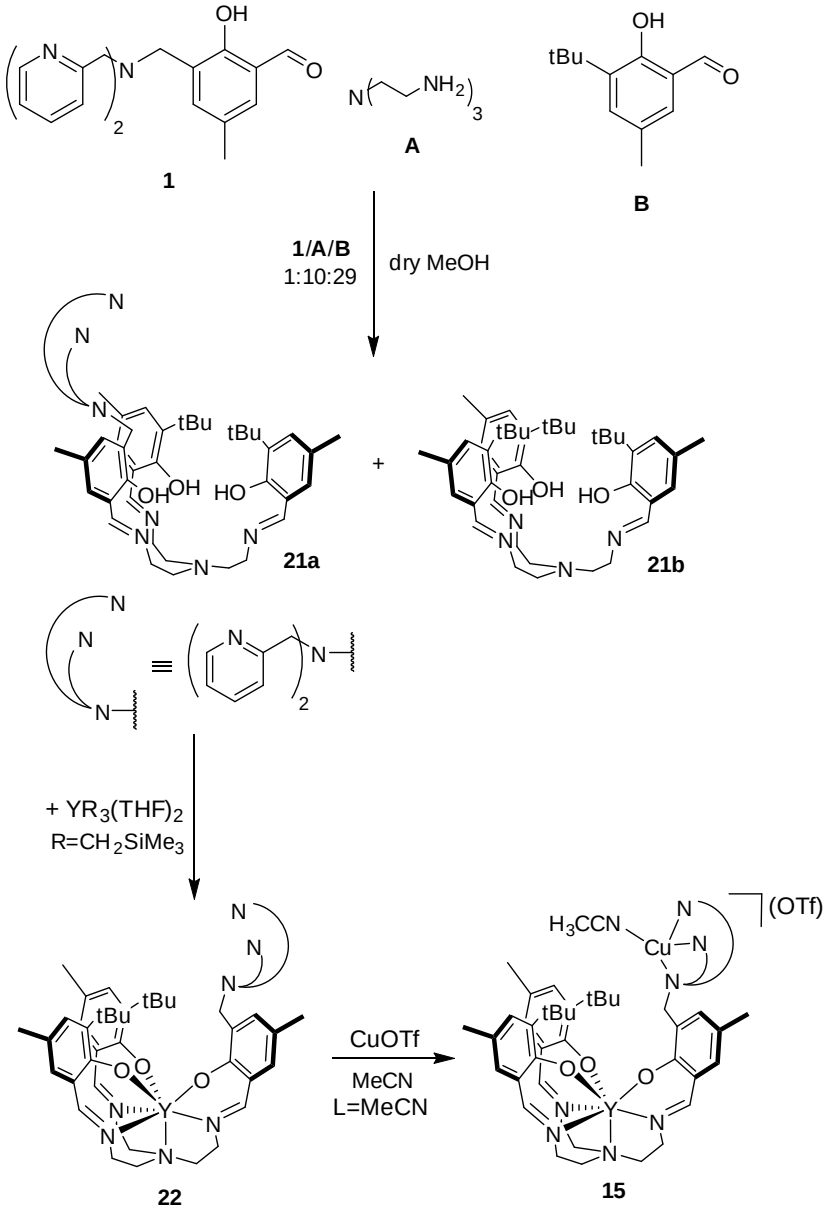

Synthesis of 15.

Yttrium-monocopper complex **15** required synthesis of the asymmetric ligand **21a** (Scheme 11) via an imine condensation route analogous to the preparation of **2**. Reaction of **1** with a large excess (10 equiv) of tris(2-aminoethyl)amine followed by addition of 29 equivalents of 3-*tert*-butylsalicylaldehyde gave a mixture of the desired

ligand (**21a**) and the symmetric trialkyl ligand **21b**, most of which precipitates from the reaction solution. Unfortunately, concentration *in vacuo* often led, in the presence of adventitious water, to scrambling of the ligand arms to give a mixture of asymmetric and symmetric ligands. A mixture (consisting mostly of **21a**, which was the only dipicolylamine-containing species) was therefore used for metalation with yttrium, analogous to preparation of **3-Y**. Yttrium complex **22** was obtained as part of a complex mixture due to the impurities in the ligand material. Thus, **22** was reacted with a substoichiometric amount of Cu^{I} salt to afford the yttrium-monocopper complex **15**.

Synthesis of 15.

In a 500 mL Schlenk flask, 1.55 mL tris(2-aminoethyl)amine (tren, 10.3 mmol, 10 equiv) was dissolved in dry methanol. **1** (0.3950 g, 1.03 mmol) was dissolved in DCM and added to the tren solution dropwise. After 15 minutes, 3-*tert*-butyl-2-hydroxybenzaldehyde (5.7619 g, 29.97 mmol, 29 equiv)[72] was added as a DCM solution. Over 20 minutes, a yellow precipitate formed. The reaction was stirred for 2 hours, after which activated 3Å molecular sieves were added to the solution. After 20 minutes, the reaction solution was opened to air and rapidly filtered through Celite to remove most of the unwanted side product and molecular sieves. The filtrate was concentrated *in vacuo*, resolubilized in DCM, and passed through a short silica gel plug. DCM (1 L) was eluted to remove as much of the symmetric trialkyl ligand (**21b**) as possible, after which ligand **21a** was eluted with methanol. Solvent was removed from the methanol fraction and the resulting yellow powder (~0.500 g) was brought into the glovebox. ^{1}H-NMR revealed a 5:1 mixture of **21a** to **21b**. **21a**: ^{1}H-NMR (300 MHz, C_6D_6): δ 8.40 (m, 2H, *o*-Py*H*), 7.77 (m, 6H, Ar*H*+ArC*H*N), 7.14 (m, 2H, Ar*H*), 7.07 (m, 3, Ar*H*), 6.54

(m, 2H, Py*H*), 5.66 (s, 3H, Ar*H*), 4.13 (m, 6H, NCH_2), 2.97 (s, 6H, NCH_2), 2.13 (m, 15H, NCH_2), 1.60 (s, 18H, ArC(CH_3)). ^{13}C-NMR (101 MHz, CD_2Cl_{20}): δ 166.66 (Ar*C*HN), 166.18 (Ar*C*HN), 159.83 (Ar), 157.93 (Ar), 157.91 (Ar), 148.78 (Ar), 136.40 (Ar), 136.05 (Ar), 130.53 (Ar), 130.19 (Ar), 129.73 (Ar), 129.61 (Ar), 126.25 (Ar), 126.19 (Ar), 122.44(Ar), 121.66(Ar), 118.38(Ar), 118.29(Ar), 67.69 (N*C*H_2), 60.05 (N*C*H_2), 58.14 (N*C*H_2), 56.11 (N*C*H_2), 51.75 (N*C*H_2), 34.50 (N*C*H_2), 29.10 (C(*C*H_3)$_3$), 25.52 (*C*(CH_3)$_3$), 20.11, 20.01 (Ar*C*H_3) ppm. ESI-MS: 824.1 (M^+).

Part of the ligand-containing mixture (0.1968 g, 0.239 mmol) was dissolved in THF and the solution frozen. Upon thawing, a thawing solution of Y(CH_2SiMe_3)$_3$(THF)$_2$ (0.1123 g, 0.227 mmol, 0.95 equiv) in THF was added dropwise. The solution was warmed to room temperature and stirred for 3 hours. The solvent was removed *in vacuo* and the resulting yellow solid was washed with hexanes, diethyl ether, toluene, and THF. The diethyl ether and toluene fractions were combined and evaporated to dryness to give a material consisting mostly of yttrium complex **22**. This complex was suspended in acetonitrile, and Cu(CH_3CN)$_4$OTf (0.100 mmol) was added as acetonitrile solution. The solution changed from colorless to yellow as **22** was complexed. The solution was filtered through Celite to remove unreacted **22** and **21b**, and the solvent was evaporated to give **15** as a golden yellow powder. ^{1}H-NMR (400 MHz, CD_3CN) δ 8.22 (m, 2H, Py*H*), 8.01 (s, 1H, ArC*H*N), 7.97 (m, 2H, ArC*H*N), 7.95 (s, 3H, ArC*H*N), 7.50 (m, 2H, Py*H*), 7.07 (m, 2H, Py*H*), 6.91 (d, 1.8 Hz, 1H, Ar*H*), 6.80 (d, 1.8 Hz, 1H, Ar*H*), 6.76 (d, 1.8 Hz, 1H, Ar*H*), 6.74 (m, 2H, Py*H*), 6.66 (d, 1.8 Hz, 1H, Ar*H*), 6.63 (d, 1.8 Hz, 1H, Ar*H*), 6.42 (d, 1.8 Hz, 1H, Ar*H*), 4.04-3.75 (m, 5H, CH_2), 3.22-2.65 (m, 13H, NCH_2), 1.97 (s, 3H, CH_3Ar), 1.85 (s, 3H, CH_3Ar), 1.84 (s, 3H, CH_3Ar), 1.01 (s,

9H, C(C*H*)$_3$), 0.77 (s, 9H, C(C*H*)$_3$) ppm. ^{13}C-NMR (101 MHz, CD_3CN): δ 168.39 (Ar*C*HN), 167.97 (Ar*C*HN), 167.55 (Ar*C*HN), 164.51 (Ar), 148.47 (Ar), 139.68 (Ar), 139.32 (Ar), 137.69 (Ar), 137.53 (Ar), 134.44 (Ar), 132.03 (Ar), 131.91 (Ar), 131.69 (Ar), 125.168 (Ar), 123.46 (Ar), 121.74 (Ar), 121.61 (Ar), 121.07 (Ar), 120.94 (Ar), 60.17 (N*C*H$_2$), 59.61 (N*C*H$_2$), 58.37 (N*C*H$_2$), 58.07 (N*C*H$_2$), 57.88 (N*C*H$_2$), 54.25 (N*C*H$_2$), 34.49 (*C*(CH$_3$)$_3$), 34.19 (*C*(CH$_3$)$_3$), 29.30 (C(*C*H$_3$)$_3$), 28.65 (C(*C*H$_3$)$_3$), 19.74 (Ar*C*H$_3$), 19.64 (Ar*C*H$_3$), 19.14 (Ar*C*H$_3$) ppm. ESI-MS: 972.4 ([M -OTf -CH_3CN]$^+$).

Synthesis of 16.

In a glovebox, **2** (0.1571 g, 138 mmol) was dissolved in toluene. Separately, Ce(O^{t}Bu)$_3$(NO$_3$) (0.0625 g, 138 mmol, 1 eq) was also dissolved in toluene. Both solutions were cooled to -40 °C, after which the cerium solution was added to the stirring ligand solution dropwise. The reaction solution turned from yellow to dark purple immediately, and after the addition was completed a dark purple solid began to precipitate. The solution was stirred for 20 minutes, after which volatiles were removed *in vacuo* to give a dark purple solid in near quantitative yield. ^{1}H-NMR (300 MHz, CD_2Cl_2): δ 8.45 (s, 3H, ArC*H*NCH$_2$), 8.38 (s, 6H, *o*-Py*H*), 7.49 (m, 15H, Ar*H*), 7.01 (m, 6H, Py*H*), 6.88 (s, 3H, Ar*H*), 4.02 (m, 9H, NC*H*$_2$), 3.43 (s, 18H, NC*H*$_2$), 3.22 (m, 9H, NC*H*$_2$), 2.33 (m, 6H, NC*H*$_2$), 1.23 (s, 9H, C*H*$_3$Ar).

Synthesis of 18.

Thiophenol-bound complex **18** was synthesized by addition of 4-*tert*-butylthiophenol (0.0103 g, 0.062 mmol, 3 equiv) to **4-Y** (0.041 g, 0.0207 mmol) in acetonitrile. The solvent was removed *in vacuo* to obtain a bright yellow powder 0.050

g, ~quantitative yield). ^{1}H-NMR (400 MHz, CD_3CN): δ 8.96 (br s, 2H, SAr*H*), *8*.49 (s, 6H, *o*-Py*H*), 8.27 (s, 3H, ArC*H*NCH$_2$), 7.76 (m, 6H, Py*H*), 7.46 (m, 2H, SAr*H*), 7.36 (m, 6H, Py*H*), 7.07 (s, 3H, Ar*H*), 7.05 (m, 6H, Py*H*), 6.86 (s, 3H, Ar*H*), 4.48-4.32 (m, 6H, NC*H*$_2$), 4.03-3.64 (m, 18H, NC*H*$_2$), 3.31 (m, 3H, NC*H*$_2$), 3.09 (m, 6H, NC*H*$_2$), 1.99 (s, 9H, C*H*$_3$Ar + s, 9H, (C*H*$_3$)$_3$Ar) ppm. ^{13}C-NMR (101 MHz, CD_3CN): δ 167.65 (Ar*C*HN), 162.75 (Ar), 151.70 (Ar), 149.75 (Ar), 149.19 (Ar), 137.67 (Ar), 137.33 (Ar), 136.70 (Ar), 133.27 (Ar), 127.77 (Ar), 126.41 (Ar), 124.12 (Ar), 123.99 (Ar), 122.73 (Ar), 121.95 (Ar), 119.74 (Ar), 119.56 (Ar), 58.87 (N*C*H$_2$), 57.77 (N*C*H$_2$), 56.97 (N*C*H$_2$), 55.87 (N*C*H$_2$), 34.23 (*C*(CH$_3$)$_3$), 30.46 (C(*C*H$_3$)$_3$), 18.89 (Ar*C*H$_3$) ppm. Elemental analysis: Calculated for $C_{102}H_{114}Cu_3F_9N_{13}O_{12}S_6Y$: C 51.98, H 4.88, N 7.73. Found: pending. ESI-MS: m/z: 2054.8 ([LYCu$_3$(ArS)$_3$OTf]$^+$).

Crystallographic Information for Complex 4

Crystallographic data have been deposited at the CCDC, 12 Union Road, Cambridge CB2 1EZ, UK and copies can be obtained on request, free of charge, by quoting the publication citation and the deposition number 846679.

Table 5. Crystal and Refinement Data for **4**

Empirical formula	$[C_{75}H_{81}N_{16}O_3Cu_3Y]^{3+}$ (see Details)
Formula weight	1534.09
Crystallization solvent	Acetonitrile/diethyl ether
Crystal habit	Blade
Crystal size	0.40 x 0.36 x 0.12 mm
Crystal color	Yellow
Type of diffractometer	Bruker KAPPA APEX II
Wavelength	0.71073 Å MoKa

Data Collection Temperature	100(2) K	
q range for 9751 reflections used in lattice determination	2.33 to 24.61°	
Unit cell dimensions	a = 14.2953(5) Å	α= 75.534(2)°
	b = 18.3037(7) Å	β= 71.127(2)°
	c = 20.8565(8) Å	γ = 74.087(2)°
Volume	4887.5(3) $Å^3$	
Z	2	
Crystal system	Triclinic	
Space group	P-1	
Density (calculated)	1.042 Mg/m^3	
F(000)	1586	
Data collection program	Bruker APEX2 v2009.7-0	
q range for data collection	2.09 to 26.58°	
Completeness to q = 26.58°	98.7 %	
Index ranges	$-17 \leq h \leq 17$, $-22 \leq k \leq 23$, $-26 \leq l \leq 26$	
Data collection scan type	w scans; 14 settings	
Data reduction program	Bruker SAINT-Plus v7.68A	
Reflections collected	135224	
Independent reflections	20138 [R_{int}= 0.0637]	
Absorption coefficient	1.275 mm^{-1}	
Absorption correction	Semi-empirical from equivalents	
Max. and min. transmission	0.7454 and 0.6174	
Structure solution program	SHELXS-97 (Sheldrick, 2008)	
Primary solution method	Direct methods	
Secondary solution method	Difference Fourier map	
Hydrogen placement	Geometric positions	
Structure refinement program	SHELXL-97 (Sheldrick, 2008)	
Refinement method	Full matrix least-squares on F^2	
Data / restraints / parameters	20138 / 13 / 893	
Treatment of hydrogen atoms	Riding	

Goodness-of-fit on F^2	3.264
Final R indices [I>2s(I), 13445 reflections]	R1 = 0.0700, *w*R2 = 0.0973
R indices (all data)	R1 = 0.1002, *w*R2 = 0.0983
Type of weighting scheme used	Sigma
Weighting scheme used	$w=1/s^2(Fo^2)$
Max shift/error	0.000
Average shift/error	0.000
Largest diff. peak and hole	1.514 and -1.134 e.Å^{-3}

Special refinement details for 4.

Crystals were mounted on a glass fiber using Paratone oil then placed on the diffractometer under a nitrogen stream at 100K. The solvent region of the crystal is very disordered, including the triflate anions. The intensities were adjusted such that the solvent region was flattened in the electron density map using SQUEEZE,[73] with the triflate anions, although being clearly present, being excluded from the final model. The volume of the solvent region is 1891Å^3, approximately 39% of the total volume. A total of 514 electrons were accounted for which is reasonable agreement for three triflate and three acetonitrile molecules per asymmetric unit. Refinement of F^2 against ALL reflections. The weighted R-factor (*w*R) and goodness of fit (S) are based on F^2, conventional R-factors (R) are based on F, with F set to zero for negative F^2. The threshold expression of $F^2 > 2\sigma(F^2)$ is used only for calculating R-factors(gt) etc. and is not relevant to the choice of reflections for refinement. R-factors based on F^2 are statistically about twice as large as those based on F, and R-factors based on ALL data will be even larger. All esds (except the esd in the dihedral angle between two l.s. planes) are estimated using the full covariance matrix. The cell esds are taken into account

individually in the estimation of esds in distances, angles and torsion angles; correlations between esds in cell parameters are only used when they are defined by crystal symmetry. An approximate (isotropic) treatment of cell esds is used for estimating esds involving l.s. planes.

REFERENCES

(1) Holm, R. H.; Kennepohl, P.; Solomon, E. I. *Chem. Rev.* **1996**, *96*, 2239.

(2) Solomon, E. I.; Sundaram, U. M.; Machonkin, T. E. *Chem. Rev.* **1996**, *96*, 2563.

(3) Bertini, I. *Biological inorganic chemistry : structure and reactivity*; University Science Books: Sausalito, Calif., 2007.

(4) Suntivich, J.; Gasteiger, H. A.; Yabuuchi, N.; Nakanishi, H.; Goodenough, J. B.; Shao-Horn, Y. *Nat. Chem.* **2011**, *3*, 647.

(5) Hong, W. T.; Risch, M.; Stoerzinger, K. A.; Grimaud, A.; Suntivich, J.; Shao-Horn, Y. *Energy Environ. Sci.* **2015**, *8*, 1404.

(6) Adler, S. B. *Chem. Rev.* **2004**, *104*, 4791.

(7) Solomon, E. I.; Heppner, D. E.; Johnston, E. M.; Ginsbach, J. W.; Cirera, J.; Qayyum, M.; Kieber-Emmons, M. T.; Kjaergaard, C. H.; Hadt, R. G.; Tian, L. *Chem. Rev.* **2014**, *114*, 3659.

(8) Jones, S. M.; Solomon, E. I. *Cell. Mol. Life. Sci.* **2015**, *72*, 869.

(9) Solomon, E. I.; Augustine, A. J.; Yoon, J. *Dalton Trans.* **2008**, 3921.

(10) Heppner, D. E.; Kjaergaard, C. H.; Solomon, E. I. *J. Am. Chem. Soc.* **2014**, *136*, 17788.

(11) Messerschmidt, A.; Ladenstein, R.; Huber, R.; Bolognesi, M.; Avigliano, L.; Petruzzelli, R.; Rossi, A.; Finazziagro, A. *J Mol Biol* **1992**, *224*, 179.

(12) Cole, A. P.; Root, D. E.; Mukherjee, P.; Solomon, E. I.; Stack, T. D. P. *Science* **1996**, *273*, 1848.

(13) Root, D. E.; Henson, M. J.; Machonkin, T.; Mukherjee, P.; Stack, T. D. P.; Solomon, E. I. *J. Am. Chem. Soc.* **1998**, *120*, 4982.

(14) Taki, M.; Teramae, S.; Nagatomo, S.; Tachi, Y.; Kitagawa, T.; Itoh, S.; Fukuzumi, S. *J. Am. Chem. Soc.* **2002**, *124*, 6367.

(15) Gupta, A. K.; Tolman, W. B. *Inorg. Chem.* **2012**, *51*, 1881.

(16) Karlin, K. D.; Gan, Q. F.; Farooq, A.; Liu, S. C.; Zubieta, J. *Inorg. Chim. Acta* **1989**, *165*, 37.

(17) Karlin, K. D.; Gan, Q. F.; Farooq, A.; Liu, S. C.; Zubieta, J. *Inorg. Chem.* **1990**, *29*, 2549.

(18) Frey, S. T.; Sun, H. H. J.; Murthy, N. N.; Karlin, K. D. *Inorg. Chim. Acta* **1996**, *242*, 329.

(19) Brown, E. C.; Johnson, B.; Palavicini, S.; Kucera, B. E.; Casella, L.; Tolman, W. B. *Dalton Trans.* **2007**, 3035.

(20) Ohi, H.; Tachi, Y.; Itoh, S. *Inorg. Chem.* **2006**, *45*, 10825.

(21) Maiti, D.; Woertink, J. S.; Ghiladi, R. A.; Solomon, E. I.; Karlin, K. D. *Inorg Chem* **2009**, *48*, 8342.

(22) Chen, P. P. Y.; Yang, R. B. G.; Lee, J. C. M.; Chan, S. I. *Proc. Natl. Acad. Sci. U.S.A.* **2007**, *104*, 14570.

(23) Battaini, G.; Granata, A.; Monzani, E.; Gullotti, M.; Casella, L. *Advances in Inorganic Chemistry Including Bioinorganic Studies, Vol 58* **2006**, *58*, 185.

(24) Walsdorff, C.; Park, S. O.; Kim, J.; Heo, J.; Park, K. N.; Oh, J.; Kim, K. *J. Chem. Soc. Dalton Trans.* **1999**, 923.

(25) Cao, R.; MuÃàller, P.; Lippard, S. J. *J. Am. Chem. Soc.* **2010**, *132*, 17366.

(26) Cao, R.; McCarthy, B. D.; Lippard, S. J. *Inorg. Chem.* **2011**, *50*, 9499.

(27) Karlin, K. D.; Gan, Q. F.; Tyeklar, Z. *Chem. Commun.* **1999**, 2295.

(28) Adams, H.; Bailey, N. A.; Dwyer, M. J. S.; Fenton, D. E.; Hellier, P. C.; Hempstead, P. D.; Latour, J. M. *J. Chem. Soc. Dalton Trans.* **1993**, 1207.

(29) Zhao, Q. L.; Betley, T. A. *Angew. Chem. Int. Ed.* **2011**, *50*, 709.

(30) Friedle, S.; Lippard, S. J. *Eur. J. Inorg. Chem.* **2009**, 5506.

(31) Tsui, E. Y.; Kanady, J. S.; Day, M. W.; Agapie, T. *Chem. Commun.* **2011**, *47*, 4189.

(32) Hatnean, J. A.; Raturi, R.; Lefebvre, J.; Leznoff, D. B.; Lawes, G.; Johnson, S. A. *J. Am. Chem. Soc.* **2006**, *128*, 14992.

(33) Guillet, G. L.; Sloane, F. T.; Dumont, M. F.; Abboud, K. A.; Murray, L. J. *Dalton Trans.* **2012**, *41*, 7866.

(34) Liu, R. L.; von Malotki, C.; Arnold, L.; Koshino, N.; Higashimura, H.; Baumgarten, M.; Mullen, K. *J. Am. Chem. Soc.* **2011**, *133*, 10372.

(35) Gonzalez-Alvarez, A.; Alfonso, I.; Cano, J.; Diaz, P.; Gotor, V.; Gotor-Fernandez, V.; Garcia-Espana, E.; Garcia-Granda, S.; Jimenez, H. R.; Lloret, F. *Angew. Chem. Int. Ed.* **2009**, *48*, 6055.

(36) Inoue, M.; Ikeda, C.; Kawata, Y.; Venkatraman, S.; Furukawa, K.; Osuka, A. *Angew. Chem. Int. Ed.* **2007**, *46*, 2306.

(37) Suh, M. P.; Han, M. Y.; Lee, J. H.; Min, K. S.; Hyeon, C. *J. Am. Chem. Soc.* **1998**, *120*, 3819.

(38) Kanady, J. S.; Tsui, E. Y.; Day, M. W.; Agapie, T. *Science* **2011**, *333*, 733.

(39) Tsui, E. Y.; Day, M. W.; Agapie, T. *Angew. Chem. Int. Ed.* **2011**, *50*, 1668.

(40) Tsui, E. Y.; Kanady, J. S.; Agapie, T. *Inorg. Chem.* **2013**, *52*, 13833.

(41) Kanesato, M.; Nagahara, K.; Igarashi, K.; Sato, K.-i.; Kikkawa, Y.; Goto, M. *Inorg. Chim. Acta* **2011**, *367*, 225.

(42) Drose, P.; Gottfriedsen, J. *Z. Anorg. Allg. Chem* **2008**, *634*, 87.

(43) Essig, M. W.; Keogh, D. W.; Scott, B. L.; Watkin, J. G. *Polyhedron* **2001**, *20*, 373.

(44) Kanesato, M.; Yokoyama, T. *Chem. Lett.* **1999**, 137.

(45) Wong, W. K.; Liang, H. Z.; Guo, J. P.; Wong, W. Y.; Lo, W. K.; Li, K. F.; Cheah, K. W.; Zhou, Z. Y.; Wong, W. T. *Eur. J. Inorg. Chem.* **2004**, 829.

(46) Fennie, M. W.; DiMauro, E. F.; O'Brien, E. M.; Annamalai, V.; Kozlowski, M. C. *Tetrahedron* **2005**, *61*, 6249.

(47) Mirica, L. M.; Ottenwaelder, X.; Stack, T. D. P. *Chem. Rev.* **2004**, *104*, 1013.

(48) Itoh, S.; Fukuzumi, S. *Bull. Chem. Soc. Jpn.* **2002**, *75*, 2081.

(49) Machonkin, T. E.; Mukherjee, P.; Henson, M. J.; Stack, T. D. P.; Solomon, E. I. *Inorg. Chim. Acta* **2002**, *341*, 39.

(50) Eisenberg, G. M. *Ind. Eng. Chem.* **1943**, *15*, 327.

(51) Lucas, H. R.; Li, L.; Sarjeant, A. A. N.; Vance, M. A.; Solomon, E. I.; Karlin, K. D. *J. Am. Chem. Soc.* **2009**, *131*, 3230.

(52) Mizukami, S.; Houjou, H.; Kanesato, M.; Hiratani, K. *Chem. Eur. J.* **2003**, *9*, 1521.

(53) Shannon, R. D. *Acta Crystallogr. A* **1976**, *32*, 751.

(54) Shearer, J.; Zhang, C. X.; Zakharov, L. N.; Rheingold, A. L.; Karlin, K. D. *J. Am. Chem. Soc.* **2005**, *127*, 5469.

(55) Mahadevan, V.; Hou, Z.; Cole, A. P.; Root, D. E.; Lal, T. K.; Solomon, E. I.; Stack, T. D. P. *J. Am. Chem. Soc.* **1997**, *119*, 11996.

(56) Abasq, M. L.; Saidi, M.; Burgot, J. L.; Darchen, A. *J. Organomet. Chem.* **2009**, *694*, 36.

(57) Cole, A. P.; V, M.; Mirica, L. M.; X, O.; Stack, T. D. P. *Inorg. Chem.* **2005**, *44*, 7345.

(58) Nurminen, E.; Lonnberg, H. *J. Phys. Org. Chem.* **2004**, *17*, 1.

(59) Schwesinger, B. *Nachr. Chem. Tech. Lab.* **1990**, *38*, 1214.

(60) Ciriano, M. V.; Korth, H. G.; van Scheppingen, W. B.; Mulder, P. *J. Am. Chem. Soc.* **1999**, *121*, 6375.

(61) Cowley, R. E.; Eckert, N. A.; Vaddadi, S.; Figg, T. M.; Cundari, T. R.; Holland, P. L. *J. Am. Chem. Soc.* **2011**, *133*, 9796.

(62) Mcmillen, D. F.; Golden, D. M. *Annu. Rev. Phys. Chem.* **1982**, *33*, 493.

(63) Osako, T.; Ohkubo, K.; Taki, M.; Tachi, Y.; Fukuzumi, S.; Itoh, S. *J. Am. Chem. Soc.* **2003**, *125*, 11027.

(64) Parsell, T. H.; Yang, M.-Y.; Borovik, A. S. *J. Am. Chem. Soc.* **2009**, *131*, 2762.

(65) Green, M. T.; Dawson, J. H.; Gray, H. B. *Science* **2004**, *304*, 1653.

(66) Borovik, A. S. *Chem. Soc. Rev.* **2011**, *40*, 1870.

(67) Warren, J. J.; Tronic, T. A.; Mayer, J. M. *Chem. Rev.* **2010**, *110*, 6961.

(68) Lappert, M. F.; Pearce, R. *J. Chem. Soc. Chem. Commun.* **1973**, 126.

(69) Bradley, D. C.; Ghotra, J. S.; Hart, F. A. *J. Chem. Soc. Dalton Trans.* **1973**, 1021.

(70) Lambert, E.; Chabut, B.; ChardonNoblat, S.; Deronzier, A.; Chottard, G.; Bousseksou, A.; Tuchagues, J. P.; Laugier, J.; Bardet, M.; Latour, J. M. *J. Am. Chem. Soc.* **1997**, *119*, 9424.

(71) Burger, B. J.; Bercaw, J. E. *ACS Symp. Ser.* **1987**, *357*, 79.

(72) Knight, P. D.; Clarkson, G.; Hammond, M. L.; Kimberley, B. S.; Scott, P. *J. Organomet. Chem.* **2005**, *690*, 5125.

(73) Vandersluis, P.; Spek, A. L. *Acta Crystallogr. A* **1990**, *46*, 194.

CHAPTER 3

A *TRANS*-HYPONITRITE INTERMEDIATE IN THE REDUCTIVE COUPLING AND DEOXYGENATION OF NITRIC OXIDE BY A TRICOPPER-LEWIS ACID COMPLEX

Abstract

The reduction of nitric oxide (NO) to nitrous oxide (N_2O) is a process relevant to biological chemistry as well as to the abatement of environmental pollutants. One of the proposed key intermediates in biological NO reduction is the hyponitrite motif ($N_2O_2^{2-}$), the direct product of N–N bond formation between two NO molecules. Model complexes of these systems have been reported that display NO reduction activity, and hyponitrite complexes of various transition metals have been reported as models of the proposed reaction intermediates, including examples in which the hyponitrite motif was derived from NO. The reactivity of an yttrium-tricopper complex with NO was studied to explore the possibility of cooperative activation by multiple metal centers. Whereas O_2 activation by this [YCu_3] complex had previously been shown to occur at the three Cu centers on a single complex, reductive coupling of NO proceeded *inter*molecularly to generate a *trans*-hyponitrite moiety supported by two [YCu_3] cores. A related mononuclear complex displayed NO disproportionation activity analogous to that of similar literature complexes, highlighting the importance of role of Y in stabilizing the hyponitrite ligand. Reaction of the hyponitrite species with Brønsted acids led to generation of N_2O, supporting the viability of the hyponitrite complex as an intermediate in NO reduction to N_2O. The synthesis and reactivity of these species are discussed. The additional reducing equivalents stored in each tricopper unit were then used in a subsequent step in which N_2O was reduced to N_2

INTRODUCTION

Nitrogen monoxide (nitric oxide, NO) has attracted much attention due to its relevance to biochemistry as well as environmental science.[1-5] Nitric oxide is involved in a number of biochemical processes, including immune response to pathogens, blood pressure regulation, and neurotransmission.[6] In bacteria, as well as several fungi and yeasts, NO is a key intermediate in the anaerobic respiration cycle, by which these organisms utilize nitrate (NO_3^-) as terminal electron acceptor in place of O_2 (Scheme 1) ultimately leading to generation of nitrous oxide (N_2O) or dinitrogen (N_2).[2,7] Reduction of NO to N_2O, accompanied by release of H_2O, is a pivotal step in this pathway, involving the formation of a N–N bond. This transformation has also been targeted for its potential to contribute to the abatement of NO_x pollutants emitted by industrial and automotive sources.[8,9]

Scheme 1. The Denitrification Process.

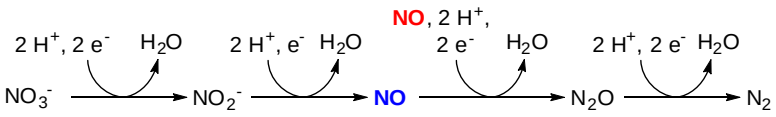

One of the biological systems responsible for the reduction of NO is the nitric oxide reductase (NOR) family of enzymes, which contain a heme/non-heme diiron active site (Figure 1a).[2,10] NORs are evolutionarily related to cytochrome *c* oxidases (CcOs,), which display a Cu center in place of the non-heme Fe site (Figure 1b).[11] Due to the similarities in their active site architectures, these two families of enzymes also share reactivity patterns – several C*c*Os have been shown to catalyze the reduction of NO to N_2O (albeit at lower efficiencies than O_2, their biological substrate) and, likewise, certain NORs display C*c*O activity, being capable of reducing O_2 to H_2O.[2,5]

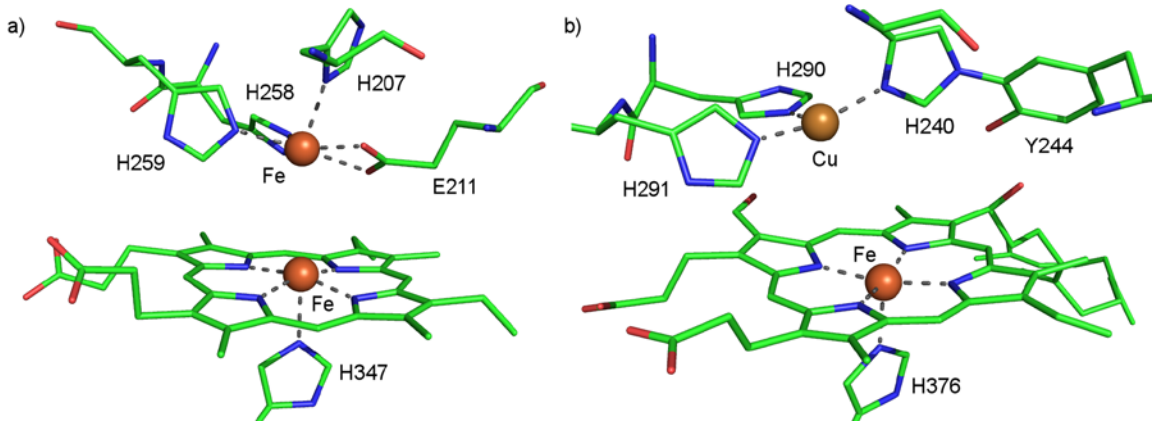

Figure 1. Structural representations of the active sites of (a) nitric oxide reductase (PDB: 3O0R)[10] and (b) cytochrome *c* oxidase (PDB: 1V54).[11]

The mechanism of NO reduction by NORs and C*c*Os has not been fully elucidated, in part due to the lack of structural information about intermediates along the reaction pathway. Nonetheless, several proposals have been put forth based on spectroscopic studies and theoretical calculations.[5,12-19] A key element in many proposals is the formation of a hyponitrite motif ($[N_2O_2]^{2-}$), the direct product of N–N bond formation between two nitric oxide molecules. Studies of NO reduction by heterogeneous catalysts have indicated that hyponitrite species are also relevant to their catalytic activity. The hyponitrite dianion can adopt a *trans* or *cis* geometry, and both isomers have been implicated in various mechanistic proposals of NO reduction, although several recent studies have favored mechanisms involving formation of *cis*-hyponitrite.[4,5]

The mechanism of the reduction of NO to N_2O has been probed in synthetic model systems based on both the metals involved in biological NO reduction (Fe, Cu).[3,5,20-36] Complexes of other transition metals have also been reported to display NO reduction activity.[3,4,20,37-41] Nonetheless, the paucity of intermediates that could be structurally or

spectroscopically characterized in these reactions has often hindered efforts to elucidate the mechanism of this transformation.

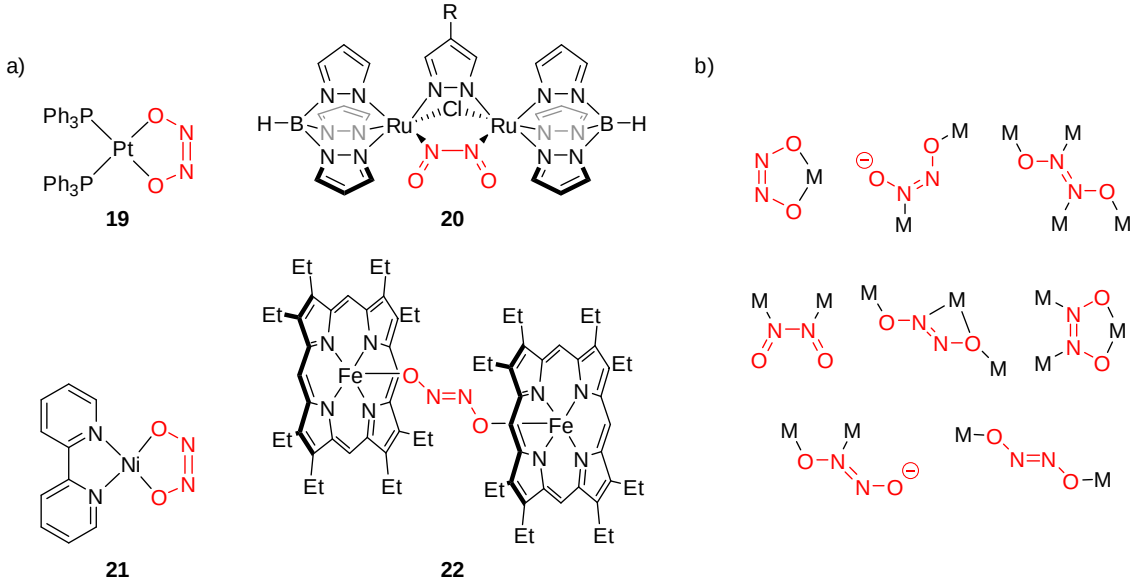

Figure 2. (a) Selected literature hyponitrite complexes; (b) binding modes of literature hyponitrite ligands

Only a handful of metal complexes that contain the hyponitrite motif, the proposed product of N–N coupling in NORs and C*c*Os, have been reported. Dimerization of NO by $Pt(PPh_3)_4$ was observed to generate the *cis*-hyponitrite-bound Pt complex **19** (Figure 2).[42,43] T*rans*-hyponitrite species were formed upon reaction of a coordinatively unsaturated Ru complex with NO.[44-47] Reaction of an yttrium–(NO^{2-}) complex with NO also led to observation of a hyponitrite complex.[48] Studies by Onishi and coworkers on a dinuclear Ru complex showed reversible formation of a *cis*-hyponitrite species (**20**) from coupling of two adjacent nitrosyl ligands.[38] Treatment of **20** with H^+ sources led to release of N_2O and formation of a μ-O complex, and the mechanism of this transformation was recently investigated by Arikawa and Yoshizawa.[41] Hayton and coworkers have recently reported the reactivity of a bipyridine-supported Ni–(NO^-)

complex, which thermally converted to Ni-hyponitrite complex **19** via coupling of two NO^- moieties.[4,39,40,49,50] Complex **19** was also shown to release N_2O upon treatment with weak acids. Notably, the only hyponitrite complex featuring biologically relevant metals (Fe, Cu) is **22**, in which a *trans*-hyponitrite ligand bridges two Fe-porphyrin.[19,51] However, the hyponitrite ligand in this complex was obtained from hyponitrous acid ($N_2O_2H_2$) rather than from reduction of NO.

We previously reported a series of [MCu_3] complexes supported by tripodal multinucleating ligand frameworks as models of the multicopper oxidases (Scheme 2).[52] [Cu^I_3] complex **4-Y** displayed intramolecular metal-metal cooperativity in reduction of O_2 at low temperature to form a $[Cu^{III}Cu^{II}_2(\mu_3\text{-}O)_2]^{3+}$ intermediate in which the O–O bond had been fully cleaved (**5-Y**). The pre-assembly of the three Cu centers in **4-Y** was found to be essential to this reactivity, as related mononuclear or [YCu] complexes failed to generate the same intermediate. The reactivity of **5-Y** was extensively studied with a variety of substrates (H-atom donors, O-atom acceptors, Brønsted acids) to gain insight into the properties of this species. Remarkably, **5-Y** was observed to react with thiophenols to generate a [Cu^I_3] species and two equivalents of disulfide, consistent with formal transfer of four H-atoms to form two H_2O molecules as byproducts.

Scheme 2. Summary of O_2 Reactivity of [MCu_3] Complexes.

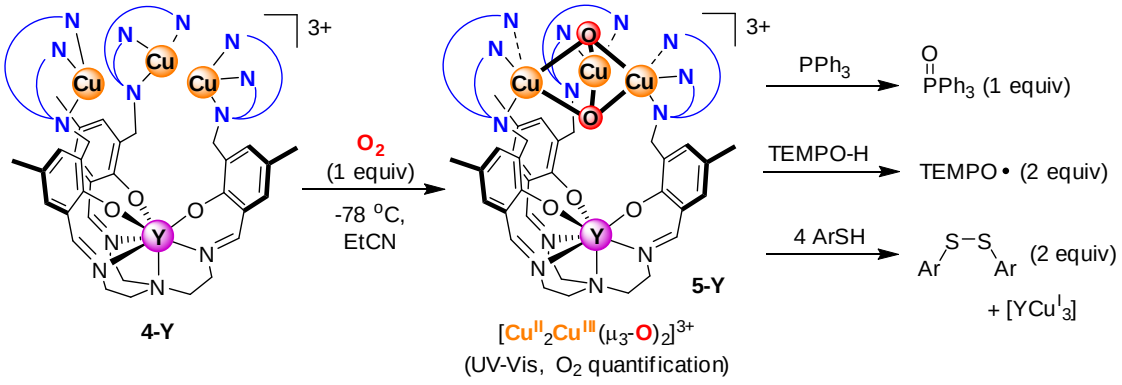

Herein, we describe the reactivity of **4-Y** with nitric oxide, which was inspired by interest in exploring the ability of the three Cu centers in this complex to engage in cooperative reactivity with other small-molecule substrates. However, instead of cooperative activation by the three Cu centers on the same molecule as was observed for O_2, activation of NO by **4-Y** proceeded by cooperative reactivity between four metal centers (two Cu and two Y centers) on two separate [YCu_3] units. Reductive coupling of two NO molecules led to formation of a *trans*-hyponitrite complex, which released N_2O upon treatment with an appropriate H^+ source. The presence of Y^{3+} was pivotal, as a related mononuclear Cu complex displayed different reactivity. The presence of additional Cu^I centers in **23** also allowed to observe further reduction of the N_2O produced *in situ* to N_2.

RESULTS AND DISCUSSION

Binding of NO to Cu^{I} complexes has been reported for a handful mono- and dinuclear complexes supported by netural and anionic ligand frameworks. These [Cu^{I}–NO]^{11} complexes are formally 19-e^{-} species, and are therefore often highly reactive.[20] While spectroscopic (and, in a few cases, structural) characterization of these species has been carried out at low temperature, NO reduction reactivity is often observed at ambient temperature conditions.[21,23,24,53,54] In the presence of excess NO, many [Cu–NO]^{11} complexes perform reductive disproportionation to generate N_2O and Cu–(NO_2^-) species, although transfer of an O^{2-} ligand to the Cu complexes themselves or sacrificial reduction by an organic substrate have also been observed.[54] In general, these reactions are proposed to occur at single Cu centers either by coupling of two bound nitrosyl or via nucleophilic attack onto a Cu-bound nitrosyl by free NO, due to the lack of evidence for bimetallic mechanisms.[24]

To explore the feasibility of cooperative activation of nitric oxide by multiple Cu centers, reactivity of tricopper complex **4-Y** with NO was explored. The multinucleating ligand scaffold supporting **4-Y** was designed to favor cooperative reactivity between three copper centers, as is observed for O_2 reduction by the multicopper oxidase enzymes.[55] In fact, O_2 activation by **4-Y** was shown to proceed via intramolecular cooperative reactivity between the three Cu centers to yield the bis(μ_3-O) species **5-Y**.[52] To test whether the pre-assembly of the three Cu centers in **4-Y** could enforce cooperative activation of NO, a degassed propionitrile (EtCN) solution of **4-Y** was exposed to a slightly suprastoichiometric (1.2 equiv.) amount of gaseous NO at -78 °C (Scheme 3). Within minutes, the color of the concentrated solution had changed from dark yellow to dark green. The solution was stirred for 6 hours at -78 °C, after

which it was allowed to warm to room temperature. Analysis of the yellow-green product obtained after removing the solvent *in vacuo* by ^{1}H NMR revealed the disappearance of the sharp signals for **4-Y** and the appearance of broad (though diamagnetic) signals, indicating the presence of fluxional processes involving the intricate ligand scaffold.

Single crystals suitable for X-ray diffraction (XRD) analysis were grown from vapor diffusion of diethyl ether into a CH_3CN solution of the product. The solid state structure revealed a dimer of [YCu_3] cores bridged by a *trans*-hyponitrite moiety resulting from reductive coupling of two NO molecules (**23**). At each [YCu_3] unit, the oxygen atom from the $N_2O_2^{2-}$ ligand was observed to bridge between a copper center and the yttrium center bound to the heptadentate site of the ligand framework (Figures 3 and 4). A second bridge between Cu and Y was provided by the oxygen of a ligand phenoxide oxygen. The hyponitrite-bound Cu center was five-coordinate and displayed a square pyramidal geometry, and was therefore assigned as Cu^{II}. The other two Cu centers remained essentially unchanged, in their distorted tetrahedral geometries, from the structure of the starting material **4-Y**,[52] and were thus assigned as having maintained the Cu^{I} oxidation state.

Scheme 3. Reaction of Complex **4-Y** with Nitric Oxide.

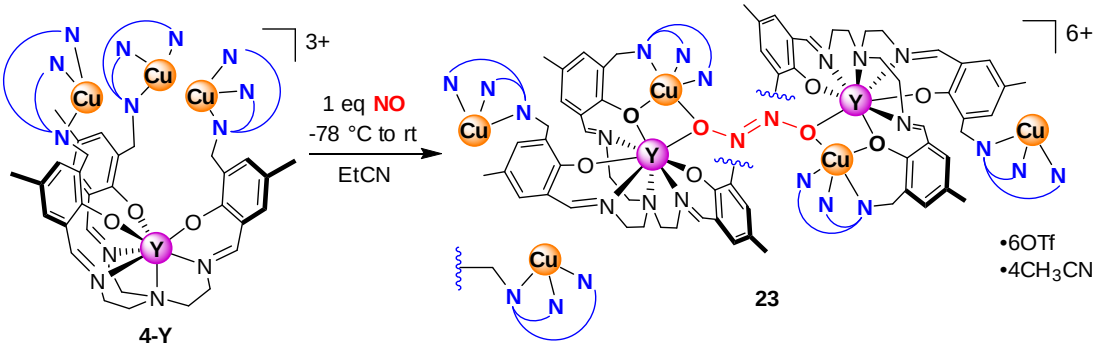

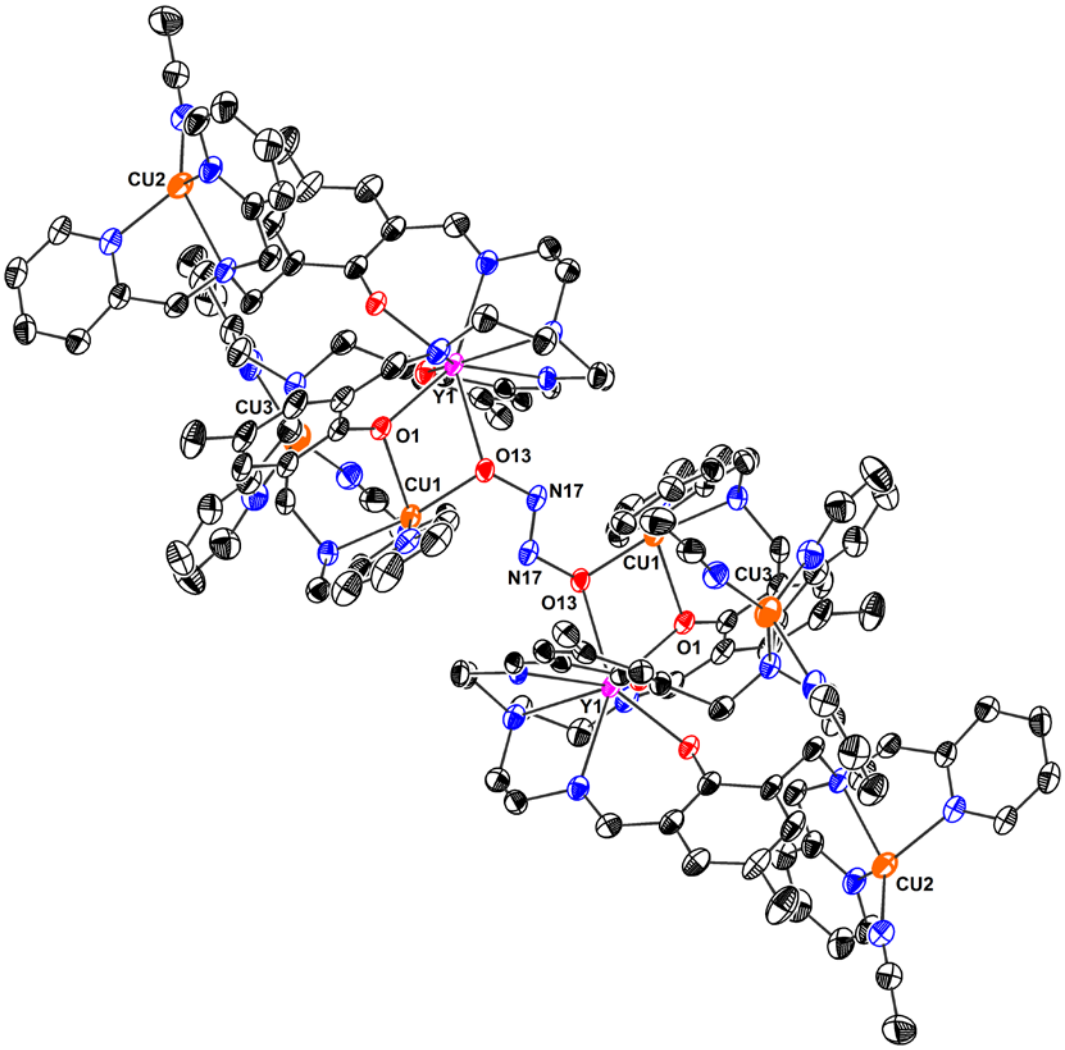

Figure 3. Solid-state structure of hyponitrite complex **23**. Six outer-sphere triflate anions and hydrogen atoms omitted for clarity. Thermal ellipsoids shown at 50% probability.

The overall reaction between **4-Y** and NO, therefore, can be described as the 2-e^- reduction of two NO molecules by two Cu^{I} centers to give $N_2O_2^{2-}$ and two Cu^{II}. The Lewis acidic Y^{3+} center was key to this transformation as it provided an additional coordination site for stabilization of the hyponitrite ligand. Coordination of hyponitrite to Y^{3+} can be viewed as a Lewis acid/base analog to the Brønsted acid/base reaction with H^+ to generate N_2O in the natural system. Remarkably, formation of **23** was the

result of *inter*molecular cooperative activation of NO by two Cu and two Y centers, a striking difference from the activation of O_2, which occurred *intra*molecularly. It is notable that although the multinucleating ligand framework was shown to hold the three Cu centers in close proximity, thereby engendering cooperative O_2 activation, it was sufficiently flexible to allow coordination of an eighth ligand to Y^{3+}, pivotal to the stabilization of the hyponitrite in **23**. Complex **23** is the first hyponitrite complex of a biologically relevant metal (Cu) in which the $N_2O_2^{2-}$ ligand was derived from nitric oxide.[4] The crystalline yield of **23** was low (~20-25%), but comparison of the ^{1}H NMR spectra for the crystalline material with that of the crude reaction mixture showed that **23** accounted for the majority of the product formed.

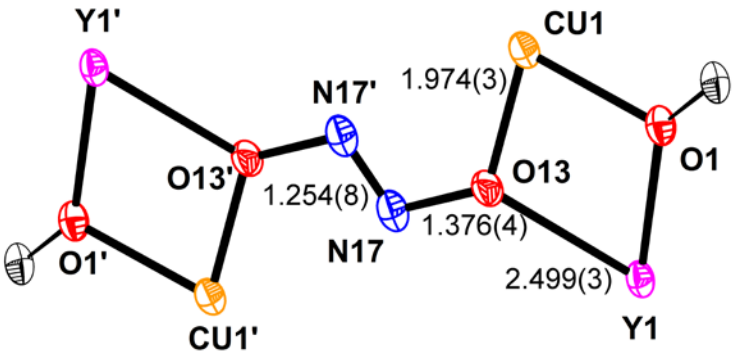

Figure 4. Truncated solid-state structure of hyponitrite complex **23** highlighting the hyponitrite motif. Relevant bond distances (in Å) are included. Thermal ellipsoids shown at the 50% probability level.

The structural parameters for hyponitrite complex **23** are listed in Table 1 alongside those for other hyponitrite complexes reported in the literature. The bond distances and angles for the hyponitrite ligand were observed to be very similar to those of analogous *trans*-hyponitrite species. Both N–N and N–O bond distances in **23** were within the range of values reported in the literature, as were the N–N–O angles. The measured distances were consisted with an N–N double bond and N–O single bonds.

Table 1. Structural Parameters for Selected *Trans*-Hyponitrite Complexes.

Complex	N–N (Å)	N-O (Å)	N–N–O (°)	Ref.
$Na_2(ONNO)$ (*trans*)	1.256(2)	1.3622(11)	112.14(9)	56
$Ru_2(CO)_4(\mu\text{-}H)(\mu\text{-}P^tBu)_2(\mu\text{-}dppm)(\mu\text{-}ONNO)$[a]	1.261(2) 1.267(2)	1.313(3) 1.357(3) 1.321(2) 1.355(2)	112.5(2) 115.5(2) 112.4(2) 114.9(2)	44,46
$[Ru_2(CO)_4(\mu\text{-}H)(\mu\text{-}P^tBu)_2(\mu\text{-}dppm)(\mu\text{-}ONNOH)][BF_4]$	1.261(3)	1.381(3) 1.341(3)	109.2(2) 111.4(2)	47
$[Ru_2(CO)_4(\mu\text{-}H)(\mu\text{-}P^tBu)_2(\mu\text{-}dppm)(\mu\text{-}ONNOMe)][BF_4]$	1.262(5)	1.384(5) 1.333 (4)	107.7(3) 110.5(3)	47
$[Ru_2(CO)_4(\mu\text{-}P^tBu)_2(\mu\text{-}dppm)(\mu\text{-}ONNOMe)][BF_4]$	1.258(5)	1.390(5) 1.325(4)	107.8(4) 111.9(3)	47
$[(Co(NO)_2(\mu\text{-}ONO)]_2(\mu\text{-}ONNO)$	1.265	1.316	112.5	57
$([(Me_3Si)_2N]_2Y)_4(\mu_3\text{-}ONNO)_2(THF)_2$	1.257(3)	1.392(2) 1.335(2)	113.2(2) 112.14(9)	48
22 (Figure 2)	1.250(3)	1.375(2)	108.5(2)	51
23	1.254(8)	1.376(4)	110.2(4)	this work

[a] Two independent molecules in the asymmetric unit.

Hyponitrite complexes have been reported to display characteristic bands in their infrared (IR) spectra corresponding to N–N and N–O stretching vibrations.[3] However, due to the symmetric nature of **23** (an inversion center is present in the middle of the hyponitrite N–N bond), the N–N (1400-1500 cm^{-1}) and symmetric N–O (900-1000 cm^{-1}) stretching vibrations were not IR active, akin to what was observed for the analogously symmetric Fe complex **22**.[51] The IR-active asymmetric N–O stretch was on the other hand observed at 980 cm^{-1} in the ATR-IR spectrum of **23** ($\nu(^{15}NO)$ = 970 cm^{-1}), similar to previously reported *trans*-hyponitrite complexes. Characterization of **23**

by electrospray ionization mass spectrometry (ESI-MS) was also unsuccessful due to the large molecular weight (~4000 g/mol) and overall charge (+6) of the complex.

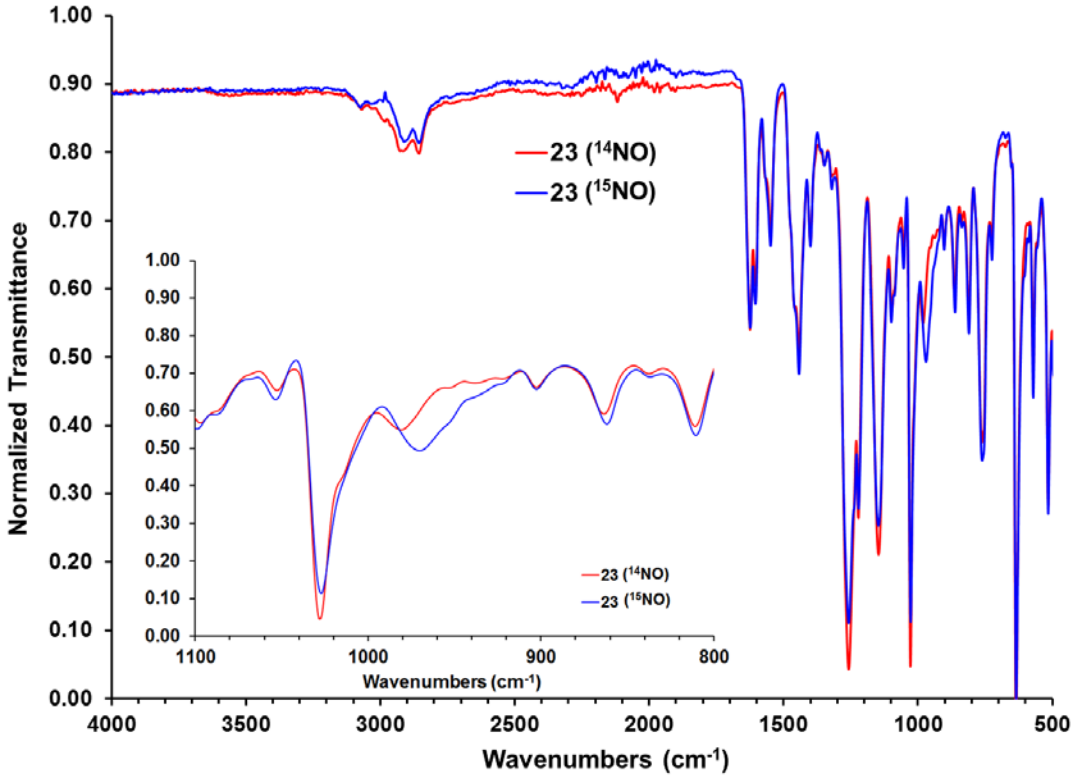

Figure 5. Solid-state ATR-IR spectra of **23** prepared from natural abundance NO (blue) and ^{15}NO (red). The N–O asymmetric stretch region is highlighted in the inset.

To shed light on the mechanism of formation of **23**, reactivity of monocopper complex **14** with NO was explored to determine whether reduction of nitric oxide could occur with a Cu complex in a similar coordination environment but without a pendant metal center for binding of a reduced intermediate. The reactivity of complex **14** with O_2 was previously studied, and it was shown that this mononuclear complex could not generate the same bis(μ_3-O) intermediate as its multimetallic analog. Furthermore, the closely related Cu^I complex $[(TMPA)Cu(CH_3CN)]^+$ (**24**, Figure 6; TMPA = tris(2-methylpyridyl)amine), in which a third picolyl group replaced the aryl ether arm in **14**, has been reported to react with NO to generate a putative [Cu–NO] complex at low

temperature that released N_2O and formed a $[Cu–O–Cu]^{2+}$ species upon warming to room temperature.

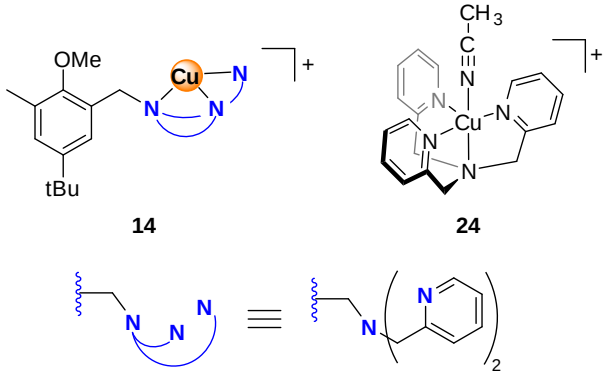

Figure 6. Mononuclear copper complexes with analogous Cu coordination environments to **4-Y**.

Absorbance features in the UV-Vis region (450-500 nm, ε~1,000-1,500 $M^{-1}cm^{-1}$) have been reported for $[Cu–NO]^{11}$ species supported by scorpionate ligands, while complex **24** gave rise to absorbances at 403, 493, 610, and 820 nm (ε = 1260, 960, 300, and 340 $M^{-1}cm^{-1}$, respectively) upon reaction with NO at low temperature. Treatment of **14** with NO at low temperature (-78 °C, EtCN) resulted in appearance of a new band in its UV-Vis spectrum (λ_{max}=365 nm, ε=1,370 $M^{-1}cm^{-1}$), together with very low-intensity features in the 500-750 nm range. The 365 nm feature, while displaying the correct intensity, was observed at substantially higher energy than in literature complexes, making assignment of the species in solution as a Cu nitrosyl uncertain. Warming of the solution to room temperature resulted in disappearance of this feature.

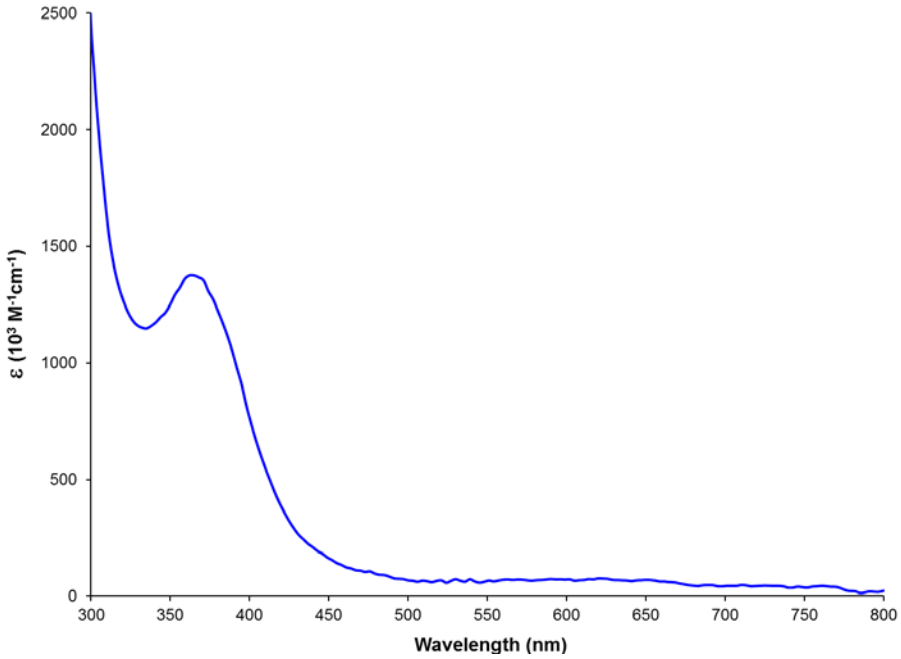

Figure 7. UV-Vis spectrum of the reaction of **14** (0.62 mM) with NO (~3 equiv) in EtCN at -78 °C.

To further characterize the species formed at low temperature, reaction of **14** with NO was monitored via *in situ* FTIR spectroscopy (Figure 8). Due to the particular instrumental setup, reliable addition of stoichiometric amount of NO to the reaction solution was impossible, and reactivity was studied with excess NO. Bubbling of NO through a 12.2 mM solution of **14** in 1:1 THF/EtCN at -78 °C resulted in a color change from golden yellow to dark green. Concurrently, a new IR feature was observed (ν=1,600 cm^{-1}). N–O stretching frequencies reported for other Cu^{I} complexes have ranged from 1600-1700 cm^{-1} for scorpionate ligands to 1460 cm^{-1} for the low-temperature intermediate obtained from **24**; thus, the vibration observed for **14** was in a reasonable range for a $[Cu–NO]^{11}$ complex (Scheme 4).[22,24,33] Warming of the solution resulted in the disappearance of the 1,600 cm^{-1} feature and concomitant appearance of a new band at 1,740 cm^{-1}. Upon further warming, the newly appeared band at 1,740 cm^{-1} was lost, and a new signal at 1,640 cm^{-1} appeared, which was maintained in the final

spectrum at room temperature. These observations were consistent with a multi-step process, although no assignment could be made for the signals observed at 1,740 and 1,640 cm^{-1}.

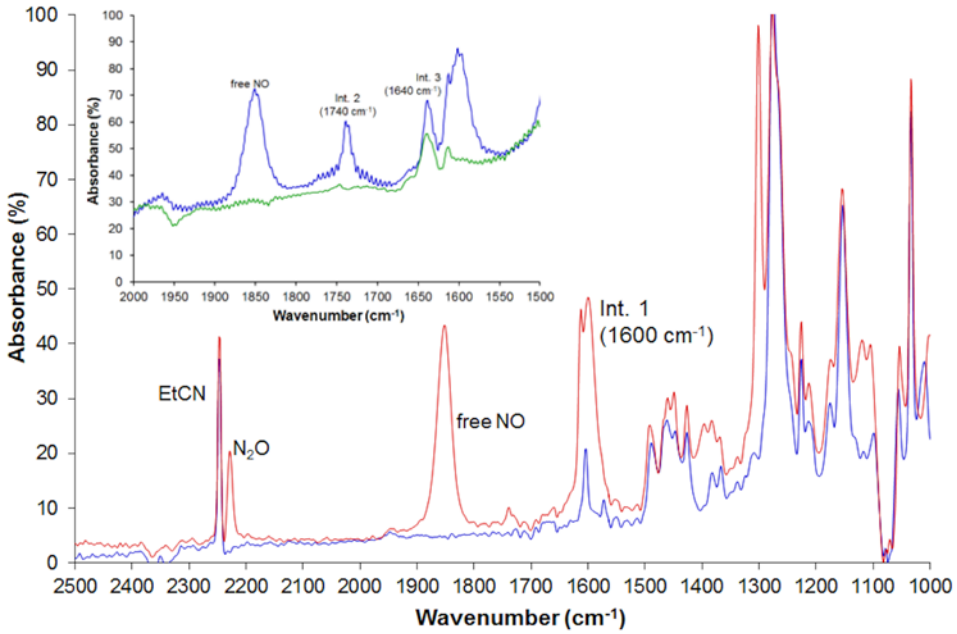

Figure 8. *In situ* solution IR monitoring of reaction of **14** with NO (THF/EtCN, -78 °C). Spectra shown before (blue) and after (red) addition of excess NO. Peaks corresponding to residual solvent, free N_2O, free NO, and intermediate species formed (see text) are marked. Inset: spectra recorded during (blue) and after warmup (green); free NO and intermediates formed are marked.

Warming of the IR cell to room temperature also resulted in a second change in the color of the solution from dark green to blue. The blue material was isolated by filtering of the slightly opaque solution and removal of the solvent *in vacuo*. Attempts to crystallize the major product formed in this reaction were unsuccessful. On the other hand, single-crystals suitable for XRD analysis were obtained for a minor product of the reaction (**25a**, Scheme 4) by vapor diffusion of diethyl ether into a CH_3CN solution of the crude mixture. The structure thus obtained showed dimerization of the mononuclear complex through a linear diatomic bridge (Figure 9). Each Cu center was

in a six-coordinate environment, bound to the three N donors from the dipicolylamine motif, the aryl ether oxygen, a triflate anion, and the diatomic bridging ligand. A third, outer-sphere triflate was also observed, indicating that the intermetallic bridge was likely a monoanionic moiety (to balance out the positive charge of the two Cu^{II} centers). The best fit for the diatomic ligand was found to be a cyanide (CN^-) moiety disordered over the two possible orientations (~70/30 ratio of the two populations). Furthermore, disorder in one of the two Cu-bound triflate anions suggested partial occupation by a triatomic moiety, successfully modeled in the refined structure as a nitrite (NO_2^-) ligand. The observation of a CN^- ligand was surprising, and was corroborated by ESI-MS, which showed several fragments containing this moiety. The source of the CN^- was unclear, although decomposition of nitriles by Cu^{II} centers in the presence of nucleophiles to generate cyanide species has been reported for a handful of systems.[58-63] Independent synthesis of complex **25a** was targeted to confirm its assignment as a cyanide species. Treatment of **14** with Ag(OTf) (1 equiv.) provided the corresponding Cu^{II} complex, from which **25a** was generated by addition of 0.5 equiv. tetrabutylammonium cyanide, as confirmed by ^{1}H NMR spectroscopy and XRD.

Scheme 4. Reactivity of **14** with NO. Wavenumber Values Refer to Signals Detected Via IR Spectroscopy Corresponding to Intermediate Species.

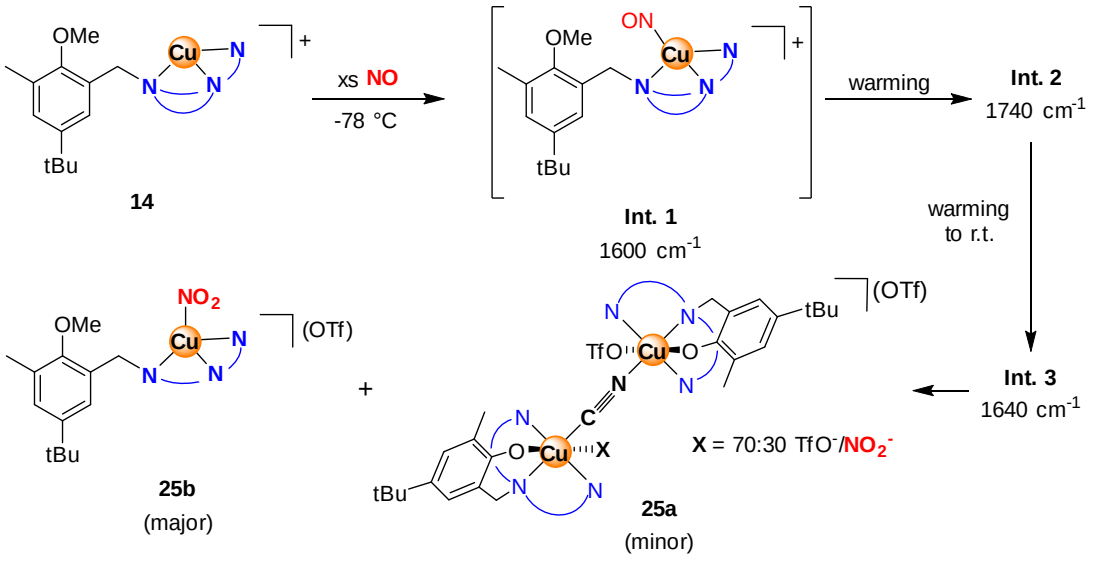

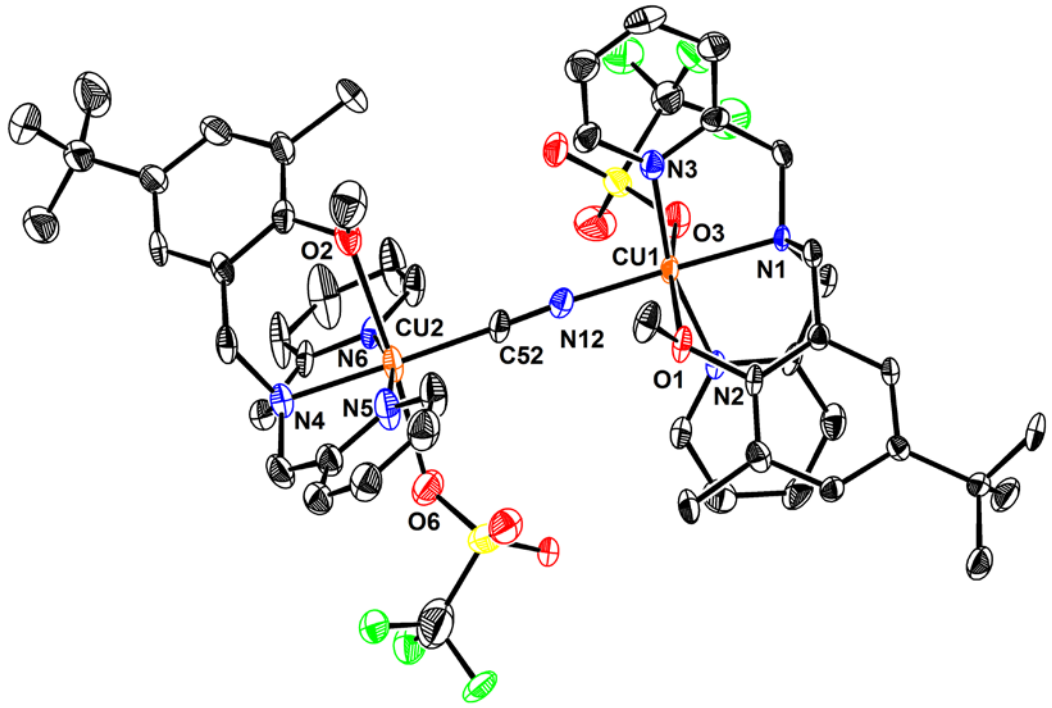

Figure 9. Solid-state structure of **25a**. Hydrogen atoms and an outer-sphere triflate anion omitted for clarity. Thermal ellipsoids shown at the 50% probability level. For disordered positions (C(52)–N(12), triflate anion containing O(6)), only fragments with higher occupancy are shown (see Experimental Section for details).

Reaction of **14** with NO was further studied via ^{1}H NMR spectroscopy. Treatment of **14** with stoichiometric NO only resulted in partial conversion to a new species with broad paramagnetic features (Figure 10). The presence of unreacted starting material indicated a different reaction stoichiometry from that of complex **4-Y**. Complete disappearance of the ^{1}H NMR signals corresponding to **14** was observed upon addition of excess NO (5 equiv.), concurrent with a change in color from yellow to blue-green. Notably, treatment of **14** with Ag(OTf) followed by addition of 1 equiv. tetrabutylammonium nitrite yielded a material displaying identical ^{1}H NMR features to that of the product of the reaction of **14** with excess NO. XRD analysis of single crystals obtained via vapor diffusion of diethyl ether into an acetonitrile solution of this material revealed formation of Cu(II) nitrite (NO_2^-) complex **25b** (Figure 11). Observation of a nitrite complex and of the different stoichiometry of the reaction of **14** with NO suggested that this complex engaged in reductive disproportionation to N_2O and NO_2^- regardless of the amount of NO added (Scheme 5) – consistent with the stoichiometry of this transformation, which requires transfer of one electron per three NO molecules, the reactivity of complex **14** with 1 equiv. NO involved disproportionation of NO by one-third of the Cu species, leaving two thirds of the starting complex **14** unreacted. Notably, formation of N_2O by **14** in the presence of excess NO was observed in the reaction monitored by solution IR (Figure 8). These observation indicated that the presence of the Y^{3+} center in **4-Y** was essential to stabilization of the bound hyponitrite moiety.

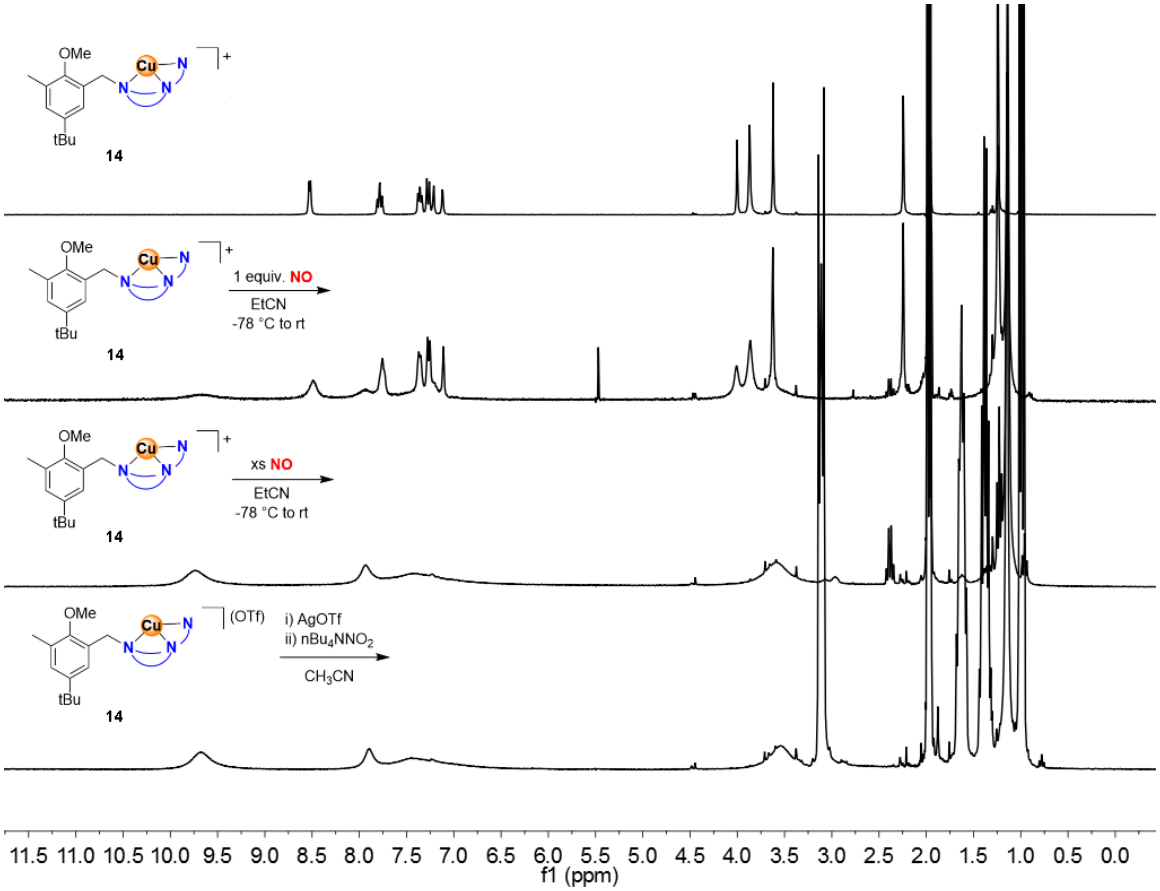

Figure 10. ^{1}H NMR spectra (CD_3CN, 300 MHz) for **14**, and of its reaction with 1 equiv. NO (EtCN, -78 °C, 2 hours), excess NO (EtCN/THF, -78 °C, 4 hours), and 1 equiv. Ag(OTf) and 1 equiv. $^{n}Bu_4NNO_2$ (CH_3CN, 1 h).

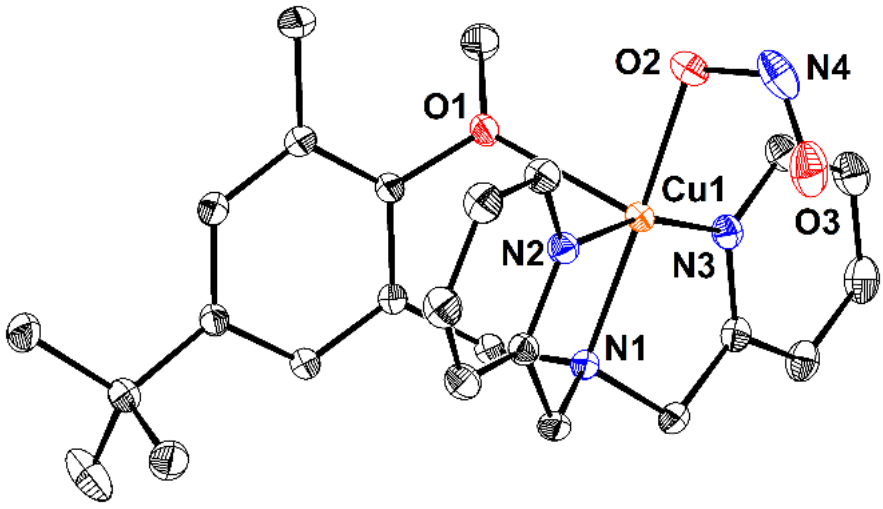

Figure 11. Solid-state structure of complex **25b**. Hydrogen atoms and an outer-sphere triflate anion omitted for clarity. Thermal ellipsoids shown at the 50% probability level.

Scheme 5. Independent Synthesis of Cu^{II} Complexes Relevant to Observed NO Reactivity of Complex **14**.

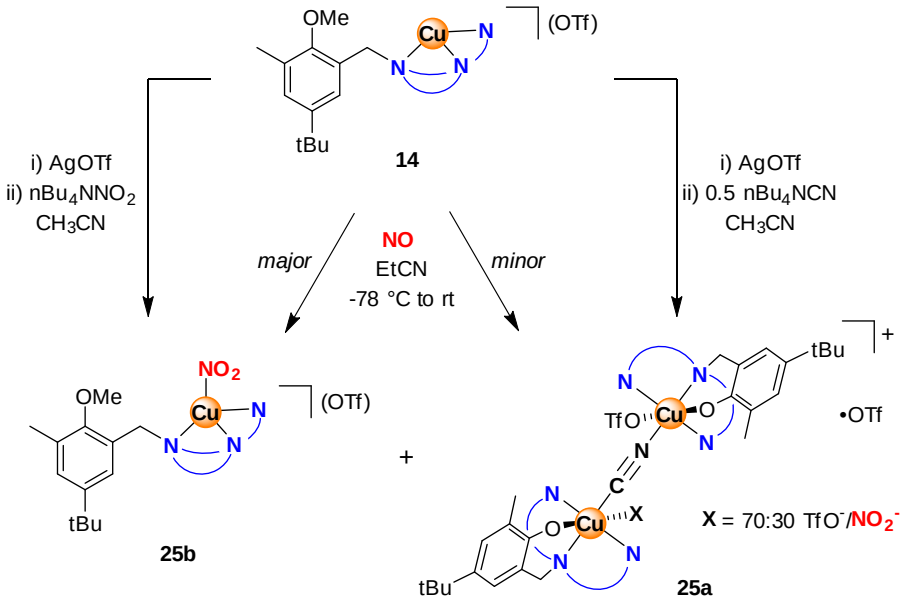

Based on the observation of intermediates for the reaction of complex **14** with NO, the reactivity of **4-Y** with NO was studied by the same spectroscopic methods to determine whether similar species were formed on the way to generation of **23**. However, monitoring of the reaction of **4-Y** with NO by low-temperature UV-Vis or IR spectroscopy did not provide conclusive evidence for the formation of [Cu–NO] species or other intermediates. UV-Vis spectra of this reaction showed the appearance of low-intensity features in the 450-500 and 650 nm ranges that could be consistent with the putative nitrosyl product obtained from **4-Y**, but the lack of a clear ~400 nm absorbance made this assignment impossible. Likewise, monitoring of the reaction via solution IR showed that no new signals appeared upon treatment of **4-Y** with NO (Figure 12).

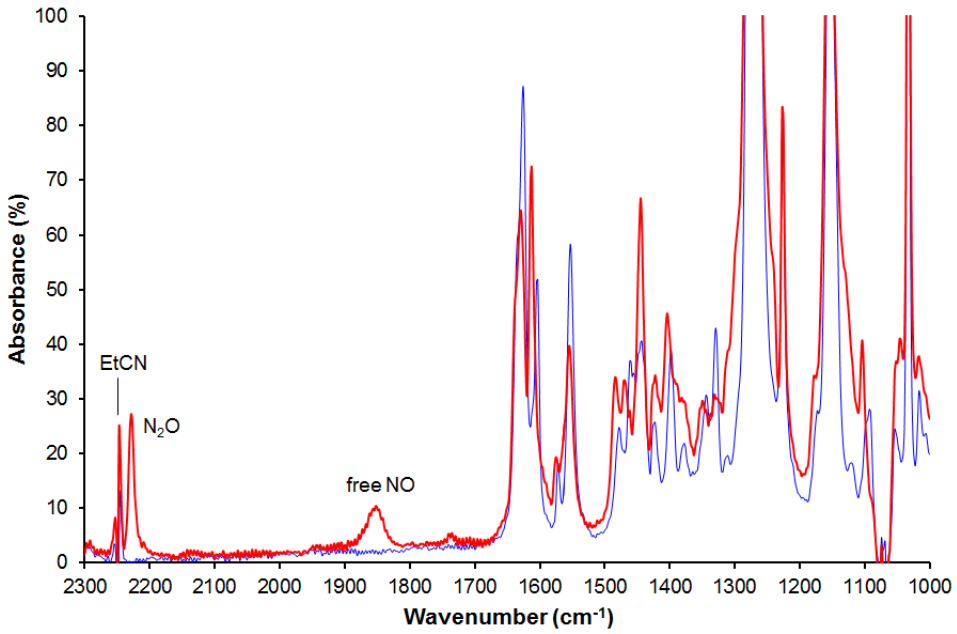

Figure 12. *In situ* solution IR monitoring of reaction of **4-Y** with NO (THF/EtCN, -78 °C). Spectra shown before (blue) and after (red) addition of excess NO. Peaks corresponding to residual solvent, free N_2O, and free NO are marked.

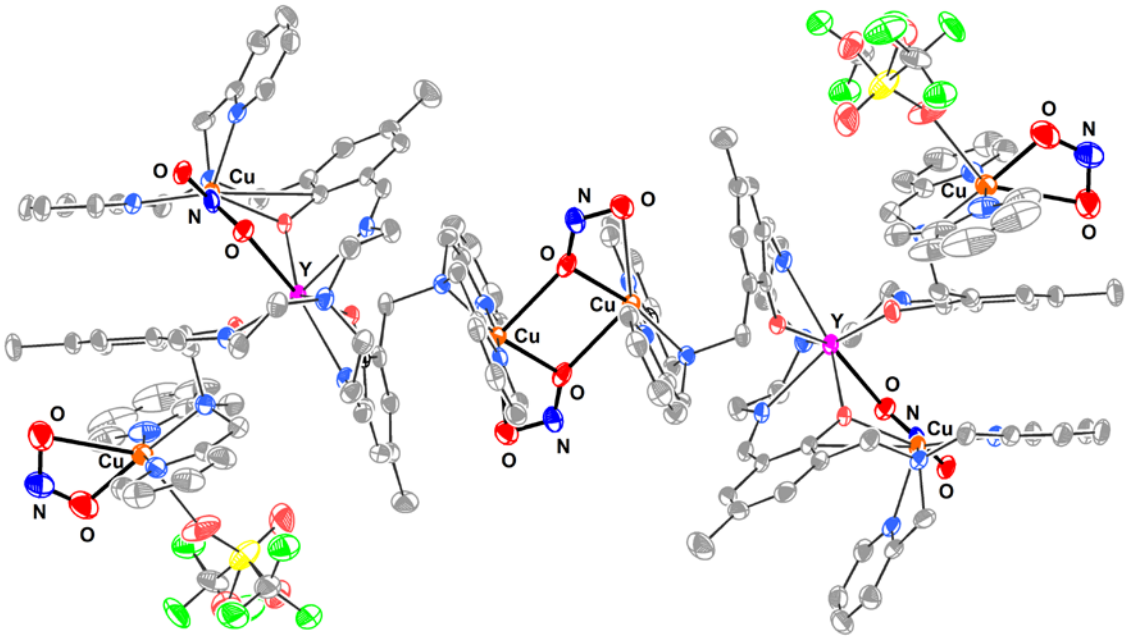

Figure 13. Preliminary solid state structure of the product of reaction of **4-Y** with excess NO. Outer-sphere triflate anions (four) not shown for clarity. Thicker lines and bolder colors emphasize interactions between metal centers and NO_2^- ligands.

Scheme 6. Synthesis of Complex **25c**.

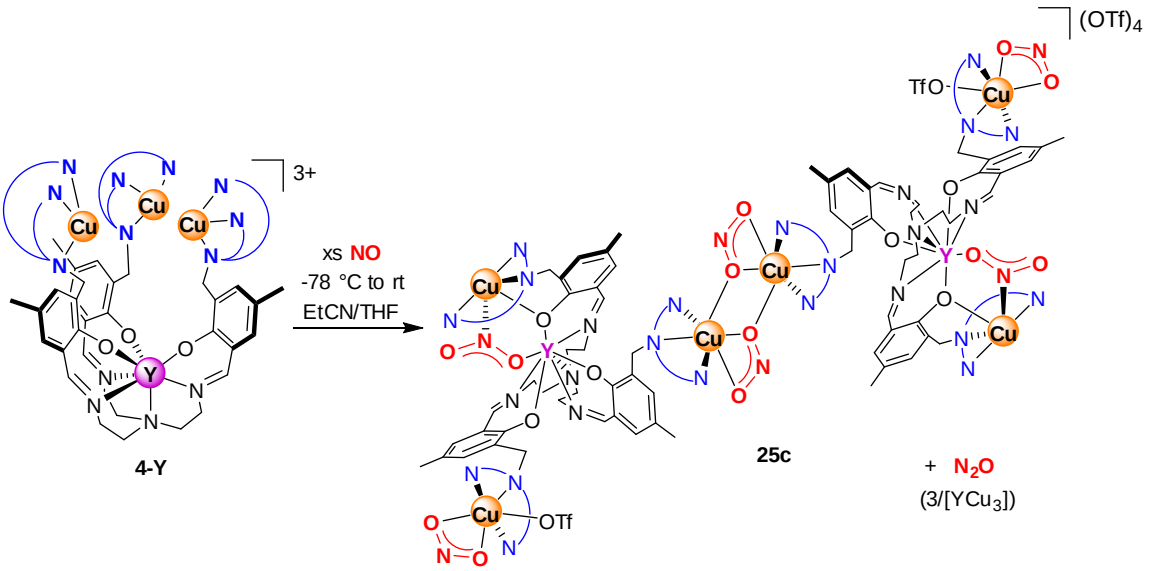

These observations could be consistent with rapid reactivity to form the hyponitrite complex **23** without accumulation of any intermediate species. However, since excess NO had to be added to the reaction for *in situ* IR monitoring, it is also possible that the lack of new features could be due to rapid disproportionation reactivity (instead of formation of **23**). Consistent with the latter possibility, N_2O was detected in the IR experiment. Furthermore, single crystals were obtained from the material that had precipitated from the reaction solution upon warming to room temperature. Although of poor quality, these crystals were sufficient for an XRD study to provide connectivity information. As hypothesized, given the observed formation of N_2O, the product contained multiple nitrite motifs (one NO_2^- per Cu center), which displayed various coordination modes to the [YCu_3] complex (**25c**, Scheme 6). As shown in Figure 13, two [YCu_3] units formed a dimer bridged by two nitrite ligands. On each tetrametallic portion, one of the Cu centers was bridged to Y by a nitrite moiety, whereas the last Cu had a κ^2-bound nitrite, as well as a bound triflate. These results confirmed that under

conditions of excess NO, disproportionation reactivity was observed for all Cu centers in **4-Y**, generating N_2O and nitrite species.

To determine whether hyponitrite complex **23** was a feasible intermediate in the reduction of NO to N_2O by **4-Y**, its reactivity with H^+ sources was explored. Complex **23** did not react with excess triethylammonium triflate (pK_a = 18.5 in CH_3CN), which had previously been shown to react with **5-Y**, the intermediate formed upon reaction with O_2. Treatment of **23** with 2 equiv. pyridinium triflate (pK_a = 12.53 in CH_3CN) resulted in a reaction as observed by ^{1}H NMR. Addition of excess acid led to further conversion (up to ~5 equiv.). The new species generated in this reaction also displayed broad NMR signals; notably, this species was identified as a possible component of mixtures obtained by keeping **23** in solution for extended periods of time for the purposes of crystallizing this species.

To study the gaseous products of this reaction, the reagents were mixed in CH_3CN in a sealed vessel. After 3 hours, N_2 was removed from the solution by freeze-pump thawing at -196 °C, and the remaining volatiles were transferred to vessels cooled to -78 °C (to trap CH_3CN) and -196 °C (to condense any produced N_2O). IR analysis of the product in a gas IR cell revealed formation of N_2O by comparison with an authentic sample (Figure 14). Likewise, treatment of **23** generated from ^{15}NO with pyridinium triflate led to generation of $^{15}N_2O$. Efforts to characterize the metal-containing products of this reaction are currently ongoing. However, observation of the formation of N_2O confirmed the viability of **23** as an intermediate in the reduction of NO by tricopper complex **4-Y**, indicating that the Y center is sufficiently Lewis acidic to favor binding of $N_2O_2^{2-}$, but not to induce N–O bond cleavage to yield N_2O, which was instead observed with a sufficiently acidic source of H^+.

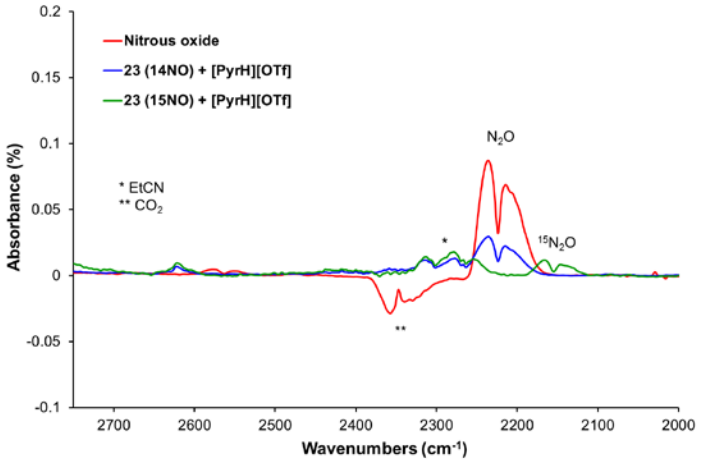

Figure 14. Red: gas-phase IR spectrum of an authentic sample of N_2O. Blue: gas-phase IR spectrum of the products of the reaction of **23** (natural abundance NO) with pyridinium triflate. Green: gas-phase IR spectrum of the products of the reaction of **23** (^{15}NO) with pyridinium triflate.

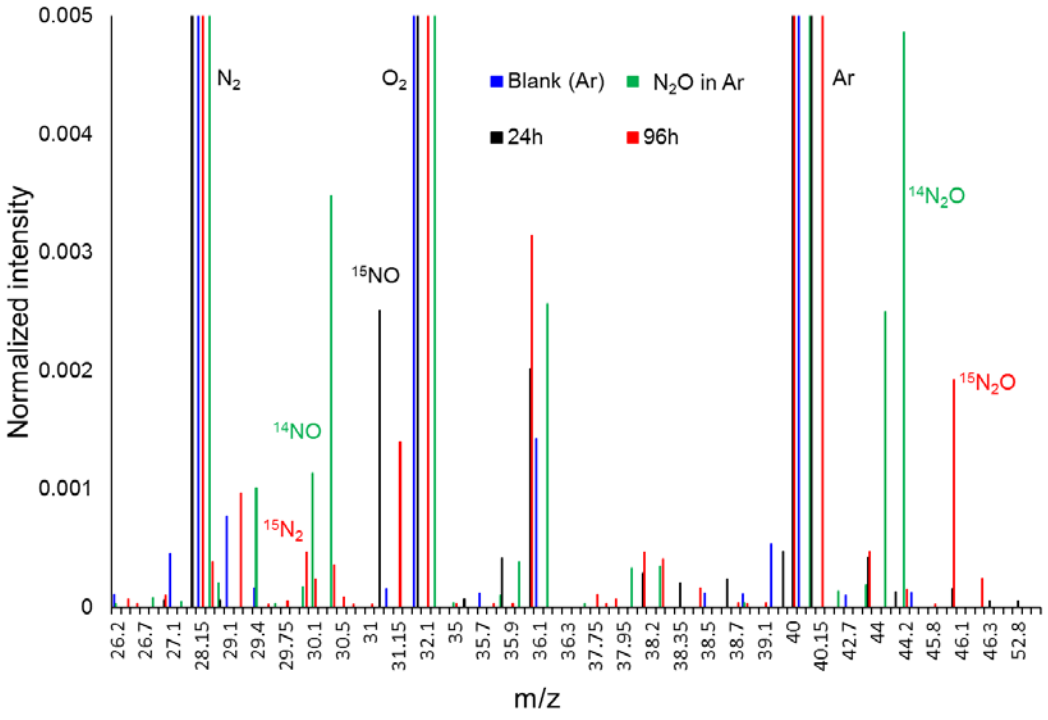

Figure 15. Comparison of GC-MS data for reaction of ^{15}N-labeled complex **23** with pyridinium triflate at various timepoints (24 and 96 h), neat Ar, and $^{14}N_2O$ in Ar.. Labels represent assignment of m/z peaks. Note: peak at m/z=30 (^{14}NO) in authentic $^{14}N_2O$ sample due to fragmentation of N_2O under mass spectrometry conditions.

Given the presence of four Cu^{I} centers in **23**, it was also hypothesized that further *in situ* reduction of N_2O (to N_2) produced upon treatment with H^+ may be possible. Notably, N_2O reduction to N_2 is performed in Nature by the nitrous oxide reductase enzyme at a unique $[Cu_4S_2]$ active site, although the exact mechanism for this transformation is under debate.[64,65]

Scheme 7. Reactivity of Complex **23** with H^+.

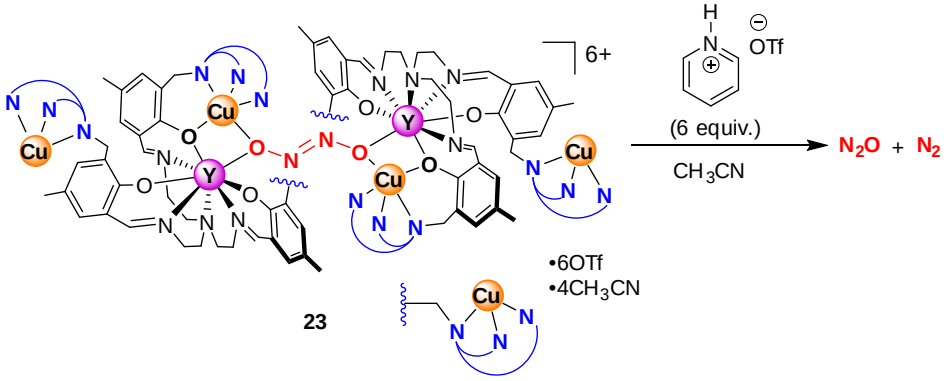

To explore the possibility of N_2 formation, the reaction of ^{15}N-labeled **23** with pyridinium triflate under an Ar atmosphere was monitored via headspace sampling and analysis by gas chromatography mass-spectrometery (GC-MS). Beginning at 48 hours, a peak at m/z=30 was observed that was absent in blank experiments as well as at earlier reaction timepoints. A peak at m/z=46 for $^{15}N_2O$ was also observed (Figure 15). This result suggested that $[Cu^{I}_3]$ complex **4-Y** could engage in nitric oxide reductase as well as nitrous oxide reductase activity, performing the overall four-electron reduction of two NO molecules to N_2 (Scheme 7) Although reduction of mononuclear Fe^{II} nitrosyl complexes by sulfite and bisulfite to generate N_2O and N_2 has been reported,[66] and heterogeneous catalysts for reduction of NO (including to N_2) have also been extensively studied,[9] the present study is the first example of the two-step reduction of NO to N_2 by a discrete multimetallic complex without the need for an external reductant.

CONCLUSIONS

Reduction of nitric oxide has been the focus of much attention due to the importance of this small molecule in biological systems and its relevance to environmental chemistry. To gain insight into the mechanism of NO reduction by model complexes containing biologically relevant metals, the reactivity with NO of the previously reported [YCu_3] complex **4-Y**, designed as a model of multicopper active sites involved in O_2 reduction, was studied. Whereas O_2 activation by **4-Y** proceeded via cooperative *intra*molecular activation by the three Cu centers, *inter*molecular activation of NO was observed. Reductive coupling of two NO molecules by two equivalents of **4-Y** resulted in formation of a *trans*-hyponitrite complex, **23**, in which each oxygen of the $N_2O_2^{2-}$ ligand was bridging between Y and a Cu center on a different [YCu_3] core. The remaining two Cu centers in each tetrametallic unit did not participate in reactivity. No intermediates in this reaction could be conclusively identified by spectroscopic methods. Reaction of related mononuclear Cu complex **14** with NO did result in intermediate species observed at low temperature via UV-Vis and IR spectroscopies, but the observed final products of these reactions indicated that NO disproportionation to N_2O and NO_2^- had occurred. These observations indicated that Y^{3+} played a key role in **23**, promoting binding of the hyponitrite intermediate without favouring N–O bond cleavage.

Reaction of **23** with an appropriate Brønsted acid led to decomposition of **23** and generation of N_2O gas as observed by IR spectroscopy. This result indicated that hyponitrite complex **23** is an intermediate in the reduction of NO to N_2O by **4-Y**. This is the first report of a Cu complex capable of reductive coupling of NO to generate N_2O for which a hyponitrite intermediate has been structurally characterized. These

results provide further substantiation for the intermediacy of hyponitrite species in reduction of NO to N_2O by biological systems. Furthermore, reduction of N_2O generated *in situ* upon treatment of the hyponitrite complex with acid was also observed, highlighting the ability of tricopper complex **4-Y** to perform both nitric oxide reductase and nitrous oxide reductase activities.

EXPERIMENTAL SECTION

Unless indicated otherwise, reactions performed under inert atmosphere were carried out in oven-dried glassware in a glovebox under a nitrogen atmosphere. Anhydrous tetrahydrofuran (THF) was purchased from Aldrich in 18 L Pure-Pac^{TM} containers. Anhydrous diethyl ether, acetonitrile, and THF were purified by sparging with nitrogen for 15 minutes and then passing under nitrogen pressure through a column of activated A2 alumina (Zapp's). Propionitrile was dried over calcium hydride and vacuum transferred over molecular sieves. CD_3CN was purchased from Cambridge Isotope Laboratories, dried over calcium hydride, degassed by three freeze-pump-thaw cycles, and vacuum-transferred prior to use. ^{1}H NMR spectra were recorded on a Varian 300 MHz instrument, with shifts reported relative to the residual solvent peak. ^{19}F NMR spectra were recorded on a Varian 300 MHz instrument, with shifts reported relative to the internal lock signal. Electrospray ionization mass spectrometry (ESI-MS) was performed in the positive ion mode using an LCQ ion trap mass spectrometer (Thermo) at the California Institute of Technology Mass Spectrometry Facility. The UV-vis spectra were recorded on a Varian Cary Bio 50 spectrophotometer. Low-temperature UV-Vis spectra were obtained using a Varian dip-probe (661.202-UV, 10 mm) and a custom-made glass vessel. The ATR-IR measurements were recorded on a Bruker APLHA ATR-IR spectrometer at 2 cm^{-1} resolution using the OPUS software

package. *In situ* solution IR spectra were recorded on an iC10 ReactIR (Mettler Toledo) equipped with a K4 conduit and a SiComp Sentinel sensor in a custom-made glass vessel. The gas-phase IR measurements were recorded on a Bio-Rad Excalibur Series spectrometer using a custom-made Schlenk cell fitted with KBr windows (pathlength = 10 cm). GC-MS analysis was performed on an Agilent 6890 gas chromatogram equipped with an Agilent 5793 mass-selective detector and an Agilent 19091S-433 column, using a 1.0 mL/min flow (He) and a 50 °C oven temperature. Elemental analyses were performed by Midwest Microlab, LLC. (Indianapolis, IN). Unless indicated otherwise, all commercial chemicals were used as received. Nitric oxide was purchased from Aldrich. ^{15}N-labeled nitric oxide was purchased from Cambridge Isotope Laboratories. Complexes **4-Y** and **14** were prepared according to previously published procedures.[52]

Synthesis of 23.

In a Schlenk tube, a solution of **4-Y** (0.212 g, 1.07 mmol) in EtCN (8 mL) was degassed by three freeze-pump-thaw cycles. The solution was cooled to -78 °C in a dry ice/acetone bath, and nitric oxide (43.5 mL, 54 mmHg, 1.24 mmol, 1.2 equiv) was added to the vessel via a volumetric gas bulb. The golden yellow solution changed to dark yellow-green in ~15 minutes. The solution was stirred at -78 °C for 6 hours, then warmed to room temperature. The solvent was removed *in vacuo*, and the residue was washed with THF and filtered through a pad of Celite. The green-yellow solid was extracted with acetonitrile. Vapor diffusion of diethyl ether into an acetonitrile solution of this product yielded crystalline **23** as green urchins, which were mechanically separated from other precipitates (0.055 g, 27% yield based on [YCu_3]). ^{1}H NMR (CD_3CN, 300 MHz): δ 8.63 (br), 8.42 (br), 7.87 (br overlapped), 7.75 (br overlapped),

7.40 (br), 7.26 (br), 6.88 (br overlapped), 6.72 (br overlapped), 3.6 (br overlapped), 3.35 (br overlapped), 2.09 (br) ppm. ^{19}F NMR (CD_3CN): δ −78.96 ppm. Anal. Calcd. For $C_{144}H_{144}Cu_6F_{18}N_{28}O_{26}S_6Y_2$: C, 45.80; H, 3.84; N, 10.39. Found: C. 46.00; H, 3.91; N, 10.27.

Synthesis of 25b.

In a Schlenk tube, a solution of **14** (0.5585 g, 0.927 mmol) in EtCN (8 mL) was degassed by three freeze-pump-thaw cycles. The solution was cooled to -78 °C in a dry ice/acetone bath, and nitric oxide (234 mL, 362 mmHg, 4.64 mmol, 5 equiv.) was added to the vessel via a volumetric gas bulb. The dark yellow solution changed to green-blue in ~1 hour. The solution was stirred at -78 °C for 6 hours, then warmed to room temperature. The solvent was removed *in vacuo*. The residue was triturated with THF and the green solution (which contained mostly desired product) was filtered through a pad of Celite. The material remaining on the Celite filter was extracted with acetonitrile, and the solvent was removed *in vacuo* to give the nitrite product **25b** as a green-blue powder (0.369 g, 61%). Single-crystals of **25b** suitable for X-ray diffraction studies were obtained via vapor diffusion of diethyl ether into an acetonitrile solution of this material. ^{1}H NMR (CD_3CN, 300 MHz): δ 9.80 (br), 7.95 (br overlapped), 7.49 (br overlapped), 3.58 (br), 1.14 (br) ppm. ^{19}F NMR (CD_3CN): δ −79.08 ppm. Anal. Calcd. For $C_{26}H_{31}CuF_3N_4O_6S$: C, 48.18; H, 4.82; N, 8.64. Found: C. 48.07; H, 4.74; N, 8.42.

Synthesis of 25c.

In a Schlenk vessel, a solution of **4-Y** (0.3024 g, 0.163 mmol) in 1:1 THF/EtCN was cooled to -78 °C. NO was bubbled through the solution via syringe needle for 1 min, during which the solution turned from yellow to dark green/brown. After stirring

at -78 °C for 4 hours, the solution was warmed to room temperature, and precipitation of a brown solid was observed. In the glovebox, the suspension was filtered through Celite, and the brown residue extracted with fresh CH_3CN. The solvent was removed *in vacuo* to give the product as a brown powder (0.241 g, 74%). Single-crystals suitable for X-ray diffraction studies were obtained via vapor diffusion of diethyl ether into an acetonitrile solution of **25c**. ^{1}H NMR (CD_3CN, 300 MHz): δ 10.0 (br overlapped), 9.4 (br overlapped), 3.4 (br) ppm. ^{19}F NMR (CD_3CN): δ −78.80 ppm. Anal. Calcd. For $C_{72}H_{72}Cu_3F_9N_{16}O_{18}S_3Y$: C, 43.32; H, 3.64; N, 11.23. Found: C. 43.29; H, 3.76; N, 11.29.

Protocol for Gas Analysis in Reactions of 23 with Acids.

Gas-phase IR: a Schlenk tube was charged with a solution of **23** in CH_3CN. On a Schlenk line, the solution was frozen in LN_2. Under positive N_2 pressure, fresh CH_3CN was layered on top of the frozen solution via syringe and frozen, after which a CH_3CN solution of pyridinium triflate (6 equiv.) was added and also frozen. The Schlenk tube was sealed, and the solution was thawed and stirred at room temperature for three hours. On a high-vacuum line, N_2 was removed from the solution via three freeze-pump-thaw cycles (the solution was frozen in LN_2 to keep any N_2O produced condensed). The volatiles in the reaction vessel were than vacuum transferred through a trap cooled to -78 °C (to condense CH_3CN) and into a liquid nitrogen-cooled Schlenk flask (to condense N_2O). The flask containing the gaseous products was then connected to an evacuated gas IR cell fitted with two greased joint connections. The gases in the Schlenk flask were allowed to expand into the cell and IR spectra were recorded.

Headspace analysis by GC-MS: in the glovebox, a 10 mL Schlenk flask was charged with a solution of **23** in CH_3CN. On a Schlenk line, the solution was degassed and placed under an argon atmosphere. The solution was frozen in a dry ice/acetone bath.

Under positive Ar pressure, fresh CH_3CN sparged with Ar was layered on top of the frozen solution via syringe and frozen, after which a CH_3CN solution of pyridinium triflate (6 equiv.) sparged with Ar was added via syringe and also frozen. The Schlenk tube was sealed with a rubber septum, and the solution was thawed and stirred at room temperature. To analyze the headspace, a gastight microsyringe purged with Ar was used to extract a headspace sample (~5 μL) and inject it into the GC-MS instrument.

Crystallographic Information

Refinement details

Crystals were mounted on a nylon loop using Paratone oil under a nitrogen stream. Low temperature (100 K) X-ray data were obtained on a Bruker APEXII CCD based diffractometer (Mo sealed X-ray tube, K_α = 0.71073 Å). All diffractometer manipulations, including data collection, integration and scaling were carried out using the Bruker APEXII software.[67] Absorption corrections were applied using SADABS.[68] Space groups were determined on the basis of systematic absences and intensity statistics and the structures were solved by direct methods using XS[69] (incorporated into SHELXTL) and refined by full-matrix least squares on F^2. All non-hydrogen atoms were refined using anisotropic displacement parameters. Hydrogen atoms were placed in idealized positions and refined using a riding model. The structures were refined (weighted least squares refinement on F^2) to convergence.

It should be noted that due to the size of **23**, its crystal included solvent accessible voids, which tended to contain disordered solvent. Although they were satisfactorily modeled, these disordered solvent molecules were largely responsible for the alerts generated by the checkCIF protocol.

Table 6. Crystal and refinement data.

	23	**25a**	**25b**
empirical formula	$C_{162}H_{179}Cu_6F_{18}N_{33}O_{28}S_6Y_2$	$C_{53.7}H_{62}Cu_2F_{8.09}N_{7.3}O_{10.7}S_{2.7}$	$C_{26}H_{31}CuF_3N_4O_6S$
formula wt	4129.79	1348.14	648.15
T (K)	100	100.15	100.0
a, Å	13.8507(13)	32.390(3)	20.569(2)
b, Å	16.8194(17)	9.0239(7)	15.5906(15)
c, Å	21.214(2)	20.1006(15)	18.3755(18)
α, deg	105.556(3)	90	90
β, deg	105.602(3)	90	104.318(3)
γ, deg	94.915(3)	90	90
V, Å^3	4518.7(8)	5875.1(8)	5709.7(10)
Z	1	4	8
cryst syst	triclinic	orthorhombic	monoclinic
space group	P-1	$Pna2_1$	C2/c
ρ_{calcd}, g/cm^3	1.518	1.524	1.508
2θ range, deg	4.384 to 55.028	4.052 to 57.772	5.226 to 79.504
μ, mm^{-1}	1.490	0.910	0.905
abs corr	Multi-scan	Multi-scan	Multi-scan
GOOF[c]	1.038	1.046	1.032
R1,[a] wR2[b] (I > 2σ(I))	0.0533, 0.1447	0.0537, 0.0997	0.0421, 0.1018

[a] $R1 = \Sigma||F_o|-|F_c|| / \Sigma|F_o|$ [b] $wR2 = [\Sigma[w(F_o^2-F_c^2)^2] / \Sigma[w(F_o^2)^2]]^{1/2}$ [c] $GOOF = S = [\Sigma[w(F_o^2-F_c^2)^2] / (n-p)]^{1/2}$

Special Refinement Details for 23

The structure of **23** displayed disorder in a handful of outer-sphere components. One of the triflate anions was disordered over two positions with ~80:20 occupancy. Due to the considerable size of the complex, large solvent voids existed that required modelling of highly disordered solvent molecules. A diethyl ether molecule was modelled fully (including H atoms) but not refined anisotropically. An acetonitrile molecule residing on a special position was satisfactorily modelled using the EADP and EXYZ commands to account for the disorder of the N atom over two position. H atoms were included but this molecule was also not refined anisotropically.

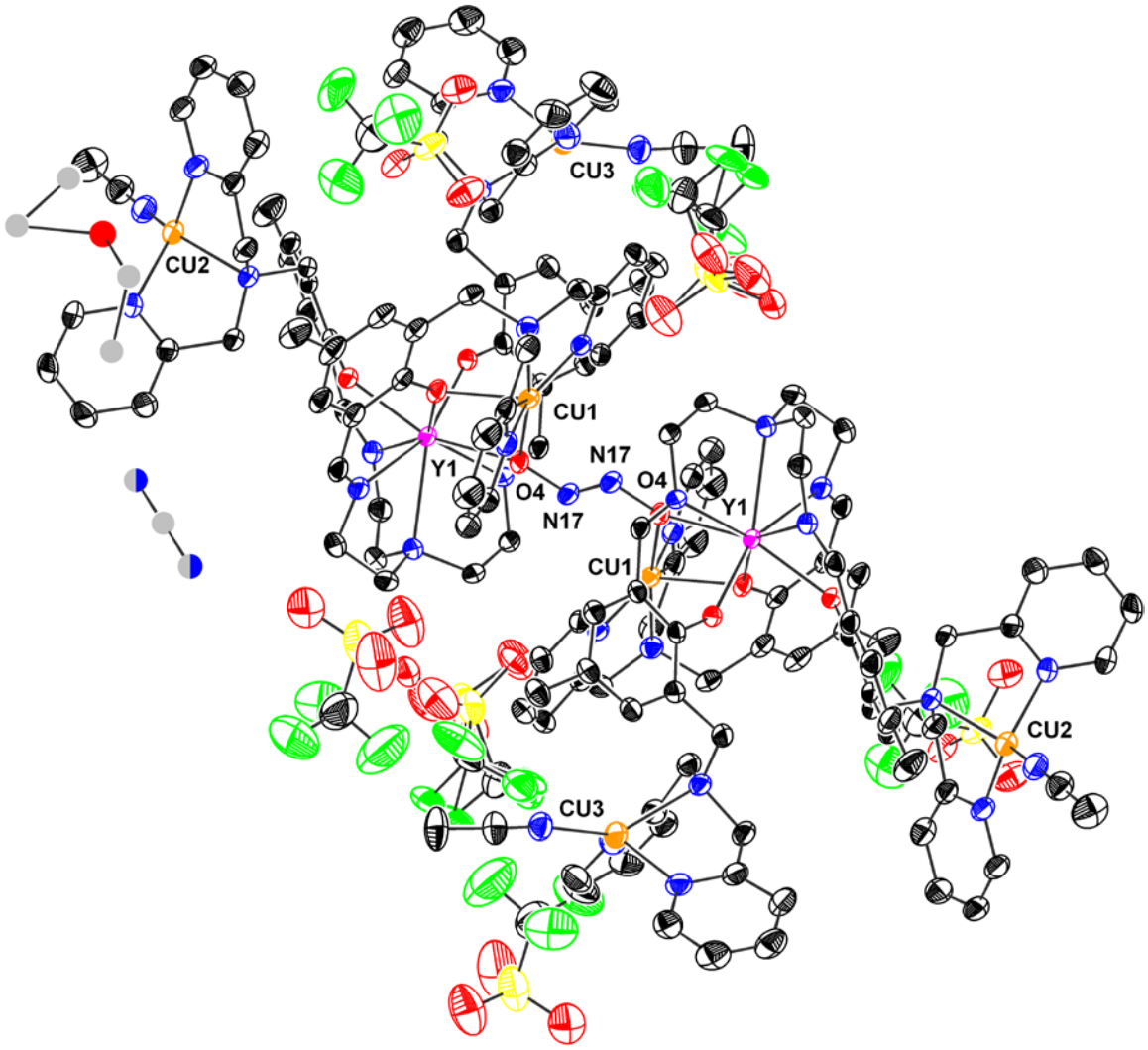

Figure 16. Full solid-state structure of complex **23**. Both components of the disordered outer-sphere triflate moiety are included. Hydrogen atoms omitted for clarity. Thermal ellipsoids shown at the 50% probability level.

Special Refinement Details for 25a

The structure of **25** contained disorder at two positions. The bridging cyanide ligand was disordered over the two possible orientations (C–N vs. N–C); this disorder was satisfactorily modeled to give a ~70:30 population ratio of the two orientations. The other disordered portion of the structure was at the site of one of the Cu(2)-bound

triflate anions, which was partially occupied by another ligand, modeled as a nitrite moiety (NO_2^-). O(6) was shared by both ligands, so its occupancy was refined as 1. The remaining portions of the two ligands (C(52), F(4), F(5), F(6), O(7), and O(8) for triflate, and N(14) and O(14) for nitrite) were placed in separate parts and refined to a total occupancy of 1, resulting in ~70:30 triflate/nitrite populations.

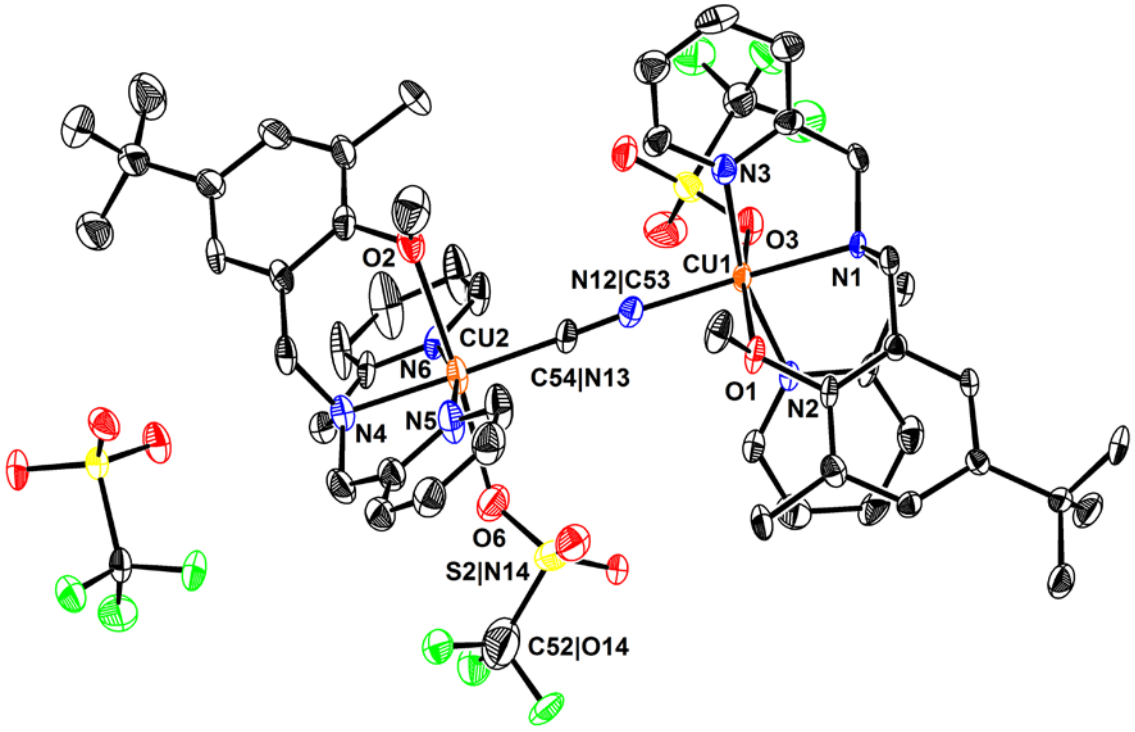

Figure 17. Full solid-state structure of complex **25a**. Hydrogen atoms omitted for clarity. Thermal ellipsoids shown at the 50% probability level.

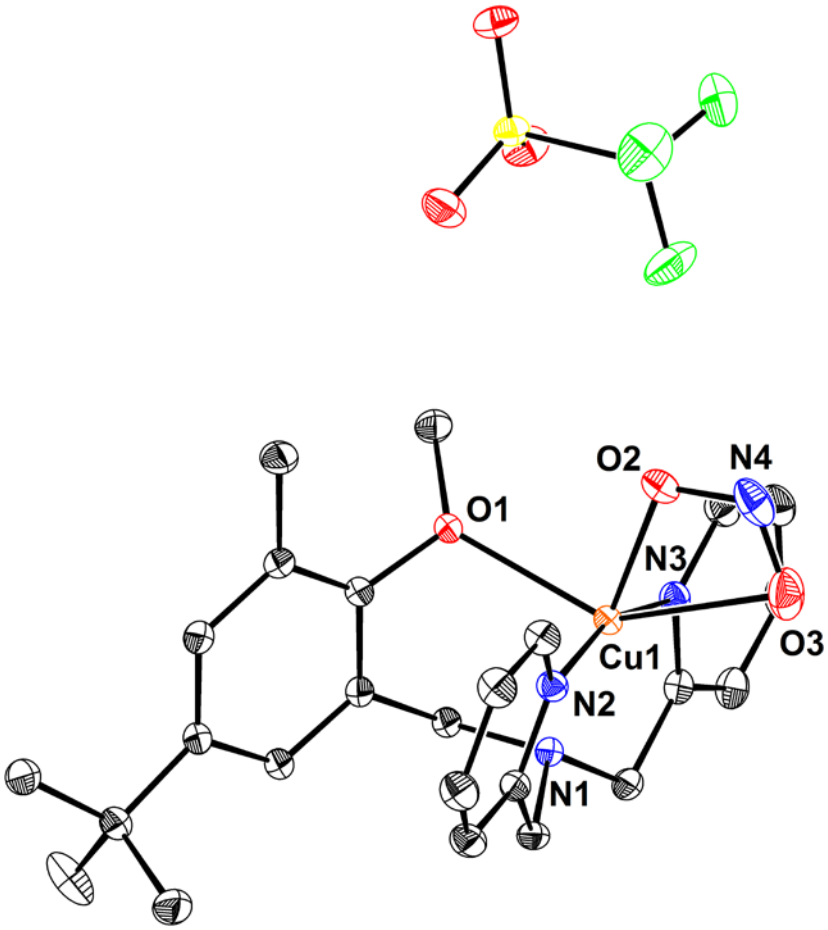

Figure 18. Full solid-state structure of complex **25b**. Hydrogen atoms omitted for clarity. Thermal ellipsoids shown at the 50% probability level.

REFERENCES

(1)Richter-Addo, G. B.; Legzdins, P.; Burstyn, J. *Chem. Rev.* **2002**, *102*, 857.

(2)Wasser, I. M.; de Vries, S.; Moenne-Loccoz, P.; Schroder, I.; Karlin, K. D. *Chem. Rev.* **2002**, *102*, 1201.

(3)Arikawa, Y.; Onishi, M. *Coord. Chem. Rev.* **2012**, *256*, 468.

(4)Wright, A. M.; Hayton, T. W. *Inorg. Chem.* **2015**, DOI: 10.1021/acs.inorgchem.5b00516.

(5)Schopfer, M. P.; Wang, J.; Karlin, K. D. *Inorg. Chem.* **2010**, *49*, 6267.

(6)*Nitric Oxide: Biology and Pathobiology*; Ignarro, L. J., Ed.; Academic Press: San Diego, 2000.

(7)Zumft, W. G. *Microbiol. Mol. Biol. Rev.* **1997**, *61*, 533.

(8)Lelieveld, J.; Crutzen, P. J. *Science* **1994**, *264*, 1759.

(9)Granger, P.; Parvulescu, V. I. *Chem. Rev.* **2011**, *111*, 3155.

(10)Hino, T.; Matsumoto, Y.; Nagano, S.; Sugimoto, H.; Fukumori, Y.; Murata, T.; Iwata, S.; Shiro, Y. *Science* **2010**, *330*, 1666.

(11)Tsukihara, T.; Shimokata, K.; Katayama, Y.; Shimada, H.; Muramoto, K.; Aoyoma, H.; Mochizuki, M.; Shinzawa-Itoh, K.; Yamashita, E.; Yao, M.; Ishimura, Y.; Yoshikawa, S. *Proc. Natl. Acad. Sci. USA* **2003**, *100*, 15304.

(12)Pinakoulaki, E.; Ohta, T.; Soulimane, T.; Kitagawa, T.; Varotsis, C. *J. Am. Chem. Soc.* **2005**, *127*, 15161.

(13)Blomberg, L. M.; Blomberg, M. R. A.; Siegbahn, P. E. M. *BBA Bioenergetics* **2006**, *1757*, 240.

(14)Blomberg, L. M.; Blomberg, M. R. A.; Siegbahn, P. E. M. *BBA Bioenergetics* **2006**, *1757*, 31.

(15)Ohta, T.; Kitagawa, T.; Varotsis, C. *Inorg. Chem.* **2006**, *45*, 3187.

(16)Moenne-Loccoz, P. *Nat. Prod. Rep.* **2007**, *24*, 610.

(17)Varotsis, C.; Ohta, T.; Kitagawa, T.; Soulimane, T.; Pinakoulaki, E. *Angew. Chem. Int. Ed.* **2007**, *46*, 2210.

(18)Pinakoulaki, E.; Varotsis, C. *J. Inorg. Biochem.* **2008**, *102*, 1277.

(19)Berto, T. C.; Xu, N.; Lee, S. R.; McNeil, A. J.; Alp, E. E.; Zhao, J. Y.; Richter-Addo, G. B.; Lehnert, N. *Inorg. Chem.* **2014**, *53*, 6398.

(20)Hayton, T. W.; Legzdins, P.; Sharp, W. B. *Chem. Rev.* **2002**, *102*, 935.

(21)Paul, P. P.; Karlin, K. D. *J. Am. Chem. Soc.* **1991**, *113*, 6331.

(22)Ruggiero, C. E.; Carrier, S. M.; Antholine, W. E.; Whittaker, J. W.; Cramer, C. J.; Tolman, W. B. *J. Am. Chem. Soc.* **1993**, *115*, 11285.

(23)Ruggiero, C. E.; Carrier, S. M.; Tolman, W. B. *Angew. Chem. Int. Ed. Engl.* **1994**, *33*, 895.

(24)Schneider, J. L.; Carrier, S. M.; Ruggiero, C. E.; Young, V. G.; Tolman, W. B. *J. Am. Chem. Soc.* **1998**, *120*, 11408.

(25)Franz, K. J.; Lippard, S. J. *J. Am. Chem. Soc.* **1999**, *121*, 10504.

(26)Kim, E.; Chufan, E. E.; Kamaraj, K.; Karlin, K. D. *Chem. Rev.* **2004**, *104*, 1077.

(27)Collman, J. P.; Dey, A.; Yang, Y.; Decreau, R. A.; Ohta, T.; Solomon, E. I. *J. Am. Chem. Soc.* **2008**, *130*, 16498.

(28)Collman, J. P.; Yang, Y.; Dey, A.; Decreau, R. A.; Ghosh, S.; Ohta, T.; Solomon, E. I. *Proc. Natl. Acad. Sci. USA* **2008**, *105*, 15660.

(29)Wang, J.; Schopfer, M. P.; Sarjeant, A. A. N.; Karlin, K. D. *J. Am. Chem. Soc.* **2009**, *131*, 450.

(30)Wang, J.; Schopfer, M. P.; Pulu, S. C.; Sarjeant, A. A. N.; Karlin, K. D. *Inorg. Chem.* **2010**, *49*, 1404.

(31)Zheng, S.; Berto, T. C.; Dahl, E. W.; Hoffman, M. B.; Speelman, A. L.; Lehnert, N. *J. Am. Chem. Soc.* **2013**, *135*, 4902.

(32)Jiang, Y. B.; Hayashi, T.; Matsumura, H.; Do, L. H.; Majumdar, A.; Lippard, S. J.; Moenne-Loccoz, P. *J. Am. Chem. Soc.* **2014**, *136*, 12524.

(33)Fujisawa, K.; Tateda, A.; Miyashita, Y.; Okamoto, K.; Paulat, F.; Praneeth, V. K. K.; Merkle, A.; Lehnert, N. *J. Am. Chem. Soc.* **2008**, *130*, 1205.

(34)Berto, T. C.; Hoffman, M. B.; Murata, Y.; Landenberger, K. B.; Alp, E. E.; Zhao, J. Y.; Lehnert, N. *J. Am. Chem. Soc.* **2011**, *133*, 16714.

(35)Berto, T. C.; Speelman, A. L.; Zheng, S.; Lehnert, N. *Coord. Chem. Rev.* **2013**, *257*, 244.

(36)Speelman, A. L.; Lehnert, N. *Angew. Chem. Int. Ed.* **2013**, *52*, 12283.

(37)Franz, K. J.; Lippard, S. J. *J. Am. Chem. Soc.* **1998**, *120*, 9034.

(38)Arikawa, Y.; Asayama, T.; Moriguchi, Y.; Agari, S.; Onishi, M. *J. Am. Chem. Soc.* **2007**, *129*, 14160.

(39)Wright, A. M.; Wu, G.; Hayton, T. W. *J. Am. Chem. Soc.* **2012**, *134*, 9930.

(40)Wright, A. M.; Zaman, H. T.; Wu, G.; Hayton, T. W. *Inorg. Chem.* **2014**, *53*, 3108.

(41)Suzuki, T.; Hiromasa, T.; Shiota, Y.; Sajith, P. K.; Arikawa, Y.; Yoshikawa, S. *Inorg. Chem.* **2015**, DOI: 10.1021/acs.inorgchem.5b00394.

(42)Cenini, S.; Lamonica, G.; Robinson, S. D. *Inorg. Chim. Acta* **1972**, *6*, 182.

(43)Bhaduri, S.; Johnson, B. F. G.; Pickard, A.; Raithby, P. R.; Sheldrick, G. M.; Zuccaro, C. I. *J. Chem. Soc. Chem. Comm.* **1977**, 354.

(44)Bottcher, H. C.; Graf, M.; Mereiter, K.; Kirchner, K. *Organometallics* **2004**, *23*, 1269.

(45)Mayer, T.; Bottcher, H. C. *Z. Anorg. Allg. Chem.* **2012**, *638*, 1071.

(46)Mayer, T.; Mayer, P.; Bottcher, H. C. *J. Organomet. Chem.* **2012**, *700*, 41.

(47)Bottcher, H. C.; Wagner, C.; Kirchner, K. *Inorg. Chem.* **2004**, *43*, 6294.

(48)Evans, W. J.; Fang, M.; Bates, J. E.; Furche, F.; Ziller, J. W.; Kiesz, M. D.; Zink, J. I. *Nat. Chem.* **2010**, *2*, 644.

(49)Wright, A. M.; Wu, G.; Hayton, T. W. *Inorg. Chem.* **2011**, *50*, 11746.

(50)Wright, A. M.; Zaman, H. T.; Wu, G.; Hayton, T. W. *Inorg. Chem.* **2013**, *52*, 3207.

(51)Xu, N.; Campbell, A. L. O.; Powell, D. R.; Khandogin, J.; Richter-Addo, G. B. *J. Am. Chem. Soc.* **2009**, *131*, 2460.

(52)Lionetti, D.; Day, M. W.; Agapie, T. *Chem. Sci.* **2013**, *4*, 785.

(53)Mahapatra, S.; Halfen, J. A.; Tolman, W. B. *J. Chem. Soc. Chem. Comm.* **1994**, 1625.

(54)Berreau, L. M.; Halfen, J. A.; Young, V. G.; Tolman, W. B. *Inorg. Chim. Acta* **2000**, *297*, 115.

(55)Solomon, E. I.; Heppner, D. E.; Johnston, E. M.; Ginsbach, J. W.; Cirera, J.; Qayyum, M.; Kieber-Emmons, M. T.; Kjaergaard, C. H.; Hadt, R. G.; Tian, L. *Chem. Rev.* **2014**, *114*, 3659.

(56)Arulsamy, N.; Bohle, D. S.; Imonigie, J. A.; Sagan, E. S. *Inorg. Chem.* **1999**, *38*, 2716.

(57)Bau, R.; Sabherwal, I. H.; Burg, A. B. *J. Am. Chem. Soc.* **1971**, *93*, 4926.

(58)Yang, L. Z.; Li, Y.; Zhuang, X. M.; Jiang, L.; Chen, J. M.; Luck, R. L.; Lu, T. B. *Chem. Eur. J.* **2009**, *15*, 12399.

(59)Lu, T. B.; Zhuang, X. M.; Li, Y. W.; Chen, S. *J. Am. Chem. Soc.* **2004**, *126*, 4760.

(60)Cui, J. H.; Huang, L. F.; Lu, Z. Z.; Li, Y. Z.; Guo, Z. J.; Zheng, H. G. *CrystEngComm* **2012**, *14*, 2258.

(61)Marlin, D. S.; Olmstead, M. M.; Mascharak, P. K. *Angew. Chem. Int. Ed.* **2001**, *40*, 4752.

(62)Zhu, Y. L.; Qu, L. L.; Zhang, J.; Ge, G. W.; Li, Y. Z.; Du, H. B.; You, X. Z. *Inorg. Chem. Commun.* **2011**, *14*, 1644.

(63)Li, L. L.; Liu, L. L.; Ren, Z. G.; Li, H. X.; Zhang, Y.; Lang, J. P. *CrystEngComm* **2009**, *11*, 2751.

(64)Pomowski, A.; Zumft, W. G.; Kroneck, P. M. H.; Einsle, O. *Nature* **2011**, *477*, 234.

(65)Pauleta, S. R.; Dell'Acqua, S.; Moura, I. *Coord. Chem. Rev.* **2013**, *257*, 332.

(66)Littlejohn, D.; Chang, S. G. *Ind. Eng. Chem. Res.* **1990**, *29*, 10.

(67)*APEX2, Version 2 User Manual, M86-E01078,*; Bruker Analytical X-ray Systems: Madison, WI, June 2006.

(68)Sheldrick, G. M.; University of Göttingen: 2008.

(69)Sheldrick, G. M. *Acta Crystallogr., Sect. A: Found. Crystallogr.* **2008**, *64*, 112.

CHAPTER 4

EFFECTS OF REDOX-INACTIVE METALS ON ELECTRON AND OXYGEN-ATOM TRANSFER PROCESSES IN HETEROMETALLIC TRIIRON CLUSTERS

The text for this chapter was reproduced in part from:

Herbert, D. E.; Lionetti, D.; Rittle, J.; Agapie, T.; *J. Am. Chem. Soc.*, **2013**, *135*, 19075

D. Lionetti, Suseno, S. Tsui, E. Y., Lu, L., Britt, R. D., Carsch, K. M., Kanady, J. S., Goddard, W. A., T. Agapie, *Manuscript in preparation*.

Abstract

The modulation of the reactivity of metal-oxo species by redox-inactive metals has attracted much interest due to the observation of redox-inactive metal effects on electron transfer processes both in Nature (the oxygen evolving complex of Photosystem II) and in heterogeneous catalysis (mixed-metal oxides). Studies of small-molecule models of these and other systems have revealed numerous instances of effects of redox-inactive metals on electron and group transfer reactivity in synthetic complexes. A series of tetranuclear oxo/hydroxo clusters comprised of three Fe centers and a redox-inactive metal (M) of varying charge is reported. Crystallographic studies showed an unprecedented $Fe_3M(\mu_4\text{-}O)(\mu_2\text{-}OH)$ core that remains intact upon changing M or the oxidation state of iron. Electrochemical studies revealed that the reduction potentials ($E_{1/2}$) span a window of 500 mV and depend upon the Lewis acidity of M. Investigations of the effects of the Lewis acidic metal on O-atom transfer reactivity of these clusters indicated that in this series of clusters, as in others previously studied in our group, the rate of OAT correlates with the Lewis acidity of the heteroatom. Efforts towards accessing and characterizing related $[Fe_3M(\mu_4\text{-}O)(\mu_2\text{-}O)]$ clusters and analysis of structural and spectroscopic data regarding reassignment of the structures of a previously reported series of $[Mn_3M(\mu_4\text{-}O)(\mu_2\text{-}O)]$ are also discussed.

INTRODUCTION

Lewis-acidic, redox-inactive metal ions are known to influence electron- and group-transfer processes in both natural and synthetic systems.[1-3] In biology, the preeminent example is that of the redox-inactive Ca^{2+} center found in the oxygen evolving complex (OEC) of Photosystem II (PSII), a Mn_4CaO_x cluster responsible for water oxidation to dioxygen in plants, algae, and cyanobacteria. Although its role has not been fully elucidated, Ca^{2+} is an essential cofactor in this system.[4,5] Redox-inactive metals likewise affect the catalytic behavior of heterogeneous mixed-metal oxides in reactions such as water oxidation and dioxygen reduction.[6-8] Alkali and alkali earth metals have also been proposed as components in heterogeneous water oxidation by cobalt and manganese oxides.[8-12]

Reports by Lau and Lee showed that the reactivity of inorganic oxidants (e.g. permanganate, chromate) with organic substrates could be modulated by Lewis acidic additives.[13-19] Collins described the effects of redox-inactive metals on the rate of phosphine oxygenation by a Mn^{V}–oxo complex.[20] In their studies on high-valent Fe- and Mn-oxo species, Nam and Fukuzumi have reported a range of effects of Lewis acidic, redox-inactive metal ions on the oxygen-atom transfer (OAT) and hydrogen-atom transfer (HAT) reactivity of these complexes, including rate enhancement, shifts in reaction mechanism, and the Lewis-acid induced O–O bond cleavage or release of O_2 from a Fe(III)-bound peroxide species.[21-32] Group 2 metal ions were also shown to enhance the rates of dioxygen activation by monometallic Mn^{II} and Fe^{II} complexes.[33,34] Valence tautomerism and effects on OAT and HAT reactions induced by the addition of Zn^{2+} were reported for Mn^{V}–O corrolazine complexes. Reports by Yin have also described the effects of Lewis acids on phosphine and sulfide oxygenation by high-

valent Mn complexes, including under catalytic conditions.[35,36] Despite the elegance of these studies, interpretation of their results with regards to the effects of redox-inactive metals on ET or OAT is challenging due to the lack of structural characterization of the actual Lewis acid-bound species active for these transformations. In most cases, active species are generated *in situ* by addition of large excesses of Lewis acid additives to high-valent metal oxo complexes. Although spectroscopic studies of the interaction of metal-oxo complexes with metal ions in solution have been described, full structural characterization of these species has rarely been reported. The only crystallographically characterized high-valent metal-oxo/redox-inactive metal ion adduct is a [Fe(IV)–O–Sc^{3+}] complex reported by Nam and Fukuzumi;[21] however, the assignment of even this complex as a Fe(IV) species has recently been challenged.[37,38]

Synthetic access to well-defined isostructural multimetallic complexes containing different redox-*inactive* metal ions allows systematic investigation of their effects upon the redox-*active* metallic constituents. Our group has reported a series of heterometallic trimanganese oxo-hydroxo clusters [$Mn_3M(\mu_4\text{-}O)(\mu_2\text{-}OH)$] (M = Na^+, Ca^{2+}, Sr^{2+}, Zn^{2+}, and Y^{3+}, Figure 1) and demonstrated that the reduction potentials of the clusters (Figure 2) are linearly correlated with the Lewis acidity of the redox-inactive metal (these clusters were originally assigned as dioxo complexes, *vide infra*).[39] A similar trend was observed for an even more extensive series of [$Mn^{IV}_3MO_4$] cubane complexes supported by the same multinucleating ligand framework (LH_3, Figure 1), that are structurally related to the $CaMn_3O_4$ cubane subsite of the OEC. These studies suggest a role for the Ca^{2+} center in tuning the reduction potential of the active site in PSII.[40-43] It was of interest to determine if the effects discovered in manganese chemistry extend to other transition metals because of the variety of metal oxides studied as catalysts for

water oxidation and O_2 reduction.[44-47] To expand this type of analysis to complexes of Fe, synthesis of a new series of tetranuclear heterometallic clusters containing three Fe centers was targeted and the effects of the heterometal on the redox chemistry of these compounds were investigated. Structural and spectroscopic data obtained for these Fe_3 clusters provided evidence for the reassignment of related Mn_3 clusters as analogous $[Mn_3MO(OH)]$ species, whereas these complexes had originally been characterized as $[Fe_3MO(O)]$ species. Studies targeting the synthesis and characterization of related $[Fe_3MO(O)]$ clusters were also undertaken to explore the effects on protonation on redox processes in these complexes.

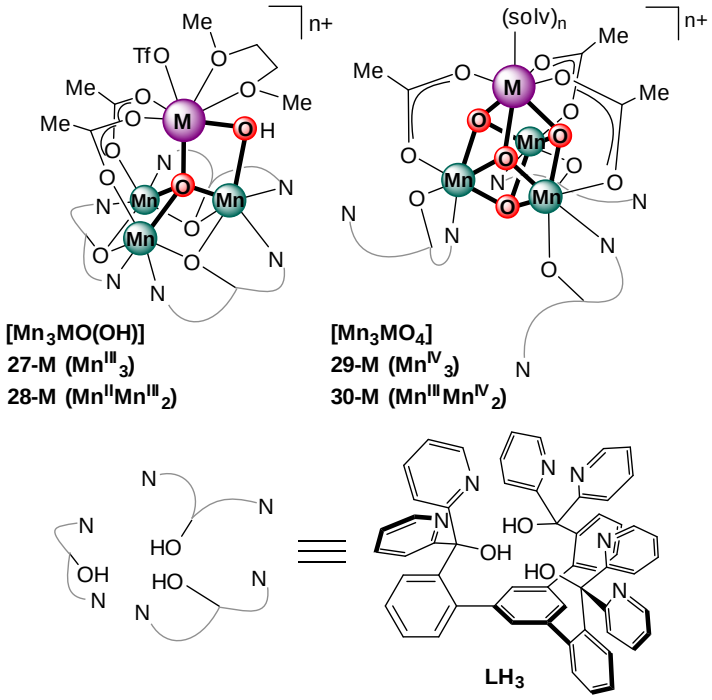

Figure 1. Previously investigated heterotetrametallic clusters and multinucleating triarylbenzene ligand scaffold.

Furthermore, the $[Fe_3MO(OH)]$ clusters were considered well-suited for further exploration of the effects of redox-inactive metals on OAT reactivity. The structurally characterized heterotetrametallic clusters provided well-defined precursors for OAT

reactions, and the availability of structurally analogous complexes containing different redox-inactive metals allowed for direct comparison of the effects of different Lewis acids. The effects of the heterometal on the OAT reactivity of [$Fe_3MO(OH)$] clusters was explored and compared with that of [Mn_3MO_n] complexes.

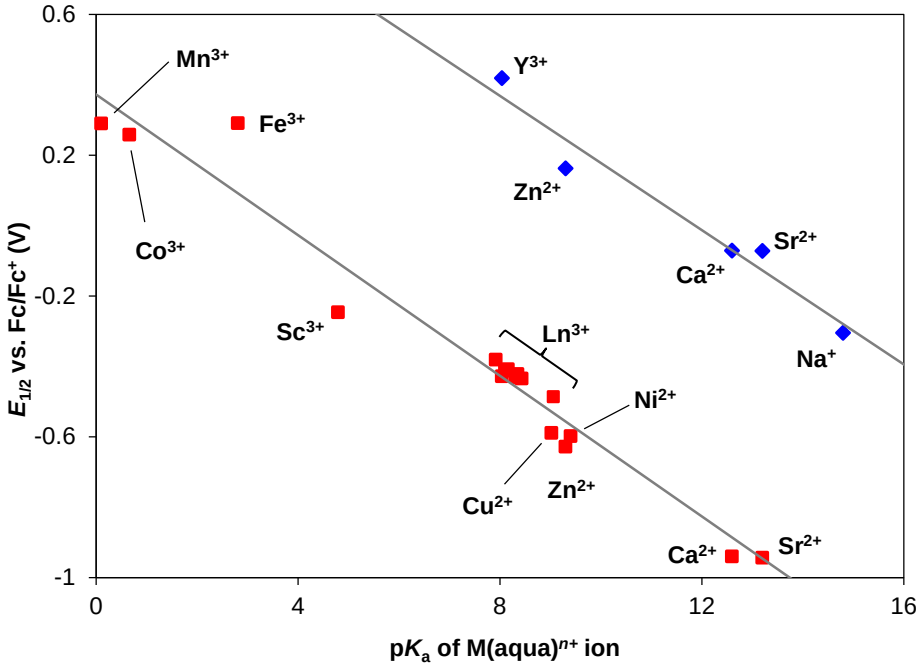

Figure 2. Lewis acid effects on redox potential of [Mn_3MO_4] (red squares) and [$Mn_3MO(OH)$] clusters (blue diamonds).

RESULTS AND DISCUSSION

Synthesis of [Fe$_3$M(O)(OH)] Complexes and Redox-Inactive Metal Effects On Redox Potential.

Scheme 1. Synthesis of Heterometallic Fe$_3$ Oxo-Hydroxo Clusters.

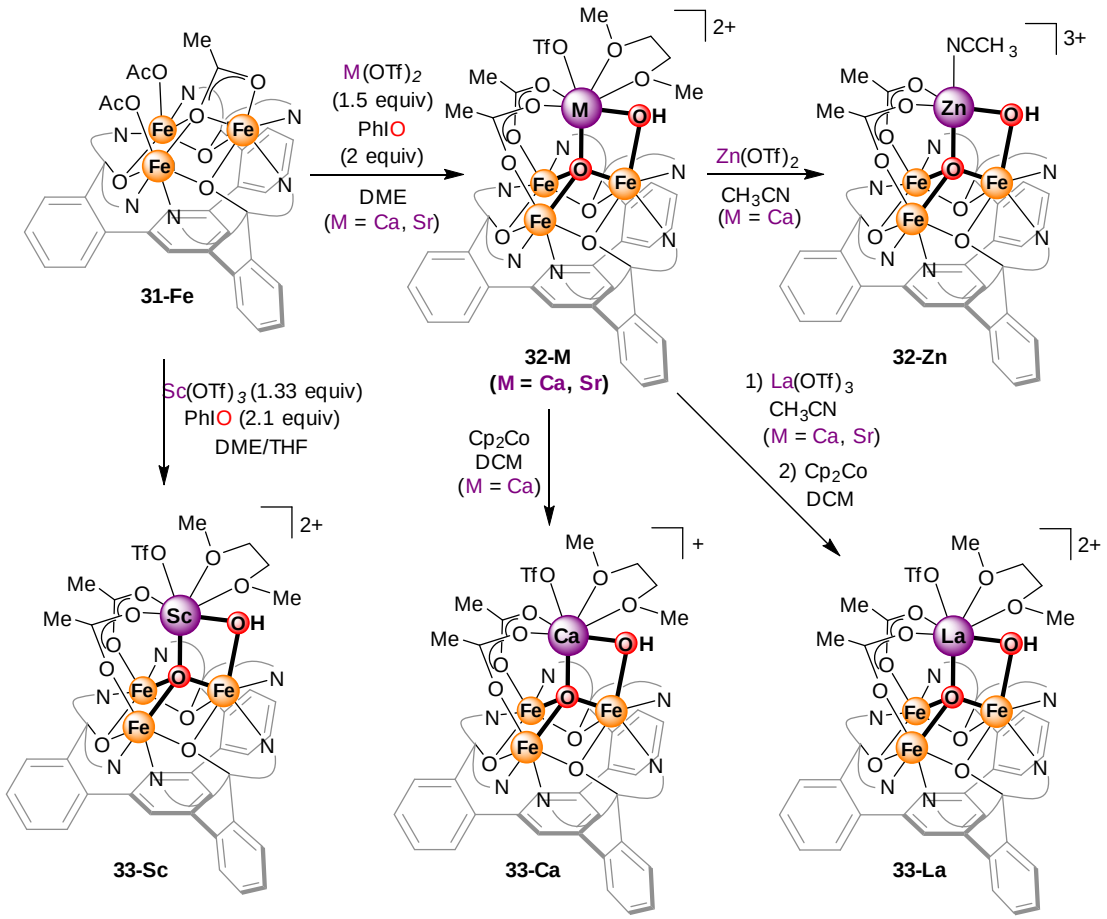

To target Fe$_3$ clusters analogous to the previously reported Mn$_3$ species, synthetic protocols similar to those developed for Mn were followed using as precursor the all-ferrous complex **31-Fe**, supported by the same multidentate architecture as used for complexes **27-**/**30-M** (Scheme 1).[48,49] Treatment of a 1,2-dimethoxyethane (DME) suspension of **31-Fe** and M(OTf)$_2$ (M = Ca^{2+}, Sr^{2+}; $^{-}$OTf = trifluoromethanesulfonate) with iodosobenzene (PhIO), afforded a new species as observed by proton nuclear magnetic resonance (^{1}H NMR) – although all the complexes described herein were paramagnetic, their broadened and shifted ^{1}H features were used as diagnostic

signatures to monitor reactivity, even if a full assignment of the signals was not made. Single crystal X-ray diffraction (XRD) studies of these products revealed tetranuclear clusters (**32-Ca** and **32-Sr**, Scheme 1). In these complexes, as in **31-Fe**, the three iron centers were bridged by three alkoxide donors from the multidentate ligand, forming a $[Fe_3(OR)_3]$ six-membered, chair cyclohexane-like ring. The pyridine N donors of each dipyridyloxymethyl moiety were coordinated to adjacent metal centers. The apical metal (M) was bridged to the triiron cluster by a μ_4-oxide ligand, to one unique iron center by a μ_2-hydroxide moiety, and to the remaining Fe centers by bridging acetate ligands. The coordination sphere of M was completed by a bidentate DME ligand and a $^-$OTf anion (Figure 3). Two additional $^-$OTf ions remained outer-sphere.

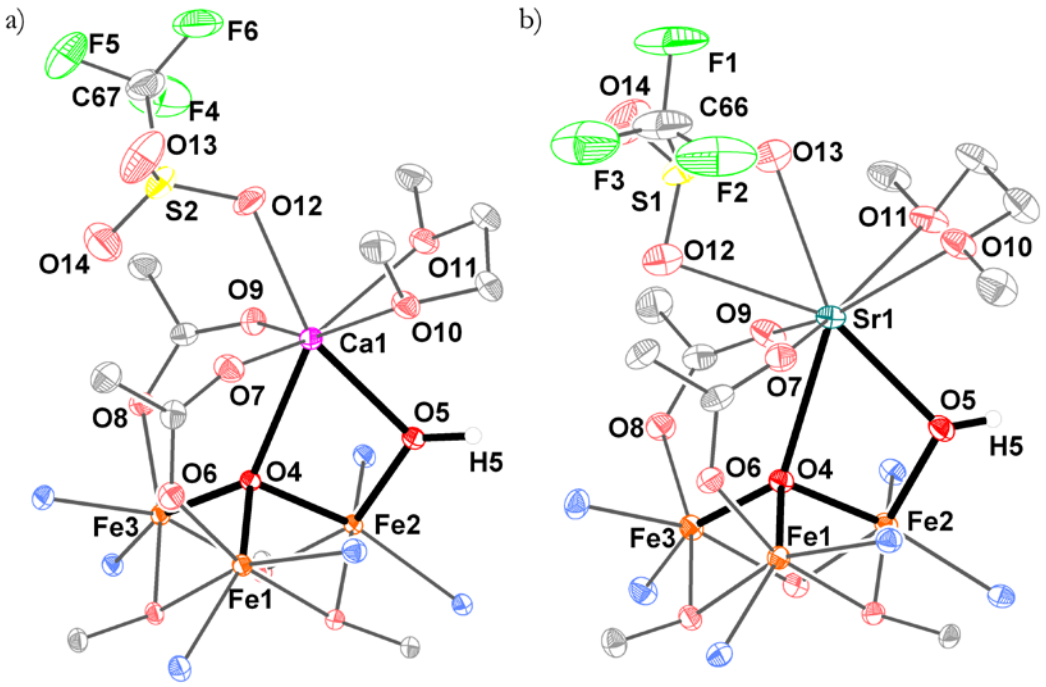

Figure 3. Truncated solid-state structures of (a) **32-Ca** and (b) **32-Sr**. Portions of the multinucleating ligand, hydrogen atoms and outer-sphere anions and solvent molecules are omitted for clarity. Thicker lines emphasize the $[MFe_3O(OH)]$ core.

In order to correctly assign the μ_2-bridging O-based ligand, conclusive information on the oxidation state of the [Fe_3] core was required. The zero-field ^{57}Fe Mössbauer spectra of **32-M** (M = Ca^{2+}, Sr^{2+}) recorded at 80 K displayed features that were best modeled as two quadrupole doublets in a 2:1 ratio, consistent with two distinct ferric sites (Figure 4). Assignment of the trimetallic core as [Fe^{III}_3] indicated that a H^+ was required for charge balance in the XRD structure. The long Fe–(μ_2-O) bond distances (**32-Ca**, 1.884(2); **32-Sr**, 1.900(6) Å) and the observation of a $^-$OTf ligand within H-bonding distance (~2.7 Å) of the μ_2 bridge supported assignment of this ligand as a hydroxide moiety. In comparison, the Fe–O bond distances for a series of μ_2-hydroxide bridges between Fe^{III} and redox-inactive dications (Ca^{2+}, Sr^{2+}, Ba^{2+}) were observed to measure between 1.859(2) and 1.872(2) Å.[34]

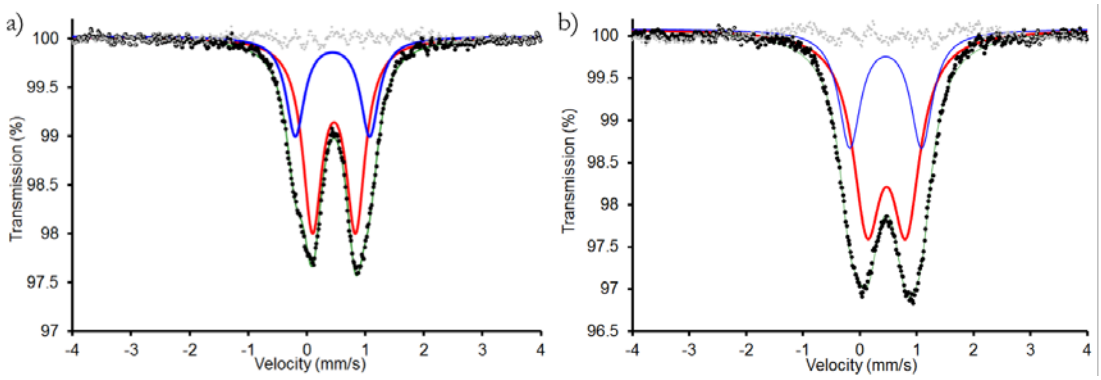

Figure 4. Zero-field ^{57}Fe Mössbauer spectrum for (a) **32-Ca** and (b) **32-Sr** at 80 K. Data: black dots; spectral fit: green line; deconvolution: red and blue lines; residual: grey dots.

The synthetic protocol above was hypothesized to involve the transfer of two O-atoms from PhIO to generate a putative, highly reactive Fe^{IV} intermediate capable of H-atom abstraction (presumably from solvent) to form **32-M**. Under the same reaction conditions, the scandium analog of **32-Ca** and **32-Sr** was isolated, albeit in the reduced [$Fe^{II}Fe^{III}_2$] oxidation state (**33-Sc**, Scheme 1). A single crystal XRD study of **7-Sc**

revealed an [$Fe_3MO(OH)$] core analogous to **32-Ca** and **32-Sr** (Figure 5a) The assignment of the iron oxidation states was based on the absence of a fourth triflate counteranion, as well as on the observation of a disparity in the Fe–(μ_4-O) distances in **33-Sc** – two of which (2.005(3), 1.931(3) Å) were similar to those in **32-Ca**, while the third one was longer (2.211(4) Å), consistent with a more reduced Fe center at one of the two positions *not* connected to the μ_2-(OH). The presence of a ferrous ion was further confirmed by the zero-field ^{57}Fe Mössbauer spectrum, which showed three distinct features best modeled as one ferrous (δ: 1.135 ^{mm}/s) and two ferric (δ: 0.466 ^{mm}/s, 0.477 ^{mm}/s) quadrupole doublets in a 1:1:1 ratio (Figure 6a), in good agreement with literature values for $Fe^{II/III}$ compounds bearing N/O ligands.[50-54] The Fe(2)–O(5)H bond in **33-Sc** is elongated compared to **32-Ca** and **32-Sr**, likely due to a combination of a more reduced [Fe_3] core and a stronger interaction of the bridging moieties with the more Lewis acidic Sc^{3+}.

To allow direct comparison between clusters with different metal composition in the same oxidation state, the one-electron reduced Ca compound was targeted. **33-Ca** was obtained by the chemical reduction of **32-Ca** using one equivalent of cobaltocene ($CoCp_2$; E^O=–1.34 V vs. Fc^+/Fc) in CH_2Cl_2 (Scheme 1). Washing with DME and crystallization from CH_2Cl_2/Et_2O afforded the reduced compound as confirmed by an XRD study (Figure 5b). The observed changes in Fe–O distances in this reduced compound are similar to those of **7-Sc**, with an elongated Fe(2)–O(5)H bond and one longer (>2.2 Å) Fe–μ_4-O distance. The zero-field Mössbauer spectrum revealed features similar to those of **33-Sc** – two quadrupole doublets in a 1:2 ratio, consistent with one ferrous (δ: 1.166 ^{mm}/s) and two ferric sites (δ: 0.475 ^{mm}/s; Figure 6b, Table 1).

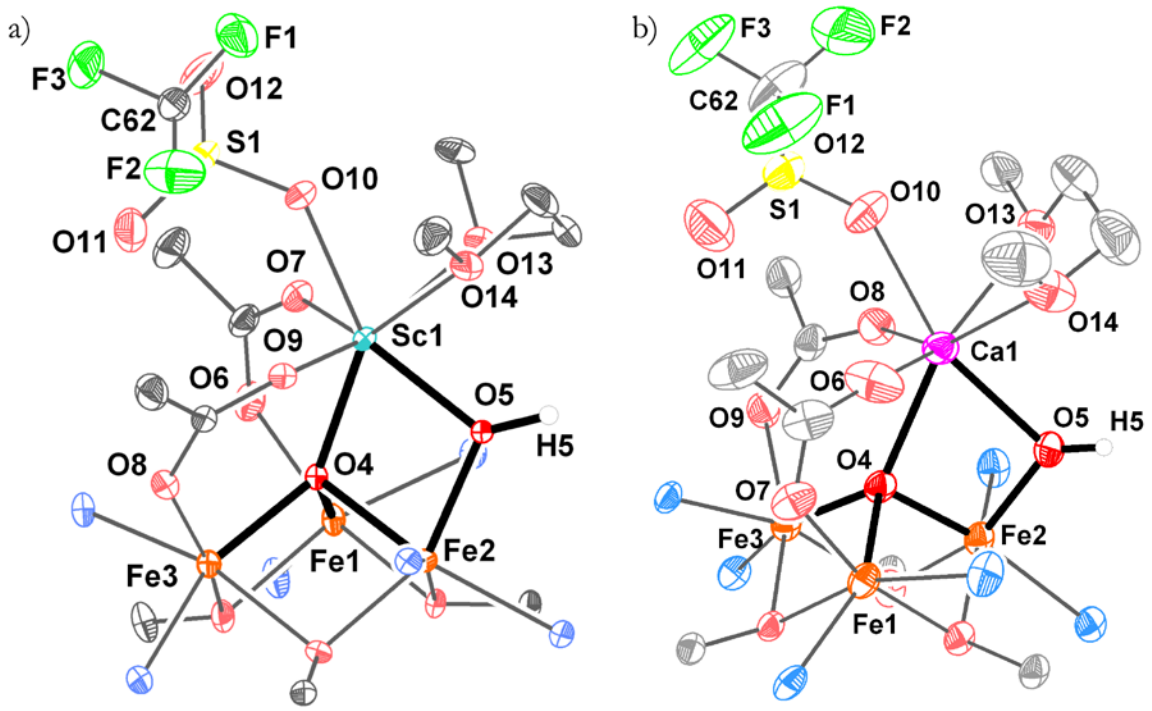

Figure 5. Truncated solid-state structures of (a) **33-Sc** and (b) **33-Ca**. Portions of the multinucleating ligand, hydrogen atoms, and outer-sphere anions and solvent molecules are omitted for clarity.

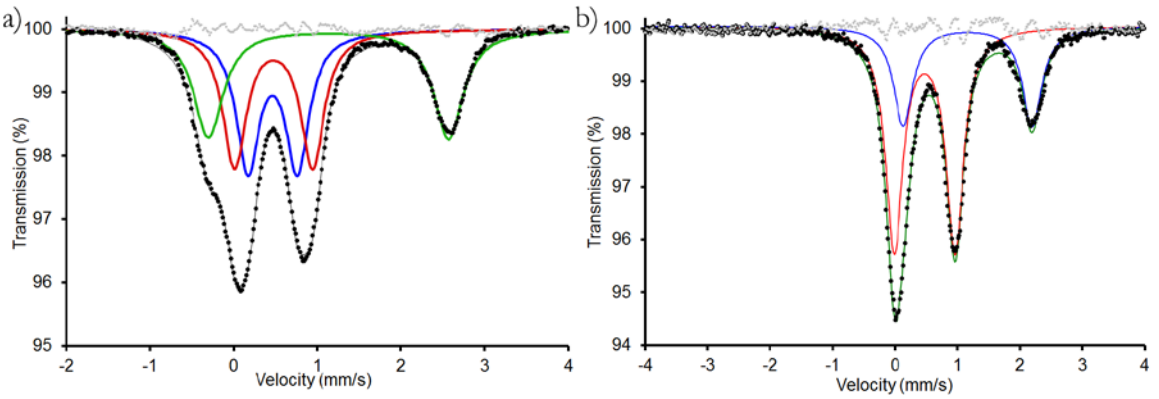

Figure 6. Zero-field ^{57}Fe Mössbauer spectrum for (a) **33-Sc** (data: black dots; spectral fit: black line; deconvolution: red, green, and blue lines; residual: grey dots) and (b) **33-Ca** (data: black dots; spectral fit: green line; deconvolution: red and blue lines; residual: grey dots) at 80 K.

Table 1. Mössbauer spectral properties (isomer shift, quadrupole splitting, linewidth, and relative areas) for compounds **32-M** and **33-M**.

	δ (mm/s)	$\lvert \Delta E_Q \rvert$ (mm/s)	LW	Relative Area (%)
32-Ca	0.465	0.735	0.405	71
	0.439	1.271	0.379	35
33-Ca	0.475	0.973	0.338	71
	1.166	2.067	0.380	35
33-Sc	0.466	0.591	0.336	37
	0.477	0.933	0.338	37
	1.135	2.869	0.429	37
32- Sr	0.470	0.686	0.605	76
	0.454	1.264	0.467	38
32-Zn	0.460	0.551	0.418	71
	0.448	0.934	0.353	36
32-La	0.463	0.663	0.343	70
	0.448	1.063	0.331	35
32-La	0.474	0.761	0.330	75
	1.157	2.830	0.430	37

Complexes containing other redox-inactive metal ions could not be isolated by analogous procedures, possibly due to solubility differences. However, when **32-Ca** was treated with $Zn(OTf)_2$ in CH_3CN (Scheme 1), a new species was obtained by ^1H NMR that was assigned as the Zn cluster **32-Zn**. A single crystal XRD study of **32-Zn** showed that this cluster had retained the $[MFe_3O(OH)]$ structural motif, although the smaller zinc center was five-coordinate and displayed a single acetonitrile solvent ligand in place of DME and ^-OTf (Figure 7a). Similar to **33-Sc**, **32-Zn** showed a longer Fe(2)–O(5) distance [1.925(4) Å] relative to **32-Ca** and **32-Sr** suggesting that the stronger

interaction between μ_2-(OH) and the more Lewis acidic Zn^{2+} resulted in a weaker interaction with Fe. Under the same reaction conditions, addition of $La(OTf)_3$ instead of $Zn(OTf)_2$ resulted in a product with ^{1}H NMR and Mössbauer spectroscopic features similar to **32-Ca**, **32-Sr** and **32-Zn** (Table 1). Structural characterization of this species was unsuccessful. Nonetheless, reduction with one equivalent of $CoCp_2$ in CH_2Cl_2 yielded the one-electron reduced $[Fe^{II}Fe^{III}_2]$ cluster, **33-La**, which was characterized crystallographically (Figure 7b) as well as by ^{1}H NMR and Mössbauer spectroscopies (Figure 8b).

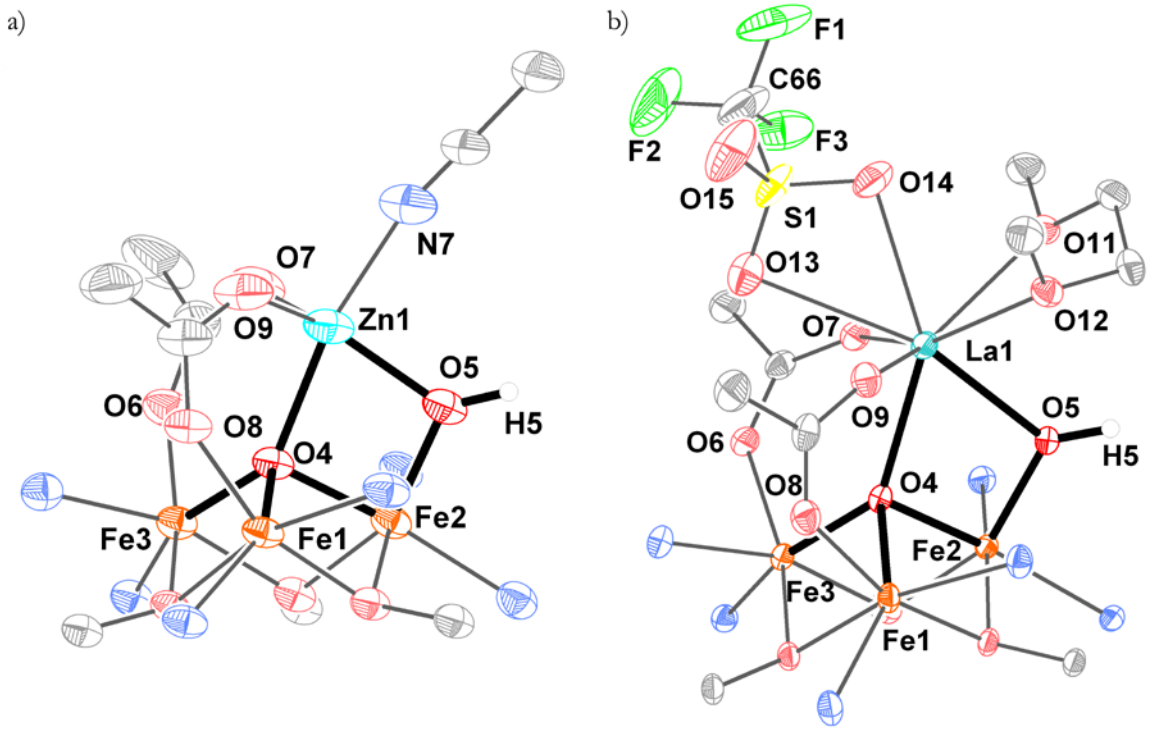

Figure 7. Truncated solid-state structures of (a) **32-Zn** and (b) **33-La**. Portions of the multinucleating ligand, hydrogen atoms, and outer-sphere anions and solvent molecules are omitted for clarity.

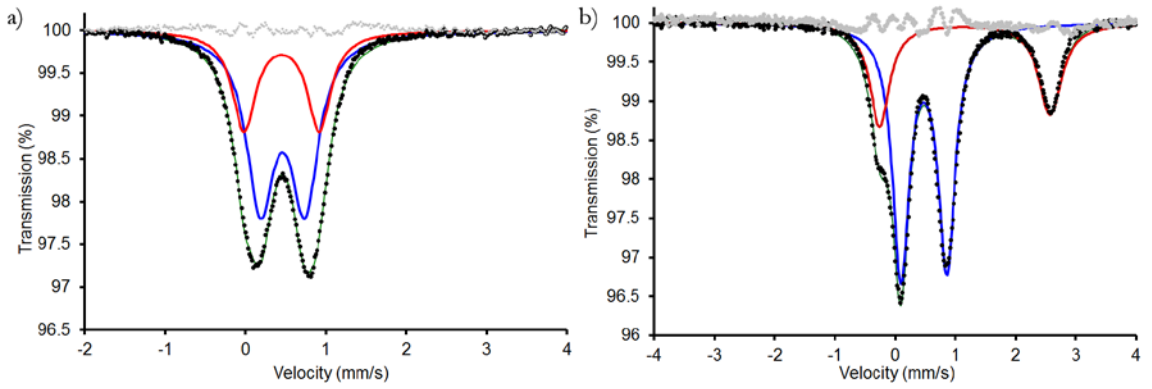

Figure 8. Zero-field ^{57}Fe Mössbauer spectrum for (a) **32-Zn** (data: black dots; spectral fit: green line; deconvolution: red and blue lines; residual: grey dots) and (b) **33-La** (data: black dots; spectral fit: black line; deconvolution: red, green, and blue lines; residual: grey dots) at 80 K.

With these complexes in hand, the effect of the redox-inactive metals on cluster electronics was investigated. Cyclic voltammograms (CV) in CH_2Cl_2/DME (9:1) with 0.1 M $^nBu_4NPF_6$ showed quasireversible redox processes assigned as the $[MFe^{III}_3O(OH)]$ /$[MFe^{III}_2Fe^{II}O(OH)]$ couple at potentials of –0.490 (**32-Ca**), –0.490 (**32-Sr**), –0.210 (**32-Zn**), –0.080 (**33-La**), and +0.070 V (**33-Sc**) vs. the Fc^+/Fc couple (Figure 9). The reduction potentials of **32-Ca** and **32-Sr** are similar ($E_{1/2}$ = –490 mV vs. Fc/Fc^+), but the reduction potential of **32-Zn** is more positive by greater than 300 mV ($E_{1/2}$ = –210 mV), even though Zn^{2+} is also a dicationic redox-inactive metal. Similarly, although both **32-La** and **32-Sc** contain tricationic redox-inactive metals and have the same overall charge, their reduction potentials differ by ca. 150 mV. This variation in redox potential is inconsistent with a purely electrostatic explanation of the differences in redox potentials.[55] The similarity of the redox potentials of the Ca and Sr variants in comparison to those of the other analogs is consistent with the observation that both Sr^{2+} and Ca^{2+} generate catalytically active OEC in PSII (although the activity of the Sr^{2+}-reconstituted active site is lower than that of the native protein).[56]

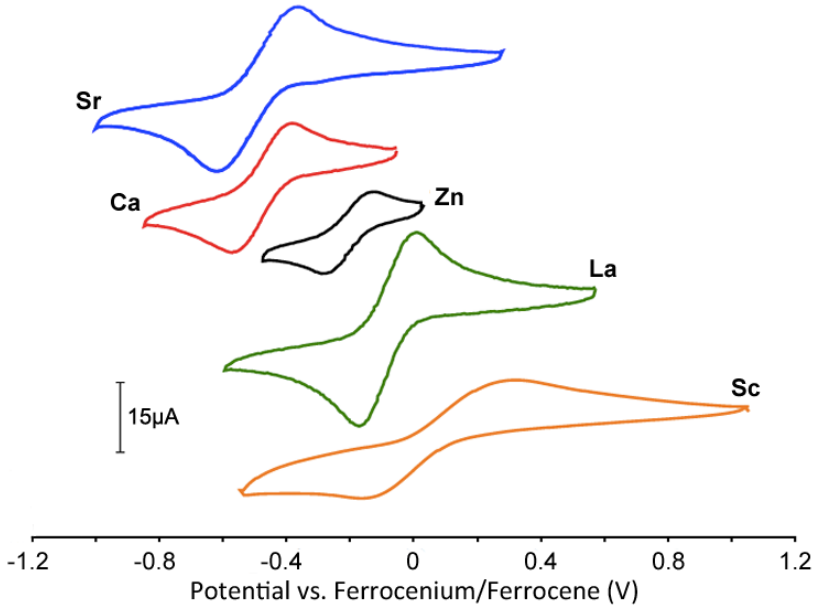

Figure 9. Cyclic voltammograms corresponding to the $[MFe^{III}_3O(OH)]$ /$[MFe^{III}_2Fe^{II}O(OH)]$ redox couple (M = Sc^{3+}, La^{3+}, Zn^{2+}, Ca^{2+}, and Sr^{2+}) in 0.1 M $^nBu_4NPF_6$ in CH_2Cl_2/DME (9:1). Scan rate of 200 mV/s. Potentials are referenced to Fc^+/Fc.

The $E_{1/2}$ values of the $[Fe^{III}_3MO(OH)]$/$[MFe^{III}_2Fe^{II}O(OH)]$ and those of previously prepared $[Mn_3MO(OH)]$ and $[Mn_3MO_4]$ complexes were plotted against the pK_a of the metal aqua ions measured in water,[57] used here as a measure of the Lewis acidity of cation M.[39-41] In all cases, a linear correlation was observed (Figure 10). Hence, the reduction potentials of the clusters could be easily tuned by the Lewis acidity of the incorporated redox inactive metal. The positive shift in reduction potential with increasing Lewis acidity was likely due to the increased electron-withdrawing effect on the bridging oxide/hydroxide ligands, which stabilizes the more reduced iron oxidation state.

The change in slope between the isostructural Fe and Mn $[M'_3MO(OH)]$ clusters (70 vs. 100 mV per pK_a unit, respectively) is notable. The similarity between the two series of compounds points to the difference in the identity of the core metal centers

as the reason for the observed differences in the Lewis acidic effects on cluster redox potential.

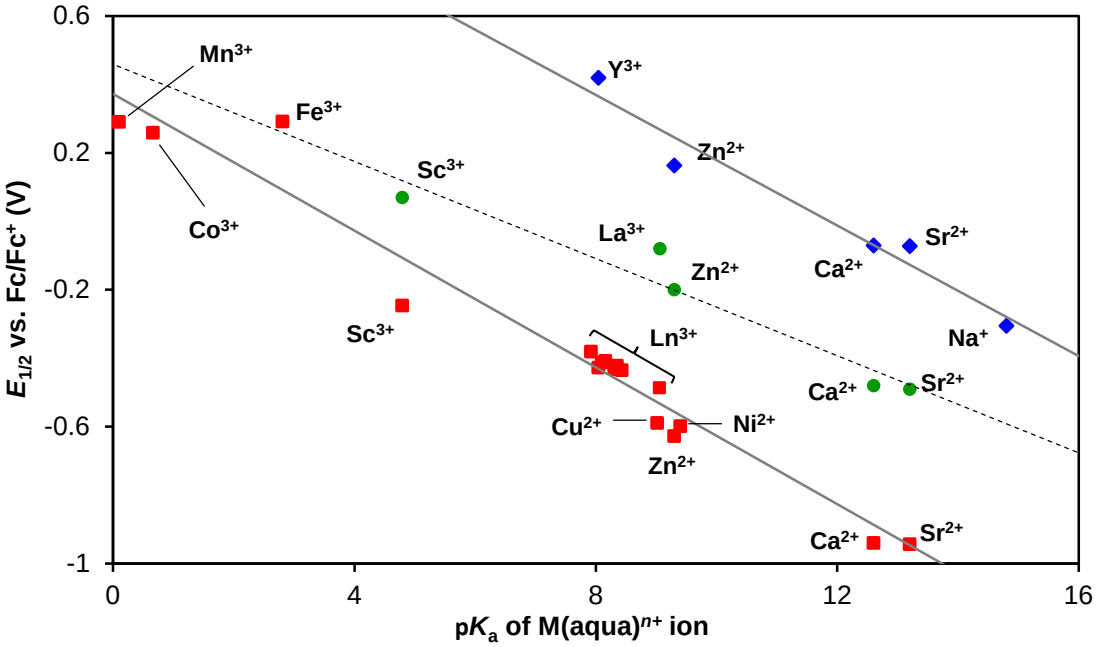

Figure 10. Lewis acid effects on redox potential of [Mn_3MO_4] (red squares), [$Mn_3MO(OH)$] (blue diamonds), and [$Fe_3MO(OH)$] clusters (green circles).

A possible explanation for this trend (previously described in Chapter 1, Section 2.2.6) is the differences in the changes in Lewis acidity between Mn and Fe upon reduction from the M^{III} to the M^{II} oxidation state. The Lewis acidity of Mn decreases considerably more than that of Fe upon one-electron reduction to the M^{II} state.[58] Consequently, interaction of a Lewis acidic ion bridged to these metal centers will strengthen more upon reduction in the case of Mn than for Fe, and as the Lewis acidity of the redox-inactive ion increases, the greater increase in available electron-density in clusters upon reduction of Mn vs. Fe will allow greater stabilization. This, in turn, will result in a larger shift in potential as the Lewis acidity of the redox-inactive metal

increases, as a stronger interaction is possible. Further studies are necessary for determining the feasibility of this hypothesis.

The [Fe^{III}_3MO(OH)] complexes displayed more negative reduction potentials than the corresponding Mn complexes, consistent with the more negative reduction potential of Fe^{III} centers (vs. Mn^{III}). Nonetheless, the similar linear dependences upon Lewis acidity of the various cluster complexes suggest that a general correlation exists between the redox potentials of mixed metal oxides and the Lewis acidity of incorporated redox-inactive metals. Such a relationship may provide a quantitative method for tuning the potentials of both homogeneous and heterogeneous metal oxide electrocatalysts by changing the redox-inactive metal in isostructural compounds. The wide range of reduction potentials found within each series cluster demonstrates that a large change in the thermodynamics of a catalyst can be effected by redox-inactive metal substitution.

Studies of the reactivity of **31-Fe** with O_2 revealed that complexes **32-M** and **33-M** could be observed in the product mixtures when **31-Fe** was exposed to O_2 in the presence of the respective $M(OTf)_n$ salts. Although in most cases the products obtained were quite impure, clean **32-Ca** was isolated from reaction of **31-Fe** and O_2 (1 atm) in the presence of 1.5 equiv. $Ca(OTf)_2$. It was hypothesized that isotopic labeling studies could provide information on the mechanism of this transformation with respect to whether both O atoms incorporated into oxo-hydroxo cluster **32-Ca** originated from the same O_2 molecule. Use of a 1:1 mixture of $^{16}O_2$ and $^{18}O_2$ and analysis of the product via ESI-MS would lead, in the case of reaction of incorporation of both O atoms from a single O_2 molecule, to the observation of only [$^{16}O(^{16}OH)$] or [$^{18}O(^{18}OH)$] clusters, provided that exchange of these ligands could not occur following the reaction.

Unfortunately, following isolation of ^{18}O-containing **32-Ca** it was discovered that mixing of this material with ^{16}O-containing **32-Ca** obtained from the regular synthetic procedure led to scrambling of the isotopic label and observation of the mixed $^{18}O^{16}O$ cluster by ESI-MS within minutes.

Reassignment of [Mn_3MO_2] Clusters: Mn_3 Oxo-Hydroxo Complexes (with Dr. Sandy Suseno).

The full characterization of a series of Fe_3 oxo-hydroxo clusters, inclusive of oxidation state assignment on the basis of Mössbauer spectroscopy, raised questions on the nature of the structurally related Mn_3 clusters. In the original analysis, these complexes were characterized as [Mn_3MO_2] clusters.[39] In the absence of an easily available technique analogous to Mössbauer spectroscopy for determination of Mn oxidation states, charge balance of the XRD structures led to assignment of the trimetallic cores as [$Mn^{IV}Mn^{III}_2$] or [Mn^{III}_3]. This description was corroborated by results from SQUID magnetometry experiments, which were consistent the respective oxidation state assignments.

As described in the previous section, interpretation of the structural parameters for clusters **32-M** and **33-M** in light of the spectroscopically determined Fe oxidation states revealed several peculiar features that were dependent on oxidation state. Most importantly, it was determined that in clusters in the reduced, [$Fe^{III}_2Fe^{II}$] oxidation state, one Fe–(μ_4-O) distance was longer than the other two (~2.15 vs <2.05 Å). This finding indicated with localized reduced character at a single Fe site (one of the two Fe centers not bound to the μ_2-(OH) ligand). The correlation between longer Fe–(μ_4-O) bond distances and reduced character at a given Fe center has since been found to be quite general for [Fe_3MO] clusters (Appendix A). In light of these findings for Fe_3 complexes, reanalysis of the structural metrics for Mn_3 clusters **27-M** and **28-M** revealed analogous

elongation of a single Mn–(μ_4-O) bond in reduced complexes **28-M**, resulting in a similar arrangement of relative bond lengths in the reduced Mn_3 clusters as in their Fe_3 counterparts (Table 2). This pattern was more consistent with a single reduced Mn center in **28-M** clusters than with the original assignment of three Mn centers in the same (+3) oxidation state. By charge balance of the solid state structures, therefore, clusters **27-M** and **28-M** were assigned as [Mn^{III}_3] and [$Mn^{III}_2Mn^{II}$], respectively, and the μ_2-bridging ligand in these complexes was assigned as $^-$OH as in the Fe_3 clusters **32-M**/**33-M**. Manipulation of the solid-state structures to account for symmetry-related outer-sphere moieties revealed the presence of a H-bonding interaction (~2.7 Å) between the μ_2 ligand and a $^-$OTf moiety in complexes **27-M**. An analogous H-bonding interaction between the μ_2-OH and a DME solvent molecule was observed in complex **28-Ca**.

Density functional theory (DFT) calculations were carried out by Kurtis M. Carsch to further corroborate the structural assignment of complexes **27-M** and **28-M**. Clusters **27-Ca** and **28-Ca** were modeled using Jaguar 8.4[59], both as originally assigned – [$Mn^{III}_2Mn^{IV}CaO_2$] (**27-Ca'**) and [$Mn^{III}_3CaO_2$] (**28-Ca'**), respectively – and according to the new proposed structural assignment – [$Mn^{III}_3CaO(OH)$] (**27-Ca"**) and [$Mn^{II}Mn^{III}_2CaO(OH)$] (**28-Ca"**). Selected bond metrics for the optimized structures as well as the values observed experimentally (XRD) are shown in Table 3. For both oxidized and reduced complexes, modeling of the clusters as the overall more reduced oxo-hydroxo species provided parameters in closer agreement with the experimental values than those calculated for the more oxidized dioxo clusters. In particular, the experimental observation of one longer (> 2.1 Å) Mn–O_1 distance in the reduced cluster **28-Ca** was well modeled by the computed parameters for **28-Ca"** but not by

those of dioxo cluster **28-Ca'**. Furthermore, the Mn_1–O_2 distance, which was expected to be sensitive to the nature of the μ_2-ligand, was calculated to be considerably shorter for clusters containing a μ_2-O^{2-} ligand (1.683 Å and 1.697 Å for **27-Ca'** and **28-Ca'**, respectively) than for hydroxide-bridged clusters (1.830Å and 1.907 Å for **27-Ca"** and **28-Ca"**, respectively). The experimental values (1.842(3) Å and 1.887(3) Å) were in better agreement with the latter set of bond distances, supporting the assignment of **27-Ca** and **28-Ca** as oxo-hydroxo clusters. Additionally, for comparison, the Mn–O bond distance for a [Mn^{III}–(OH)–Ca] complex reported by Borovik and coworkers was 1.829(2) Å.

Table 3. Comparison of Selected Bond Distances (in Å) for Fe_3 and Mn_3 Complexes derived from XRD studies and calculated via DFT methods**.**

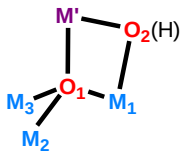

	32-Ca	**33-Ca**	**27-Ca**	**28-Ca**	**27-Ca'**	**27-Ca"**	**28-Ca'**	**28-Ca"**
Method	XRD	XRD	XRD	XRD	DFT	DFT	DFT	DFT
M_3 core	Fe_3	Fe_3	Mn_3	Mn_3	Mn_3	Mn_3	Mn_3	Mn_3
μ_4, μ_2 ligands	O, OH	O, OH	O, OH	O, OH	O, O	O, OH	O, O	O, OH
Mn_1-O_1	2.023(2)	1.928(5)	1.958(3)	1.860(3)	1.972	2.006	2.141	1.894
Mn_2-O_1	1.927(2)	1.904(5)	1.913(3)	2.159(3)	1.889	1.918	1.906	2.195
Mn_3-O_1	1.945(2)	2.140(5)	2.017(3)	1.939(3)	2.054	1.944	1.848	1.907
Mn_1-O_2	1.881(2)	1.923(5)	1.842(3)	1.887(3)	1.683	1.830	1.697	1.907

The new structural assignment for clusters **27-M** and **28-M**, was further supported by electron paramagnetic resonance (EPR) spectroscopy (Luo Lu, R. David Britt; UC Davis). Normal-mode X-band EPR characterization obtained in CH_2Cl_2 glass at

cryogenic temperatures revealed a weak signal for **27-Ca** and **27-Sr** (Figure 11a, c), indicative of integer-spin systems, and stronger signal for **28-Ca** and **28-Sr** (Figure 11b, d), consistent with half-integer spin systems. These observations were inconsistent with the original oxidation state assignment for these clusters: a $[Mn^{III}_2Mn^{IV}]$ complex would be a half-integer spin system (d^4, d^4, d^3), whereas a $[Mn^{III}_3]$ one would be an integer-spin system (d^4, d^4, d^4). The EPR data was however consistent with the newly proposed assignments of **27-M** as $[Mn^{III}_3]$ (an integer-spin system) and of **28-M** as $[Mn^{III}_2Mn^{II}]$ (a half-integer spin system – d^4, d^4, d^5). Studies aimed at observing coupling between the unpaired spins on the metal centers and the $^-$OH proton via electron nuclear double resonance (ENDOR) EPR are currently ongoing.

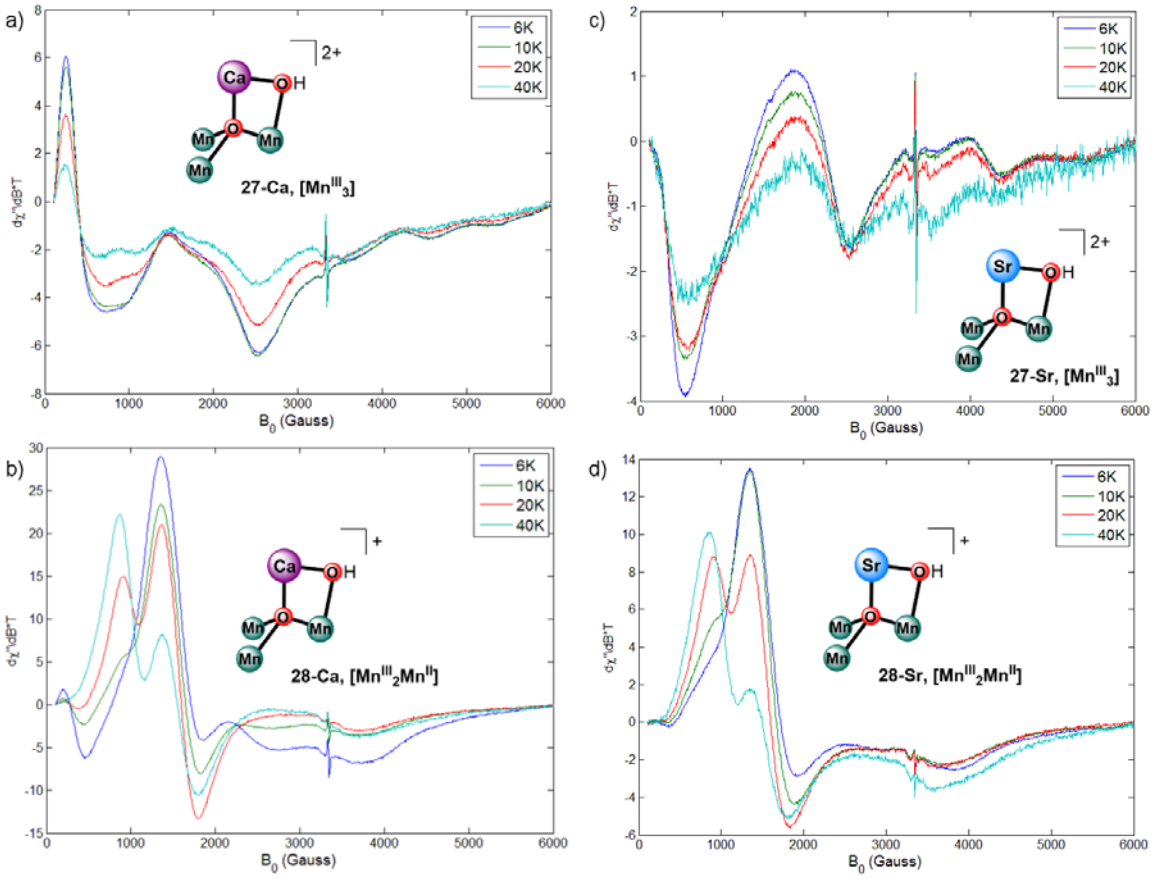

Figure 11. Normal mode EPR spectra of **27-Ca** (a), **28-Ca** (b), **27-Sr** (c), and **28-Sr** (d) obtained in CH_2Cl_2 glass at 6-40K.

It should be noted here that the proposed changes in assignment of the oxidation states and identity of bridging ligands in clusters **27-M** and **28-M** bear no effect on the conclusions of earlier studies on these complexes. All comparisons within this series of complexes remain valid, as changes affect compounds across the entire series. Although efforts to access dioxo clusters synthetically are currently ongoing, reactivity studies were limited to the available oxo-hydroxo complexes.

Targeting [Fe_3MO_2] Clusters

Before the spectroscopic, structural, and computational support for the reassignment of clusters **27-M**/**28-M** was obtained, interest in targeting [Fe_3MO_2] clusters had been driven by a desire to compare the effects of redox-inactive metal cations on OAT reactivity on a series of Fe_3 complexes isostructural with their Mn_3 counterparts. Furthermore, access to dioxo clusters would provide a platform to study the effects of protonation on electron transfer (proton-coupled electron transfer), a key aspect of many enzymatic redox processes.

Two synthetic approaches were envisioned for accessing [Fe_3MO_2] clusters from the previously synthesized [$Fe_3MO(OH)$] complexes: deprotonation of **32-M** or **33-M** clusters and hydrogen-atom transfer (HAT) from **33-M** precursors. Lanthanum complexes **32-La** and **33-La** proved to be the most amenable to these types of conversions. Treatment of **32-La** with 1,8-diazabicyclo[5.4.0]undec-7-ene (DBU, pK_a = 24.34 in acetonitrile) in CH_3CN for 20 minutes resulted in generation of a new species (**34-La**) whose ^{1}H NMR features were typical of [Fe^{III}_3] complexes, which exhibit very broad ^{1}H NMR signatures (Figure 12). The product was precipitated from the reaction mixture with Et_2O to separate it from protonated DBU, which was removed by washing with DME and observed by ^{1}H NMR. Extraction with CH_3CN afforded the

product in ~80% yield. Single crystals of this species suitable for XRD analysis have not been obtained to date, preventing conclusive identification of the product. Mössbauer spectroscopy, nonetheless, confirmed the [Fe^{III}_3] oxidation state assignment suggested by NMR data (Figure 14).

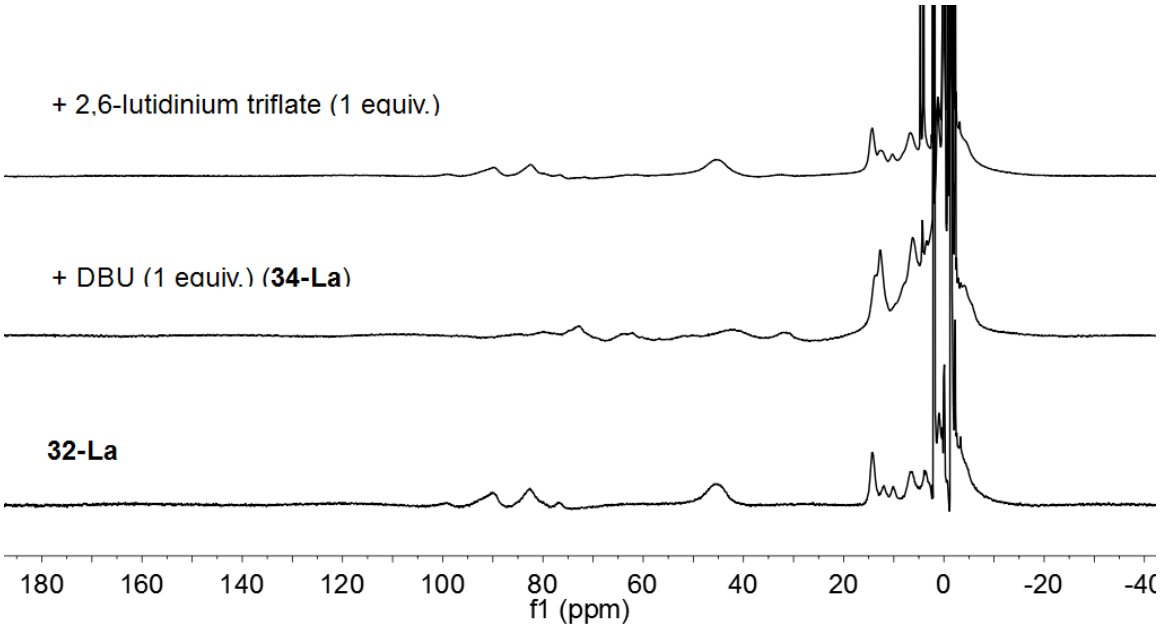

Figure 12. ^{1}H NMR (300 MHz, CD_3CN) of reaction of **32-La** with DBU, followed by reaction with 2,6-lutidinium triflate.

To confirm the identity of **34-La** as the desired [Fe_3LaO_2] complex, its reactivity with various substrates was studied (Scheme 2). **34-La** was found to react with 1 equiv. 2,6-lutidinium triflate to regenerate **32-La** via protonation (Figure 12). Furthermore, treatment with 0.5 equiv. 1,2-diphyenylhydrazine (DPH) led to conversion of this species to the previously characterized cluster **33-La**, concurrent with formation of azobenzene (as observed by ^{1}H NMR), consistent with HAT from DPH to the cluster. The observed reactivity patterns were therefore consistent with assignment of **34-La** as a dioxo cluster, in which the μ_2-(OH) ligand has been deprotonated. To further corroborate this designation, **33-La** was treated with 10 equiv. 2,4,6-tri-*tert*-

butylphenoxyl radical (a stable radical often employed as an H-atom abstractor), resulting in formation of a new species with the same ^{1}H NMR features as those of the product of reaction of **32-La** with DBU. Concomitant formation of 2,4,6-tri-*tert*-butylphenol was observed by ^{1}H NMR.

To access an analogous dioxo cluster containing a different redox-inactive metal, the H-atom transfer protocols were extended to cluster **33-Sc**. Treatment of **33-Sc** with 10 equiv. 2,4,6-tri-*tert*-butylphenoxyl radical resulted in observation of a new species by ^{1}H NMR (Figure 13), with spectral features consistent with a [Fe^{III}_3] complex (formation of 2,4,6-tri-*tert*-butylphenol was also observed). As for **34-La**, no XRD-suitable single-crystals of this species could be obtained, although Mössbauer spectroscopy confirmed the [Fe^{III}] assignment (Figure 14b). Its reactivity with DPH (0.5 equiv) to generate **33-Sc** and azobenzene supported its assignment as dioxo cluster **34-Sc**.

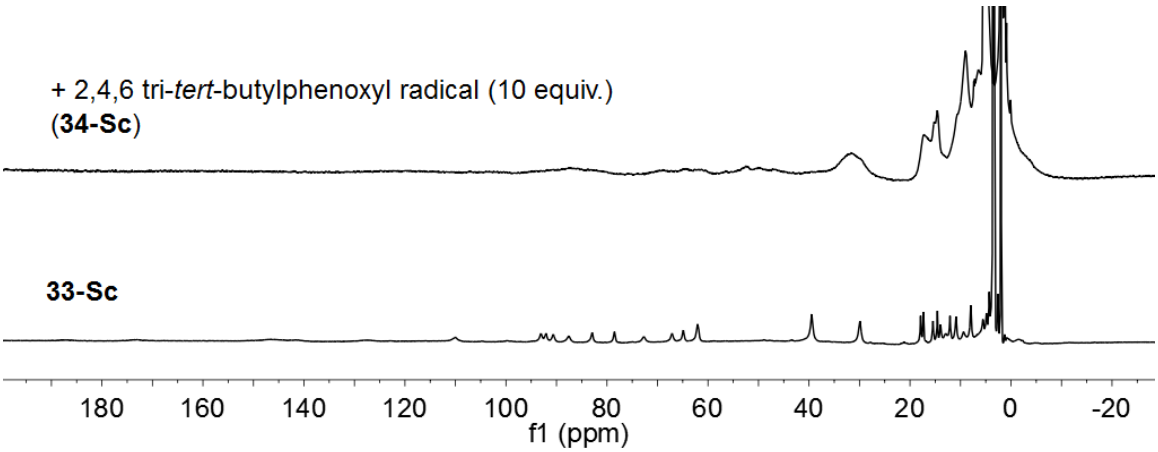

Figure 13. ^{1}H NMR (300 MHz, CD_3CN) of reaction of **33-Sc** with 2,4,6-tri-*tert*-butylphenoxyl radical (10 equiv.).

Given the inaccessibility of the oxidized cluster **32-Sc**, no deprotonation-based synthetic route was available to corroborate the HAT results (attempts to protonate **34-Sc** with 2,6-lutidinium triflate were inconclusive). IR spectroscopic studies aimed at confirming the conversion of **33-M** (M = Sc^{3+}, La^{3+}) to their dioxo analogues **34-M** via

the loss of signal corresponding to the O–H bond stretching vibration were inconclusive. Likewise, investigation into the identity of these clusters via EPR spectroscopy (including ENDOR techniques) has not been successful to date.

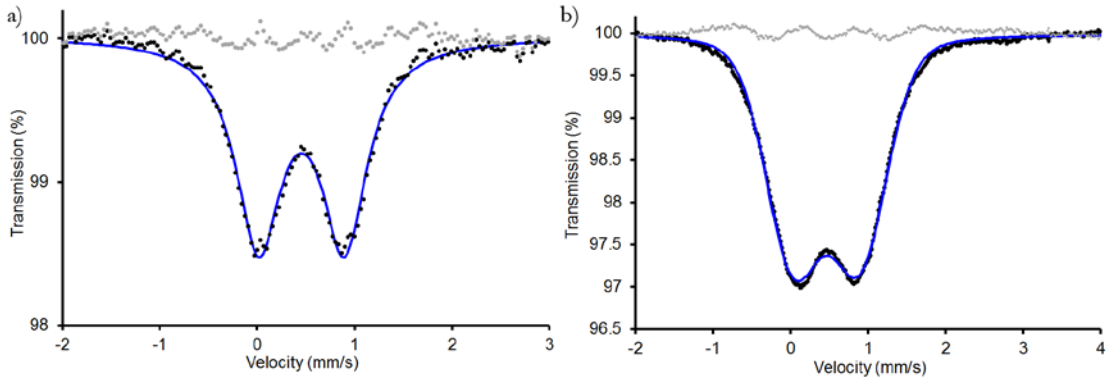

Figure 14. Zero-field ^{57}Fe Mössbauer spectrum for (a) **8-La** and (b) **8-Sc** at 80 K. Data: black dots; spectral fit: blue line.

Finally, the analogous Ca cluster **34-Ca** was targeted. Despite occasional productive reactivity of **33-Ca** with 2,4,6-tri-*tert*-butylphenoxyl radical, however, synthesis of **34-Ca** proved to be extremely hard to reproduce, and efforts to access this cluster were therefore abandoned.

Scheme 2. Reactivity of Complexes **32-M** and **33-M** Targeting Dioxo Clusters **34-M**.

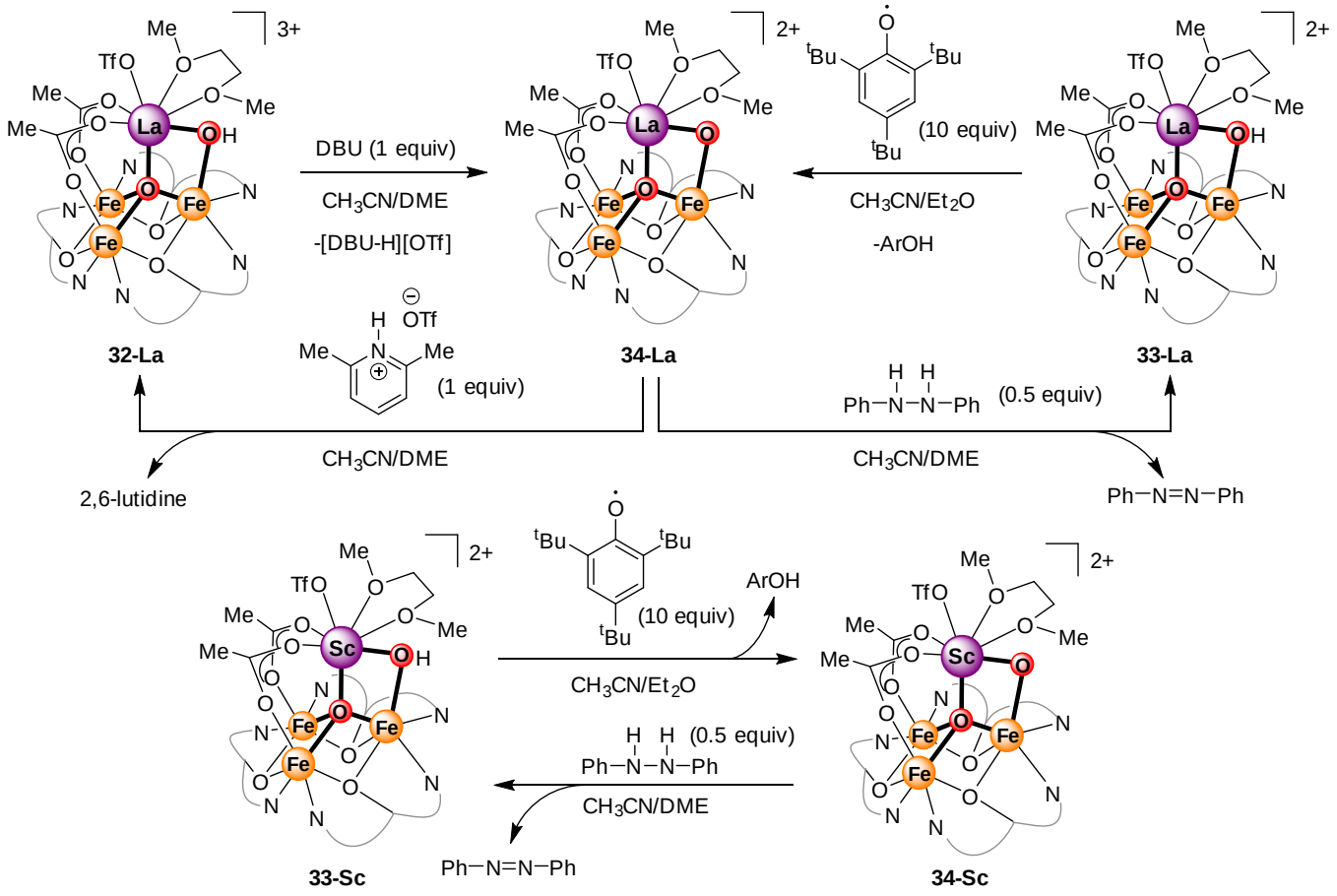

The successful isolation of a complex whose spectroscopic features and reactivity patterns were consistent with its identification as dioxo cluster **34-La**, coupled with the numerous failed attempts to target the analogous **34-Ca** cluster, highlights the delicate balance that must be struck to effect the desired conversion with these complex clusters. Brønsted bases were often too reducing (e.g. benzyl potassium, sodium hexamethyldisilazide, trimethylamine), and electron transfer, rather than deprotonation, was observed for some clusters. Coordination of these bases to clusters (likely via the apical metal) was observed to lead to electron transfer even when the redox potentials between cluster and reductant were not well-matched. As the Lewis acidity of the apical metal increased (from Ca^{2+}, to La^{3+}, to Sc^{3+}), the μ_2-(OH) ligands became more acidic, facilitating deprotonation, but the reduction potential of the clusters also shifted positively, promoting reduction. In the end, the availability of appropriate reagents (in this case, bases of sufficient strength but with positive oxidation potentials and, at least in some cases, larger steric profiles) appeared to dictate the products that could be accessed.

Based on the reactivity data obtained for cluster **33-La**, it was possible to construct a partial thermodynamic square based on Hess' law to outline the interplay between redox potential and pK_a in these clusters, as described by Mayer and coworkers (Scheme 3).[60] Using the known pK_as of DBU and 2,6-lutidine in CH_3CN (24.34 and 14.1, respectively),[61] the redox potential of **32-La** (-0.07 V vs, Fc^+/Fc),[62] and the BDFE of 2,4,6-tri-*tert*-butylphenol (77.1 kcal/mol)[60] approximate values for the pK_a of **32-La** and the bond dissociation free energy (BDFE) of the O–H bond in **33-La** could be obtained. Based on these calculations, the pK_a of **32-La** was determined to be between 14.1 and 17.55, whereas the $BDFE_{O–H}$ of **33-La** was between 72.4 and 77.1 kcal/mol.

These value ranges were consistent with the observed reactivity of **34-La** with DPH ($BDFE_{N–H} \approx 70$ kcal/mol),[60] and **32-La** with DBU ($pK_a = 24.34$). Partial deprotonation of **32-La** by PMe_3 ($pK_a = 15.5$)[63] observed under certain reaction conditions (*vide infra*) was also consistent with these values.

Scheme 3. Thermodynamic Square for [Fe_3La] Oxo-Hydroxo/Dioxo Clusters.

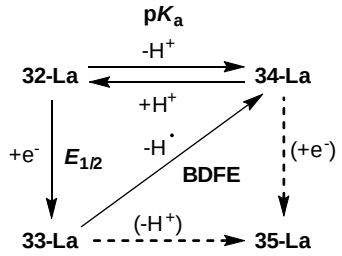

$14.1 < pK_a(\textbf{32-La}) < 17.55$

$72.4 < \textbf{BDFE (33-La)} < 77.1$

To explore the effects of protonation on the electron transfer properties of these multimetallic clusters, electrochemical studies of **34-Sc** were undertaken. Cyclic voltammetry of **34-Sc** showed that the [Fe^{III}_3]/[$Fe^{III}_2Fe^{II}$] couple was shifted negatively from **33-Sc** by ~250 mV to ~-0.17 V vs. Fc^+/Fc (Figure 15). This shift in redox potential upon deprotonation was strikingly smaller than that reported by Borovik and coworkers for a mononuclear [Fe–OH] complex, whose [Fe^{IV}]/[Fe^{III}] couple shifted negatively by >800 mV upon deprotonation. The reason for the reduced influence of the protonation state on the redox potential of cluster **34-Sc** was proposed to arise from the separation between the basic and redox sites. As described above, reduction of **33-Sc** was observed to be localized at a Fe site *not* bound to the μ_2-(OH) ligand. The protonation state of this moiety, therefore, did not affect the ET behavior of the distal redox-active site as intensely as the $O^{2–}/{}^{–}OH$ ligand directly bound to the Fe center engaging directly in ET.

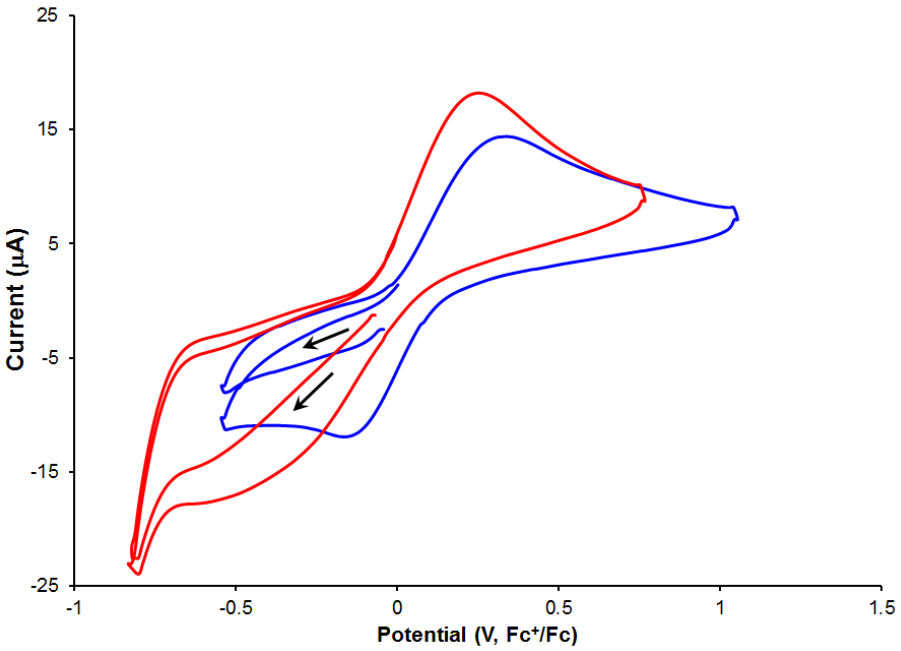

Figure 15. Cyclic voltammograms corresponding to the $[Fe^{III}_3]/[Fe^{III}_2Fe^{II}]$ redox couple for **33-Sc** (blue) and **34-Sc** (red) in 0.1 M $^nBu_4NPF_6$ in CH_2Cl_2/DME (9:1). Scan rate of 200 mV/s. Potentials were referenced to Fc^+/Fc.

OAT Reactivity of Fe_3M Clusters

Previous work by a number of researchers in our group (Dr. Emily Y. Tsui, Dr. Jacob S. Kanady, and Dr. Sandy Suseno) had shown that the Lewis acidity of the apical metal in $[Mn_3MO_n(H)]$ clusters influenced the rate of oxygen atom transfer from the clusters to phosphine substrates. Clusters containing more Lewis acidic metals displayed faster reactivity and were capable of transferring oxygen atom equivalents to less electron-rich phosphines. In the case of cubane clusters **30-M** (M = Sc^{3+}, Mn^{3+}, Gd^{3+}, Co^{3+}) the cluster products of OAT were the corresponding trioxo complexes **36-M**, which corresponded to the transfer of a single O atom. Mn^{3+}, the most Lewis acidic metal in this set, led to the fastest rates of OAT (15 minutes), whereas conversion with Gd^{3+} (the least Lewis acidic in the set) required >2 weeks. Although their oxidation potentials were more positive, oxidized clusters **29-M** generally displayed low OAT

reactivity, likely due to the kinetic barrier to dissociation of carboxylate, necessary for substrate access to the cluster core and calculated to be the first step of the OAT process.[64] The more oxidizing oxo-hydroxo clusters **27-M** and **28-M** exhibited much faster rates of OAT, and could oxidize triaryl phosphines as well as trialkyl variants (Scheme 4). As in the cubane series, these clusters displayed OAT rates that were dependent on the Lewis acidity of the redox-inactive metal they contained, with **27-Y** and **28-Y** leading to faster phosphine oxidation rates than **27-Ca** and **28-Ca**, respectively. The metal-containing products of these reactions could not be structurally characterized, although their extremely broad ^{1}H NMR features were similar to those of trinuclear [Mn^{II}_{3}] complexes that had previously been described. The observation of such species indicated that **27-M**/**28-M** clusters were capable of transferring both their O-atoms.

The well-defined nature of these clusters is a key advantage in studying heterometallic effects on reactivity of these species. Literature examples of the effects of Lewis acidity of metal cations on reactivity rarely provide structural characterization for reactive species (for ET, OAT, or HAT), and the deconvolution of pre-equilibrium processes and direct effects on reactivity can be challenging. The clusters described herein, however, have been unambiguously characterized structurally by solid-state methods, and therefore provide well-defined precursors for the study of the effects of Lewis acidity of redox-inactive metals on redox reactivity.

Scheme 4. OAT Reactivity of Mn_3 Clusters.

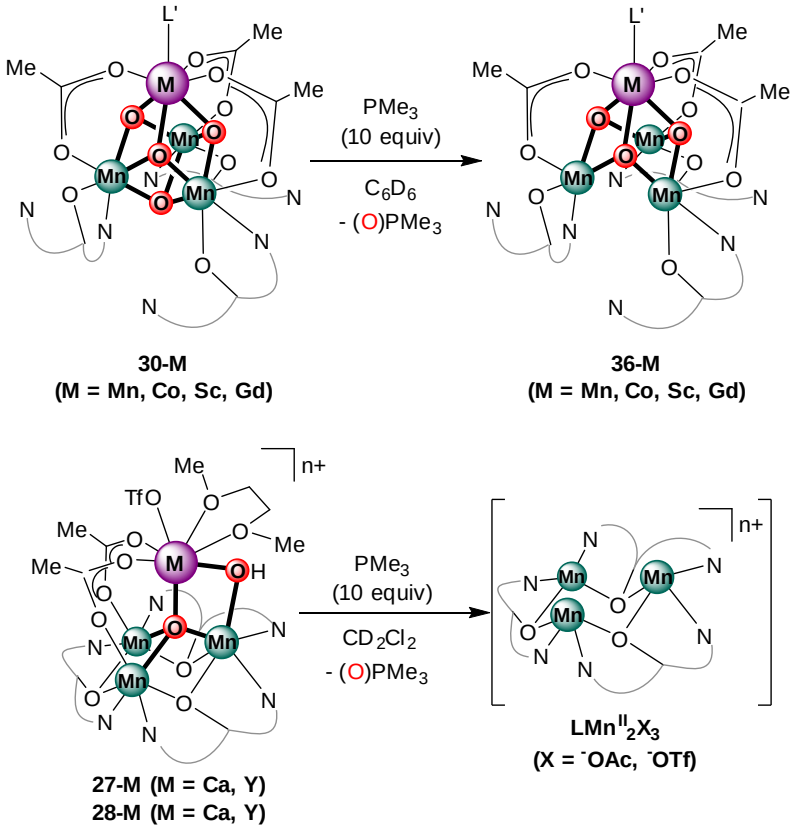

Studies of the OAT reactivity of clusters **32-M** and **33-M** was carried out with phosphine substrates in an analogous manner to those of cubane and oxo-hydroxo [Mn_3] clusters. As alluded to earlier, treatment of cluster **32-La**, containing three Fe^{III} centers, with electron-rich phosphines such as PMe_3, resulted in partial deprotonation. At longer reaction times, evidence for one-electron reduction to **33-La** was also observed, indicating that PMe_3 was not a suitable substrate for this study involving complex **32-La**. Therefore, the OAT behavior of **32-M** clusters was studied with the more electron-poor substrate triphenylphosphine (PPh_3, Scheme 5). **32-Ca** displayed very low conversion in the presence of PPh_3 (10 equiv, Figure 16). Conversely, **32-La** reacted to completion with PPh_3 (10 equiv) over 14 hours, generating $(O)PPh_3$ as

observed via ^{31}P NMR (Figure 17). The relative reactivity of these two clusters was in agreement with the relative Lewis acidities of Ca^{2+} (pK_a = 12.6) and La^{3+} (pK_a = 9.06).

Scheme 5. OAT Reactivity of **32-M** and **33-M** Oxo-Hydroxo Fe_3 Clusters.

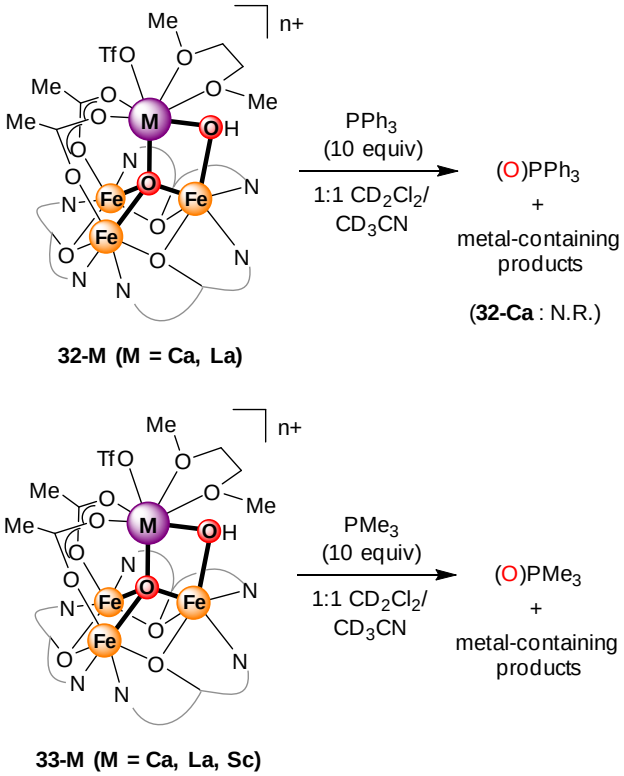

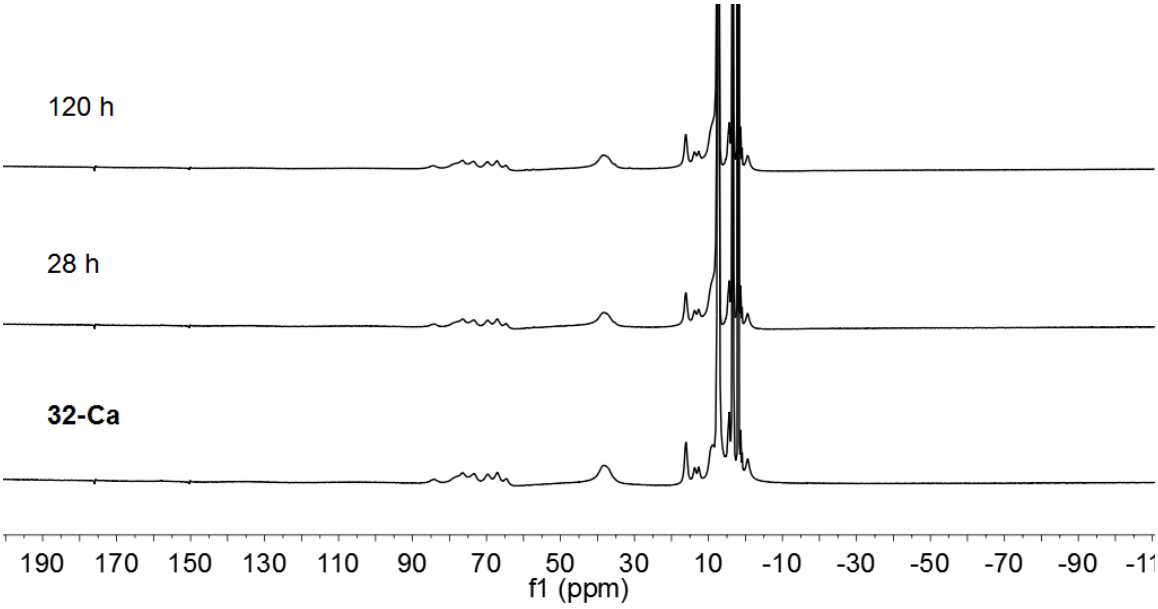

Figure 16. ^{1}H NMR (300 MHz, CD_3CN) of reaction of **32-Ca** with PPh_3 (10 equiv).

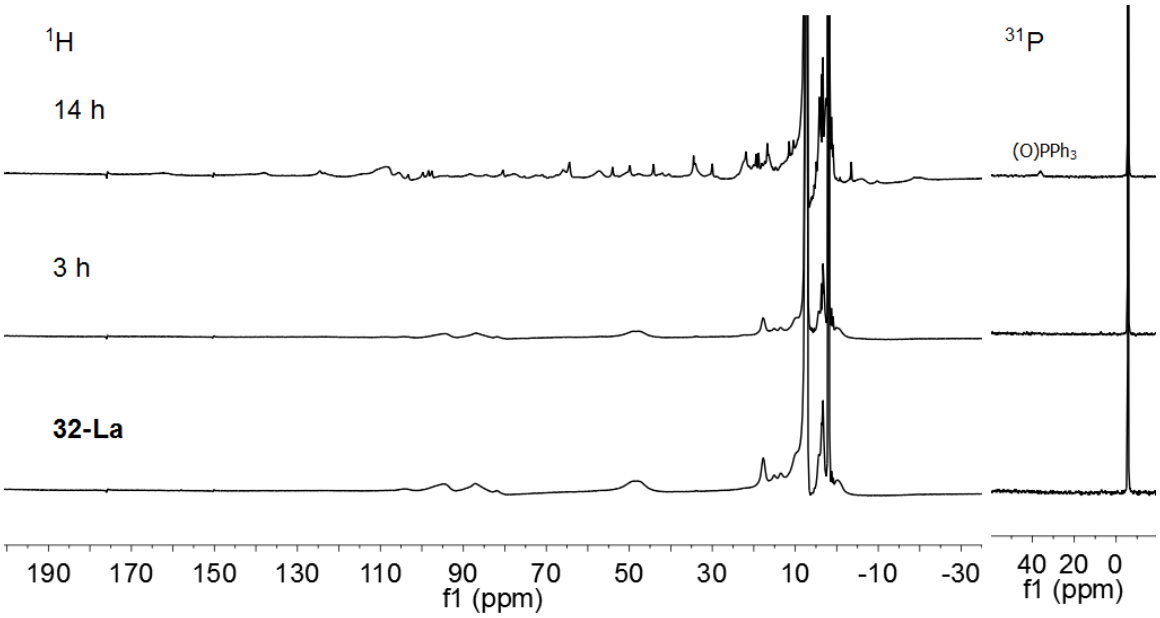

Figure 17. ^{1}H NMR (300 MHz, CD_3CN) and ^{31}P NMR (121 MHz) of reaction of **32-La** with PPh_3 (10 equiv).

OAT reactivity of reduced clusters **33-M**, in the $[Fe^{III}_2Fe^{II}]$ oxidation state, was studied using PMe_3 as substrate. In the presence of a 10-fold excess of PMe_3, **33-Sc** displayed complete conversion to new products in 60 hours – slower than for the more oxidized cluster **32-La** even with a more reducing substrate. The $(O)PMe_3$ product generated (~1 equiv.) was observed during the reaction via ^{31}P NMR (Figure 18). It should be noted that it is possible that some of the phosphine oxide product could be bound to paramagnetic species, which could broaden its ^{31}P NMR signal, making assignment of the reaction stoichiometry with respect to the amount of phosphine oxide produced difficult. Treatment of clusters **33-La** and **33-Ca** with 10 equiv. PMe_3 resulted in slower reactivity, as these starting complexes were fully converted in 130 h and 270 h, respectively. As in the case with **33-Sc**, generation of $(O)PMe_3$ (~1 and ~1.5 equiv., respectively) was confirmed via ^{31}P NMR as the reaction proceeded (Figures 19 and 20). Similar to what was observed for Mn_3 complexes, OAT reactivity of Fe_3 oxo-

hydroxo complexes **33-M** was affected by the Lewis acidity of the redox-inactive metal. **33-Ca**, containing the least Lewis acidic Ca^{2+} (pK_a = 12.6), reacted more slowly than clusters **33-La** and **33-Sc**, which contained more Lewis acidic metals (pK_a: La^{3+} = 9.06, Sc^{3+} = 4.8). The metal-containing products of these clusters could not be structurally characterized. The sharp ^{1}H NMR features were consistent with [Fe_3] cores containing Fe^{II} centers, but distinction between [Fe^{II}_3] and [$Fe^{III}Fe^{II}_2$] via this technique was not possible.

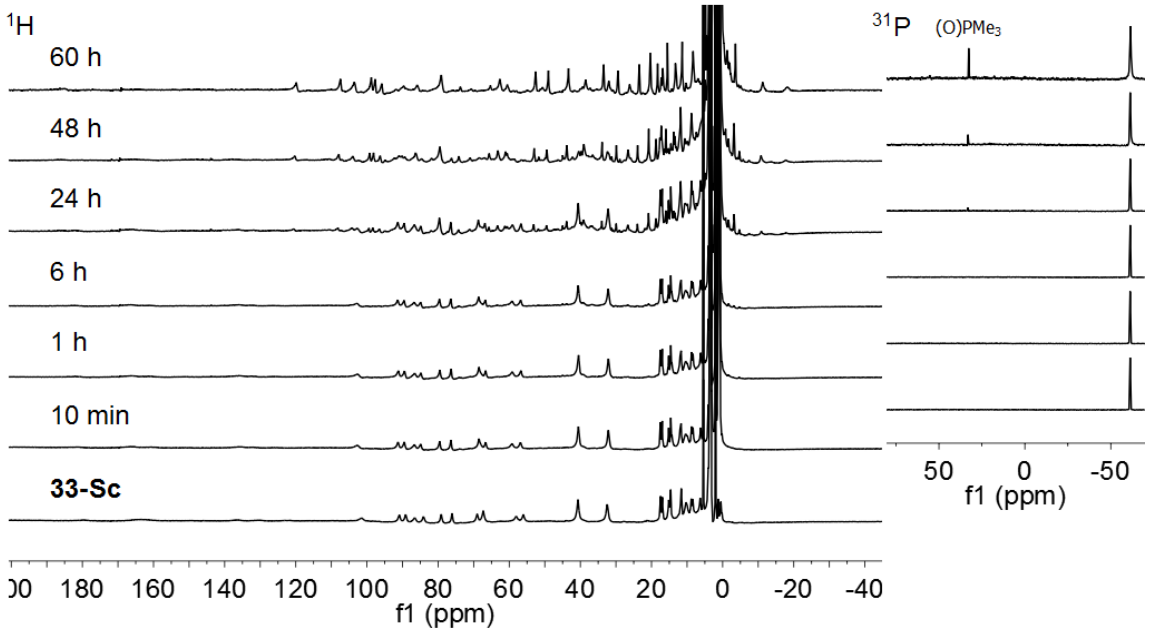

Figure 18. ^{1}H NMR (300 MHz, 1:1 CD_3CN/CD_2Cl_2) and ^{31}P NMR (121 MHz) of reaction of **33-Sc** with PMe_3 (10 equiv).

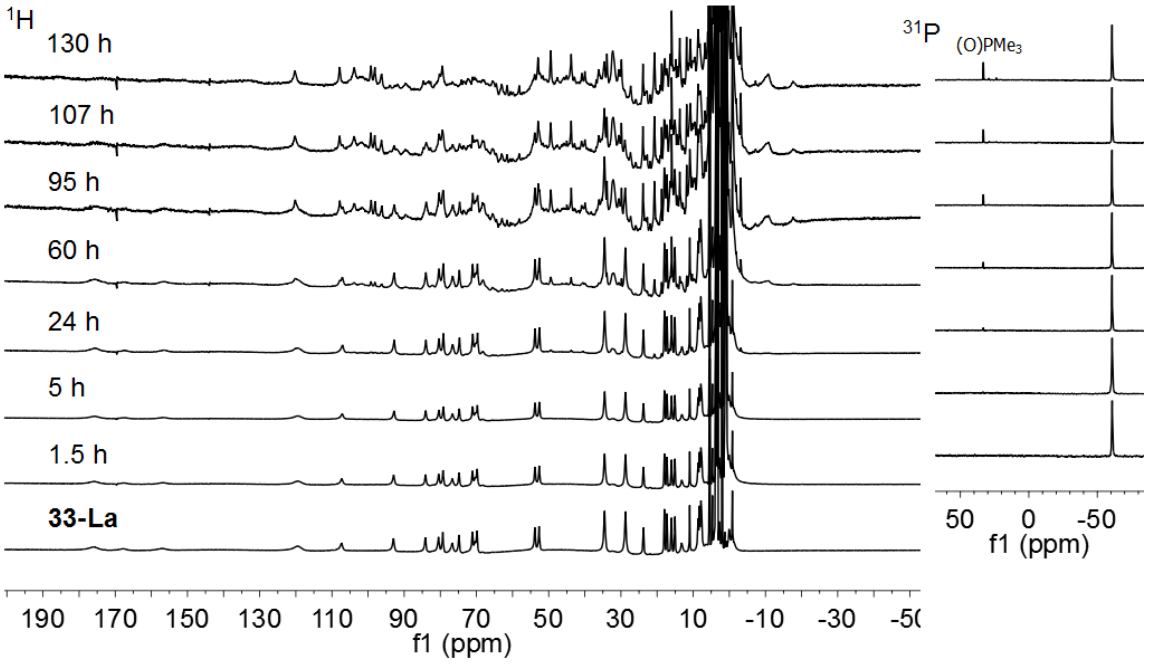

Figure 19. ^{1}H NMR (300 MHz, C_6D_6) and ^{31}P NMR (121 MHz) of reaction of **33-La** with PMe_3 (10 equiv).

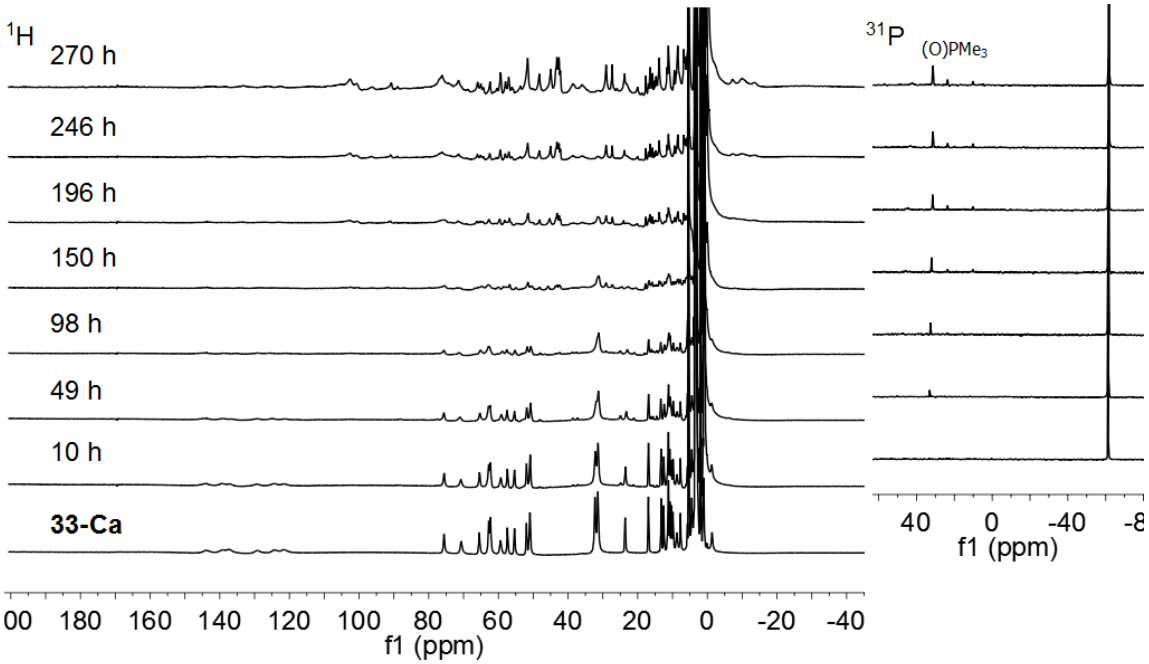

Figure 20. ^{1}H NMR (300 MHz, C_6D_6) and ^{31}P NMR (121 MHz) of reaction of **33-Ca** with PMe_3 (10 equiv).

Although conclusive structural identification was not available, preliminary studies of reactivity of dioxo clusters **34-M** (M = La^{3+}, Sc^{3+}) were carried out with the available materials. **34-La** was fully converted in the presence of 10 equiv. PMe_3 in ~50 hours (Figure 21), while conversion of **34-Sc** under the same conditions required ~25 hours (Figure 22). Once again, the Lewis acidity of the heterometal in these clusters affected their rates of OAT, with the more Lewis acidic Sc^{3+} resulting in faster reactivity. Complexes **32-La** and **34-La** provided the only available comparison of the OAT reactivity of oxo-hydroxo and dioxo clusters. **34-La** displayed slower reactivity with a more electron-rich phosphine (PMe_3) than **32-La** (PPh_3). This observation was consistent with the assumption that **34-La** would have a more negative reduction potential than **32-La** (akin to what was observed for **33-**/**34-Sc**). At the same time, it was expected that **34-La** could undergo direct OAT to phosphine, whereas this pathway is likely not available to **32-La**. The observed relative reactivities may hint to an electron transfer step preceding transfer of the oxygen atom – similar to what has been proposed for Lewis acid-bound Fe- and Mn-oxo complexes – resulting in slower reactivity in the case of the less oxidizing cluster.

Preliminary reactivity of a putative Ca dioxo cluster (**34-Ca**) did afford single-crystals suitable for XRD analysis, which revealed formation of a mono-oxo species containing a single Ca^{2+} center and of a trimetallic mono-oxo species bearing chloride ligands (Figure 23). This observation indicated that abstraction of a single O-atom from these clusters was at least a possibility. Nonetheless, the difficulties in accessing Ca^{2+} dioxo complexes reproducibly, as well as the observation of Cl^- incorporation – clearly a result of further cluster decomposition – limited the usefulness of this result.

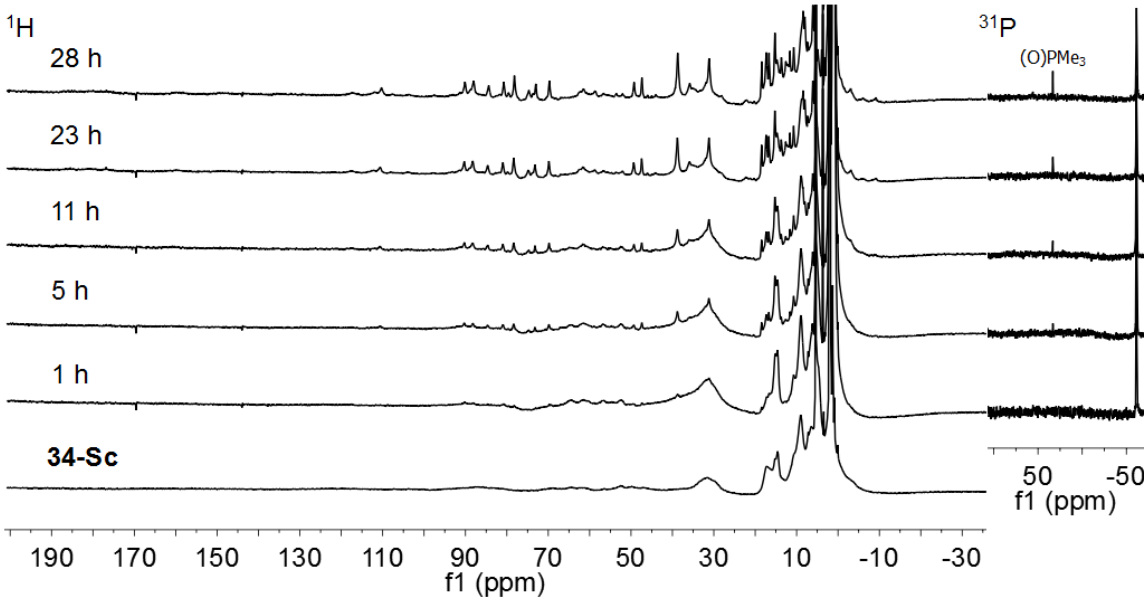

Figure 21. ^{1}H NMR (300 MHz, C_6D_6) and ^{31}P NMR (121 MHz) of reaction of **34-Sc** with PMe_3 (10 equiv).

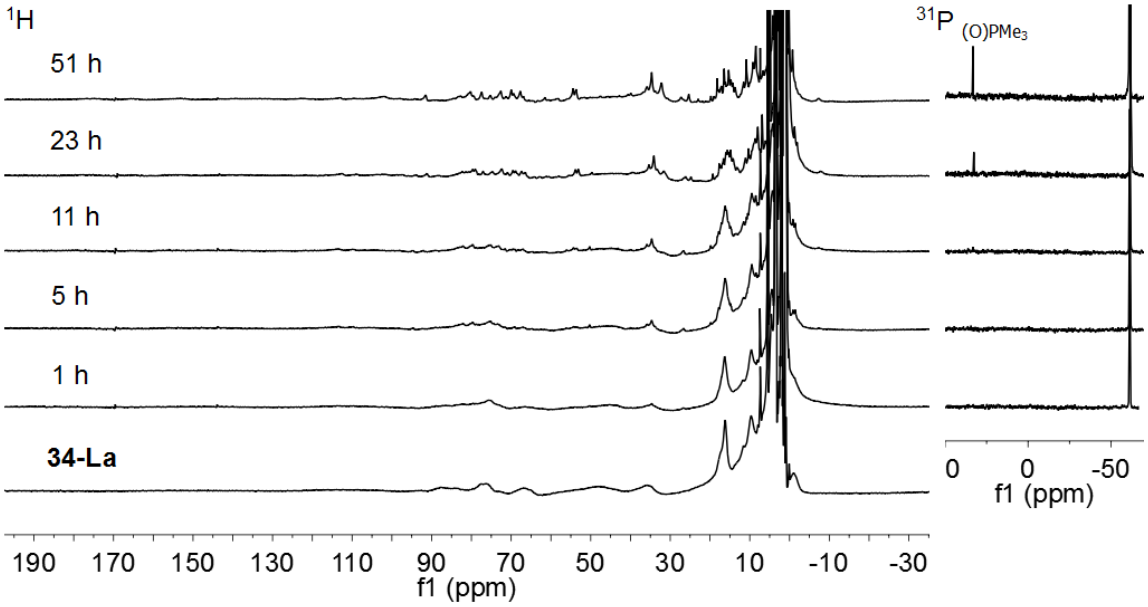

Figure 22. ^{1}H NMR (300 MHz, C_6D_6) and ^{31}P NMR (121 MHz) of reaction of **34-La** with PMe_3 (10 equiv).

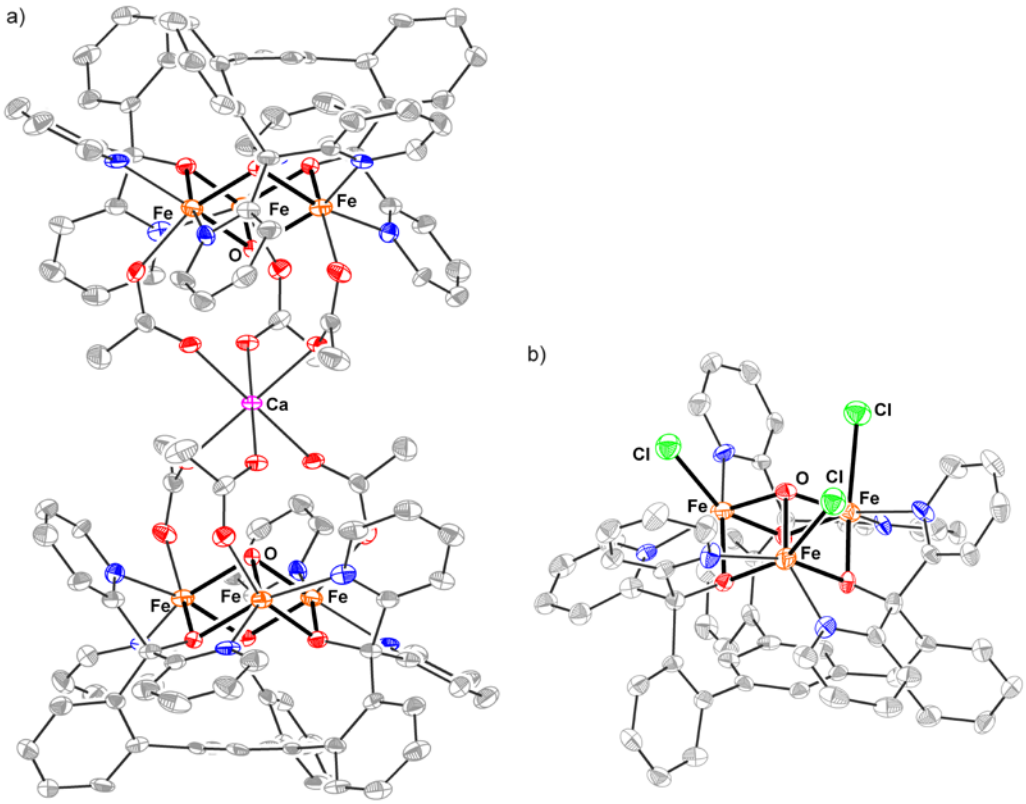

Figure 21. Preliminary solid-state structure of reaction of a putative Ca^{2+} dioxo complex (**34-Ca**) with PMe_3, indicating potential products of reaction of oxo-hydroxo Fe_3 clusters with phosphine substrates: (a) dimeric subunit; (b) monomeric subunit.

The OAT reactivity data for cubane and Mn_3 and Fe_3 oxo-hydroxo clusters is summarized in Table 4. For each individual series, the rate of OAT increased with increasing Lewis acidity (i.e. decreasing pK_a) of the fourth, apical metal center present in the clusters. For both series of Mn_3 and Fe_3 oxo-hydroxo complexes, clusters in the higher oxidation state displayed faster OAT reactivity than their reduced counterparts. The case of cubane clusters is more complex, as the high kinetic barrier to dissociation of an acetate ligand from the Mn^{IV}_3 core in oxidized clusters **29-M** hindered the OAT process as described above. Comparison of OAT reactivity across different series of complexes was possible with clusters containing redox-inactive metals of similar Lewis

Table 4. OAT Reactivity of Mn_3 and Fe_3 Clusters.[65]

Complex	M_3 Ox. State	pK_a[a]	Substrate (equiv.)	Time	T(°C)
29-Sc[64]	Mn^{IV}_3	4.8	PMe_3 (2)	N.R.[b]	r.t.
29-Ca[64]	Mn^{IV}_3	12.6	PMe_3 (2)	N.R.	r.t.
30-Mn	$Mn^{IV}_2Mn^{III}$	0.1	PMe_3 (2)	15 min	r.t.
30-Co	$Mn^{IV}_2Mn^{III}$	0.66	PMe_3 (2)	2 h	r.t.
30-Sc	$Mn^{IV}_2Mn^{III}$	4.8	PMe_3 (10)	1.5 weeks	r.t.
30-Sc	$Mn^{IV}_2Mn^{III}$	4.8	PMe_3 (10)	35 h	50 °C
30-Gd	$Mn^{IV}_2Mn^{III}$	8.4	PMe_3 (10)	>2 weeks	r.t.
30-Gd	$Mn^{IV}_2Mn^{III}$	8.4	PMe_3 (10)	50 h	50 °C
(27-Y)$_2$[c]	Mn^{III}_3	8.6	PEt_3 (10)	15 min	r.t.
(27-Y)$_2$[c]	Mn^{III}_3	8.6	PPh_3 (10)	30 min	r.t.
27-Ca	Mn^{III}_3	12.6	PEt_3 (10)	3 h	r.t.
27-Ca	Mn^{III}_3	12.6	PPh_3 (10)	20 h	r.t.
28-Y	$Mn^{III}_2Mn^{II}$	8.6	PEt_3 (10)	30 min	r.t.
28-Y	$Mn^{III}_2Mn^{II}$	8.6	PPh_3 (10)	1 h	r.t.
28-Ca	$Mn^{III}_2Mn^{II}$	12.6	PEt_3 (10)	36 h	r.t.
32-La	Fe^{III}_3	9.06	PPh_3 (10)	24 h	r.t.
32-Ca	Fe^{III}_3	12.6	PPh_3 (10)	N.R.	r.t.
33-Sc	$Fe^{III}_2Fe^{II}$	4.8	PMe_3 (10)	14 h	r.t.
33-La	$Fe^{III}_2Fe^{II}$	9.06	PMe_3 (10)	130 h	r.t.
33-Ca	$Fe^{III}_2Fe^{II}$	12.6	PMe_3 (10)	270 h	r.t.
34-Sc	Fe^{III}_3	4.8	PMe_3 (10)	25 h	r.t.
34-La	Fe^{III}_3	9.06	PMe_3 (10)	55 h	r.t.

[a] pK_a of $M(aqua)^{n+}$ complex.[66] [b] N.R. = no reaction. [c] complex **27-Y** was isolated as a dimer

acidity, such as **30-Gd**, **28-Y**, and **33-La**, which contained heterometals with similar pK_as (Gd^{3+} = 8.4, Y^{3+} = 8.6, La^{3+} = 9.06). Cubane cluster **30-Gd** reacted more slowly (>2 weeks at r.t.) with PMe_3 than **33-La** (120 h), which in turn displayed slower OAT activity than **28-Y** (30 min, PEt_3). These observations are in agreement with the reported one-electron redox potentials for the three series of clusters, as the Fe_3 oxo-hydroxo clusters display potentials that are intermediate between those of cubane clusters (more negative) and Mn_3 oxo-hydroxo complexes (more positive).[39,40,62] The mechanism of OAT from Fe_3 (and Mn_3) oxo-hydroxo clusters is however not fully understood. Direct OAT involving the hydroxide ligand is unlikely. Either proton transfer (deprotonation of the hydroxide by substrate phosphine) or electron transfer (reduction of cluster by phosphine) are therefore likely required as initial steps in this conversion. The occasional observation of either one-electron reduction or deprotonation of oxidized oxo-hydroxo clusters by phosphines indicated that either pathway may contribute to the observed reactivity. Further studies are necessary to shed more light on the mechanism of these OAT reactions, although the promiscuous reactivity (ET/PT/OAT) of several reagents with these clusters makes these investigations challenging.

CONCLUSIONS

A series of [Fe_3MO(OH)] clusters substituted with divalent and trivalent redox-inactive metals were prepared. This series of compounds allowed for the systematic study of the electrochemical effect of the Lewis acidic metal ions on the iron reduction potentials. Varying the Lewis acidity of the capping metal from Ca^{2+} to Sc^{3+} shifted the redox potentials of these clusters by over 0.5 V. These results supported the generality

of the role redox-inactive metals can play in modulating the redox potential of the redox-active centers via μ-O or μ-OH ligands.

The Lewis acidity of redox-inactive metal centers incorporated in heterometallic Mn_3 and Fe_3 clusters was also found to have a remarkable effect on the rate of oxygen atom transfer to phosphine substrates. Lewis acidity of the heterometal in cubane [Mn_3MO_4], oxo-hydroxo [$Mn_3MO(OH)$], and [$Fe_3MO(OH)$] clusters correlated with the qualitative rate of OAT, similar to what had been previously observed for the one-electron redox potentials of the same series of clusters. Although effects of Lewis acidic, redox-inactive metals on redox processes such as group transfer reactivity have been previously reported, this study is the first to be based on heterometallic systems for which an unambiguous structural assignment of the OAT precursors is available. While in previous literature reports redox-inactive metal centers were included as additives (often in suprastoichiometric amounts), generating the species responsible for OAT *in situ*, the use of well-defined heterometallic clusters simplifies the interpretation of the observed reactivity. When redox-inactive metal additives are used in excess to generate adducts with high-valent metal oxo species *in situ*, the effects of the Lewis acidity of these metal centers on the dynamic binding processes involved in adduct formation must be accounted for when studying the effects of Lewis acidity on the reactivity of the adducts themselves. In the present systems, however, the redox-inactive metal centers are incorporated in clusters that can be isolated and structurally characterized, and no equilibrium between bound and unbound species is operative in solution. Therefore, the observed differences in reactivity can conclusively be ascribed to the electronic effects of the redox-inactive metals incorporated in the clusters. Studies to

further probe the effects of heterometal Lewis acidity on chemical transformations involving these clusters are ongoing

EXPERIMENTAL SECTION

General Considerations

Unless indicated otherwise, reactions performed under inert atmosphere were carried out in oven-dried glassware in a glovebox under a nitrogen atmosphere. Anhydrous tetrahydrofuran (THF) was purchased from Aldrich in 18 L Pure-Pac™ containers. Anhydrous dichloromethane, diethyl ether, and THF were purified by sparging with nitrogen for 15 minutes and then passing under nitrogen pressure through a column of activated A2 alumina (Zapp's). Anhydrous 1,2-dimethoxyethane (DME) was dried over sodium/benzophenone ketyl and vacuum-transferred onto molecular sieves. CD_2Cl_2 and CD_3CN were purchased from Cambridge Isotope Laboratories, dried over calcium hydride, then degassed by three freeze-pump-thaw cycles and vacuum-transferred prior to use. ^{1}H NMR spectra were recorded on a Varian 300 MHz instrument, with shifts reported relative to the residual solvent peak. ^{19}F NMR spectra were recorded on a Varian 300 MHz instrument, with shifts reported relative to the internal lock signal. Elemental analyses were performed by Robertson Microlit Laboratories, NJ. Electrospray ionization mass spectrometry (ESI-MS) was performed in the positive ion mode using a LCQ ion trap mass spectrometer (Thermo) at the California Institute of Technology Mass Spectrometry Facility.

Unless indicated otherwise, all commercial chemicals were used as received. $Ca(OTf)_2$, and $Zn(OTf)_2$ were purchased from Aldrich. Cobaltocene was purchased from Strem and sublimed before use. $La(OTf)_3$ was purchased from Strem. $Sr(OTf)_2$ and 2,4,6-tri-*tert*-butylphenoxyl radical were prepared according to literature procedures.[67,68] **31-Fe** was prepared according to previously published procedures.[49]

Synthesis of 32-Ca

In the glovebox, a round-bottom flask equipped with a stir bar was charged with **31-Fe** (0.600 g, 0.500 mmol) and suspended in 50 mL of DME. $Ca(OTf)_2$ (0.270 g, 0.798 mmol, 1.6 equiv) was added leading the orange suspension to lighten in color, and the yellow-orange suspension was stirred at room temperature for 10 min. Iodosobenzene (0.242 g, 1.10 mmol, 2.2 equiv) was added as a solid, and the mixture was stirred at room temperature for 10 h, turning from yellow-orange to dark-brown and ultimately to a orange-brown suspension. The orange-brown solid was collected via filtration, washed with DME (3 x 10 mL), then extracted with dichloromethane (~ 10 mL). The orange-brown solution was dried, re-extracted with dichloromethane, filtered over Celite and layered with diethylether to yield an orange-brown solid (0.650 g, 74%). ^{1}H NMR (CD_2Cl_2, 300 MHz): δ 85 (v br overlapped), 80 (v br overlapped), 74 (v br overlapped), 68 (v br overlapped), 63 (v br overlapped), 39 (v br), 16 (br), 14, 13, 9, 4 (br, overlapped), 3 (br overlapped), 1, 0 ppm (v br). ^{19}F NMR (CD_2Cl_2): δ −76.6 (br) ppm. Anal. Calcd. For $C_{68}H_{56}CaF_9Fe_3N_6O_{20}S_3$: C, 46.62; H, 3.22; N, 4.80. Found: C, 46.35; H, 3.01; N, 4.69.

Synthesis of 33-Ca

In the glovebox, a 20 mL vial equipped with a stir bar was charged with **32-Ca** (0.246 g, 0.140 mmol) and 8 mL of CH_2Cl_2. A solution of cobaltocene (0.0277 g, 0.148 mmol, 1.06 equiv; 2 mL CH_2Cl_2) was added drop-wise. The mixture was stirred for 45 min then dried *in vacuo*. The residue was washed with DME until the washings were colorless to remove cobaltocenium triflate (identified by ^{1}H, ^{19}F NMR). The dark brown residue was recrystallized from DME/CH_2Cl_2/Et_2O to yield the product as a dark

brown solid (0.172 g, 76%). ^{1}H NMR (CD_2Cl_2, 300 MHz): δ 144 (br, overlapped), 139 (br, overlapped), 129 (br, overlapped), 126 (br, overlapped), 123 (br, overlapped), 74.6, 68.8, 65.4, 62.9 (overlapped), 62.1 (overlapped), 58.5 (overlapped), 57.5 (overlapped), 54.6, 52.1 (overlapped), 51.3 (overlapped), 33.8 (overlapped), 32.3 (overlapped), 22.8, 17.0, 13.1, 12.4, 11.6, 11.1, 10.6 (overlapped), 10.2 (overlapped), 9.9 (overlapped), 8.7, 8.0, 4.7 (br, overlapped with solvent), 3.6 (overlapped), 3.3 (overlapped), 2.8, 1.2, 0.9, -1.9 ppm. ^{19}F NMR (CD_2Cl_2): δ −74.4 ppm. Anal. Calcd. for $C_{67}H_{56}CaF_6Fe_3N_6O_{17}S_2$: C, 50.20; H, 3.52; N, 5.24. Found: C, 50.04; H, 3.70; N, 5.15.

Synthesis of 32-Sr

In the glovebox, a round bottom flask equipped with a stir bar was charged with **31-Fe** (0.400 g, 0.333 mmol) and 40 mL DME. Solid $Sr(OTf)_2$ (0.206 g, 0.534 mmol, 1.6 equiv) was added and the mixture was stirred at room temperature for 10 min. PhIO (0.161 g, 0.733 mmol, 2.2 equiv) was added as a solid to the vial, and the yellow suspension was stirred at room temperature for 10 h, turning dark brown then to an orange-brown suspension. The brown-orange precipitate was collected over Celite and washed with DME (2 x 10 mL), then extracted with CH_2Cl_2. The brown-orange CH_2Cl_2 filtrate was dried *in vacuo*, redissolved in CH_2Cl_2 and filtered once more over Celite. DME (1 mL) was added to the solution and diffusion of ether into the mixture led to formation of the product as an orange-brown solid (0.476 g, 79%). ^{1}H NMR (CD_2Cl_2, 300 MHz): δ 79 (br overlapped), 73 (br overlapped), 71 (br overlapped), 68 (br overlapped), 65 (br overlapped), 63 (br overlapped), 38 (v br), 16 (overlapped), 14.5 (overlapped), 13.3 (overlapped), 9.6 (br overlapped), 9.5 (br overlapped), 4.3 (br overlapped with solvent), 3.6 (overlapped), 3.5 (overlapped), 1.2, -0.1 (br) ppm. ^{19}F

NMR (CD_2Cl_2): δ −75.7 ppm. Anal. Calcd. for $C_{68}H_{56}F_9Fe_3N_6O_{20}S_3Sr$: C, 45.39; H, 3.14; N, 4.67. Found: C, 45.15; H, 3.00; N, 4.60.

Synthesis of 7-Sc

In the glovebox, a scintillation vial equipped with a stir bar was charged with **31-Fe** (0.1108 g, 0.0908 mmol), $Sc(OTf)_3$ (0.0594 g, 0,1208 mmol, 1.33 equiv), and 10 mL 1:1 THF/DME. The mixture was stirred at room temperature for 10 minutes during which time the orange suspension turned into a nearly homogenous yellow solution. PhIO (0.0419 g, 0.1906 mmol, 2.1 equiv) was added as a solid to the reaction mixture. While stirring at room temperature for 15 h, a brown precipitate formed, leaving a light brown solution behind. The precipitate was collected over Celite and washed with 3 x 10 mL DME, then extracted with CH_2Cl_2. The filtrate was dried in vacuo. The resulting powder was redissolved in CH_2Cl_2,; DME (2 mL) was added, and diffusion of diethyl ether into the mixture led to precipitation of the product as a brown solid (0.1049 g, 66%). ^{1}H NMR (CD_2Cl_2, 300 MHz): δ 179 (br overlapped), 173 (br overlapped), 156 (br), 146 (br), 94 (br overlapped), 92 (br overlapped), 88, 86, 76 (overlapped), 74, 73, 59, 48, 46, 42, 36, 19.5, 17.2, 16.5, 14.8, 11.1 (br overlapped), 9.7 (br overlapped), 8.7 (br overlapped), 8.1 (br overlapped), 4.8 (overlapped with solvent), 2.8, 0.4 (overlapped with solvent), -1.6 (br) ppm. ^{19}F NMR (CD_2Cl_2): δ −76.7 ppm. Anal. Calcd. For $C_{68}H_{56}F_9Fe_3N_6O_{20}S_3Sc$: C, 46.49; H, 3.21; N, 4.78. Found: C, 46.22; H, 3.46; N, 4.79.

Synthesis of 32-Zn

In the glovebox, a scintillation vial equipped with a stir bar was charged with **32-Ca** (0.099 g, 0.056 mmol) and $Zn(OTf)_2$ (0.021 g, 0.058 mmol, 1.04 equiv) in CH_3CN (10 mL). The red solution was stirred at room temperature for 2 h, then dried in vacuo. The resulting orange-red solid was dissolved in CH_2Cl_2 with a few drops of CH_3CN and filtered over Celite. The orange-red solution was dried, re-extracted with CH_2Cl_2 and a few drops of CH_3CN and concentrated. Diffusion of Et_2O into the solution at room temperature produced dark red crystals (0.095 g, 98%). ^{1}H NMR (CD_2Cl_2, 300 MHz): δ 95 (br, overlapped), 88 (br, overlapped), 82 (br, overlapped), 76 (br, overlapped), 73 (br, overlapped), 69 (br, overlapped), 46 (br), 16.8, 12.2 (overlapped), 10.1 (overlapped), 4.5 (overlapped with solvent), 3.4, 2.1, 1.2, -1.1, -2.2 ppm. ^{19}F NMR (CD_2Cl_2): δ −74.2 ppm. Anal. Calcd. For $C_{66}H_{49}F_9Fe_3N_7O_{18}S_3Zn$: C, 45.87; H, 2.86; N, 5.67. Found: C, 45.66; H, 2.98; N, 5.64.

Synthesis of 32-La

In the glovebox, a scintillation vial equipped with a stir bar was charged with **32-Ca** (0.146 g, 0.0832 mmol) and 5 mL CH_3CN. $La(OTf)_2$ (0.100 g, 0.171 mmol, 2 equiv) was added as a solid and the red solution was stirred at room temperature for 2 h, then dried *in vacuo*. The resulting orange-red paste was washed with neat CH_2Cl_2 then extracted with CH_2Cl_2 with a few drops of CH_3CN and filtered over Celite. The orange-red solution was concentrated and 1 mL of DME was added. Diffusion of Et_2O into the solution at room temperature produced a dark red oil that was dried extensively *in vacuo* to give an orange-red powder that was again washed with Et_2O (0.100 g, 60%). ^{1}H NMR (CD_2Cl_2, 300 MHz): δ 102 (br overlapped), 94 (br, overlapped), 87 (br,

overlapped), 84 (br, overlapped), 81 (br, overlapped), 49 (br), 18, 15.7, 13.6, 9.9, 7.3, 4.3 (overlapped with solvent), 3.5 (overlapped), 3.3 (overlapped), 1.9, 1.1, -2.5 ppm. ^{19}F NMR (CD_2Cl_2): δ −76.5 ppm.

Synthesis of 33-La

In the glovebox, a 20 mL vial equipped with a stir bar was charged with **32-La** (0.1095 g, 0.0548 mmol) and 10 mL of CH_2Cl_2 and a few drops of CH_3CN. A solution of cobaltocene (0.0104 g, 0.0548 mmol, 1 equiv; 2 mL CH_2Cl_2) was added drop-wise. The mixture was stirred for 10 min then dried *in vacuo*. The residue was washed with DME until the washings were colorless. The dark brown residue was extracted with CH_2Cl_2, and the solvent evaporate *in vacuo*. The resulting brown powder was precipitated from DME/CH_2Cl_2/Et_2O to yield the product as a dark brown solid (0.0850 g, 84%). ^{1}H NMR (CD_2Cl_2, 300 MHz): δ 173 (br), 165 (br), 153 (br), 131 (br), 100 (b), 90 (br), 81.9 (overlapped), 80.9 (overlapped), 76.0 (overlapped), 75.1 (overlapped), 72.8, 68.4, 58.7 (br, overlapped), 56.3 (br, overlapped), 36.3 (overlapped), 33.7 (br, overlapped), 21.5, 18.0, 16.4 (overlapped), 15.6 (overlapped), 15.0 (overlapped), 11.2, 8.5, 4.0 (br, overlapped), 3.4 (overlapped), 1.2, -0.5 ppm. ^{19}F NMR (CD_2Cl_2): δ −74.8 ppm. Anal. Calcd. for $C_{68}H_{56}LaF_9Fe_3N_6O_{20}S_3$: C, 44.13; H, 3.05; N, 4.54. Found: C, 43.88; H, 3.24; N, 4.48.

Synthesis of 34-La

In the glovebox, a 20 mL vial equipped with a stir bar was charged with **6-La** (0.1428 g, 0.0714 mmol) in CH_3CN/DME (1:1). DBU (10.7 μL, 0.0714 mmol, 1 equiv.) was added as a CH_3CN solution, and the reaction solution was stirred for 30 minutes. Et_2O

(10 volumes) was added to crash out the product and the suspension was filtered over Celite. The residue was washed with DME (2 x 3 mL) to remove protonated DBU, and the residue was then extracted with CH_3CN. The solvent was removed *in vacuo* to give an orange powder (0.130 g, 98%), which was stored at -40 °C. ^{1}H NMR (CD_3CN, 300 MHz): δ 85 (br overlapped), 80 (br, overlapped), 73 (br, overlapped), 64 (br, overlapped), 62 (br, overlapped), 51 (br overlapped), 42 (br overlapped), 32 (br overlapped), 13 (overlapped), 12.6 (overlapped), 13.6, 9.9, 7.3, 4.3 (overlapped with solvent), 3.5 (overlapped), 3.3 (overlapped), 6.3, -4 (br overlapped), -5 (br overlapped) ppm. ^{19}F NMR (CD_2CN): δ −80.0 (br) ppm.

Synthesis of 34-Sc.

Preparation of **34-Sc** was most reproducible when carried out in small batches, which were then quickly used for further reactivity (although once isolated **34-Sc** was stable for weeks if stored at -40 °C).

In the glovebox, a 20 mL vial equipped with a stir bar was charged with **33-Sc** (0.0288 g, 0.0164 mmol) in CH_3CN/Et_2O (1:2) to which was added a solution of 2,4,6-tri-*tert*-butylphenoxyl radical (0.0429 g, 0.164 mmol, 10 equiv.) in Et_2O. The mixture was stirred for three hours, after which full consumption of starting material was determined via ^{1}H NMR. Excess Et_2O was added to crash out the metal product. Filtration through Celite separated the orange solids from the blue solution. The orange residue was washed with Et_2O (4x), C_6H_6 (2x), and Et_2O again (2x), then extracted with minimal CH_3CN. Evaporation of the solvent *in vacuo* yielded the product as an orange powder (0.0267 g, 93%). ^{1}H NMR (CD_3CN, 300 MHz): δ 87 (br overlapped), 83 (br, overlapped), 69 (br, overlapped), 64 (br, overlapped), 61 (br, overlapped), 56 (br), 52

(br overlapped), 50 (br overlapped), 47 (br overlapped), 32 (br), 17 (overlapped), 14.6 (overlapped), 10.5 (br overlapped), 9 (br overlapped), -3.3 (br overlapped) ppm. ^{19}F NMR (CD_2CN): δ -77.4 (br) ppm.

Mössbauer Spectroscopy

Spectra were recorded on a spectrometer from SEE Co. operating in the constant acceleration mode in a transmission geometry. Spectra were recorded with the temperature of the sample maintained at 80 K. The sample was kept in an SVT-400 Dewar from Janis, at zero field. Application of a magnetic field of 54 mT parallel to the γ-beam did not cause detectable changes in the spectra recorded at 80 K. The quoted isomer shifts are relative to the centroid of the spectrum of a metallic foil of α-Fe at room temperature. Samples were prepared by grinding polycrystalline material into a fine powder and then mounted in a cup fitted with a screw cap as a boron nitride pellet. Data analysis was performed using the program WMOSS (www.wmoss.org) and quadrupole doublets were fit to Lorentzian lineshapes.

Electrochemical Measurements

Electrochemical measurements were recorded with a Pine Instrument Company AFCBP1 bipotentiostat using the AfterMath software package. Cyclic voltammograms were recorded on ca. 3 mM solutions of the relevant complexes in the glovebox at 20 °C with an auxiliary Pt-coil electrode, a Ag^+/Ag reference electrode (0.01 M $AgNO_3$, 0.1 M $^nBu_4NPF_6$ in CH_3CN), and a 3.0 mm glassy carbon electrode disc (BASI). The electrolyte solutions were 0.1 M $^nBu_4NPF_6$ in CH_2Cl_2:DME (9:1) for all compounds. All reported values are referenced to an internal ferrocenium/ferrocene couple.

Table 5. $E_{1/2}$ values of the $[MFe_3O(OH)]^{n+5}/[MFe_3O(OH)]^{n+4}$ couple vs. Fc^+/Fc using a glassy carbon electrode (GCE). Values are reported in 9:1 CH_2Cl_2/DME.

Complex	GCE (V)
32-Ca	-0.490
32-Sr	-0.490
32-Zn	-0.210
33-La	-0.080
33-Sc	+0.070
34-Sc	-0.170

Protocol for reactivity studies of metal-oxo clusters with phosphine substrate

In an inert-atmosphere glovebox, a J. Young NMR tube was charged with a solution (~12-15 mM) of the desired cluster complex, which was dissolved (~12-15 mM) in an appropriate NMR solvent (CD_2Cl_2, CD_3CN, or C_6D_6). Phosphine (PPh_3, PEt_3, or PMe_3; 2-10 equiv) was added neat via gas-tight microsyringe or as a stock solution. Reaction progress was monitored via ^1H and ^{31}P NMR as appropriate until full (>95%) conversion was observed by disappearance of signal corresponding to starting material. Samples requiring heating were kept at elevated temperature in mineral oil baths. When phosphine oxide products were not observed during reaction via ^{31}P NMR, samples were returned to a glovebox, where volatiles were removed *in vacuo*. On the benchtop, the resulting residue was dissolved in dichloromethane, filtered through a short silica plug, and further eluted with methanol. The resulting solution was analyzed by GC-MS to confirm the presence of phosphine oxide product.

Crystallographic Information

CCDC 966986-966991 contain the supplementary crystallographic data for this paper. These data can be obtained free of charge from The Cambridge Crystallographic Data Centre via www.ccdc.cam.ac.uk/data_request/cif.

Refinement details

In each case, crystals were mounted on a glass fiber or nylon loop using Paratone or Framblin oil under a nitrogen stream. Low temperature (100 K) X-ray data were obtained on a Bruker APEXII CCD based diffractometer (Mo sealed X-ray tube, K_α = 0.71073 Å). All diffractometer manipulations, including data collection, integration and scaling were carried out using the Bruker APEXII software.[69] Absorption corrections were applied using SADABS.[70] Space groups were determined on the basis of systematic absences and intensity statistics and the structures were solved by direct methods using XS[71] (incorporated into SHELXTL) and refined by full-matrix least squares on F^2. All non-hydrogen atoms were refined using anisotropic displacement parameters. Hydrogen atoms were placed in idealized positions and refined using a riding model. The structure was refined (weighted least squares refinement on F^2) to convergence.

It should be noted that due to the size of these compounds, most crystals included solvent accessible voids, which tended to contain disordered solvent. In addition, due to a tendency to desolvate, the long range order of these crystals and amount of high angle data we were able to record was in some cases not ideal. These disordered solvent molecules were largely responsible for the alerts generated by the checkCIF protocol. In some cases, this disorder could be modeled satisfactorily, while in **32-Sr** the disordered solvent was removed using the SQUEEZE protocol included in

PLATON.[72,73] In this case, we are confident this additional electron density is attributable to solvent included in the crystal lattice and not unaccounted for counterions.

Table 6. Crystal and refinement data.

	32-Ca	**33-Ca**	**32-Sr**	**33-Sc**	**32-Zn**	**33-La**
empirical formula	$C_{82}H_{89}CaF_9Fe_3N_7O_{24}S_3$	$C_{77.25}H_{81.63}CaF_6Fe_3N_6O_{20.56}S_2$	$C_{68}H_{56}F_9Fe_3N_6O_{20}S_3Sr$	$C_{77}H_{77}Cl_2F_9Fe_3N_6O_{23}S_3Sc$	$C_{66}H_{49}F_9Fe_3N_7O_{18}S_3Zn$	$C_{66}H_{56}F_9Fe_3LaN_6O_{20}S_3$
formula wt	2031.41	1808.93	1799.54	2005.03	1728.22	2089.28
T (K)	100	100	100	100	100	100
a, Å	15.0308(6)	11.8543(18)	16.2788(6)	14.5972(18)	14.292(3)	14.949(5)
b, Å	25.1917(10)	26.583(4)	26.1544(9)	25.161(3)	14.592(3)	25.335(8)
c, Å	23.7066(10)	25.731(4)	20.0612(7)	23.470(3)	18.666(4)	23.827(8)
α, deg	90	90	90	90	72.48(3)	90
β, deg	103.928(2)	93.023(8)	105.979(2)	102.693(7)	72.06(3)	102.574(8)
γ, deg	90	90	90	90	70.67(3)	90
V, Å^3	8712.6(6)	8097(2)	8211.3(5)	8409.4(17)	3407.8 (12)	8808(5)
Z	4	4	4	4	2	4
cryst syst	Monoclinic	Monoclinic	Monoclinic	Monoclinic	Triclinic	Monoclinic
space group	P2(1)/c	P2(1)/c	P2(1)/n	P2(1)/c	P1	P2(1)/c
d_{calcd}, g/cm^3	1.549	1.484	1.456	1.584	1.684	1.576
θ range, deg	2.18 to 34.03	2.20 to 22.66	1.43 to 26.37	1.6 to 36	(φ rotation only)	2.41 to 34.18
μ, mm^{-1}	0.722	0.734	1.331	0.82	(φ rotation only)	1.147
abs cor	Multi-scan	Multi-scan	Semi-empirical from equivalents	Semi-empirical from equivalents	Empirical	Multi-scan
GOOF[c]	1.032	1.042	0.965	1.10	0.829	1.086
R1,[a] wR2[b] (I > 2σ(I))	0.0664, 0.1675	0.0986, 0.2377	0.0389, 0.1190	0.1248, 0.3287	0.0869, 0.2457	0.0567, 0.1458

[a] $R1 = \Sigma||F_o|-|F_c|| / \Sigma|F_o|$ [b] $wR2 = [\Sigma[w(F_o^2-F_c^2)^2] / \Sigma[w(F_o^2)^2]]^{1/2}$ [c] $GOOF = S = [\Sigma[w(F_o^2-F_c^2)^2] / (n-p)]^{1/2}$

Table 7. Comparison of key structural parameters for clusters **32-M** and **33-M** (all distances in Å).

Complex (**32-**/**33-M**)	**32-Ca**	**32-Sr**	**33-Sc**	**32-Zn**	**33-Ca**	**33-La**
M–O(m^4)	2.483(2)	2.491(6)	2.121(3)	2.090(3)	2.388(5)	2.384(2)
M–O(H)	2.332(2)	2.692(6)	2.069(3)	1.997(4)	2.359(5)	2.401(2)
Fe–O(H)	1.881(2)	1.884(2)	1.937(3)	1.923(4)	1.923(5)	1.927(2)
Fe(2)–O(μ^4); Fe(1,3)– O(μ^4)	2.023(2); 1.927(2), 1.945(2)	2.021(2); 1.929(2), 1.884(2)	2.005(3); 1.931(3), 2.211(4)	2.006(4); 1.950(3), 1.965(3)	1.928(5); 1.904(5), 2.140(4)	1.996(2); 1.915(2), 2.225(2)

Computational Protocol (Kurtis M. Carsch)

Density functional theory (DFT) calculations were carried out on complexes [LMn(III)$_2$ Mn(IV)CaO$_2$(OTf)(DME)[OTf]$_2$ (**27-Ca'**), [LMn(III)$_3$CaO(OH)(OTf)(DME)][OTf]$_2$ (**27-Ca"**), [LMn(III)$_3$O$_2$Ca(OTf)(DME)[OTf] (**28-Ca'**), and [LMn(II)Mn(III)$_2$CaO(OH)(OTf)(DME)][OTf] (**28-Ca"** and **28-Ca"-noH**) to elucidate the structure of complexes **27-Ca** and **28-Ca**. Complexes **27-Ca'** and **28-Ca'** were optimized using the solid-state structure without outer-sphere solvent molecules as the initial geometry input whereas complexes **27-Ca"** and **28-Ca"** were modified by placing one triflate in the vicinity (~ 3.0 Å) of the bridging hydroxo motif for the initial geometry input. To decrease computational expenses, a "truncated ligand" approximation was employed in which the three carbon atoms connecting the bipyridine motifs were spatially constrained, and the remaining ligand scaffold connecting each carbon atom to the phenyl backbone was substituted with three

protons. This approximation is expected not to influence bond parameters for the [Mn_3O_2Ca] core.

Schrodinger computational products Jaguar 8.4[59] and Maestro were employed respectively to perform gas-phase geometry optimization and measure the bond lengths and angles in the optimized complexes. Calculations were accomplished with the basis set/functional pairing of unrestricted dispersion-corrected B3LYP[74-76]-d3[77] and basis set lacvp** for non-metals C, H, N, O, S, and F along with basis set lacv3p** for Mn and Ca.[78,79] Successful ground-state optimizations were assessed by the forces on all atoms residing below 10^{-5} hartrees/bohr as well as total energy remaining unchanged by 10^{-4} between the final SCF iterations. Oxidation states of clusters **27-Ca'**, **27-Ca"**, **28-Ca'**, and **28-Ca"** were tabulated through Mullikan spin populations and inspection of the spin-density plots. For structure **28-Ca"**, wavefunctions with (**28-Ca"**) and without (**28-Ca"-noH**) hydrogen bonding between triflate and the hydroxide motif were isolated.

Table 8. Bond Parameters (Measured in Å) from Computation

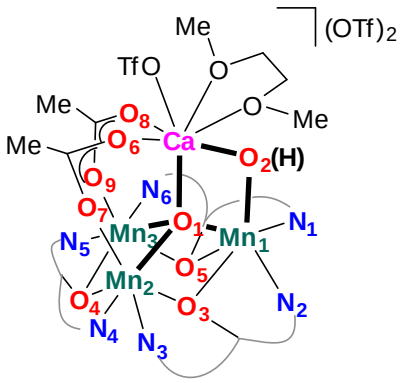

Bond	27-Ca (XRD)	27-Ca'	27-Ca"	28-Ca (XRD)	28-Ca'	28-Ca"	28-Ca"-noH
Mn2-N4	2.095	2.122	2.140	2.089	2.176	2.278	2.277
Mn2-N3	2.241	2.292	2.251	2.341	2.264	2.254	2.341
Mn2-O3	1.884	1.908	1.893	1.936	1.876	2.101	2.106
Mn2-O4	2.265	2.224	2.248	2.111	2.281	2.282	2.262
Mn2-O7	1.913	1.922	1.906	1.971	1.922	2.096	2.094
Mn2-O1	1.913	1.889	1.918	2.159	1.906	2.203	2.195
Mn3-N5	2.161	2.107	2.255	2.290	2.287	2.256	2.194
Mn3-N6	2.124	2.166	2.125	2.205	2.142	2.219	2.170
Mn3-O5	2.232	2.226	2.379	2.322	2.149	2.308	2.397
Mn3-O4	1.872	1.857	1.911	2.092	1.935	1.939	1.910
Mn3-O9	1.910	1.896	1.867	2.129	1.938	1.928	1.884
Mn3-O1	2.017	2.054	1.944	1.939	1.848	1.827	1.907
Mn1-N1	2.170	2.208	2.161	2.211	2.151	2.278	2.303
Mn1-N2	2.129	2.145	2.143	2.156	2.187	2.131	2.159
Mn1-O3	2.215	2.279	2.261	2.250	2.281	2.142	2.178
Mn1-O5	1.878	1.908	1.896	1.900	2.029	1.941	1.912
Mn1-O1	1.958	1.972	2.006	1.860	2.141	1.958	1.894
Mn1-O2	1.842	1.683	1.830	1.887	1.697	1.837	1.907
Ca1-O1	2.452	2.445	2.479	2.397	2.474	2.424	2.410
Ca1-O2	2.349	2.556	2.422	2.368	2.394	2.389	2.504
O2-OTf	2.742	--	2.692	2.847[a]	--	2.664	--

[a] In **28-Ca**, the OH ligand displayed a H-bonding interaction with a DME solvent molecule rather than a triflate anion.

Calculation of Mulliken Spin Populations

Mulliken population analysis was employed to assign oxidation states of all atoms based on the number of unpaired spins. The bridging alkoxides exhibited α spins on

the order of ~0.10 due to the highly covalent Mn-O bonds.* Spin on the remaining scaffold was found to be negligible (<0.02 α spins per remaining atoms). For **28-Ca"**, Mulliken spin population revealed an alternative oxidation state assignment in which Mn_2 is assigned as Mn(II) as Mn_3 is assigned as Mn(III).

Table 9. Mulliken Spin Populations.

Atom	27-Ca'	27-Ca"	28-Ca'	28-Ca"	28-Ca"-noH
Mn1	3.49	3.83	3.72	3.82	3.85
Mn2	3.87	3.87	3.88	3.86	3.87
Mn3	3.86	3.88	3.84	4.82	4.81
Ca1	0.01	0.00	0.00	0.00	0.00
O1	0.00	0.00	0.00	0.00	0.00
O2	-0.61	0.00	0.18	0.00	0.00

REFERENCES

(1) Fukuzumi, S. In *Progress in Inorganic Chemistry*; Karlin, K. D., Ed.; John Wiley & Sons Inc: New York, 2009; Vol. 56, p 49.

(2) Tsui, E. Y.; Kanady, J. S.; Agapie, T. *Inorg. Chem.* **2013**, *52*, 13833.

(3) Fukuzumi, S. *Chem. Lett.* **2008**, *37*, 808.

(4) Umena, Y.; Kawakami, K.; Shen, J. R.; Kamiya, N. *Nature* **2011**, *473*, 55.

(5) Yano, J.; Yachandra, V. *Chem. Rev.* **2014**, *114*, 4175.

(6) Suntivich, J.; Gasteiger, H. A.; Yabuuchi, N.; Nakanishi, H.; Goodenough, J. B.; Shao-Horn, Y. *Nat. Chem.* **2011**, *3*, 647.

(7) Suntivich, J.; May, K. J.; Gasteiger, H. A.; Goodenough, J. B.; Shao-Horn, Y. *Science* **2011**, *334*, 1383.

(8) Zaharieva, I.; Najafpour, M. M.; Wiechen, M.; Haumann, M.; Kurz, P.; Dau, H. *Energy Environ. Sci.* **2011**, *4*, 2400.

(9) Risch, M.; Klingan, K.; Ringleb, F.; Chernev, P.; Zaharieva, I.; Fischer, A.; Dau, H. *Chemsuschem* **2012**, *5*, 542.

(10) Wiechen, M.; Zaharieva, I.; Dau, H.; Kurz, P. *Chem. Sci.* **2012**.

(11) Najafpour, M. M.; Pashaei, B.; Nayeri, S. *Dalton Trans.* **2012**, *41*, 4799.

(12) Najafpour, M. M.; Ehrenberg, T.; Wiechen, M.; Kurz, P. *Angew. Chem. Int. Ed.* **2010**, *49*, 2233.

(13) Lau, T. C.; Mak, C. K. *J. Chem. Soc. Chem. Comm.* **1993**, 766.

(14) Lau, T. C.; Wu, Z. B.; Bai, Z. L.; Mak, C. K. *J. Chem. Soc. Dalton Trans.* **1995**, 695.

(15) Ho, C. M.; Lau, T. C. *New J. Chem.* **2000**, *24*, 587.

(16) Lai, S.; Lee, D. G. *Tetrahedron* **2002**, *58*, 9879.

(17) Yiu, S. M.; Wu, Z. B.; Mak, C. K.; Lau, T. C. *J. Am. Chem. Soc.* **2004**, *126*, 14921.

(18) Yiu, S. M.; Man, W. L.; Lau, T. C. *J. Am. Chem. Soc.* **2008**, *130*, 10821.

(19) Du, H. X.; Lo, P. K.; Hu, Z. M.; Liang, H. J.; Lau, K. C.; Wang, Y. N.; Lam, W. W. Y.; Lau, T. C. *Chem. Commun.* **2011**, *47*, 7143.

(20) Miller, C. G.; Gordon-Wylie, S. W.; Horwitz, C. P.; Strazisar, S. A.; Peraino, D. K.; Clark, G. R.; Weintraub, S. T.; Collins, T. J. *J. Am. Chem. Soc.* **1998**, *120*, 11540.

(21) Fukuzumi, S.; Morimoto, Y.; Kotani, H.; Naumov, P.; Lee, Y. M.; Nam, W. *Nat. Chem.* **2010**, *2*, 756.

(22) Morimoto, Y.; Kotani, H.; Park, J.; Lee, Y. M.; Nam, W.; Fukuzumri, S. *J. Am. Chem. Soc.* **2011**, *133*, 403.

(23) Yoon, H.; Lee, Y. M.; Wu, X.; Cho, K. B.; Sarangi, R.; Nam, W.; Fukuzumi, S. *J. Am. Chem. Soc.* **2013**, *135*, 9186.

(24) Bang, S.; Lee, Y. M.; Hong, S.; Cho, K. B.; Nishida, Y.; Seo, M. S.; Sarangi, R.; Fukuzumi, S.; Nam, W. *Nat. Chem.* **2014**, *6*, 934.

(25) Park, J.; Morimoto, Y.; Lee, Y. M.; Nam, W.; Fukuzumi, S. *Inorg. Chem.* **2014**, *53*, 3618.

(26) Lionetti, D.; Agapie, T. *Nature* **2014**, *513*, 495.

(27) Fukuzumi, S.; Morimoto, Y.; Kotani, H.; Naumov, P.; Lee, Y.-M.; Nam, W. *Nat. Chem.* **2010**, *2*, 756.

(28) Park, J.; Morimoto, Y.; Lee, Y. M.; Nam, W.; Fukuzumi, S. *J. Am. Chem. Soc.* **2011**, *133*, 5236.

(29) Lee, Y. M.; Bang, S.; Kim, Y. M.; Cho, J.; Hong, S.; Nomura, T.; Ogura, T.; Troeppner, O.; Ivanovic-Burmazovic, I.; Sarangi, R.; Fukuzumi, S.; Nam, W. *Chem. Sci.* **2013**, *4*, 3917.

(30) Nam, W.; Lee, Y. M.; Fukuzumi, S. *Acc. Chem. Res.* **2014**, *47*, 1146.

(31) Li, F. F.; Van Heuvelen, K. M.; Meier, K. K.; Munck, E.; Que, L. *J. Am. Chem. Soc.* **2013**, *135*, 10198.

(32) Chen, J.; Lee, Y. M.; Davis, K. M.; Wu, X.; Seo, M. S.; Cho, K. B.; Yoon, H.; Park, Y. J.; Fukuzumi, S.; Pushkar, Y. N.; Nam, W. *J. Am. Chem. Soc.* **2013**, *135*, 6388.

(33) Park, Y. J.; Ziller, J. W.; Borovik, A. S. *J. Am. Chem. Soc.* **2011**, *133*, 9258.

(34) Park, Y. J.; Cook, S. A.; Sickerman, N. S.; Sano, Y.; Ziller, J. W.; Borovik, A. S. *Chem. Sci.* **2013**, *4*, 717.

(35) Yin, Y. D.; Wang, P.; Yang, X. X.; Li, X.; He, C.; Sheng, X. *Chem. Commun.* **2012**, *48*, 7413.

(36) Dong, L.; Wang, Y. J.; Lv, Y. Z.; Chen, Z. Q.; Mei, F. M.; Xiong, H.; Yin, G. C. *Inorg. Chem.* **2013**, *52*, 5418.

(37) Swart, M. *Chem. Commun.* **2013**, *49*, 6650.

(38) Prakash, J.; Rohde, G. T.; Meier, K. K.; Jasniewski, A. J.; Van Heuvelen, K. M.; Munck, E.; Que, L. *J. Am. Chem. Soc.* **2015**, *137*, 3478.

(39) Tsui, E. Y.; Tran, R.; Yano, J.; Agapie, T. *Nat. Chem.* **2013**, *5*, 293.

(40) Tsui, E. Y.; Agapie, T. *Proc. Natl. Acad. Sci. USA* **2013**, *110*, 10084.

(41) Kanady, J. S.; Tsui, E. Y.; Day, M. W.; Agapie, T. *Science* **2011**, *333*, 733.

(42) Lin, P. H.; Takase, M. K.; Agapie, T. *Inorg. Chem.* **2015**, *54*, 59.

(43) Suseno, S.; Agapie, T., *Manuscript in preparation*.

(44) Singh, A.; Spiccia, L. *Coord. Chem. Rev.* **2013**, *257*, 2607.

(45) Bockris, J. O.; Otagawa, T. *J. Electrochem. Soc.* **1984**, *131*, 290.

(46) Cheng, F. Y.; Chen, J. *Chem. Soc. Rev.* **2012**, *41*, 2172.

(47) Neburchilov, V.; Wang, H. J.; Martin, J. J.; Qu, W. *J. Power Sources* **2010**, *195*, 1271.

(48) Tsui, E. Y.; Day, M. W.; Agapie, T. *Angew. Chem. Int. Ed.* **2011**, *50*, 1668.

(49) Tsui, E. Y.; Kanady, J. S.; Day, M. W.; Agapie, T. *Chem. Commun.* **2011**, *47*, 4189.

(50) Reynolds, R. A.; Coucouvanis, D. *Inorg. Chem.* **1998**, *37*, 170.

(51) Schmitt, W.; Anson, C. E.; Pilawa, B.; Powell, A. K. *Z. Anorg. Allg. Chem.* **2002**, *628*, 2443.

(52) Chardon-Noblat, S.; Horner, O.; Chabut, B.; Avenier, F.; Debaecker, N.; Jones, P.; Pecaut, J.; Dubois, L.; Jeandey, C.; Oddou, J. L.; Deronzier, A.; Latour, J. M. *Inorg. Chem.* **2004**, *43*, 1638.

(53) Singh, A. K.; Jacob, W.; Boudalis, A. K.; Tuchagues, J. P.; Mukherjee, R. *Eur. J. Inorg. Chem.* **2008**, 2820.

(54) Lalia-Kantouri, M.; Papadopoulos, C. D.; Hatzidimitriou, A. C.; Bakas, T.; Pachini, S. *Z. Anorg. Allg. Chem.* **2010**, *636*, 531.

(55) Horwitz, C. P.; Ciringh, Y. *Inorg. Chim. Acta* **1994**, *225*, 191.

(56) Ghanotakis, D. F.; Babcock, G. T.; Yocum, C. F. *FEBS Lett.* **1984**, *167*, 127.

(57) Perrin, D. D. *Ionisation Constants of Inorganic Acids and Bases in Aqueous Solution*; Pergamon Press: New York, 1982.

(58) Hawkes, S. J. *J. Chem. Educ.* **1996**, *73*, 516.

(59) Bochevarov, A. D.; Harder, E.; Hughes, T. F.; Greenwood, J. R.; Braden, D. A.; Philipp, D. M.; Rinaldo, D.; Halls, M. D.; Zhang, J.; Friesner, R. A. *Int. J. Quantum Chem.* **2013**, *113*, 2110.

(60) Warren, J. J.; Tronic, T. A.; Mayer, J. M. *Chem. Rev.* **2010**, *110*, 6961.

(61) Kaljurand, I.; Kutt, A.; Soovali, L.; Rodima, T.; Maemets, V.; Leito, I.; Koppel, I. A. *J. Org. Chem.* **2005**, *70*, 1019.

(62) Herbert, D. E.; Lionetti, D.; Rittle, J.; Agapie, T. *J. Am. Chem. Soc.* **2013**, *135*, 19075.

(63) Haav, K.; Saame, J.; Kutt, A.; Leito, I. *Eur. J. Org. Chem.* **2012**, 2167.

(64) Kanady, J. S.; Mendoza-Cortes, J. L.; Tsui, E. Y.; Nielsen, R. J.; Goddard, W. A.; Agapie, T. *J. Am. Chem. Soc.* **2013**, *135*, 1073.

(65) Lionetti, D.; Suseno, S.; Tsui, E. Y.; Lu, L.; Britt, R. D.; Carsch, K. M.; Agapie, T., *Manuscript in preparation*.

(66) Perrin, D. D.; International Union of Pure and Applied Chemistry. Commission on Equilibrium Data. *Ionisation constants of inorganic acids and bases in aqueous solution*; 2nd ed.; Pergamon Press: Oxford Oxfordshire ; New York, 1982.

(67) Forsberg, J. H.; Spaziano, V. T.; Balasubramanian, T. M.; Liu, G. K.; Kinsley, S. A.; Duckworth, C. A.; Poteruca, J. J.; Brown, P. S.; Miller, J. L. *J. Org. Chem.* **1987**, *52*, 1017.

(68) Manner, V. W.; Markle, T. F.; Freudenthal, J. H.; Roth, J. P.; Mayer, J. M. *Chem. Commun.* **2008**, 256.

(69) *APEX2, Version 2 User Manual, M86-E01078,*; Bruker Analytical X-ray Systems: Madison, WI, June 2006.

(70) Sheldrick, G. M., "SADABS (version 2008/1): Program for Absorption Correction for Data from Area Detector Frames", University of Göttingen, 2008

(71) Sheldrick, G. M. *Acta Crystallogr., Sect. A: Found. Crystallogr.* **2008**, *64*, 112.

(72) Spek, A. L., "PLATON – A Multipurpose Crystallographic Tool", Utrecht University, Utrecht, The Netherlands, 2006

(73) Spek, A. L. *Acta Crystallogr., Sect. C: Cryst. Struct. Commun.* **2015**, *71*, 9.

(74) Becke, A. D. *J. Chem. Phys.* **1993**, *98*, 5648.

(75) Becke, A. D. *Phys. Rev. A* **1988**, *38*, 3098.

(76) Lee, C. T.; Yang, W. T.; Parr, R. G. *Phys. Rev. B* **1988**, *37*, 785.

(77) Grimme, S. *J. Chem. Phys.* **2006**, *124*.

(78) Francl, M. M.; Pietro, W. J.; Hehre, W. J.; Binkley, J. S.; Gordon, M. S.; DeFrees, D. J.; Pople, J. A. *J. Chem. Phys.* **1982**, *77*, 3654.

(79) Hehre, W. J.; Ditchfield, R.; Pople, J. A. *J. Chem. Phys.* **1972**, *56*, 2257.

APPENDIX A

TARGETING HETERONUCLEAR CLUSTERS FOR THE STUDY OF HETEROMETALLIC EFFECTS ON SMALL-MOLECULE ACTIVATION

Abstract

The study of the interactions between different metal centers in heterometallic complexes and their effects on activation of small molecules can provide insight into the mechanism of the reactivity with similar substrates of heterometallic assemblies found in biological active sites and heterogeneous catalysts. In order to accurately model these systems, strategies to rationally target different structural motifs with heteronuclear metal clusters are needed. Various novel synthetic protocols have been developed to attempt to access new classes of cluster complexes supported by a multidentate ligand framework. Incorporation of several new supporting ligands into cluster structures was targeted to provide suitable precursors to study small-molecule activation and develop systematic approaches to the study of heterometallic effects on these processes. Despite several unsuccessful results, a handful of new classes of compounds were isolated and characterized displaying novel structural motifs, including new supporting ligands (pyrazolates, oximates) and bridging ligands (sulfide, nitride). The reactivity of some of these compounds with substrates (e.g. O_2) was explored. These studies have contributed to the expansion of the library of clusters available for the study of reactivity of multimetallic complexes and have provided new synthetic protocols to complement the previously reported strategies for cluster synthesis.

INTRODUCTION

The rational synthesis of discrete metal clusters is an attractive target due to the role of multimetallic complexes in both natural enzymes and heterogeneous catalysis.[1-7] Enzymes utilize multimetallic active sites to facilitate small-molecule transformations that require the transfer of multiple electrons. In heterogeneous materials such as the mixed-metal oxides that catalyze the reduction of dioxgyen and the oxidation of water, cooperative reactivity between different metal centers is proposed to play an important role in catalysis.[4,8,9] Understanding how metal-metal interactions influence the properties and the reactivity of multimetallic clusters is key to designing new catalysts for the activation and transformation of small molecules.

Efforts in targeting discrete heteromultimetallic complexes have often relied on self-assembly of clusters from mixtures of metal salts and organic ligands. In a number of cases, this strategy has been successful at providing discrete models of enzymatic or heterogeneous active sites,[7,10-12] as in the case of the [Mn_5CaO_4] cluster recently reported by Zhang and coworkers as a model of the oxygen evolving complex (OEC) of Photosystem II (PSII).[13] Nonetheless, self-assembly synthetic protocols fail to reliably provide adequate control on the structure of the resulting complexes and on the stoichiometry of metals and ligands that are incorporated in these assemblies. These shortcomings make structure-function relationship studies on multimetallic systems extremely challenging, as systematically effecting changes to either ligand or metal stoichiometry or to structural motifs may require entirely different protocols. As a result, synthetic efforts towards multimetallic clusters have increasingly relied on multinucleating ligand scaffolds which can arrange multiple metal centers in close proximity, facilitating cooperative reactivity.[11,14-20] Introduction of systematic changes

in multimetallic complexes via this strategy is facilitated by the control over metal identity and structure afforded by the multinucleating platform, which can bias the system towards formation of specific desired complexes.

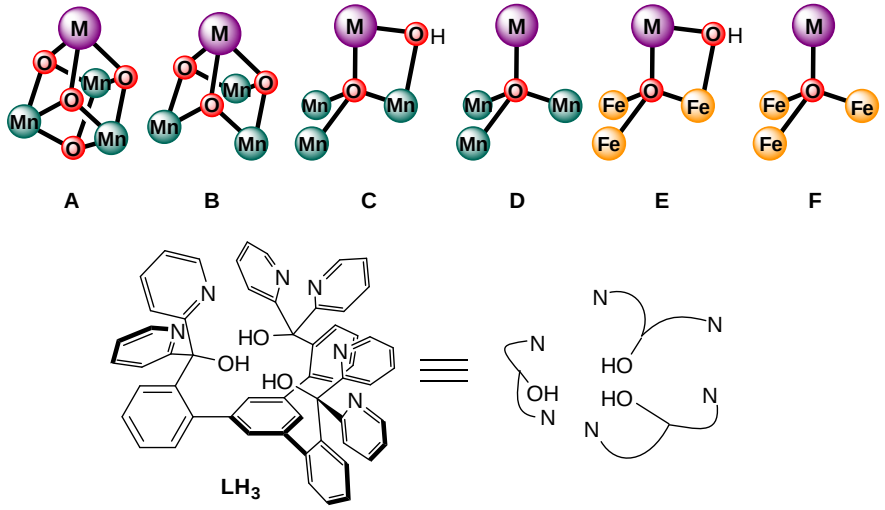

Figure 1. Metal-oxo structural motifs supported by the multinucleating ligand platform **L**.

In our group, we have successfully employed a multinucleating ligand framework (**LH_3**, Figure 1) bearing six pyridine and three alkoxide donors to support numerous multinuclear metal-oxo clusters. Complexes with different structural motifs, metal composition, and extent of oxygen atom incorporation were accessed via modulation of the reaction conditions.[19-28] In several cases, isostructural complexes were synthesized in which only the metal center in a specific site was varied, affording series of clusters in which the effects of metal composition on cluster properties (such as redox potential and group transfer reactivity) could be explored. Through the study of three separate series of heterometallic clusters – [Mn_3MO_4] 'cubane' complexes (**A**, Figure 1), and [$Mn_3MO(OH)$] and [$Fe_3MO(OH)$] oxo-hydroxo complexes (**C**, **E**) – it was shown that the redox potential of these clusters could be tuned by varying the Lewis acidity of the apical heterometal, with potentials shifting positively with

increasing Lewis acidity of this metal center.[21,23,24,26,28,29] Likewise, Lewis acidity was shown to affect the rate of oxygen atom transfer from these clusters to phosphine substrates.[30]

The clusters that have been previously studied in our group provided insight into some of the metal-metal interactions that might play a role in the activity of heterometallic systems in both biology and heterogeneous catalysis. Tuning of redox potential has been proposed as one of the roles for the Ca^{2+} center in the OEC,[6] and redox-inactive metal cations have also been observed to influence the activity of mixed-metal oxide catalysts for the oxygen evolution reaction (OER) and the oxygen reduction reaction (ORR).[8] With an interest in expanding the library of complexes to extend the range of structural motifs and metal compositions that could be accessed and studied for their properties and reactivity, further studies on the synthesis of clusters supported by the same multinucleating ligand framework were undertaken. In particular, clusters were targeted that might provide useful insight into the mechanism of the activation and conversion of small molecules by heterometallic systems.

Two general approaches were developed to synthesize clusters for the study of small molecule reactivity. First, clusters designed to model the mixed-metal heterogeneous materials involved in processes such as the ORR were targeted. This strategy involved desymmetrization of previously characterized clusters (most of which have *pseudo*-C_3 symmetry) and unveiling of a heterometallic, dinuclear edge site within the cluster (Scheme 1a) to explore the effects of changes in the complex (oxidation state, metal composition) on the reactivity with small molecules at this site. The second strategy was designed to target tetranuclear complexes in which small-molecule reactivity would take place at an open coordination site on the apical metal, and the effects of various

structural elements (supporting ligands, μ_4 bridging ligand, metal identity and oxidation state, etc.) on this reactivity would be studied (Scheme 1b). Via this approach, the trimetallic core and the four bridging ligands will be considered in practical terms as a 'tetradentate ligand' for the apical metal, with the ability to store reducing or oxidizing equivalents into the three metal centers in the 'ligand' core. Efforts to develop the desired synthetic protocols to access these clusters and to study their reactivity will be described herein.

Scheme 1. Proposed Strategies for Targeting of New Heterometallic Tetranuclear Clusters: (a) Edge Site Reactivity; (b) Reactivity at Apical Metal.

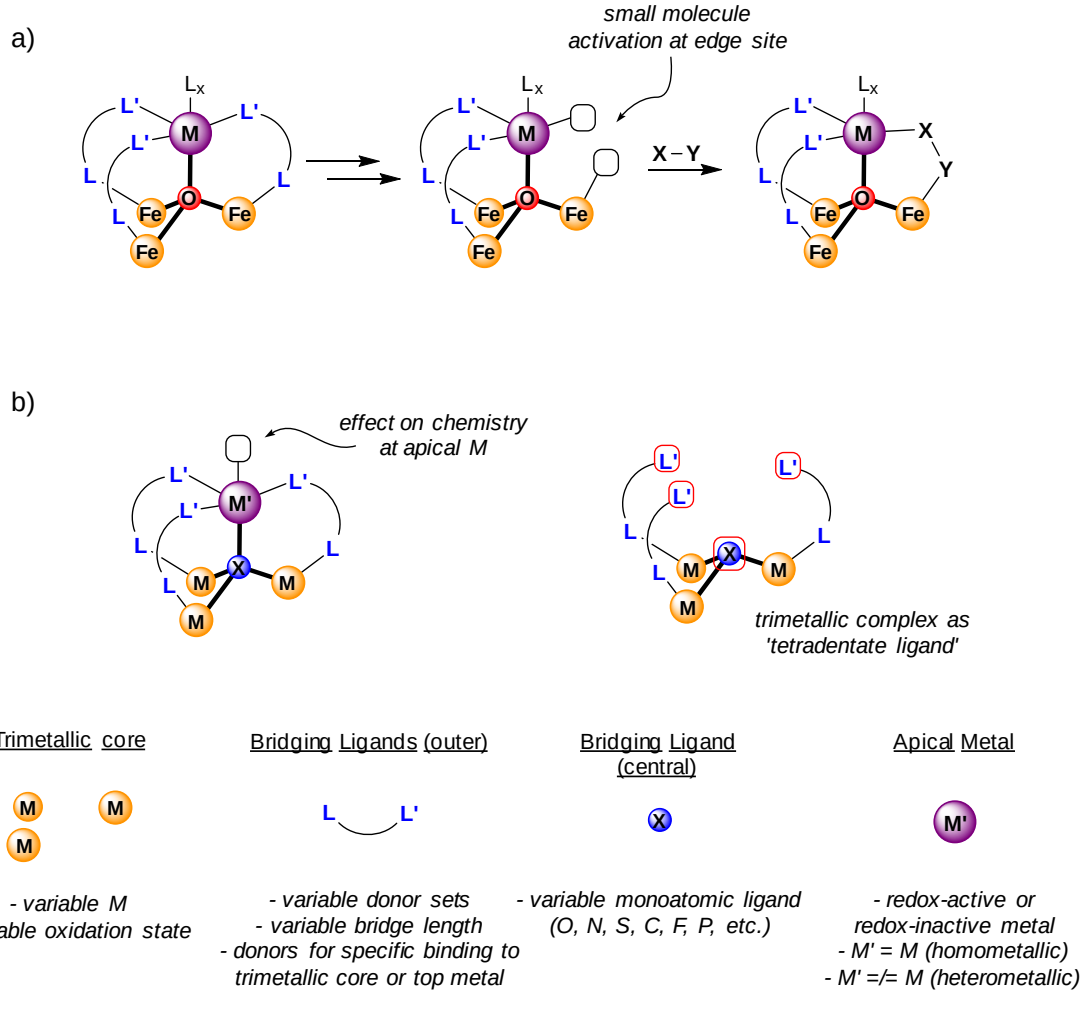

RESULTS AND DISCUSSION

Clusters for Edge Site Reactivity

As the desire for carbon-neutral, environmentally friendly sources of energy has increased, much interest in the scientific community has focused on devices capable of generating electrical current from renewable fuels that generate harmless byproducts.[31,32] In a H_2-fueled fuel cell, use of dioxygen from air as terminal oxidant yields water as the only chemical product of fuel cell operation. The oxygen reduction reaction (ORR) is therefore a key transformation for the generation of power from fuel cells, and efficient catalysis of the reduction of O_2 to H_2O would improve the overall efficiency of such a device. Although mixed-metal oxide materials – based on both transition and redox-inactive metals – have been studied as inexpensive alternatives for O_2 reduction catalysis, mechanistic studies that could inform the design of new materials have been lacking.[33-36]

Scheme 2. Synthesis of [Fe_3ZnO] Clusters and Reactivity with O_2.

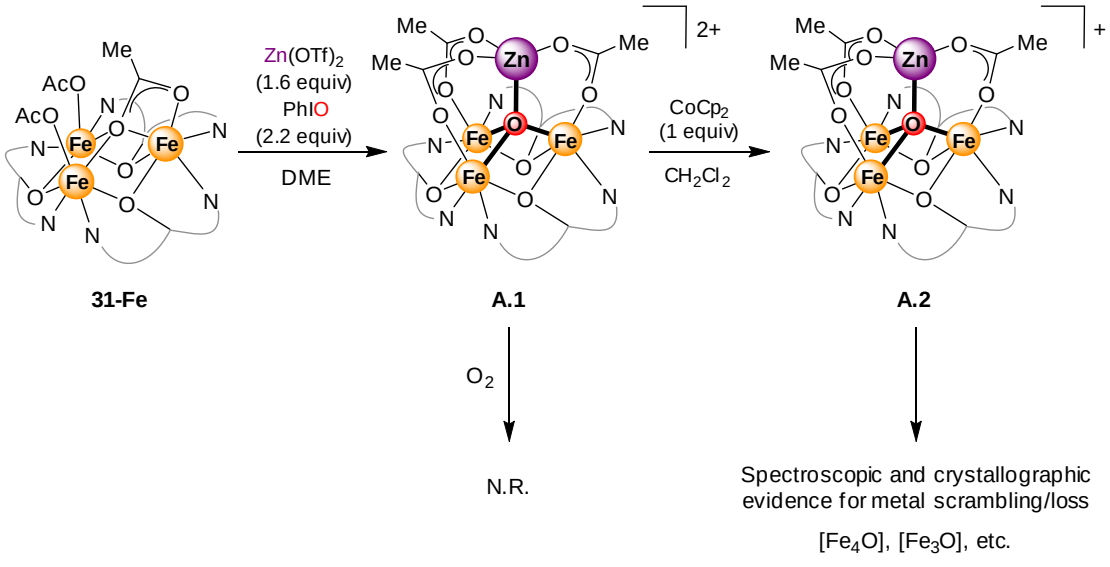

It was envisioned that the edge sites obtained by removal of a supporting ligand from tetranuclear, homo- and heterometallic clusters could serve as mimics of binuclear

sites within extended metal oxide materials, and might therefore afford useful insight on the mechanism of the activation of small molecules such as O_2. Complex **A.1**, a [Fe_3ZnO] cluster previously characterized in our group by Dr. David E. Herbert, was chosen as an initial target due to the several reports of iron oxides capable of O_2 reduction.[8] Complex **A.1** was synthesized from [Fe^{II}_3] precursor **31-Fe** in the [$Fe^{III}_2Fe^{II}$] oxidation state, and the one-electron reduced [$Fe^{III}Fe^{II}_2$] complex (**A.2**) could be accessed via reduction with cobaltocene ($CoCp_2$, Scheme 2). While oxidized cluster **A.1** was unreactive towards O_2 at room temperature, exposure of **A.2** to O_2 resulted in observation of several new species by proton nuclear magnetic resonance (^{1}H NMR) spectroscopy. The increased reactivity of **A.2** was likely due to its more negative oxidation potential or to the greater lability of its acetate ligands. Although the appearance and disappearance of several intermediate species could be observed by ^{1}H NMR, reaction of **A.2** with O_2 eventually led to species which displayed electrospray ionization mass spectrometry (ESI-MS) features consistent with loss of the Zn^{2+} center as well as metal scrambling (i.e. replacement of Zn^{2+} in the apical site by Fe^{n+}). These observations were corroborated by preliminary X-ray diffraction (XRD) studies on crystalline samples obtained from the products of this reaction.

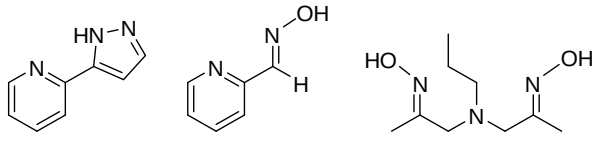

A.3 **A.4** **A.5**

Figure 2. Ligand precursors used for substitution of acetates in [Fe_3MO] clusters.

The observed decomposition of **A.2** indicated that the cluster scaffold was insufficiently robust to withstand reaction with O_2. To reinforce the [Fe_3ZnO] core in **A.1**-**2**, substitution of one or more of the supporting acetate groups in these clusters

with ligands bearing additional donor moieties was targeted. Oximate and pyrazolate groups had been previously shown to substitute carboxylate groups and bridge between a core metal center and the apical site in related Mn clusters. Therefore, pyrazole **A.3** and oxime **A.4**, each bearing an additional pyridine donor for further binding to the apical metal center, were studied.

Scheme 3. Introduction of Oximate and Pyrazolate Ligands in [Fe_3ZnO] Clusters.

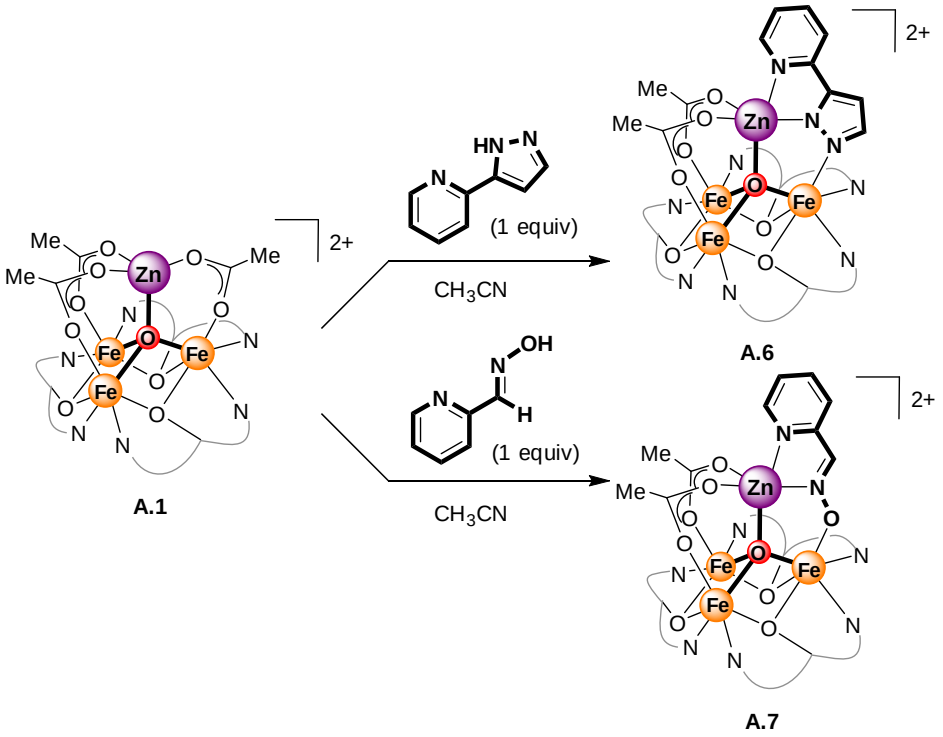

Attempts to carry out ligand substitution with complex **A.2** were unsuccessful in yielding pure materials. On the other hand, reaction of **A.3** and **A.4** with complex **A.1** resulted in generation of pure, asymmetric species as observed by ^{1}H NMR. ESI-MS data for these reactions was also consistent with protonolysis of an $^-$OAc group by **A.3** and **A.4** to form the pyrazolate and oximate complexes **A.6** and **A.7**, respectively. Reduction of these clusters with $CoCp_2$ led to a change in color from brown to dark

purple, similar to the color changes observed upon reduction of **A.1** to **A.2**. ^{1}H NMR spectra of these products were consistent with formation of new asymmetric species.

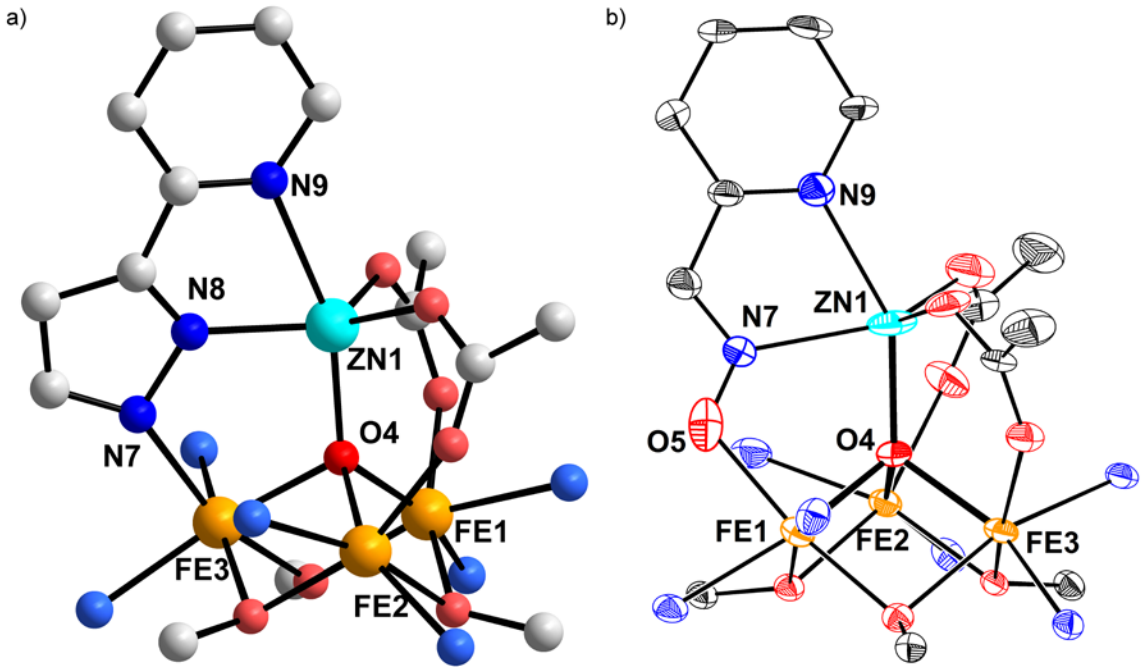

Figure 3. Solid-state structures of (a) **A.8** and (b) **A.9**. Hydrogen atoms, outer sphere anions, and part of the multinucleating ligand scaffold omitted for clarity. Ellipsoids shown at 50% probability. Only one of the two oximate orientations with approximate equal occupancy shown in (b). See Experimental Section for details.

Characterization of these reduced products by XRD showed that the clusters displayed the desired structures, with the pyrazolate and oximate ligands having substituted one of the acetate bridges (Figure 3). The Zn center, four-coordinate in **A.1**, was five-coordinate in both **A.8** and **A.9** due to binding of the additional pyridine donor on the pyrazolate/oximate ligands. As observed in oxo-hydroxo clusters **32-M** and **33-M**, Fe–(μ_4-O) distances in these complexes could be used as reporters of Fe oxidation state. In the solid-state structure of **A.8**, two Fe–(μ_4-O) distances were elongated with respect to the third one (2.162 and 2.089 Å vs. 1.936 Å), indicative of two Fe^{II} sites and one Fe^{III} center (see Table 1 for extensive comparison of Fe–O bond distances).

However, due the disorder over two positions of the oximate group in **A.9** (better quality of the overall structure notwithstanding), analysis of the Fe–(μ_4-O) distances was impossible. Nonetheless, the balancing of the charges in this structure was consistent with the proposed oxidation state of the Fe centers as [$Fe^{III}Fe^{II}_2$].

Scheme 4. Reduction of Asymmetric [Fe_3ZnO] Clusters and Their O_2 Reactivity.

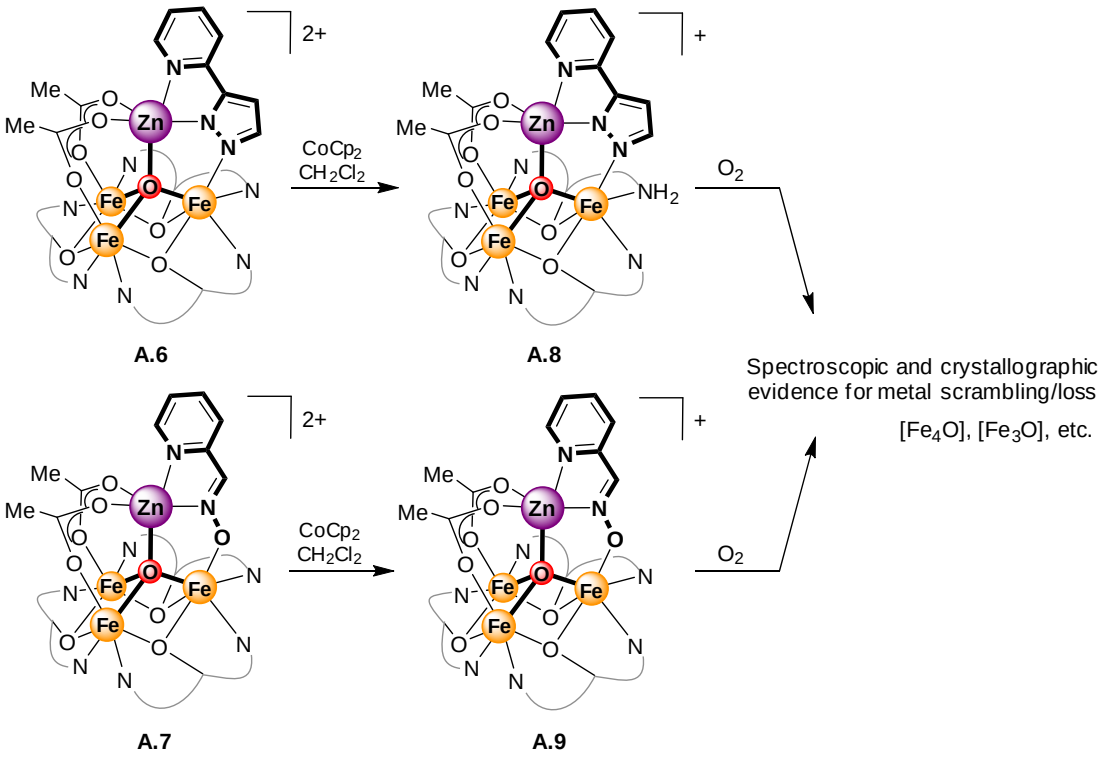

Unfortunately, substitution of $^{-}$OAc for ligands with larger non-polar substituents in **A.8** and **A.9** led to a shift in their solubility – unlike **A.2**, **A.8** and **A.9** were very soluble in tetrahydrofuran (THF), making separation of the clusters from the byproduct of reduction ($CoCp_2^+$) impossible – in fact, [CoCp][OTf] was observed in the solid-state structure of **A.9**. The reactivity of these complexes with O_2 was nonetheless studied, accounting for the presence of $CoCp_2^+$. Unfortunately, results were similar to the studies of all-acetate cluster **A.2**, with evidence of decomposition of the cluster (especially loss of Zn^{2+}) observed by ESI-MS. Clearly, the addition of a donor moiety

to a single bridging ligand did not provide sufficient stabilization for the tetrametallic core.

Attempts to introduce a second equivalent of oximate or pyrazolate ligand were unsuccessful – binding of a second pyridine donor to Zn in **A.8** and **A.9** was impossible due to the steric hindrance from the pyridine moiety from the first bound ligand. Therefore, a new supporting ligand was targeted that could substitute two $^{-}$OAc groups and provide additional donor(s) for the apical Zn center. Bis(oxime) **A.5** (Figure 2) has been previously reported to chelate to Ni^{II} centers via its three N donors while leaving the oxime moieties protonated, indicating that it could be possible to chelate the apical metal in a tetranuclear cluster with the three N donors in **A.5**, and for the two oximate groups to bridge to the basal metals in the cluster.[37] Reaction of **A.5** with **A.1** resulted in conversion to a single new species by ^{1}H NMR. ESI-MS data was consistent with substitution of two $^{-}$OAc ligands by the bis(oximate) scaffold (Scheme 5). Characterization via XRD confirmed formation of the bis(oximate)-substituted cluster **A.10** (Figure 4). Notably, the Fe–(μ_4-O) bond distance for the Fe still bound to an $^{-}$OAc was ~0.13 Å longer than the ones for Fe centers coordinated to the oximate groups (Table 1). This observation was consistent with the [$Fe^{III}_2Fe^{II}$] oxidation state of the cluster, and also indicated that the more oxidized Fe centers were bound to the more electron-rich oximate groups (vs. the more electron-poor acetate).

One-electron reduction of **A.10** with $CoCp_2$ led to conversion to [$Fe^{III}Fe^{II}_2$] cluster **A.11** as observed by ^{1}H NMR, providing the desired cluster for exploration of O_2 reactivity. Exposure of **A.11** to O_2, however, led to complete recovery of the 1-e^{-} oxidized cluster **A.10**. This result confirmed that the two-armed oximate ligand imparted sufficient stability to the tetrametallic core to undergo O_2 reactivity without

metal loss or metal scrambling. However, the observation of a 1-e⁻ process to return the cluster to its oxidized state indicated that the complex could simply be involved in outer-sphere electron transfer rather than binding and activation of O_2.

Scheme 5. Synthesis and Reactivity of Bis(oximate)-Substituted Clusters.

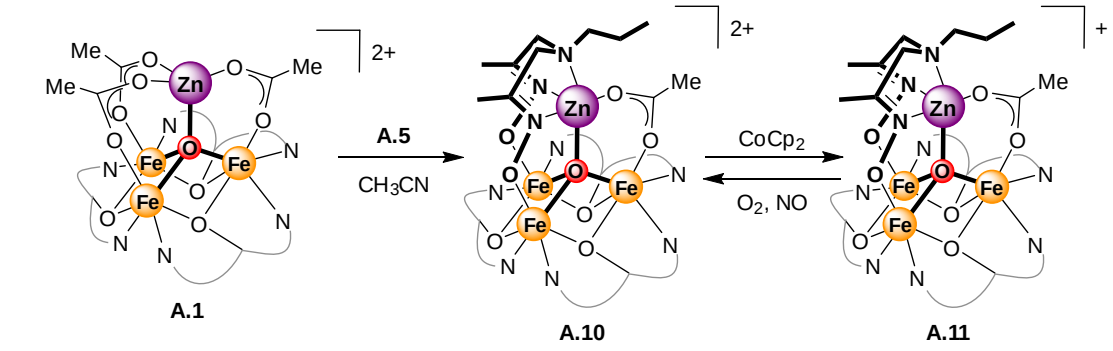

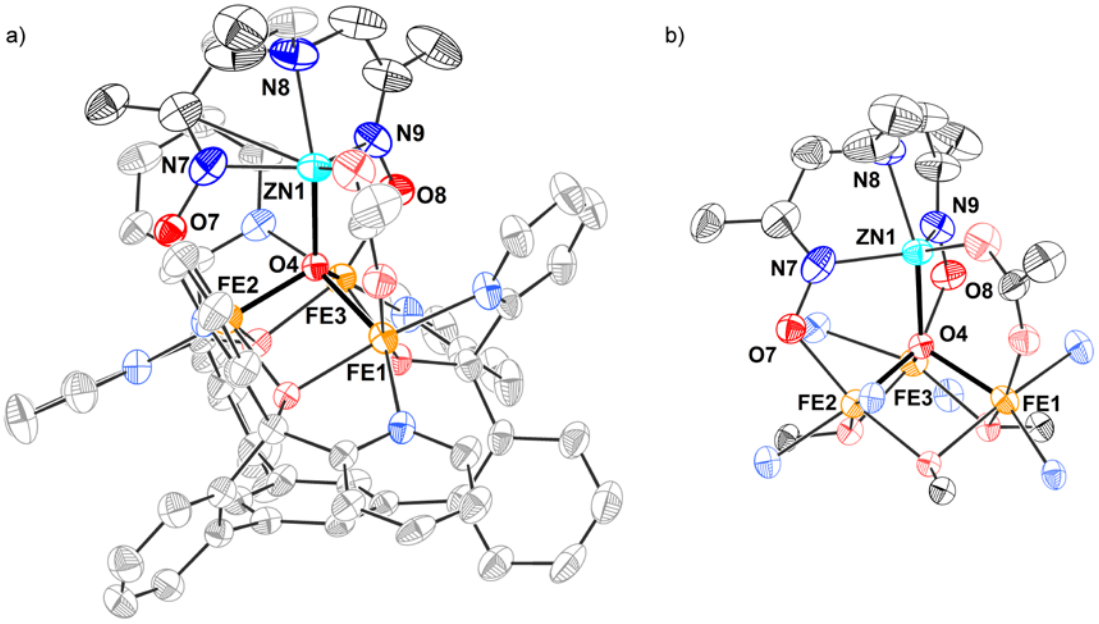

Figure 4. (a) Solid-state structure of **A.10**, hydrogen atoms, outer-sphere anions, and solvent molecules omitted for clarity; (b) cropped representation highlighting the tetrametallic core. Thermal ellipsoids shown at the 50% probability level.

It was hypothesized that if the acetate ligand in **A.11** was bound too strongly to either Fe or Zn, outer-sphere electron transfer would be favored due to the lack of a binding site at Fe or of an open site on Zn to stabilize a partially reduced species. In an

attempt to favor an inner-sphere process, abstraction of the remaining $^{-}$OAc ligand on **A.11** was targeted to provide the open edge site for O_2 activation. Reaction of **A.11** with trimethylsilyltriflate ($(CH_3)_3SiOTf$), previously shown to be a suitable reagent for abstraction of acetate ligands on $[Mn_4O_4]$ cubane clusters,[22] led to formation of **A.10** via oxidation by $[(CH_3)_3Si]^+$ (Scheme 6). Due to instability of **A.11** towards oxidation, milder abstracting agents (e.g. metal salts such as $Zn(OTf)_2$) could not be employed as their reactivity with **A.11** was too slow to afford new species before significant decomposition to **A.10** was observed. Use of methyl triflate (MeOTf), however, yielded promising results. Treatment with MeOTf, a strong electrophile but a poorer oxidant than $(CH_3)_3SiOTf$, gave rise to a new set of ^{1}H NMR features in ~120 minutes. Although formation of a small amount of **A.10** was also observed, it was not expected to contribute to reactivity, and preliminary reactivity studies of putative triflate cluster **A.12** were undertaken with this mixture. Reaction with O_2 led to the disappearance of all ^{1}H NMR features assigned to **A.12**, but no product could be identified. On the other hand, **A.12** did not react with pyridine, which had previously been used to stabilize the product of acetate abstraction from a cubane cluster.

Scheme 6. Attempts at Abstraction of an Acetate Ligand from **A.11**.

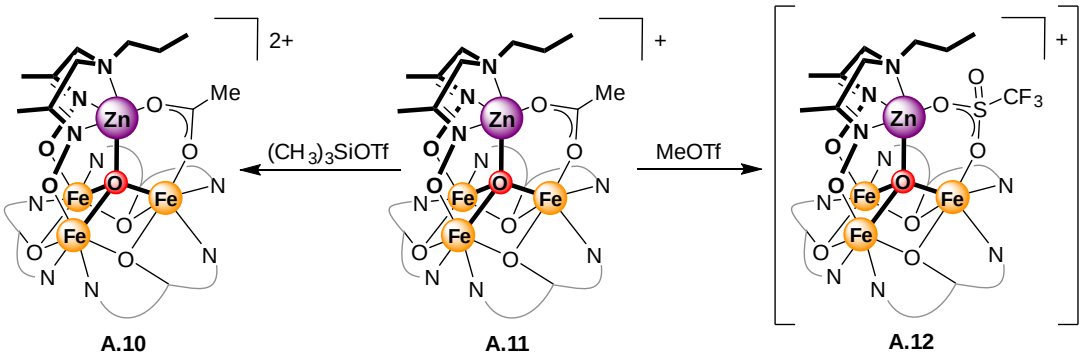

Finally, reactivity of **A.11** with nitric oxide (NO) was explored to determine whether a different substrate could yield more promising results. Treatment of **A.11** with ~1 equiv. NO led to complete conversion to oxidized cluster **A.10** in ~2 hours. Consistent with O_2 reactivity, this process likely occurred through outer-sphere electron transfer. Detection of the products of NO reduction (likely N_2O and NO_2^-, the products of reductive disproportionation) was not attempted. Notably, the all-acetate parent cluster **A.2** was also shown to react with NO. Partial conversion of **A.2** to a new asymmetric species was observed in the presence of an excess of NO (~15 equiv.). Evacuation of the reaction solution led to partial regeneration of **A.2**, consistent with a reversible process – likely binding of NO. Only over longer periods of time (several hours) in the presence of NO did **A.2** show evidence of further reactivity, indicating possible electron transfer. The difference in the reactivity between **A.11** and **A.2** with NO was likely due to the more electron-rich nature of the bis(oximate) ligand in **A.11** making this complex more reducing and leading to more facile electron transfer to NO.

The lack of a viable protocol to remove the last acetate group from **A.11**, notwithstanding the successful desymmetrization of the cluster, precluded any further studies of the reactivity of this product. Other bis(oximate) ligands were briefly investigated, but with no structural characterization of the respective bis(oximate)-bound cluster species these investigations could not be furthered.

Concurrently with the studies on [Fe_3ZnO] clusters, investigations into the synthesis of analogous homometallic [Fe_4O] monooxo complexes were undertaken. The formation of [Fe_4] clusters had previously been observed as decomposition products of other species, such as [Fe_3Zn] clusters. A low-quality structure of [Fe_4] complex **A.13**

had been obtained by Dr. David E. Herbert by crystallization of the product of transmetallation from [Fe_3NaO] cluster **A.14** (Scheme 7).

Scheme 7. Synthetic Protocols for Preparation of [Fe_4O] Cluster **A.13**.

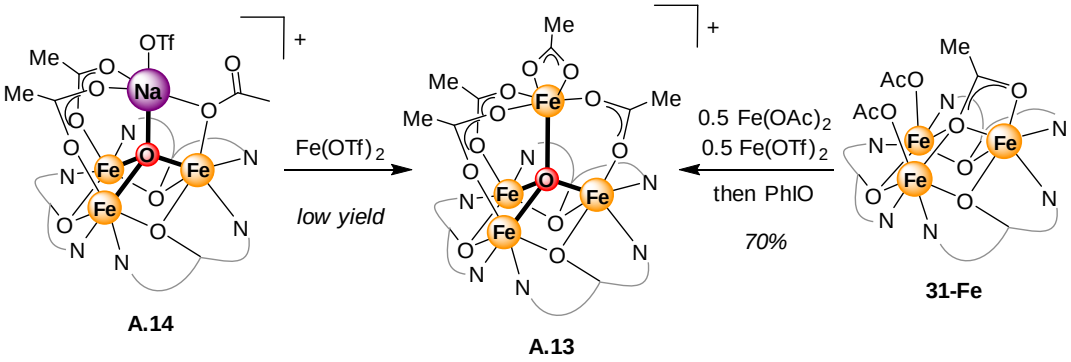

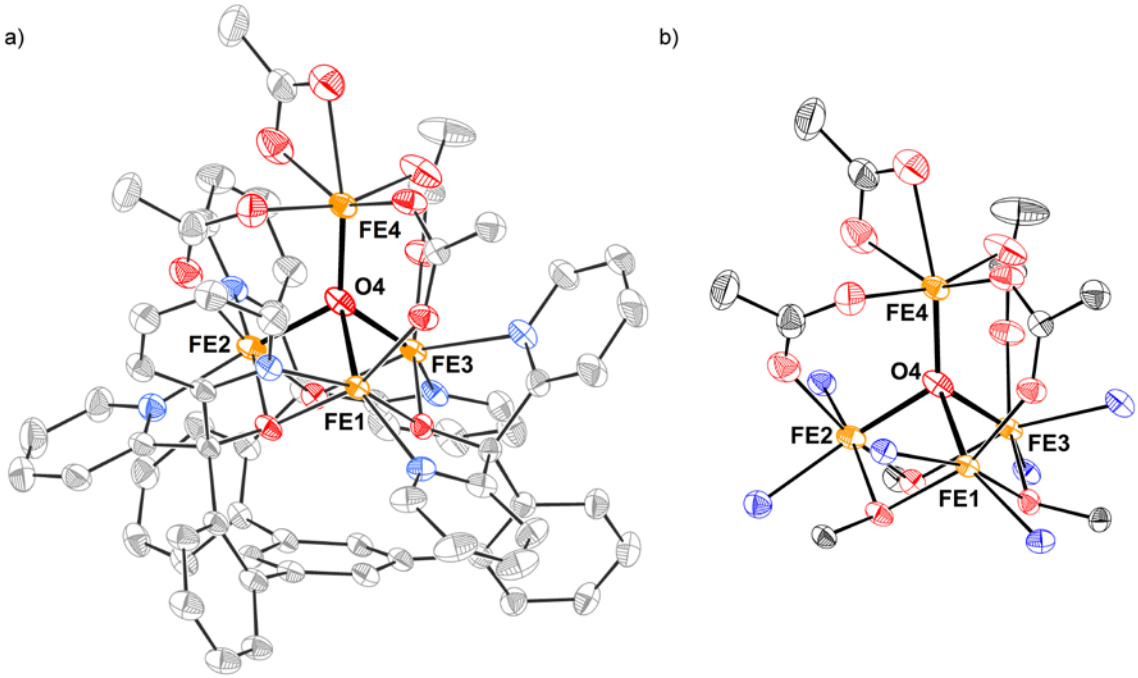

Figure 5. (a) Solid-state structure of **A.13**, hydrogen atoms, outer-sphere anions, and solvent molecules omitted for clarity; (b) cropped representation highlighting the tetrametallic core. Thermal ellipsoids shown at the 50% probability level.

Observation of binding of a fourth acetate anion to the apical iron center and the consequent assignment of the oxidation states of the Fe centers as [$Fe^{III}_2Fe^{II}_2$] led to the formulation of an improved synthetic protocol to generate **A.13**. Treatment of [Fe^{II}_3] complex **31-Fe** with 0.5 equiv. $Fe(OAc)_2$ and 0.5 equiv. $Fe(OTf)_2$, followed by addition

of iodosobenzene (PhIO), led to isolation of **A.13** in 70% yield. A higher-quality solid-state structure of this species was also obtained (Figure 5). Analysis of the Fe–(μ_4-O) bond distances for the basal Fe centers revealed two longer bonds (2.250(4) and 2.117(4) Å) and one shorter one (1.987(3) Å), indicating that two Fe^{II} centers were present in the base of the cluster, and that the apical Fe was in the Fe^{III} oxidation state (Table 1). κ^2-binding of a fourth acetate ligand at the apical Fe completed its octahedral coordination environment.

Despite preliminary indications by cyclic voltammetry that reduced states of complex **A.13** could be accessed, attempts at chemical reduction resulted in loss of the apical metal. Therefore, analogous strategies to those employed for Zn clusters were devised for stabilization of the [Fe_4O] core – namely, substitution of acetate groups for ligands bearing additional donor moieties for binding to the apical metal. Unfortunately, perhaps due to the presence of the fourth acetate ligand, attempts at ligand substitution on the preformed cluster were unsuccessful (depending on the ligand, either no reaction or cluster decomposition was observed). To circumvent this problem, substitution of the acetate ligand was carried out before formation of the tetranuclear cluster. Reaction of 1 equiv. of oxime **A.4** or pyrazole **A.3** with trimetallic precursor **31-Fe** (Scheme 8) generated the mono-substituted, bis(acetate) species **A.15** and **A.16** as confirmed by their asymmetric ^{1}H NMR spectra and by ESI-MS (due to the reactive nature of these species, incorporation of an O atom under ESI conditions was often observed for [Fe^{II}_3] complexes, as it was in these cases).

Scheme 8. Ligand Substitution on [Fe_4O] Complexes.

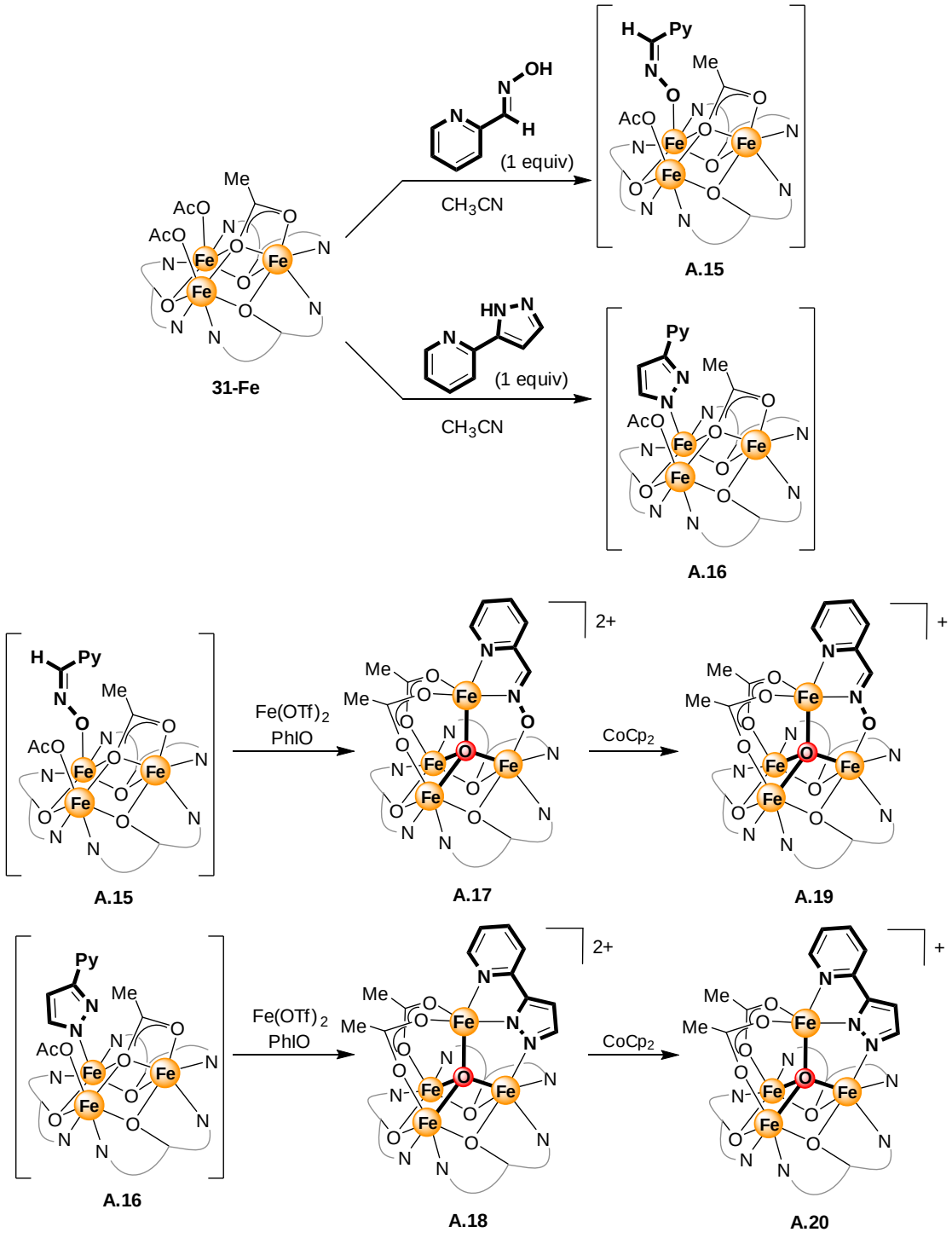

Treatment of these complexes with $Fe(OTf)_2$ (1 equiv.) and PhIO yielded the asymmetric [Fe_4O] clusters. Incorporation of the additional pyridine donor to the apical metal center appeared to obviate the need for binding of a fourth acetate ligand.

Although no solid-state structural characterization could be obtained for these clusters, the comparison of their ^{1}H NMR and ESI-MS spectroscopic features with those of the respective [Fe_3ZnO] clusters **A.6** and **A.7** supported their assignment as **A.17** and **A.18**. Unlike their all-acetate counterpart, **A.17** and **A.18** could be reduced by one electron with $CoCp_2$, generating relatively clean new species by ^{1}H NMR (again also supported by ESI-MS), indicating that the stabilization provided by the extra donor on these ligands prevented cluster decomposition at least in the case of reduction.

Scheme 9. Reactivity of Reduced Fe_4 Clusters with O_2.

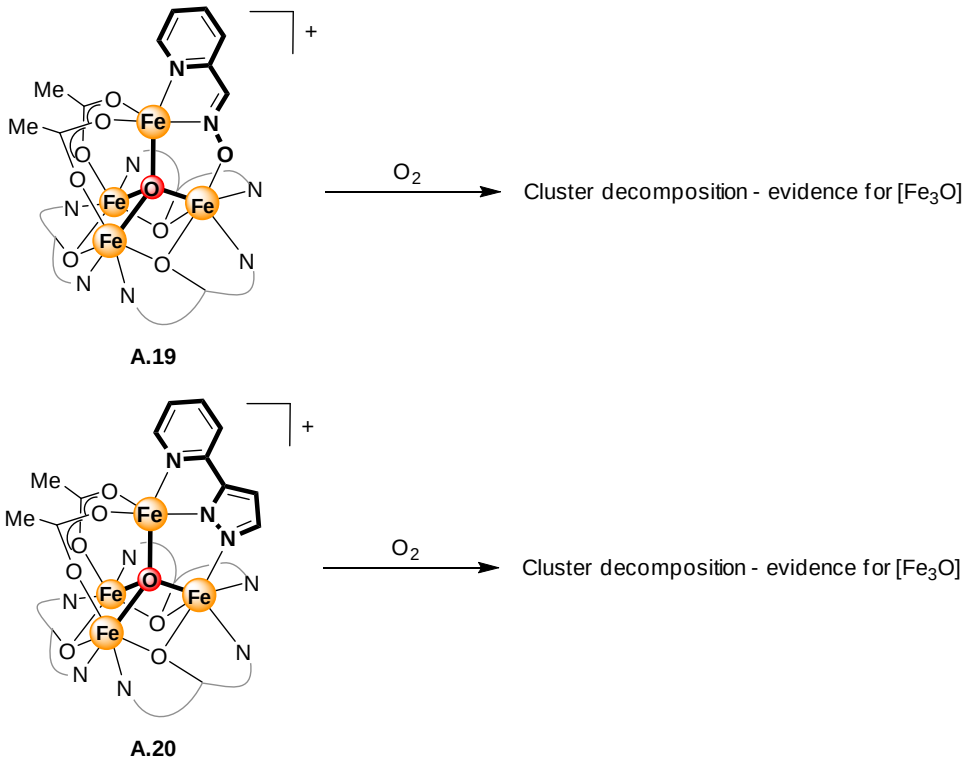

A.19

A.20

Unfortunately, much like the Zn clusters **A.8** and **A.9**, reaction of **A.19** and **A.20** with O_2 led to decomposition to complex mixtures, in which evidence for loss of the apical metal was observed (Scheme 9). Targeting a more robust [Fe_4O] cluster, substitution of two acetate ligands on **A.13** was attempted with bis(oxime) **A.5**. However, while the protonolysis reaction between **A.5** and the bis(oxime) was

promising, reduction of this species resulted in a species with symmetric ^{1}H NMR features, consistent with decomposition to a Fe_3 cluster.

While monooxo clusters incorporating different redox-inactive metals were targeted via transmetallation from Na complex **A.14** and Zn complexes **A.1**-**2**, no structural characterization for any of these species was obtained, and no further description of their studies is reported here. A peculiar monooxo cluster was however obtained from a different route, involving the attempted substitution of the acetate groups in oxo-hydroxo cluster **32-Ca** (Scheme 10). To target a cluster with no acetate ligands and a hydroxide bridge, **32-Ca** was reacted with bis(oxime) **A.5**. Subsequent one-electron reduction with $CoCp_2$ yielded a relatively symmetric species by ^{1}H NMR. XRD analysis of single crystals of this species revealed that both acetate groups were still present, while the hydroxide bridge had been protonolyzed (**A.21**). One of the oxime groups remained protonated and only bound to Ca via the N donor (Figure 6).

Scheme 10. Reactivity of Oxo-Hydroxo Cluster **32-Ca** with Bis(oxime) **A.5**.

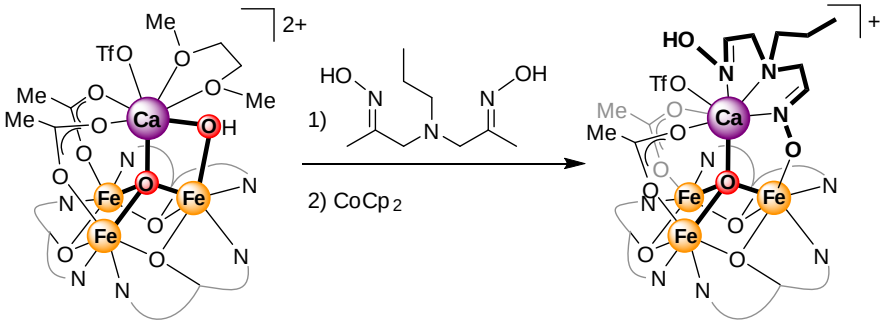

32-Ca **A.21**

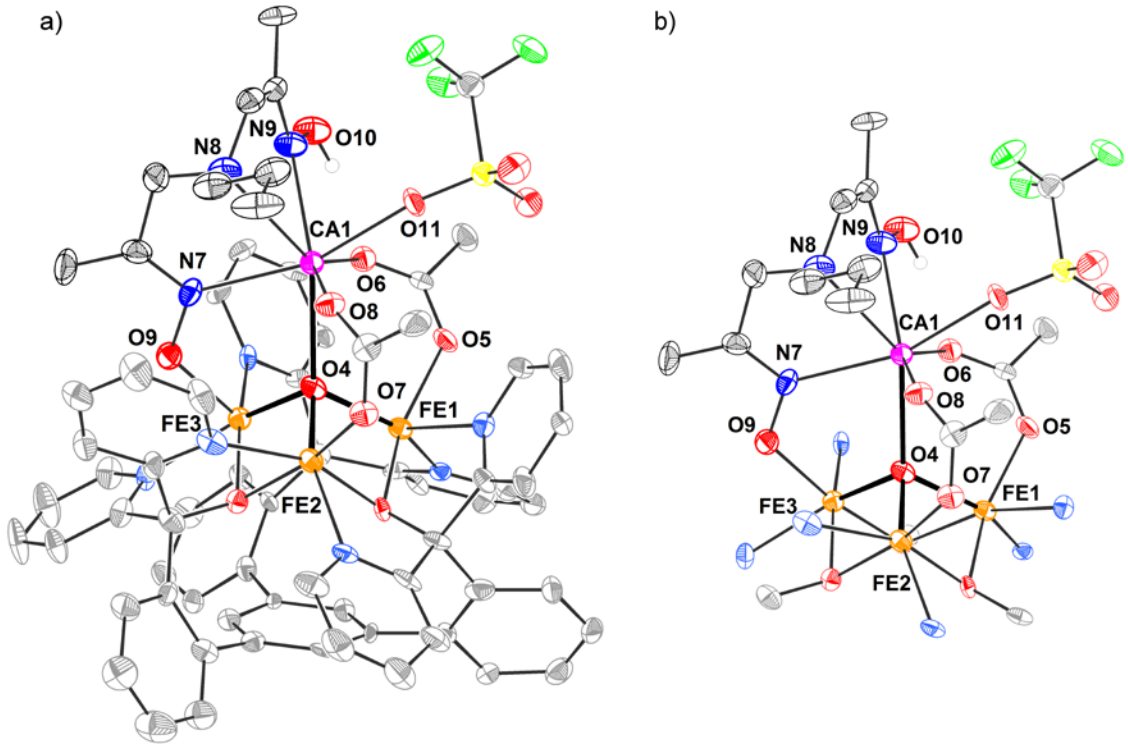

Figure 6. (a) Solid-state structure of **A.21**, hydrogen atoms, outer-sphere anions, and solvent molecules omitted for clarity; (b) cropped representation highlighting the tetrametallic core. Thermal ellipsoids shown at the 50% probability level.

Complex **A.21** was the first Ca^{2+}-containing monooxo cluster that displayed an interaction between the Ca^{2+} center and the bridging oxide ligand, which was presumably enforced by the bis(oximate) moiety. When only carboxylate ligands are present, in fact, Ca-monooxo clusters usually adopt a heptanuclear structure in which two trimetallic cores with μ_3-O ligands are bridged by a single Ca^{2+} center that does not interact directly with the oxide bridges, rather only with carboxylate ligands.

In summary, despite substantial synthetic efforts, targeting of asymmtetric clusters bearing more supporting ligands to stabilize the tetrametallic core did not provide complexes suitable to the study of small-molecule activation. Nonetheless, the synthetic protocols developed for the preparation of these compounds were useful in improving

our understanding of the chemistry of these clusters with respect to ligand exchange and some of its effects on cluster properties. The lessons learned from these studies were later implemented in the synthesis of other asymmetric clusters.

Trinuclear Complexes as Tetradentate Ligands: Varying Supporting Ligands

The second approach to the synthesis of novel tetranuclear clusters was aimed at developing complexes with an open coordination site at the apical metal to study the effects of the properties of the rest of the cluster (trimetallic core metal identity and oxidation state, supporting ligands, etc.) on small molecule activation at this site. These studies could provide insight into the factors that regulate reactivity at multimetallic sites in biology and heterogeneous catalysts. The proposed investigation would include the study of the effects of cluster elements that had not previously been varied, such as the monoatomic μ_4 bridges, for which oxide ligands had been used almost exclusively thus far. The desire to introduce this type of variation into tetranuclear clusters analogous to the ones that were previously studied required a redesign of our synthetic protocols, as the use of oxygen atom transfers had been the dominant strategy to assemble higher-nuclearity complexes from trimetallic precursors. Efforts to develop these new structural motifs were focused on the synthesis of sulphide clusters from various trimetallic precursors, the synthesis of clusters with redox-inactive trimetallic cores, and the targeting of tetrairon clusters supported by novel bridging ligands (at both μ_4 and μ_2 bridges).

Assembly of multimetallic clusters containing oxide and hydroxide ligands has proved to be extremely facile, due in part also to the availability of suitable oxygen atom transfer reagents such as iodosobenzene (PhIO), potassium superoxide (KO_2), and O_2 itself. Promising results were observed from the use of xenon difluoride (XeF_2) as an

F• source to incorporate an F^- ligand into $[Mn_3]$ precursors (Dr. Sandy Suseno). In simultaneous studies, non-oxidative routes to incorporate X^{n-} ligands into reduced $[M^{II}_3]$ complexes had shown that trimetallic sulfide clusters could be accessed with Fe and Mn via use of the bis(trimethylsilyl)sulphide ($(Me_3Si)_2S$) reagent (Kyle Horak, Dr. Sandy Suseno). Removal of an acetate group from complexes **31-Fe** and **31-Mn**, either *in situ* or in a separate step, provided a species with only two $^-$OAc ligands (**A.22-M**), which underwent nucleophilic attack on the trimethylsilyl groups of $(Me_3Si)_2S$ to generate μ_3-sulfide species (**A.23-M**) and Me_3SiOAc as byproduct (Scheme 11). To expand these studies to other first-row transition metal complexes, $[M_3S]$ ($M = Zn^{2+}$, Cu^{2+}) clusters were targeted. Preparation of Cu sulfide complex **A.23-Cu** was of interest due to the presence of a $[Cu_4S]$ assembly in the active site of the nitrous oxide reductase enzyme.[38,39] A $[Cu_3S]$ complex was viewed as a potential precursor for the synthesis of a synthetic model of this active site. Sulfide complex **A.23-Cu** was accessed from the previously reported tris(acetate) cluster **31-Cu** by treatment with 1 equiv. $(Me_3Si)_2S$. As observed by ^{1}H NMR spectroscopy, a new species was obtained with features similar to **31-Cu**. XRD analysis of single-crystals of **A.23-Cu** revealed the desired $[Cu_3S]$ structure (Figure 7; the poor quality of the structure and the rhombohedral symmetry of the crystal made any analysis beyond the determination of connectivity impossible). Unfortunately, it was discovered that this species was quite unstable in solution, with insoluble material precipitating from solution whenever **A.23-Cu** was solubilized in various solvents. This observation was ascribed to the formation of copper sulfide, indicating that the multidentate ligand could not sufficiently stabilize the trinuclear sulfide species with respect to loss of CuS. This result precluded the use of **A.23-Cu** as a precursor to higher-nuclearity clusters.

Scheme 11. Synthesis of [M_3S] Clusters (M = Fe, Mn, Cu, Zn).

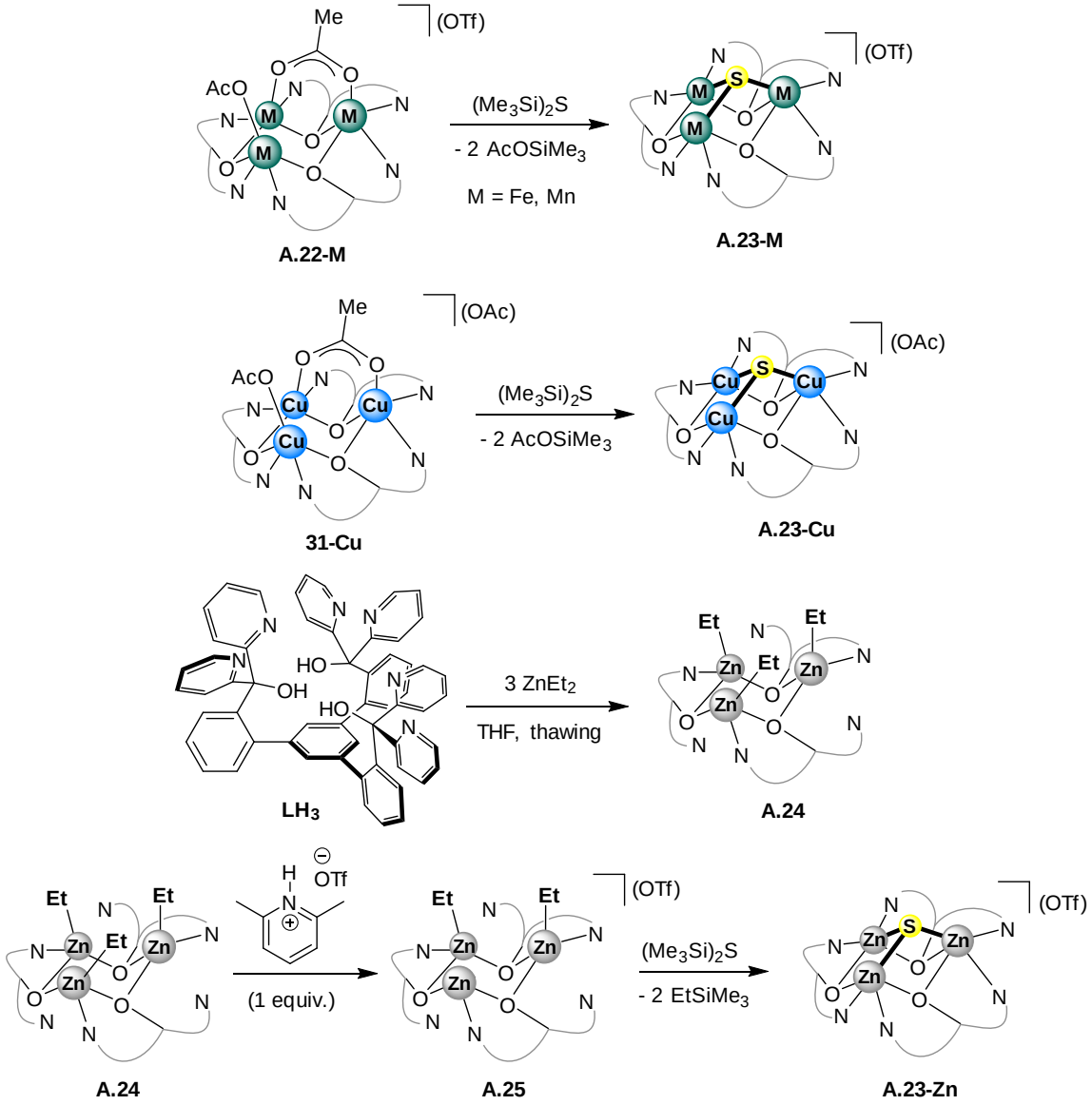

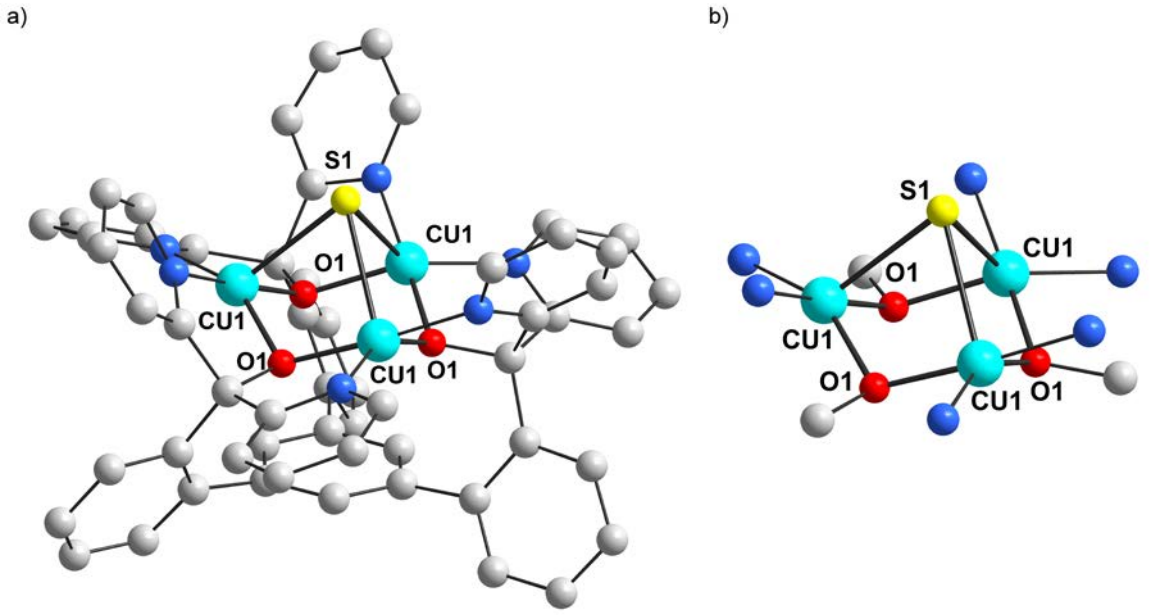

Figure 7. (a) Preliminary solid-state structure of **A.23-Cu**, outer-sphere anions and solvent molecules omitted for clarity; (b) cropped representation highlighting the [Cu_3S] core. Thermal ellipsoids shown at the 50% probability level.

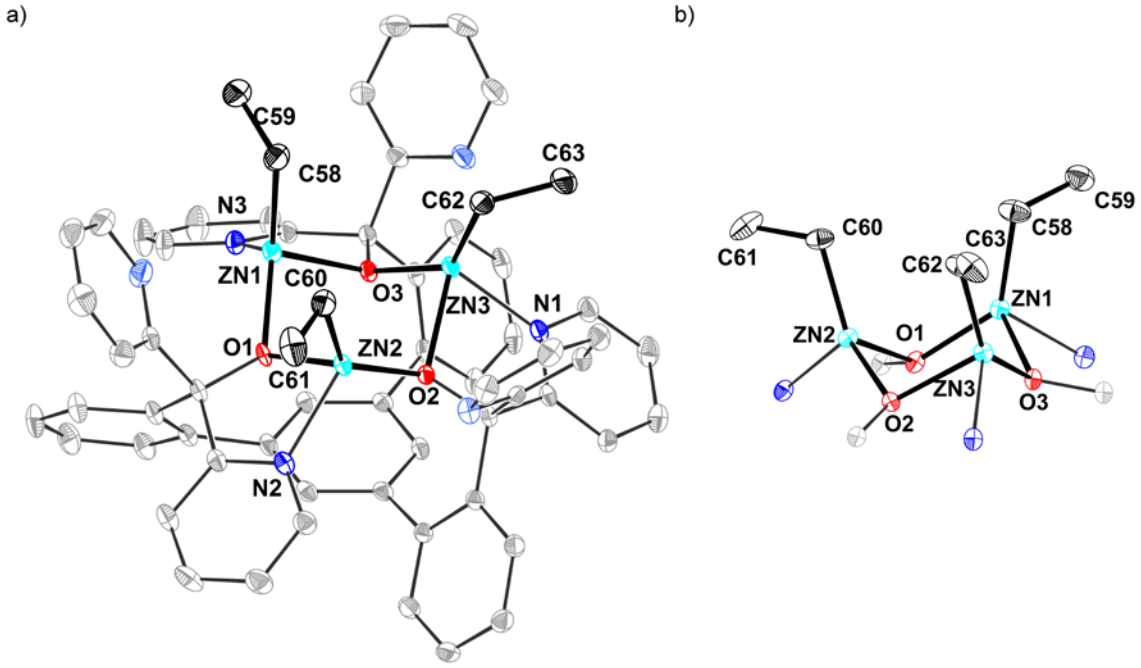

Figure 8. (a) Solid-state structure of **A.23-Zn**, hydrogen atoms and solvent molecules omitted for clarity; (b) cropped representation highlighting the [Zn_3] core. Thermal ellipsoids shown at the 50% probability level.

To access a redox-inactive analog of these sulfide clusters, [Zn_3S] complex **A.23-Zn** was targeted. In this case, a suitable trimetallic precursor was obtained from a Zn_3 triethyl complex (**A.24**) that had been synthesized by a visiting student in our laboratory, Yuji Niishi. Complex **A.24** was accessed by metallation of the multidentate ligand with $ZnEt_2$ to give a Zn_3 species with three ethyl groups (Scheme 11). This complex was considered an intriguing precursor to higher-nuclearity clusters, as installation of new bridging ligands could be carried out via protonolysis of the alkyl groups. It was in fact shown that addition of 1 equiv. of 2,6-lutidinium triflate led to isolation of a diethyl complex (**A.25**), and that all ethyl groups could be removed by addition of 3 equiv. of acid to yield a tris(triflate) complex, whose identity was confirmed via independent synthesis. Treatment of diethyl complex **A.25** with $(Me_3Si)_2S$ resulted in conversion over several hours to a new species displaying ^{1}H NMR features consistent with formation of a new symmetric species. XRD analysis of this product confirmed the structural assignment of this product as the sulfide complex **A.23-Zn** (Figure 9).

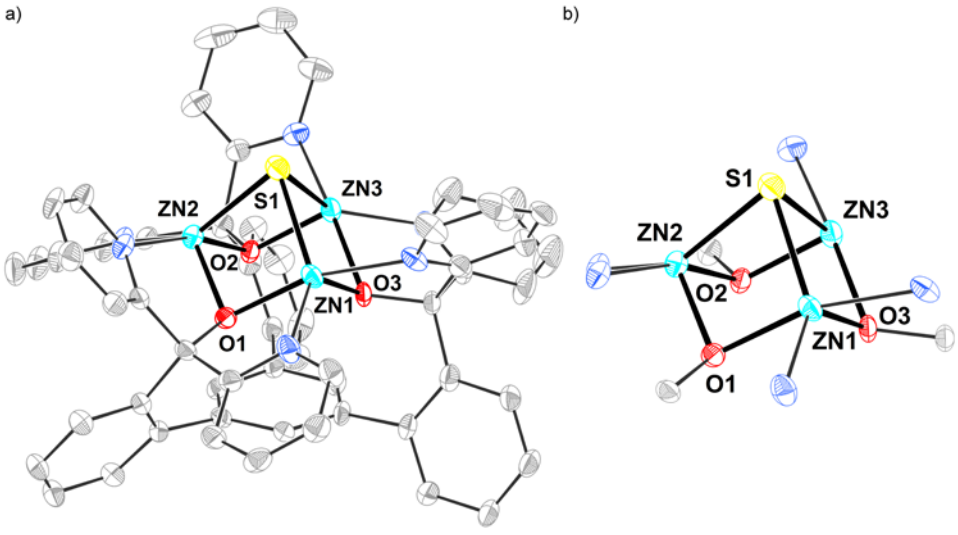

Figure 9. (a) Preliminary solid-state structure of **A.23-Zn**, hydrogen atoms, outer-sphere anions, and solvent molecules omitted for clarity; (b) cropped representation highlighting the [Zn_3S] core. Thermal ellipsoids shown at the 50% probability level.

The isolation of a series of μ_3-sulfide complexes provided insight into the feasibility of incorporating a μ_4-S bridge in tetranuclear clusters. Unfortunately, due to the size of the sulfur atom and to the consequently longer S–M bonds with respect to M–O ones, the distance between the S^{2-} ligand and the trimetallic plane was much larger than that observed for oxide ligands in tetranuclear clusters (Table 1). The distance between S and the centroid of the trimetallic plane was up to ~0.5 Å longer than longest such distance for the oxide ligand in tetranuclear clusters (found in complex **A.13**). Such an elevation of the μ_3-S from the base of the cluster resulted in a distortion of the geometry at the three metal centers, which did not bind a sixth ligand as seen in oxide clusters. Rather, these metal centers remained five-coordinate, making incorporation of ligands to bridge to a fourth metal unfeasible. The sulfide ligand was therefore considered incompatible with formation of tetranuclear clusters analogous to those supported by μ_4-O ligands.

Table 1. Comparison of Fe–X Bond Distances (Å) in Fe_3 Monooxo and Sulfide Clusters.

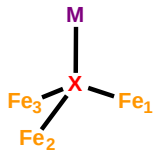

	A.2	**A.8**	**A.9**	**A.10**	**A.13**	**A.23-Fe**
X	O	O	O	O	O	S
M	Zn^{2+}	Zn^{2+}	Zn^{2+}	Zn^{2+}	Fe^{3+}	-
Basal Fe_3 ox. st.	$Fe^{III}Fe^{II}_2$	$Fe^{III}Fe^{II}_2$	$Fe^{III}Fe^{II}_2$	$Fe^{III}Fe^{II}_2$	$Fe^{III}_2Fe^{II}$	Fe^{II}_3
Fe_1–O	2.014(3)	1.94	1.962(4)	2.065(4)	2.250(4)	2.375(1)
Fe_2–O	2.000(4)	2.16	2.010(3)	1.940(4)	1.987(3)	2.412(1)
Fe_3–O	2.041(3)	2.10	2.089(4)	1.939(4)	2.117(4)	2.403(1)
M–O	1.916(3)	1.94	1.937(3)	1.972(4)	1.852(4)	-
[Fe_3]–O[a]	0.944	1.03	1.021	0.898	1.130	1.685
Fe Coord. #	6	6	6	6	6[b]	5

[a] M_3–X = distance between centroid of Fe_3 core and X ligand. [b] Both core Fe centers and apical Fe were six-coordinate.

The possibility of installing ligand motifs on a [Zn_3] core via protonolysis of the ethyl groups in complex **A.24** was recognized as a potential unique entry into new cluster scaffolds. Numerous attempts to incorporate a variety of bridging ligands, from thiolates to pyrazolates to secondary phosphine oxides, via protonolysis from their conjugate acids, were undertaken. However, in most cases **A.24** was found to be less reactive than initially assumed. In fact, ESI-MS studies of **S.24** revealed partial retention of the ethyl groups even under the forcing and not water-free ESI conditions, indicating that protonolysis of this species was not as facile as originally thought. Protonolysis with various proligands did not proceed at all at low temperatures even in the presence of an excess of H^+ sources. In the few cases in which reactivity was observed, complex mixtures were often observed, suggesting that multiple processes were occurring.

Scheme 12. Proposed Synthesis of [Zn_3Fe] Clusters **A.26**-**27**.

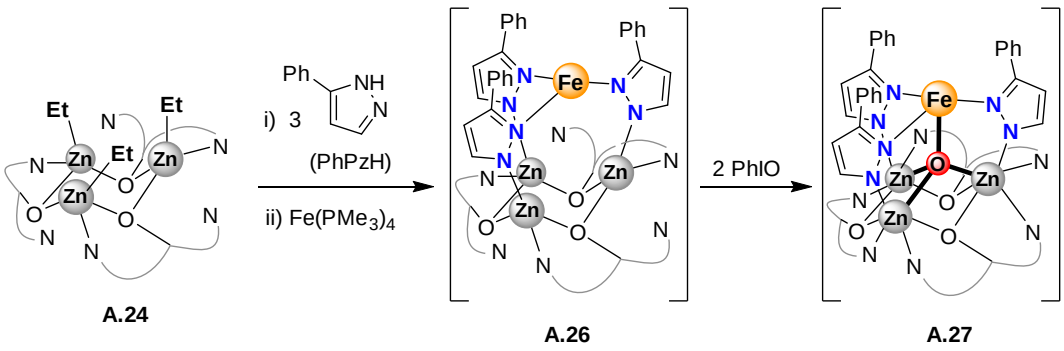

The most promising results were obtained when a pyrazolate-supported [Zn_3Fe] cluster was targeted. It had been previously observed that treatment of **A.24** with phenyl pyrazole (PhPzH) in the absence of additional metal sources led to precipitation of an isoluble material that could not be further characterized. When addition of 3 equiv. of PhPzH to **A.24** was immediately followed by addition of $Fe(PMe_3)_4$, however, the solution remained homogeneous. The brown species thus obtained displayed no features in the paramagnetic region of its ^{1}H NMR spectrum. While the diamagnetic

region was rather complex, the observation of a single feature in the ^{31}P NMR spectrum was promising. Furthermore, ESI-MS analysis showed a small peak corresponding to the mass of the desired cluster **A.26** with incorporation of an O atom (possibly an artefact due to ESI conditions). This species was therefore tentatively assigned as a [Fe_3Zn] cluster with a vacant intermetallic site in which the apical Fe center was capped by a PMe_3 ligand (Scheme 12). To chemically install the μ_4-oxide ligand that appeared to be incorporated under ESI conditions, this species was treated with 2 equiv. PhIO – an additional equivalent was added to account for PMe_3, which has been shown to be capable of abstracting O atoms from related clusters. The product thus generated was lighter in color and displayed no features by ^{1}H and ^{31}P NMR. ESI-MS studies, however, showed that the peak corresponding to the mass of [**A.26**+O], previously observed as a small signal, was now the major feature. The product was therefore assigned as [Zn_3FeO] cluster **A.27**. Despite several attempts, no structural characterization of this species could be obtained, and its further reactivity remains unexplored. However, complex **A.27** may serve as a useful spectroscopic and reactivity comparison for [Fe_4O] complexes supported by pyrazolate ligands that have recently been studied in the group. In **A.27** the three basal metals are redox-inactive, and study of its reactivity would therefore afford insight into the behavior of the apical Fe center in the absence of additional oxidizing or reducing equivalents in the trimetallic core.

Further efforts towards the synthesis of novel tetranuclear clusters focused on the installation of hitherto unexplored ligand motifs in [Fe_4] clusters. The chief goals of these studies were the synthesis of clusters supported by secondary phosphine oxide (SPO) ligands and the non-oxidative incorporation of μ_4 bridging ligands (both

strategies targeting lower-valent complexes than the ones studied to date) as well as the synthesis of [Fe_4] complexes incorporating new μ_4 bridging ligands.

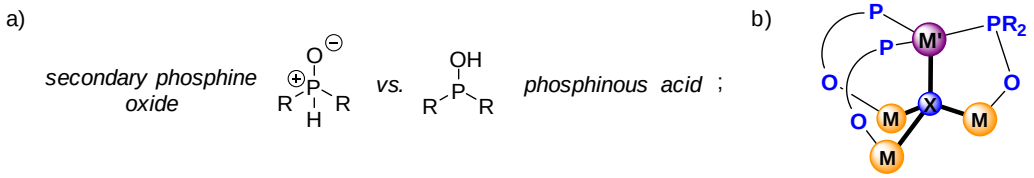

Figure 10. (a) Structure of secondary phosphine oxides (SPOs) and phosphinous acids; (b) proposed mode of binding of SPOs to tetranuclear clusters.

It was theorized that a set of soft donor moieties bound to the apical Fe center in a [Fe_4] cluster would favor its reduction, which would in turn facilitate binding of certain small molecules (CO, N_2, etc.). SPOs have been studied as ligands to low-valent metal centers, albeit mostly for late- and second-/third-row transition metals. Incorporation of three equivalents of the SPO ligand was expected to be potentially difficult due to the large steric profile of the substituent on phosphorous. Di-*i*-butylphosphine oxide was chosen as a first target because of a balance between ease of manipulation (diethyl- and dimethylphosphine oxide, while precedented, are difficult to prepare and handle) and expected steric requirements (the majority of the steric bulk in this ligand was separated from the P donor by a methylene unit). ^{i}Bu$_2$P(O)H was synthesized according to a literature procedure,[40] and substitution of the acetate groups in **A.13** was attempted. No reactivity was observed upon addition of ^{i}Bu$_2$P(O)H to **A.13**, which was not surprising given the reluctance of **3** to undergo ligand substitution reactions with other motifs (*vide supra*). Salt metathesis was attempted via use of [^{i}Bu$_2$P(O)]K, obtained by deprotonation of ^{i}Bu$_2$P(O)H with benzyl potassium. While a reaction with **A.13** was observed, deconvolution of the product mixtures was not possible. Additions of [^{i}Bu$_2$P(O)]K to **A.13** and other clusters were performed at cold temperatures and with

varying number of equivalents of the SPO salt, but similar results were obtained. ESI-MS data was promising, as m/z peaks above the molecular mass of the starting material were observed. However, these peaks were often assignable to species incorporating both [^{t}Bu$_2$P(O)] *and* additional oxygen atoms. The reason for this observation was discovered via a salt metathesis reaction attempted in the presence of Ca(OTf)$_2$ as an acetate scavenger. The ^{1}H NMR spectrum of the product of this reaction was consistent with loss of the apical Fe and of the bridging oxide ligand, indicating that [^{t}Bu$_2$P(O)]$^-$ was sufficiently reducing to undergo oxygen atom transfer to the SPO to form phosphinite species.

Since ligand substitution in the preformed cluster was once again unsuccessful, trimetallic precursors were targeted that could undergo this ligand exchange process. Surprisingly, it was found that [Fe$^{II}_3$] complex **31-Fe** was rather unreactive towards ligand substitution via salt metathesis, partly due to its insoluble nature in most organic solvents (**31-Fe** is only soluble in CH_2Cl_2). It had been previously shown, however, that a single $^-$OAc group in **31-Fe** could be substituted with a non-coordinating $^-$OTf by treatment with Ca(OTf)$_2$, and bis(acetate) complex **A.22-Fe** reacted more readily with various salts.

To further facilitate installation of other ligand motifs, a [Fe$_3$] complex with no acetate groups was targeted. Treatment of **31-Fe** with MeOTf (3 equiv.) resulted in a change in color from orange to yellow and to the observation of new ^{1}H NMR features still consistent with a symmetric species. Although the product of this reaction was originally assigned as the tris(triflate) complex **A.28**, a preliminary solid-state structure of this species was eventually obtained, and revealed that a single acetate ligand remained bound to the Fe$_3$ core (**A.29**, Figure 11). Incorporation of SPO ligands using

bis(triflate) species **A.29** as precursor was attempted. Reaction of this material with [^{t}Bu$_2$P(O)K] and M^0 sources (Fe(PMe$_3$)$_4$ or Mo(CH$_3$CN)$_3$(CO)$_3$) led to the observation of some promising spectroscopic data, but no structural characterization of these complexes was obtained.

Scheme 13. Reactivity of Complex **31-Fe** with Methyl Triflate.

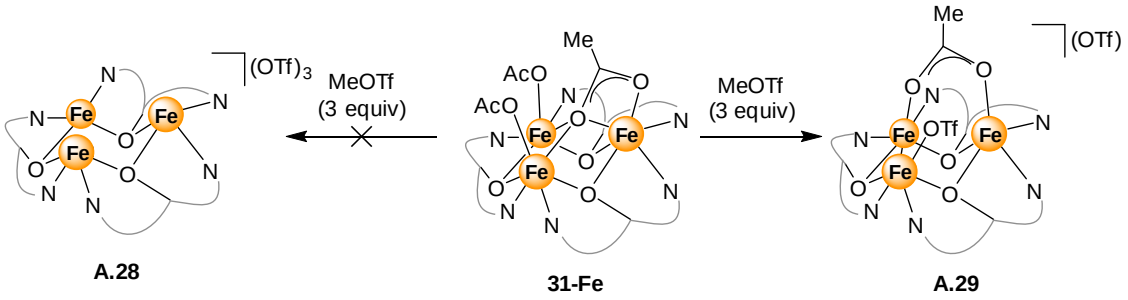

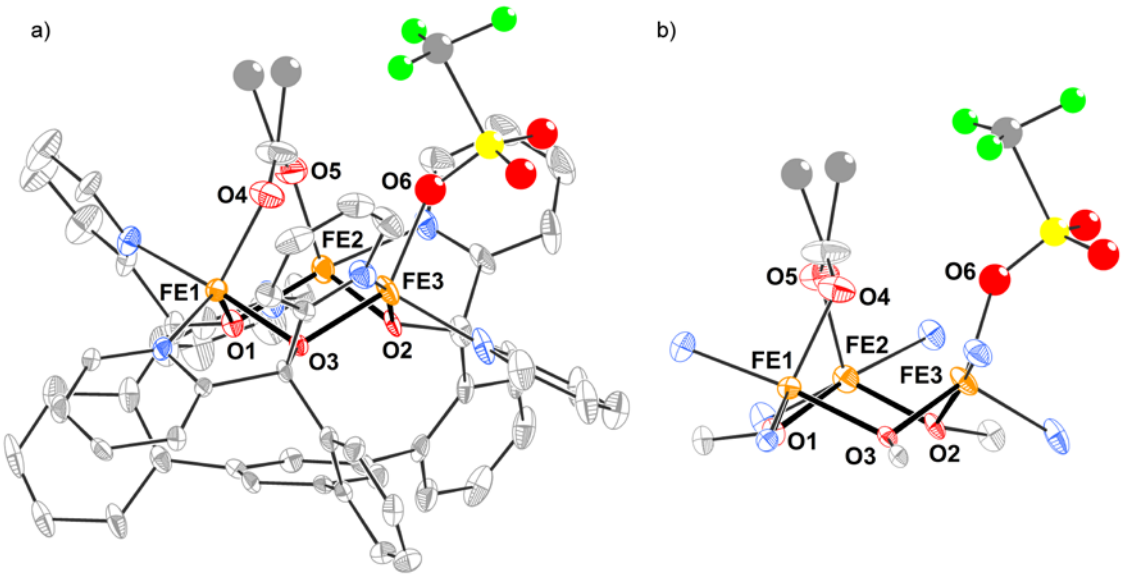

Figure 11. (a) Preliminary solid-state structure of **A.29**, hydrogen atoms, outer-sphere anions, and solvent molecules omitted for clarity, disordered fragments shown as ball-and-stick models (b) cropped representation highlighting the trimetallic core. Thermal ellipsoids shown at the 50% probability level.

Non-oxidative incorporation of an oxide ligand was observed as a decomposition product from a putative tris(pyrazolate) complex obtained via salt metathesis from **A.29** with 3 equiv. sodium phenylpyrazolate (Dr. Graham deRuiter). This species, or analogous complexes showing incorporation of oxide or hydroxide clusters without the use of oxidizing agents, was targeted via rational synthesis. Complex **A.29** was found to react with sources of hydroxide such as Et_4NOH. Despite the initial observation of promising features in the ^1H NMR spectra of these reactions, these signals disappeared when the products were kept in solution for several hours (for crystallization purposes).

Among the decomposition products, single-crystals of a complex displaying a hitherto unobserved motif were obtained. In complex **A.30** (Figure 12), two $[Fe_3]$ units are bridged by a single Fe center via three hydroxide (or, potentially, oxide) bridges per $[Fe_3]$ motif. The presence of three triflate anions per $[Fe_7]$ unit suggested that the two $[Fe_3]$ cores were in the $[Fe^{II}_3]$ oxidation state, the central Fe center was Fe^{III}, and that all the monoatomic bridges were hydroxide moieties. The structural motif observed in **A.30** suggested that tetranuclear clusters without μ_4 bridging ligands could be supported by three monoatomic bridges, provided that the coordination sphere of the apical metal could be filled suitably.

A final set of experiment in these studies was aimed at introducing μ_3 or μ_4 bridging ligands other than oxide. In particular, as clusters containing oxide and fluoride ligands had been accessed, clusters incorporating a nitride were targeted. Both oxidative and non-oxidative routes to incorporate a N^{3-} ligand were explored. All attempts to introduce $[NH_n]^{n-3}$ ligands into $[Fe^{II}_3]$ complexes via salt metathesis or protonolysis were unsuccessful. To install a nitride ligand oxidatively, reactivity of $[Fe_3]$ precursors with azide reagents was explored.

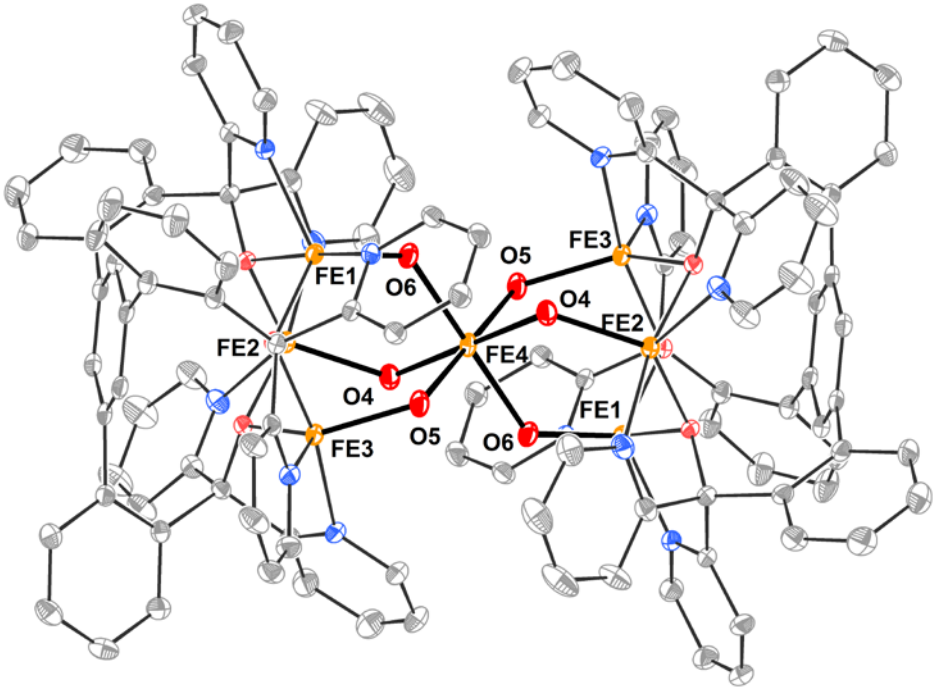

Figure 12. Solid-state structure of **A.30**. Hydrogen atoms, three outer-sphere triflate anions, and solvent molecules omitted for clarity. Thermal ellipsoids shown at the 50% probability level.

Treatment of tris(acetate) complex **31-Fe** with tetrabutylammonium azide ($^{n}Bu_4NN_3$) in the presence of a Lewis acid ($Zn(OTf_2)$ led to slow conversion to a new species (Scheme 14). Although the ^{1}H NMR spectrum of this product indicated low purity, XRD-quality crystals were obtained and showed a $[Fe_3]$ unit with three different anions: a κ^2-acetate bridging between two Fe centers, an azide bound to the third Fe, and an outer-sphere triflate (Figure 13).

Scheme 14. Synthesis of Azide Complex **A.31**.

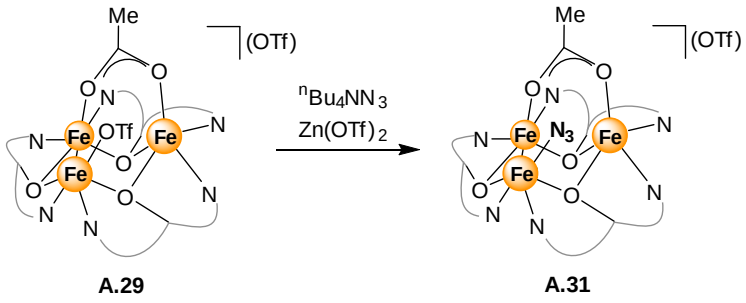

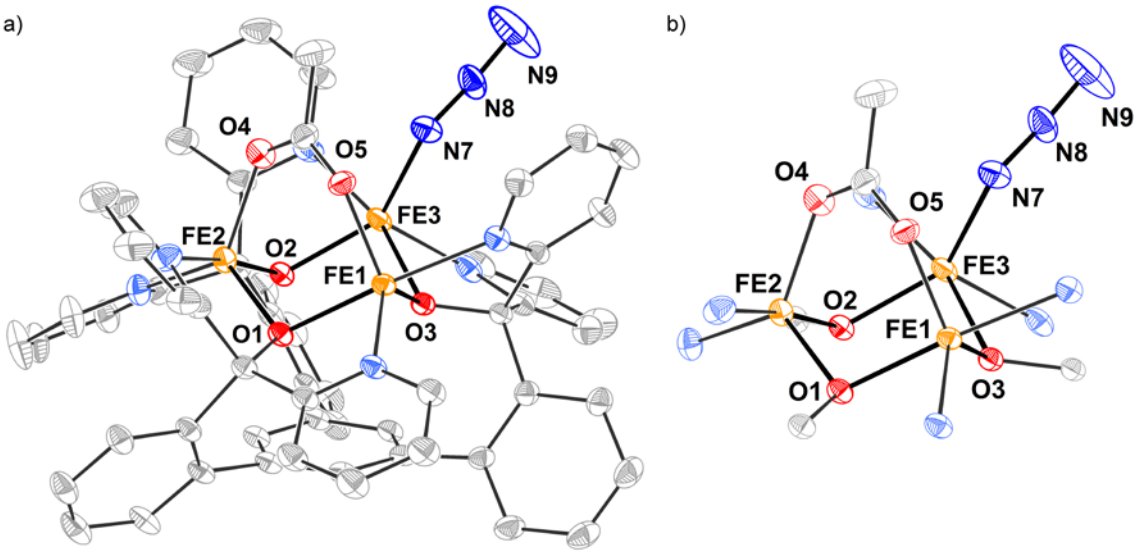

Figure 13. (a) Solid-state structure of **A.31**, hydrogen atoms, outer-sphere anions, and solvent molecules omitted for clarity; (b) cropped representation highlighting the tetrametallic core. Thermal ellipsoids shown at the 50% probability level.

This result indicated that azide binding to the trimetallic complex was possible, which opened the possibility for thermal or photolytic conversion of the azide moiety to install the desired N^{3-} ligand. Photolysis of solutions of **31-Fe** and azide sources ($^{n}Bu_4NN_3$ or Me_3SiN_3) in the presence of an additional equivalent of $Fe(OAc)_2$ showed formation of two new species by ^{1}H NMR (Figure 14), concomitantly with production of some of oxide cluster **A.13** (Scheme 15). Formation of oxo cluster **A.13** was ascribed to residual water present in $Fe(OAc)_2$ despite repeated attempts at drying this material. ESI-MS analysis of the reaction showed a major peak at m/z=1329 (Figure 15), consistent with the mass of a $[LFe_4N(OAc)_3]^{+}$ species (by the same technique, complex **A.13** showed the same ion peak at m/z=1331).

Scheme 15. Synthesis of Proposed Nitride Cluster **A.32**.

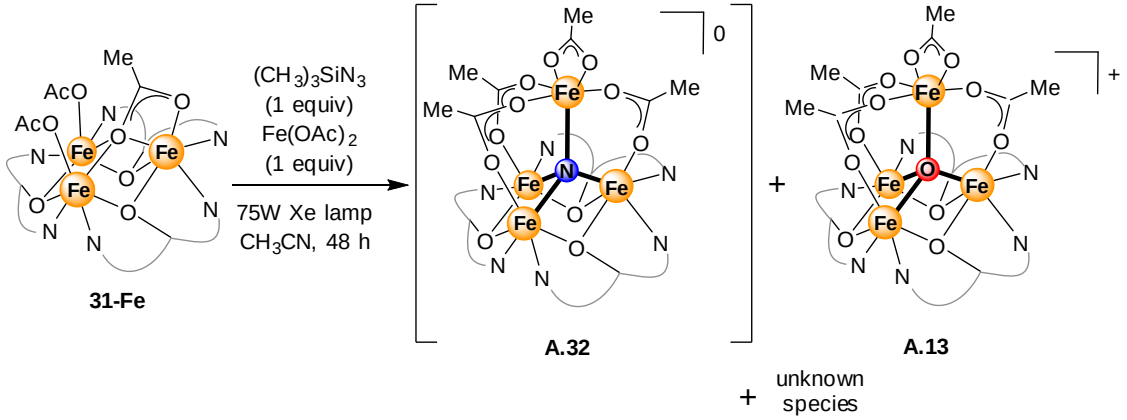

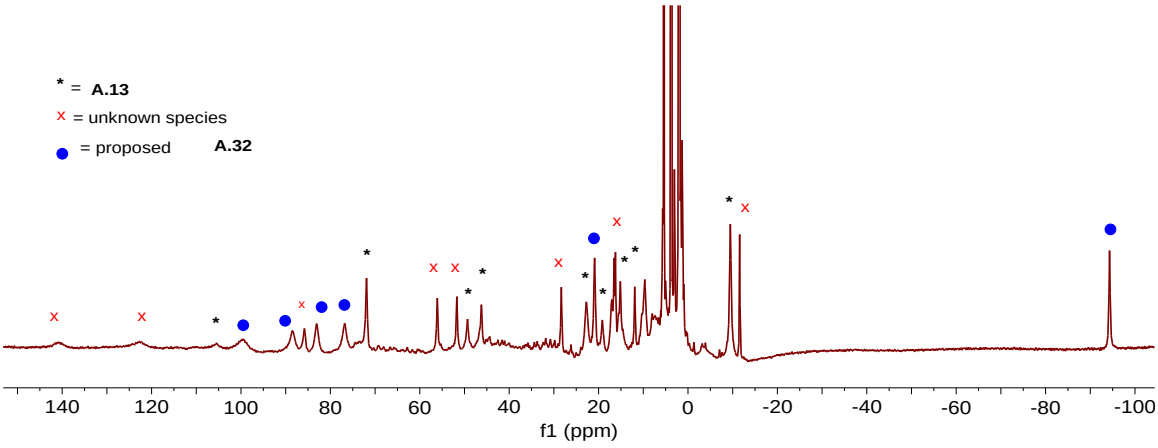

Figure 14. ^{1}H NMR spectrum (CD_2Cl_2, 300 MHz) of the product mixture from the reaction of **31-Fe** with Me_3SiN_3 and $Fe(OAc)_2$ under photolysis conditions. Peaks corresponding to monooxo cluster **A.13**, proposed nitride cluster **A.32**, and an unknown species that was produced are marked.

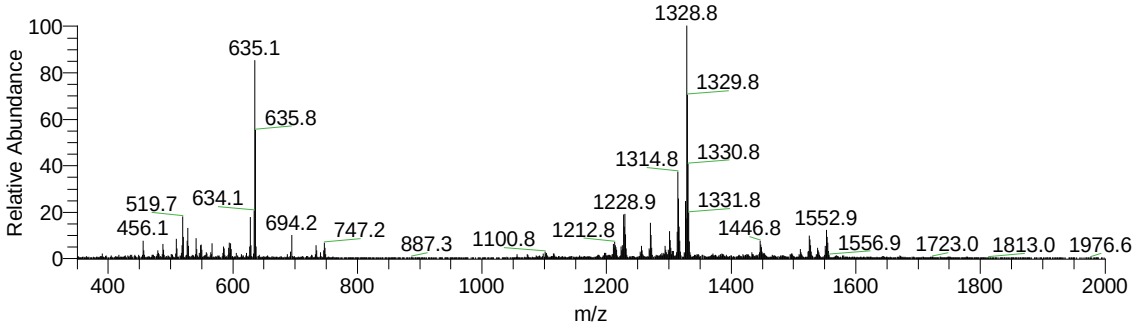

Figure 15. ESI-MS spectrum in CH_2Cl_2 of product mixture from reaction of **31-Fe** with Me_3SiN_3 and $Fe(OAc)_2$ under photolysis conditions (Scheme 15). Peaks at m/z = 1329 and 1331 correspond to proposed nitride cluster **A.32** and oxo cluster **A.13**, respectively.

These observations indicated that nitride cluster **A.32** could be accessed via photolysis of an azide species. Unfortunately, all attempts to structurally characterize this species have failed. Furthermore, nitride complex **A.32** appeared to easily decompose if kept in solution (it is unclear if this decomposition led to formation of oxo cluster **A.13**).

Synthesis of a nitride cluster supported by pyrazolate ligands was also attempted, in this case via a non-oxidative route. Tetramethyldisilylamine ($(Me_2HSi)_2NH$) did not react with bis(acetate) complex **A.22-Fe** over several hours; however, addition of lithium phenylpyrazolate and $Fe(OTf)_2$ to the mixture resulted in a change in color from yellow to dark orange-red. ^{1}H NMR analysis of the product revealed formation of two species –previously reported [Fe_4O] pyrazolate cluster **A.33** (Dr. Graham deRuiter) and a hitherto unobserved species (Scheme 16). This second component of the mixture displayed a considerably upfield-shifted ^{1}H NMR signal, similar to the NMR of the species proposed to be nitride cluster **A.34** (Figure 16), and also similar to [Fe_4F] clusters under investigation at the same time (Christopher Reed).

Scheme 16. Synthesis of Proposed Nitride Cluster **A.34**.

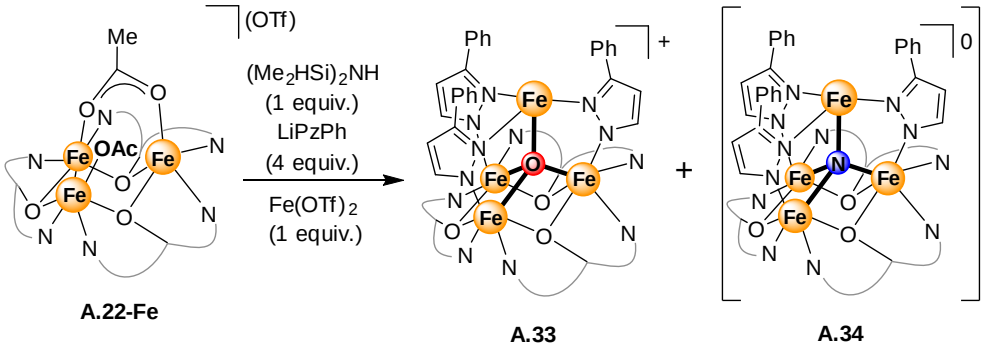

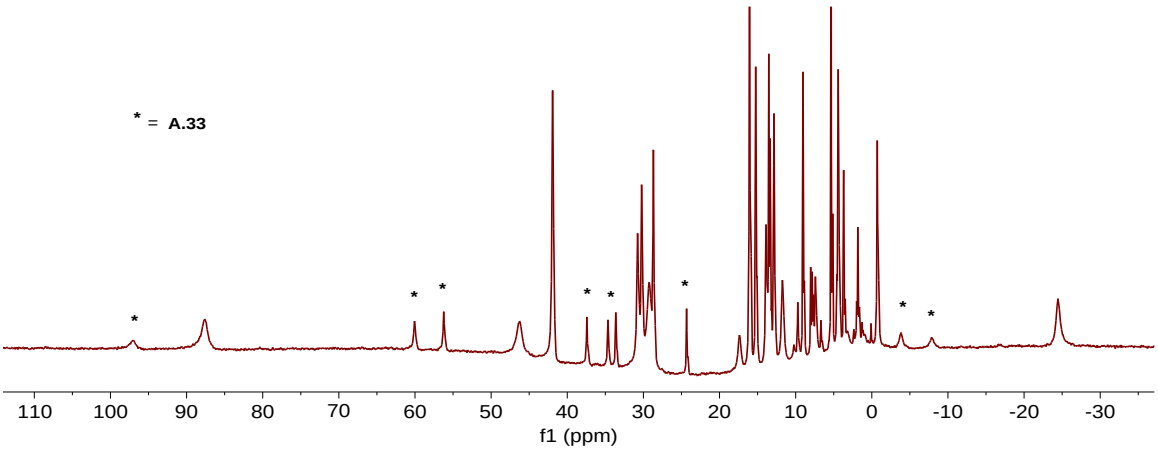

Figure 16. ^{1}H NMR spectrum (CD_2Cl_2, 300 MHz) of the product mixture from the reaction of **A.22-Fe** with $(Me_2HSi)_2NH$, LiPzPh, and $Fe(OTf)_2$. Peaks corresponding to monooxo cluster **A.33** (Scheme 16) are marked with asterisks.

ESI-MS analysis of this product was inconclusive, possibly due to the large signals observed for oxo complex **A.33** even in mixtures in which it is but a minor component. However, on the basis of the similarities observed by ^{1}H NMR, the product of this reaction was tentatively identified as nitride cluster **A.34**. An attempt at reproducing this reaction was unsuccessful, and mostly oxo complex **A.33** was obtained – again likely due to the presence of water in the $Fe(OTf)_2$ salt. It should also be noted that the oxo cluster obtained from this reaction was in the $[Fe^{III}_3Fe^{II}]$ oxidation state, indicating that a 1-e^- oxidation had taken place, probably by $[Me_2SiH]^+$ species. These observations supported the possibility of incorporating nitride ligands into $[Fe_4]$ clusters, hopefully opening a door into the exploration of the effect of a μ_4 bridging ligand on chemical reactivity at the apical iron over a series of three main group elements (F^-, O^{2-}, N^{3-}).

CONCLUSIONS

The many studies reported herein are part of the continued effort to expand the library of multinuclear clusters aimed at unveiling the interactions between metal centers and their effects on chemical reactivity. The synthesis and manipulation of these multinuclear clusters is a complex process, requiring many attempts at targeting specific species. Many of the investigations presented here were not successful in achieving their original goals. Nonetheless, useful information about how these complexes can be accessed, isolated, and modified was often obtained. Studies on the incorporation of various ligands – from oximates, to pyrazolates, to SPOs – provided insight into ligand exchange processes in both tri- and tetranuclear clusters. Efforts to open coordination sites on [Fe_3] complexes resulted in precursors that have proved useful in the synthesis of higher-nuclearity clusters by other researchers in our laboratory. Furthermore, characterization of the many complexes isolated by various spectroscopic and structural techniques have provided extremely useful lessons on assignment of cluster properties, such as metal oxidation states, based on these methods.

A few notable results should be recalled here. Study of bis(oximate) cluster **A.11** showed that this motif is quite robust, and further investigations of its reactivity may be possible. Synthesis of [Cu_3S] and [Zn_3S] complexes was carried out successfully, and study of these and other complexes in the same series of first-row transition metal μ_3-sulfides may inform on the possibility of building higher-nuclearity clusters from these precursors. Finally, although structural characterization for these species could not be obtained, two complexes (**A.32** and **A.34**) were assigned as clusters containing a μ_4-N^{3-} ligand. Further studies on the synthesis and properties of these clusters will be of interest for comparison with related oxide and fluoride clusters.

EXPERIMENTAL SECTION

General Considerations

Unless indicated otherwise, reactions performed under inert atmosphere were carried out in oven-dried glassware in a glovebox under a nitrogen atmosphere. Anhydrous tetrahydrofuran (THF) was purchased from Aldrich in 18 L Pure-Pac^{TM} containers. Anhydrous dichloromethane, diethyl ether, DME, and THF were purified by sparging with nitrogen for 15 minutes and then passing under nitrogen pressure through a column of activated A2 alumina (Zapp's). Anhydrous 1,2-dimethoxyethane (DME) was dried over sodium/benzophenone ketyl and vacuum-transferred onto molecular sieves. CD_2Cl_2 and CD_3CN were purchased from Cambridge Isotope Laboratories, dried over calcium hydride, then degassed by three freeze-pump-thaw cycles and vacuum-transferred prior to use. ^{1}H NMR spectra were recorded on a Varian 300 MHz instrument, with shifts reported relative to the residual solvent peak. ^{19}F NMR spectra were recorded on a Varian 300 MHz instrument, with shifts reported relative to the internal lock signal. Electrospray ionization mass spectrometry (ESI-MS) was performed in the positive ion mode using a LCQ ion trap mass spectrometer (Thermo) at the California Institute of Technology Mass Spectrometry Facility.

Unless indicated otherwise, all commercial chemicals were used as received. $Ca(OTf)_2$, $Zn(OTf)_2$, $(CH_3)_3SiOTf$, MeOTf, and $[(CH_3)_3Si]_2S$ were purchased from Aldrich. Cobaltocene was purchased from Strem and sublimed before use. Bis(oxime) **A.5** and di-*i*-butylphosphine oxide were prepared as reported in the literature. [37] [40] **5-Fe** and **5-Cu** were prepared according to previously published procedures.[19,20]

Synthesis of A.6

In the glovebox, **A.1** (0.0205 g, 0.013 mmol) was dissolved in 3 mL CH_3CN in a 20 mL scintillation vial. 2-Pyridylpyrazole (0.013 mmol from a stock solution in CH_3CN) was added, and the solution was stirred for 12 hours. Solvents were removed *in vacuo* to obtain the desired product in quantitative yield. ^{1}H NMR (CD_3CN, 300 MHz): δ 158 (br), 153 (br), 149 (br), 144 (br), 133 (br), 121 (br), 116, 101, 95, 92, 76, 75, 74, 73, 71, 70, 69.5, 68, 62, 53, 52, 40, 37, 33, 23, 18.3, 17.4, 16.7, 15.4, 14, 11.9, 11.5, 10.7, 9.3, 7.4, 7.2, 6.8, 6.1, 5.6, 5.5, 5.2, 4.5, 3.1, 0.6, -0.2, -0.6, -1.4, -1.6, -4.0, -8.9 ppm. ^{19}F NMR (CD_3CN): δ −79.2 ppm.

Synthesis of A.7

In the glovebox, **A.1** (0.024 g, 0.0152 mmol) was dissolved in 3 mL CH_3CN in a 20 mL scintillation vial. 2-Pyridylcarboxaldehyde oxime (0.0152 mmol from a stock solution in CH_3CN) was added, and the solution was stirred for 12 hours. Solvents were removed *in vacuo* to obtain the desired product in quantitative yield. ^{1}H NMR (CD_3CN, 300 MHz): δ 185 (br), 158 (br), 148 (br), 134 (br), 131 (br), 90, 88, 85, 81, 77, 74, 72, 64, 62, 58.2, 57.6, 41, 31, 19.0, 17.7, 16.5, 14.4, 13.8, 13.6, 12.8, 12.2, 11.6, 11.0, 9.8, 8.2, 7.8, 7.1, 6.4, 0, -0.9, -5.0, -5.8, -22 ppm. ^{19}F NMR (CD_3CN): δ −79.2 ppm.

Synthesis of A.8

In the glovebox, **A.6** (0.0209 g, 0.0126 mmol) was dissolved in 3 mL CH_2Cl_2 in a 20 mL scintillation vial. $CoCp_2$ (0.0126 mmol from a stock solution in CH_3CN) was added, and the solution was stirred for 20 minutes. Solvents were removed *in vacuo*. The product could not be separated from the $[CoCp_2]^+$ byproduct; the mixture was used for

reactivity studies. XRD-quality crystals (of sufficient quality solely for the determination of connectivity) of **A.8** were grown by vapour diffusion of diethyl ether into a solution of **A.8** in CH_2Cl_2. ^{1}H NMR (CD_2Cl_2, 300 MHz): δ 147 (br), 130 (br), 126 (br), 121 (br), 114 (br), 105 (br), 93, 85.4, 84.7, 82.5, 74, 71.5, 68, 66.3, 65.8, 64, 59, 56.8, 56.2, 51, 44.8, 44.1, 43.3, 40, 38, 29.1, 27.3, 23.4, 19.5, 17.8, 17.1, 15.5, 14.5, 14.1, 12.2, 11.8, 11.1, 10.6, 7.4, 6.6, 5.0, 4.6, 4.1, 4.0, 2.0, 1.9, 1.1, 1.0, -2.3 (br), -11.3 (br) ppm. ^{19}F NMR (CD_3Cl_2): δ −78.6 ppm.

Synthesis of A.9

In the glovebox, **A.7** (0.0162 g, 0.0099 mmol) was dissolved in 3 mL CH_2Cl_2 in a 20 mL scintillation vial. $CoCp_2$ (0.0099 mmol from a stock solution in CH_3CN) was added, and the solution was stirred for 20 minutes. Solvents were removed *in vacuo*. The product could not be separated from the $[CoCp_2]^+$ byproduct; the mixture was used for reactivity studies. XRD-quality crystals of **A.9** were grown by vapour diffusion of diethyl ether into a solution of **A.9** in CH_2Cl_2. ^{1}H NMR (CD_2Cl_2, 300 MHz): δ 191 (br), 184 (br), 101 (br), 97 (br), 92, 89, 78, 74, 69.1, 68.6, 52, 49, 45, 41, 34, 30, 26.7 (br), 25.7, 22.7, 21.6, 18.8, 17.4, 16.9, 15.5, 13.3, 13.0, 11.7, 9.8, 9.2, 8.8, 7.5, 6.6, 3.6, 3.5, 3.2, 1.8, 1.3, 0.9, -1.4, -4.1, -11.2, -15.8 (br) 93, 85.4, 84.7, 82.5, 74, 71.5, 68, 66.3, 65.8, 64, 59, 56.8, 56.2, 51, 44.8, 44.1, 43.3, 40, 38, 29.1, 27.3, 23.4, 19.5, 17.8, 17.1, 15.5, 14.5, 14.1, 12.2, 11.8, 11.1, 10.6, 7.4, 6.6, 5.0, 4.6, 4.1, 4.0, 2.0, 1.9, 1.1, 1.0, -2.3 (br), -11.3 (br) ppm. ^{19}F NMR (CD_3Cl_2): δ −78.7 ppm.

Synthesis of A.10

In the glovebox, **A.1** (0.0224 g, 0.0142 mmol) was dissolved in a mixture of CH_3CN and CH_2Cl_2 in a 20 mL scintillation vial. Bis(oxime) **A.5** (0.0142 mmol from a stock solution in CH_2Cl_2) was added, and the solution was stirred for 12 hours. Solvents were removed *in vacuo* to obtain the desired product in quantitative yield. XRD-quality crystals of **A.10** were grown by vapour diffusion of diethyl ether into a solution of **A.10** in CH_2Cl_2. ^{1}H NMR (CD_2Cl_2, 300 MHz): δ 156 (br), 150 (br), 140 (br), 125 (br), 99, 97, 91, 88, 87, 80, 68, 66, 62.7, 61.5, 59, 57, 55, 48, 41, 32, 18.7, 18.3, 18.0, 17.7, 17.1, 16.3, 10.4, 9.3, 9.1, 6.74, 6.1, 4.2, 3.6, 1.3, 0.9, 0.5, -1.5, -2.7, -3.3, -4.3, -8.5 ppm. ^{19}F NMR (CD_2Cl_2): δ −77.9 ppm.

Synthesis of A.11

In the glovebox, **A.10** (0.0206 g, 0.0124 mmol) was dissolved in 3 mL CH_2Cl_2 in a 20 mL scintillation vial. $CoCp_2$ (0.0124 mmol from a stock solution in CH_2Cl_2) was added, and the solution was stirred for 20 minutes, during which the color changed from yellow-brown to dark red-brown. Solvents were removed *in vacuo*, and the residue washed with DME to remove $[CoCp_2]^+$. The product was then extracted with CH_2Cl_2 and the solvent removed *in vacuo* to obtain the reduced product **A.11** (0.0154 g, 82 %). ^{1}H NMR (CD_2Cl_2, 300 MHz): δ 164 (br), 158 (br overlapped), 155 (br overlapped), 114 (br), 95 (br), 93, 87, 72.7, 72.3, 71, 63.7, 63.1, 61, 55, 53, 49, 42, 39, 38, 35, 31, 23.9, 19.8, 18.9, 17.8, 16.2, 14.5, 14.2, 13.5, 11.1, 7.3, 6.8, 6.5, 5.1, 3.1, 2.8, 2.2, 1.7, -0.4, -1.2, -8.5, -11.8 ppm. ^{19}F NMR (CD_3Cl_2): δ −78.4 ppm.

Synthesis of A.13

In the glovebox, **31-Fe** (0.0362g, 0.0297 mmol) was suspended in DME in a 20 mL scintillation vial. $Fe(OTf)_2$ and $Fe(OAc)_2$ (0.0148 mmol, 0.5 equiv. each) and PhIO (0.0065 g, 0.0297 mmol, 1 equiv.) were added as DME suspensions. The solution slowly turned brown and remained heterogeneous. After 15 h, the suspension was filtered and washed with DME. The residue was extracted with CH_2Cl_2, and the solvent was removed *in vacuo* to give **A.13** as a brown powder (0.0305 g, 70%). XRD-quality crystals of **A.13** were grown by vapour diffusion of diethyl ether into a solution of **A.13** in CH_2Cl_2. ^{1}H NMR (CD_2Cl_2, 300 MHz): δ 105 (br overlapped), 101 (br overlapped), 73 (br overlapped), 72 (overlapped), 49, 46, 22.6, 19.0, 15.1, 11.9, 10.2, 5.7, 3.0, -11.6 ppm. ^{19}F NMR (CD_3Cl_2): δ −76.6 ppm.

Synthesis of A.15

In the glovebox, **31-Fe** (0.0214 g, 0.0175 mmol) was dissolved in 3 mL 3:1 CH_2Cl_2/CH_3CN in a 20 mL scintillation vial. 2-Pyridylcarboxaldehyde oxime (0.0175 mmol from a stock solution in CH_2Cl_2) was added, and the solution was stirred for 1.5 hours. Solvents were removed *in vacuo* to obtain the desired product **A.15** in quantitative yield as a brown powder. ^{1}H NMR (CD_2Cl_2, 300 MHz): δ 121 (br), 110 (br), 104 (br), 79, 73.0, 72.3, 68.7, 68.3, 67, 65, 60, 56 (br), 54, 49, 45.4, 45.0, 43.6, 39.6, 37.7, 36.3, 36.0, 30.0, 28.1, 27.7, 27.1, 26.0, 23.2, 22.4, 16.6, 15.4, 13.7, 11.0, 10.2, 9.5, 8.5, 8.4, 8.1, 7.7, 7.3, 4.7, 3.6, 2.1, 1.3, 0.0, -6.5, -7.5, -11.5, -16.7 ppm.

Synthesis of A.16

In the glovebox, **31-Fe** (0.0250 g, 0.0205 mmol) was dissolved in 3 mL 3:1 CH_2Cl_2/CH_3CN in a 20 mL scintillation vial. 2-Pyridylpyrazole (0.0205 mmol from a stock solution in CH_2Cl_2) was added, and the solution was stirred for 1.5 hours. Solvents were removed *in vacuo* to obtain the desired product **A.16** in quantitative yield as a light brown powder. ^{1}H NMR (CD_2Cl_2, 300 MHz): δ 113 (br), 104 (br), 100 (br), 96, 91, 83 (br), 77, 76.1, 75.7, 70, 69, 64, 62, 59, 53, 51, 45, 41.8 (br overlapped), 41.4 (overlapped), 39, 36.9, 36.6, 33.5, 30.5, 28.2, 27.9, 26.9, 26.4, 24.8, 23.8, 20.5, 15.8 (br overlapped), 15.3 (br overlapped), 14.4, 12.7 (overlapped), 12.4 (overlapped), 11.3, 9.7, 8.9, 8.7, 8.6, 7.9, 7.6, 7.1, 6.9, 6.5, 6.3, 4.1, 3.3, 2.0, 1.2, -3.3, -3.5-5.6, -6.3, -11.4, -18.3 ppm.

Synthesis of A.17

In the glovebox, **A.15** (0.0225 g, 0.0175 mmol) was suspended in 4 mL DME in a 20 mL scintillation vial. $Fe(OTf)_2$ (0.0062 g, 0.0175 mmol, 1 equiv) and PhIO (0.039 g, 0.0175 mmol, 1 equiv) were added as DME suspensions. Over 1 hour, the solution turned dark brown and became homogeneous. After 12 hours, the solvent was removed *in vacuo* and the residue resolubilized in minimal DME and filtered. The solvent was evaporated to obtain **A.15** as a brown powder (0.0252 g, 83%). ^{1}H NMR (CD_2Cl_2, 300 MHz): δ 204, 170 (br), 157 (br), 152 (br), 134 (br), 111 (br), 106(br), 100, 95, 77, 75, 74, 72, 68, 65, 63, 55, 50, 26.2, 24.1, 21.9, 18.9, 17.2, 16.6, 15.9, 13.0, 11.8, 11.4, 9.9, 8.5, 8.0, 7.7, 7.4, 7.1, 5.8, 3.7, 2.4, 2.1, 1.3, 0.9, 0.1, -0.5, -2.6, -4.0, -5.7, -15.5, -18.9 ppm. ^{19}F NMR (CD_3Cl_2): δ −77.5 ppm.

Synthesis of A.18

In the glovebox, **A.16** (0.0344 g, 0.0264 mmol) was suspended in 4 mL DME in a 20 mL scintillation vial. $Fe(OTf)_2$ (0.093 g, 0.0264 mmol, 1 equiv) and PhIO (0.058 g, 0.0264 mmol, 1 equiv) were added as DME suspensions. Over 1 hour, the solution turned dark brown and became homogeneous. After 12 hours, a brown precipitate had formed, and was collected by filtration over a Celite pad. The residue was then extracted with CH_2Cl_2 and CH_3CN, and the solvents were evaporated *in vacuo* to obtain **A.18** as a brown powder (0.0375 g, 81%). ^{1}H NMR (CD_2Cl_2, 300 MHz): δ 121 (br), 126 (br), 120 (br overlapped), 118 (br overlapped), 99, 98, 97, 77, 73.7, 73.4, 70, 60, 58, 53, 51, 50, 47, 33, 26.5, 25.3, 22.0, 20.5, 18.7, 16.6, 16.5, 16.1, 14.1, 12.7, 11.1, 8.8, 8.2, 7.8, 5.8, 4.8, 4.0, 1.6, 1.1, -0.6, -5.4, -7.0, -9.8, -10.3, -12.2, -23.4 ppm. ^{19}F NMR (CD_3Cl_2): δ −78.0 ppm.

Synthesis of A.19

In the glovebox, **A.17** (0.0161 g, 0.0092 mmol) was dissolved in 3 mL CH_2Cl_2 in a 20 mL scintillation vial. $CoCp_2$ (0.0092 mmol from a stock solution in CH_2Cl_2) was added, and the solution was stirred for 20 minutes, during which the color changed from brown to red-brown. Solvents were removed *in vacuo*. The product could not be separated from the $[CoCp_2]^+$ byproduct; the mixture was used for reactivity studies. ^{1}H NMR (CD_2Cl_2, 300 MHz): δ 121 (br), 97 (br), 92 (br), 89 (br overlapped), 87 (br overlapped), 63, 60, 55, 49.7, 48.6, 46.5, 43.2, 42.5, 41.5, 40.6, 38.7, 33.7, 31.7, 24.7, 24.8, 17.7, 16.2, 14.5, 14.0, 13.3, 12.6, 11.4, 10.3, 8.6, 7.0, 4.2, 4.0, 2.9, 1.3, 0.4, -1.6, -7.1, -11.5 ppm. ^{19}F NMR (CD_3Cl_2): δ −78.6 ppm.

Synthesis of A.20

In the glovebox, **A.18** (0.0252 g, 0.0145 mmol) was dissolved in 3 mL CH_2Cl_2 in a 20 mL scintillation vial. $CoCp_2$ (0.0145 mmol from a stock solution in CH_2Cl_2) was added, and the solution was stirred for 20 minutes, during which the color changed from brown to red-brown. Solvents were removed *in vacuo*. The product could not be separated from the $[CoCp_2]^+$ byproduct; the mixture was used for reactivity studies. ^{1}H NMR (CD_2Cl_2, 300 MHz): δ 121 (br), 113 (br), 105, 97, 95, 87, 82, 73 (br overlapped), 72 (overlapped), 68, 67, 59, 53, 49, 47, 46.1, 45.5, 40, 36, 35, 31, 26.1, 25.7, 23.1, 22.7, 21.0, 19.0, 15.1, 14.1, 12.9, 12.7, 9.3, 3.2, 3.0, 1.3, 0.9, 0.5, 0.1, -2.0, -2.2, -8.0, -8.8, -11.5, -23.6, -43.7 ppm. ^{19}F NMR (CD_3Cl_2): δ −78.7 ppm.

Synthesis of A.24

In the glovebox, **LH_3** (0.3273 g, 0.381 mmol) was dissolved in 5 mL THF in a 20 mL scintillation vial. The solution was frozen in a LN_2-cooled cold well, and upon thawing a solution of $ZnEt_2$ (0.1459 g, 1.18 mmol, 3.1 equiv.) was added. The solution was allowed to warm to room temperature, and stirred for 4 hours. The solvent was removed *in vacuo* and the residue suspended in toluene. The suspension was filtered, and the residue extracted with copious amounts of THF. The solvent was evaporated to give the desired product **A.24** as a light yellow powder (0.330 g, 76%). Complex **A.24** is not indefinitely stable in CH_2Cl_2 but NMR characterization was carried out in CD_2Cl_2 for the purposes of observing resonances in the aromatic region. XRD-quality crystals of **A.24** were grown by vapour diffusion of pentane into a solution of **A.24** in benzene. ^{1}H NMR (CD_2Cl_2, 300 MHz): δ 8.73 (m, 3H, Py*H*), 7.99 (m, 3H, Ar*H*), 7.72 (m, 3H, Py*H*), 7.57, (m, 3H, Py*H*), 7.45 (m, 3H, Py*H*), 7.18 (m, 12H, Py*H*+Ar*H*), 6.98 (m, 3H,

Py*H*), 6.79 (m, 3H, Py*H*), 6.68 (m, 3H, Py*H*), 5.20 (s, 3H, Ar*H*), 0.43 (t, 8.0 Hz, 9H, $ZnCH_2CH_3$), -1.14 (q, 8.0 Hz, 6H, $ZnCH_2CH_3$) ppm.

Synthesis of A.25

In the glovebox, **A.24** (0.0223 g, 0.019 mmol) was dissolved in 3 mL toluene in a 20 mL scintillation vial and cooled to -40 °C. A solution of 2,6-lutidinium triflate (0.005 g, 0.019 mmol, 1 equiv.) in toluene was added dropwise, and a precipitate formed immediately. The suspension was filtered and washed with toluene, and the residue extracted with CH_2Cl_2 which was then rapidly evaporated to minimize decomposition. The product **A.25** was obtained as a light yellow powder containing a small amount of impurities. Complex **A.25** is not indefinitely stable in CH_2Cl_2 but characterization and further reactivity studies were carried out in this solvent because of lack of solubility of **A.25** in other organic solvents. ^{1}H NMR (CD_2Cl_2, 300 MHz): δ 8.69 (m, 2H, Py*H*), 8.48 (m, 1H, Py*H*), 8.31 (m, 1H, Py*H*), 8.15 (m, 2H, Py*H*+Ar*H*), 7.95 (m, 2H, Py*H*+Ar*H*), 7.75, (m, 2H, Py*H*+Ar*H*), 7.67 (m, 2H, Py*H*+Ar*H*), 7.23-7.60 (m, 12H, Py*H*+Ar*H*), 7.05 (m, 2H, Py*H*+Ar*H*), 6.94 (m, 2H, Py*H*+Ar*H*), 6.77 (m, 3H, Ar*H*), 6.65 (m, 3H, Ar*H*), 5.98 (s, 1H, Ar*H*), 5.16 (s, 2H, Ar*H*), 0.37 (t, 8.0 Hz, 6H, $ZnCH_2CH_3$), -1.17 (q, 8.0 Hz, 4H, $ZnCH_2CH_3$) ppm. ^{19}F NMR (CD_3Cl_2): δ −78.7 ppm.

Synthesis of A.23-Zn

In a J.Young NMR tube, **A.24** (0.0177 g, 0.0141 mmol) was dissolved in 0.5 mL CD_2Cl_2. Bis(trimethylsilyl)sulfide (14.8 μL, 0.0703 mmol, 5 equiv.) was added via a gas-tight microsyringe, and the reaction progress was monitored by ^{1}H NMR. After 20 h, the starting material had been converted to a new major product. The solution was returned to the glovebox and the solvents removed *in vacuo*. The residue was washed with THF to give a fraction containing some of the desired product together with other impurities. The remaining material was extracted with CH_2Cl_2, and the solvent was evaporated to give the desired product **A.23-Zn** as an off-white powder (0.0094 g, 54 %). XRD-quality crystals were grown by vapour diffusion of diethyl ether into a solution of **A.23-Zn** in CH_2Cl_2. ^{1}H NMR (CD_2Cl_2, 300 MHz): δ 8.65 (m, 3H, Py*H*), 8.07 (m, 3H, Py*H*), 7.97 (m, 3H, Py*H*), 7.87 (m, 6H, Py*H*+Ar*H*), 7.46 (m, 3H, Py*H*), 7.31, (m, 3H, Py*H*), 7.19 (m, 12H, Py*H*+Ar*H*), 7.05 (m, 3H, Py*H*), 5.72 (s,3H, Ar*H*), 0.37 (t, 8.0 Hz, 6H, $ZnCH_2CH_3$), -1.17 (q, 8.0 Hz, 4H, $ZnCH_2CH_3$) ppm. ^{19}F NMR (CD_3Cl_2): δ −78.7 ppm.

Synthesis of A.29

In the glovebox, **31-Fe** (0.1065 g, 0.0887 mmol) was dissolved in 6 mL CH_2Cl_2 in a 20 mL scintillation vial. Methyl triflate (29.2 μL, 0.266 mmol, 3 equiv.) was added as a CH_2Cl_2, and the solution immediately turned from orange to bright yellow. After 20 min, the volume of the solution was reduced to ~3 mL, and 15 mL Et_2O was added to precipitate the product. The suspension was filtered and washed with copious amounts of Et_2O. The residue was then extracted with CH_2Cl_2 and the solvent evaporated to give **A.29** as a yellow powder (0.117 g, 90%). XRD-quality crystals of **A.29** were grown

by vapour diffusion of diethyl ether into a solution of **A.29** in CH_2Cl_2. ^1H NMR (CD_2Cl_2, 300 MHz): δ 101, 85, 76, 48, 46, 37, 34, 30, 26, 11, 1.2, 0.6, -5.1 ppm. ^{19}F NMR (CD_3Cl_2): δ −50.5 (br) ppm.

Crystallographic Information

Refinement details

In each case, crystals were mounted on a glass fiber or nylon loop using Paratone or Framblin oil under a nitrogen stream. Low temperature (100 K) X-ray data were obtained on a Bruker APEXII CCD based diffractometer (Mo sealed X-ray tube, K_α = 0.71073 Å). All diffractometer manipulations, including data collection, integration and scaling were carried out using the Bruker APEXII software.[41] Absorption corrections were applied using SADABS.[42] Space groups were determined on the basis of systematic absences and intensity statistics and the structures were solved by direct methods using XS[43] (incorporated into SHELXTL) and refined by full-matrix least squares on F^2. All non-hydrogen atoms were refined using anisotropic displacement parameters. Hydrogen atoms were placed in idealized positions and refined using a riding model. The structure was refined (weighted least squares refinement on F^2) to convergence. Due to the size of these compounds, most crystals included solvent accessible voids, which tended to contain disordered solvent. In addition, due to a tendency to desolvate, the long range order of these crystals and amount of high angle data we were able to record was in some cases not ideal. These disordered solvent molecules were largely responsible for the alerts generated by the checkCIF protocol. In some cases, this disorder could be modeled satisfactorily, while in others disordered solvent was refined isotropically.

Table 2. Crystal and refinement data.

	A.9	**A.10**	**A.13**	**A.21**
empirical formula	$C_{84.7}H_{61.17}Cl_{2.44}CoF_6Fe_3N_8O_{16.23}S_2Zn$	$C_{78.35}H_{59}F_{5.67}Fe_3N_9O_{15.67}S_{1.89}Zn$	$C_{44.37}H_{33.96}Cl_{0.91}F_2Fe_{2.63}N_4O_{10}S_{0.67}$	$C_{74}H_{66}CaF_6Fe_3N_{10}O_{16}S_2$
formula wt	2006.99	1778.56	1021.51	1737.11
T (K)	100	100	100	100
a, Å	14.5861(7)	19.4338(7)	27.5978(11)	13.311(3)
b, Å	27.8888(14)	16.6130(6)	12.3159(5)	13.921(3)
c, Å	21.6516(11)	26.0379(9)	19.5245(8)	42.698(9)
α, deg	90	90	90	90
β, deg	105.059(3)	111.551(2)	90	90
γ, deg	90	90	90	90
V, Å^3	8505.1(7)	7818.8(5)	6636.2(5)	7912(3)
Z	4	4	6	4
crystal system	monoclinic	monoclinic	orthorhombic	orthorhombic
space group	$P2_1/c$	$P2_1/c$	$Pca2_1$	$P2_12_12_1$
d_{calcd}, g/cm^3	1.56	1.511	1.534	1.458
2θ range, deg	3.51 to 55.442	3.33 to 63.956	3.614 to 73.824	4.34 to 54.942
μ, mm^{-1}	1.179	0.985	1.011	0.745
abs cor	Multi-scan	Multi-scan	Multi-scan	Multi-scan
GOF[c]	1.118	1.120	1.089	1.057
R1,[a] wR2[b] ($I > 2\sigma(I)$)	0.0777, 0.1771	0.1035, 0.2518	0.0693, 0.1646	0.0890, 0.2198

	A.24	**A.30**	**A.31**
empirical formula	$C_{69}H_{60}N_6O_3Zn_3$	$C_{63.04}H_{39}Cl_{4.7}F_{4.42}Fe_{3.5}N_6O_{11.03}S_{1.46}$	$C_{61}H_{43}Cl_2F_3Fe_3N_9O_8S$
formula wt	1217.34	1549.63	1357.55
T (K)	100	100	100
a, Å	12.6332(14)	36.184(2)	16.9576(9)
b, Å	13.5649(15)	14.3462(9)	17.4846(9)
c, Å	18.979(2)	25.3404(15)	19.7687(10)
α, deg	91.973(5)	90	90
β, deg	108.205(5)	94.127(3)	92.582(3)
γ, deg	109.719(4)	90	90
V, Å^3	2872.6(6)	13120.1(14)	5855.4(5)
Z	2	8	4
cryst syst	triclinic	monoclinic	monoclinic
space group	P-1	C2/c	Cc
d_{calcd}, g/cm^3	1.407	1.569	1.540
θ range, deg	3.23 to 66.948	3.054 to 64.55	3.874 to 80.818
μ, mm^{-1}	1.297	1.075	0.934
abs cor	Multi-scan	Multi-scan	Multi-scan
GOF[c]	1.005	1.049	1.063
R1,[a] wR2[b] ($I > 2\sigma(I)$)	0.0400, 0.0811	0.0529, 0.1282	0.0567, 0.1571

[a] $R1 = \Sigma||F_o|-|F_c|| / \Sigma|F_o|$ [b] $wR2 = [\Sigma[w(F_o^2-F_c^2)^2] / \Sigma[w(F_o^2)^2]]^{1/2}$ [c] $GOF = S = [\Sigma[w(F_o^2-F_c^2)^2] / (n-p)]^{1/2}$

Special Refinement Details for A.9

In the solid-state structure of complex **A.9**, two different orientations of the oximate ligand were observed, in a 60:40 population ratio, and this disorder was modeled satisfactorily. Non-coordinated solvent molecules were present with partial occupations ranging from 40% to 100%. One of these (a CH_2Cl_2 molecule) was modeled anisotropically, while the other two (one CH_2Cl_2 and an Et_2O molecule in two separate orientations) were modeled isotropically. The asymmetric unit of complex **A.9** also contained a co-crystallyzed $[CoCp_2][OTf]$ moiety (modeled satisfactorily).

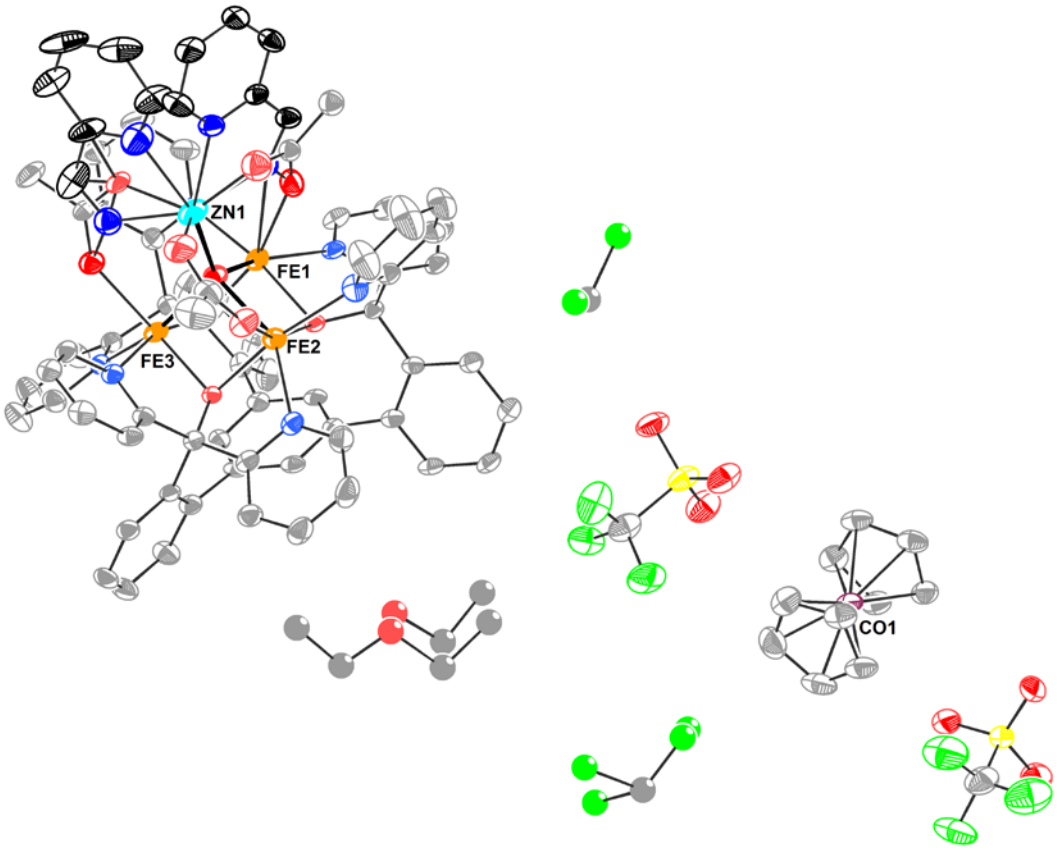

Figure 17. Full representation of the solid-state structure of complex **A.9**. Hydrogen atoms omitted for clarity.

Special Refinement Details for A.10

In the solid-state structure of complex **A.10**, one of the two outer-sphere triflate anions was disordered over two positions, and this disorder was modeled satisfactorily, with both moieties modeled anisotropically. A non-coordinated Et_2O solvent molecule was also disorderd over two positions – these two molecules were refined isotropically to a total occupancy of 1.

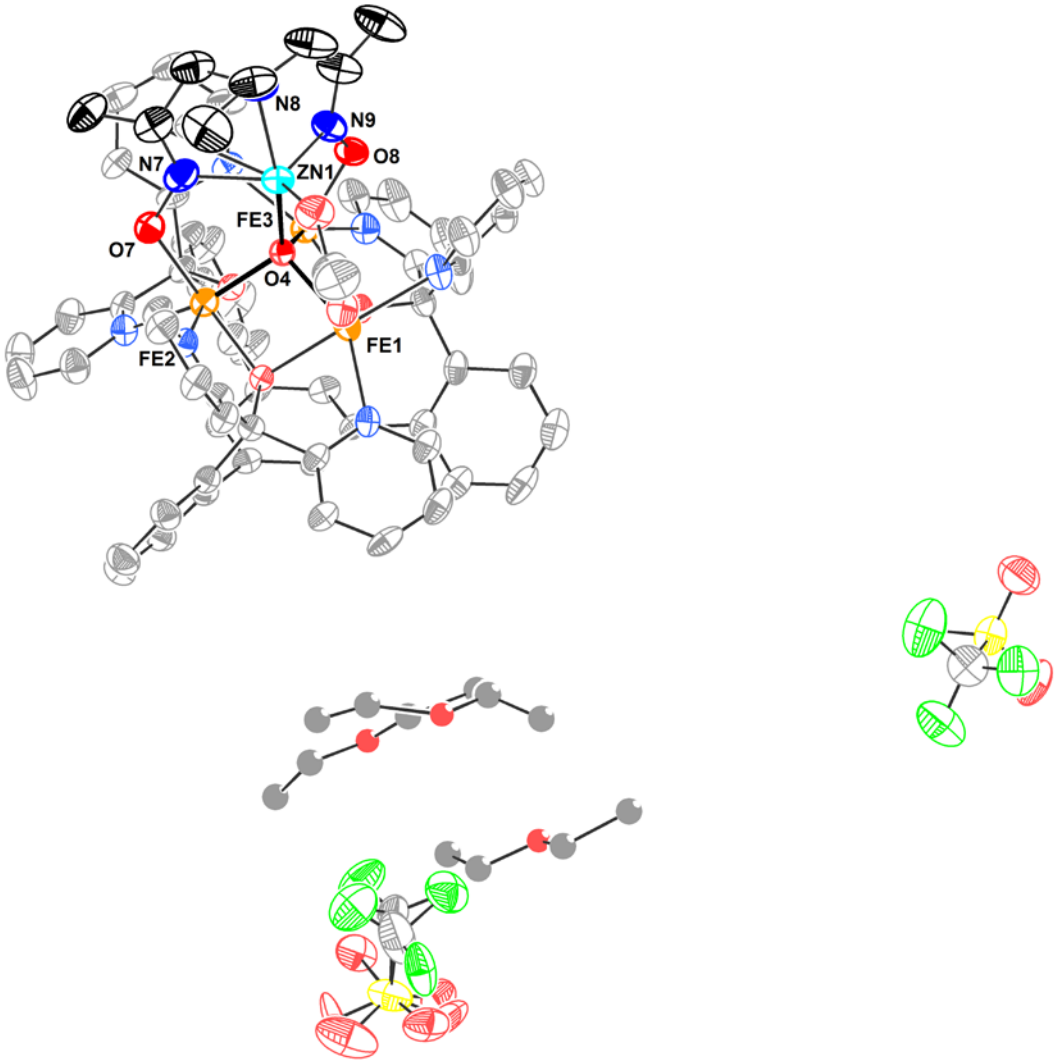

Figure 18. Full representation of the solid-state structure of complex **A.10**. Hydrogen atoms omitted for clarity.

Special Refinement Details for A.13

In the solid-state structure of complex **A.13**, two non-coordinated CH_2Cl_2 molecules were isotropically refined to free occupancies of 47% and 21%.

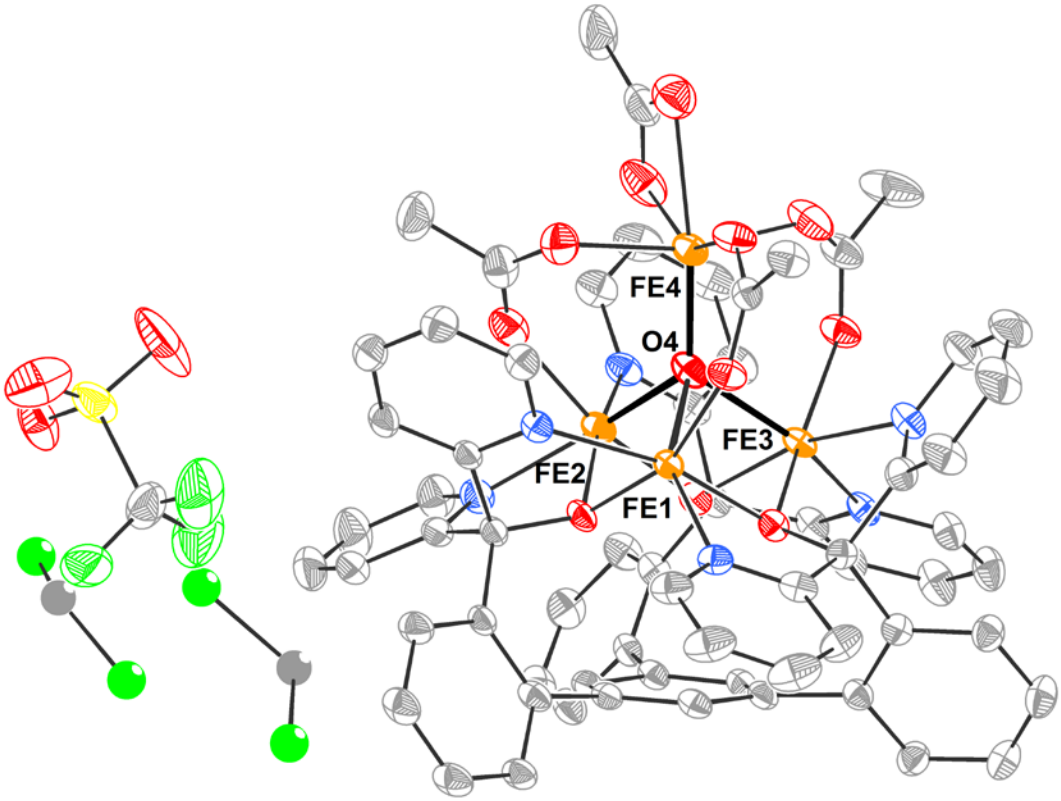

Figure 19. Full representation of the solid-state structure of complex **A.13**. Hydrogen atoms omitted for clarity.

Special Refinement Details for A.21

One outer-sphere CH_3CN molecule was present in the solid-state structure of complex **A.21,** and it was satisfactorily modeled anisotropically.

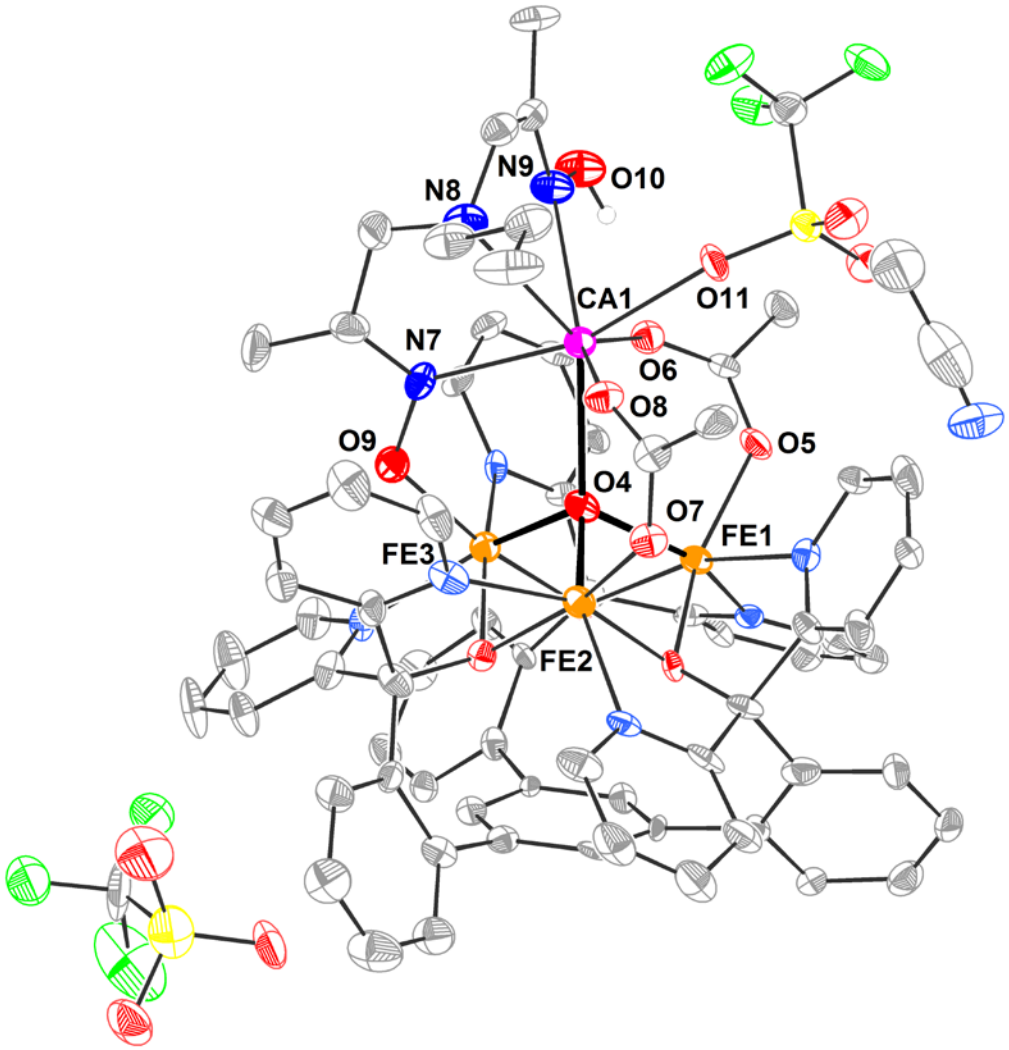

Figure 20. Full representation of the solid-state structure of complex **A.21**. Hydrogen atoms omitted for clarity.

Special Refinement Details for A.24

Two halves of C_6H_6 molecules were present in the asymmetric unit of the solid-state structure of complex **A.24**, which were modeled anisotropically.

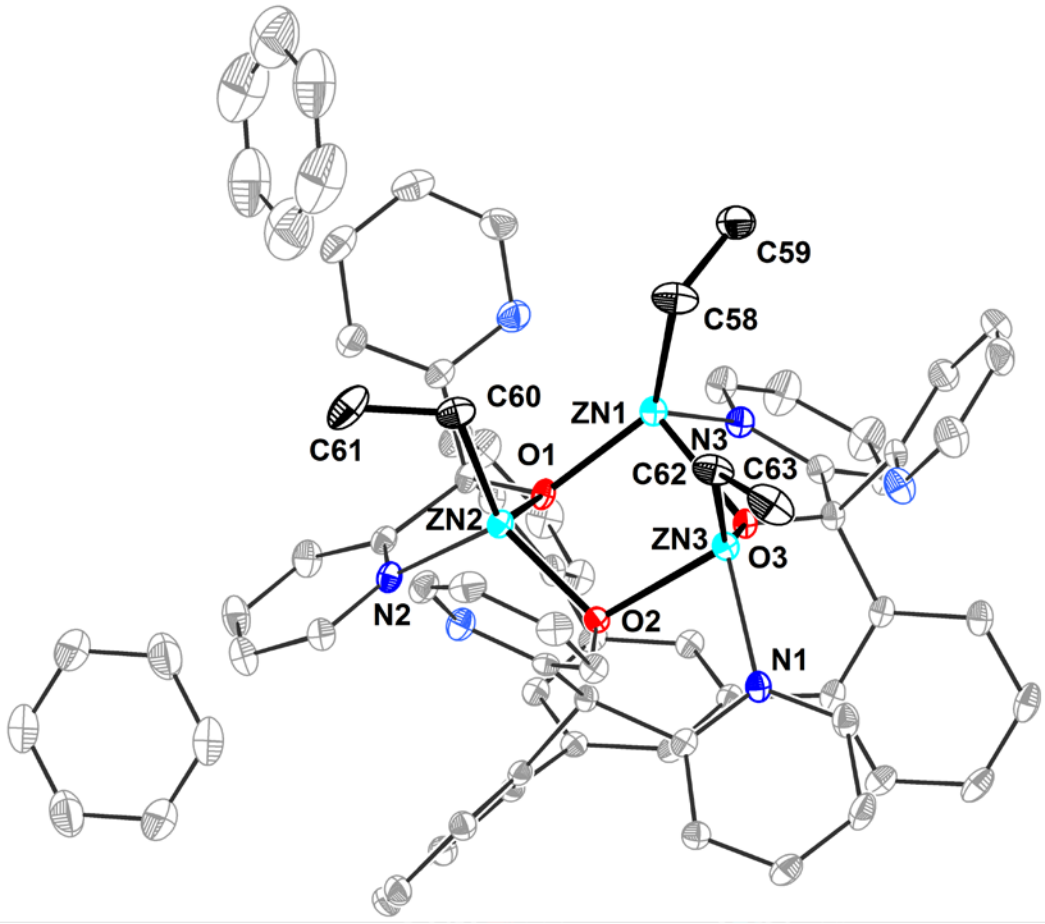

Figure 21. Full representation of the solid-state structure of complex **A.24**. Hydrogen atoms omitted for clarity.

Special Refinement Details for A.30

In the solid-state structure of complex **A.30**, a disordered triflate anion was located on a crystallographic symmetry element, resulting in disorder split into two symmetry-related asymmetric units. This disorder was modeled and all atoms in this moiety were refined anisotropically. An outer-sphere CH_2Cl_2 molecule was disordered over two positions, modeled in a 54:46 ratio and refined anisotropically. Another CH_2Cl_2 molecule was present in partial occupancy in the same site as an Et_2O molecule. These two moieties were modeled to a total occupancy of 1 and were refined isotropically. Finally, a third CH_2Cl_2 molecule was present in 90% occupancy and was refined anisotropically.

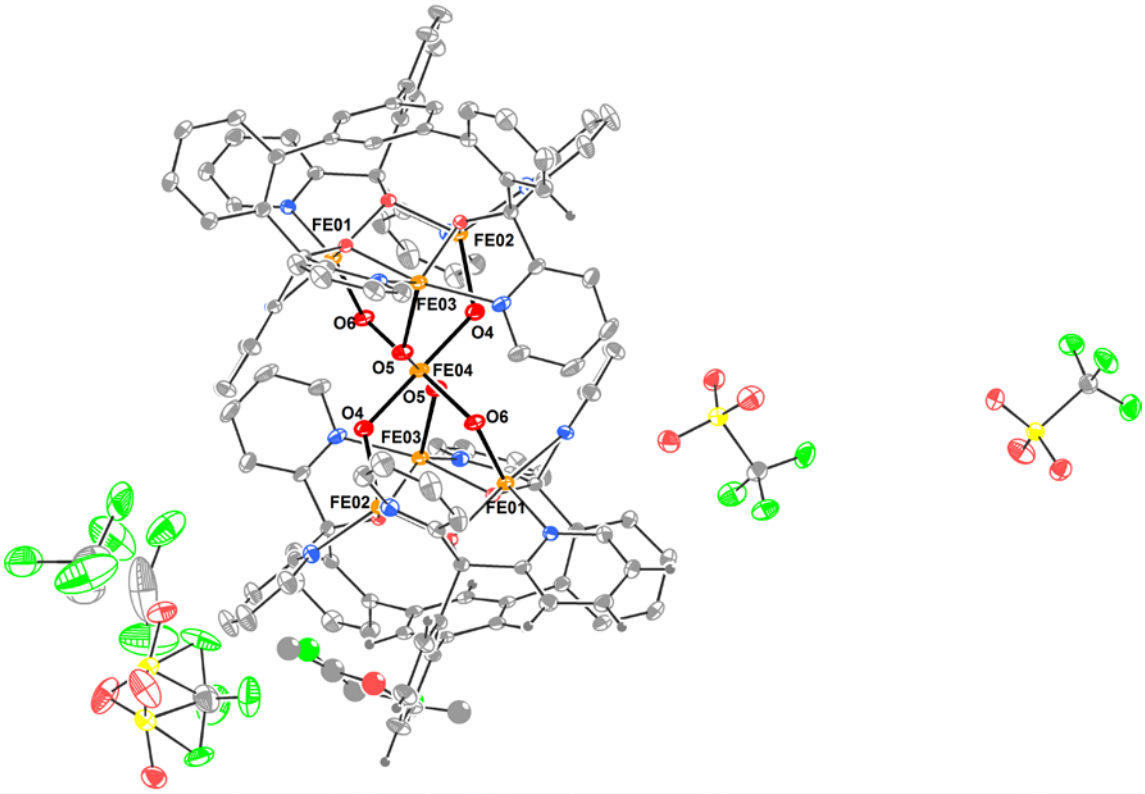

Figure 22. Full representation of the solid-state structure of complex **A.30**. Hydrogen atoms omitted for clarity.

Special Refinement Details for A.31

One outer-sphere CH_2Cl_2 molecule was present in the solid-state structure of **A.31** and was refined anisotropically.

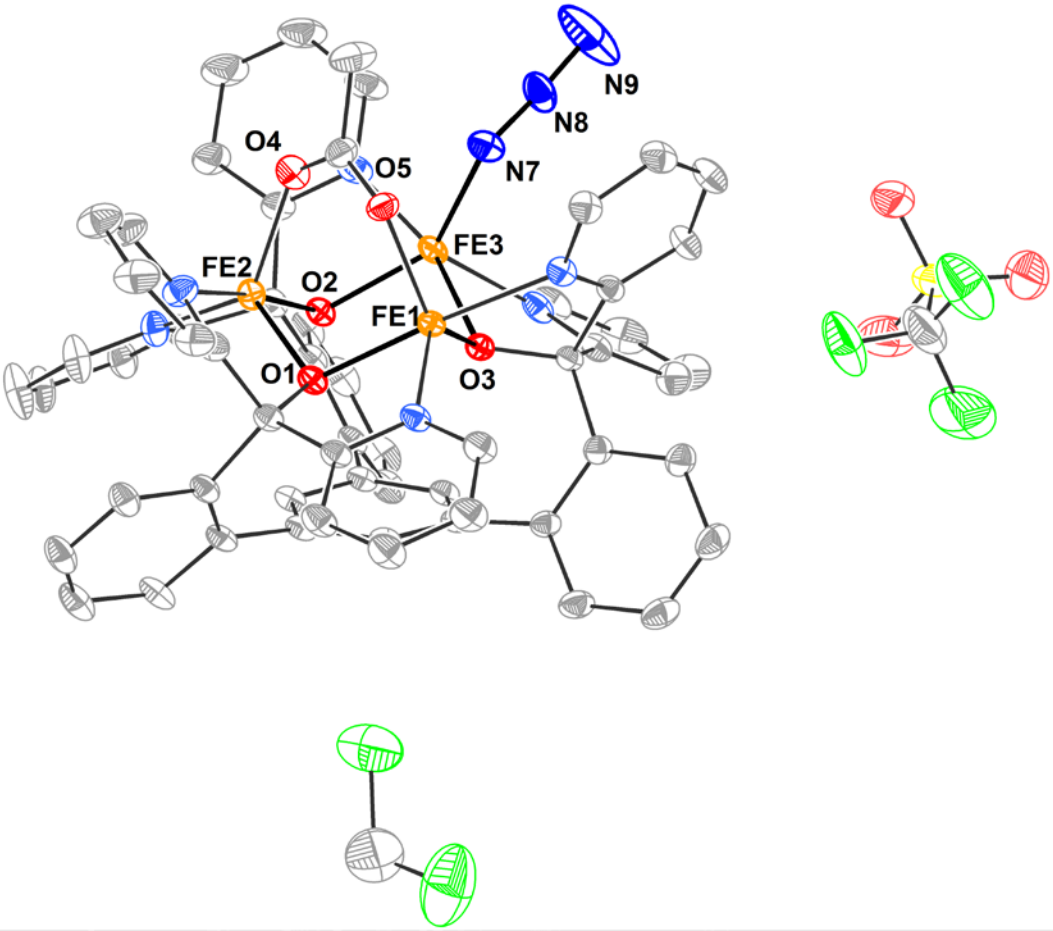

Figure 23. Full representation of the solid-state structure of complex **A.31**. Hydrogen atoms omitted for clarity.

REFERENCES

(1) Holm, R. H.; Kennepohl, P.; Solomon, E. I. *Chem. Rev.* **1996**, *96*, 2239.

(2) Holm, R. H.; Solomon, E. I. *Chem. Rev.* **2004**, *104*, 347.

(3) Du, P. W.; Eisenberg, R. *Energy Environ. Sci.* **2012**, *5*, 6012.

(4) Smith, R. D. L.; Prevot, M. S.; Fagan, R. D.; Zhang, Z. P.; Sedach, P. A.; Siu, M. K. J.; Trudel, S.; Berlinguette, C. P. *Science* **2013**, *340*, 60.

(5) Karkas, M. D.; Verho, O.; Johnston, E. V.; Akermark, B. *Chem. Rev.* **2014**, *114*, 11863.

(6) Yano, J.; Yachandra, V. *Chem. Rev.* **2014**, *114*, 4175.

(7) Buchwalter, P.; Rose, J.; Braunstein, P. *Chem. Rev.* **2015**, *115*, 28.

(8) Suntivich, J.; Gasteiger, H. A.; Yabuuchi, N.; Nakanishi, H.; Goodenough, J. B.; Shao-Horn, Y. *Nat. Chem.* **2011**, *3*, 546.

(9) Suntivich, J.; May, K. J.; Gasteiger, H. A.; Goodenough, J. B.; Shao-Horn, Y. *Science* **2011**, *334*, 1383.

(10) Mukherjee, S.; Stull, J. A.; Yano, J.; Stamatatos, T. C.; Pringouri, K.; Stich, T. A.; Abboud, K. A.; Britt, R. D.; Yachandra, V. K.; Christou, G. *Proc. Natl. Acad. Sci. USA* **2012**, *109*, 2257.

(11) Tsui, E. Y.; Kanady, J. S.; Agapie, T. *Inorg. Chem.* **2013**, *52*, 13833.

(12) Rodriguez, M. M.; Bill, E.; Brennessel, W. W.; Holland, P. L. *Science* **2011**, *334*, 780.

(13) Zhang, C. X.; Chen, C. H.; Dong, H. X.; Shen, J. R.; Dau, H.; Zhao, J. Q. *Science* **2015**, *348*, 690.

(14) Lee, S. C.; Lo, W.; Holm, R. H. *Chem. Rev.* **2014**, *114*, 3579.

(15) Powers, T. M.; Gu, N. N. X.; Fout, A. R.; Baldwin, A. M.; Sanchez, R. H.; Alfonso, D. M.; Chen, Y. S.; Zheng, S. L.; Betley, T. A. *J. Am. Chem. Soc.* **2013**, *135*, 14448.

(16) Clouston, L. J.; Siedschlag, R. B.; Rudd, P. A.; Planas, N.; Hu, S. X.; Miller, A. D.; Gagliardi, L.; Lu, C. C. *J. Am. Chem. Soc.* **2013**, *135*, 13142.

(17) Tereniak, S. J.; Carlson, R. K.; Clouston, L. J.; Young, V. G.; Bill, E.; Maurice, R.; Chen, Y. S.; Kim, H. J.; Gagliardi, L.; Lu, C. C. *J. Am. Chem. Soc.* **2014**, *136*, 1842.

(18) Lionetti, D.; Day, M. W.; Agapie, T. *Chem. Sci.* **2013**, *4*, 785.

(19) Tsui, E. Y.; Day, M. W.; Agapie, T. *Angew. Chem. Int. Ed.* **2011**, *50*, 1668.

(20) Tsui, E. Y.; Kanady, J. S.; Day, M. W.; Agapie, T. *Chem. Commun.* **2011**, *47*, 4189.

(21) Kanady, J. S.; Tsui, E. Y.; Day, M. W.; Agapie, T. *Science* **2011**, *333*, 733.

(22) Kanady, J. S.; Tran, R.; Stull, J. A.; Lu, L.; Stich, T. A.; Day, M. W.; Yano, J.; Britt, R. D.; Agapie, T. *Chem. Sci.* **2013**, *4*, 3986.

(23) Tsui, E. Y.; Tran, R.; Yano, J.; Agapie, T. *Nat. Chem.* **2013**, *5*, 293.

(24) Tsui, E. Y.; Agapie, T. *Proc. Natl. Acad. Sci. USA* **2013**, *110*, 10084.

(25) Kanady, J. S.; Mendoza-Cortes, J. L.; Tsui, E. Y.; Nielsen, R. J.; Goddard, W. A.; Agapie, T. *J. Am. Chem. Soc.* **2013**, *135*, 1073.

(26) Herbert, D. E.; Lionetti, D.; Rittle, J.; Agapie, T. *J. Am. Chem. Soc.* **2013**, *135*, 19075.

(27) Kanady, J. S.; Lin, P. H.; Carsch, K. M.; Nielsen, R. J.; Takase, M. K.; Goddard, W. A.; Agapie, T. *J. Am. Chem. Soc.* **2014**, *136*, 14373.

(28) Lin, P. H.; Takase, M. K.; Agapie, T. *Inorg. Chem.* **2015**, *54*, 59.

(29) Suseno, S.; Agapie, T., *Manuscript in preparation*.

(30) Lionetti, D.; Suseno, S.; Tsui, E. Y.; Lu, L.; Britt, R. D.; Carsch, K. M.; Agapie, T., *Manuscript in preparation*.

(31) Armand, M.; Tarascon, J. M. *Nature* **2008**, *451*, 652.

(32) Service, R. F. *Science* **2009**, *324*, 1257.

(33) Bockris, J. O.; Otagawa, T. *J. Electrochem. Soc.* **1984**, *131*, 290.

(34) Meadowcroft, D. B. *Nature* **1970**, *226*, 847.

(35) Suntivich, J.; Gasteiger, H. A.; Yabuuchi, N.; Nakanishi, H.; Goodenough, J. B.; Shao-Horn, Y. *Nat. Chem.* **2011**, *3*, 647.

(36) Suntivich, J.; Gasteiger, H. A.; Yabuuchi, N.; Shao-Horn, Y. *J. Electrochem. Soc.* **2010**, *157*, B1263.

(37) Goldcamp, M. J.; Edison, S. E.; Squires, L. N.; Rosa, D. T.; Vowels, N. K.; Coker, N. L.; Bauer, J. A. K.; Baldwin, M. J. *Inorg. Chem.* **2003**, *42*, 717.

(38) Pauleta, S. R.; Dell'Acqua, S.; Moura, I. *Coord. Chem. Rev.* **2013**, *257*, 332.

(39) Pomowski, A.; Zumft, W. G.; Kroneck, P. M. H.; Einsle, O. *Nature* **2011**, *477*, 234.

(40) Achard, T.; Giordano, L.; Tenaglia, A.; Gimbert, Y.; Buono, G. *Organometallics* **2010**, *29*, 3936.

(41) *APEX2, Version 2 User Manual, M86-E01078,*; Bruker Analytical X-ray Systems: Madison, WI, June 2006.

(42) Sheldrick, G. M., "SADABS (version 2008/1): Program for Absorption Correction for Data from Area Detector Frames", University of Göttingen, 2008

(43) Sheldrick, G. M. *Acta Crystallogr., Sect. A: Found. Crystallogr.* **2008**, *64*, 112.

APPENDIX B

ADDITIONAL STRUCTURES

INTRODUCTION

Structural information was obtained for a handful of additional compounds outside the confines of the investigations covered in the previous chapters, and are therefore included here. Three of the compounds described herein were observed during studies of Cu systems for activations of small molecules as described in chapters 2 and 3. The final complex was encountered as an undesired side-product in studies of the deprotonation of the Fe_3 oxo-hydroxo clusters described in chapter 4.

RESULTS AND DISCUSSION

In early attempts to target multimetallic complexes with two or more Cu centers in close proximity, a zirconium dicopper species was prepared with a dianionic, tetradentate ligand scaffold supporting the Zr center and each Cu center bound to a dipicolylamine moiety on a pendant monodentate phenoxide ligand (**B.1**). Despite the lack of structural characterization for this complex, its reactivity with O_2 was explored to determine the feasibility of cooperative activation by the two Cu centers. Instead, reaction with dioxygen did not result in observation of intermediates at low temperature, and yielded as one of the final products a dicopper(II) complex supported by two dipicolylamine-phenoxide ligands (**B.2**, Scheme 1), which was characterized by X-ray diffraction (XRD) methods. The same product was obtained by treating [$ZrCu_2$] complex **B.1** with hydrogen peroxide. The loss of the Zr portion of the complex indicated that this framework was not sufficiently robust to allow study of O_2 activation.

Scheme 1. Reactivity of [$ZrCu_2$] Complex **B.1** with O_2 and H_2O_2.

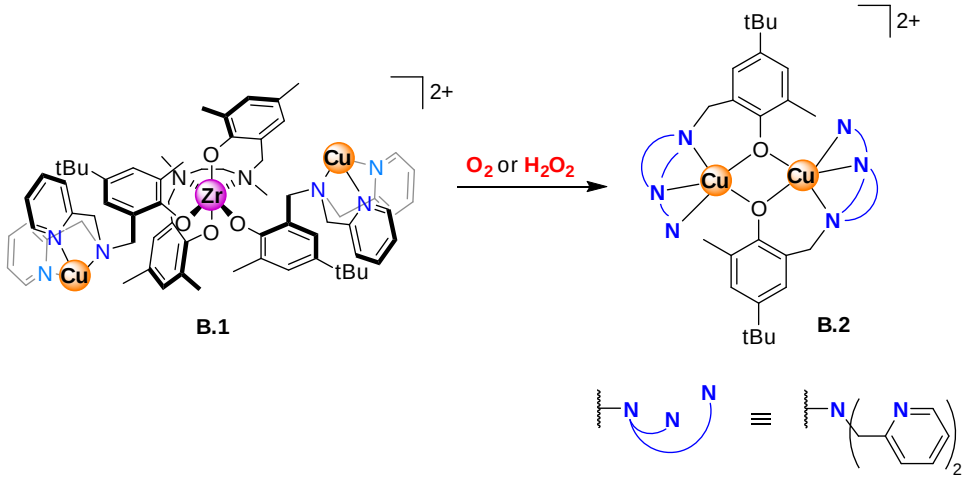

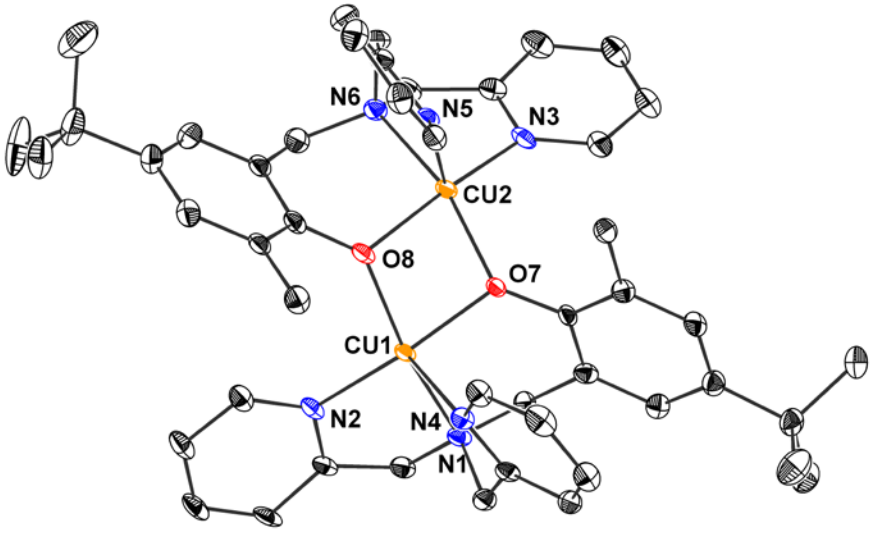

Figure 1. Solid-state structure of complex **B.1**. H-atoms and outer-sphere anions omitted for clarity. Thermal ellipsoids shown at the 50% probability level.

In an effort to obtain structural evidence of cooperative reactivity of the three Cu centers in yttrium tricopper complex **4-Y**, exchange of the trifluoromethanesulfonate anions with carboranes ($CB_{11}H_{12}^-$) was attempted (Scheme 2), followed by treatment with sodium persulfide (Na_2S_2). The only product that could be characterized crystallographically was an yttrium trisodium complex with carborane counteranions (**B.3**, Figure 2).

Scheme 2. Anion Exchange and Reactivity with Persulfide of Yttrium-Tricopper(I) Complex **4-Y**

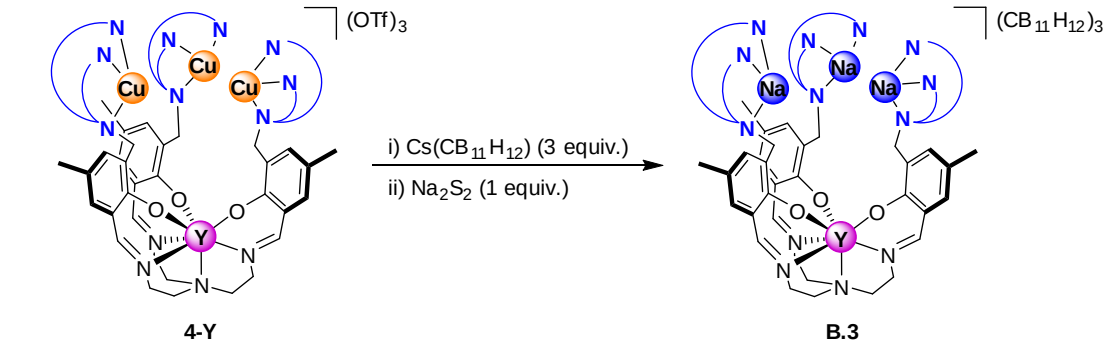

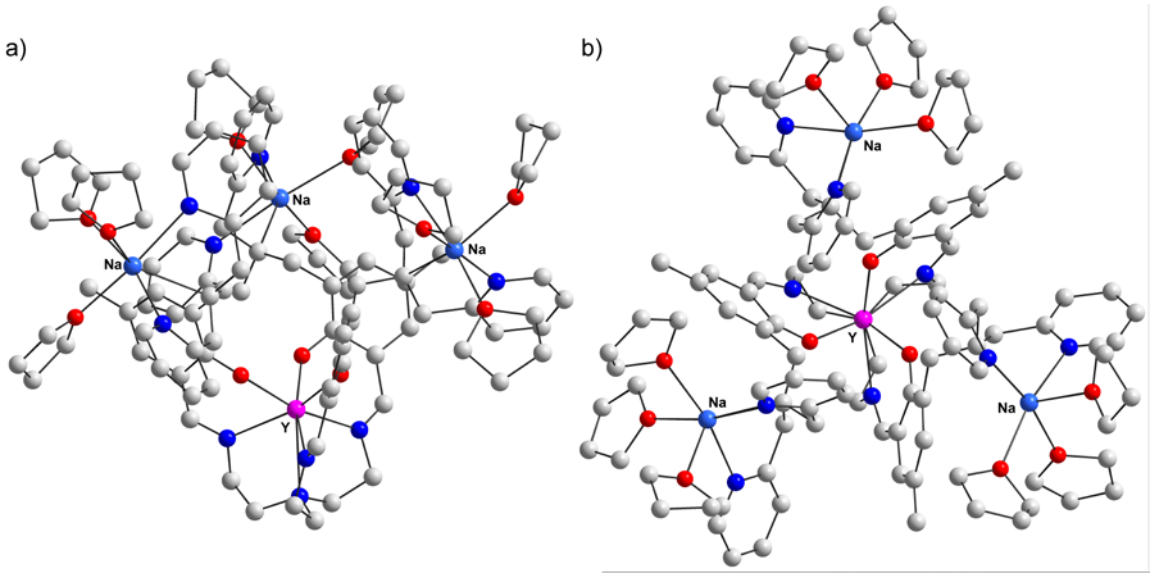

Figure 2. Preliminary solid-state structure of complex **B.3**: (a) side view; (b) top-down view.

In studies of the reactivity of Cu complexes with nitric oxide (chapter 3), a mononuclear Cu^{II} nitrite (NO_2^-) complex was targeted via independent synthesis to provide a spectroscopic benchmark for studies on NO reduction and disproportionation by the analogous Cu^{I} complex. Treatment of the mononucleating ligand **B.4** with $Cu(SO_4)$, followed by treatment with excess sodium nitrite ($NaNO_2$) resulted in isolation of a green powder from which poor-quality crystals were grown

(Scheme 3). XRD studies of these crystals provided a preliminary structure supporting the successful synthesis of a Cu^{II} complex bearing two nitrite ligands (**B.5**, Figure 3).

Scheme 3. Synthesis of Dinitrite Complex **B.5**.

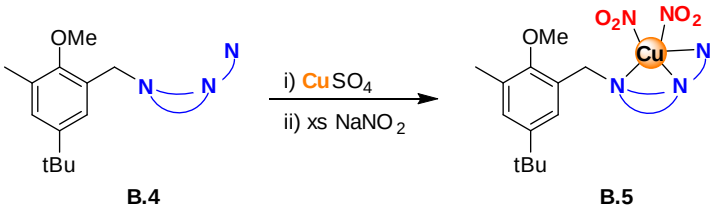

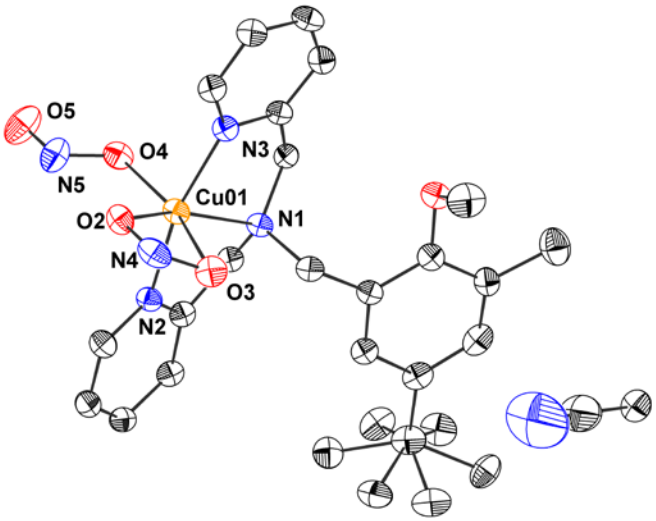

Figure 3. Preliminary solid-state structure of complex **B.5** showing incorporation of two NO_2^- ligands.

While exploring possible protocols to deprotonate Fe_3 oxo-hydroxo clusters supported by a different multinucleating ligand scaffold, an undesired but nonetheless unique species was obtained by treating [Fe^{III}_3] calcium oxo-hydroxo cluster **32-Ca** with sodium hexamethyldisilazide ($NaN(SiMe_3)_2$, Scheme 4). XRD analysis of crystals grown from the material obtained from this reaction showed a hitherto never observed incorporation of the large Ca dication in the trimetallic cluster core, substituting one of the Fe centers (Figure 4). Dimerization via multiple oxide/hydroxide bridges, likely generated by decomposition of additional equivalents of oxo-hydroxo complex, led to

observation of an octametallic core which two partial cubane-like motifs. Notably, terminal as well as μ_2, μ_3, and μ_4 oxygen-based bridges were present. Based on XRD data, the μ_2 and μ_3 bridging ligands were assigned as hydroxides. It was on the other hand impossible to conclusively assign the terminal O ligand (O(7), Figure 4) as a hydroxide or water ligand on the basis of XRD data; however, charge balance indicated that the more likely assignment was as a neutral water ligand, consistent with [Fe^{III}_6] complex (Fe^{IV} has not been observed in any complex supported by the present multinucleating framework.).

This type of product, in which a large metal ion had been incorporated in the trimetallic core, was the result of a metal-exchange process that had only rarely been observed previously (and then only with similarly-sized transition metal ions). Although it showcased the flexibility of the ligand scaffold, the lack of a rational protocol for synthesis of heterotrimetallic cores made this result less notable.

Scheme 4. Reactivity of Oxo-Hydroxo Complex **32-Ca** with $NaN(SiMe_3)_2$.

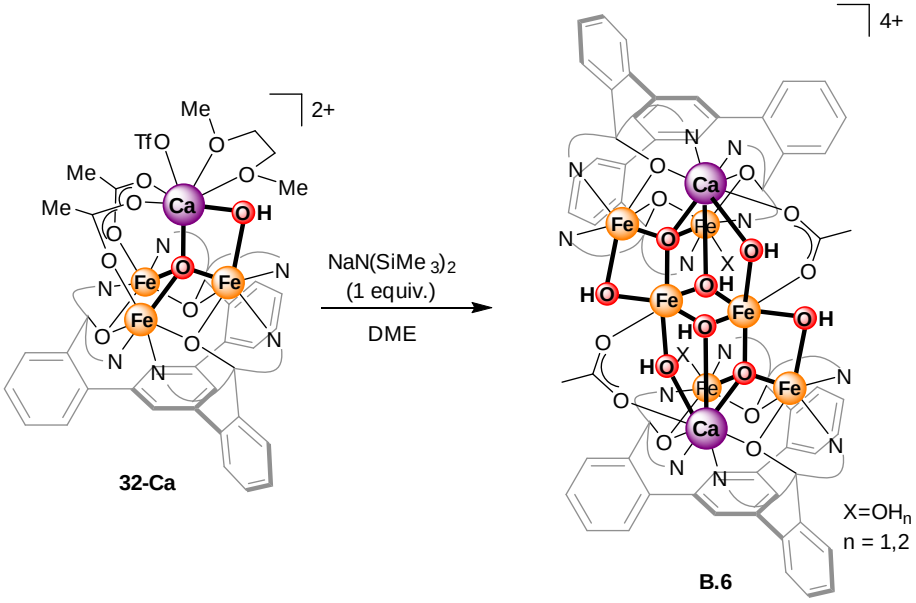

32-Ca B.6

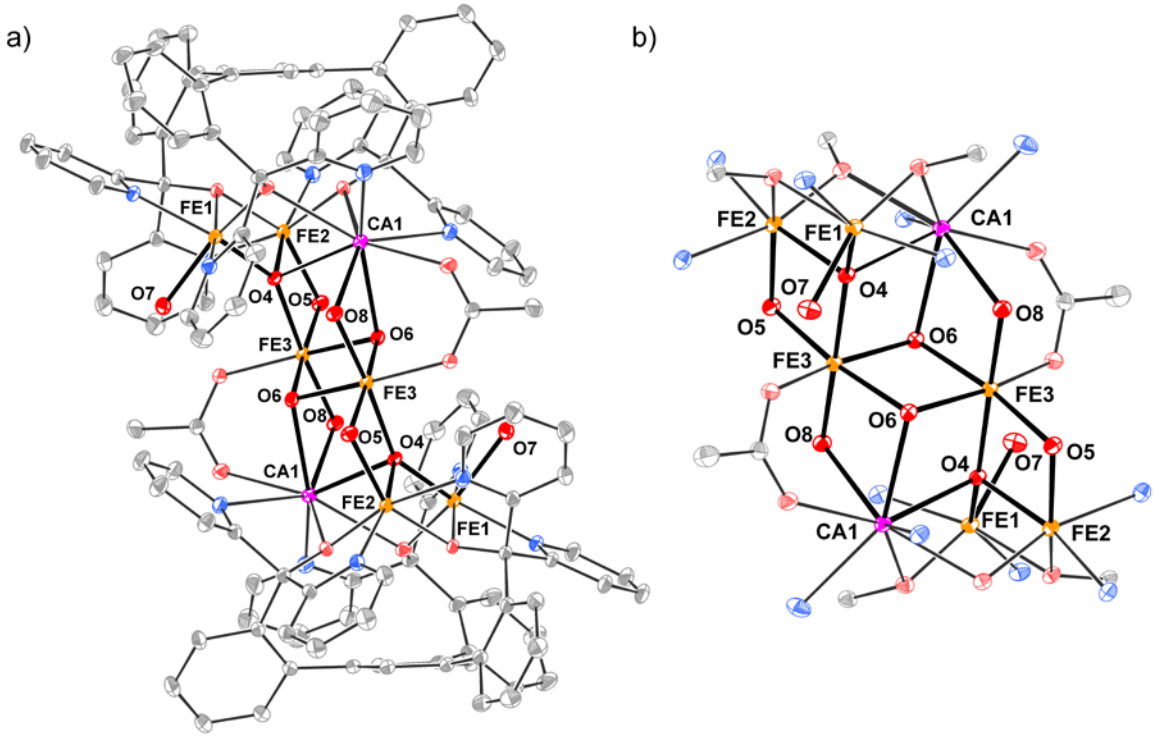

Figure 4. (a) Preliminary solid-state structure of octametallic complex **B.6**; H-atoms and outer-sphere anions and solvent molecules omitted for clarity. Thermal ellipsoids shown at the 50% probability level. (b) Cropped view highlighting the octametallic core.

APPENDIX C

NMR SPECTRA

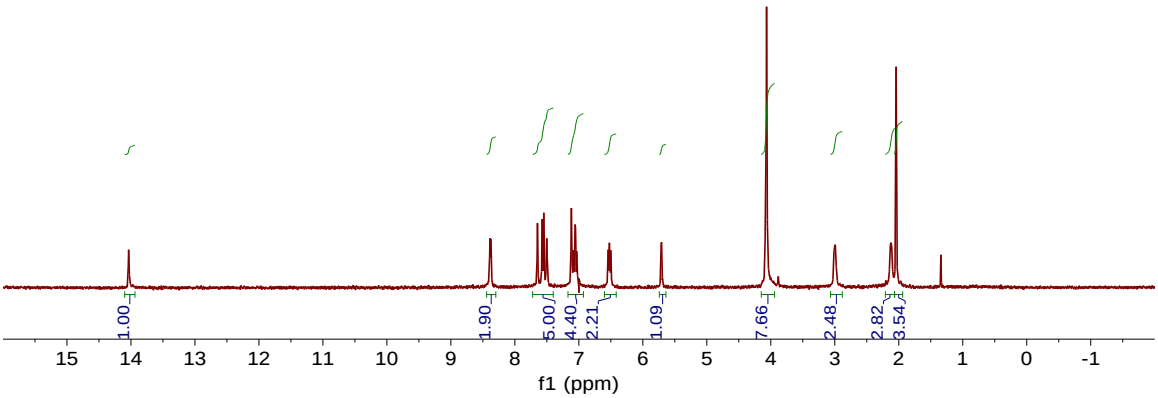

Figure 1. ^{1}H NMR spectrum of **2** in C_6D_6.

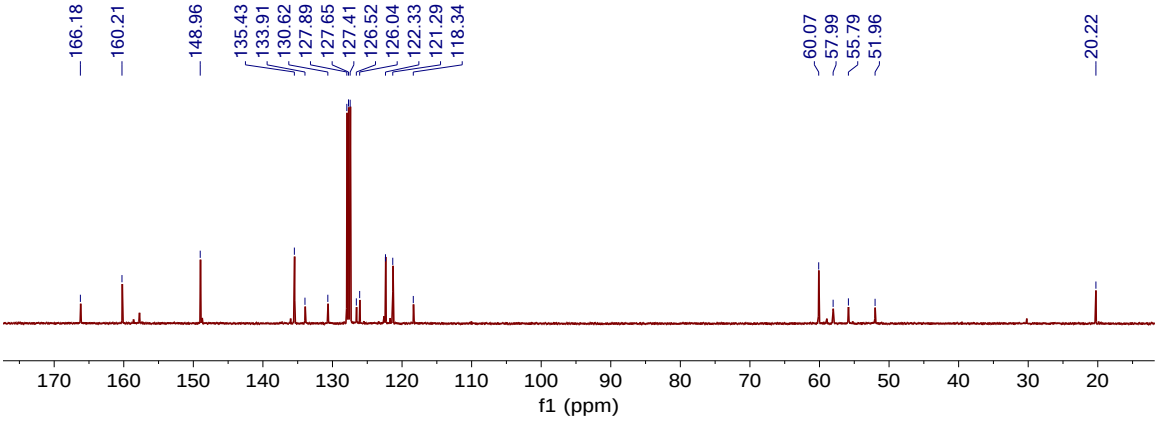

Figure 2. ^{13}C NMR spectrum of **2** in C_6D_6.

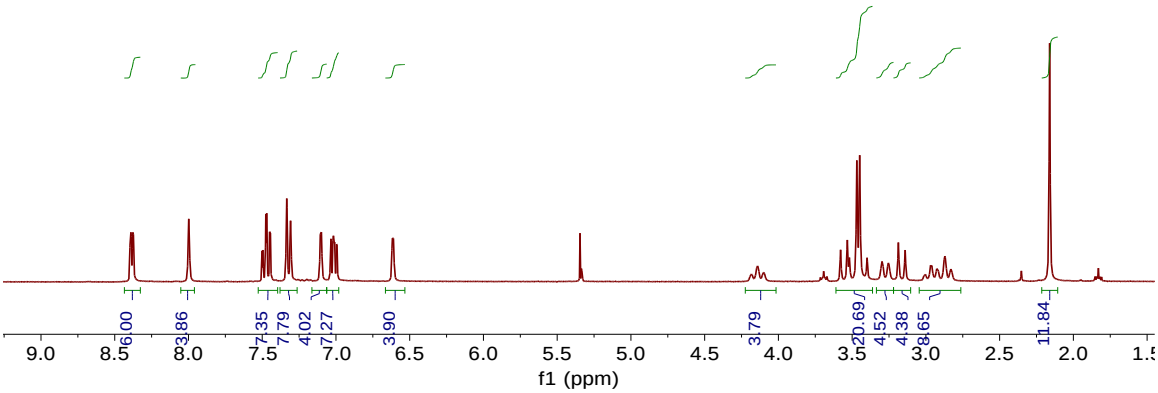

Figure 3. ^{1}H NMR spectrum of **3-Y** in CD_2Cl_2.

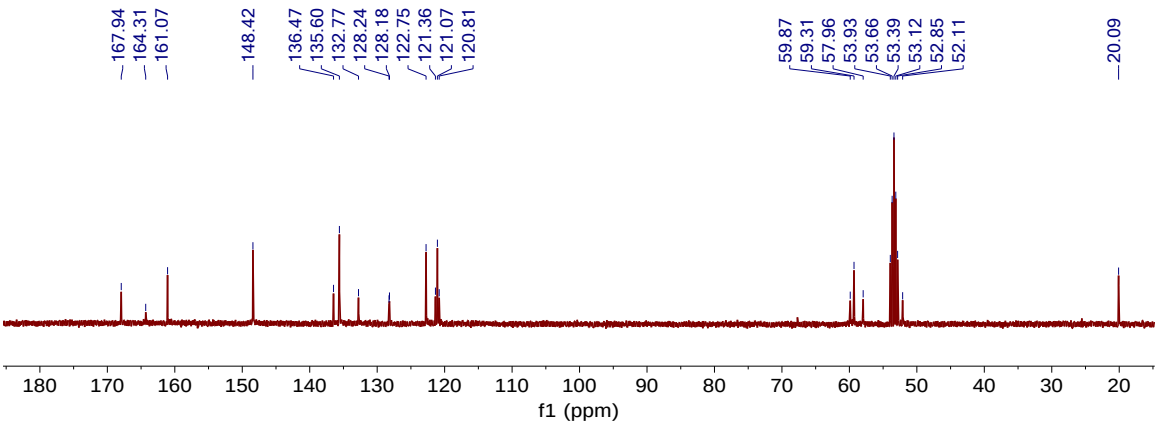

Figure 4. ^{13}C NMR spectrum of **3-Y** in CD_2Cl_2.

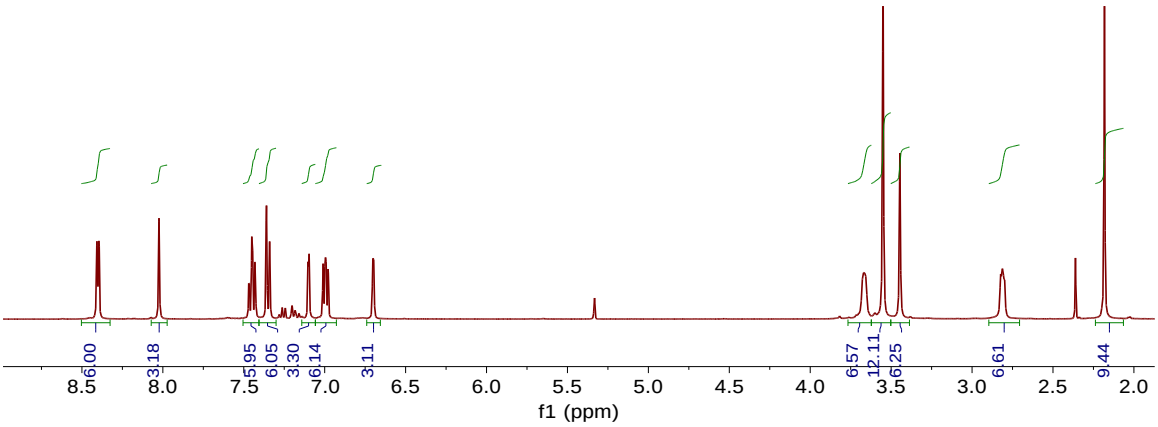

Figure 5. ^{1}H NMR spectrum of **3-La** in CD_2Cl_2.

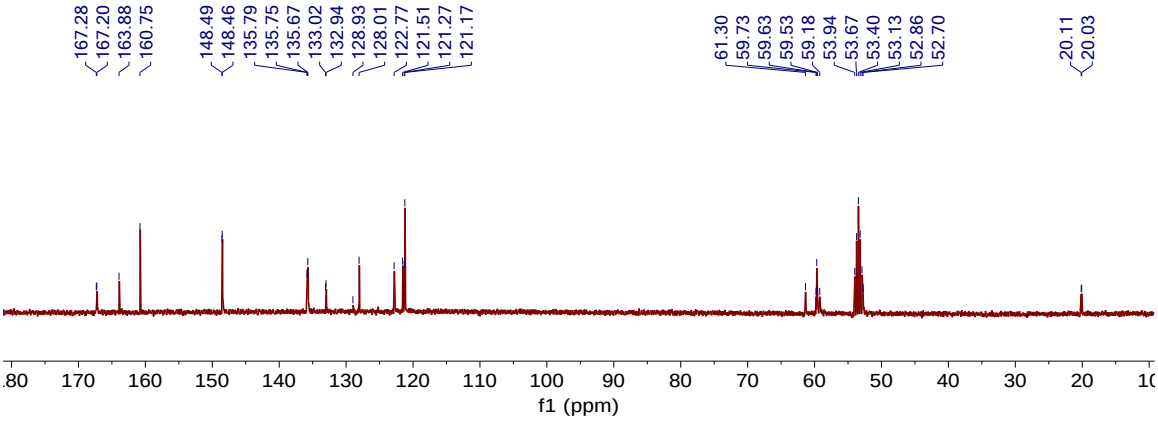

Figure 6. ^{13}C NMR spectrum of **3-La** in CD_2Cl_2.

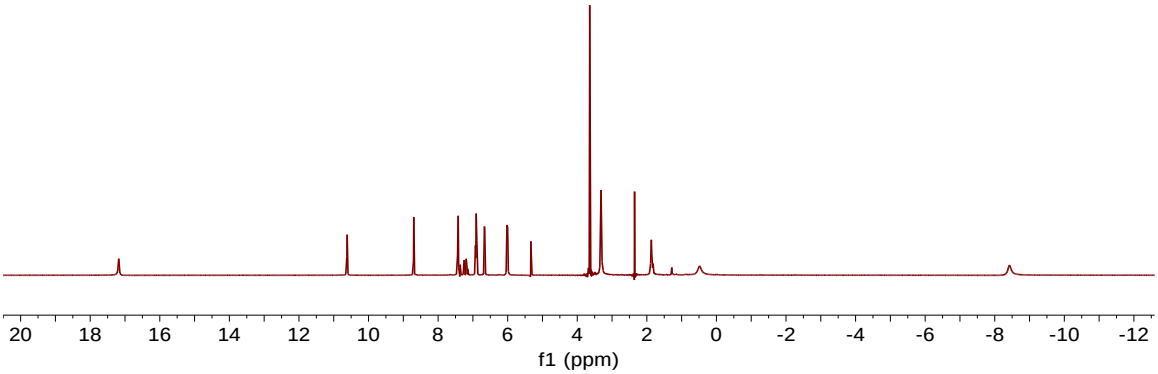

Figure 7. ^{1}H NMR spectrum of **3-Ce** in CD_2Cl_2.

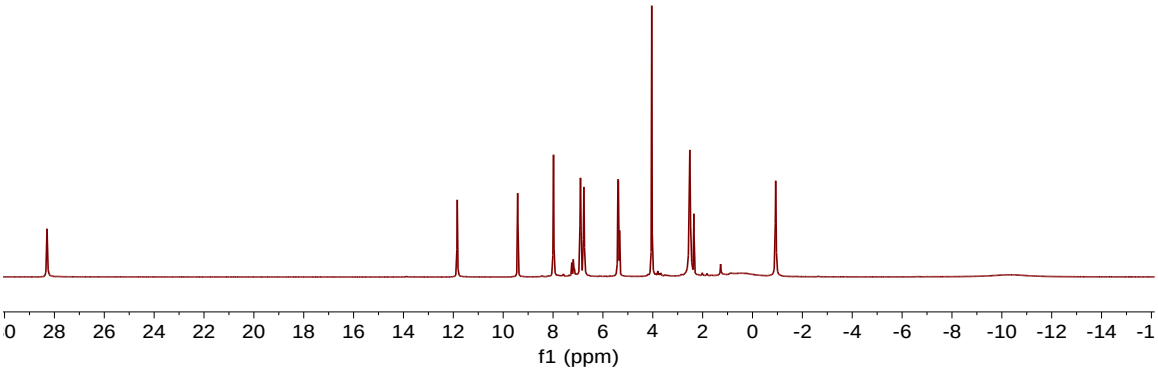

Figure 8. ^{1}H NMR spectrum of **3-Nd** in CD_2Cl_2.

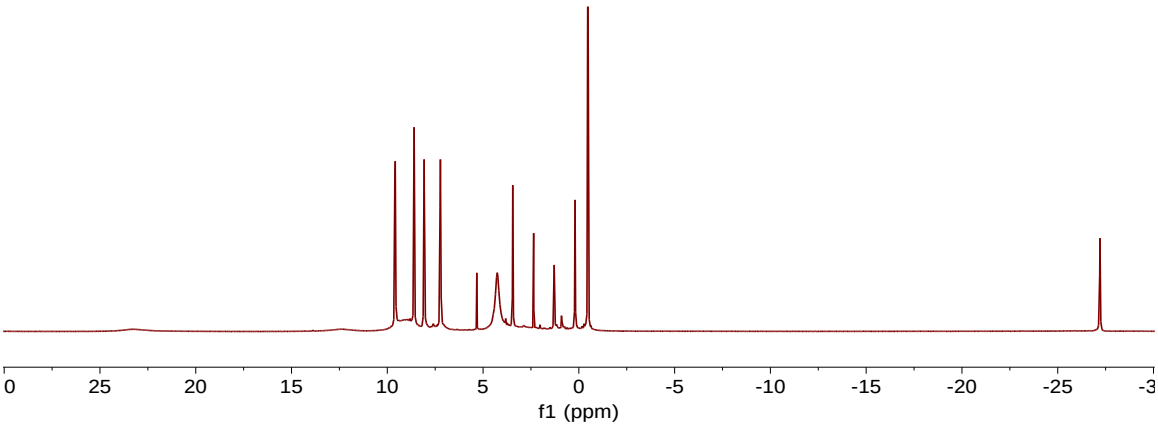

Figure 9. ^{1}H NMR spectrum of **3-Eu** in CD_2Cl_2.

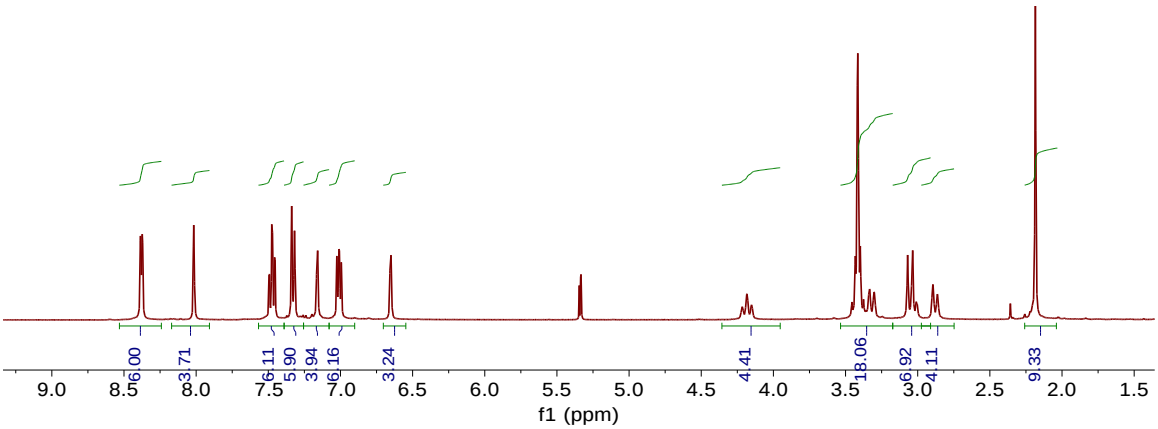

Figure 10. ^{1}H NMR spectrum of **3-Lu** in CD_2Cl_2.

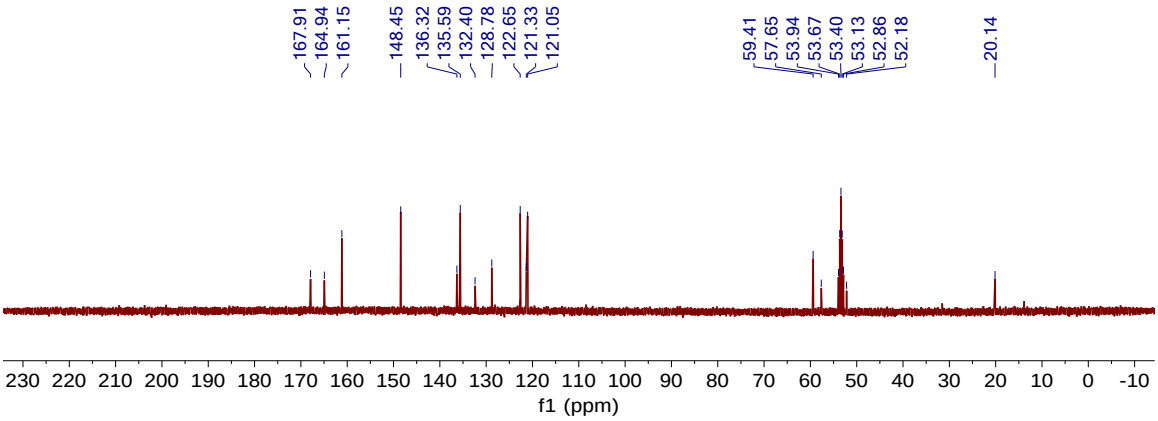

Figure 11. ^{13}C NMR spectrum of **3-Lu** in CD_2Cl_2.

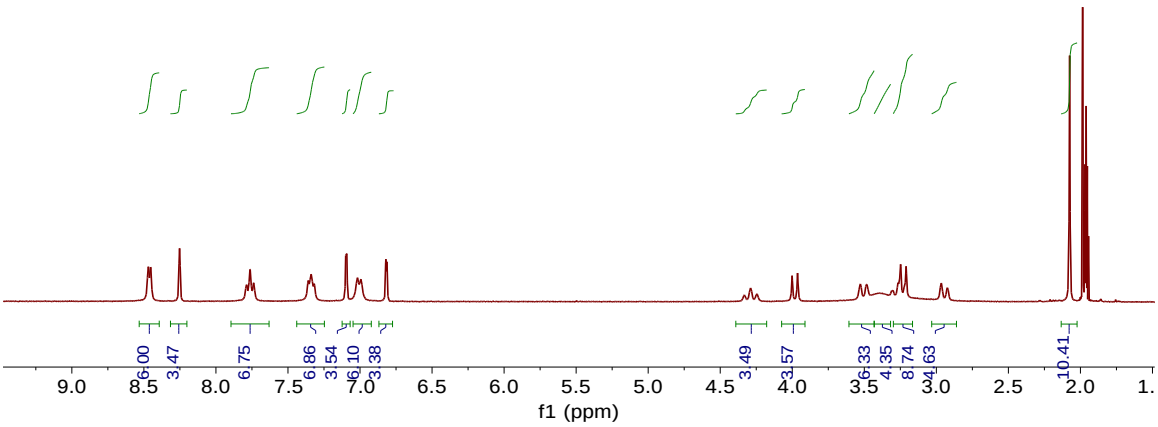

Figure 12. ^{1}H NMR spectrum of **4-Y** in CD_3CN.

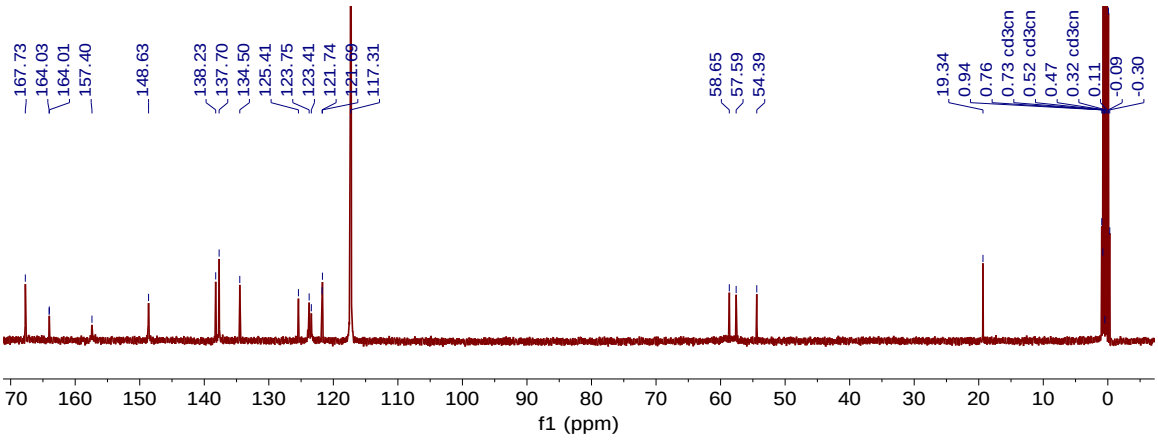

Figure 13. ^{13}C NMR spectrum of **4-Y** in CD_3CN.

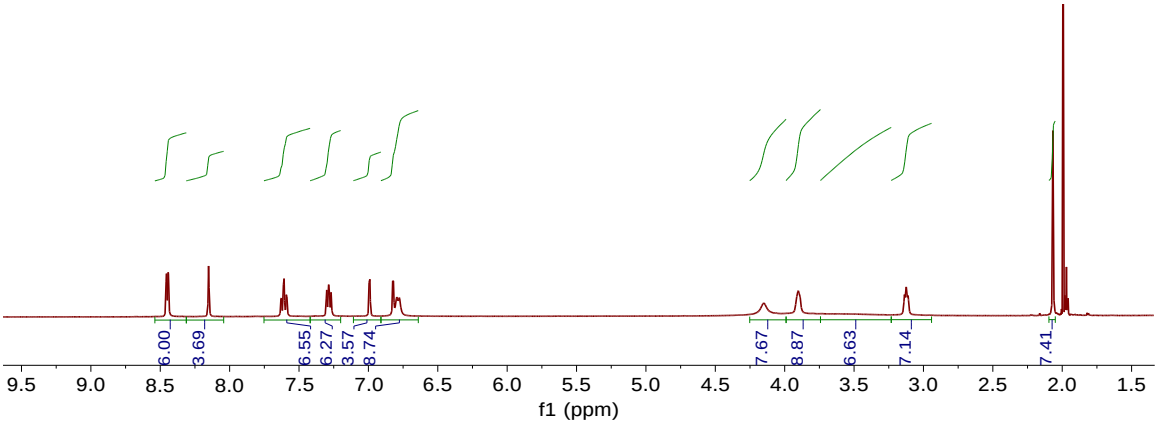

Figure 14. ^{1}H NMR spectrum of **4-La** in CD_3CN.

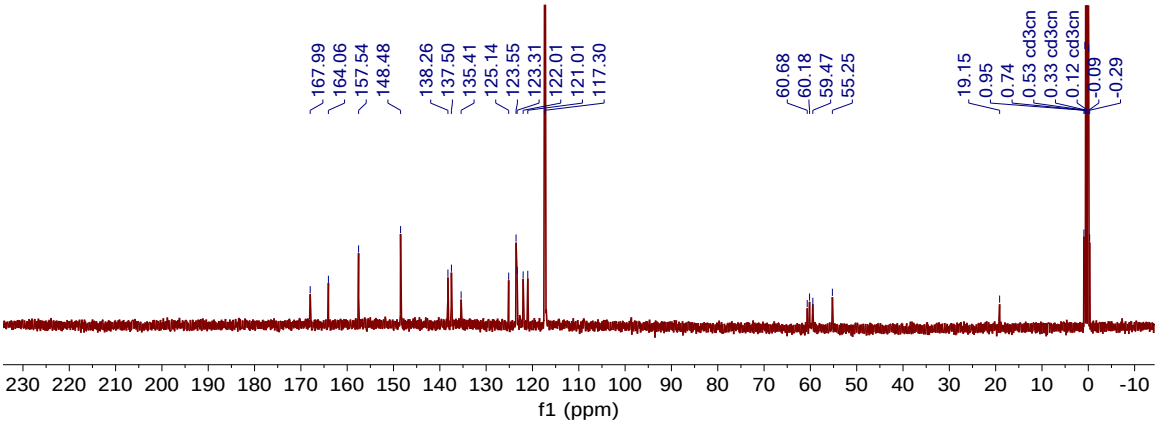

Figure 15. ^{13}C NMR spectrum of **4-La** in CD_3CN.

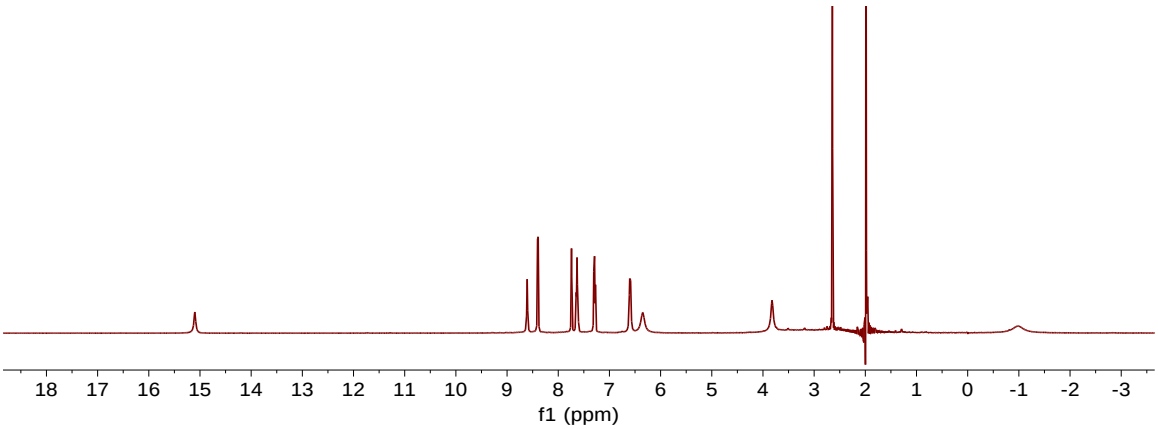

Figure 16 ^{1}H NMR spectrum of **4-Ce** in CD_3CN.

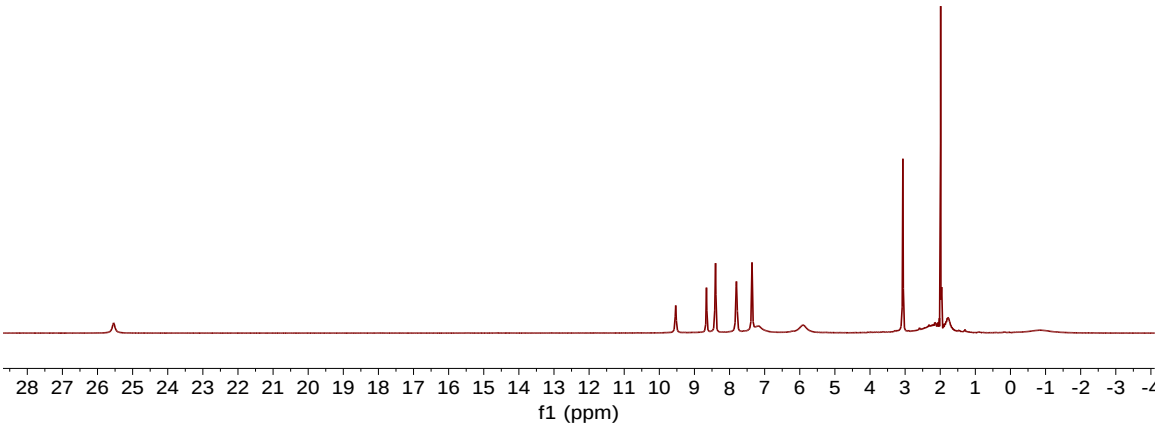

Figure 17. ^{1}H NMR spectrum of **4-Nd** in CD_3CN.

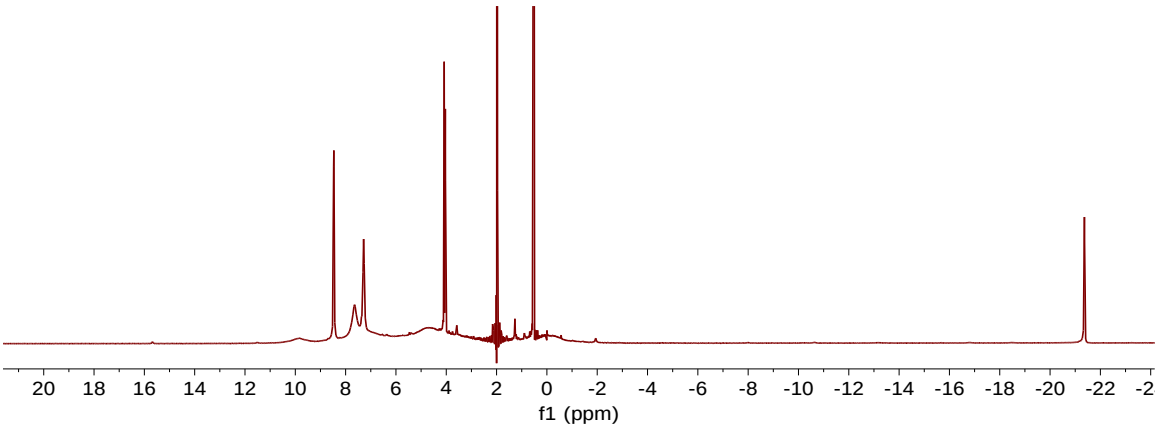

Figure 18. ^{1}H NMR spectrum of **4-Eu** in CD_3CN.

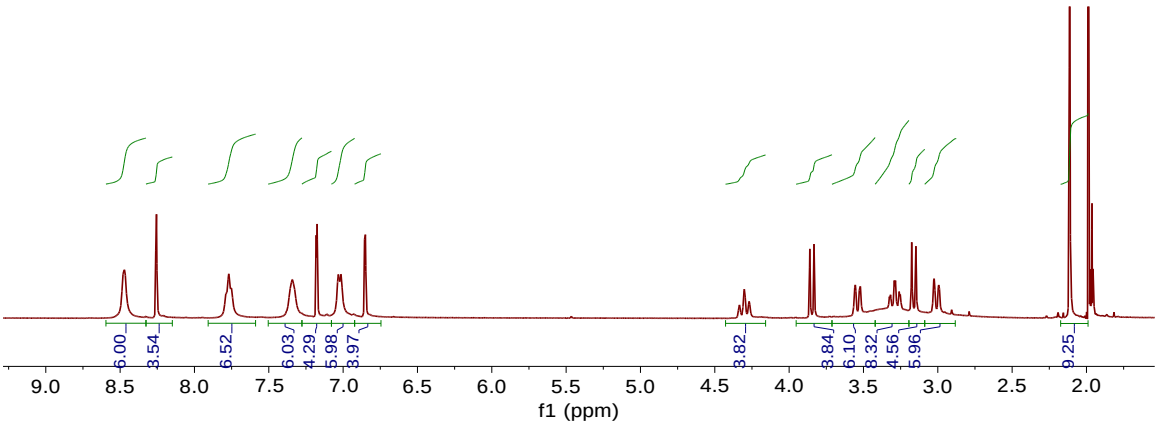

Figure 19. ^{1}H NMR spectrum of **4-Lu** in CD_3CN.

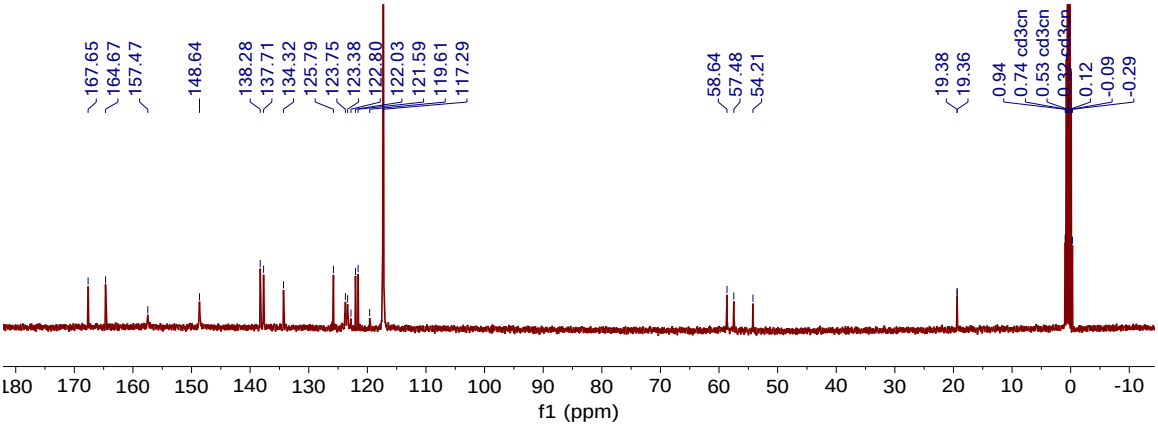

Figure 20. ^{13}C NMR spectrum of **4-Lu** in CD_3CN.

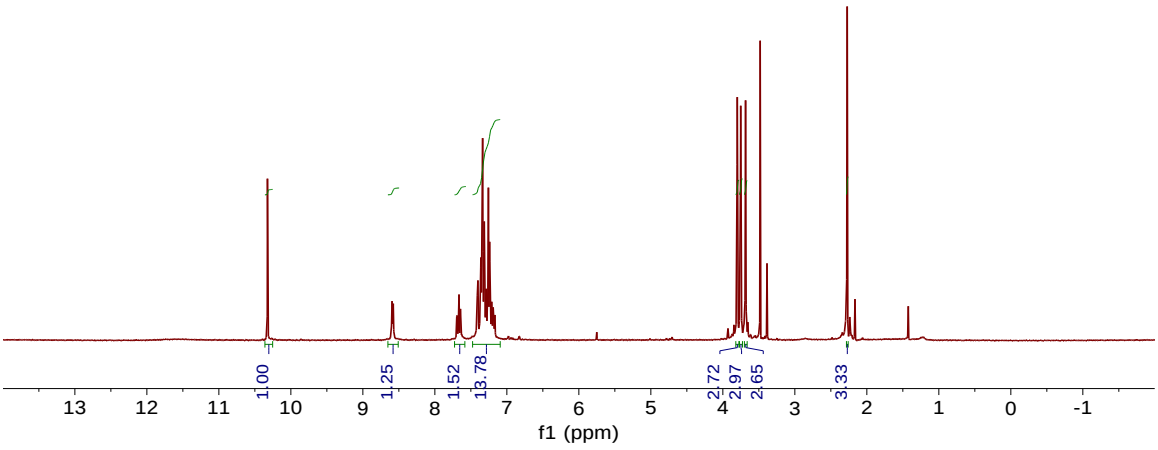

Figure 21 ^{1}H NMR spectrum of **9** in C_6D_6.

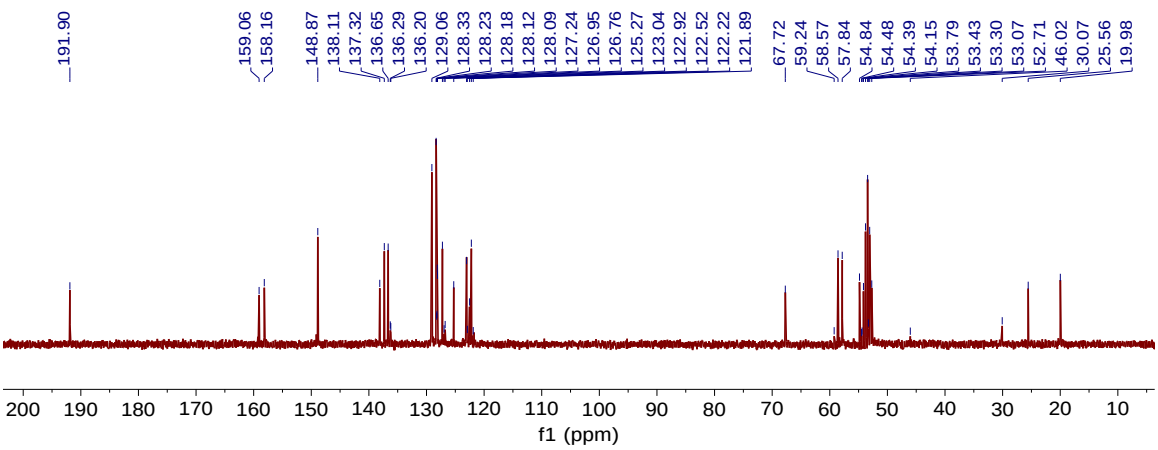

Figure 22. ^{13}C NMR spectrum of **9** in C_6D_6.

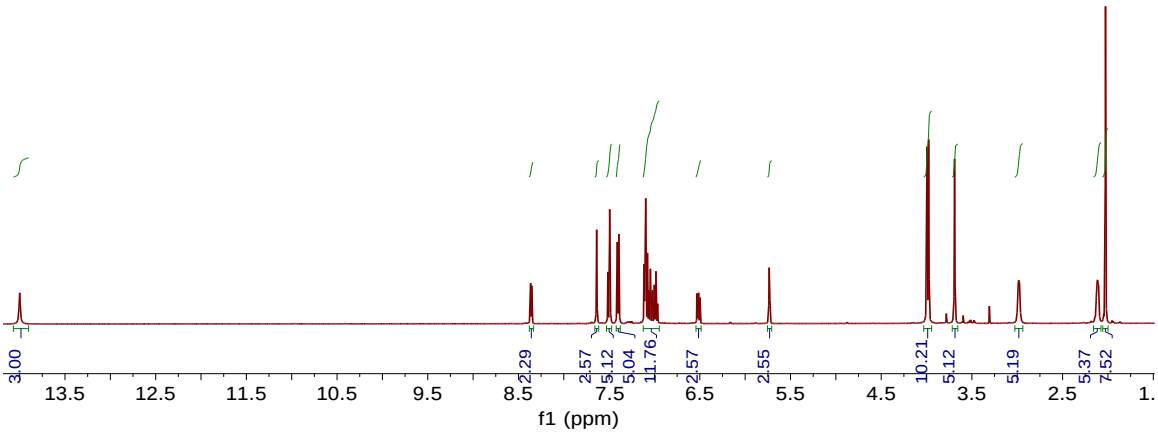

Figure 23. ^{1}H NMR spectrum of **10** in C_6D_6.

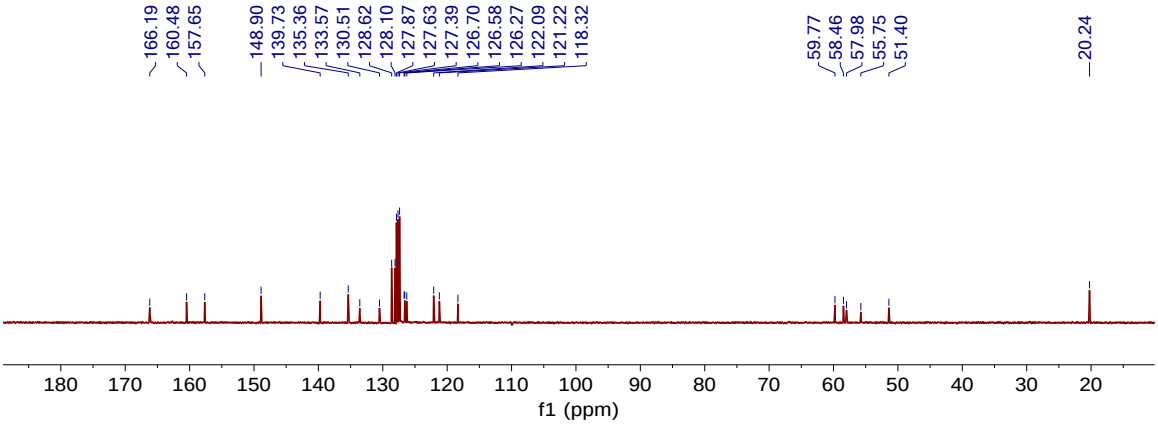

Figure 24. ^{13}C NMR spectrum of **10** in C_6D_6.

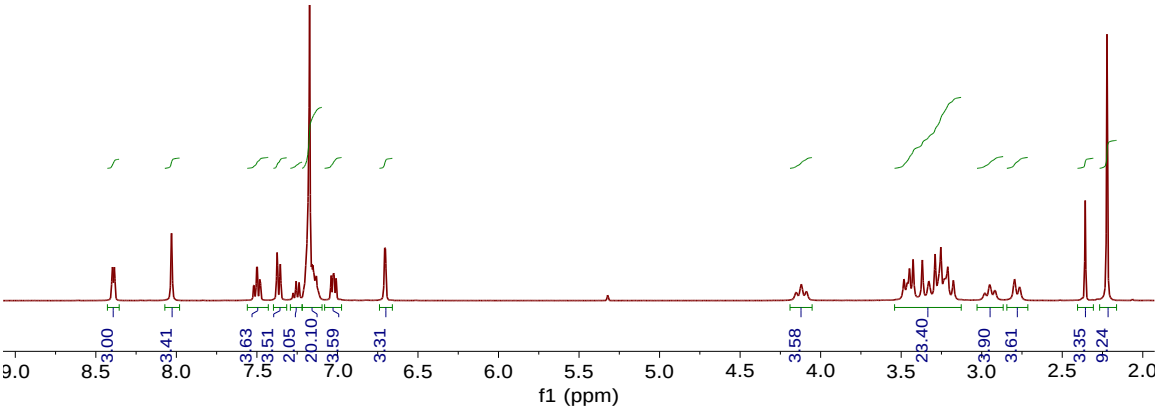

Figure 25. ^{1}H NMR spectrum of **11-Y** in CD_2Cl_2.

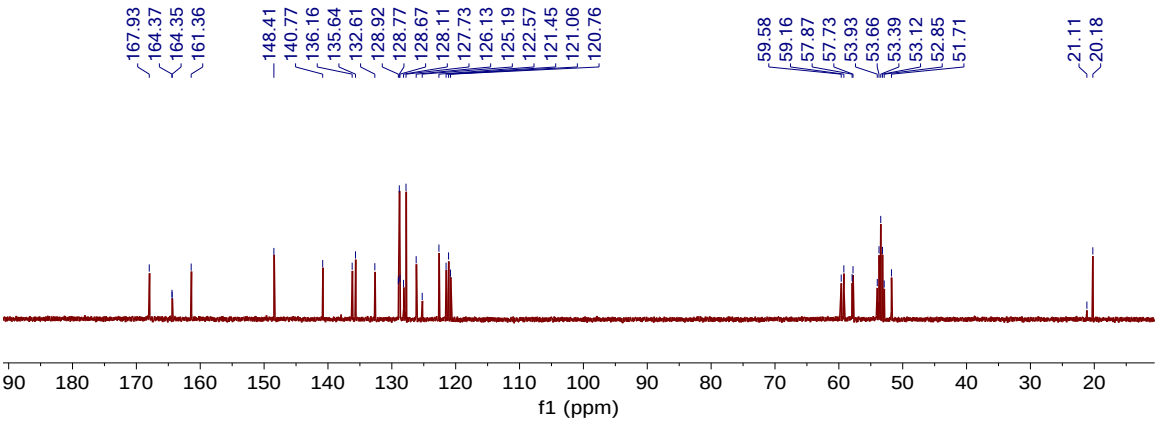

Figure 26. ^{13}C NMR spectrum of **11-Y** in CD_2Cl_2.

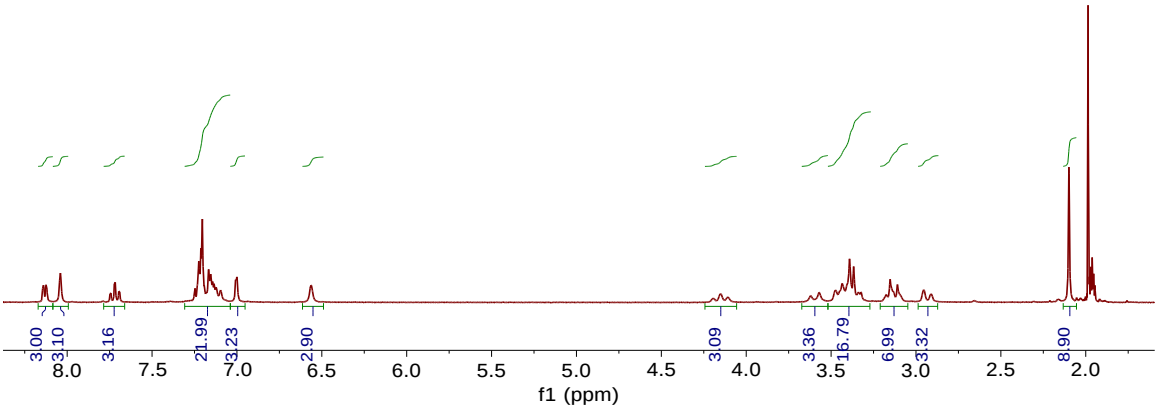

Figure 27. ^{1}H NMR spectrum of **12-Y** in CD_3CN.

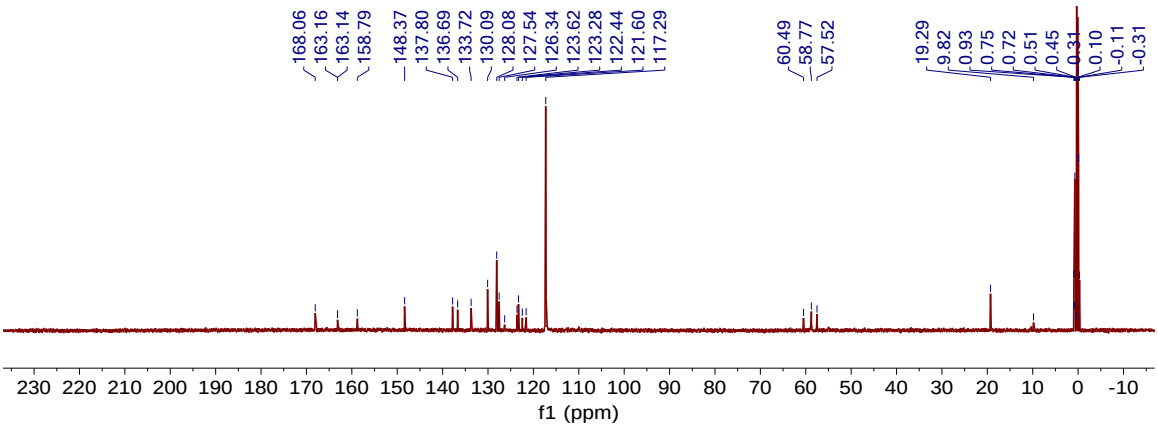

Figure 28. ^{13}C NMR spectrum of **12-Y** in CD_3CN.

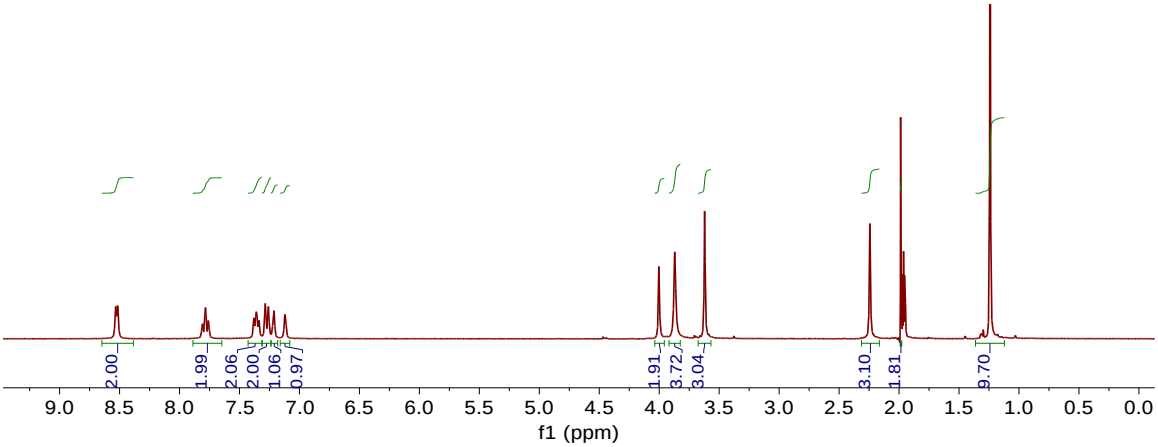

Figure 29. ^{1}H NMR spectrum of **14** in CD_3CN.

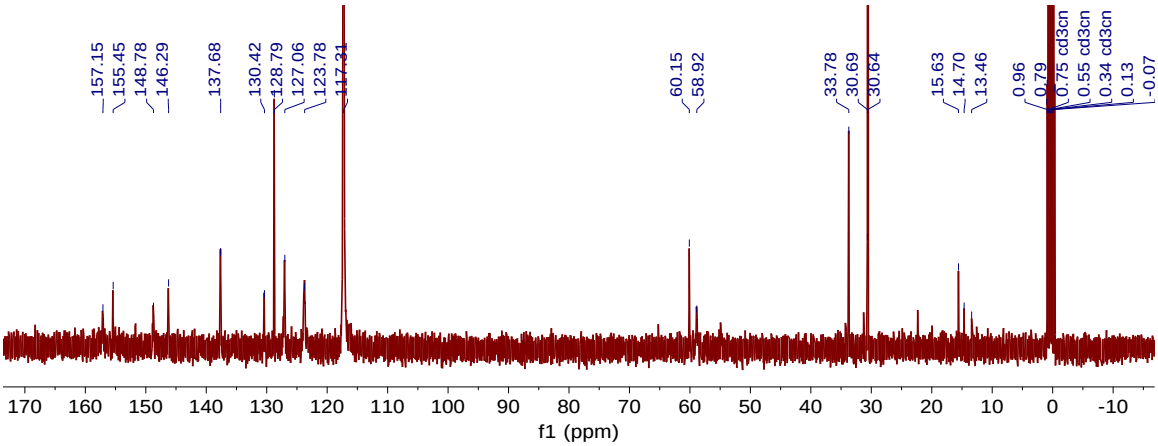

Figure 30. ^{13}C NMR spectrum of **14** in CD_3CN.

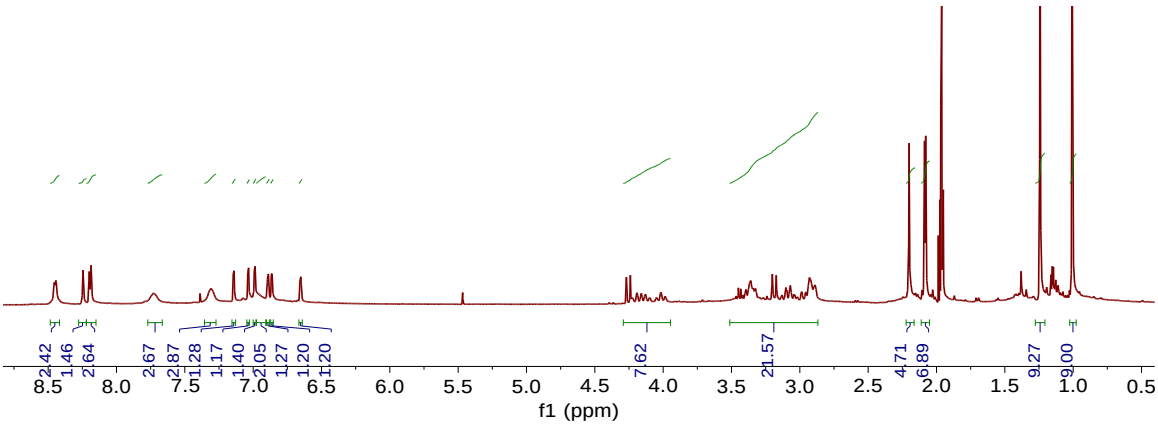

Figure 31. ^{1}H NMR spectrum of **15** in CD_3CN.

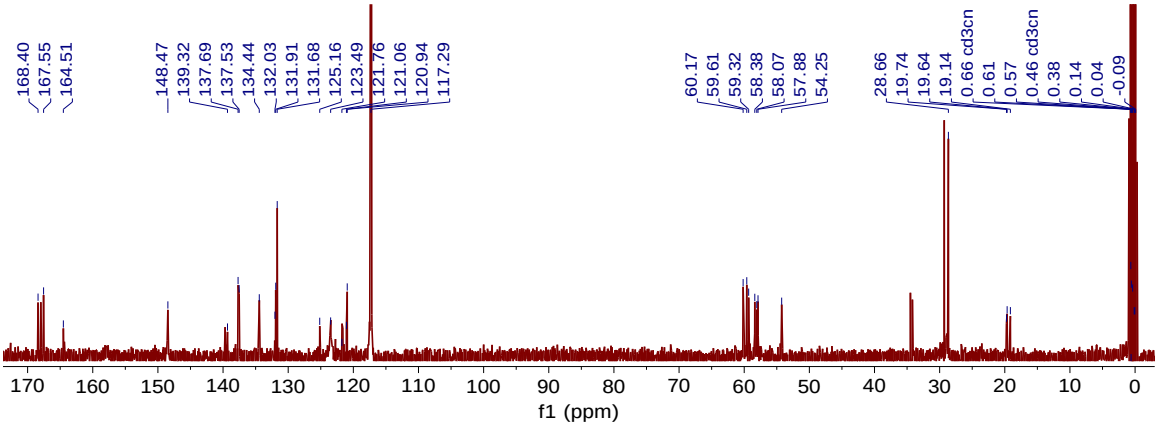

Figure 32. ^{13}C NMR spectrum of **15** in CD_3CN.

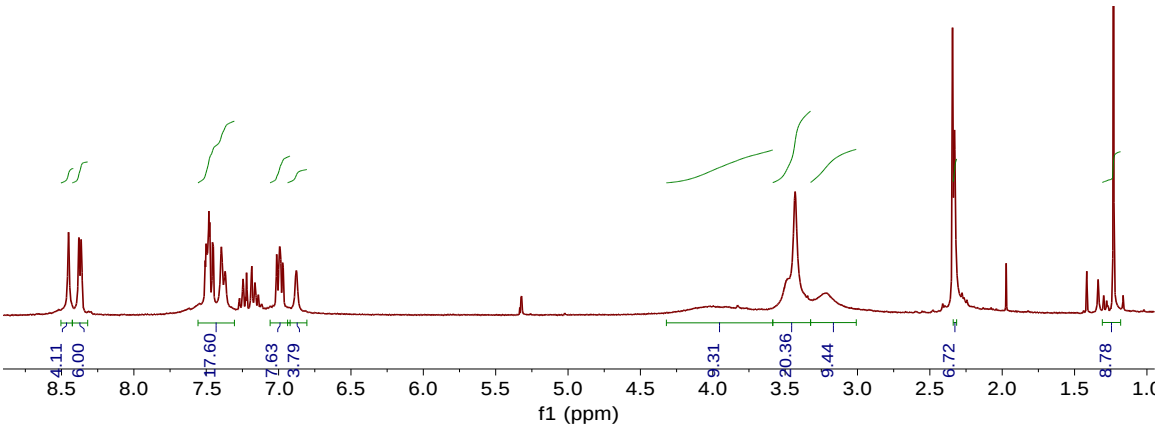

Figure 33. ^{1}H NMR spectrum of **15** in CD_2Cl_2.

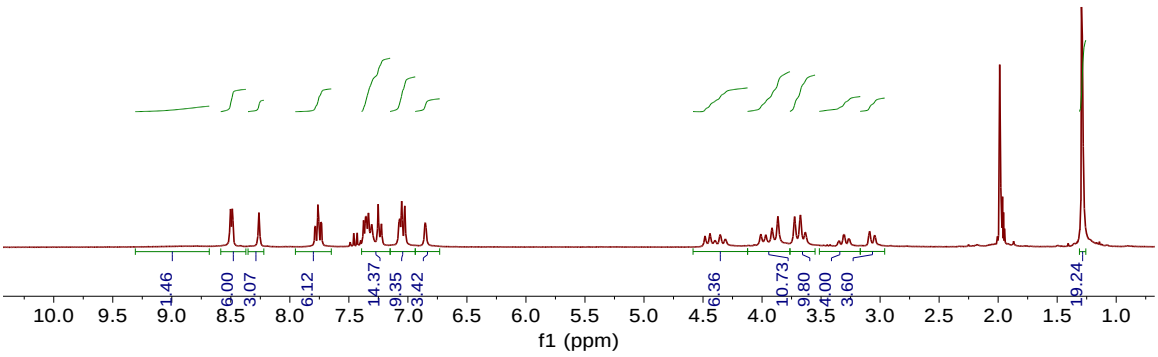

Figure 34. ^{1}H NMR spectrum of **18** in CD_3CN.

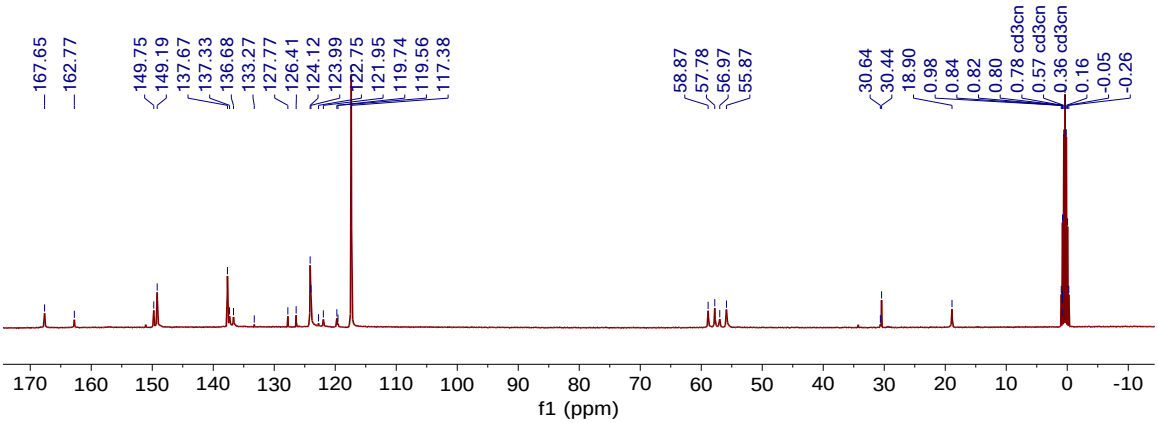

Figure 35. ^{13}C NMR spectrum of **18** in CD_3CN.

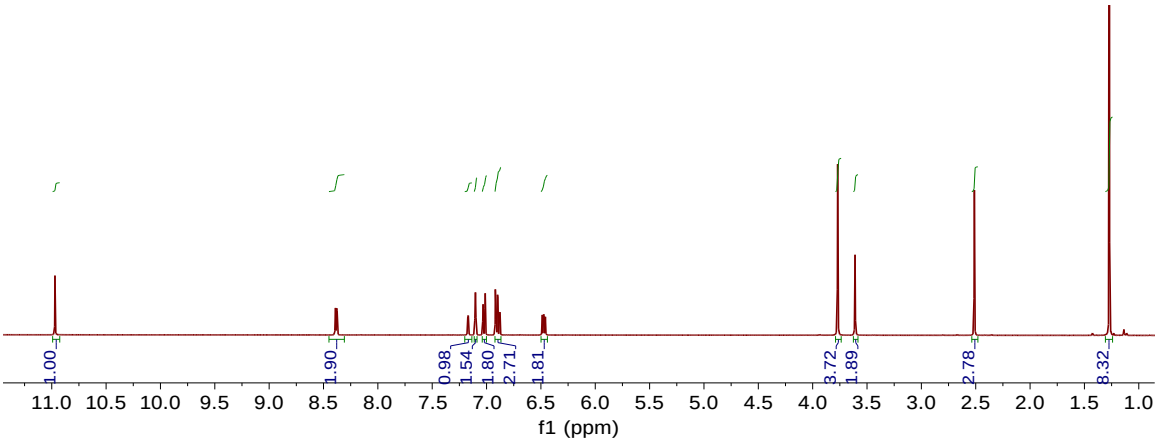

Figure 36. ^{1}H NMR spectrum of **19** in C_6D_6.

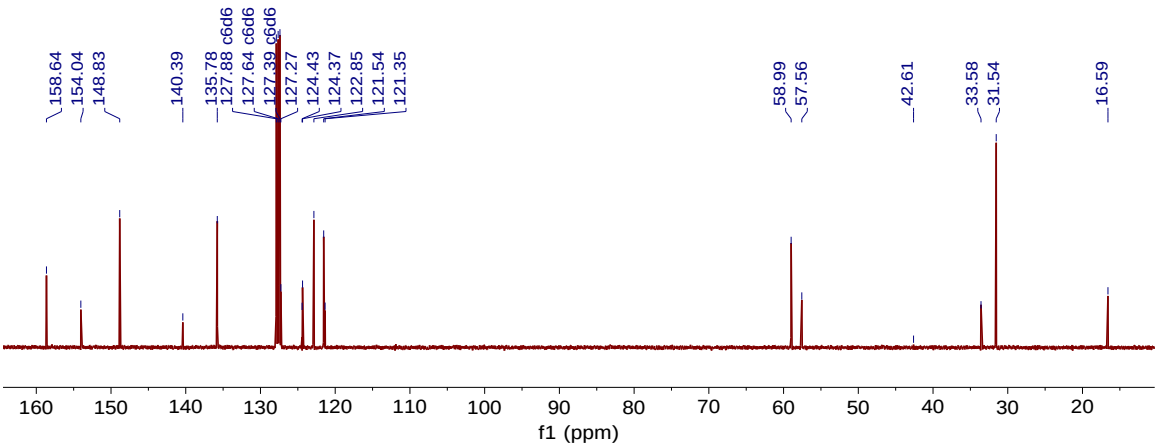

Figure 37. ^{13}C NMR spectrum of **19** in C_6D_6.

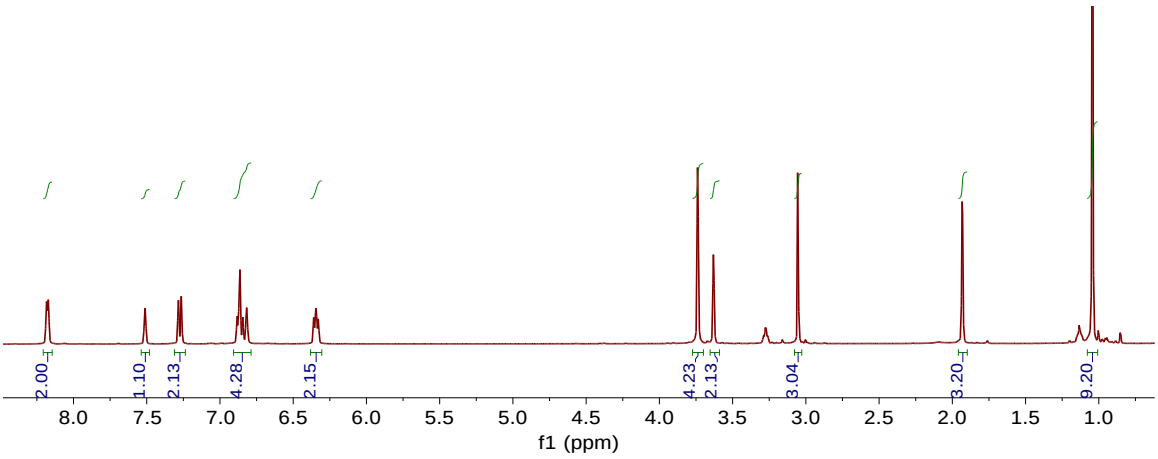

Figure 38. ^{1}H NMR spectrum of **20** in CD_3CN.

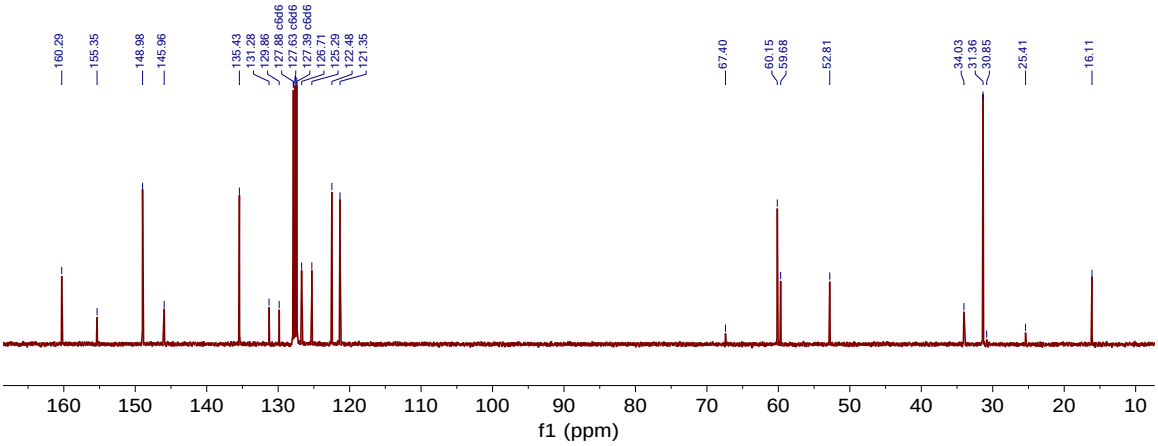

Figure 39. ^{13}C NMR spectrum of **20** in CD_3CN.

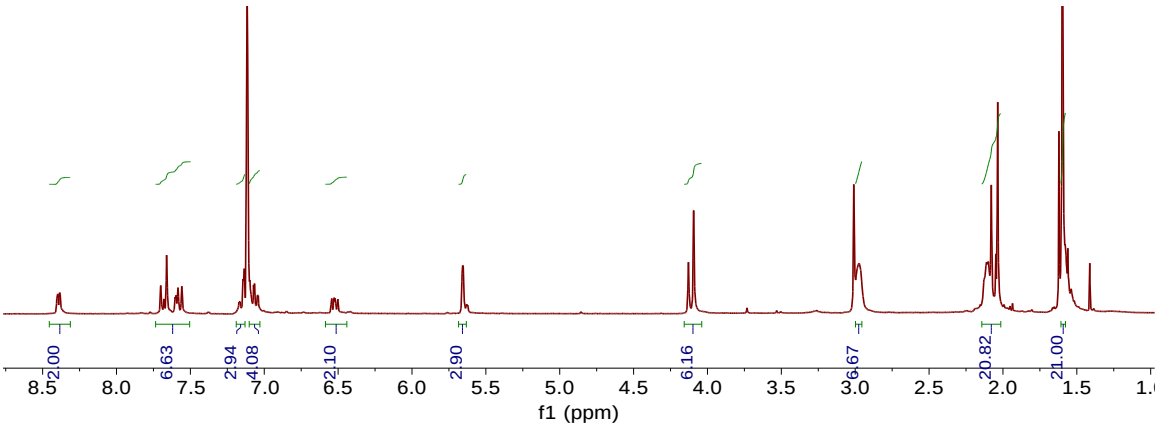

Figure 40. ^{1}H NMR spectrum of **21a** in CD_2Cl_2.

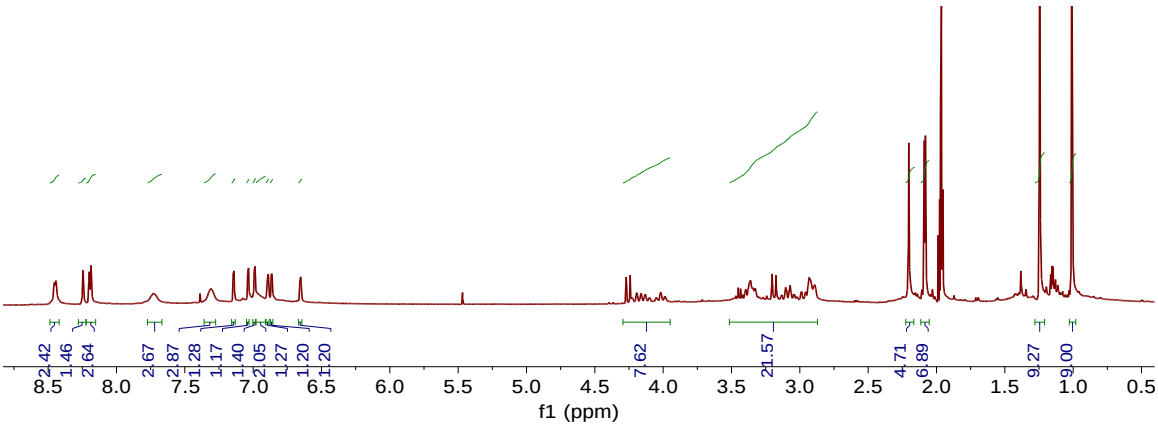

Figure 41. ^{13}C NMR spectrum of **21a** in CD_2Cl_2.

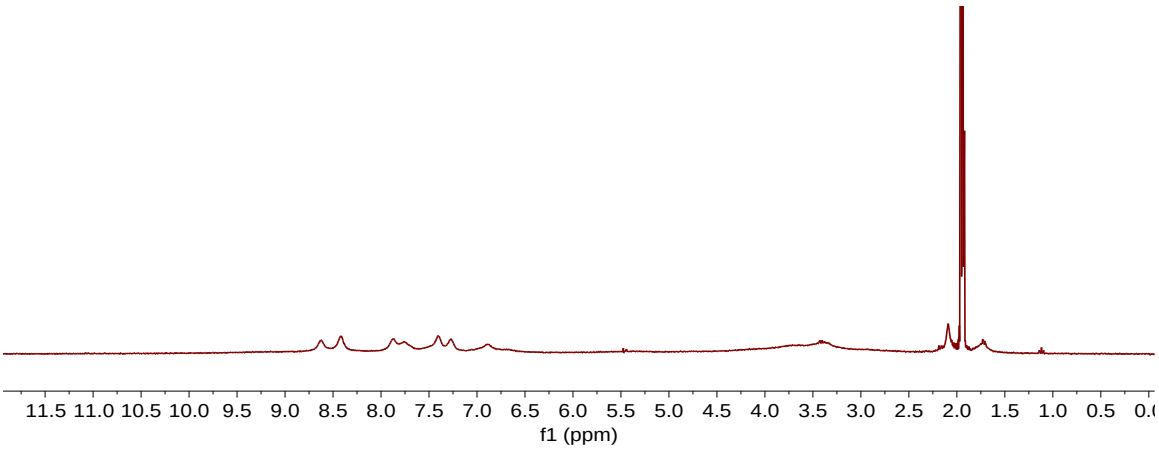

Figure 42. ^{1}H NMR spectrum of **23** in CD_3CN.

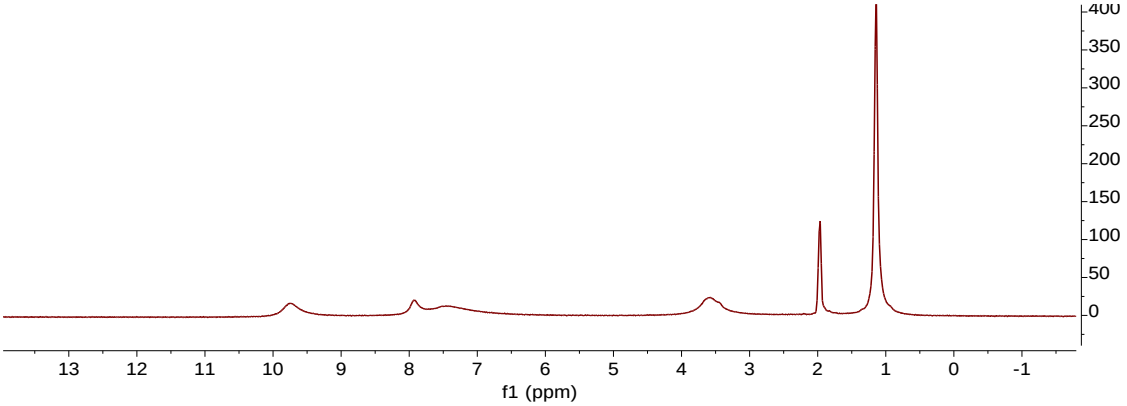

Figure 43. ^{1}H NMR spectrum of **25b** in CD_3CN.

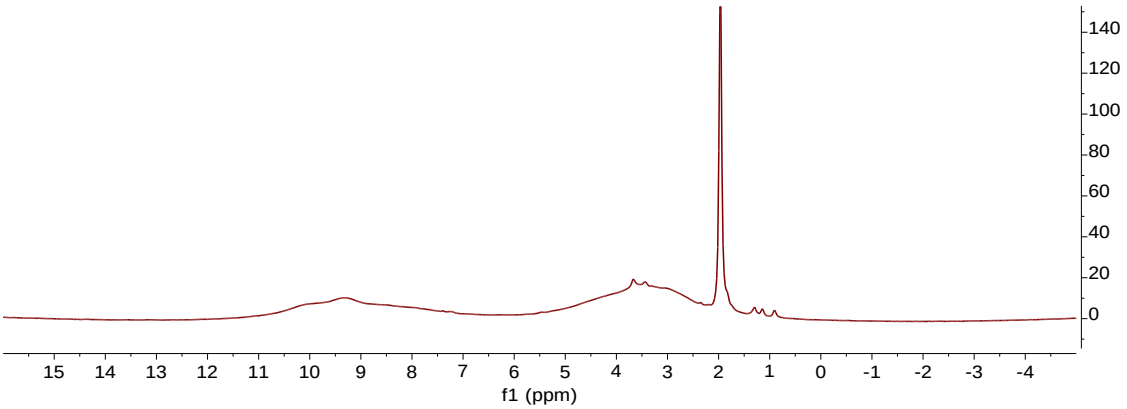

Figure 44. ^{1}H NMR spectrum of **25c** in CD_3CN.

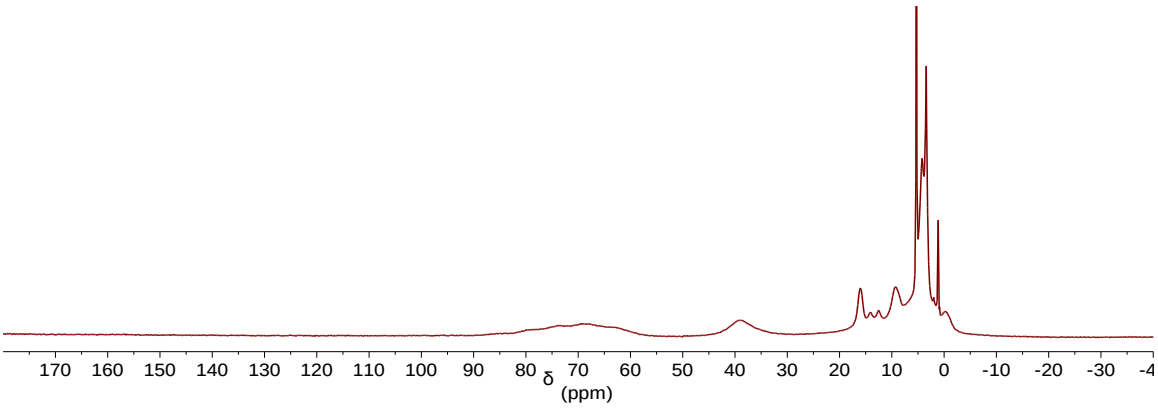

Figure 45. ^{1}H NMR spectrum of **32-Ca** in CD_2Cl_2.

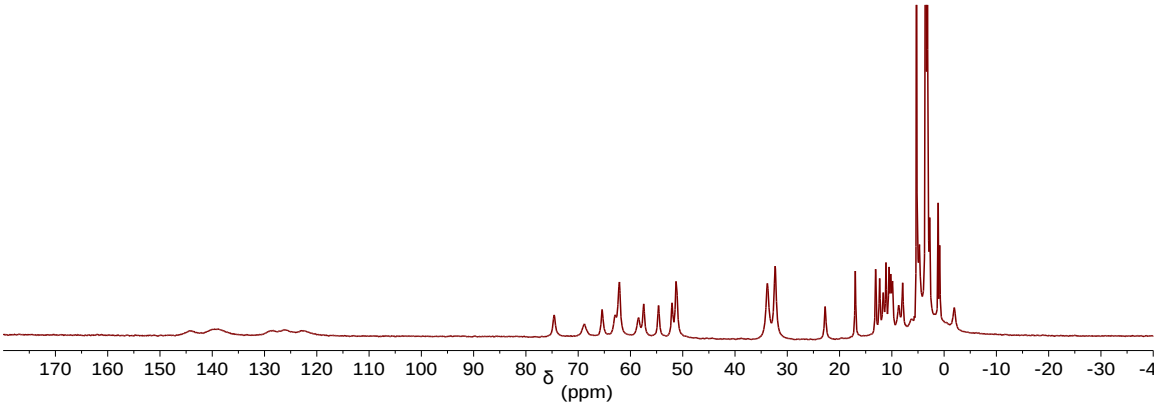

Figure 46. ^{1}H NMR spectrum of **33-Ca** in CD_2Cl_2.

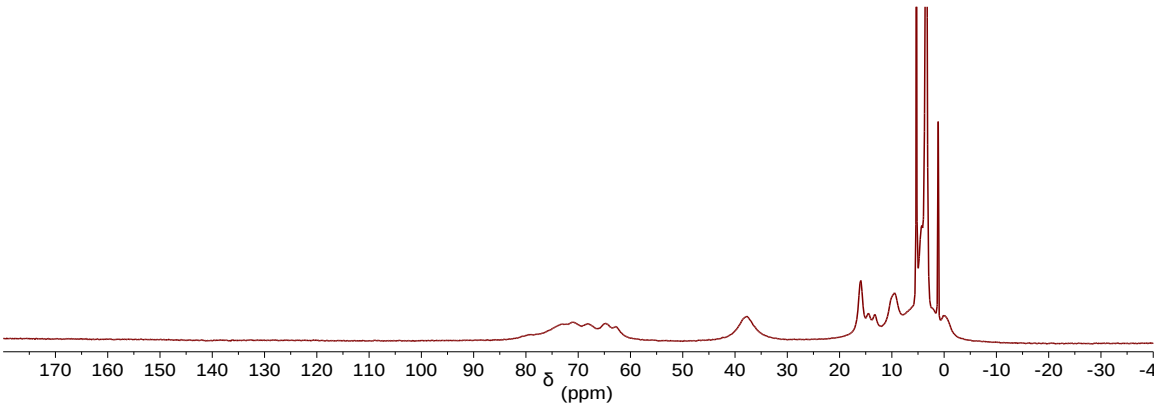

Figure 47. ^{1}H NMR spectrum of **32-Sr** in CD_2Cl_2.

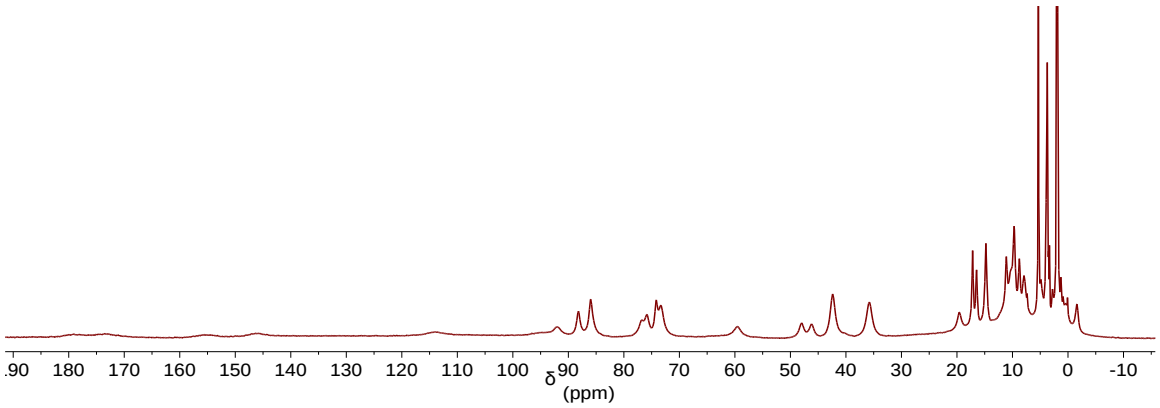

Figure 48. ^{1}H NMR spectrum of **33-Sc** in CD_2Cl_2.

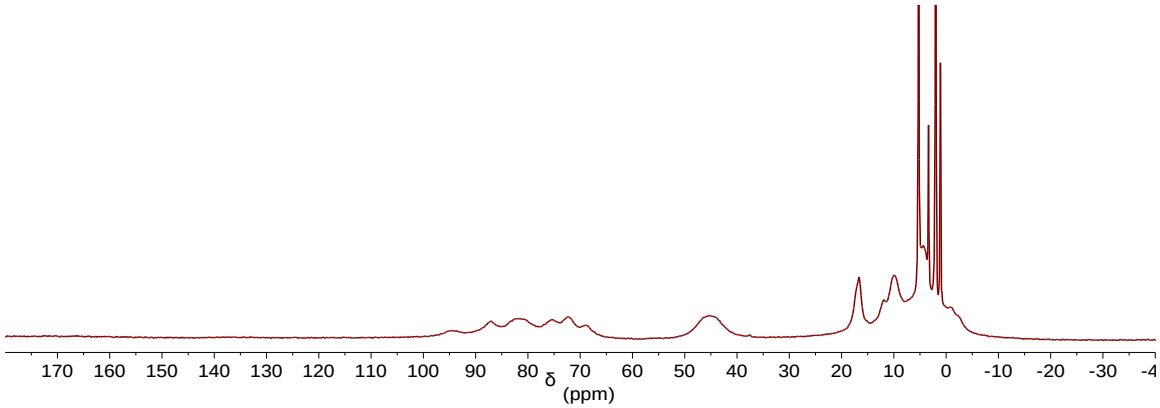

Figure 49. ^{1}H NMR spectrum of **32-Zn** in CD_2Cl_2.

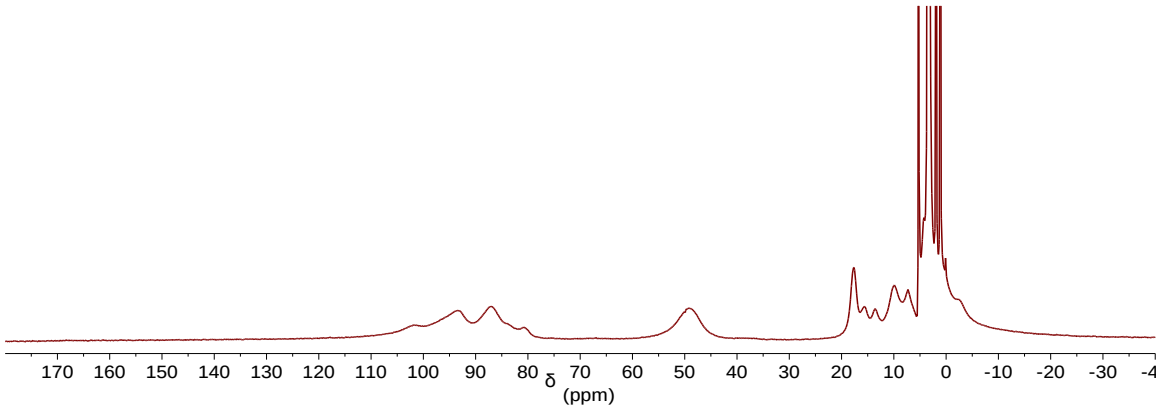

Figure 50. ^{1}H NMR spectrum of **32-La** in CD_3CN.

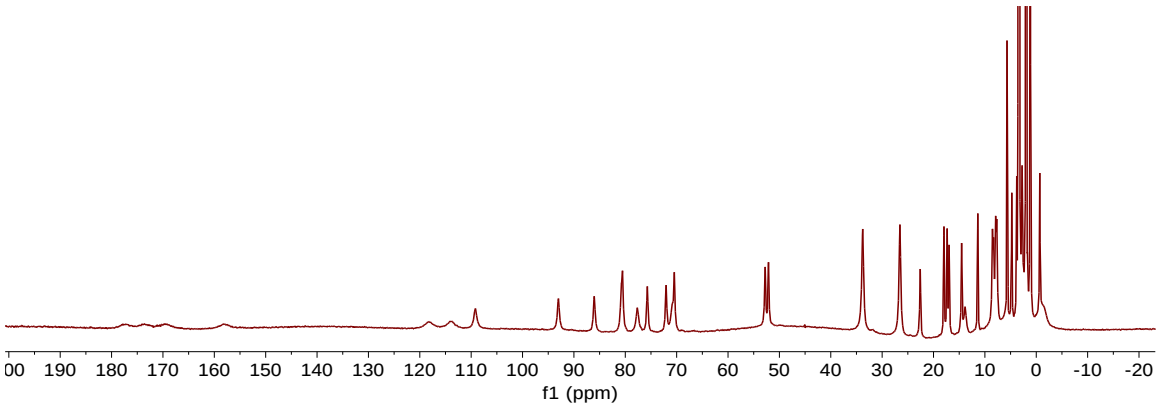

Figure 51. ^{1}H NMR spectrum of **33-La** in CD_2Cl_2.

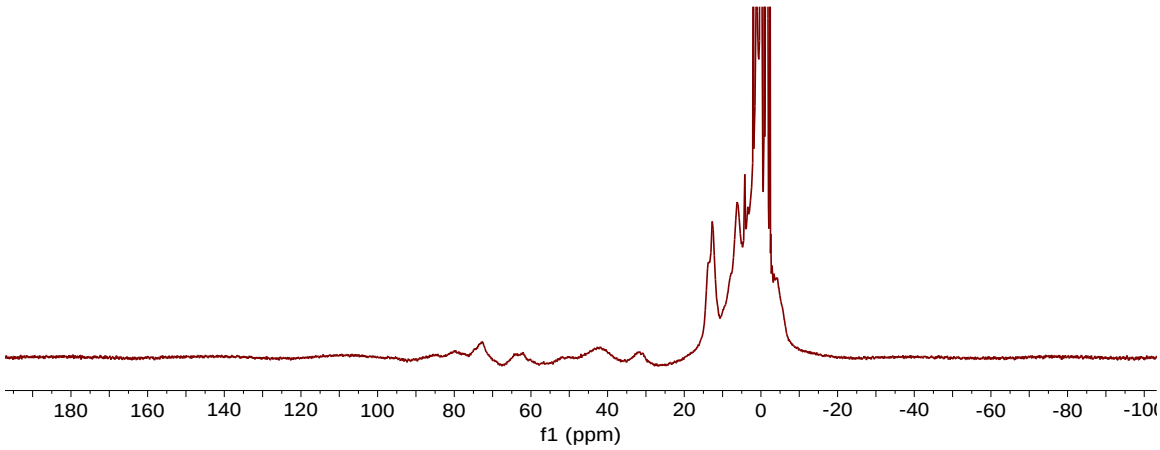

Figure 52. ^{1}H NMR spectrum of **34-La** in CD_3CN.

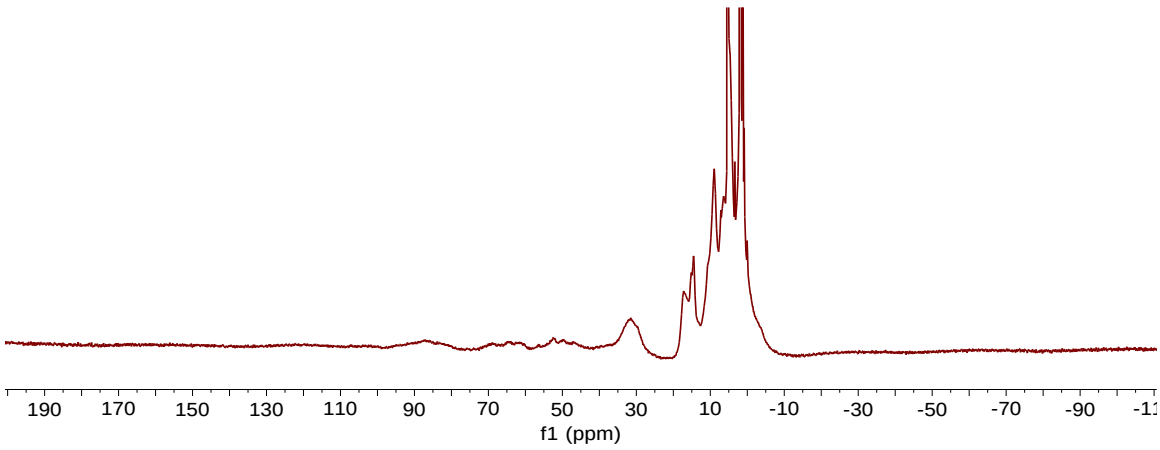

Figure 53. ^{1}H NMR spectrum of **34-Sc** in CD_3CN.

APPENDIX A

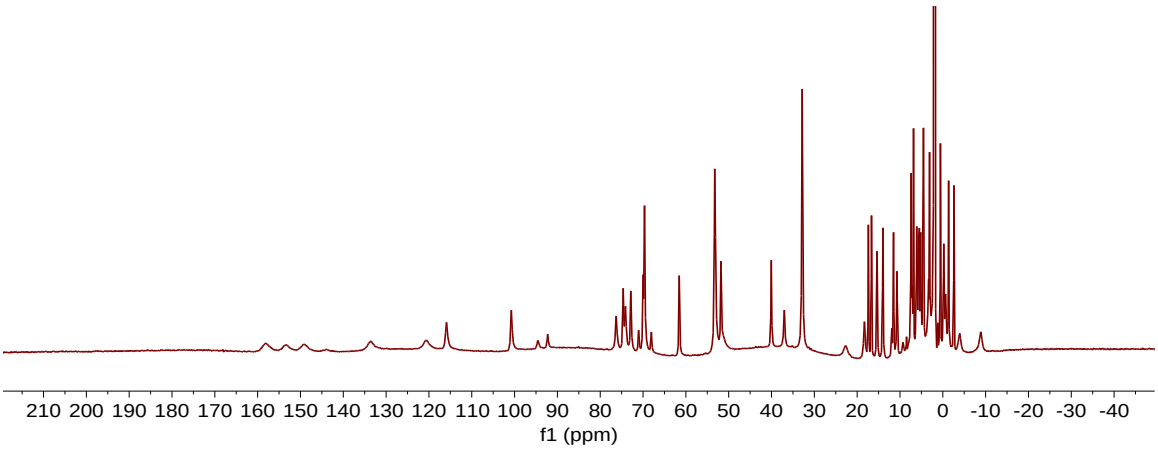

Figure 54. ^{1}H NMR spectrum of **A.6** in CD_3CN.

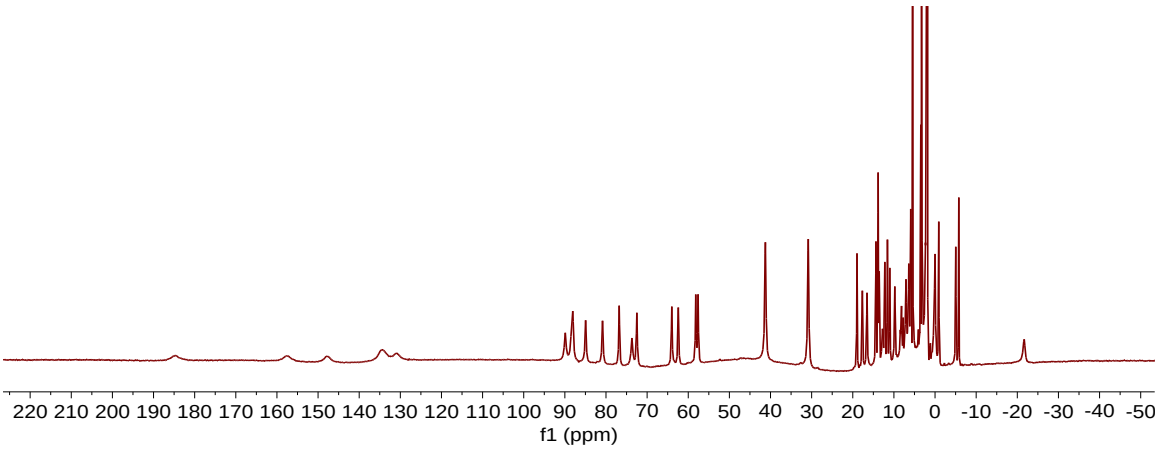

Figure 55. ^{1}H NMR spectrum of **A.7** in CD_3CN.

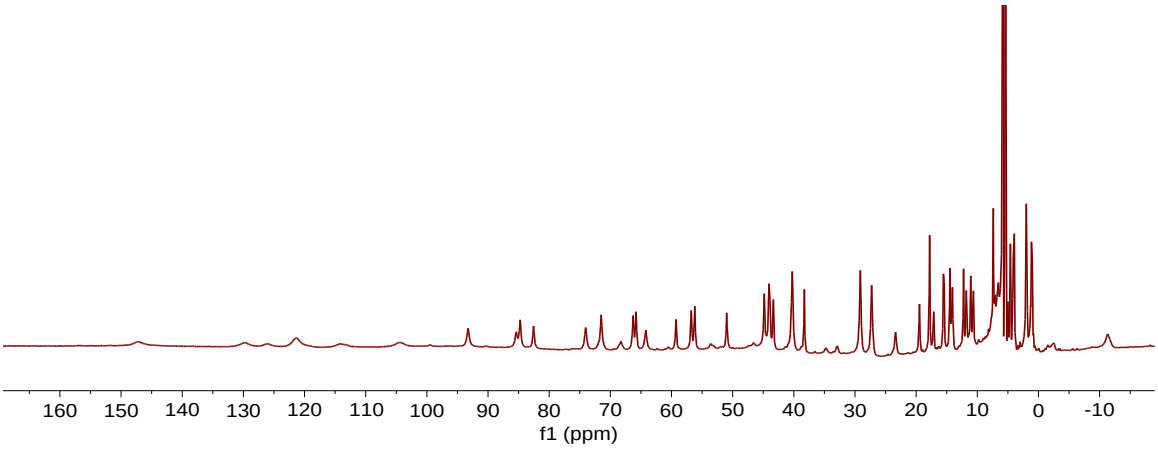

Figure 56. ^{1}H NMR spectrum of **A.8** in CD_3CN.

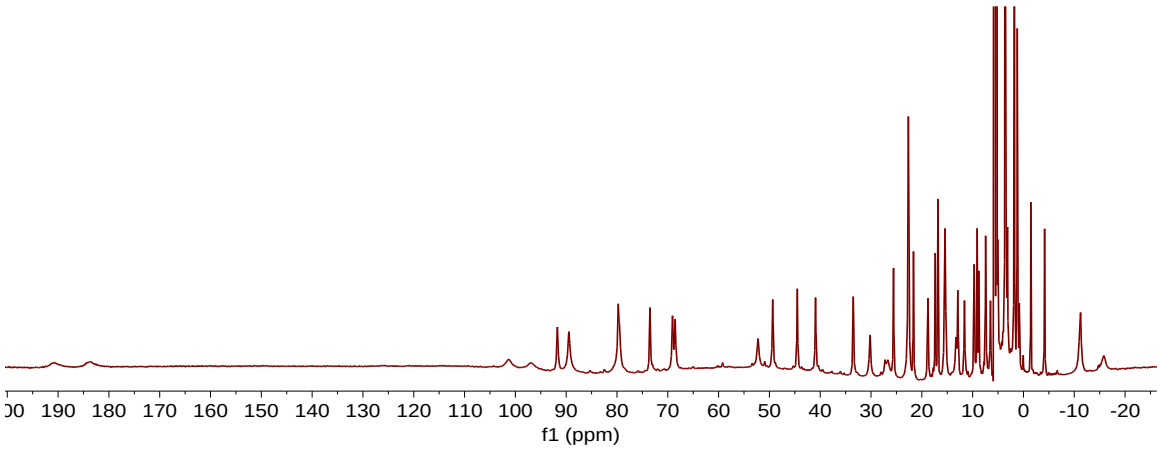

Figure 57. ^{1}H NMR spectrum of **A.9** in CD_2Cl_2.

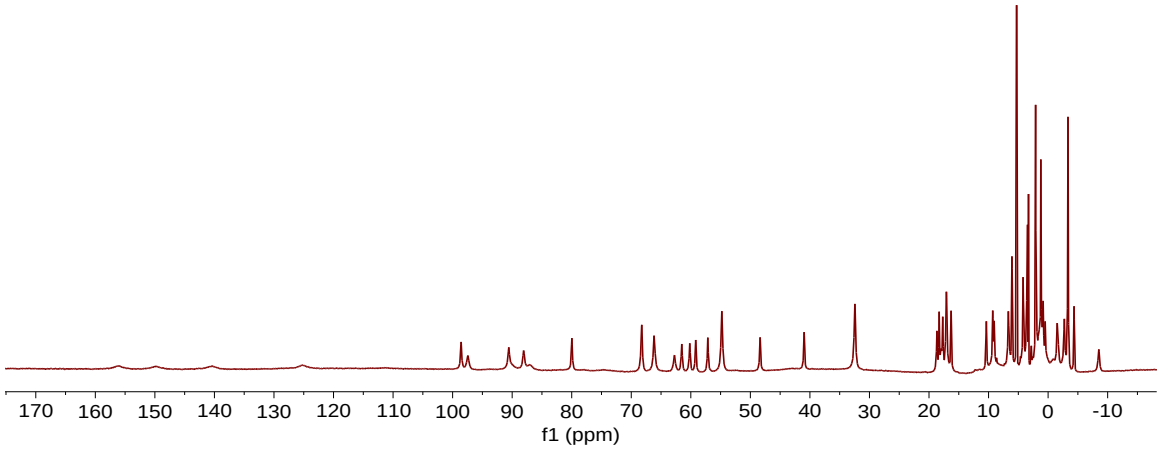

Figure 58. ^{1}H NMR spectrum of **A.10** in CD_2Cl_2.

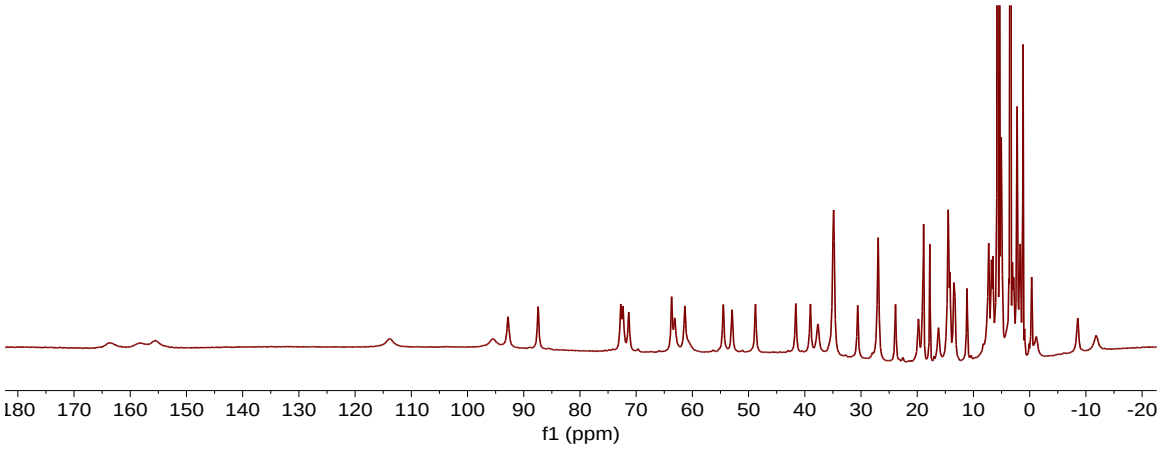

Figure 59. ^{1}H NMR spectrum of **A.11** in CD_2Cl_2.

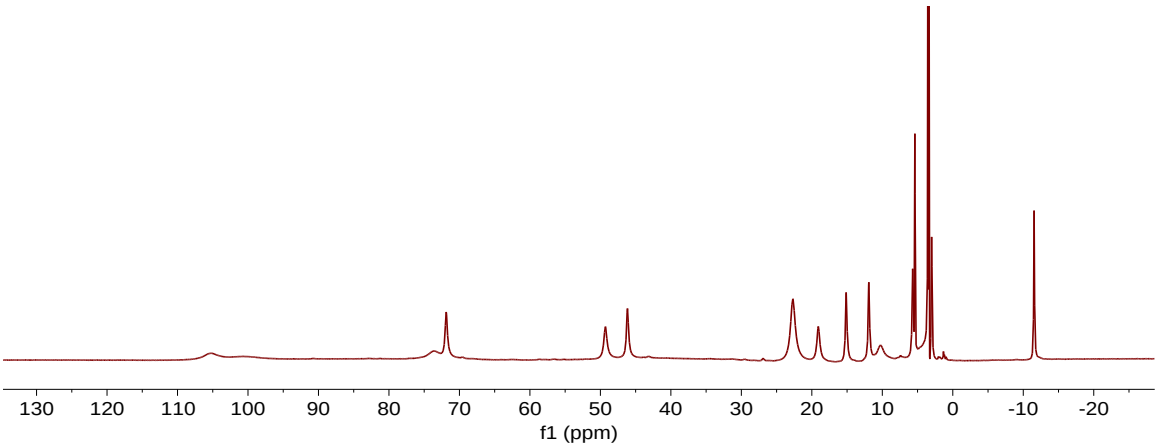

Figure 60. ^{1}H NMR spectrum of **A.13** in CD_2Cl_2.

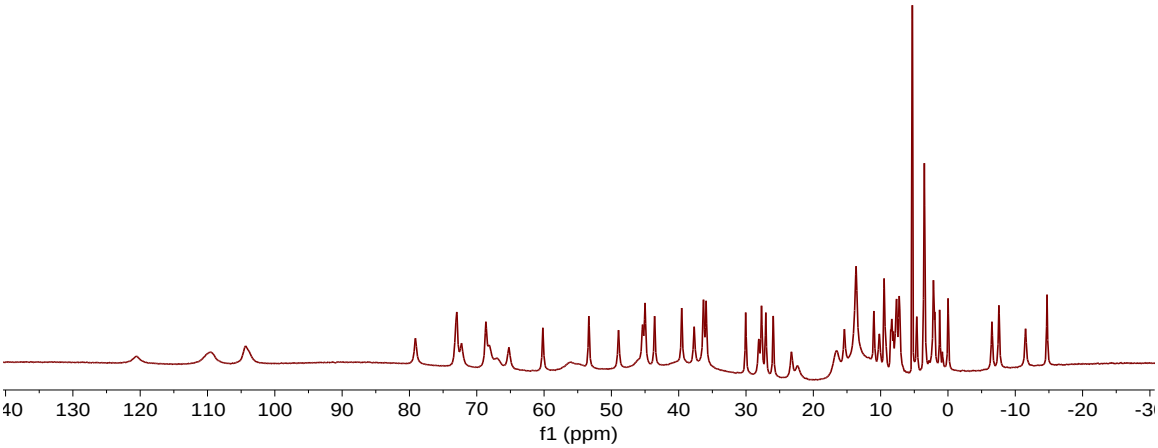

Figure 61. ^{1}H NMR spectrum of **A.15** in CD_2Cl_2.

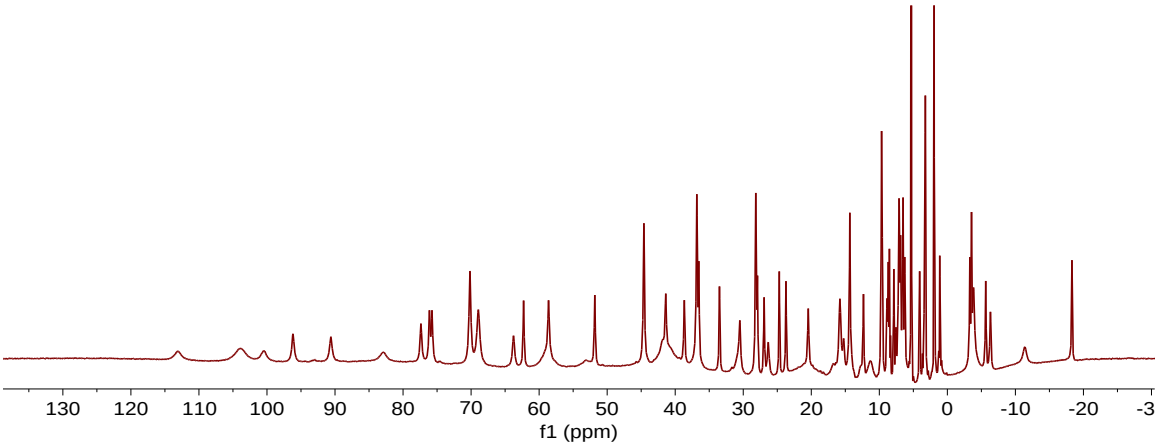

Figure 62. ^{1}H NMR spectrum of **A.16** in CD_2Cl_2.

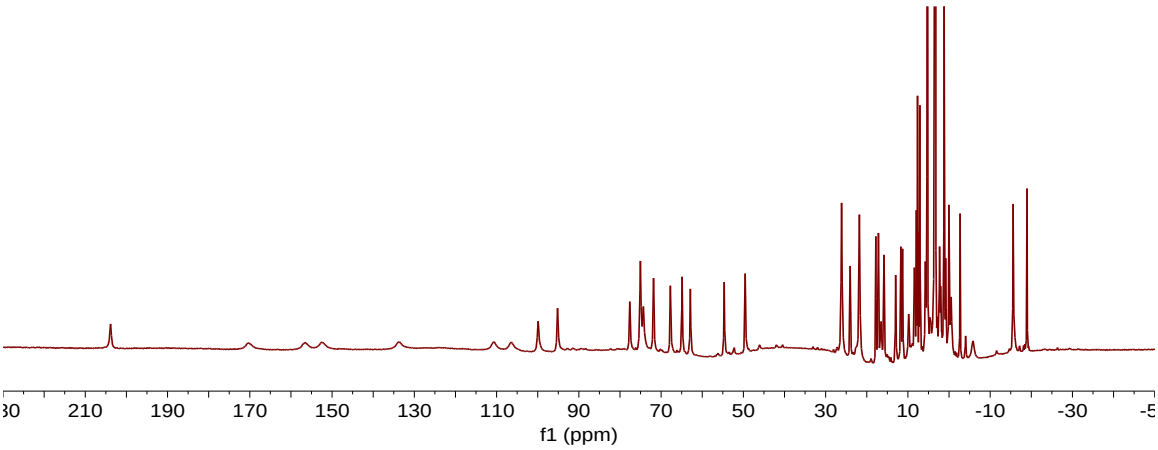

Figure 63. ^{1}H NMR spectrum of **A.17** in CD_2Cl_2.

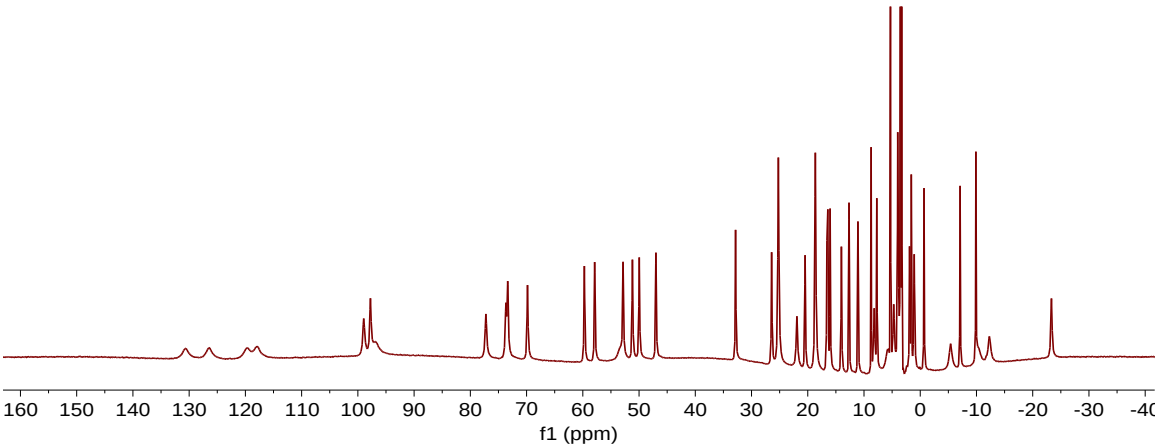

Figure 64. ^{1}H NMR spectrum of **A.18** in CD_2Cl_2.

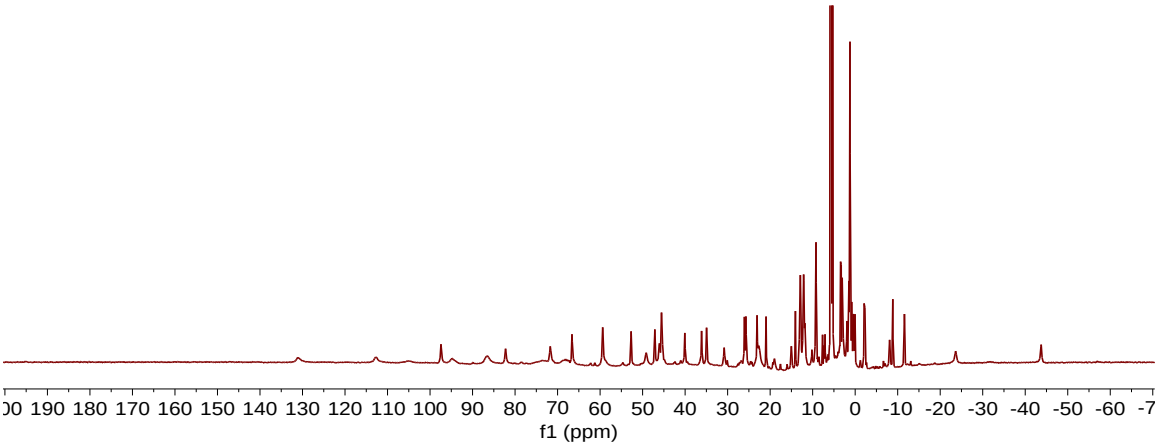

Figure 65. ^{1}H NMR spectrum of **A.19** in CD_2Cl_2.

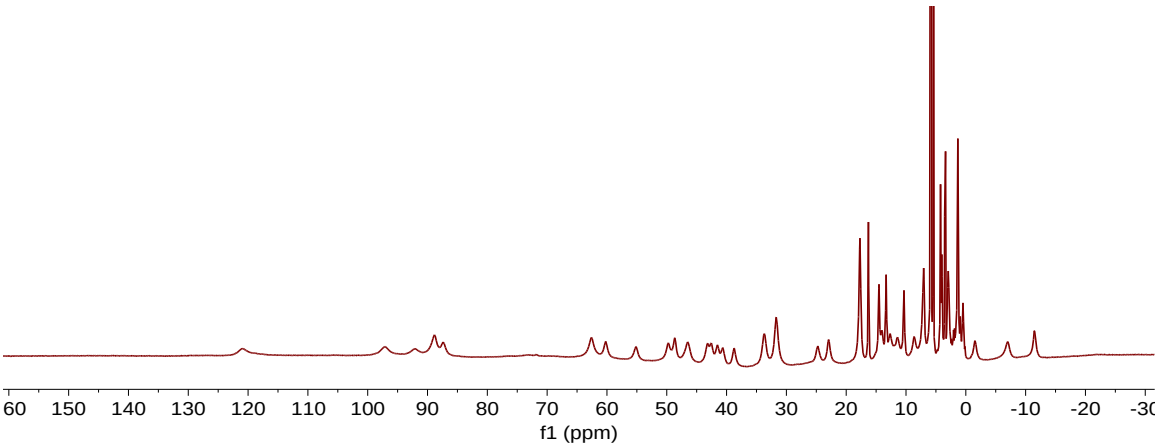

Figure 66. ^{1}H NMR spectrum of **A.20** in CD_2Cl_2.

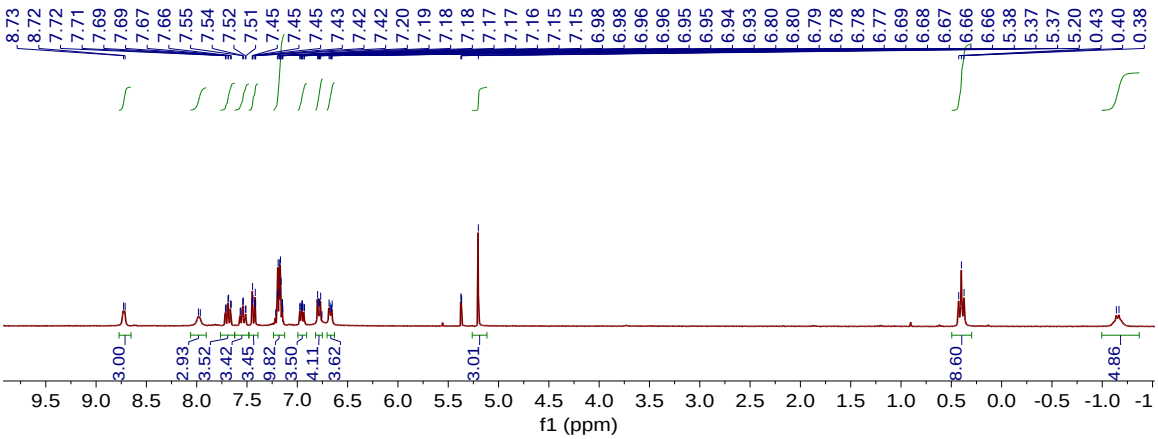

Figure 67. ^{1}H NMR spectrum of **A.24** in CD_2Cl_2.

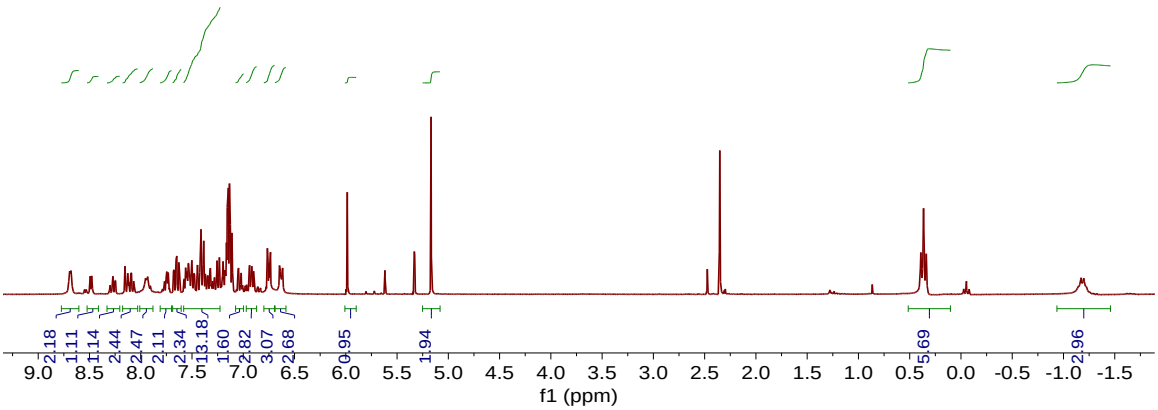

Figure 68. ^{1}H NMR spectrum of **A.25** in CD_2Cl_2.

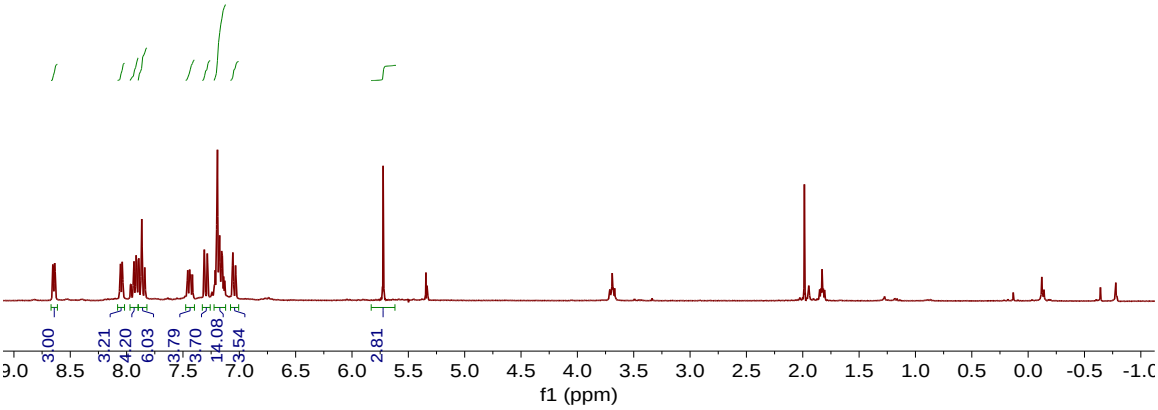

Figure 69. ^{1}H NMR spectrum of **A.23-Zn** in CD_2Cl_2.

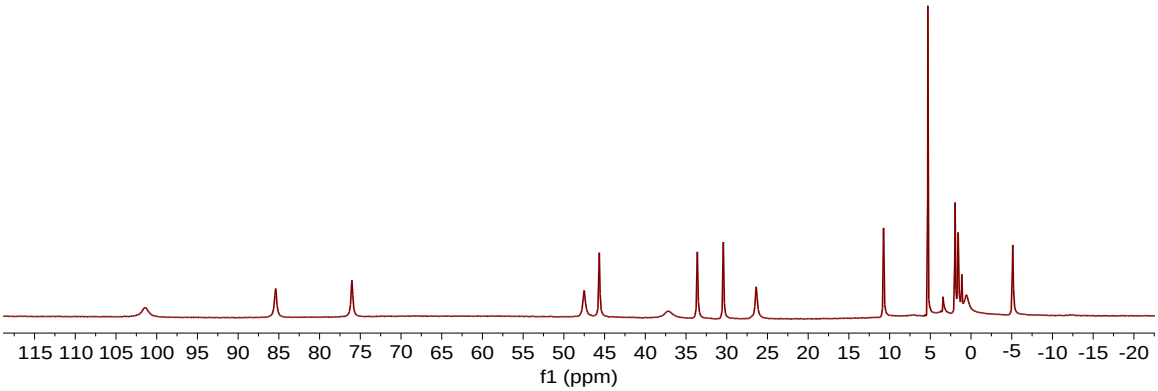

Figure 70. ^{1}H NMR spectrum of **A.29** in CD_2Cl_2.

"Lo duca e io per quel cammino ascoso
intrammo a ritornar nel chiaro mondo;
e sanza cura aver d'alcun riposo,

salimmo su, el primo e io secondo
tanto ch'i' vidi de le cose belle
che porta 'l ciel, per un pertugio tondo.

E quindi uscimmo a riveder le stelle."

Dante Alighieri
Comedia, Inferno, Canto XXXIV, 133-139